NASA Conference Publication 3177
Part 2

Fifth NASA/DoD Controls-Structures Interaction Technology Conference

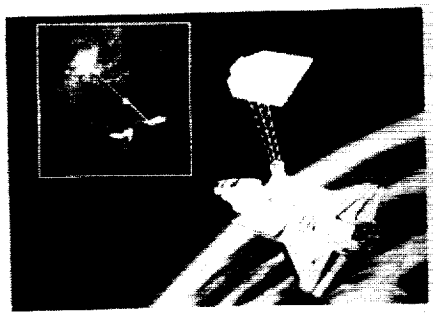

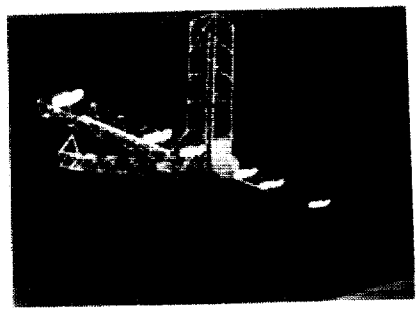

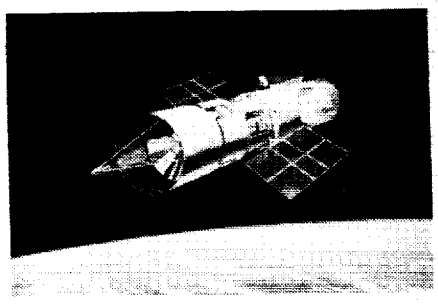

Proceedings of a conference held in
Lake Tahoe, Nevada
March 3–5, 1992

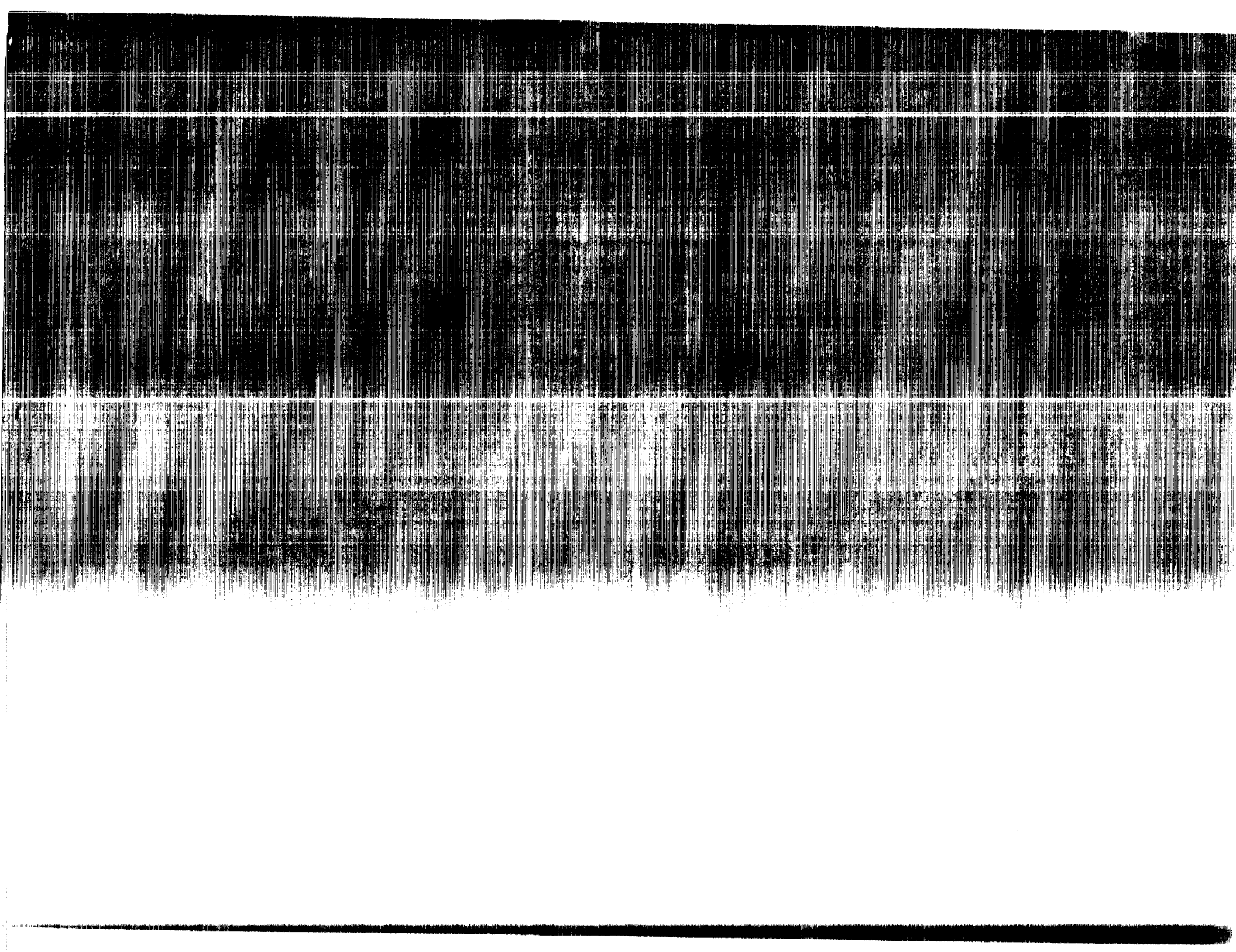

NASA Conference Publication 3177
Part 2

Fifth NASA/DoD Controls-Structures Interaction Technology Conference

Compiled by
Jerry R. Newsom
NASA Langley Research Center
Hampton, Virginia

Proceedings of a conference sponsored by the National Aeronautics and Space Administration, Washington, D.C., and the Department of Defense, Washington, D.C., and held in Lake Tahoe, Nevada March 3–5, 1992

NASA
National Aeronautics and Space Administration
Office of Management
Scientific and Technical Information Program
1993

PREFACE

The National Aeronautics and Space Administration (NASA) and the Department of Defense (DoD) are actively involved in the development of a validated technology data base in the area of controls-structures interaction (CSI) for flexible spacecraft. The development of this technology is essential to the efficient and confident development of future spacecraft to meet stringent goals in performance and cost. Both NASA and DoD have programs in CSI, structural dynamics, and controls. The activities of these programs provide a systematic approach to address technology voids through development and validation of analytical tools, extensive ground testing of representative structures, and future in-space experiments for verification of analysis and ground test methods.

In order to promote timely dissemination of technical information acquired in these programs, the NASA Langley Research Center and the Wright Laboratory alternately sponsor a conference to report to industry, academia, and government agencies on the current status of controls-structures interaction technology. This publication is a compilation of the papers presented at the fifth NASA/DoD CSI Technology Conference.

Jerry R. Newsom
Technical Program Chairman

CONTENTS

*Part 1 is presented under separate cover.

POSTER SESSION

SESSION III

Chairman: Robert A. Laskin
Co-Chairman: Richard Martin

Part 2

SESSION IV

Chairman: Kevin Slimak
Co-Chairman: William L. Grantham

SESSION V

Chairman: Brantley R. Hanks
Co-Chairman: Capt. Chuck Sherwin

ATTENDEES

Nandu S. Abhyankar
Bus. Phone: 805-275-5526
Dynacs Engineering Company
C/O OLAC PL/STS
Edwards AFB, CA 93523-5000

Scott Adams
Bus. Phone: 215-531-5199
General Electric
751 Vandenburg Road
King of Prussia, PA 19406

Gregory S. Agnes
Bus. Phone: 513-255-5236 X408
Wright Laboratory
WL/FIBGC
WPAFB, OH 45433

Dr. James J. Allen
Bus. Phone: 505-844-6764
Sandia National Laboratories
Structural Dynamics Division, 1434
Albuquerque, NM 87185

Dr. Willard W. Anderson
Bus. Phone: 804-864-1718
NASA Langley Research Center
Mail Stop 479
Hampton, VA 23665-5225

Peter M. Bainum
Bus. Phone: 202-806-6612
Howard University
Dept. of Mechanical Engineering
2300 6th Street, NW
Washington, DC 20059

Prof. A. V. Balakrishnan
Bus. Phone: 310-825-2180
University of California at LA
Electrical Engineering Department
Engr. IV Bldg., room 56-125B
UCLA (Mail Code #159410)
Los Angeles, CA 90024

Dr. Michael F. Barrett
Bus. Phone: 612-782-7286
Honeywell SRC
3660 Technology Drive
Minneapolis, MN 55418

Bob Bauer
Bus. Phone: 602-561-3257
Honeywell
P. O. Box 52199
Phoenix, AZ 85072-2199

Victor M. Beazel
Bus. Phone: 805-275-5798
USAF
OLAC PL/STS
Edwards AFB, CA 93523-5000

Dr. Georges A. Becus
Bus. Phone: 513-556-3222
University of Cincinnati
AsE/EM Department
Mail Location #70
Cincinnati, OH 45221-0070

Dr. W. Keith Belvin
Bus. Phone: 804-864-4319
NASA Langley Research Center
Mail Stop 230
Hampton, VA 23665-5225

Dr. Peter L. Bender
Bus. Phone: 303-492-6793
University of Colorado
Joint Institute for Laboratory Astro.
Campus Box 440
Boulder, CO 80309

Dr. Andrew S. Bicos
Bus. Phone: 714-896-1534
McDonnell Douglas Space Systems Co.
5301 Bolsa Avenue
M/S A3-Y857-13-3
Huntington Beach, CA 92647

Ross M. Blankinship
Bus. Phone: 505-262-2626
Lockheed Missiles and Space Company
1601 Randolph Road, SE, Suite 210 S
Albuquerque, NM 87106

Dr. Bob J. Boan
Bus. Phone: 407-729-7133
Harris Corporation
P. O. Box 94000
Melbourne, FL 32902

Ed B. Bokhour
Bus. Phone: 617-868-8086
Payload Systems Inc.
270 Third Street
Cambridge, MA 02142

Dr. John Breakwell
Bus. Phone: 408-743-7806
Lockheed Missiles & Space Company
P. O. Box 3504
Sunnyvale, CA 94088-3504

Dr. Hugh C. Briggs
Bus. Phone: 818-354-8192
Jet Propulsion Laboratory
Mail Stop T1710
4800 Oak Grove Drive
Pasadena, CA 91109

Patsy Brito
Bus. Phone:
USAF
Kirtland AFB, NM 87117

Ms. Angie Bukley
Bus. Phone: 205-544-0054
NASA Marshall Space Flight Center
Mail Stop ED12
Huntsville, AL 35812

Thomas F. Burns
Bus. Phone:
U. S. Government
13126 Thornapple Place
Herndon, VA 22071

Dr. Alain C. Carrier
Bus. Phone: 415-424-2735
Lockheed Missiles & Space Co., Inc.
3251 Hanover Street
Building 281, Org. 92-30
Palo Alto, CA 94304-1191

Cheng-Chih Chu
Bus. Phone: 818-354-7457
Jet Propulsion Laboratory
Mail Stop 198-326
4800 Oak Grove Drive
Pasadena, CA 91109

Lt. Derek F. Cossey
Bus. Phone: 805-275-5350
Phillips Laboratory - USAF - AFSC
OLAC PL/STSS
Edwards AFB, CA 93523-5000

Prof. Roy R. Craig, Jr.
Bus. Phone: 512-471-4172
University of Texas at Austin
ASE-EM Department
Austin, TX 78712-1085

Dr. Edward F. Crawley
Bus. Phone: 617-253-7510
Massachusetts Inst. of Technology
Building 37-351
77 Massachusetts Avenue
Cambridge, MA 02139

Dr. J. F. Creedon
Bus. Phone: 804-864-6033
NASA Langley Research Center
Mail Stop 113
Hampton, VA 23665-5225

Darby A. Davis
Bus. Phone: 408-743-1206
Lockheed Missiles and Space Company
1111 Lockheed Way
O/77-50 B/551
Sunnyvale, CA 94089-3504

Hugh W. Davis
Bus. Phone: 303-939-4022
Ball Electro-Optics/Cryogenics Div.
P. O. Box 1062
Boulder, CO 80306

L. Porter Davis
Bus. Phone: 602-561-3483
Honeywell, Inc. Satellite Systems Div
19019 N. 59th Avenue
Glendale, AZ 85308-9650

William M. Day
Bus. Phone: 205-922-7574
McDonnell Douglas Space Systems Co.
Mail Stop 15A1
689 Discovery Drive
Huntsville, AL 35806

Geoffrey S. Dean
Bus. Phone: 504-257-2454
Martin Marietta Manned Space System
P. O. Box 29304
Department 3041
New Orleans, LA 70189

Martha E. Demeo
Bus. Phone: 804-864-8045
Vigyan, Inc.
NASA Langley Research Center
Mail Stop 298
Hampton, VA 23665-5225

Keith K. Denoyer
Bus. Phone: 805-275-6187
USAF
Phillips Laboratory
OLAC PL/VTSS
Edwards AFB, CA 93523-5000

Robert J. Denton, Jr.
Bus. Phone: 315-330-4441
USAF/Rome Laboratory
OCDS
Griffiss AFB, NY 13441-5700

John W. Dettmer
Bus. Phone:
Lockheed Missiles and Space Company
1601 Randolph Road, SE
Suite 210 South
Albuquerque, NM 87119

Ted A. Doederlein
Bus. Phone: 805-275-5483
Air Force
OLAC PL/STSS
Edwards AFB, CA 93523

Daniel B. Eldred
Bus. Phone: 818-354-6519
Jet Propulsion Laboratory
Mail Stop 198-326
4800 Oak Grove Drive
Pasadena, CA 91109

Dr. Kenny B. Elliott
Bus. Phone: 804-864-4359
NASA Langley Research Center
Mail Stop 230
Hampton, VA 23665-5225

Andy M. Engelhardt
Bus. Phone: 602-561-3482
Honeywell, Inc.
P. O. Box 52199
Phoenix, AZ 85072-2199

Dr. James L. Fanson
Bus. Phone: 818-354-7014
Jet Propulsion Laboratory
Mail Stop 157-316
4800 Oak Grove Drive
Pasadena, CA 91109

Clarence J. Fennell
Bus. Phone: 505-846-4703
Phillips Laboratory
PL/VTS
Kirtland AFB, NM 87117-6008

Dr. Shalom "Mike" Fisher
Bus. Phone: 202-767-3914
Naval Research Laboratory
Code 8240.1
Washington, DC 20375-5000

Anthony Fontana
Bus. Phone: 804-864-6491
NASA Langley Research Center
Mail Stop 298
Hampton, VA 23665-5225

Eugene R. Fosness
Bus. Phone: 505-846-1338
Phillips Laboratory
PL/VTSA
Kirtland AFB, NM 87117-6008

Rodney Galloway
Bus. Phone: 505-846-1338
Phillips Laboratory
PL/VTSA
Kirtland AFB, NM 87117-6008

Dr. Joseph F. Garibotti
Bus. Phone: 714-545-8825
Ketema
Advanced Materials Group
3611 South Harbor Boulevard
Suite 225
Santa Ana, CA 92704-6928

Michael Garnek
Bus. Phone: 215-354-3827
General Electric Company
Astro Space Division
P. O. Box 8555, Bldg 100, M4018
Philadelphia, PA 19101

Margaret N. Gieseking
Bus. Phone: 804-864-6493
NASA Langley Research Center
Mail Stop 298
Hampton, VA 23665-5225

Ray E. Gogan
Bus. Phone: 407-727-6293
Harris Corporation
P. O. Box 94000
Melbourne, FL 32902

Stephen C. Gould
Bus. Phone: 505-846-1338
Phillips Laboratory
PL/VTSA
Kirtland AFB, NM 87117-6008

Joel Greenstein
Bus. Phone: 407-352-3700
Coleman Research Corporation
5950 Lakehurst Drive
Orlando, FL 32819

Steven F. Griffin
Bus. Phone: 805-275-5304
USAF
OLAC PL/STSS
Edwards AFB, CA 93523

Angel Garnica
Bus. Phone: 818-354-1903
Jet Propulsion Laboratory
4800 Oak Grove Drive
Mail Stop 158/224
Pasadena, CA 91109

Michael G. Gilbert
Bus. Phone: 804-864-2839
NASA Langley Research Center
Mail Stop 297
Hampton, VA 23665-5225

A. Ernesto (Ernie) Golan
Bus. Phone: 714-531-7340
Consultant
11069 Sudith Avenue
Fountain Valley, CA 92708

William L. Grantham
Bus. Phone: 804-864-6494
NASA Langley Research Center
Mail Stop 298
Hampton, VA 23665-5225

Joseph W. Gregory
Bus. Phone: 804-864-4358
Lockheed Engineering and Sciences
NASA Langley Research Center
Mail Stop 230
Hampton, VA 23665-5225

Marc Gronet
Bus. Phone: 408-756-5673
Lockheed Missiles and Space Company
ORG/6N-24, Bldg 579
1111 Lockheed Way
Sunnyvale, CA 94089-3504

Sandeep Gupta
Bus. Phone: 804-864-4054
Vigyan, Inc.
NASA Langley Research Center
Mail Stop 230
Hampton, VA 23665-5225

Dr. Fred Y. Hadaegh
Bus. Phone: 818-354-8777
Jet Propulsion Laboratory
Mail Code 198-318
4800 Oak Grove Drive
Pasadena, CA 91109

Nesbitt W. Hagood
Bus. Phone: 617-253-2738
Massachusetts Inst. of Technology
77 Massachusetts Avenue
Room 33-313
Cambridge, MA 02139

Mike Hagopian
Bus. Phone: 301-286-7854
NASA Goddard Space Flight Center
Mail Code 716.5
Greenbelt, MD 20771

Brian J. Hamilton
Bus. Phone: 602-561-3554
Honeywell
P. O. Box 52199, Mail Stop 2P9
Phoenix, AZ 85072-2199

Brantley Hanks
Bus. Phone: 804-864-4322
NASA Langley Research Center
Mail Stop 297
Hampton, VA 23665-5225

Robert J. Hayduk
Bus. Phone: 202-453-2962
NASA Headquarters
Code RM
Washington, DC 20546

John M. Hedgepeth
Bus. Phone: 805-569-1344
Astro Aerospace Corporation
202 E. Pedregosa Street
Santa Barbara, CA 93101

John Higgins
Bus. Phone: 505-846-1338
Phillips Laboratory
PL/VTSA
Kirtland AFB, NM 87117-6008

Lucas G. Horta
Bus. Phone: 804-864-4352
NASA Langley Research Center
Mail Stop 230
Hampton, VA 23665-5225

J. Warren Hoskins
Bus. Phone: 408-742-6560
Lockheed Missiles and Space Company
P. O. Box 3504
B/551, D/77-50
Sunnyvale, CA 94088-3504

Stuart Hsu
Bus. Phone: 602-561-3485
Honeywell, Inc.
P. O. Box 52199
Phoenix, AZ 85072

Tuyen Hua
Bus. Phone: 713-483-8296
NASA Johnson Space Center
Mail Code EG2
Houston, TX 77058

Daniel J. Inman
Bus. Phone: 716-636-2733
State Univ. of New York at Buffalo
Department of Mech. and Aero.
Buffalo, NY 14260

A. Dean Jacot
Bus. Phone: 206-773-8629
Boeing Aerospace Company
P.O. Box 3999, MS 82-23
Seattle, WA 98124

Robert N. Jacques
Bus. Phone: 617-253-3267
Massachusetts Inst. of Technology
77 Massachusetts Avenue
Room 37-391
Cambridge, MA 02139

Bruce G. Johnson
Bus. Phone: 617-661-0540 x207
SatCon Technology Corporation
12 Emily Street
Cambridge, MA 02139-4507

Conor D. Johnson
Bus. Phone: 415-494-7351
CSA Engineering, Inc.
2850 W. Bayshore Road
Palo Alto, CA 94306-3843

Victoria L. Jones
Bus. Phone: 205-882-2650
Logicon Control Dynamics
600 Blvd. S., Suite 304
Huntsville, AL 35802

Dr. Jer-Nan Juang
Bus. Phone: 804-864-4351
NASA Langley Research Center
Mail Stop 297
Hampton, VA 23665-5225

Prof. John L. Junkins
Bus. Phone: 409-845-3912
Texas A&M University
Aerospace Engineering Department
Room 701 Bright Building
College Station, TX 77843-3141

Claude R. Keckler
Bus. Phone: 804-864-1716
NASA Langley Research Center
Mail Stop 479
Hampton, VA 23665-5225

Sean P. Kenny
Bus. Phone: 804-864-6612
NASA Langley Research Center
Mail Stop 230
Hampton, VA 23665-5225

Dr. Farshad Khorrami
Bus. Phone: 718-260-3227
Polytechnic University
Dept. of Electrical Engineering
Six Metrotech Center
Brooklyn, NY 11201

Dr. Narendra S. Khot
Bus. Phone: 513-255-6992
WL/FIBRA
WPAFB, OH 45433-6553

Jim A. King
Bus. Phone: 407-727-2140
Harris Corporation
Government Aerospace Systems Div.
Mail Stop 22/4847
P. O. Box 94000
Melbourne, FL 32902

Andy Kissil
Bus. Phone: 818-354-8479
Jet Propulsion Laboratory
Building 157-410
4800 Oak Grove Drive
Pasadena, CA 91109

Robert L. Kittyle
Bus. Phone: 719-472-4088
USAF
HQ USAFA/DFAS
USAF Academy, CO 80840

Roy E. Klusendorf
Bus. Phone: 805-684-6641
Astro Aerospace Corporation
6384 Via Real
Carpinteria, CA 93013-2920

Timothy Kreitinger
Bus. Phone: 505-846-1338
Phillips Laboratory
PL/VTSA
Kirtland AFB, NM 87117-6008

Thomas J. H. Lange
Bus. Phone: 49-8153-28-1177
DLR/GSOC
Munchnerstr. 20
D-8031 Oberpfeffenhofen
GERMANY

Charles R. Larson
Bus. Phone: 310-922-2031
Rockwell International
Mail Stop AD88
12214 Lakewood Boulevard
Downey, CA 90241

Robert W. Lashlee, Jr.
Bus. Phone: 314-341-6172
USAF
UMR Rolla MO
1105 Joyce Avenue
Rolla, MO 65401

Dr. Robert A. Laskin
Bus. Phone: 818-354-5086
Jet Propulsion Laboratory
Mail Stop 198-326
4800 Oak Grove Drive
Pasadena, CA 91109

James P. Lauffer
Bus. Phone: 505-844-5176
Sandia National Laboratories
Org. 2743
P. O. Box 5800
Albuquerque, NM 87185

Marie B. Levine-West
Bus. Phone: 818-354-6273
Jet Propulsion Laboratory
4800 Oak Grove Drive
Mail Stop 157-316
Pasadena, CA 91109

Dr. Kyong B. Lim
Bus. Phone: 804-864-4342
NASA Langley Research Center
Mail Stop 161
Hampton, VA 23665-5225

Chiang Lin
Bus. Phone: 713-333-7061
Lockheed Engineering & Science
2400 NASA Road 1
Houston, TX 77058-3799

Yeongching Lin
Bus. Phone: 333-8502
Dynacs Engineering Co., Inc.
1110 NASA Road One, Suite 650
Houston, TX 77058

Doug Looze
Bus. Phone: 413-545-0973
University of Massachusetts
Dpt of Electrical and Computer Eng
Amherst, MA 01003

Boris J. Lurie
Bus. Phone: 818-354-3690
Jet Propulsion Laboratory
4800 Oak Grove Drive
Mail Stop 198/326
Pasadena, CA 91109

Lt. John R. Mackaman
Bus. Phone: 513-255-5236 X406
Wright Laboratory, USAF
WL/FIBG
WPAFB, OH 45433-6553

H. Bruce Mackay
Bus. Phone: 619-458-4702
SAIC
4161 Campus Point Court
San Diego, CA 92121

Dr. Peiman G. Maghami
Bus. Phone: 804-864-4039
NASA Langley Research Center
Mail Stop 230
Hampton, VA 23665-5225

Richard M. Martin
Bus. Phone: 805-275-5354
USAF
OLAC PL/STS
Edwards AFB, CA 93523-5000

David R. Martinez
Bus. Phone: 505-844-1457
Sandia National Laboratories
Org. 1434
P. O. Box 5800
Albuquerque, NM 87185

Mark D. McLaren
Bus. Phone: 415-852-4767
Space Systems/LORAL
Mail Stop G76
3825 Fabian Way
Palo Alto, CA 94303

Dr. David W. Miller
Bus. Phone: 617-253-3288
Massachusetts Inst. of Technology
Space Engineering Research Center
Room 37-371
70 Vassar Street
Cambridge, MA 02139

Mark H. Milman
Bus. Phone: 818-354-3627
Jet Propulsion Laboratory
Mail Stop 198-326
4800 Oak Grove Drive
Pasadena, CA 91109

Jerrel R. Mitchell
Bus. Phone: 614-593-1566
Ohio University
Stocker Center 327
Athens, OH 45701

Michael G. Moeller
Bus. Phone: 407-729-7141
Harris Corporation
Gov. Aerospace & Systems Division
P. O. Box 94000, MS 19-4737
Melbourne, FL 32902

James B. Mohl
Bus. Phone: 303-939-5064
Ball Space Systems Division
Mail Stop CO-10B
P. O. Box 1062
Boulder, CO 80306-1062

Dr. Raymond C. Montgomery
Bus. Phone: 804-864-6615
NASA Langley Research Center
Mail Stop 161
Hampton, VA 23665-5225

R. Jorge Montoya
Bus. Phone: 919-541-6807
Research Triangle Institute
P. O. Box 12194
Research Triangle Park, NC 27709

Dr. Ibrahaim A. Murra
Bus. Phone: 416-790-2800X4787
SPAR Aerospace Limited
9445 Airport Road
Brampton, Ontario
CANADA L6S4J3

James J. Murray
Bus. Phone: 703-834-3796
General Electric
924 Riva Ridge Drive
Great Falls, VA 22066-1619

Gregory W. Neat
Bus. Phone: 818-354-0584
Jet Propulsion Laboratory
Mail Stop 198-326
4800 Oak Grove Drive
Pasadena, CA 91109

Jerry R. Newsom
Bus. Phone: 804-864-6488
NASA Langley Research Center
Mail Stop 298
Hampton, VA 23665-5225

R. Rory Ninneman
Bus. Phone: 505-846-4699
Phillips Laboratory
PL/VTSA
Kirtland, NM 87117-6008

John F. O'Brian
Bus. Phone: 818-354-1250
Jet Propulsion Laboratory
4800 Oak Grove Drive
Pasadena, CA 91109

Robert P. O'Donnell
Bus. Phone: 703-385-0723
MRT, Inc.
10455 White Granite Drive
Oakton, VA 22124

Dr. Eric K. Parsons
Bus. Phone: 415-424-2654
Lockheed Missiles & Space Co., Inc.
Research and Development
Department 92-30, Building 281
3251 Hanover Street
Palo Alto, CA 94304-1191

Janet Perrault
Bus. Phone: 805-275-5219
USAF
OLAC PL/STS
Edwards AFB, CA 93523-5000

Doug J. Phillips
Bus. Phone: 407-727-6239
Harris Corporation
P. O. Box 94000
Melbourne, FL 32901

Tom Pollock
Bus. Phone: 409-845-1686
Texas A&M University
Aerospace Engineering
College Station, TX 77843-3141

Karim S. Qassim
Bus. Phone: 505-846-4704
Phillips Laboratory
PL/VTSA
Kirtland AFB, NM 87117-6008

Hayrani Oz
Bus. Phone: 614-292-3843
Ohio State University
Bolz Hall
2036 Neil Avenue Mall, Rm 328
Columbus, OH 43210

Jerome Pearson
Bus. Phone: 513-255-6622
Wright Laboratory
WL/FIBG
WPAFB, OH 45433-6553

Lee D. Peterson
Bus. Phone: 303-492-1743
University of Colorado
Campus Box 429
Boulder, CO 80309-0429

Brett J. Pokines
Bus. Phone: 716-636-2199
State Univ. of New York at Buffalo
Mechanical & Aerospace Engineering
1012 Furnus Hall
Amherst, NY 14260

Dr. Douglas B. Price
Bus. Phone: 804-864-6605
NASA Langley Research Center
Mail Stop 161
Hampton, VA 23665-5225

Ralph W. Quan
Bus. Phone: 719-472-3122
United States Air Force Academy
Frank J. Seiler Lab, USAFA
Colorado Springs, CO 80840

Zahidul H. Rahman
Bus. Phone: 818-354-3659
Jet Propulsion Laboratory
4800 Oak Grove Drive
Mail Stop 157-316
Pasadena, CA 91109

Prof. Vittal S. Rao
Bus. Phone: 314-341-6371
University of Missouri-Rolla
Intelligent Systems Center
Rolla, MO 65401

Dr. Kenneth E. Richards, Jr.
Bus. Phone: 303-971-9376
Martin Marietta Astronautics
P. O. Box (MS H4330)
Denver, CO 80201

John M. Richardson
Bus. Phone: 505-846-4693
Phillips Laboratory
PL/VTSA
Kirtland AFB, NM 87117-6008

Linda B. Rowell
Bus. Phone: 804-864-1718
NASA Langley Research Center
Mail Stop 479
Hampton, VA 23665-5225

Chris A. Sandridge
Bus. Phone: 804-864-2816
Lockheed Engineering & Sciences Co.
NASA Langley Research Center
Mail Stop 230
Hampton, VA 23665-5225

Celeste M. Satter
Bus. Phone: 818-354-9246
Jet Propulsion Laboratory
Mail Stop 157-410
4800 Oak Grove Drive
Pasadena, CA 91109

Ian R. Scarle
Bus. Phone: 206-773-2046
Boeing Defense & Space Group
P. O. Box 3999
Mail Stop 82-97
Seattle, WA 98124

Dr. Eric Schmitz
Bus. Phone: 303-971-2732
Martin Marietta Civil Space & Comm.
MS 4372
P. O. Box 179
Denver, CO 80201

Sherman Seltzer
Bus. Phone: 205-379-3428
Consultant
2786 Hurricane Road
New Market, AL 35761

Kendall W. Sherman
Bus. Phone: 804-864-6488
NASA Langley Research Center
Mail Stop 298
Hampton, VA 23665-5225

Samuel W. Sirlin
Bus. Phone: 818-354-8484
Jet Propulsion Laboratory
Mail Stop 198-326
4800 Oak Grove Drive
Pasadena, CA 91109

Joseph C. Slater
Bus. Phone: 716-636-3977
State Univ. of New York at Buffalo
Mechanical & Aerospace Engineering
Buffalo, NY 14260

Andrew J. Smith
Bus. Phone: 505-846-4706
Phillips Laboratory
PL/VTSA
Kirtland AFB, NM 87117-6008

Dr. Suzanne W. Smith
Bus. Phone: 606-257-4584
University of Kentucky
Dept. of Engineering Mechanics
467 Anderson Hall
Lexington, KY 40506-0046

Monty J. Smith
Bus. Phone: 805-275-5348
DOD Phillips Laboratory
Lancaster, CA 93536

Rudeen Smith-Taylor
Bus. Phone: 804-864-6490
NASA Langley Research Center
Mail Stop 298
Hampton, VA 23665-5225

Rose Marie Snow
Bus. Phone: 513-255-5200 X251
Wright Laboratory
WL/FIBG
WPAFB, OH 45433-6553

John T. Spanos
Bus. Phone: 818-354-6572
Jet Propulsion Laboratory
Mail Stop 198-326
4800 Oak Grove Drive
Pasadena, CA 91109

Dean W. Sparks, Jr.
Bus. Phone: 804-864-4349
NASA Langley Research Center
Mail Stop 230
Hampton, VA 23665-5225

Dr. Victor A. Spector
Bus. Phone: 310-814-6304
TRW Inc.
R9/2181
One Space Park
Redondo Beach, CA 90278

Captain Daniel J. Stech
Bus. Phone: 719-472-3122
FJSRL/NA
USAF Academy, CO 80840-6528

Tzu-Jeng Su
Bus. Phone: 804-864-4395
NASA Langley Research Center - NRC
National Research Council
Mail Stop 230
Hampton, VA 23665-5225

John Sudey, Jr.
Bus. Phone: 301-286-8908
NASA Goddard Space Flight Center
Mail Code 716.0
Greenbelt, MD 20771

Jeff L. Sulla
Bus. Phone: 804-864-4348
Lockheed Engineering & Sciences Co.
NASA Langley Research Center
Mail Stop 230
Hampton, VA 23665-5225

George A. Tan
Bus. Phone: 804-864-6621
Lockheed Engineering & Sciences Co.
NASA Langley Research Center
Mail Stop 161
Hampton, VA 23665-5225

Lawrence W. Taylor, Jr.
Bus. Phone: 804-864-4040
NASA Langley Research Center
Mail Stop 489
Hampton, VA 23665-5225

Dr. A. Fernando Tolivar
Bus. Phone: 818-354-6215
Jet Propulsion Laboratory
4800 Oak Grove Drive
MS 198-330
Pasadena, CA 91109

Dr. Hubert Troidl
Bus. Phone: 089/6088-3905
IABG
Department TRV
Einsteinstrabe 20
D-8012 Ottobrunn
GERMANY

Dr. Henry B. Waites
Bus. Phone: 205-544-1441
NASA Marshall Space Flight Center
Mail Stop ED12
MSFC, AL 35812

Lee F. Sword
Bus. Phone: 818-354-1908
Jet Propulsion Laboratory
4800 Oak Grove Drive
Mail Stop 158-224
Pasadena, CA 91109

Ms. Sharon E. Tanner
Bus. Phone: 804-864-4353
NASA Langley Research Center
Mail Stop 230
Hampton, VA 23665-5225

Nimfa C. Teneza
Bus. Phone: 202-404-8338
Naval Research Laboratory
Code 8240
Washington, DC 20375-5000

Dr. John J. Tracy
Bus. Phone: 714-896-1534
McDonnell Douglas Space Systems Co.
5301 Bolsa Avenue
Mail Station A3-Y857-13/3
Huntington Beach, CA 92647

Ben K. Wada
Bus. Phone: 818-354-3600
Jet Propulsion Laboratory
Mail Stop 157-507
4800 Oak Grove Drive
Pasadena, CA 91109

J. M. (Mel) Waldman
Bus. Phone: 408-756-4498
Lockheed Missiles and Space Company
P. O. Box 3504
Building 579, Organization 6N-24
Sunnyvale, CA 94088-3504

David W. Walsh
Bus. Phone: 602-561-4116
Honeywell
P. O. Box 52199
Phoenix AZ 85072-2199

Dr. Shyh J. (Don) Wang
Bus. Phone: 818-354-7288
Jet Propulsion Laboratory
Mail Stop TR1711
4800 Oak Grove Drive
Pasadena, CA 91109

Major Steven G. Webb
Bus. Phone: 719-472-2196
USAF Academy
HQ USAFA/DFEM
USAF Academy, CO 80840-5000

Edward V. White
Bus. Phone: 314-232-1479
McDonnell Douglas Missile Systems
Mail Code 3064275
P. O. Box 516
Saint Louis, MO 63166

Chin (John) Won
Bus. Phone: 804-864-8225
Lockheed Engineering and Sciences
NASA Langley Research Center
Mail Stop 230
Hampton, VA 23665-5225

Shih-Chin Wu
Bus. Phone: 804-864-4355
Lockheed Engineering & Sciences Co.
NASA Langley Research Center
Mail Stop 230
Hampton, VA 23665-5225

James F. Walton
Bus. Phone: 518-785-2477
Mechanical Technology Incorporated
968 Albany Shaker Road
Latham, NY 12110

Donald C. Washburn
Bus. Phone: 505-846-1338
Phillips Laboratory
PL/VTSA
Kirtland AFB, NM 87117-6008

Mark S. Webster
Bus. Phone: 818-354-1212
Jet Propulsion Laboratory
4800 Oak Grove Drive
Mail Stop 157-316
Pasadena, CA 91109

Dr. Trevor Williams
Bus. Phone: 513-556-3221
University of Cincinnati
Dept. of Aero. Eng. & Eng. Mechanics
ML 70
Cincinnati, OH 45221

Stanley E. Woodard
Bus. Phone: 804-864-4053
NASA Langley Research Center
Mail Stop 230
Hampton, VA 23665-5225

Spencer T. Wu
Bus. Phone: 202-767-6962
AFOSR
Bolling AFB
Washington, DC 20332-6448

Y. C. Yiu
Bus. Phone: 408-742-4048
Lockheed Missiles & Space Co., Inc.
1111 Lockheed Way
B/551, O/7750
Sunnyvale, CA 94089-3504

Brad J. Yost
Bus. Phone: 805-275-5304
Wyle Laboratories
OLAC PL/VTSS E
Edwards AFB, CA 93523-5000

Joseph S.C. Yuan
Bus. Phone: 416-745-9682X6763
SPAR Aerospace Limited
1700 Ormont Drive
Weston, Ontario
CANADA M9L2W7

Dr. David C. Zimmerman
Bus. Phone: 904-392-6229
University of Florida
231 Aerospace Building
Gainesville, FL 32611

Total Number of Attendees: 184

PART 2

SESSION IV

Chairman: Kevin Slimak
Phillips Laboratory
Edwards AFB, California

Co-Chairman: William L. Grantham
NASA Langley Research Center
Hampton, Virginia

CSI Related Dynamics and Control Issues in Space Robotics

Authors: Eric Schmitz and Madison Ramey

Robotics and Advanced Controls Section
Martin Marietta Astronautics Group

Outline

- CSI issues in space robotics
- Control of elastic payloads:
  - 1-DOF example
  - 3-DOF Harmonic Drive arm with elastic beam
- Control of large space arms with elastic links:
  - Testbed description
  - Modelling
  - Experimental implementation of colocated PD and end-point tip position controllers
- Conclusions

CSI MODELLING AND CONTROL ISSUES	SMALL, DEXTEROUS MANIPULATORS		LARGE, CRANE-LIKE MANIPULATORS	
	dynamics	*controls*	*dynamics*	*controls*
Lumped compliance due to actuator geartrain	Dominant Effect (free-free resonance modes in the 10-30 Hz range, ζ=0.1 for FTS-like arms with Harmonic Drive gearings)	Active damping of geartrain mode is achieved with either analog/digital colocated rate feedback or analog output torque feedback.	Effect is as or more important than distributed flexibility (lowest locked joint frequency for RMS in the 0.1 to 2 Hz range, depending on load)	RMS control system is based on analog/digital colocated rate control (PI). Active CSI controller using links and wrist-mounted sensors have been demonstrated in the lab.
Distributed flexibility in the links	No significant effect except for lumped compliances arising from mechanical interfaces, actuator housing and end-effectors.	Control system should include active filters to gain stabilize flexible modes due to lumped compliances. Other approach is to use passive damping if it is feasible.	Significant effect, especially for the cases of very large payloads (RMS dominant elastic mode in the 0.03 to 0.4 Hz range, depending on load.	RMS control system based on colocated rate feedback damps out elastic modes but at the expense of rigid-body bandwidth. Laboratory systems are currently testing CSI-based controllers using links and wrist-mounted sensors. Future space arms will have control modes based on proximity/vision sensing systems.
Rigid & elastic payloads with lightly damped vibration modes	Important effect as dexterous robots will be used for spacecraft servicing (dominant payload frequencies can be inside or outside the robot control system nominal bandwidth) (typically, ω= 1 to 3 Hz)	No general control approach developed yet. Conventional robot controllers can be tuned to act as vibration absorber for elastic payload. Robot controller acts as a colocated controller for the elastic payload.	For each flown payload detailed pre-flight simulations are run for the RMS. Special studies need to be run to assess dynamic coupling when payload fundamental vibration mode (clamped interface) is below 0.5 Hz. Future RMS-like arm will need to handle massive and elastic systems.	No general control approach yet developed. As for rigid arms, conventional colocated rate controllers will not destabilize the payload elastic modes. For performance, additional sensors will be needed to increase active damping on dominant payload modes as necessary. A general approach will have to consider the cooperative use of the payload attitude control system together with the arm controller.
Compliant base or free-flying base	Important effect for dexterous arms mounted on a space station node or on a stabilizer arm or at the end of a long, flexible RMS-like manipulator.	Practical engineering solutions will have to be developed. Use of wrist mounted or body-mounted sensors for active feedback of base mode will be key to effective control. Passive energy dissipation mechanisms (friction brakes, viscoelastic mounts) will need to be designed.	The Space Shuttle/RMS system is the first free-flyer servicing spacecraft. Free-flying base effect becomes more important as payload mass becomes comparable to Shuttle mass/inertia. Compliance of Space-Station RMS mount on truss needs to be accounted for in design. Cooperative use of the base and the arm controllers will be needed for future autonomous operations.	Effect of base compliance shows up as pairs of lightly damped poles and zeroes in each joint open-loop transfer function. Effective damping of these modes can be increased through a combination of colocated control and wrist/base-mounted sensors (accelerometers and/or inertial position sensors)

CSI Issues in Space Robotics

Control of Elastic Payloads: 1-DOF Example

- 1-DOF rigid arm with 1-DOF elastic payload:

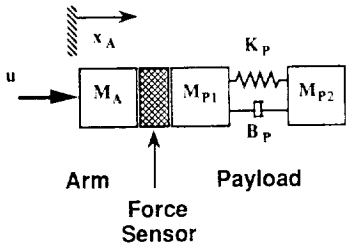

- M_A = Arm Mass
- $M_P = M_{P1} + M_{P2}$ = Payload Mass
- B_P is small (lightly damped elastic mode)

- Payload dynamics can be defined by its dynamic stiffness:

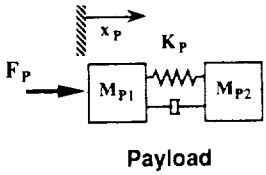

$$Z_P(s) = \frac{F_P(s)}{x_P(s)} = M_P s^2 \frac{s^2 + 2\zeta\omega_P s + \omega_P^2}{s^2 + 2\zeta'\Omega_P s + \Omega_P^2} \frac{\Omega_P^2}{\omega_P^2}$$

$$\omega_P^2 = K_P\left[\frac{1}{M_{P1}} + \frac{1}{M_{P2}}\right] \qquad \Omega_P^2 = \frac{K_P}{M_{P2}}$$

- Equations of motion for arm/payload system can be expressed in terms of the INDIVIDUAL arm & payload dynamics:

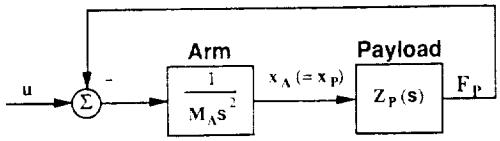

- Assume standard PD control for robot arm:

$$u = -k_A(x_A - x_A^c) - k_R x_A$$

- Arm is acting as a colocated actuator/ sensor pair for payload.

⇒ ELASTIC MODE ALWAYS STABLE

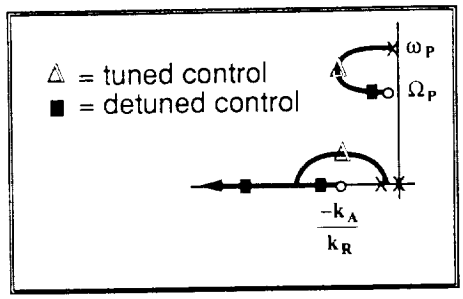

- Payload closed-loop elastic mode is a function of the ratio $\frac{\omega_A}{\Omega_P}$ where:

ω_A = Rigid Arm Closed-Loop Bandwidth

Ω_P = First Cantilevered Vibration Frequency of the payload

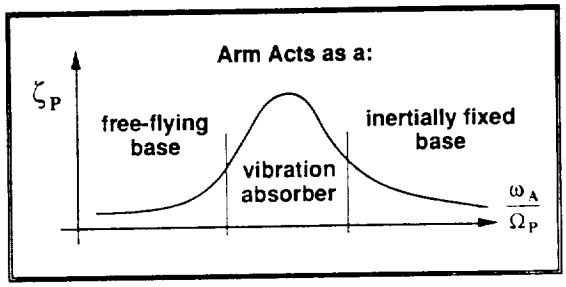

Control of Elastic Payloads: 1-DOF Example (cont'd)

- For cases where arm controller is "detuned" ($\omega_A >> \Omega_P$), we can implement an additional IMPEDANCE control law to actively damp the payload's elastic mode:

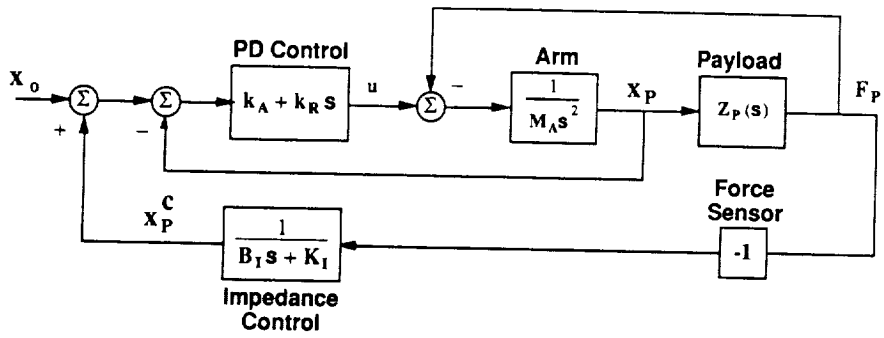

- **We Have:** $x_P \cong x_P^c$ (High-Gain PD Control)

$$x_P^c = \frac{-F_P}{B_I s + K_I} \quad \text{(Impedance Control)} \quad \Big\} \quad F_P = -(B_I s + K_I)\, x_P$$

⇒ Force F_P applied to payload acts as a virtual spring/damper selected by the user !!

- Root-Locus vs. Force Sensor Gain:

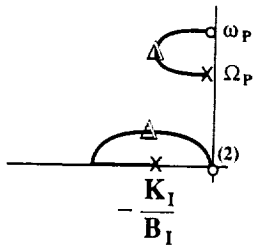

⇒ With proper choice of $[K_I, B_I]$ gains, payload elastic mode is actively damped !

Control of Elastic Payloads: Planar Arm Example

- Three DOF Arm with Elastic Beam Payload:

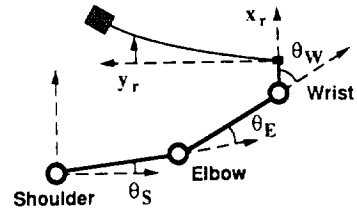

- Payload linearized dynamics model is obtained from FEM techniques applied to elastic body on moving base:

$$\begin{bmatrix} M_{rr} & M_{re} \\ M_{re}^t & M_{ee} \end{bmatrix} \begin{bmatrix} \ddot{q}_r \\ \ddot{q}_e \end{bmatrix} + \begin{bmatrix} \underline{0}_{3}\underline{0}_{3n} \\ \underline{0}_{n3} D_{ee} \end{bmatrix} \begin{bmatrix} \dot{q}_r \\ \dot{q}_e \end{bmatrix} + \begin{bmatrix} \underline{0}_{3}\underline{0}_{3n} \\ \underline{0}_{n3} K_{ee} \end{bmatrix} \begin{bmatrix} q_r \\ q_e \end{bmatrix} = \begin{bmatrix} F_p \\ \underline{0} \end{bmatrix}$$

$q_r = \begin{bmatrix} x_C \\ y_C \\ \phi_C \end{bmatrix}$ = rigid interface DOFs $\quad F_p = \begin{bmatrix} F_x \\ F_y \\ T_\Phi \end{bmatrix}$ = external forces/torque exterted on payload by arm.

- In summary:

$$\begin{bmatrix} F_x(s) \\ F_y(s) \\ T_\Phi(s) \end{bmatrix} = Z_p(s) \begin{bmatrix} x_C(s) \\ y_C(s) \\ \phi_C(s) \end{bmatrix} \text{ where } Z_p(s) = \text{DYNAMIC STIFFNESS of ELASTIC PAYLOAD}$$

- Arm dynamics linearized around given configuration:

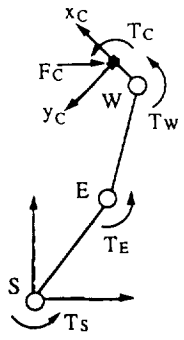

$$M(\underline{\theta}_0)\,\ddot{\underline{\theta}} = \underline{T}_A + J^T(\underline{\theta}_0)\,\underline{F}_C \quad \text{with}$$

$\underline{\theta} = \begin{bmatrix} \theta_S \\ \theta_E \\ \theta_W \end{bmatrix}$ $\quad \underline{T}_A = \begin{bmatrix} T_S \\ T_E \\ T_W \end{bmatrix}$ $\quad \underline{F}_C = \begin{bmatrix} T_{x_C} \\ T_{y_C} \\ T_{\phi_C} \end{bmatrix}$

$M(\underline{\theta}_0)$ = 3x3 inertia matrix

$J(\underline{\theta}_0)$ = Jacobian matrix expressed in end-effector frame

Can be transformed in terms of end-effector coordinates xc:

$$M(\underline{x}_0)\,\ddot{\underline{x}}_C = J^{-T}(\underline{\theta}_0)\,\underline{T}_A + \underline{F}_C \quad \text{with} \quad M(\underline{x}_0) = \text{"Cartesian" inertia matrix}$$

$$= J^{-T}(\underline{\theta}_0)\,M(\underline{\theta}_0)\,J^{T}(\underline{\theta}_0)$$

- Coupled arm / payload dynamics:

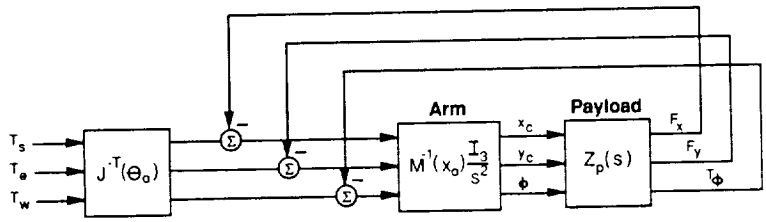

Control of Elastic Payloads: Planar Arm Example

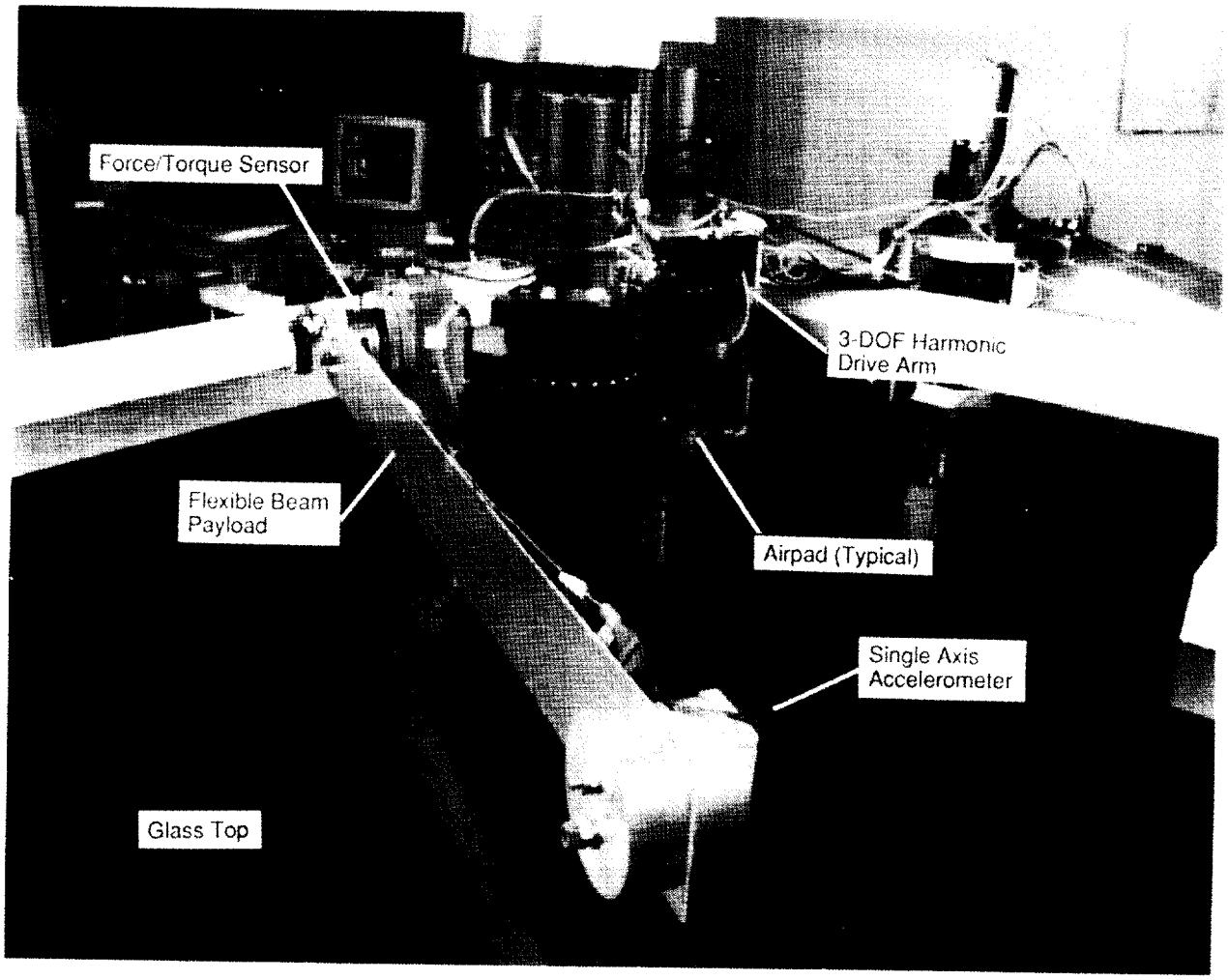

ORIGINAL PAGE
BLACK AND WHITE PHOTOGRAPH

Control of Elastic Payloads: Planar Arm Example

- System Block Diagram:

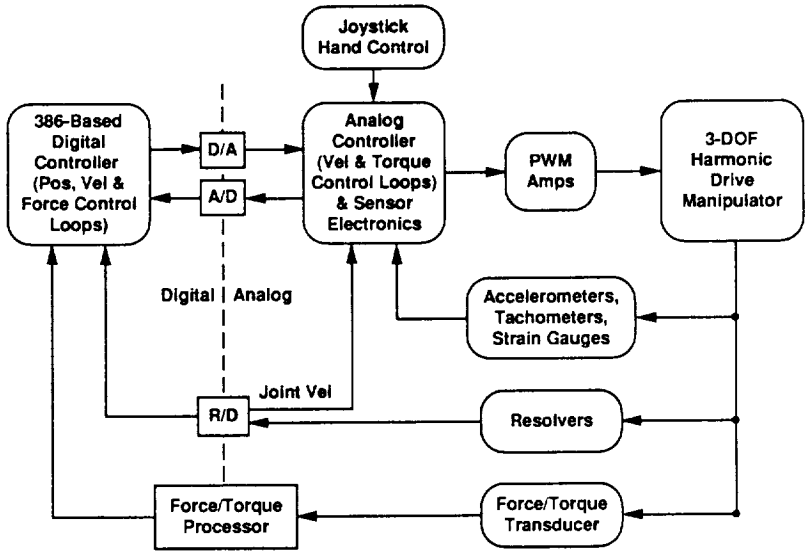

- Characteristic frequencies for 3-DOF Arm & Payload dynamic system (derived using TREETOPS multi-body software):

	F_1 (Hz)	F_2 (Hz)	F_3 (Hz)
Arm Joints Locked	1.2	14.0	42.2
Arm Joints Free	2.1	14.3	42.3

- Arm Mass Properties:

Link	Mass (kg)	Center of Mass (m)	MOI (kg-m ^{2})	Link Length (m)
Shoulder	13.8	0.406	0.77	0.56
Elbow	10.1	0.37	0.607	0.56
Wrist	13.7	0.14	0.106	0.254

- Payload Mass Properties:

Part	Mass (kg)	Center of Mass (m)	EI (N-m ^{2})	Link Length (m)
Beam	0.4	0.38	7.28	0.765
Tip Mass	0.7	—	—	—

Control of Elastic Payloads: Planar Arm Example (cont'd)

- **Arm controller is designed assuming a rigid payload:**
  - Independent analog torque loop controllers (elastic gearmotors behave as direct drive actuators)
  - Standard nonlinear control law: $T_a = M_{rr}(\theta)\left[-K_P(\theta - \theta^c) - K_R\dot{\theta}\right]$
    - For a rigid arm, closed-loop dynamics is approximated by 3 decoupled second-order integrators.
    - For a rigid arm with elastic payload, arm can be treated as a virtual cartesian 3-dof colocated actuator/sensor pair.
- **Dominant payload closed-loop elastic mode is a function of the ratio $\frac{\omega_A}{\Omega_P}$ where:**

ω_A = Rigid Arm Closed-Loop Bandwidth

Ω_P = First Clamped Vibration Frequency of the Payload

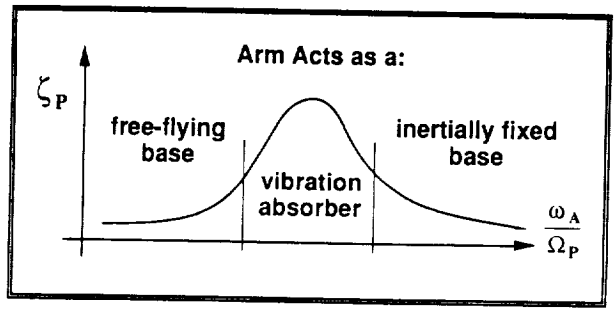

Experimental time responses for an initial payload elastic deformation:

Arm acts as a vibration absorber: $\frac{\omega_A}{\Omega_P} = 1$

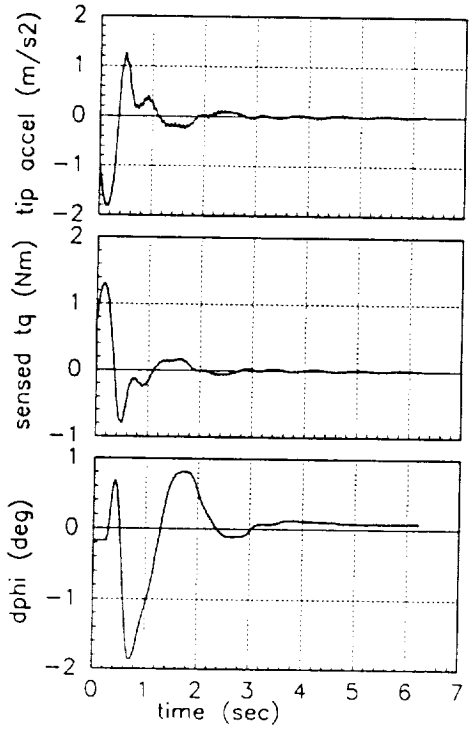

Arm acts as a rigid base: $\frac{\omega_A}{\Omega_P} = 2$

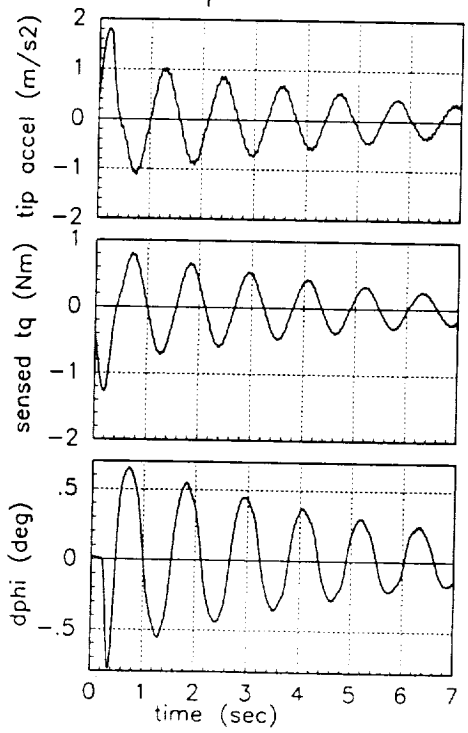

Control of Elastic Payloads: Planar Arm Example (cont'd)

- **For cases where arm controller is detuned ($\omega_a > \Omega_p$), we can implement an impedance control law to actively damp dominant payload elastic modes:**

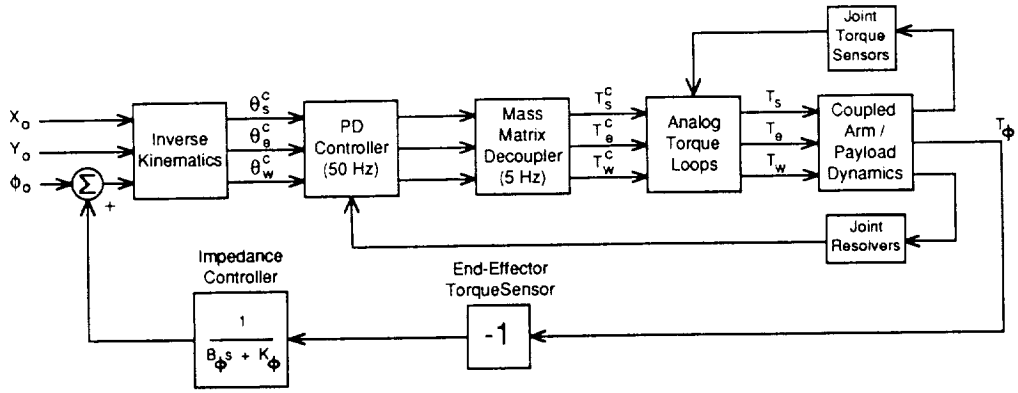

- **We Have:** $\phi \cong \phi^c$ (High-Gain PD Control)

$$\phi^c = \frac{-T_\phi}{B_\phi s + K_\phi} \quad \text{(Impedance Control)} \qquad \Big\} \quad T_\phi \cong -(B_\phi s + K_\phi)\phi$$

⇒ Torque T_ϕ applied to payload acts as a <u>virtual</u> spring/damper selected by the user !!

Experimental time responses for an initial payload elastic deformation:

Impedance controller:

$\frac{\omega_A}{\Omega_P} = 2$

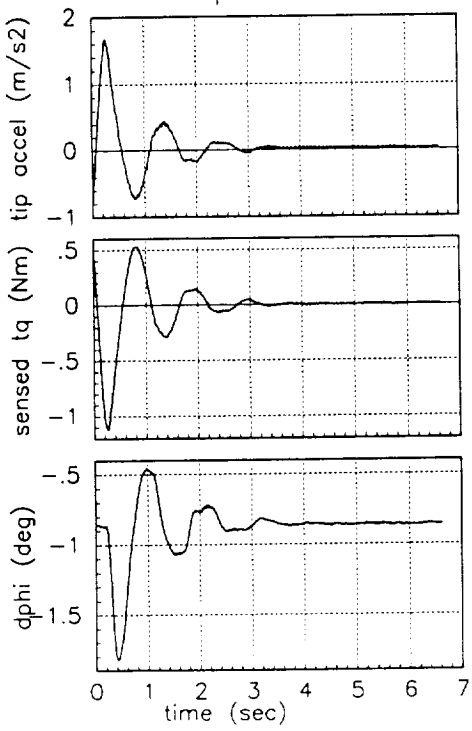

Arm acts as a rigid base:

$\frac{\omega_A}{\Omega_P} = 2$

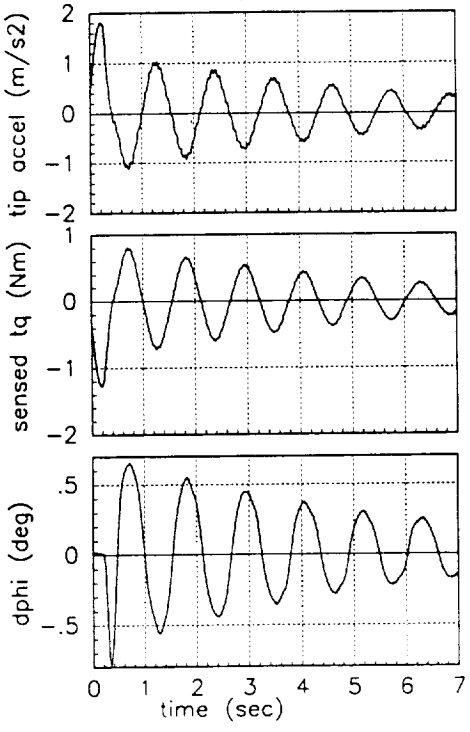

Control of Elastic Arms: Testbed Description

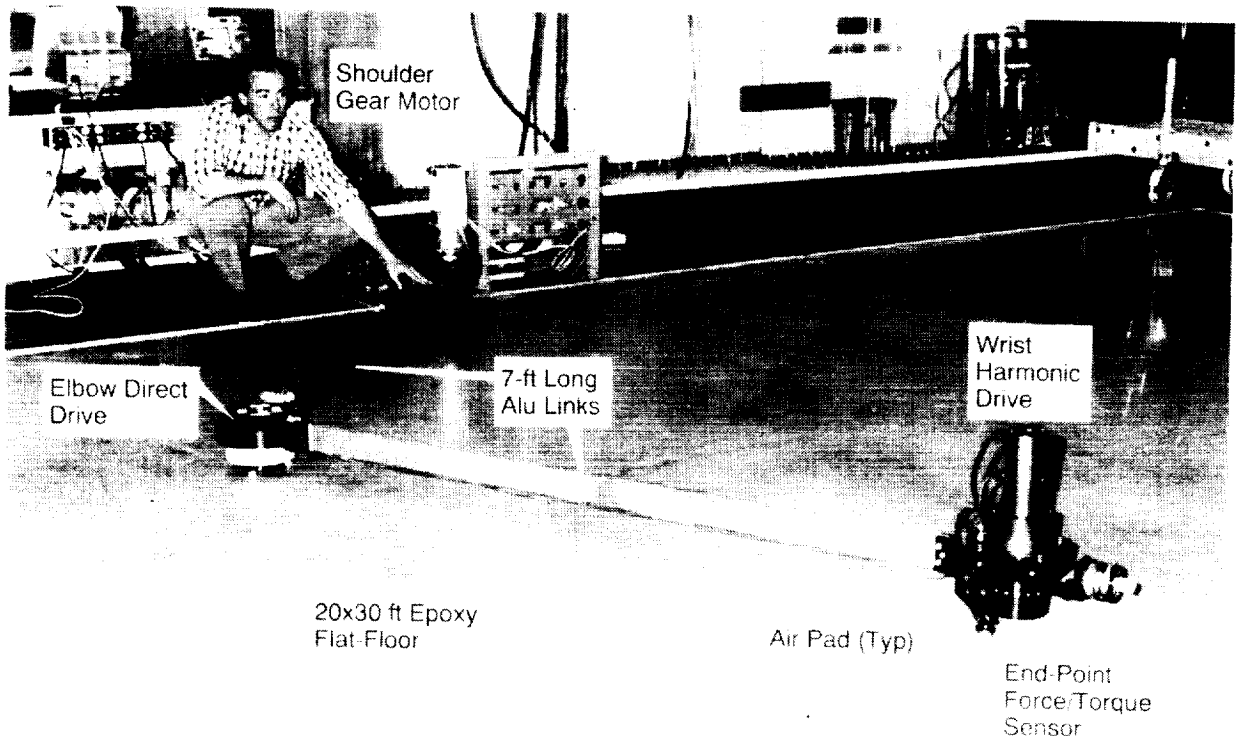

ORIGINAL PAGE
BLACK AND WHITE PHOTOGRAPH

Control of Elastic Arms: Testbed Description (cont'd)

- **System Block Diagram:**

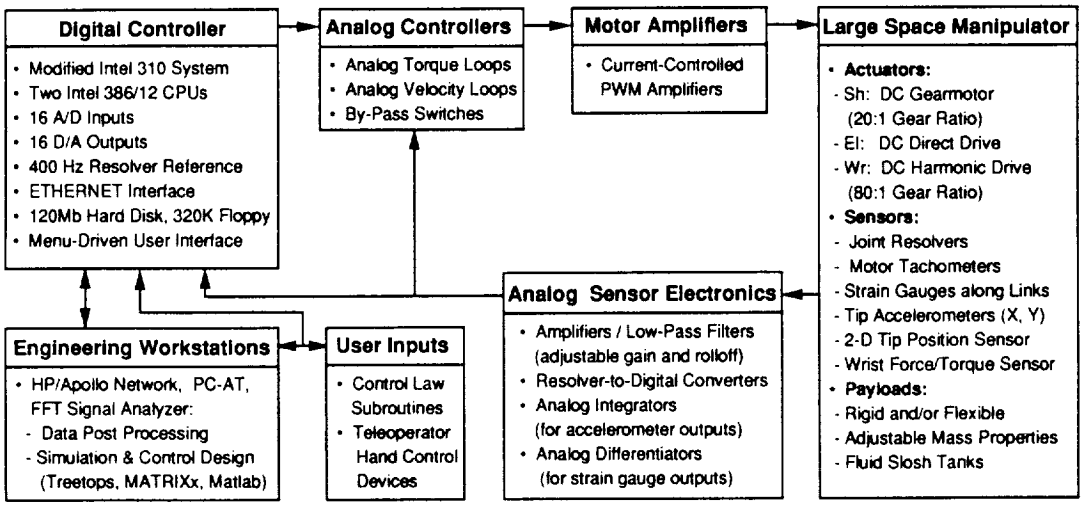

Control of Elastic Arms: Dynamic Modelling

- **Modelling tool is the multi-flexible body dynamic analysis code TREETOPS:**
  - Code developed by Dynacs for NASA-MSFC can simulate controlled dynamics of a general chain of articulated rigid and elastic bodies.
  - Preprocessor generates finite element mass, damping and stiffness matrices for each link with user-selectable end boundary conditions.
  - Linearized models can be loaded in the control analysis software packages MATLAB and MATRIXx.
  - Nonlinear TREETOPS simulation can be run with the MATRIXx/System-Build nonlinear simulator. This allows to easily design and simulate control laws with the TREETOPS-generated dynamic models.
- **Simple analytical models have also been derived to understand the basic characteristics of the system to control: linear and nonlinear models for a 1-DOF, and 2-DOF planar slender elastic arms with a rigid payload and with nonlinear or linear geared actuators.**

Control of Elastic Arms: Dynamic Modelling (cont'd)

- **Equations of motion for 2-DOF elastic arm numerically assembled by TREETOPS:**

$$\begin{bmatrix} M_{rr}(x_r) & M_{re}(x_r) \\ M_{re}^{t}(x_r) & M_{ee} \end{bmatrix} \begin{bmatrix} \ddot{X}_r \\ \ddot{X}_e \end{bmatrix} + \begin{bmatrix} D_{rr} & \underline{0}_{2n} \\ \underline{0}_{n2} & D_{ee} \end{bmatrix} \begin{bmatrix} \dot{X}_r \\ \dot{X}_e \end{bmatrix} + \begin{bmatrix} \underline{0}_2 & \underline{0}_{2n} \\ \underline{0}_{n2} & K_{ee} \end{bmatrix} \begin{bmatrix} X_r \\ X_e \end{bmatrix} = \begin{bmatrix} I_2 \\ \underline{0}_{n2} \end{bmatrix} \begin{bmatrix} T_s \\ T_e \end{bmatrix} + \begin{bmatrix} \mathcal{J}_{RR}^{t} \\ \mathcal{J}_{ee}^{t} \end{bmatrix} \begin{bmatrix} F_{Tx} \\ F_{Ty} \end{bmatrix}$$

where X_r and X_e are respectively the joint angles and the generalized elastic coordinates

- **Equations of motion are linearized around a given arm configuration. A state-space model is derived with the two control actuators as inputs. The model outputs are the joint angles, motor rates and linearized tip displacements (dx,dy).**
- **Characteristic System frequencies: JL= free joints FF = joint locked.**

System Frequencies (Hz) for No Payload Configuration				
Mode No.	$\theta_e = 0°$		$\theta_e = 90°$	
	JL	FF	JL	FF
1	0.29	5.12	0.36	5.00
2	1.50	6.70	0.94	6.54
3	7.53	18.3	7.27	18.2
4	14.5	25.3	14.3	25.1
5	27.1	40.9	26.6	40.9
6	38.7	63.2	38.6	63.1

Control of Elastic Arms: Colocated PD Control

- **Closed-loop system block diagram:**

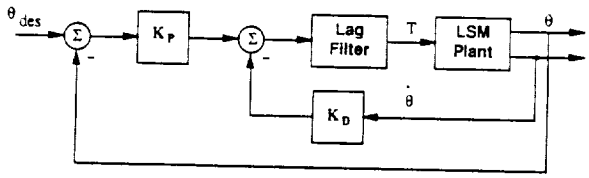

- **PD controller with joint position and motor velocity feedback:**

$$T_S = -\left[k_{PS}(\theta_S - \theta_S^c) + k_{RS}\dot{\theta}_S \right] L_{2S}(s)$$

$$T_e = -\left[k_{Pe}(\theta_e - \theta_e^c) + k_{Re}\dot{\theta}_e \right] L_{2e}(s)$$

where L_{2S} and L_{2e} are two second-order lag filters:

$$L_2(s) = \frac{S^2 + 2\zeta_z \omega_z s + \omega_z^2}{S^2 + 2\zeta_p \omega_p s + \omega_p^2} \frac{\omega_p^2}{\omega_z^2}$$

Control of Elastic Arms: Colocated PD Control (cont'd)

- **Example of gain-stabilization of the 4th vibration mode (85 Hz) with PD controller implemented at 200 Hz. Second-order lag filter provides high-frequency roll-off in compensator:**

Open-loop shoulder transfer function G (s) K (s)

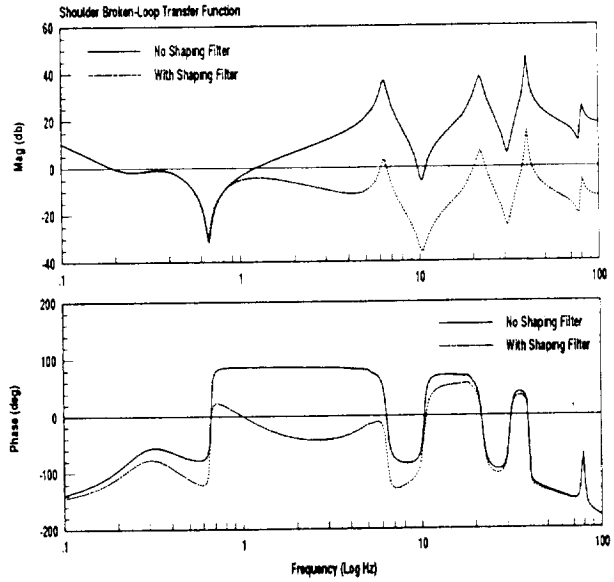

Control of Elastic Arms: End-point Controller

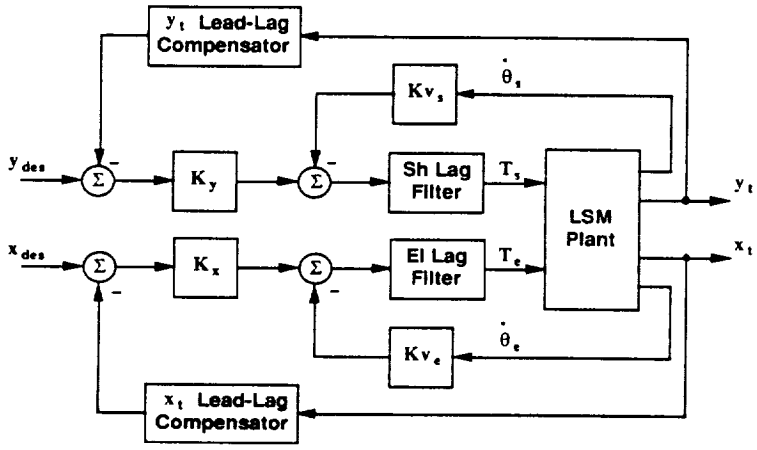

- **End-point controller is designed for configurations with the elbow angle nearly equal to 90 degrees:**
  - Tip sensor Xt channel is fed back to elbow actuator.
  - Tip sensor Yt channel is fed back to shoulder actuator.
- **For each channel, the tip controller consists of a second-order lead compensator with motor rate feedback:**

$$T_i = -\left[k_{Pi} \frac{(s+a)}{(s+b)(s+c)} (z_i - z_i^c) + k_{Ri} \dot{\theta}_i \right] L_{2i}(s)$$

with $\{a << b \ \& \ c\}$ and L_{2i} is a second-order lag filter.

Control of Elastic Arms: PD Control vs End-point Control

- **Arm is commanded to move along a straight line in the y-direction:**
  - A fifth-order spline command profile is used for the tip position command
  - For the independent joint controller, equivalent joint command profiles are computed using inverse kinematics (assuming arm is rigid).

- **Arm configuration for reference slew maneuver:**

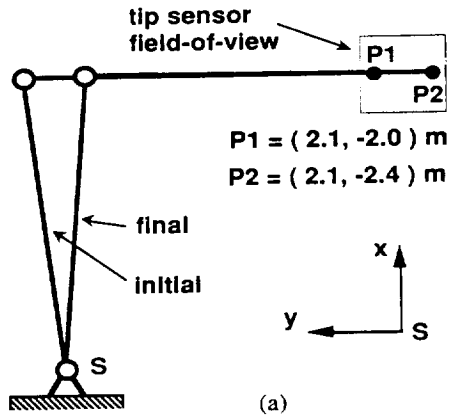

(a)

Experimental Time Responses for Slew Maneuver

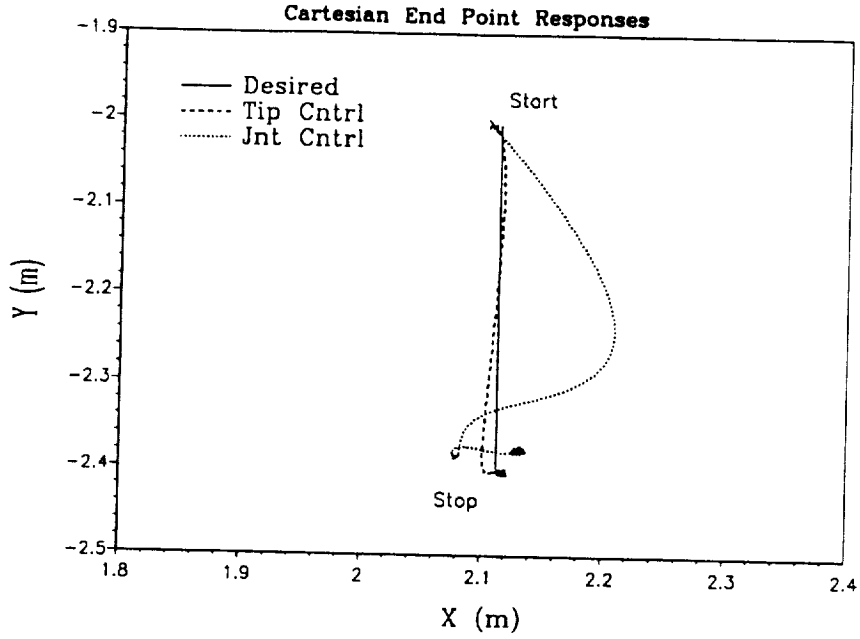

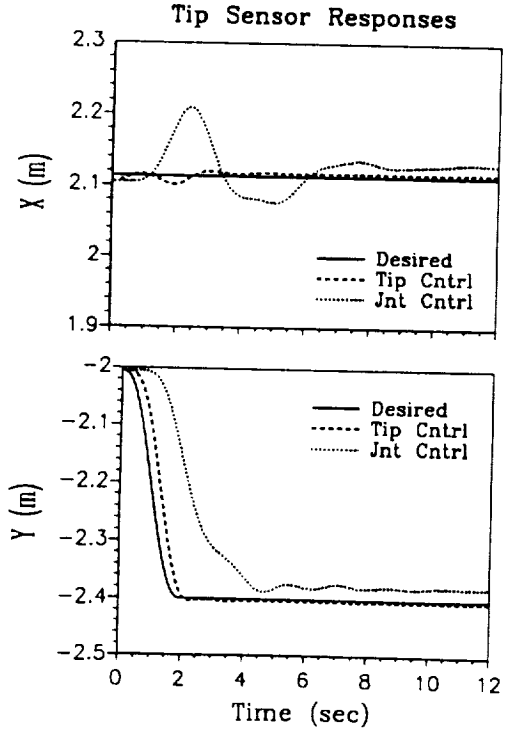

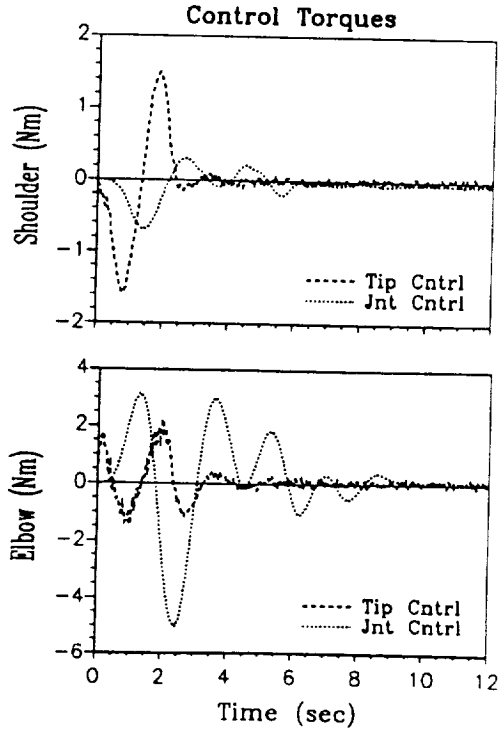

Control of Elastic Arms: Disturbance Response to Tip Forces

- Experimental set-up:

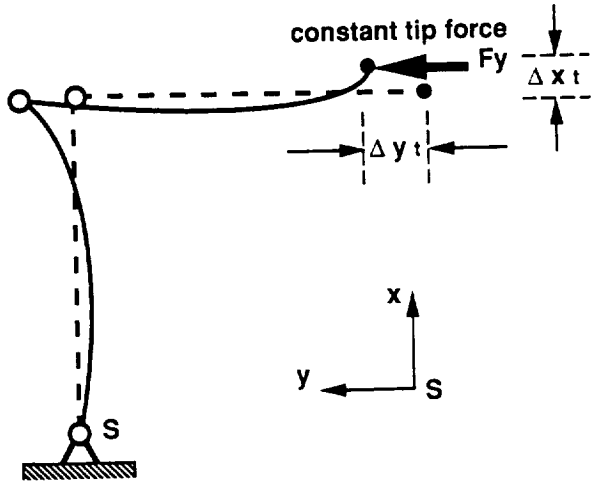

- The arm is under closed-loop control in a given configuration (joint or tip control).
- A constant force is applied at the tip using a force gage.
- After steady-state has occurred, tip force is removed.

Control of Elastic Arms: Disturbance Response toTip Forces (cont'd)

Experimental Data for 0.5 Lb Tip Force Applied along Y axis:

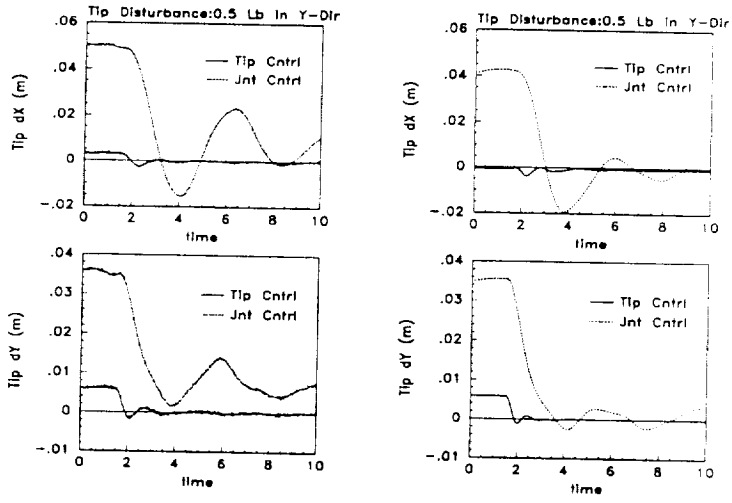

- Effective cartesian stiffness with tip position control is one order of magnitude larger than with joint feedback.
- With joint control, tip disturbance forces excite fundamental low-frequency and the lightly-damped elastic mode of the arm (0.5 Hz frequency). With tip controller, transient response is well damped.

Conclusions

- **With additional sensing capability, simple and robust control laws can be used for active damping of space robots:**
  - wrist-mounted force/torques sensors can be used to damp out large elastic payload vibration modes with a simple impedance control law.
  - sensors which directly sense the wrist motion can be used to damp out link elastic modes for RMS-class arms.
  - output torque sensors can also be used to damp out gearmotor elastic modes.

- **Experimental testbeds have been designed to validate modelling techniques and to demonstrate in 2-D the feasibility of new control/sensing implementation for FTS/SPDM-class and RMS-class manipulators. These testbeds are useful as a complement to 3-D simulation studies.**

- **Space-based experiments should be planned to demonstrate CSI-technology for FTS/SPDM-class and RMS-class manipulators.**

OPTIMIZATION FOR EFFICIENT STRUCTURE-CONTROL SYSTEMS

Hayrani Öz
Department of Aeronautical and Astronautical Engineering
The Ohio State University, Columbus OH 43210-1276

and

Narendra S. Khot
Flight Dynamics Directorate, Wright Laboratory (WL/FIBRA)
Wright-Patterson Air Force Base, Ohio 45433-6553

INTRODUCTION

The efficiency of a structure-control system is a nondimensional parameter which indicates the fraction of the total control power expended usefully in controlling a finite-dimensional system. The balance of control power is wasted on the truncated dynamics serving no useful purpose towards the control objectives. Recently, it has been demonstrated that the concept of efficiency can be used to address a number of control issues encountered in the control of dynamic systems such as the spillover effects, selection of a good input configuration and obtaining reduced order control models. Reference (1) introduced the concept and presented analyses of several Linear Quadratic Regulator designs on the basis of their efficiencies. Encouraged by the results of Ref. (1), Ref. (2) introduces an efficiency modal analysis of a structure-control system which gives an internal characterization of the controller design and establishes the link between the control design and the initial disturbances to affect efficient structure-control system designs. The efficiency modal analysis leads to identification of principal controller directions (or controller modes) distinct from the structural natural modes. Thus ultimately, many issues of the structure-control system revolve around the idea of insuring compatability of the structural modes and the controller modes with each other, the better the match the higher the efficiency. A key feature in controlling a reduced order model of a high dimensional (or ∞-dimensional distributed parameter system) structural dynamic system must be to achieve high efficiency of the control system while satisfying the control objectives and/or constraints. Formally, this can be achieved by designing the control system and structural parameters simultaneously within an optimization framework. The subject of this paper is to present such a design procedure.

An important aspect of the efficiency approach to structure-control system is that the behavior of the full-order system can be ascertained based on the reduced-order design model without any knowledge of the truncated system dynamics. In case of finite element models (FEM) of structural systems the full order system is the high-dimensional first-cut model of the system known as the N^{th}

order evaluation model, where N is the total finite-element model structural degrees of freedom. In the case of distributed parameter partial differential equation formulation, the full-order model is the ∞-dimensional system.

Two types of efficiency are defined for structure-control systems in Ref. 1. The first is the global efficiency e^* which compares the total control power expended on the full-order system by a spatially discrete finite number of point inputs, to the control power that would have been expended to control the full-order system by a spatially continuous input field. Thus, the global efficiency is a predominant indicator of the effect of nature of input configuration on utilizing the available control power. The second efficiency e compares the control power lost to the truncated dynamics thereby not serving the purpose of control to the total control power expended on the full-order physical system via the reduced-order control design model. In the case of global efficiency there is an interest in the performance of a spatially distributed control design which is dynamically similar (Ref. 3) to the point-input control design. The performance of the distributed input design constitutes a globally optimal performance. In the case of relative model efficiency e, both control powers compared pertain to the same control design model employing point-inputs, hence e constitutes a relative measure of power performance. In this paper, the focus will be on the relative model efficiency. References 1, 2, and 4 include more details on the efficiency approach to structure-control systems.

The subject of structure-control systems is inherently multidisciplinary. A variety of objectives and constraints can be proposed both at the system-level and subsystem level (structure or control subsystems) to bring about an interdisciplinary study of the problem. For space-structures an ultimate objective is to have a minimum mass structure subject to structural and/or control system constraints. References 5-8 include a variety of optimization formulations of the problem. One aspect of structural-control system optimization seems to be the variety of objective and constraint function formulations that are proposed. While abundance of various formulations is desirable at one hand, many different formulations also point out the need for being able to pose objective and constraint functions that are truly multidisciplinary and therefore can address a variety of design issues for the structure-control system. It is here that the power efficiency of the structure-control system as a non-dimensional indicator of the merit of the system design seems to offer a unique potential.

In our recent work in Ref. 9, as a further enhancement of the optimization formulation presented in Ref. 10, we included a lower bound on the minimum efficiency achievable under all possible initial disturbances as a system-level constraint. Other constraints included in Refs. 9, 10 were on closed-loop damped frequencies and damping ratios. Furthermore, the question of a reduced-order design model was not addressed in Ref. 10. The inclusion of the efficiency constraint in Ref. 9, on

the other hand, brought the controller reduction problem into the picture which is implicit in the definition of the relative model efficiency. The feasibility of the optimization procedure for minimum mass including an efficiency constraint was clearly demonstrated in Ref. 9, by several examples using the ACOSS-FOUR structure (Fig. 1). The evaluation model had 12 degrees of freedom and the reduced order control design model included the lowest 8 structural modes. The control law was designed via the linear quadratic regulator theory (LQR) for apriori assumed unit weighting parameters for the states and the control inputs. The design variables were the 12 cross-sectional areas of the members of the structure.

From a broader perspective for the structure-control system, the design variables can and should include control system design parameters as well as structural system design variables. To this end, if the control law is designed via the LQR theory, the state and control weighting parameters can be considered as additional design variables. Recently, Ref. 11 included the control and state weighting parameters as design variables along with the member cross-sectional areas of the ACOSS-FOUR structure for an optimization problem with robustness constraints. However, Ref. 11 used the full-order (12 modes, 24 states) system model in its illustrations.

In view of the illustrations given in Refs. 9 and 11, the next evolution in optimization of the structure-control system with a focus on the efficiency of the design with a reduced-order model is to include the control weighting parameters as design variables along with the structural design variables. This paper represents this next step in the system optimization. Thus an optimization problem that is not only of more practical interest but also of a more genuine interdisciplinary character is presented in this paper.

EFFICIENCY ANALYSIS FOR A STRUCTURE-CONTROL SYSTEM

Consider an N^{th} order FEM evaluation model of the structural system

$$\mathbf{M}\ddot{\underset{\sim}{q}} + \mathbf{E}\dot{\underset{\sim}{q}} + \mathbf{K}\underset{\sim}{q} = \mathbf{D}\underset{\sim}{F}(t) \tag{1}$$

where M, K and D are the mass, stiffness and input influence matrices. $q(t)$ is the N-vector of nodal displacements and $\underset{\sim}{F}_{(t)}$ is the m-vector of point inputs. To control the structure described by (1), reduced-order modal state-space equations are considered

$$\dot{\underset{\sim}{x}} = \mathbf{A}\underset{\sim}{x} + \mathbf{B}\underset{\sim}{F}(t) \tag{2}$$

$$\underset{\sim}{x} = [\,\eta_c^T \quad \dot{\eta}_c\,]^T$$

where η_c^T are the $n < N$ structural modes controlled. Hence, considering the structural modal problem associated with (1) and denoting the orthonormalized modal matrix Φ of the full order evaluation model we have

$$\underset{\sim}{q} = \Phi\eta = \begin{bmatrix} \Phi_c & \Phi_R \end{bmatrix} \begin{bmatrix} \eta_c \\ \eta_R \end{bmatrix} \tag{3}$$

where R denotes truncated structural modes. The modal-state space system of (2) is the reduced $2n^{th}$ order control design-space model. The A and B matrices have the form

$$\mathbf{A} = \left[\begin{array}{c|c} \mathbf{0} & \mathbf{I} \\ \hline -\omega^2 & \mathbf{0} \end{array}\right], \qquad \mathbf{B} = \left[\begin{array}{c} \mathbf{0} \\ \hline \Phi_c^T \mathbf{D} \end{array}\right] \tag{4,5}$$

where $\omega^2 = \text{diag}\,[\omega_1 .... \omega_n]$ with ω_r a natural frequency and I is the n^{th} order identity matrix.

Due to any arbitrary input $F(t)$ the control power associated with the input on the actual full-order evaluation system (1) is given by the integral

$$S^R = \int \underset{\sim}{F}^T \mathbf{D}^T \mathbf{M}^{-1} \mathbf{D} \underset{\sim}{F} \mathrm{d}t \tag{6a}$$

The portion of this total expended power on the actual physical system that is projected onto a reduced-order dynamic system represented by (2) is

$$S_C^M = \int \underset{\sim}{F}^T \mathbf{B}^T \mathbf{B} \underset{\sim}{F} \mathrm{d}t \tag{6b}$$

We refer to S^R as the real (total) control power expended and S_C^M as the modal control power expended on the modal control design model. One has (Ref. 1)

$$S^R \geq S_C^M \tag{7}$$

and the control power wasted to the truncated dynamics is

$$S_U^M = S^R - S_C^M \tag{8}$$

The relative model input power efficiency is defined as

$$e\% = \frac{S_C^M}{S^R} \times 100 \tag{9}$$

with a maximum possible efficiency of 100%.

Associated with e, a power spillover quotient can be defined as

$$Sq\% = \frac{S_U^M}{S^R} \times 100 = (1 - e) \times 100 \tag{10}$$

We note that while S_C^M is indicative of a quantity for the reduced control design model through the appearance of the B matrix, S^R is a quantity for the evaluation model through the appearance

of the evaluation model mass matrix M. This observation establishes that the model efficiency relates the power performance of the full-order evaluation model of the actual physical system. Most importantly the definition of model efficiency is valid regardless of the specific functional dependence of the input field $F(t)$ which is the physical input to the real system. For example, it does not matter from the point of definition whether $F(t)$ is a control input or not.

Specifically, however, if the input $F(t)$ on the physical system has the functional form of the state-feedback of the reduced-control design model (2) as:

$$\underset{\sim}{F}(t) = -\mathbf{G}\underset{\sim}{x} \tag{11}$$

where G is a stabilizing constant control feedback gain matrix of dimension $m \times 2n$, then it can be shown that S_C^M, S^R become:

$$S^R = \underset{\sim}{x}_o^T \mathbf{P}^R \underset{\sim}{x}_o, \qquad S_C^M = \underset{\sim}{x}_o^T \mathbf{P}_C^M \underset{\sim}{x}_o, \qquad \underset{\sim}{x}_o = \underset{\sim}{x}(t_o) \tag{12}$$

P^R and P_C^M are symmetric positive definite matrices referred to as real and modal control power matrices, respectively. They are the solutions of the Lyapunov equations associated with the closed-loop control system

$$\mathbf{A}_{cl}^T \mathbf{P}^R + \mathbf{P}^R \mathbf{A}_{cl} + \mathbf{G}\mathbf{D}^T \mathbf{M}^{-1} \mathbf{D}\mathbf{G} = 0 \tag{13}$$

$$\mathbf{A}_{cl}^T \mathbf{P}_C^M + \mathbf{P}_C^M \mathbf{A}_{cl} + \mathbf{G}\mathbf{B}^T \mathbf{B}\mathbf{G} = 0 \tag{14}$$

$$\mathbf{A}_{cl} = \mathbf{A} + \mathbf{B}\mathbf{G} \tag{15}$$

Both power matrices are $2n^{th}$ order; they are computed based on the reduced control design model. However, note that the real power matrix P^R still inherently involves the evaluation model. It follows that, for a stable structure-control system, the model efficiency becomes

$$e = \frac{\underset{\sim}{x}_o^T \mathbf{P}_C^M \underset{\sim}{x}_o}{\underset{\sim}{x}_o^T \mathbf{P}^R \underset{\sim}{x}_o} \tag{16}$$

Hence, the efficiency of the system in general depends on the initial disturbance state and the structure and control system parameters carried into the power matrices via the Lyapunov Equations (13, 14). As simple as definition (16) of efficiency of the system appears, it does hold a host of internal information about the working of the structure and control system thereby characterizing the control/structure interactions uniquely as we outline below.

Since the control power matrices are Hermitian matrices, the efficiency quotient (16) essentially represents a Rayleigh's quotient. Consider the eigenvalue problem associated with the power matrices (Ref. 2)

$$\mathbf{P}_C^M t_i = \lambda_i^e \mathbf{P}^R t_i \qquad i = 1, 2, \ldots, 2n \tag{17}$$

where λ_i^e and t_i are defined as the i^{th} characteristic efficiency and the i^{th} controller efficiency mode, respectively. The eigenvector t_i is also referred to as the principal controller direction. Introducing the efficiency modal matrix T:

$$\mathbf{T} = [\, t_1 \quad t_2 \quad \ldots \quad t_{2n} \,] \tag{18}$$

the following orthonomality relations can be stated

$$\mathbf{T}^T \mathbf{P}^R \mathbf{T} = \mathbf{I}_{2n \times 2n}, \qquad \mathbf{T}^T \mathbf{P}_C^M \mathbf{T} = \Lambda^e \tag{19}$$

where

$$\Lambda^e = \text{diag}\,[\, \lambda_1^e \quad \lambda_2^e \quad \ldots \quad \lambda_{2n}^e \,], \qquad \lambda_1^e \leq \ldots \leq \lambda_{2n}^e \leq 1 \tag{20}$$

From the properties of a Rayleigh's quotient, for any arbitrary vector (initial disturbance state) x_o, the value of the quotient (16) is bracketed by

$$\lambda_1^e \leq e \leq \lambda_{2n}^e \leq 1 \tag{21}$$

where the upper bound of 1 follows from the property (7). We shall refer to λ_1^e as the fundamental efficiency. It is the minimum efficiency achievable by the structure-control system regardless of the initial state x_o.

Again, since the Rayleigh's quotient is stationary around an eigenvalue λ_i^e it follows that if the initial disturbance $x_o = t_i$, that is if it matches the i^{th} controller efficiency mode exactly, the efficiency will be exactly λ_i^e. Next, defining an efficiency modal transformation

$$\underline{x} = \mathbf{T}\underline{\epsilon}, \qquad \underline{x}_o = \mathbf{T}\underline{\epsilon}_o \tag{22}$$

an efficiency expansion expression can be written as

$$e = \sum_{i=1}^{2n} e_i, \qquad e_i = c_i^2 \lambda_i^e, \qquad c_i^2 = \frac{\epsilon_{io}^2}{\|\epsilon_o\|^2} \tag{23}$$

where ϵ_i and e_i represent the i^{th} efficiency state and the i^{th} efficiency component, respectively. From the above analysis, we note that the controller efficiency modal matrix T and the characteristic efficiencies λ_i^e are uniquely determined for a particular structure-control system design. For different initial disturbances x_o, the resulting efficiency e can readily be computed via the efficiency expansion of Eqs. (23). There will be no need for reanalysis of the system when the disturbance changes. The controller efficiency modal analysis presented above and characterized by $\{\Lambda^e, T\}$ is unique for the structure-control system and is in addition to the purely structural modal properties characterized by $[\omega^2, \Phi]$. For the sake of brevity and without elaborating further, the structure and control system analysis revolves around how compatible the modal properties Φ and T are. The modal matrix T

gives an internal characterization of the structure-control system and should prove to be a valuable analysis/design tool (Ref. 4).

OPTIMIZATION PROBLEM FORMULATION

In the design of structural-control systems it is natural to strive for a high model efficiency e regardless of initial state disturbances. The consequence is that a high efficiency of any given reduced-order control design model will imply that there is low control power spillover to the truncated dynamics and hence minimized residual interaction with the design model. Furthermore, by definition, a high efficiency simply means a more efficient use of resources available, which is a common sense engineering design principle. We can then pose a structure-control optimization problem which incorporates the system efficiency.

Optimization Problem

Objective:

$$\textit{Minimize the total structural weight} \tag{24}$$

subject to

Constraints on the reduced-order control design model:

$$\xi_{i\ \min} \geq \xi_i^* \tag{25a}$$

$$\omega_i \geq \omega_i^* \qquad i\epsilon\{1,2,\ldots,n\} \tag{25b}$$

$$e\% \geq e^*\% \tag{25c}$$

Control System Design Performance Index (CDPI):

$$\text{CDPI} = \text{Minimize} : \frac{1}{2}\int_O^\infty (\underset{\sim}{x}^T \overline{Q}\underset{\sim}{x} + \underset{\sim}{f}^T \overline{R}\underset{\sim}{f})dt \tag{26}$$

where $\overline{Q} \geq O$, $\overline{R} > O$ are weighting matrices defined by

$$\overline{Q} = \delta Q, \quad \overline{R} = \gamma R \tag{27a,b}$$

where Q and R are specified constant matrices and δ and γ are the control system design variables.

Design Variables: {Structural design variables, γ, δ}

In (25), i denotes a chosen set of modes from a set of n modes in the design space. ζ_i is the damping ratio of the controlled system and ω_i is the closed-loop frequency. An * denotes minimum desirable constraint values. The minimum weight optimization problem using only the first two types of constraints has been studied in Ref. (10). The novel feature of the problem posed here is the inclusion of the nondimensional structure control system parameter, the efficiency e in addition to the already too familiar other nondimensional parameter, the damping ratio ζ. The constraint on ζ reflects a concern on the quality of response, whereas the constraint on e reflects a concern on the use of the control power. An equally important feature of this optimization formulation is that the goodness of the reduced order design model relative to the full order system is explicitly but intricately incorporated to the design via the introduction of the efficiency constraint.

Returning to the efficiency constraint (25c) and the definition of efficiency (16) it is certain that the solution of the problem will also be sensitive to the initial modal state disturbance which is affected by the structural design variables. To circumvent this dependence of the problem solution on x_o we invoke a feature noted in the previous section that the minimum efficiency achievable is the fundamental efficiency λ_1^e regardless of the initial disturbance. Hence, the efficiency constraint (25c) can be substituted by a constraint on the fundamental efficiency

$$\lambda_1^e > \epsilon^* \tag{25d}$$

guaranteeing a lower bound on the model efficiency regardless of initial disturbances where sensitivity of λ_1^e depends only on the system matrices via the efficiency eigenvalue problem (17). Hence, we solve the optimization problem subject to the constraints (25a), (25b) and (25d).

The sensitivity expressions for the objective function and the damping ratio ζ and the closed-loop frequencies ω_i are exactly the same as given in Ref. (10) where it is assumed that the control gain matrix G is the steady-state solution of the $2n^{th}$ order matrix Riccati equation associated with the minimization of the Control Design Performance Index (CDPI). The sensitivity expression of efficiency λ_1^e is given in Ref. 9. The sensitivities with respect to the control design variables are given in Ref. (11).

ILLUSTRATIVE EXAMPLES

The ACOSS-FOUR structure shown in Fig. 1 was used to design a minimum weight structure with constraints on the closed-loop eigenvalues and the fundamental efficiency. This structure has twelve degrees of freedom ($N = 12$) and four masses of two units each attached at nodes 1 through 4. The dimensions and the elastic properties of the structure are specified in consistent nondimensional units in Ref. (7). Six colocated actuators and sensors are in six bipods. The control approach used is the linear quadratic regulator with steady-state gain feedback via minimizing the control design

performance index, (Eqs. 26, 27). In Eqs. 27, the weighting matrices Q and R for the state and control variables were assumed to be equal to the identity matrices and the parameters δ and γ were used as design variables along with the 12 structural member cross-sectional areas.

The nominal initial design is denoted by Design A with cross-sectional areas of the members equal to those given in Table 1. This initial design weighs 43.69 units. The initial values for the control parameters δ and γ were chosen as unity.

The constraints imposed on the optimum designs were as follows:

$$\omega_1 \geq 1.425 \tag{28a}$$

$$\omega_2 \geq 1.757 \tag{28b}$$

$$\zeta_1 \geq 1.5\ \zeta_1(\text{initial}) \tag{28c}$$

$$\lambda_1 = e_{min} \geq 1.75\ \lambda_1(\text{initial}) = 1.75\ e_{min}(\text{initial}) \tag{28d}$$

The first two constraints on the closed-loop damped frequencies correspond to a 10% increase over the initial closed-loop damped frequencies which were practically equal to the corresponding structural natural frequencies. The damping constraint demands a 50% increase in the damping of the first mode over that of the initial design. The fundamental efficiency constraint, which is the minimum possible efficiency (the worst case) for all conceivable initial state disturbances x_o, requires a 75% increase over the minimum efficiency of the initial design. We should note that the designation with subscript "1" in this constraint has no connotation with the first structural mode, quite differently it refers to the first efficiency mode or first principal controller mode, the significance of which is brought about through the definition of concept of efficiency of the structure-control system.

The NEWSUMT-A software based on the extended interior penalty function method with Newton's method of unconstrained minimization (Ref. 12) was used to obtain optimum designs. Two optimization problems were solved each with a different reduced-order control design model and a different input configuration. These designs were denoted as Design B and Design C. Design B used the first eight natural structural modes in the reduced-order control design model ($n = 8$) with 6 inputs ($m = 6$) located on the six bipods of the structure. Design C used the first six natural structural modes in the reduced order control design model ($n = 6$) with 2 inputs ($m = 2$) located on the two bipods attached to node 2.

The results of optimizations are given in Table 2 which includes values obtained for the constrained quantities $\omega_1, \omega_2, \lambda_1^e$ and ζ_1 and the objective functions, weights of the structures. In addition, the resulting real control powers expended, S^R and the amount of this power that was absorbed by the reduced-order design models, S_C^M and the respective model efficiencies, $e\%$ are

listed in Table 2. As the initial disturbance state x_o, a unit displacement in the x-direction at node 2 was assumed. Note that the initial disturbance affects only the value of model efficiency ϵ, but not the value of the fundamental efficiency λ_1^e.

The design variables, cross-sectional areas of elements and the control weighting parameters are listed in Table 1 for all Designs A-C. The structural frequencies, the characteristic controller power efficiency spectrum and the damping ratios of the closed-loop designs are also listed in Tables 3-5, respectively.

It is observed from Table 2 that all optimum designs result in considerable weight reduction in comparison to the initial weight and the constraints are satisfied. Particularly, fundamental efficiencies of optimum designs have been increased resulting in significant improvements also in the model efficiencies as intended. From Table 2 we note that the total control powers S^R expended on the 12^{th} order evaluation models have been affected with larger percentages of them absorbed by the 8^{th} and 6^{th}-order control design models of the optimum designs. While the control design models of the optimum designs have higher structural frequencies than the initial design, the truncated frequencies have been lowered, thus making the response of the truncated dynamics more susceptible to excitation by the control powers spilled over inefficiently in the optimum design. Thus it becomes even of more concern that the optimum designs have higher efficiencies than the initial design. For both control design models this has been achieved.

The control power S_C^M absorbed by a design model increases with the cube of the structural frequencies and may increase or decrease with the damping ratios depending on the separation between the closed-loop natural frequencies (moduli of the closed-loop eigenvalues) and the open-loop structural natural frequencies (Ref. 13). Therefore, the increases in the control powers S_C^M absorbed by both of the optimum designs are expected. From an alternate perspective, the initial strain energies in the design models of the optimum designs B and C are higher than the initial design A for the assumed unit initial displacement at node 2. However, much higher damping ratios realized in the optimum designs as listed in Table 5 by virtue of the required increase in the damping ratio of the fundamental structural mode, result in considerable decrease in the settling time of the closed-loop system. Thus, from this perspective also, power absorbed by the optimum designs S_C^M must increase to remove higher levels of initial strain energy in a much shorter time. Again note that the optimum designs have higher levels of efficiencies in using the control powers.

The line-of-sight error responses at node 1 of both optimum designs for the evaluation models and the control design models are shown in Figures 2 and 3 for $(n = 6, m = 2)$ and $(n = 8, m = 6)$, respectively. Figure 2a shows the responses of the 12-mode evaluation models of the initial design (Design A - solid curve) and the optimum design (Design C - dashed curve) for the control design model of 6 lowest natural modes and 2 inputs. Design C has an efficiency of 95.1% versus the 53.6%

efficiency of the initial Design A. Figure 2b shows the responses of the 12-mode evaluation model (solid curve) and the 6-mode control design model (dashed curve) of optimum Design C. Similarly, for the control design model of 8 lowest natural modes and 6 inputs, Figure 3a shows the responses of the 12-mode evaluation models of the initial design (Design A - solid curve) and the optimum design (Design B - dashed curve) with respective efficiencies of 61.5% and 88.6%. Figure 3b shows the responses of the 12-mode evaluation model (solid curve) and the 8-mode control design model (dashed curve) of optimum Design B.

The relative model efficiency e is a figure of merit which can also be used to ascertain the quality of response of the evaluation model of a controlled structure based on the study and simulation of a reduced-order control design model without any need for simulation of the evaluation model which can be very taxing on computational resources. It is shown in Ref. 4 that the mean square response of truncated dynamics is inversely proportional to the fourth power of the truncated natural frequencies and directly proportional to the time-weighted control power spilled over to the truncated dynamics which is quantified by the spillover quotient-inefficiency defined by Eq. (10). Certainly, if the controlled frequencies and the truncated frequencies are well-separated, specifically, if the truncated frequencies are high frequencies and a high system efficiency is realized, then one would hardly expect any degradation of the response of the reduced-order control design model due to excitation of truncated dynamics. In other words, in such cases, the inefficiency figure would further be attenuated when it is translated to its effect on the system response. In contrast, if the truncated frequencies are not well-separated from the controlled frequencies and they are of low natural frequencies, then the inefficiency figure will further be magnified when it is correlated to the system response. In case of such low frequencies in the truncated dynamics it becomes even of more concern to obtain very high system efficiencies. With efficiency of the system obtained based on the reduced-order design model and its implications on the evaluation model response known apriori through such observations, the designer will not have to simulate the evaluation model. Due to such aspects of the structure-control system, consideration of the efficiency of the system becomes essential for the designer. Furthermore, even if the effect of truncated dynamics on the response is ascertained to be insignificant, still striving for higher efficiency to conserve control power makes sound design engineering.

As for the optimum designs B and C illustrated in this paper, from Table 3 it is noted that the first truncated frequencies, mode 9 for Design B and mode 7 for Design C are almost coincident with the highest controlled frequencies, modes 8 and 6, respectively. Thus although the highest controlled frequencies and the first truncated frequencies are clearly separated in the initial Designs A, in the optimum designs, this feature is lost. In spite of the higher efficiencies obtained for the optimum Designs B and C one may expect that the near resonance excitation of the truncated mode 7 for Design C and the truncated mode 9 for Design B by the 6^{th} and 8^{th} modes, respectively, will

be discernible in the evaluation model responses over the responses of the reduced control design models. This is clearly verified in the evaluation model responses, especially in Fig. 2b, in spite of the 95% efficiency obtained for the optimum design. One may seek to improve the situation by either attempting a higher efficiency design or by putting a frequency separation constraint between the control design model and the truncated frequencies.

Finally, some remarks are in order as to the choice of different input configurations for the two optimum designs B and C. As discussed in Ref. 1, efficiency is a genuine parameter that reflects the interdisciplinary nature of the structure-control system design. As such it is also an indicator of the effects of changes in the input configuration and the design model order as well as of the compatability of the particular input configuration with the reduced-order design model. Indeed, it is illustrated in Ref. 1 that for the initial Design A with the 6-mode design model inclusion of inputs 3-6 degrades the efficiency of the system, whereas their inclusion improves the efficiency of the system for the 8-mode design model. Thus, for the optimization problems formulated and illustrated in this paper with the objective of improving the efficiencies of the 8-mode and 6-mode reduced-order designs, from the study of efficiencies of the initial design A, the input configurations were chosen with 6 inputs and the first 2 inputs, respectively, culminating in satisfaction of our objectives for both designs.

CONCLUSIONS

Incorporation of the efficiency concept as a norm of the structure-control system design and analysis enhances the overall quality of the system. Structure-Control system efficiency is a physically based nondimensional parameter indicating the degree of usefulness of a fundamental quantity in the design and analysis of many engineering disciplines, namely, the power. Our work heretofore demonstrates that a focus on the system efficiency does not curtail the designer's ability in monitoring other important quantities of the overall design; on the contrary, it brings in an added, but necessary, dimension to the structure-control system which is a time-tested proven concept in engineering design. The improvement of efficiency, in the least, simply makes better use of available control power since it results in reduced power spillover to the unmodelled dynamics. Furthermore, this reduction is not merely qualitative but it is quantified via efficiency. Consequently, monitoring of efficiency of the system is tantamount to gauging the goodness of any reduced-order control design model relative to the full-order physical system, which is characterized typically by a higher-order evaluation model in the case of FEM models or the ∞-dimensional model in the case of distributed parameter systems. More importantly, all control design computations only involve the reduced-order control design model while extracting information about the behavior of the full-order system which makes efficiency a practical design tool for the structure-control engineer. Our work

demonstrates that efficiency is an essential feature that must be addressed in the design of structure-control systems for flexible systems.

REFERENCES

1. Öz, H., Farag, K., and Venkayya, V. B. "Efficiency of Structure-Control Systems," *Journal of Guidance, Control and Dynamics*, Vol. 12, No. 3, May-June 1990, pp. 545-554.

2. Öz, H., "Efficiency Modes Analysis of Structure-Control Systems," AIAA - Paper No. 90-1210, Proceedings of the AIAA Dynamics Specialist Conference, April 1990, Long Beach CA, pp. 176-188.

3. Öz, H., "Dynamically Similar Control Systems and a Globally Optimal Minimum Gain Control Technique: IMSC," *Journal of Optimization Theory and Applications*, Vol. 59, No. 2, 1988, pp. 183-207.

4. Öz, H., "A Theoretical Approach to Analysis and Design of Efficient Reduced-Control for Space Structures." WRDC, FDL, Final Report, 1990, WRDC-TR-90-3027.

5. Salama, M., Hamidi, M., Demsetz, L., "Optimization of Controlled Structure." Proceedings of the JPL Workshop on Identification and Control of Flexible Space Structures, San Diego CA, 1984.

6. Messac, A., Turner, J., Soosar, K., "An Integrated Control and Minimum Mass Structural Optimization Algorithm for Large Space Structures." Proceedings of the JPL Workshop on Identification and Control of Flexible Space Structures, San Diego CA, 1984.

7. Khot, N. S., Eastep, F. E., Venkayya, V. B., "Optimal Structural Modifications to Enhance the Optimal Active Vibration Control of Large Flexible Structures." Proceedings of the 26^{th} SDM Conference, Orlando FL, pp. 134-142.

8. Khot, N. S., Öz, H., Grandhi, R. V., Eastep, F. E., Venkayya, V. B., "Optimal Structural Design with Control Gain Norm Constraint," AIAA Journal, Vol. 26, No. 5, 1988, pp. 604-611.

9. Öz, H., Khot, N. S., "Structure-Control System Optimization with Fundamental Efficiency Constraint," Proceedings of the 8^{th} VPI&SU Symposium on Dynamics and Control of Large Structure, May 1991, Blacksburg VA.

10. Khot, N. S., "Structure/Control Optimization to Improve the Dynamic Response of Space Structures," *Computational Mechanics*, Vol. 3, 1988, pp. 179-186.

11. Khot, N. S., Veley, D. E., "Use of Robustness Constraints in the Optimum Design of Space Structures," Journal of Intelligent Mater. Syst. and Struct., Vol. 2 - April 1991.

12. Thareja, R., Haftka, R. T., "NEWSUMT-A: A Modified Version of NEWSUMT for Inequality and Equality Constraints," VPI Report, Aerospace Engineering Department, March 1985.

13. Öz, H., Adigüzel, E., "Generalized Natural Performance Charts for Control of Flexible Systems," AIAA No. 84-1951, Guidance and Control Conference, Seattle WA, 1984.

Table 1: Design Variables

Element Number	Design A	Design B n = 8, m = 6	Design C n = 6, m = 2
1	1000.0	246.9	126.5
2	1000.0	403.6	280.7
3	100.0	175.4	575.5
4	100.0	257.2	576.2
5	1000.0	228.2	407.9
6	1000.0	253.9	271.1
7	100.0	54.2	84.7
8	100.0	226.1	68.2
9	100.0	224.6	547.8
10	100.0	528.2	171.8
11	100.0	604.9	416.2
12	100.0	597.4	270.8
Weight	43.69	21.97	26.79
δ	1.00	4.24	2.45
γ	1.00	0.24	0.41

Table 2: Optimum Designs

Constraints	Design A Initial Design n = 8, 6	Design B n = 8 modes m = 6 inputs	Design C n = 6 modes m = 2 inputs
ω_1	1.295	1.425	1.425
ω_2	1.596	1.757	1.757
ζ_1	0.056, 0.031	0.290	0.130
$\lambda_1\%$	40.7, 52.5	71.2	92.1
S^R	4.88, 17.88	89.00	26.02
S_C^M	3.00, 9.59	78.91	24.74
e%	61.5, 53.6	88.6	95.1
Weight	43.69	21.97	26.79

Table 3: Structural Frequencies ω_s^2

Structural Mode	Design A	Design B n = 8, m = 6	Design C n = 6, m = 2
1	1.68	2.11	2.06
2	2.55	3.27	3.15
3	7.31	7.83	8.43
4	7.52	11.17	13.85
5	9.98	17.34	19.27
6	16.06	22.80	24.17
7	20.01	44.61	24.43
8	20.17	50.40	43.32
9	66.24	50.52	55.84
10	77.46	96.96	70.42
11	97.42	107.40	92.49
12	151.30	110.70	112.86

Table 4: Characteristic Efficiency Spectrum $|\lambda|$ %

Controller Efficiency Mode	Design A n = 8, 6	Design B n = 8, m = 6	Design C n = 6, m = 2
1	99.98, 59.95	99.89	97.85
2	99.98, 59.95	99.82	97.85
3	99.62, 59.95	99.22	97.83
4	99.57, 59.95	98.56	97.83
5	98.32, 59.95	94.01	97.77
6	98.10, 59.95	93.78	97.73
7	76.90, 52.65	92.88	92.24
8	76.21, 52.65	91.99	92.23
9	62.92, 52.65	89.57	92.16
10	61.98, 52.65	88.51	92.14
11	56.92, 52.65	81.21	92.14
12	53.29, 52.65	78.98	92.14
13	42.87, -	76.88	-
14	42.81, -	74.14	-
15	42.77, -	72.63	-
16	40.77, -	71.24	-

Table 5: Closed-Loop Damping Ratios ζ

Mode	Design A n = 8, 6	Design B n = 8, m = 6	Design C n = 6, m = 2
1	0.056, 0.031	0.290	0.130
2	0.067, 0.034	0.107	0.171
3	0.074, 0.009	0.335	0.121
4	0.081, 0.063	0.106	0.120
5	0.085, 0.077	0.100	0.160
6	0.087, 0.049	0.189	0.124
7	0.076, -	0.205	-
8	0.072, -	0.196	-

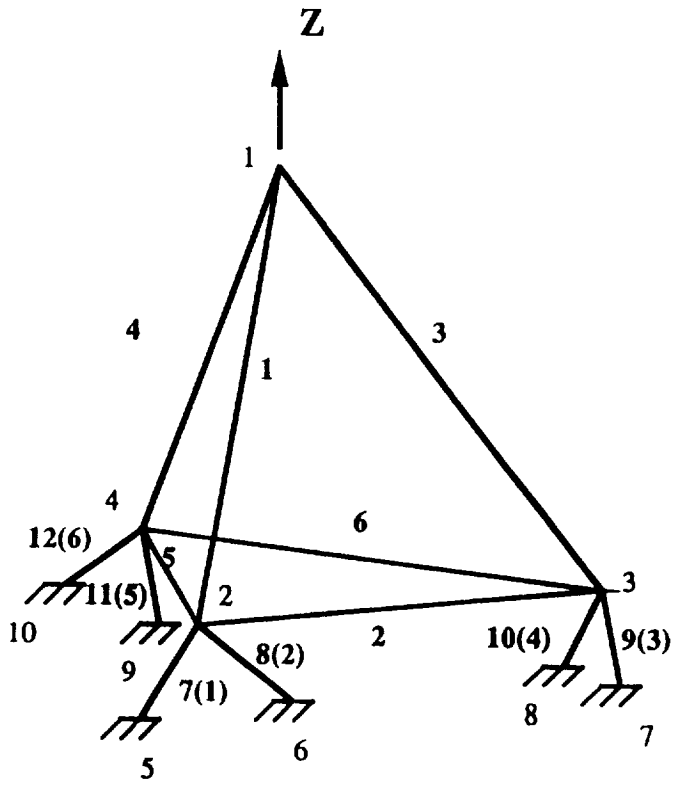

Figure 1: Tetrahedral ACOSS-FOUR structure (actuator numbers are in parentheses)

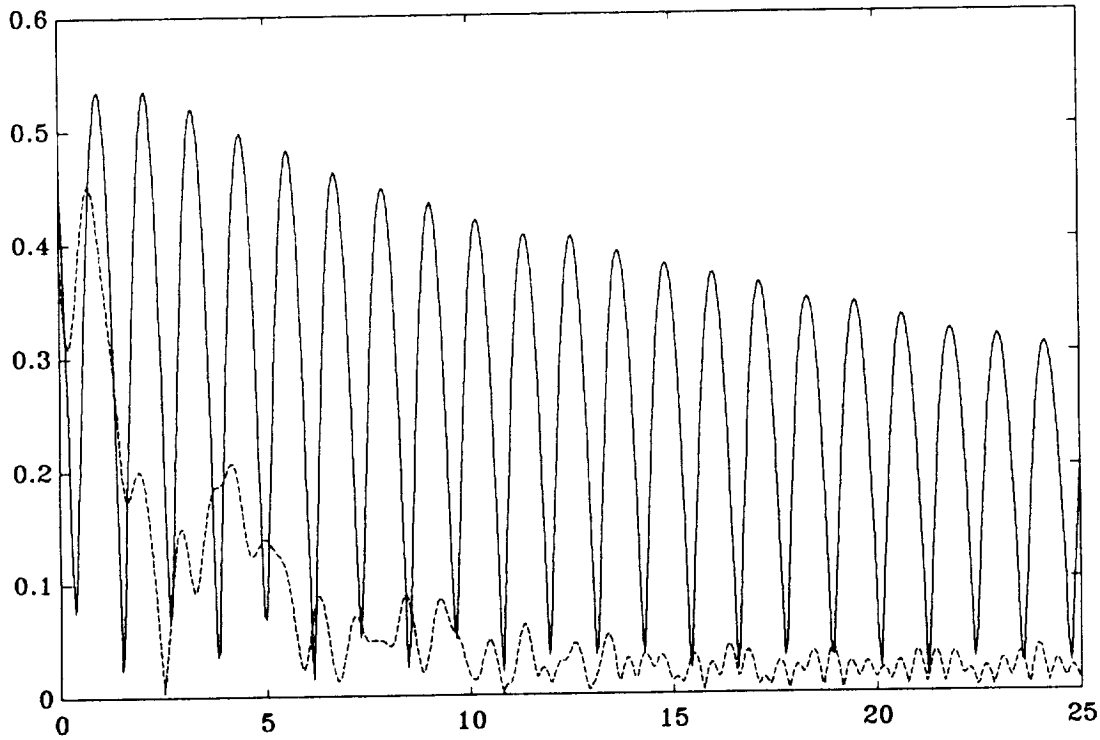

Figure 2a: Line-of-sight error evaluation model responses for the 6^{th} order control design model; initial design A (solid) and optimum design C (dashed)

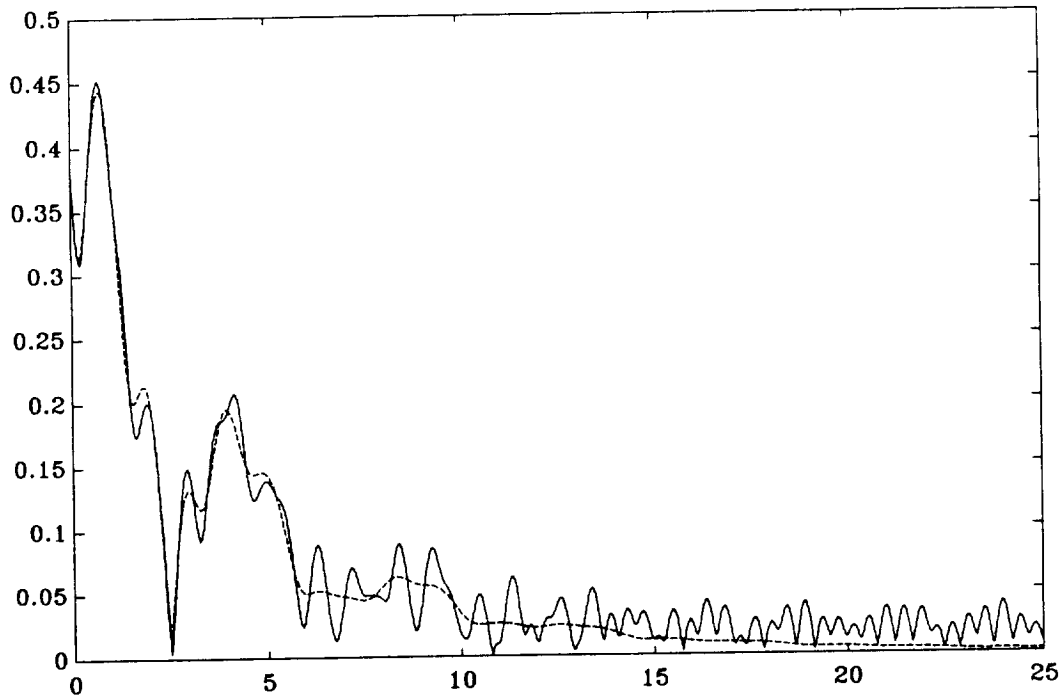

Figure 2b: Line-of-sight error responses of the evaluation model (solid) and 6^{th} order control design model (dashed) for optimum design C

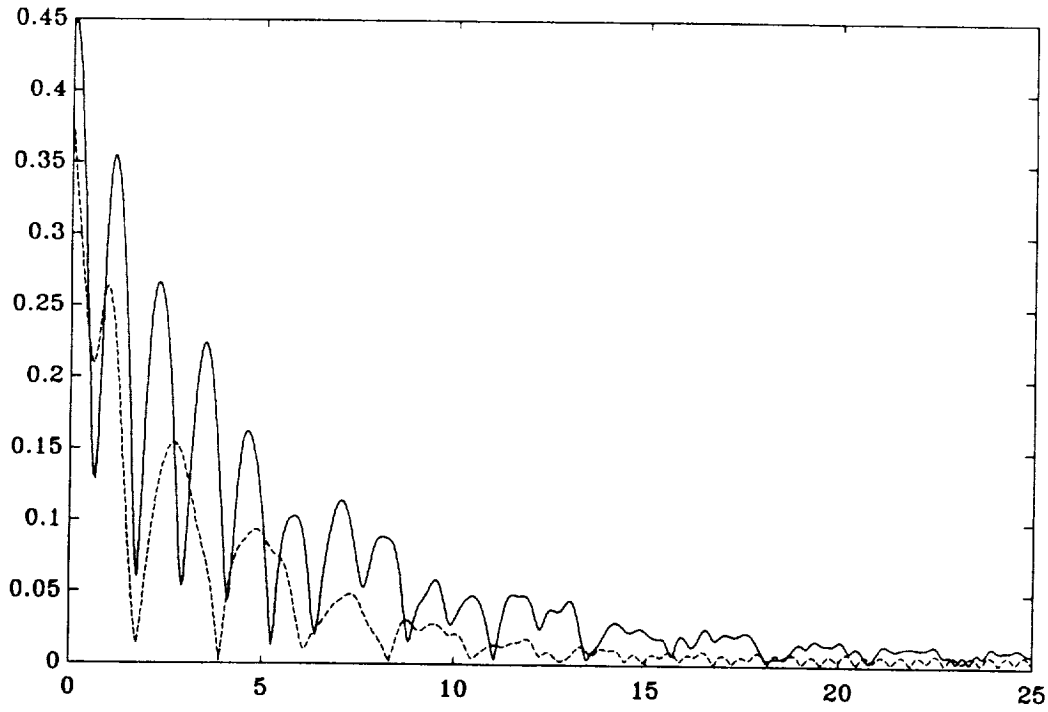

Figure 3a: Line-of-sight error evaluation model responses for the 8^{th} order control design model; initial design A (solid) and optimum design B (dashed)

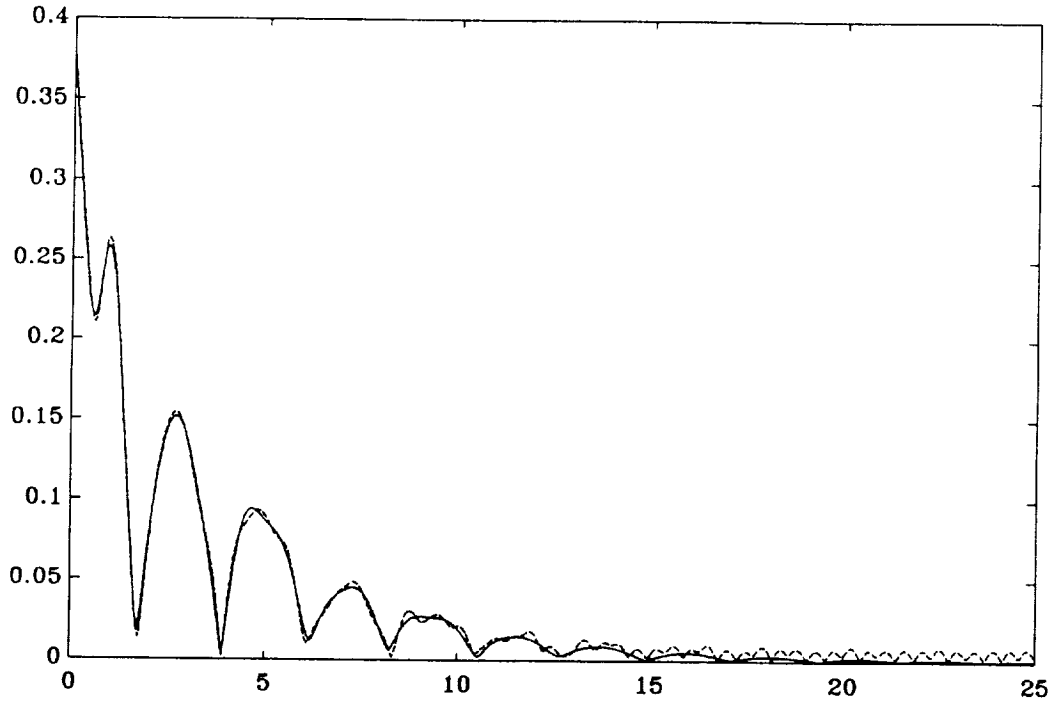

Figure 3b: Line-of-sight error responses of the evaluation model (dashed) and 8^{th} order control design model (solid) for optimum design B

C-SIDE: THE CONTROL-STRUCTURE INTERACTION DEMONSTRATION EXPERIMENT

James B. Mohl and Hugh W. Davis
Ball Aerospace Systems Group
Boulder, CO

INTRODUCTION

The Control-Structure Interaction Demonstration Experiment (C-SIDE) is sponsored by the Electro-Optics and Cryogenics Division of Ball Aerospace Systems Group. Our objective is to demonstrate methods of solution to structure control problems utilizing currently available hardware in a system that is an extension of our corporate experience. The larger space structures with which Ball has been associated are the SEASAT radar antenna, Shuttle Imaging Radar (SIR) -A, -B and -C antennas and the Radarsat spacecraft. The motivation for the C-SIDE configuration is to show that integration of active figure control in the radar's system-level design can relieve antenna mechanical design constraints.

The radar system's effectiveness depends on the success of antenna orientation and structural motion control. Orientation control has been provided by the attitude control system of the supporting vehicle. Figure control has been passive by means of exotic materials, construction and deployment techniques. Active figure control, however, offers advantages from the standpoints of adaptability and enhanced response. For example, equipment-, crew- and maneuver-induced vibrations may be damped or anticipated to both steady the platform and maintain the figure of the radiating surface. Related applications where active structure control can be the final stage of a precision controller are large optical systems and pointing systems.

This presentation is primarily an introduction to the C-SIDE testbed. Its physical and functional layouts, and major components are described. The sensor is of special interest as it enables direct surface figure measurement from a remote location. The Remote Attitude Measurement System (RAMS) makes high-rate, unobtrusive measurements of many locations, several of which may be collocated easily with actuators. The control processor is a 386/25 executing a reduced order model-based algorithm with provision for residual mode filters to compensate for structure interaction. The actuators for the ground demonstration are non-contacting, linear force devices. Results presented illustrate some basic characteristics of control-structure interaction with this hardware.

The testbed will be used for evaluation of current technologies and for research in several areas. A brief indication of the evolution of the C-SIDE is given at the conclusion.

CURRENT SYNTHETIC APERATURE RADAR SYSTEM

The challenges when defining a spaceborne radar system are observing the packaging and launch weight constraints while maintaining precise geometry of the operational antenna. The current approach is to use very stiff antenna panels and to maintain strict alignment and thermal control. The fixed arrays are relatively heavy with sophisticated mechanisms for deployment from their launch envelopes. An example of the current technology is the Radarsat spacecraft shown in figure 1.

Radarsat is a Canadian Space Agency program to operate a synthetic aperature radar (SAR) satellite for research and commerical remote sensing applications. The C-band radar module, built by Spar Aerospace, has an antenna which is 15 meters tip to tip, 1.4 meters wide and supported from behind by an extendible support structure. The radiating surface is a series of waveguides which give it a steering capability in the elevation (cross-track) direction. Since the waveguides provide substantial structure, the operational antenna is quite stiff. The antenna's in-plane and out-of-plane bending modes occur near 4.2 and 5.2 Hz. The solar arrays are less substantial with out-of-plane and in-plane bending modes near 0.3 and 0.9 Hz. The attitude control system (ref. 1), in the bus module built by Ball Space Systems Division, has sufficiently low bandwidth to avoid interaction with the solar arrays and yet provides pointing stability to 0.1 deg. The primary attitude determination system provides attitude knowledge to better than 0.05 deg to facilitate registration of images by ground processing.

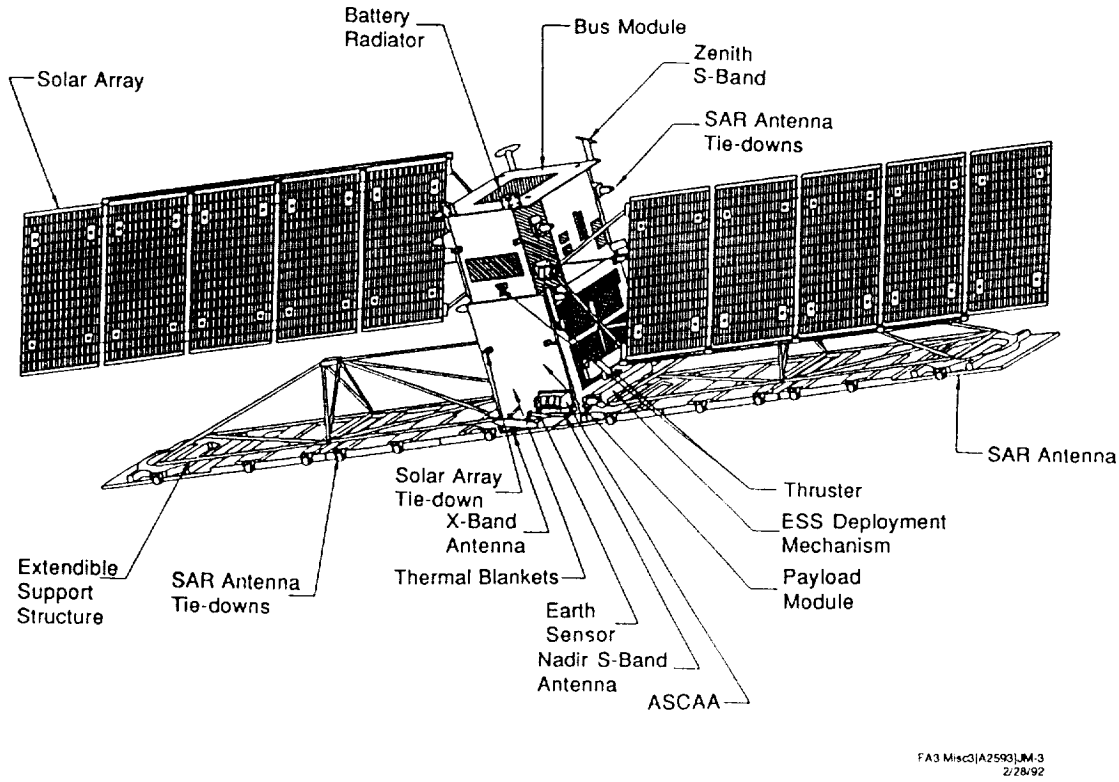

Figure 1. Radarsat uses precision deployment mechanisms and material stiffness to maintain antenna figure and strict attitude stability requirements for orientation control.

ACTIVE FIGURE CONTROL BENEFITS

A functional diagram for anSAR system is shown in figure 2. Microwave energy is generated, passed through the transmitters and phase shifters and radiated by the antenna to illuminate the target. The return energy is collected by the antenna, passed back through phase shifters and receiver and saved in mass storage. Some image processing is done on-board but much of the post-processing is a ground operation.

Benefits accrue from integration of active figure control through relief of antenna and spacecraft mechanical design constraints. A physically large antenna can have finer control to produce a more planar outgoing wavefront; shaping techniques to lower the sidelobes of the beam used in ground-based radars can be considered. Static misalignments at hingelines or distortion of panels can be readily removed; when extreme mechanical precision is not required, on-orbit assembly is an option. Low frequency, dynamic distortions can also be removed, such as those due to thermal shocks passing through an eclipse; this would reduce the need for strict thermal management. Lightweight construction or novel deployment options can be considered. Disturbance from the attitude control system, equipment or crew motion can be rejected so that operational restrictions can be relaxed.

The figure control system is independent of the radar function as shown by the loop at the bottom of figure 2. The sensors and actuators interface the antenna to the core structure. The figure control system maintains the position of the antenna relative to the core.

- Potential benefits
  - Larger antenna
  - Correct static alignment
  - Compensate thermal shock
  - Lighter construction
  - Lower precision mechanisms

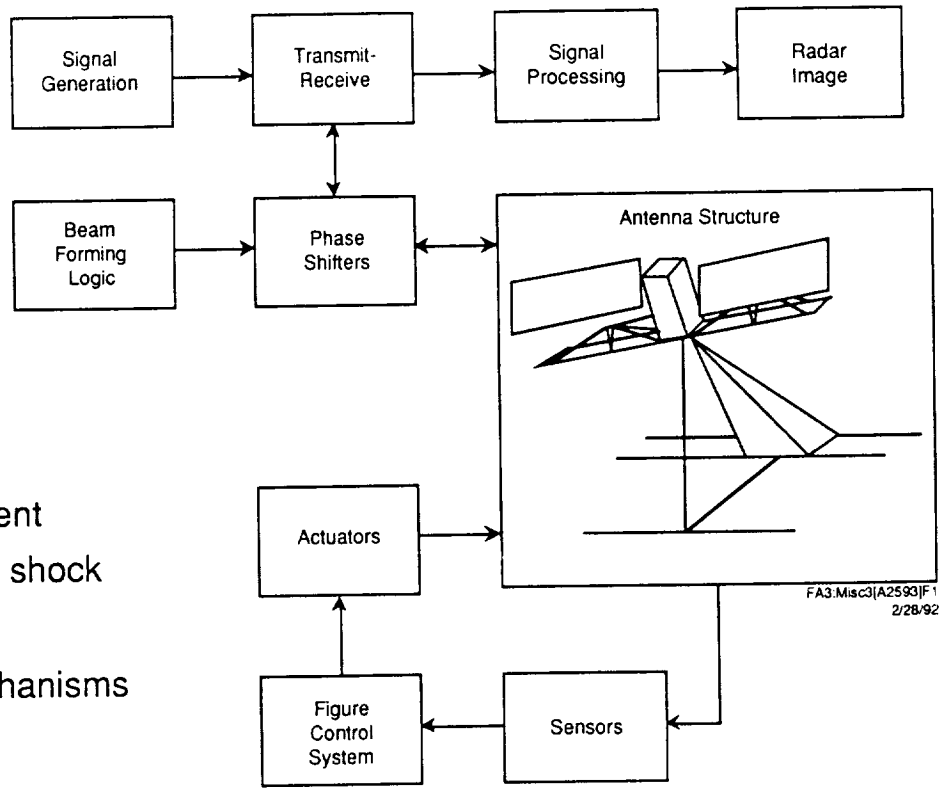

Figure 2. Integration of figure control in the radar system definition relieves mechanical design constraints.

ENHANCEMENT FOR DISTRIBUTED ELEMENT RADAR SYSTEM

The radar platform contains the basic features of control-structure interaction that are the motivation for C-SIDE. However, there is an extension of the figure control capability peculiar to an antenna with a distributed element architecture. Control beyond the attempted correction of physical figure is possible because the radar system can use the results of the control process in a second path, shown in figure 3. The outgoing wavefront would become planar to fractions of a wavelength.

The figure control system uses a modal state estimator that can provide figure error estimates over the entire antenna face. The individual radiating elements receive phase shift commands appropriate for the estimated error at their physical position on the surface. Phase shifts of 1/32 of a wavelength are practical; that corresponds to a linear distance of 10 to 1 mm for an L- to X- band.

The spacecraft's attitude determination system provides the orientation of the core structure and defines the antenna boresight. This information could be used as other input to the beam forming logic to provide wide angle steering. Time delay in the transmission from widely separated portions of the array allows steering away from the antenna boresight. This has implication in the spacecraft design by allowing the antenna to be operated from a convenient attitude rather than being articulated by the vehicle.

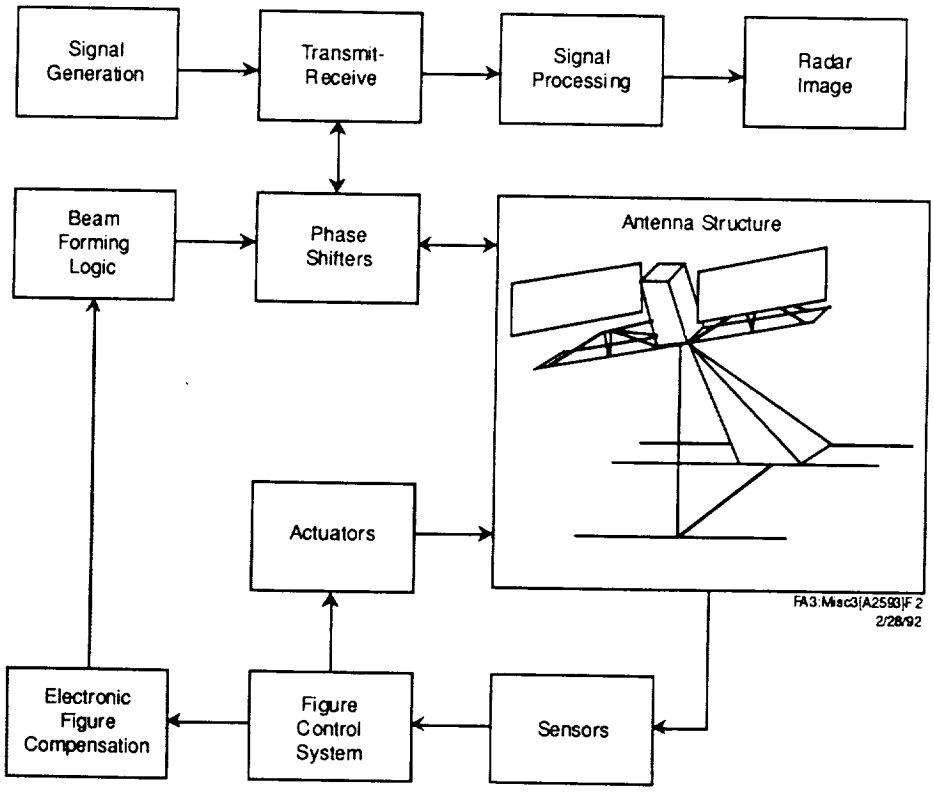

Figure 3. Figure control system facilitates on-board electronic compensation by the radar system for enhanced performance.

C-SIDE OVERVIEW

In the initial demonstration, we are assembling one-half of an antenna-like structure which is cantilevered from a massive central body as illustrated in figure 4. The "antenna" is a thin flexible facesheet one meter in height, three meters in length and 1.5 millimeters thick. A graphite/PEEK truss is placed behind the facesheet to act as a reaction structure. The figure control system is composed of a pair of single-axis Remote Attitude Measurement Systems (RAMS), up to ten linear force actuators and a single digital processor.

The physical size of our "large structure" is modest to reduce laboratory space requirements but is scaled to provide features modelling the large structure problem. The frequencies for the controlled surface start below 1 Hz. The low frequencies have the added advantages of reducing computational loading on the control system processor and lessening the impact of air damping in the laboratory environment. The reaction structure is specially fabricated to have bending frequencies starting in the neighborhood of the facesheet's sixth mode.

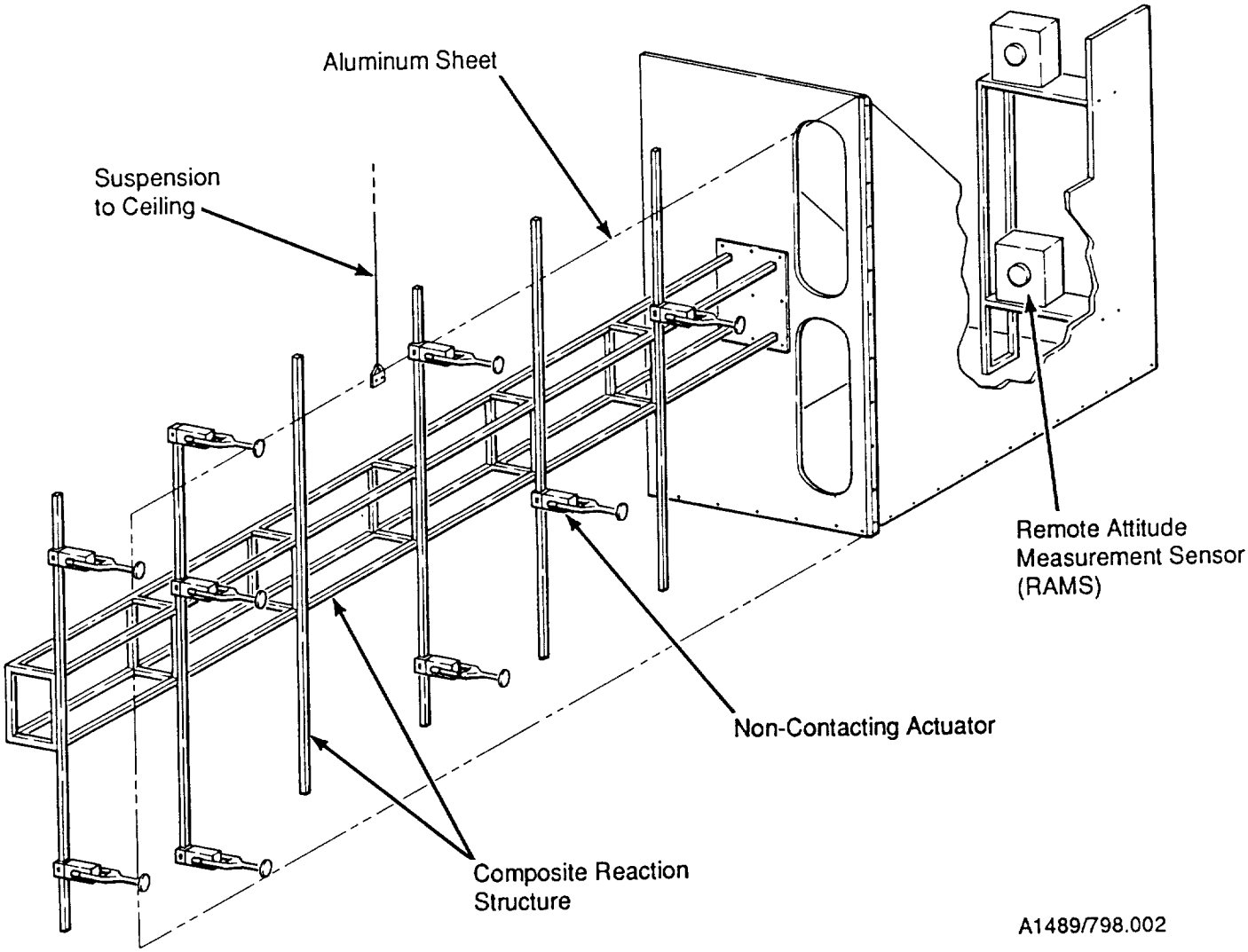

Figure 4. The C-SIDE is representative of a lightweighted spaceborne radar system that requires figure control of a thin, flexible plate supported by a structure from the rear.

FUNCTIONAL BLOCK DIAGRAM

The block diagram in figure 5 indicates the layout of the equipment and control system. The displacements of several facesheet locations are obtained by the RAMS by viewing targets on struts. The RAMS data is transferred through the interface box to the system controller. The controller interprets the RAMS data, performs the digital control algorithms and transmits the calculated actuator commands. The commands are distributed to the remote actuator drivers through the interface box. The actuators create motion in the facesheet and react on the reaction structure.

The interface box contains the force command decoder and the ±15 volt DC power supply. Its front panel allows access to the computer's analog input/output channels for use with the structural dyanmics analyzer. The ±24 volt DC actuator drive power is supplied externally.

The system controller is an 80386 with a coprocessor operating at 25 Mhz. There are three communication support cards. The digital I/O card is required for communication with the RAMS. One digital to analog channel is multiplexed for commanding the remotely located actuator electronics. Five other digital to analog channels are available for real-time display of selected "probe" points within the control algorithm. An analog to digital card allows injection of analog test signals and command waveforms into the digital system. MATLAB is available for control system design, data post-processing, analysis and documentation. Programming for the executable programs is done in Microsoft C 6.0.

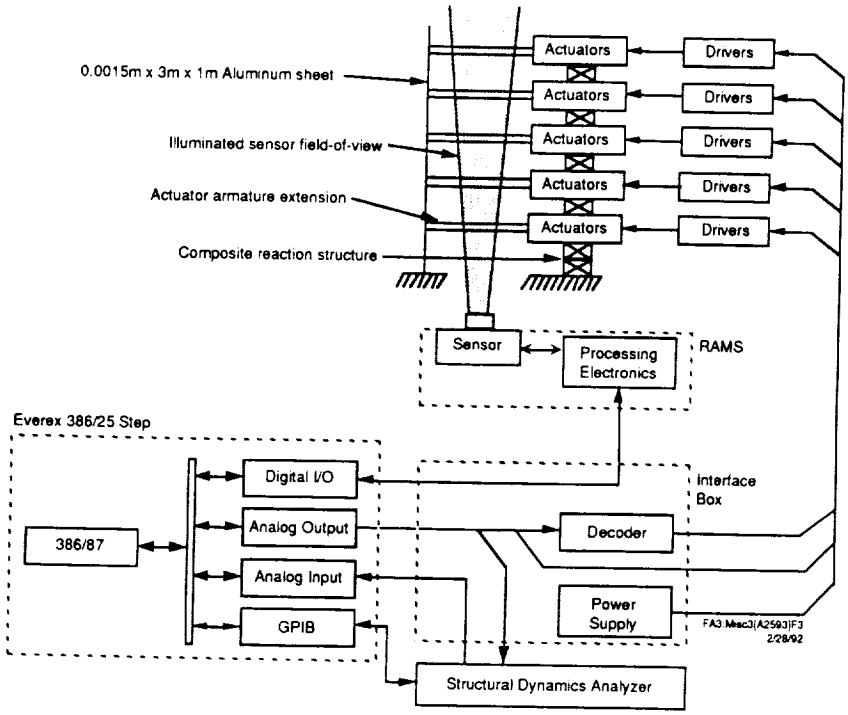

Figure 5. The initial C-SIDE provides physical figure control for the passive facesheet using a distributed array of actuators.

ASSEMBLED HARDWARE

Our control objective is to maintain the facesheet position, as measured by a remote sensor, by actuating against a well-behaved "reaction base" employing active or passive damping. Stiffness of the reaction structure provides one component of the reaction base with a passive "recentering" action. The mass of the reaction structure, augmented by the mass of cabling and drive electronics placed along its length, provides an inertial component to the reaction base. The reaction structure is placed well behind the facesheet to reduce interference with the RAMS field of view and to provide a standoff for actuator mounting. Abnormal stiffness is not to be required in the reaction structure as it is only necessary to maintain the actuators in the vicinity of their nominal positions.

Obtaining a stiff structure would not be a problem for this size of experiment. To get a better scaling for the large structure problem, a unique attribute of composite material fabrication is used to intentionally reduce material stiffness and lower the bending frequencies. The lamination orientation of the fiber is changed from alignment with the truss member axis to a 45 deg offset which reduces the modulus from 10 Mpsi to 2 Mpsi. The truss bay dimensions are small also, for appropriate scale: 0.11 m wide by 0.50 m long by 0.16 m high. The resulting modes shapes are: bending in the vertical plane at 2.8 Hz, first and second torsions about its long axis at 3.3 and 8.4 Hz, and bending in the horizontal plane at 4.0 Hz. The reaction structure is shown in figure 6. It is supporting its own mass of 11 kg and 65 kg of other components.

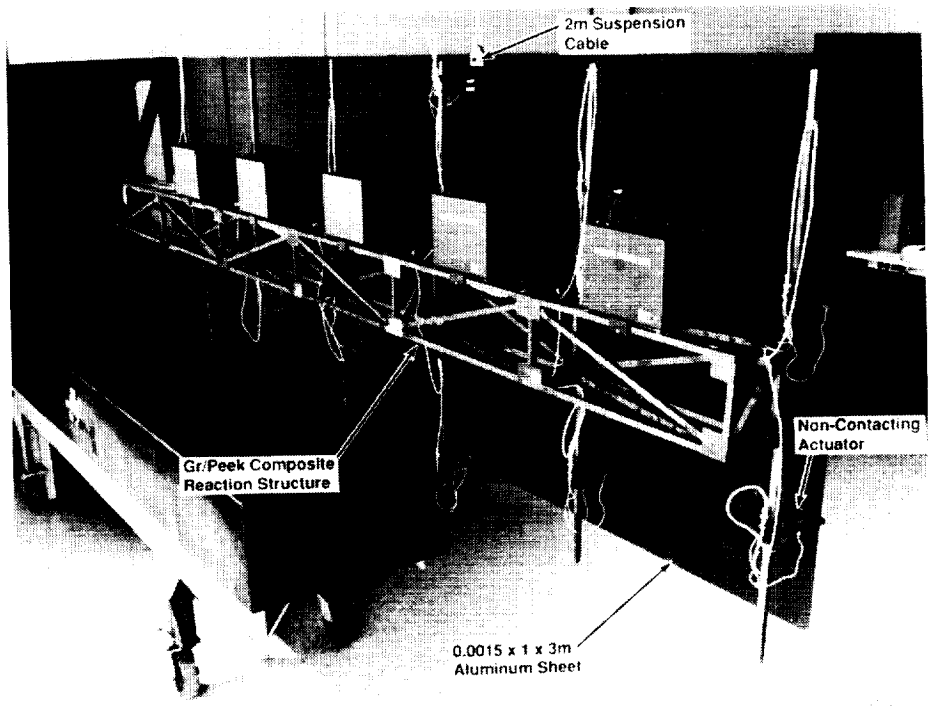

Figure 6. This view of C-SIDE shows the facesheet backside, reaction structure, actuators, drive electronics and cabling.

FACESHEET ACTUATOR

The non-contacting actuators shown in figure 7 reduce damping of the facesheet motion and avoid the nonlinear effects of stiction. The heavy, iron section (the stator) is attached to the reaction structure. The iron completes the magnetic circuit for two samarium cobalt magnets to establish a fixed field across the two air gaps. The light, coil section of the actuator (the armature) is attached to the facesheet by a yoke. The actuators produce force proportional to the coil current in the direction normal to the facesheet. The range of motion is ± 17 mm. The lateral and longitudinal clearances were modified in-house but are as small as practical to avoid compromising the actuator's force capability. Restraint of the facesheet motion is provided by the captured armature configuration. Overtravel snubbers protect the actuator element from excessive disturbance inputs (from overzealous observers). The force output capability is 2.5 N.

The armatures are mounted on spreader bars extended in the vertical direction from the reaction structure. The actuator locations are adjustable along the spreader bar. The connection of the armature to the facesheet is a slotted hole that allows small lateral adjustments.

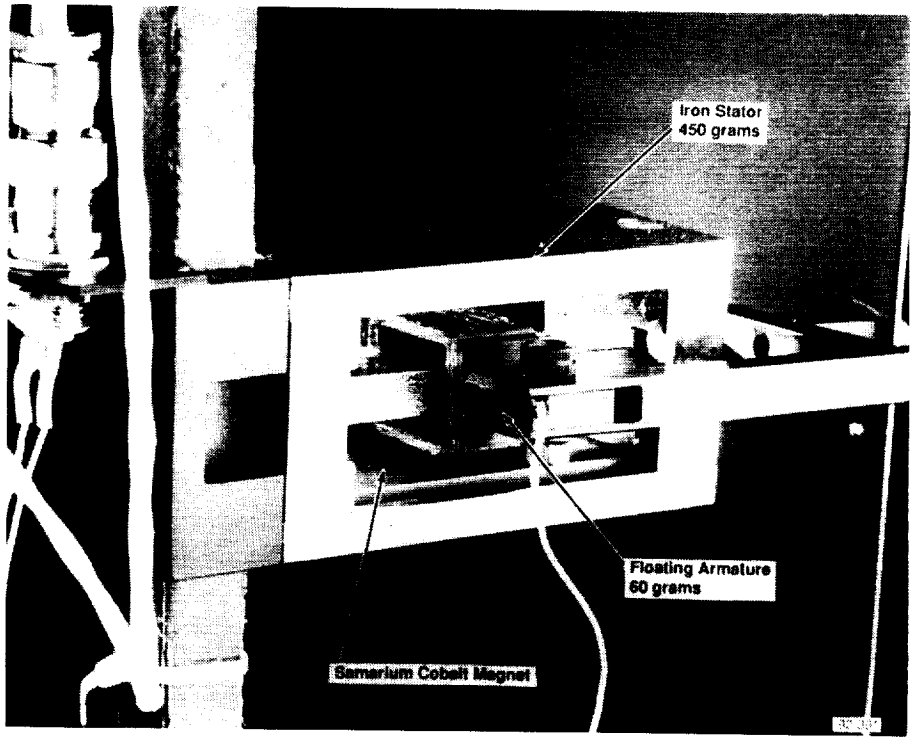

Figure 7. Non-contacting actuator reduces damping for demonstration purposes.

ACTUATOR DRIVE ELECTRONICS

Five remotely located decode and drivers electronics units are commanded from the control processor. Actuator commands are output in two parts. A single digital to analog converter channel transmits amplitude. A digital code is transmitted simultaneously to select the actuator drive circuit which reacts to the command. The five remote driver boxes each support two actuators. Each box contains sample and hold circuitry, to maintain the force command amplitude between updates, and linear drive, current loop electronics to energize the actuators. Figure 8 shows the closed loop bandwidth of the current loop is 32 kHz; actuator gain and phase errors can be ignored since our frequency range of interest will be below 100 Hz.

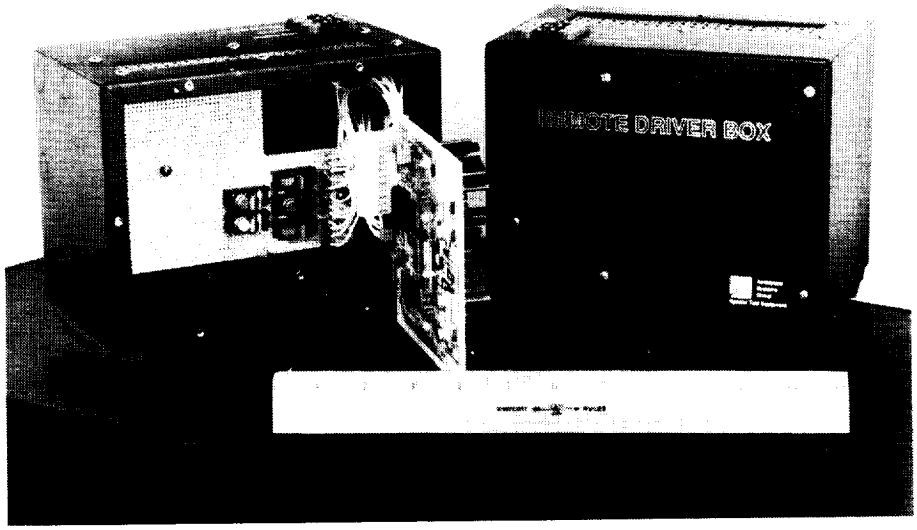

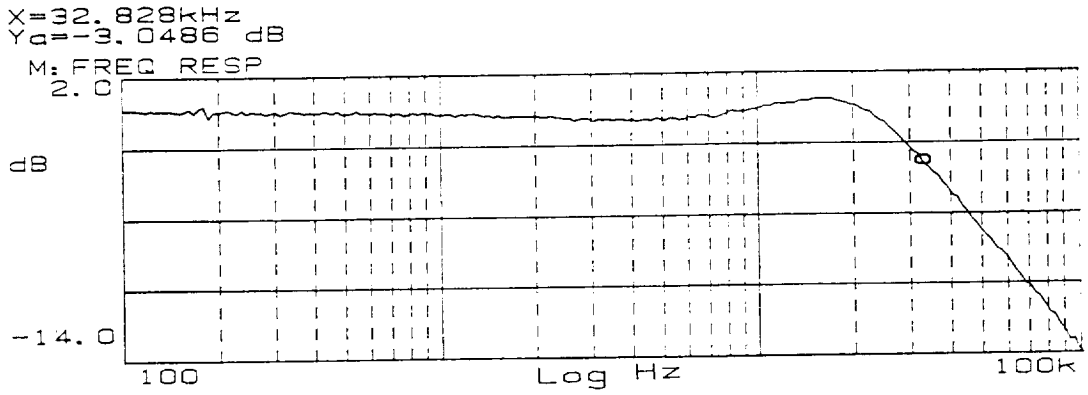

Figure 8. Actuator drive reponse is unity gain for frequencies below 10 kHz. No adjustment for actuator dynamics is required in system modelling.

REMOTE ATTITUDE MEASUREMENT SYSTEM

Measurement of the facesheet surface figure is required for feedback to the control system. RAMS can provide data for a small number of target locations at a high rate (to capture local, high frequency motions) or data for many targets at a lower rate (for identification of distributed effects over the entire structure). The passive retro-reflective target tape used by RAMS is lightweight and can be located on the actuator armature. It eliminates the added complexity and weight of power and signal lines to each sensor location.

The RAMS optics are positioned to view most of the facesheet backside and a portion of the reaction structure. A single-axis RAMS is sufficient for this case since only facesheet-normal translations are of interest; the location of targets in the other two dimensions on the facesheet can be measured. An operational schematic for RAMS is shown in figure 9. The view shown would be looking down from the ceiling for the C-SIDE installation. The RAMS boresight is at a high angle of incidence so that the field of view fans out over a large target area. The resolution in the sensitive direction varies along the facesheet. The worst condition is at the free end, farthest from RAMS; motions of 0.015 mm are resolvable there. Targets on the facesheet are placed on the actuator armature yokes. Targets on the reaction structure are also provided for system identification. The view looking out of the RAMS porthole is shown at the right of the figure.

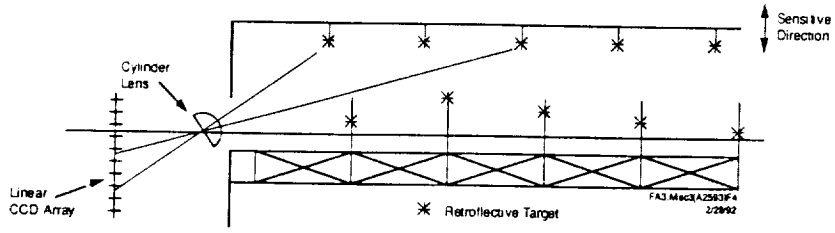

Exaggerated Top View

- Insensitive to vertical target placement
- Resolution is most coarse for distant targets

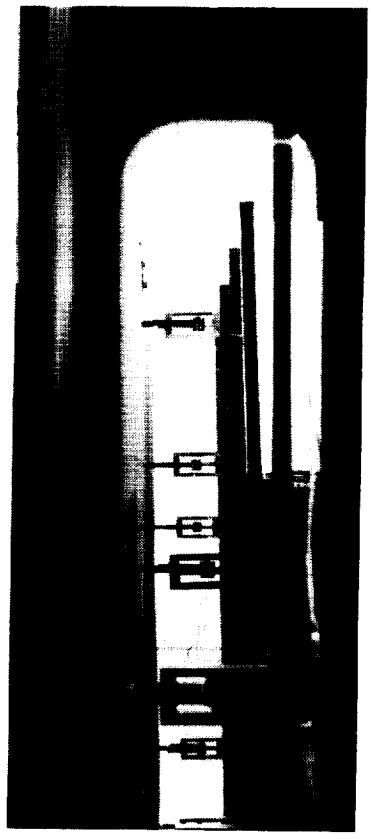

Figure 9. Each single-axis RAMS measures horizontal position at actuators and locations on the reaction structure.

The orientation of the facesheet is chosen to reduce modification to the familiar low frequency "cantilevered modes". However, this requires the facesheet to be supported along its length to prevent buckling due to gravity. Lateral stiffness of the support is reduced by using a long suspension wire with only small displacements being allowed.

The facesheet is solid aluminum stock, rather than honeycomb, expressly to create low frequency modes. The mass of the facesheet is less than 14 kg and needs only a single support wire at 2 m from the base. The support wire length is limited by the lab ceiling height to about 2 m. NASTRAN results for this thin, constrained, cantilevered beam under the influence of gravity are given as mode shapes in figure 10. The first and second modes are predominantly cantilevered beam modes occurring at 0.28 and 0.89 Hz. The third mode is torsion about the longitudinal axis at 1.08 Hz. The fourth mode is another beam mode at 2.55 Hz. The fifth and sixth modes are torsional.

Note that compensation for gravity has a major qualitative effect on the experiment. If the facesheet were in zero-g, NASTRAN would predict the first beam mode at 0.15 Hz and the first torsional mode at 0.8 Hz. The support wire adds significant resistance against the first beam (effectively quadrupling the stiffness) and causes a neutrally stable torsional mode to become a stable double-pendulum-like mode.

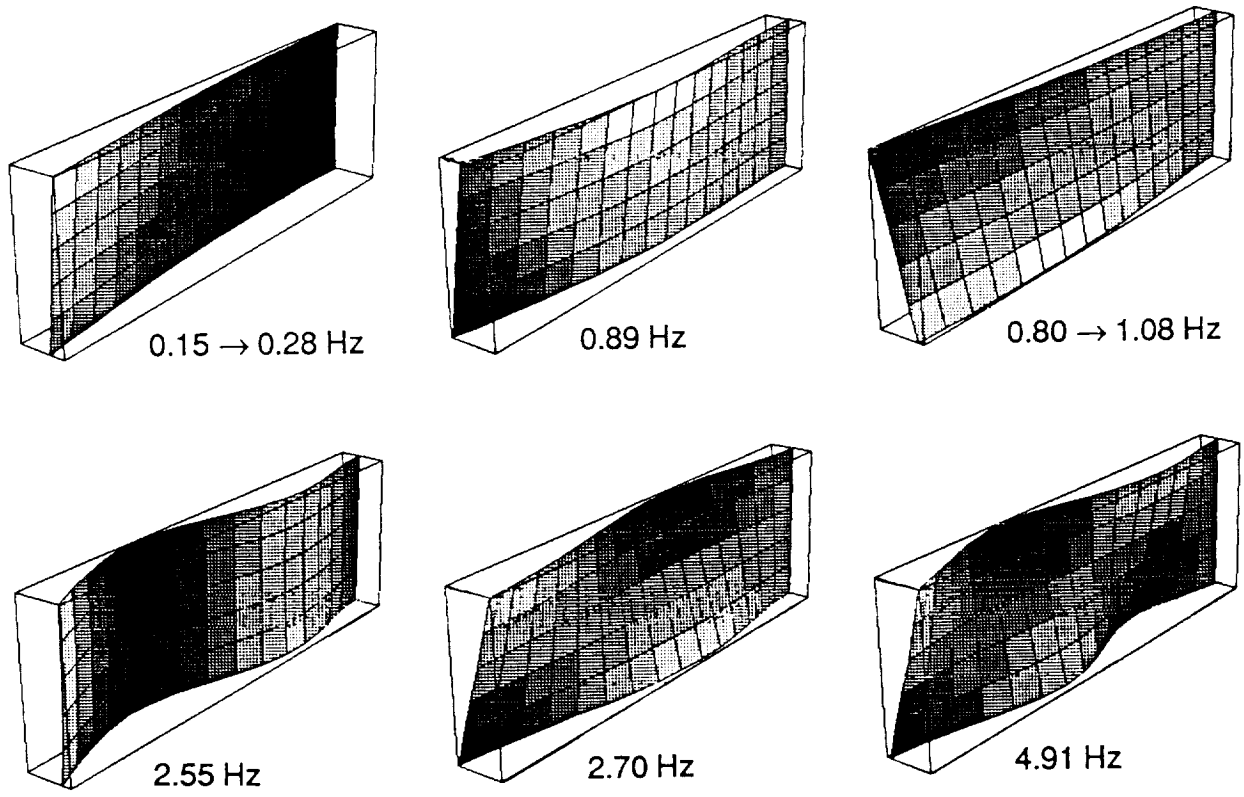

Figure 10. Suspension cable modifies the first cantilever and torsional mode frequencies most significantly.

REDUCED ORDER MODEL-BASED CONTROL

The control algorithm is based on a reduced order model of the significant vibration dynamics of the facesheet represented in modal coordinates. The definition of "significant" is determined by the system performance requirements. For the purposes of demonstration, the control actions are applied so that disruptive interaction with unmodelled flexible dynamics occurs. It is subsequently suppressed to restore desirable performance.

The context of the ROM controller is given in figure 11. The system to be controlled includes the actuator and sensor dynamics as well as those of the structure. The ROM controller takes a subset of the system dynamics, which must include any open-loop unstable modes, to be used in an state estimator model. It receives a set of measurements from the system and returns a set of actuation commands. A by-product of the process is its estimate of physical measurements at the sensors (and possibly other locations) for the modelled modes. The states of the estimator can be given an external reference command to position the system. This general configuration can be viewed as the control system for the figure of a surface, the pointing of a gimbal set, or the rigid body attitude of a spacecraft.

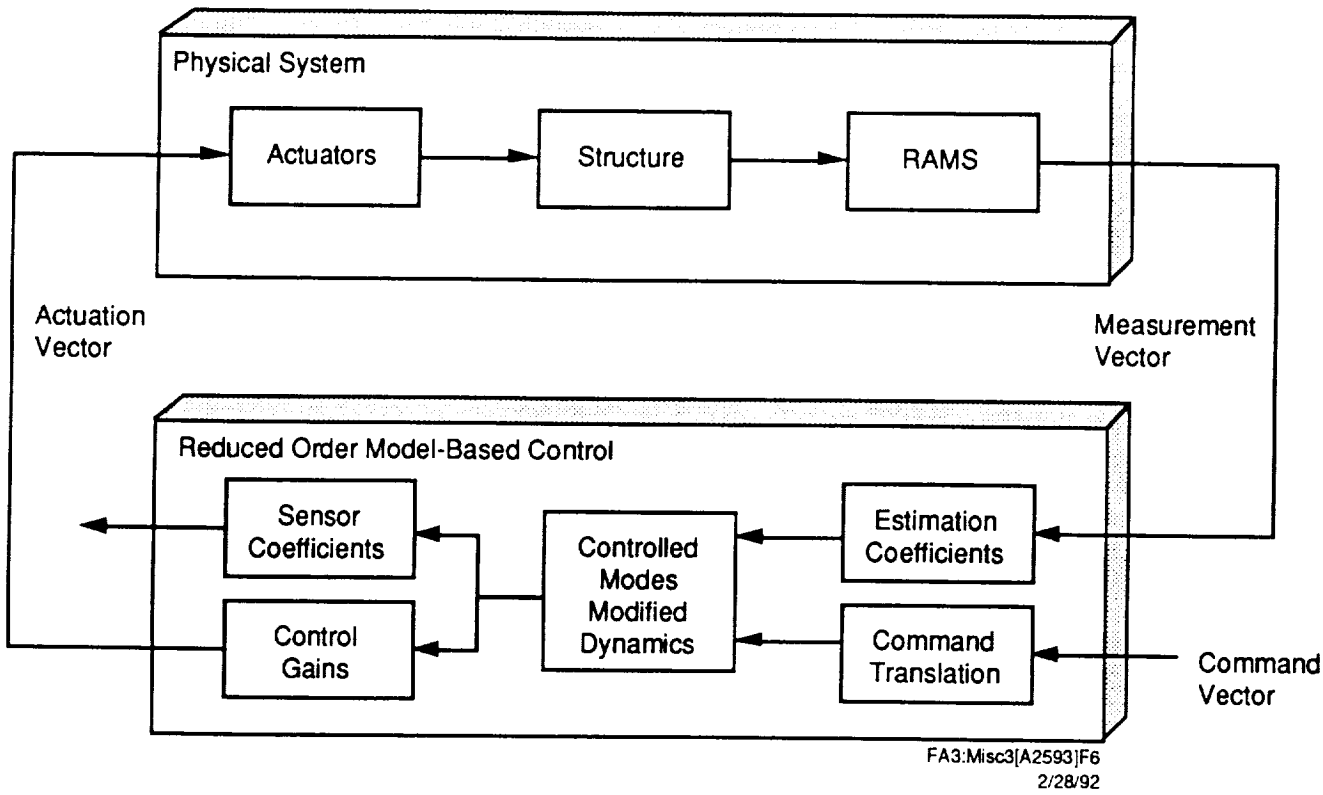

Figure 11. Reduced order model-based (ROM) control processes sensor measurements to define actuation commands.

CONTROL FOR FIRST TWO MODES

The performance objective for the initial demonstration is to increase the response frequency and damping of the first two beam modes of the facesheet. MATLAB's pole placement routine defines gains for the ROM controller. The algorithm selects the actuator and sensor locations with the highest modal gains. To control the first two modes, two collocated actuator-sensor pairs are used: at the free end of the facesheet and at the bottom below the suspension cable.

Pole placement is so aggressive in this case that it gives a pathologically interesting result. The root locus for the combined controller and structure model is shown in figure 12 with the control gains being varied from 0 to 100 percent of their design values. The first seven modes of the facesheet are used with a natural damping of 1 percent assumed. The first and second modes begin migrating in the desired direction. The third mode is immediately driven unstable. The interaction with unmodelled dynamics at higher gains causes the controlled modes to move to the right and destablizes the first mode. Some damping is applied to higher frequency cantilever modes while higher frequency torsional modes are slightly destabilized.

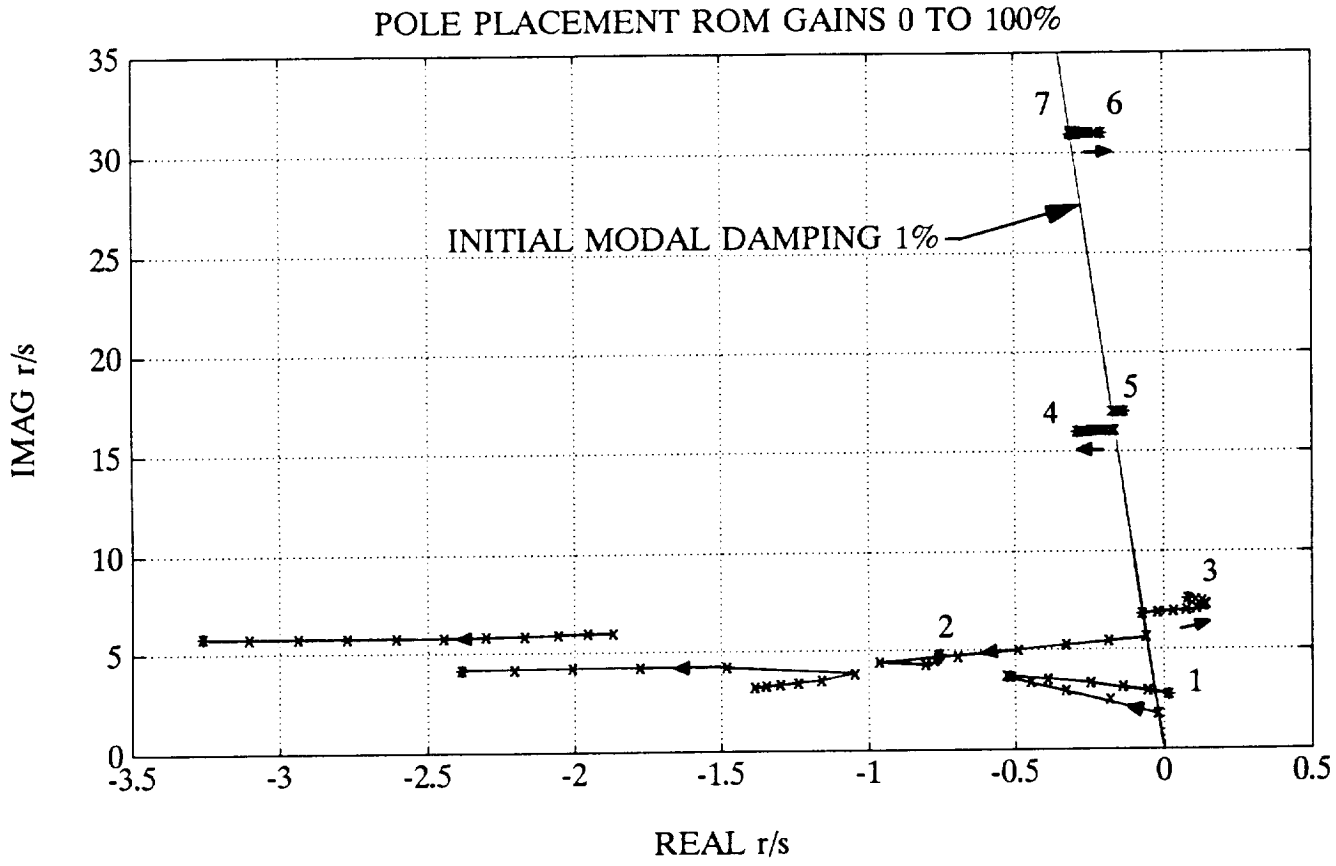

Figure 12. ROM control is intended to add damping and stiffness to the first two modes. Interaction with dynamics not modelled in the controller causes instability in both the first and third mode.

ROM CONTROL ALONE

The response for this ROM controller alone is unstable as expected. The result in figure 13 is the response to a 1 N, 0.02 sec pulse applied at the free end of the facesheet, 30 cm below center. This location drives all the cantilever and torsional modes well. This same perturbation is used for the other transient cases to follow. The sensed position and input locations are shown below.

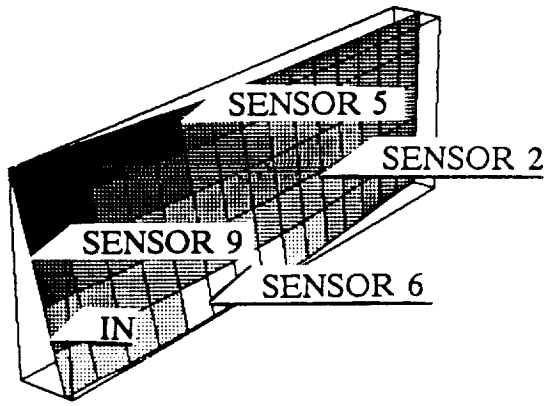

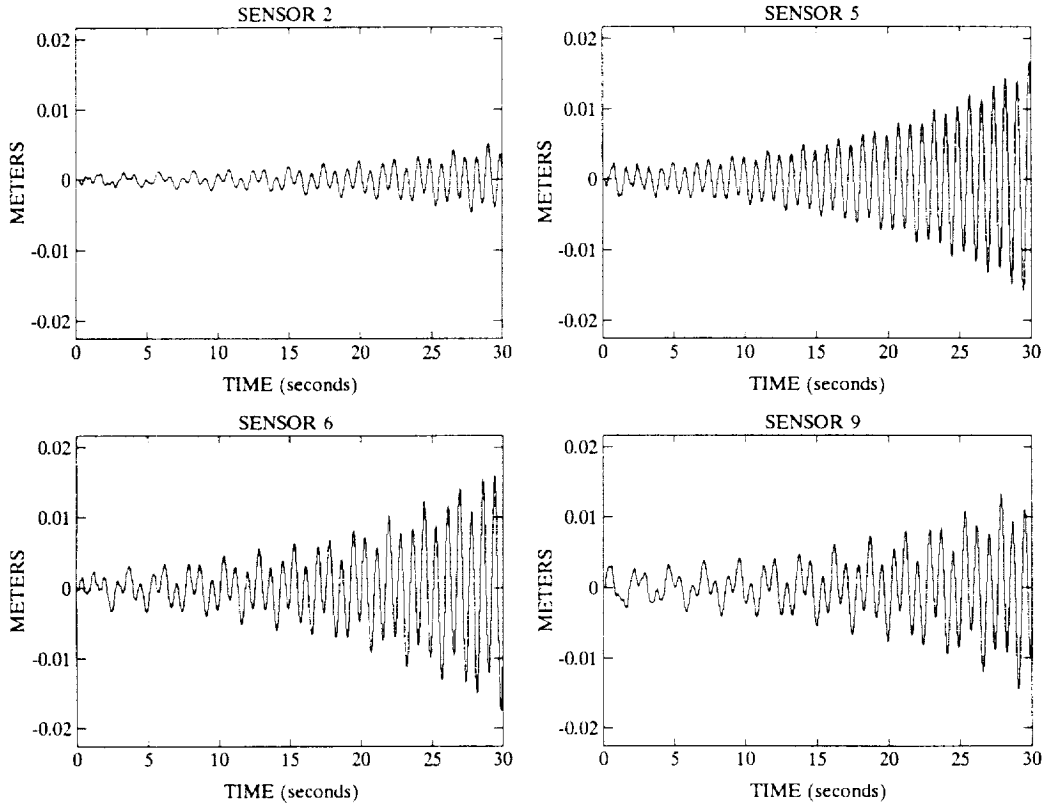

Figure 13. The pole placement design ROM controller alone cannot recover from a perturbation.

RESIDUAL MODE FILTER

The ROM design ignores the effect the control system may have on the rest of the modes of the structure, i.e., the residual system. As was shown, it is possible for some small number of the residual modes to be driven unstable by the ROM controller. The residual mode filter (RMF) is introduced at this point to correct the problem (ref. 3). The RMF is added in parallel to the controlled system, as shown in figure 14, to process the commanded control action and define expected responses at the sensor locations. The signal is subtracted from the incoming sensor measurements, having the effect of opening the feedback path for the destabilized modes. This action returns the destabilized modes to their uncontrolled, stable response character. The RMF signal is well-phased to actual motions and does not suffer from the phase error introduced by a series notch-filter.

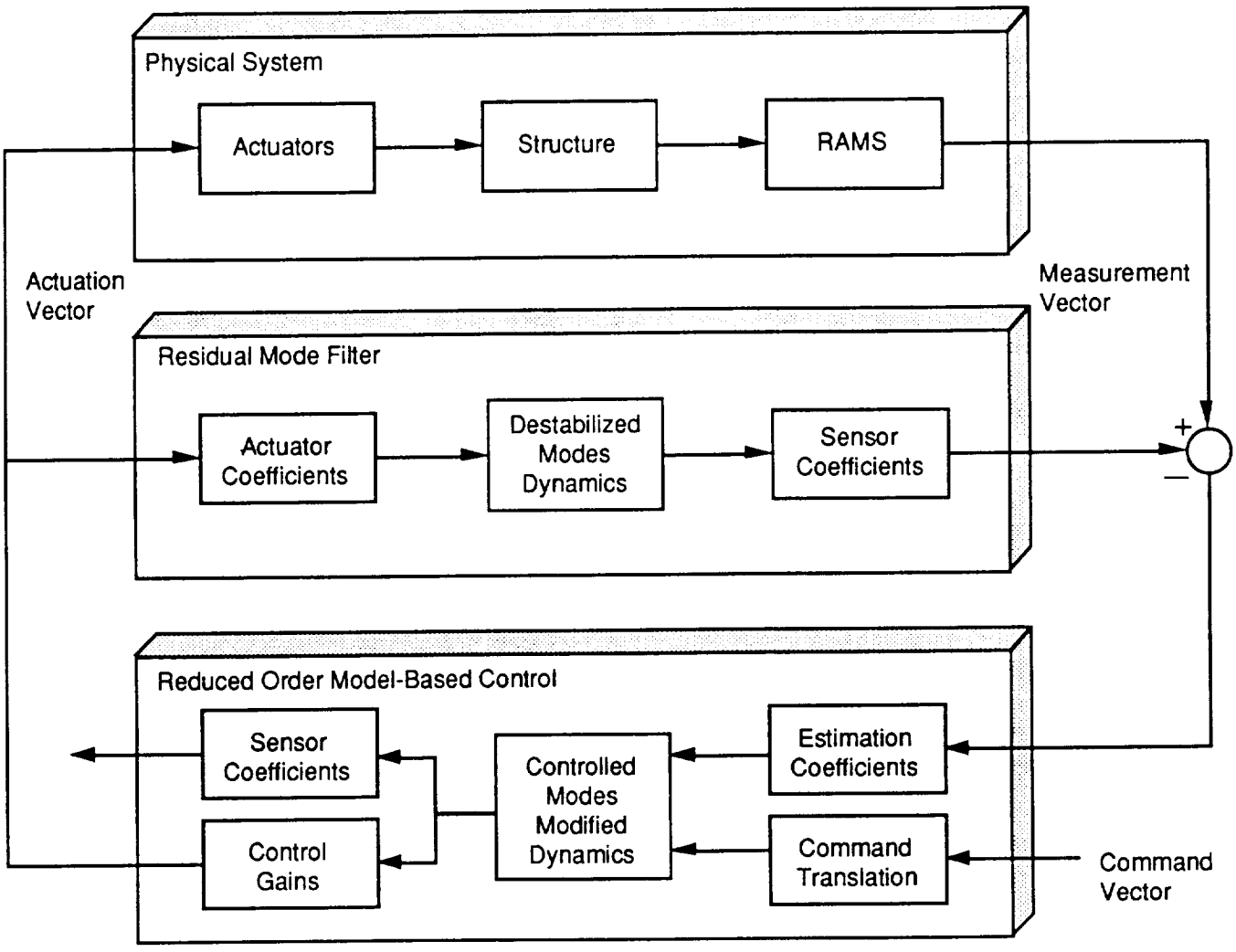

Figure 14. Residual mode filter (RMF) removes destabilizing interaction with unmodelled dynamics.

The root locus for inclusion of the RMF in figure 15 shows the third mode returns to its uncontrolled location. Removal of the strong third mode interaction allows the controlled structural modes and the state estimator poles to migrate toward their intended positions. In general, these roots approach, but do not achieve, the locations specified in the ROM control design. This is due to the remaining interaction with stable, uncompensated, high frequency modes. This is not usually a notable discrepancy because the interaction is seldom so severe.

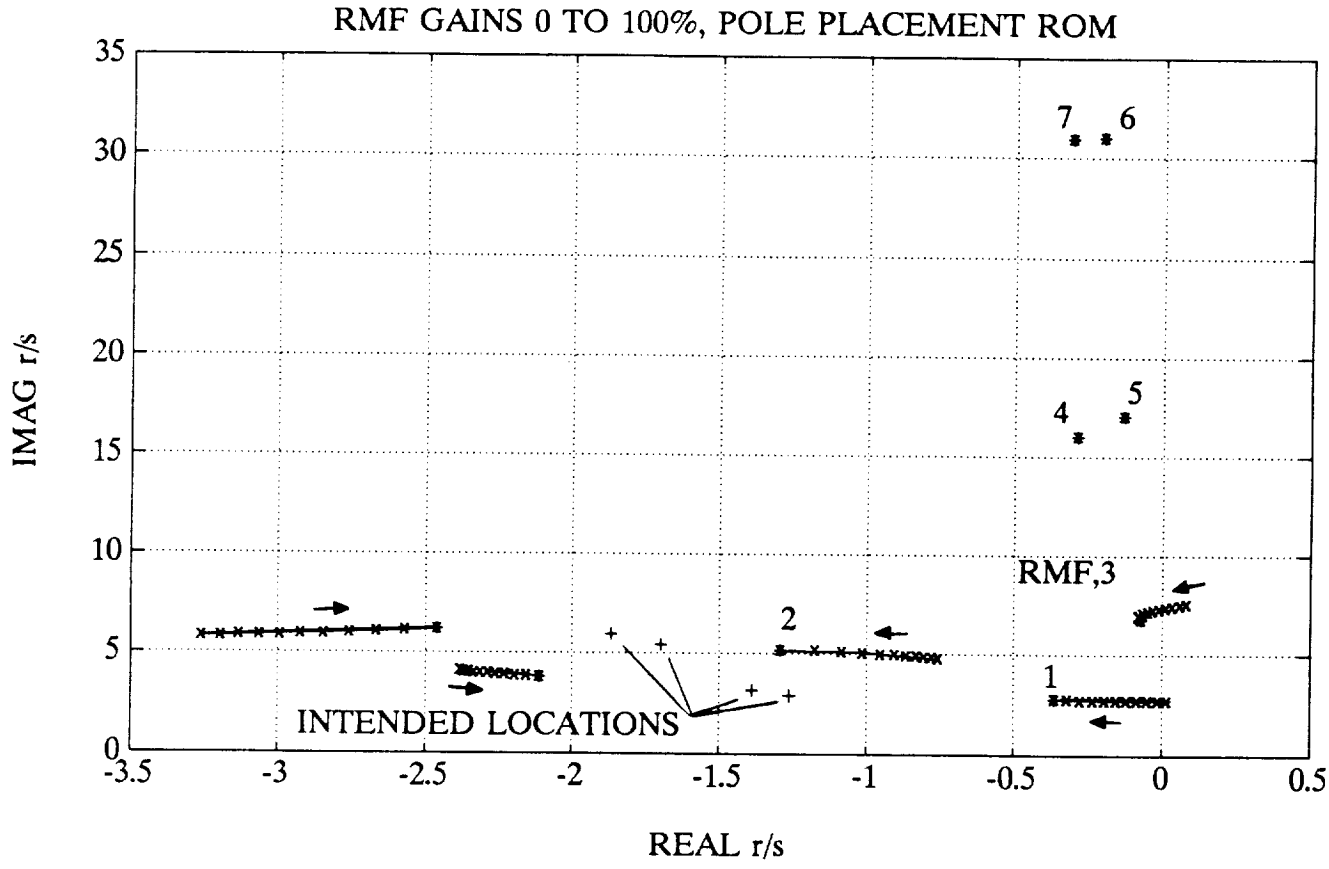

Figure 15. The RMF returns the third mode to its uncontrolled character and allows the first mode to become stable.

RMF REMOVES INSTABILITY

The response given in figure 16 is for the same perturbation as before. It is stable now but the performance is hardly acceptable. This result motivates a second design that includes control of the third mode.

This example is included as a reminder that residual modes can be driven by the ROM control. For the present case, the second mode control frequency is essentially the same as the uncontrolled third mode. Energy used for damping the second mode is also input to the third mode. The amplitude of the third mode excursion continues to increase until the control input for the second mode settles. Residual mode motion persists until it can be damped by material properties.

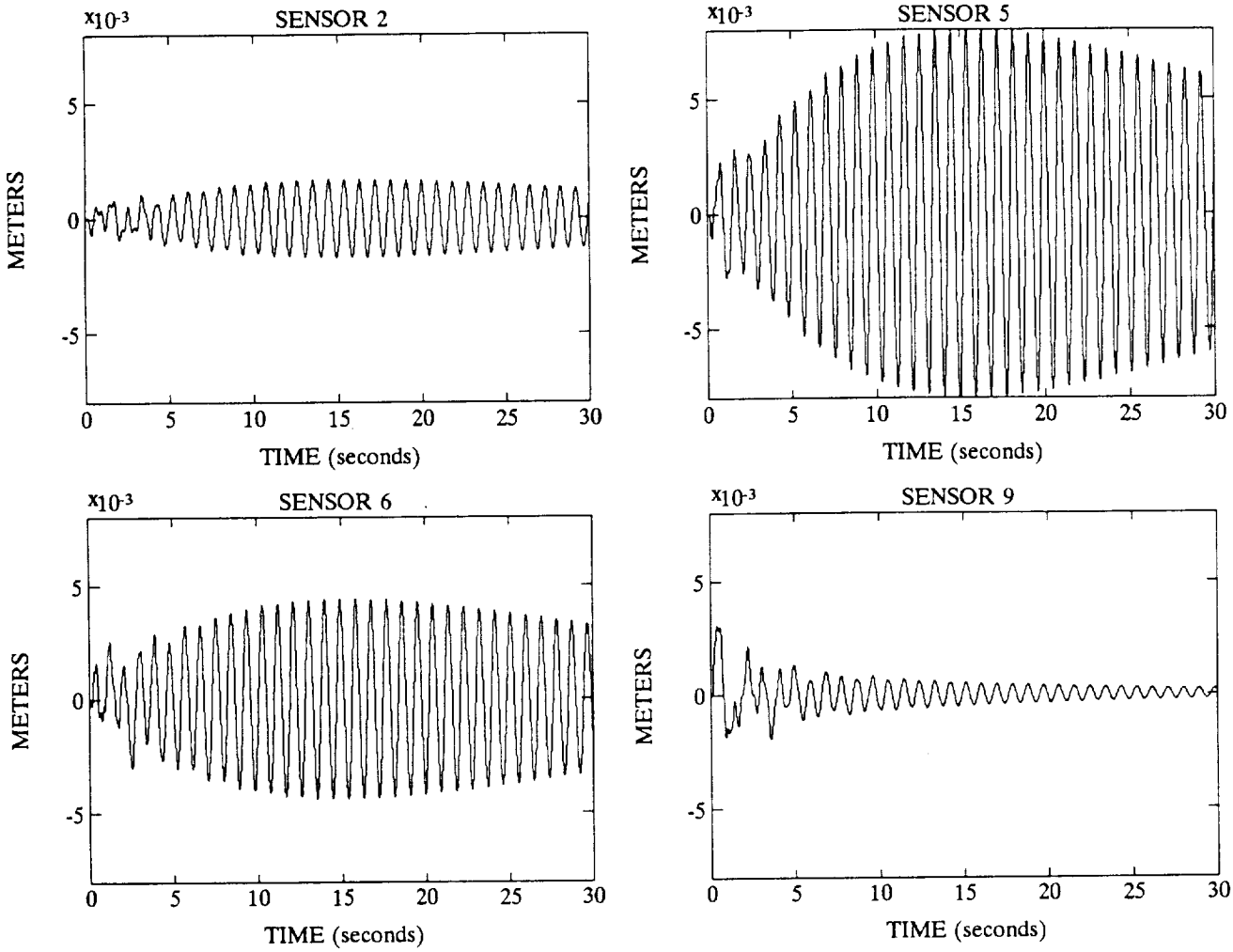

Figure 16. Control for an impact at the free end of the facesheet drives the uncontrolled residual mode. This motion will be damped by mechanical properties only.

LQR CONTROLLER

A pole placement design for three modes could be used and is better behaved than the preceding case. However, consider a frequency weighted (ref. 4) linear quadratic regulator (LQR) and estimator design for the first three modes. The weightings, in the Q matrix of the performance index for the modal displacement and velocity states, are set as the square of each mode frequency. The control weightings, in the R matrix, are the identity matrix multiplied by a parameter, α. The LQR solution is less aggressive and drives controlled roots to the left on the root locus plot along trajectories of constant frequency; the damping factors for all controlled modes increase at approximately the same rate. An RMF is not required for this design with $\alpha = 1$.

The response for the same pulse is shown in figure 17. This ROM controller settles quickly to the desired flat surface figure. The fourth and fifth modes are harder to drive with commanded actuation so there is little residual motion.

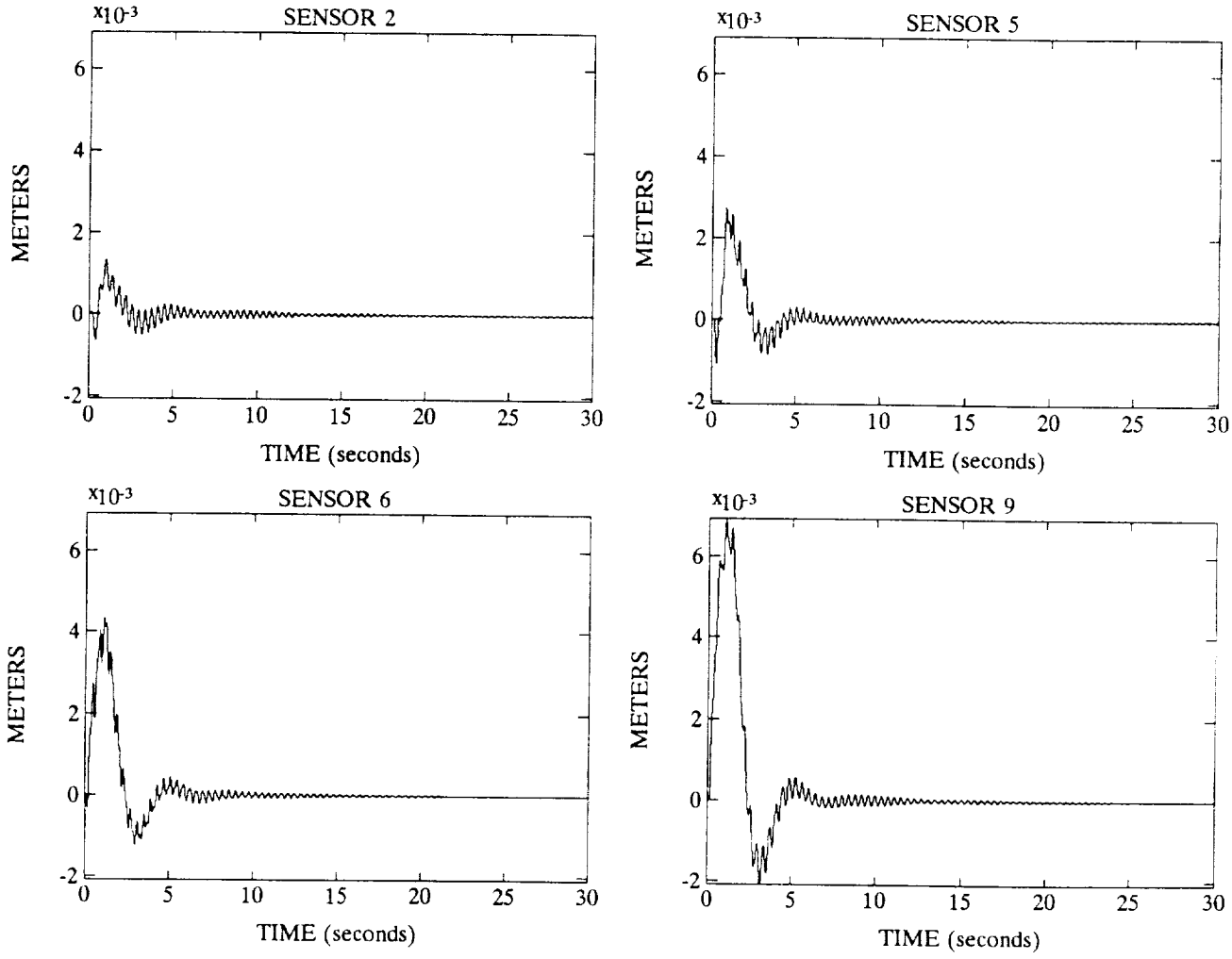

Figure 17. The LQR controller designed to create equal damping coefficients for the first three modes succesfully recovers from the impact.

FUTURE DIRECTIONS

The immediate usage of C-SIDE is for technology evaluation and research in several areas: structures, actuators, sensors, control, and processing.

The composite structure was fabricated under a separate internal development effort. It may be upgraded as new materials and fabrication methods are investigated and converted to an active (smart) structure. Current activities include embedded, distributed actuation and sensing. Eventually, these may be incorporated in an active facesheet.

Possibilities for future enhancements to the sensing capabilities include alignment transfer, inertial sensors and local sensing at the actuators. There is interest in using combinations of RAMS units to provide alignment transfer from a remote "navigation base" back to the core structure. Inertial sensors may be used to stabilize the structure against local laboratory vibrations. This is of interest for isolated benches in optical experiments. Local position sensing can be added at the actuators. The relative position is useful in localized control to recenter the actuator at low bandwidth or in a distributed control to drive an active reaction structure.

Several different actuator mechanisms can be applied to the structure and interfaced to the control system. A precision actuator for the reaction structure is a small reaction wheel. Interesting issues here are the effect of stored momentum during repositioning of structure sections and momentum unloading schemes. Active struts may be used as a primary control source between the facesheet and reaction structure or at the root of the structure. Thrusters probably are most applicable for coarse positioning of the reaction structure behind the vernier positioning system on the facesheet. Experience with many actuators types will enable recognition of novel solutions to difficulties in current and future products.

C-SIDE will provide experience with various strategies for ROM design such as variations on the basic LQR, Positivity and H_∞ methods. We are also investigating system identification techniques such as the eigensystem realization (ref. 5) and residue identification (ref. 6) algorithms. We have had success with feedforward and recursive neural networks functioning as RMFs in the C-SIDE simulation (ref. 7); verification with the hardware is planned for this year. Research areas include adaptive residual mode filters and the possibility of control during assembly of an additional structure.

Computational capabilities can be increased by segregating the control functions. The formulation of the ROM structure model and RMF bank lends itself to use of parallel processors. Additional control functions, such as disturbance accommodation and system identification, can be delegated to other processors with results being passed to the main control processor.

Although control-structure interaction is most often associated with large, flexible space structures, it is not necessary to narrowly limit its consideration. The expertise developed on C-SIDE is transferable to other high performance products: whenever a structure supports, or is itself, an actively positioned device. With processing speed increases, parallel processing and hybrid circuitry, the control method will be targeted at smaller structures also.

REFERENCES

1. Mohl, J.B.; Dieter, R.J.; and Muckle, A.M.: Attitude Determination and Control for the Radarsat Spacecraft. AAS 92-011, Feb. 1992.

2. Davis, H.W.; Sharkey, J.P.; and Carrington, C.K.: Structural Control Sensors for CASES. AAS 90-044, Feb 1990.

3. Balas, M.J.: Finite-Dimensional Controllers for Linear Distributed Parameter Systems: Exponential Stability Using Residual Mode Filters. *J. Math. Analysis and Appl.*, 1988.

4. Mackison, D.L.: Guaranteed Cost Control of Flexible Space Structures. PhD Thesis, University of Colorado - Boulder, 1988.

5. Juang, J.-N.; and Pappa, R.S.: An Eigensystem Realization Algorithm for Modal Parameter Identification and Model Reduction. *J. Guidance, Navigation and Control*, Vol. 8, No. 5, Sep.-Oct. 1985, pp. 620-627.

6. Medina, E.A.; Irwin, R.D.; Mitchell, J.R.; and Buckley, A.P.: MIMO System Indentification Using Frequency Response Data. AAS 92-065, Feb. 1992.

7. Bowman, C.; and Roorda, J.J.: Spacecraft Smart Structure Neural Network Adaptive Control. *Proc. of Government Neural Network Symposium*, Huntsville, AL, Sep. 1991.

AN EXPLICIT SOLUTION TO THE OPTIMAL LQG PROBLEM FOR FLEXIBLE STRUCTURES WITH COLLOCATED RATE SENSORS*

A. V. Balakrishnan

Electrical Engineering Department
UCLA
Los Angeles, California

ABSTRACT

We present a class of compensators in explicit form (not requiring numerical computer calculations) for stabilizing flexible structures with collocated rate sensors. They are based on the explicit solution, valid for both Continuum and FEM Models, of the LQG problem for minimizing mean square rate. They are robust with respect to system stability (will not destabilize modes even with mismatch of parameters), can be instrumented in state space form suitable for digital controllers, and can be specified directly from the structure modes and mode "signature" (displacement vectors at sensor locations). Some simulation results are presented for the NASA LaRC Phase-Zero Evolutionary Model — a modal Truth model with 86 modes — showing damping ratios attainable as a function of compensator design parameters and complexity.

1. INTRODUCTION

In this paper we present a class of compensators for stabilizing flexible structures with collocated rate sensors for Continuum as well as Finite Element or truncated Modal models. They are derived by solving explicitly the optimal control corresponding to an LQG problem. The Compensator Transfer Functions are strictly positive real and as a result they are robust with respect to system stability. They can be determined based solely on the mode frequencies and mode "signatures" (displacements at the sensor sites) and can be instrumented directly in "state-space" form.

We begin in Section 2 with the LQG problem and its solution. Section 3 highlights the features of the Compensator Transfer Function. Section 4 is devoted to Continuum models where the transfer function is nonrational. The main result on controller design is in Section 5 which shows how to design the compensator from a modal model of the structure, and in particular, how to construct a hierarchy of compensators of increasing order. Simulation results, confined to stability properties (damping ratios), are by no means exhaustive and are presented in Section 6 based on the modal model of the NASA LaRC CSI Phase-Zero Evolutionary Model [4]† Noise response performance is not included but is expected to be good because of the LQG criterion optimization. Conclusions are in Section 7.

* Research supported in part under NAS-1-19158, NASA LaRC.

† References 1-6 are cited in text.

For recent related work on controller design for collocated sensors see [5, 6] and the references therein.

2. THE LQG PROBLEM AND ITS SOLUTION

To state the LQG problem, we begin with the canonical time-domain dynamics of a flexible structure with collocated rate sensors which, whether it is a Finite Element Model (and hence finite dimensional) or Continuum Model (and hence infinite-dimensional) can be expressed in the form:

$$\left.\begin{aligned} M\ddot{x}(t) + Ax(t) + Bu(t) + BN_a(t) &= 0 \\ \mathrm{v}(t) &= B^*\dot{x}(t) + N_r(t) \end{aligned}\right\} \tag{2.1}$$

where in the case of FEM,

M	is the mass matrix (nonsingular, nonnegative definite)
A	is the stiffness matrix (nonsingular, nonnegative definite)
B	is the control matrix (rectangular matrix)
$u(\cdot)$	is the control vector ($n\times 1$, assuming n actuators)
$x(\cdot)$	is the "displacement" vector
$N_a(\cdot)$	is the actuator noise assumed white Gaussian with spectral density $d_a I$, I being the $n\times n$ Identity matrix
$\mathrm{v}(\cdot)$	is the sensor output
B^*	represents the transpose of B
$N_r(\cdot)$	is the sensor noise assumed white Gaussian with spectral density $d_r I$.

For the Continuum Model such a representation is still possible with $x(\cdot)$ now allowed to range in a Hilbert space (however complicated the structure), with A, M, and B being linear operators:

M	bounded linear, self-adjoint, nonnegative definite with M^{-1} bounded;
A	closed linear, self-adjoint, nonnegative definite with compact resolvent, resolvent, the resolvent set including zero
B	maps E^n Euclidean n-space into $\mathcal{H}$, and
B^*	represents the adjoint.

See [1], [2].

The LQG problem we shall consider is that of finding the control $u(\cdot)$ (or compensator) that minimizes the mean square time average:

$$\lim_{T\to\infty} \left\{ \frac{1}{T} \int_0^T \|B^*\dot{x}(t)\|^2 \, dt + \frac{\lambda}{T} \int_0^T \|u(t)\|^2 \, dt \right\} \tag{2.2}$$

where $\lambda > 0$. The optimal compensator transfer function ($n \times n$ matrix function) can be given in explicit form (see [1]):

$$\psi(p) = gpB^*(p^2M + A + \gamma pBB^*)^{-1}B \, , \qquad \text{Re. } p > 0 \tag{2.3}$$

where

$$g = \frac{\sqrt{d_a/d_r}}{\sqrt{\lambda}} \, ; \qquad \gamma = \sqrt{d_a/d_r} + \frac{1}{\sqrt{\lambda}} \tag{2.4}$$

under the assumption that

$$B^*\phi_k \neq 0 \tag{2.5}$$

for any k, where ϕ_k are the modes orthonormalized with respect to the mass matrix:

$$A\phi_k = \omega_k^2 \phi_k \, ; \qquad [M\phi_k, \phi_k] = 1 \, . \tag{2.6}$$

In the finite-dimensional (e.g., FEM) case, the compensator can be realized in the (finite-dimensional) state space form:

$$u(t) = gB^*\dot{Y}(t) \tag{2.7}$$

$$M\ddot{Y}(t) + AY(t) + \gamma BB^*\dot{Y}(t) = Bv(t) \, . \tag{2.8}$$

The corresponding mean square control power:

$$\lim_{T\to\infty} \frac{1}{T} \int_0^T \|u(t)\|^2 \, dt = \frac{d_a}{2\sqrt{\lambda}} \text{Tr. } (B^*MB)^{-1} \, . \tag{2.9}$$

The corresponding mean square displacement:

$$\lim_{T\to\infty} \frac{1}{T} \int_0^T \|B^*x(t)\|^2 \, dt = \left(\sqrt{d_a/d_r} + \frac{\sqrt{\lambda}\, d_a}{2} \right) \text{Tr. } B^*A^{-1}B \, . \tag{2.10}$$

Formulas (2.9) and (2.10) hold as well in the infinite-dimensional (Continuum Model) case.

3. FEATURES OF THE COMPENSATOR TRANSFER FUNCTION

Some significant features of the compensator transfer function which are noteworthy are:

(i) As $\lambda \to 0$, $\psi(p) \to I\sqrt{d_a/d_r}$ we note that

$$\psi(p) = I\sqrt{d_a/d_r}$$

is the optimal "static" or "direct connection" or "PID" controller. Note that as $\lambda \to 0$, the control power given by (2.9) becomes infinite, as we expect.

(ii) $\psi(p)$ is "positive real" — that is to say:

$\psi(p)$ holomorphic in $\mathrm{Re}.p > 0$

$\psi(p) + \psi(p)^*$ nonsingular, and positive definite, for $\mathrm{Re}.p > 0$

where $*$ denotes conjugate transpose. Of course $\psi(\cdot) \in \mathcal{H}_\infty$.

For the importance of positive realness for robustness, see [6].

Let a compensator transfer function be defined by (2.3) where g and γ are arbitrary, subject only to the condition that

$$\gamma^2 \geq 4g . \tag{3.1}$$

Then for $d_a = 0$ (no actuator noise), the corresponding mean square displacement

$$\lim_{T\to\infty} \frac{1}{T}\int_0^T \|B^*x(t)\|^2\, dt = \frac{d_r\, g}{2\gamma}\,\mathrm{Tr.}\,(B^*A^{-1}B) . \tag{3.2}$$

This follows from [1, (6.11)].

4. EXAMPLES: CONTINUUM MODELS

For a given Continuum Model for structures (see [1], [3]) it is possible to reduce (2.3) further to yield finite-dimensional matrix transfer functions which are, however, not rational functions of p. Thus (2.3) becomes:

$$\psi(p) = gpB_u^*(p^2M_b + T(p) + \gamma pB_uB_u^*)^{-1}B_u$$

where

$T(p)$: self-adjoint nonnegative definite nonsingular matrix for $p \geq 0$. Nonrational meromorphic function of p, $\mathrm{Re}.p > 0$.

B_u is $d \times n$ where

d : number of nodes $\times$ dimension of displacement vector at each node

n : number of actuators/sensors

M_b is the $d\times d$ mass/moment of inertia matrix corresponding to the nodes. For the SCOLE configuration [1], $d = n = 5$,

$$B_uB_u^* = I_{5\times 5}$$

and an explicit expression for $T(p)$ is given in [3], and involves hyperbolic sine and cosine functions of p. An example where $d \neq n$ is given by the NASA LaRC Phase Zero Evolutionary Model [4] for which $n = 8$ and $d = 48$. See also [3] for some "textbook" examples for $d = n = 1$, Bernoulli beam bending or torsion.

The system modes are given by

$$M_bp^2 + T(p) = 0 . \tag{4.1}$$

5. MODAL APPROXIMATION

Let $\{\phi_k\}$ denote the eigenvectors (mode "shapes") of the stiffness operator A with ω_k the corresponding eigenvalue (angular frequency). Let b_k denote the corresponding mode "signature" row vector:

$$b_k = (B^*\phi_k)^* \qquad 1\times n \text{ row vector}$$

where n is the number of actuators. Let for each $N \geq 1$,

$$B_N = \begin{vmatrix} b_1 \\ \vdots \\ b_N \end{vmatrix}, \qquad D_N = \text{Diagonal } (\omega_1^2, \ldots, \omega_N^2) .$$

For arbitrary $g, \gamma > 0$, define the compensator transfer function

$$\psi_N(p) = gpB_N^*(p^2 I_N + D_N + \gamma p B_N B_N^*)^{-1} B_N , \qquad \text{Re. } p \geq 0 . \tag{5.1}$$

Then

(a) $\psi_N(\cdot)$ is positive real as soon as $B_N^* B_N$ is nonsingular;

(b) For g, γ defined by (2.4), $\psi_N(p)$ converges to the optimal compensator $\psi(p)$ given by (2.3) as $N \to \infty$ (and holds *a fortiori* in the finite-dimensional case, where the sequence terminates).

Note that the modal approximation requires only the modes and the "modal signature": modal displacement at the sensor sites. Note also that (5.1) automatically yields a strictly positive real *rational* transfer function approximation for the case of the Continuum Model — yielding, in fact, a new technique for such approximation. Moreover it has the direct state space representation:

$$\left.\begin{aligned} u(t) &= gB_N^* \dot{Y}(t) \\ \ddot{Y}(t) + D_N Y(t) + \gamma B_N B_N^* \dot{Y}(t) &= B_N v(t) . \end{aligned}\right\} \tag{5.2}$$

It is also important to note that for a given finite-dimensional modal model with m modes, say, we can choose any N modes for the approximation, not necessarily the first N. Moreover the stability properties of the system are determined by the ("closed-loop") eigenvalues of the "system" $2(m+N) \times 2(m+N)$ matrix:

$$W = \begin{vmatrix} 0_{m\times m} & I_{m\times m} & 0_{m\times N} & 0_{m\times N} \\ -D_m & 0_{m\times m} & 0_{m\times N} & -gB_m B_N^* \\ 0_{N\times m} & 0_{N\times m} & 0_{N\times N} & I_{N\times N} \\ 0_{N\times m} & B_N B_m^* & -D_N & -\gamma B_N B_N^* \end{vmatrix} \tag{5.3}$$

This is readily seen to be a stable matrix under our condition that $B_N B_N^*$ is nonsingular and $g, \gamma > 0$. Moreover, including a damping matrix $D \geq 0$ in the Truth Model (replace $0_{m\times m}$ in (5.3) by $-D$), we see that

$$\text{Trace } W = -\text{Tr. } D - \gamma \text{ Tr. } B_N^* B_N = 2(\text{sum of real parts of eigenvalues}) \tag{5.4}$$

again illustrating the robustness. Also we have

$$\text{product of roots} = |W| = |D_m| \cdot |D_N| \tag{5.5}$$

where $|\cdot|$ denotes determinant. Finally let us note that the eigenvalues are the roots of

$$|pI - W| = |p^2 + D_m + pD|\, |p^2 + D_N + \gamma p B_N B_N^* + p^2 g B_N B_m^* (p^2 + D_m + pD)^{-1} B_m B_N^*| = 0 \tag{5.6}$$

where the first factor is an $m\times m$ determinant and the second factor is an $N\times N$ determinant, if $g = 0$ structure modes are unaffected. We can see from (5.4) - (5.6) that the total damping increases as γ is increased but the damping in the structure modes can decrease depending on how large γ is. Thus, for each fixed value of the gain g, there is apparently an optimal choice for γ, which may depend on the mode frequency in general.

6. SIMULATION RESULTS: PHASE ZERO EVOLUTIONARY MODEL, NASA LaRC

For evaluating control performance by simulation, the NASA LaRC CSI Phase-Zero Evolutionary model data [4] is used — specifically, the modes and modal signatures.

We denote by m the number of modes in the truth model of the structure, and let N = the number of modes in the compensator, as in (5.2) and (5.3). The compensator is thus characterized by the "gain" parameter g, the "damping" parameter γ, and N the number of "control" modes (or $2N$ = number of states). Note that for each N

$$\psi_N(p) \to kI \qquad (\sim \text{"direct connection" or "static controller"})$$

as $g \to \infty$, $\gamma \to \infty$, keeping the ratio

$$\frac{g}{\gamma} = k \tag{6.1}$$

fixed. Also for $N = m$, we can use (3.2) to determine the mean square displacement where now

$$\text{Tr. } B^* A^{-1} B = \sum_1^m \frac{\|b_k\|^2}{\omega_k^2} ,$$

so that the mean square displacement can be expressed

$$= \frac{d_r g}{2\gamma} \sum_1^m \frac{\|b_k\|^2}{\omega_k^2} , \qquad \gamma^2 > 4g , \tag{6.2}$$

and thus increases with g and decreases as γ increases.

Data for the modal model of the NASA LaRC Phase Zero Evolutionary Model is taken from [4]. Here $n = 8$ so that each b_k is 8×1, and m for the Truth model is 86, and $D = 0$ (no damping). In this case the optimal compensator will use all 86 modes. Table I[§] shows the mode frequencies and a typical mode shape (b_7). $B_8^* B_8$ is nonsingular.

Figures 1, 2, and 3 show the behavior of the damping ratio for fixed g as a function of the damping parameter γ, for angular frequencies 314 (the 86th mode), 106 (the 43rd mode) and 9.25 (the 7th mode), respectively. Note the occurrence of the maximum for all around $\gamma = 8$. Figures 4, 5, and 6 show the attainable damping ratios for a compensator with $N = 30$, and the same gain

§ Personal communication, S. M. Joshi, NASA LaRC, 1992.

Mode Number	(Angular) Frequency rad/sec	Mode Number	(Angular) Frequency rad/sec	Mode Number	(Angular) Frequency rad/sec	Mode Number	(Angular) Frequency rad/sec
1 =	0.9243	23 =	38.8269	45 =	120.5899	67 =	195.1799
2 =	0.9365	24 =	39.1489	46 =	133.1399	68 =	196.9100
3 =	0.9752	25 =	40.6580	47 =	137.8399	69 =	198.1300
4 =	4.5872	26 =	41.9080	48 =	139.5700	70 =	198.7400
5 =	4.6985	27 =	46.3219	49 =	147.2599	71 =	203.3300
6 =	5.4913	28 =	52.1080	50 =	154.2500	72 =	209.7299
7 =	9.2580	29 =	52.8380	51 =	156.5399	73 =	231.7400
8 =	10.9209	30 =	53.1319	52 =	156.9199	74 =	232.9499
9 =	11.8310	31 =	55.4410	53 =	161.0299	75 =	239.8899
10 =	14.4600	32 =	56.0859	54 =	164.6499	76 =	241.4499
11 =	15.9259	33 =	56.3370	55 =	165.1399	77 =	244.9299
12 =	17.8349	34 =	58.0239	56 =	166.9100	78 =	244.9900
13 =	21.4850	35 =	59.8600	57 =	170.8300	79 =	247.8300
14 =	21.9050	36 =	62.2190	58 =	173.7700	80 =	255.7700
15 =	22.5400	37 =	78.4509	59 =	180.0099	81 =	268.6499
16 =	25.2250	38 =	85.5439	60 =	181.9100	82 =	270.5499
17 =	25.3349	39 =	89.9440	61 =	183.1300	83 =	275.7200
18 =	26.4249	40 =	92.4779	62 =	186.6199	84 =	287.5299
19 =	27.5949	41 =	99.8170	63 =	187.7500	85 =	308.7500
20 =	31.6009	42 =	105.8899	64 =	191.2400	86 =	314.2399
21 =	31.6289	43 =	106.7699	65 =	192.0599		
22 =	34.5660	44 =	116.1500	66 =	193.7899		

Mode Shape b_7

-0.9084100127220	-0.0009229300194	0.4756200015545	0.0040255999193
0.0009075700073	-0.4345000088215	-0.0070441002026	1.1181999444962

Table I. Mode Frequencies And Sample Mode Shape

g (= 20), but here there is no maximum for the mode frequency of 314 which is not included in the controller modes. For the mode frequencies 9 and 106, the maximum occurs around $\gamma = 5$ and $\gamma = 30$, respectively. Table II shows the damping ratios for all (angular) frequencies (both control and structure modes; the former have higher damping) between 1 and 150 for $g = 20$ and $\gamma = 5$ for the optimal compensator ($N = 86$). Table III shows the same for $N = 30$. The damping ratios are seen to compare favorably with those reported in [5, 6], depending of course on the appropriate gain setting, but detailed comparative evaluation will need further study. Table IV shows the damping ratios for zero gain ($g = 0$) with $N = 86$ and $\gamma = 10$ which should help distinguish the control modes from structure modes (the latter have zero damping). Figure 7 shows the damping ratio as a function of g for $N = 86$, $\gamma = 10$ and mode frequency 21.485. The damping increases for the structure mode and decreases for the control mode.

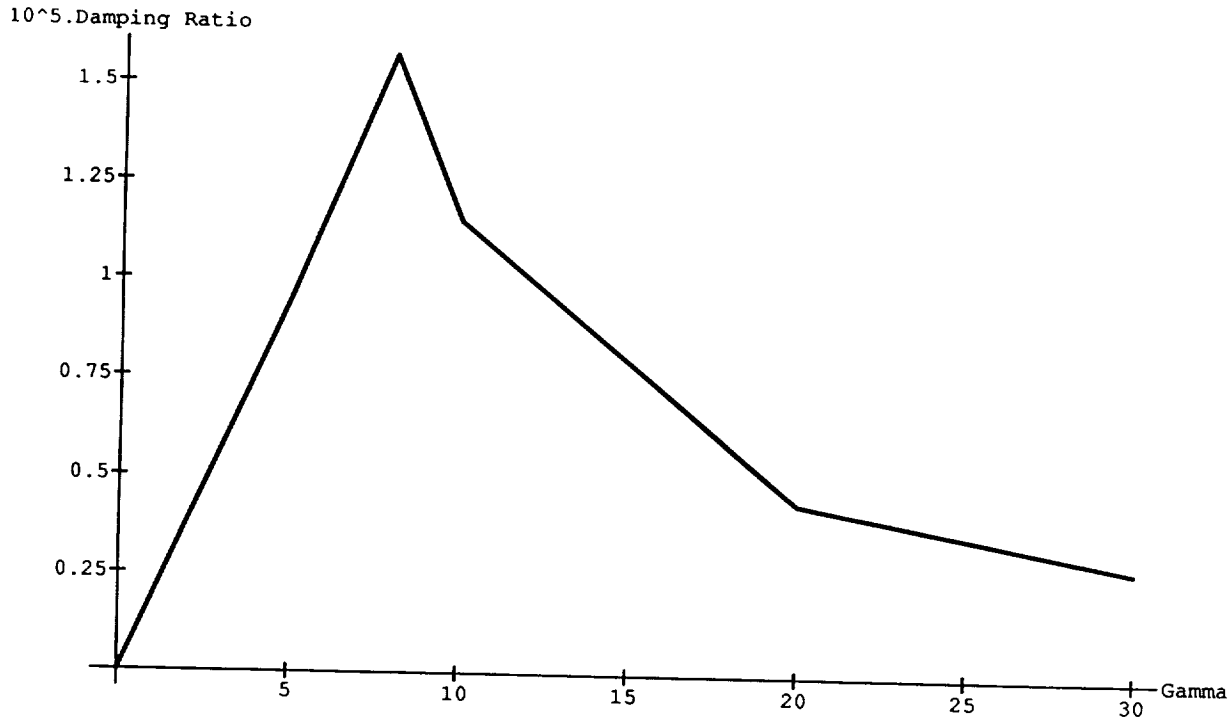

Figure 1. Damping ratio vs. damping parameter γ: mode angular frequency 314; $N = 86$.

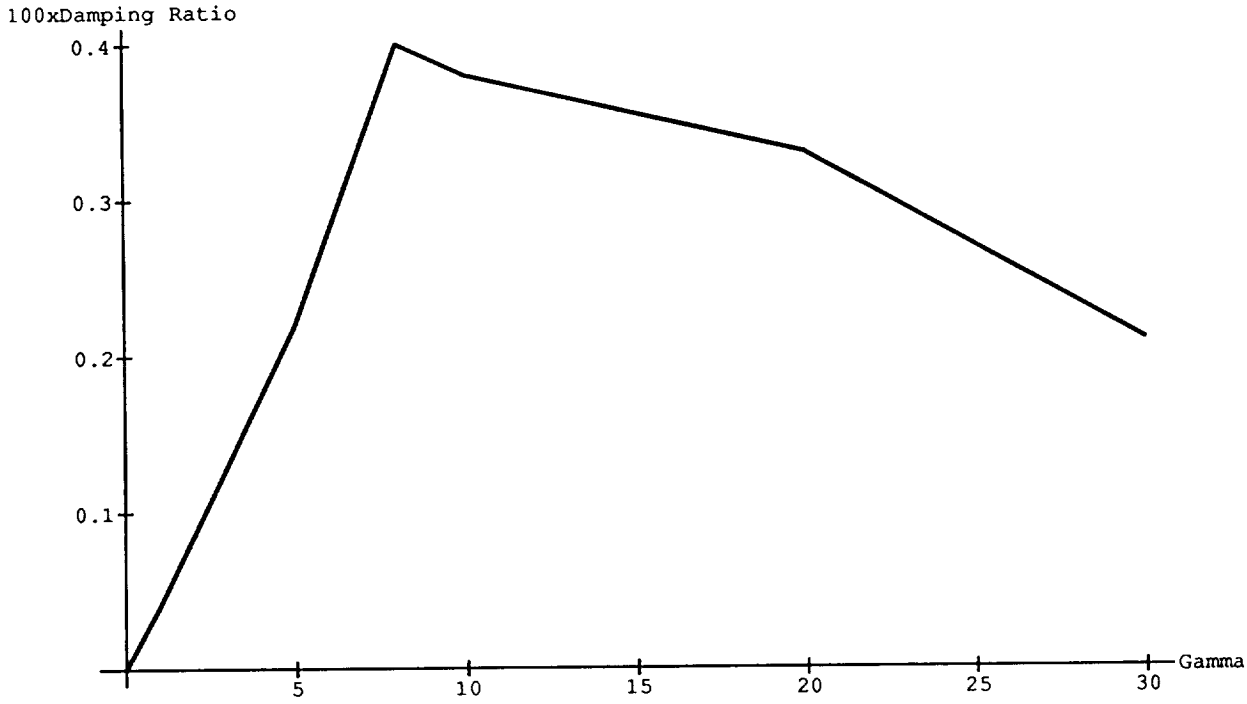

Figure 2. Damping ratio vs. damping parameter γ: mode angular frequency 106; N = 86.

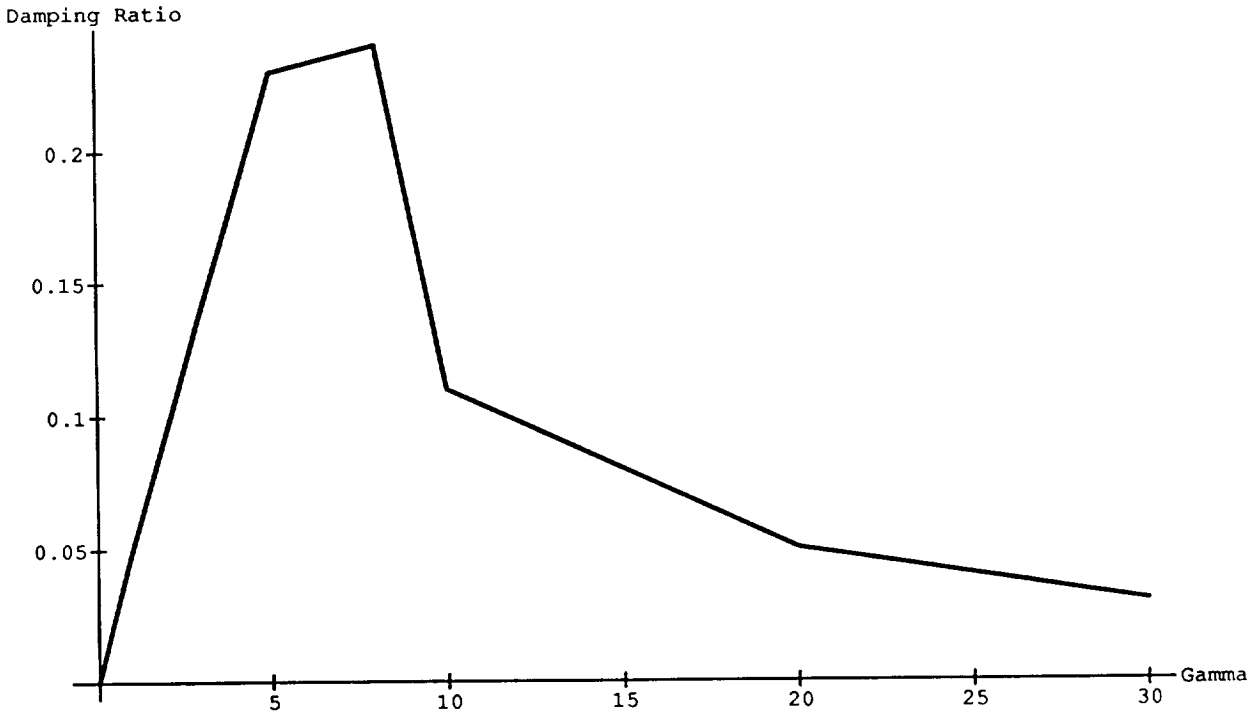

Figure 3. Damping ratio vs. damping parameter γ: mode angular frequency 9.25; N = 86.

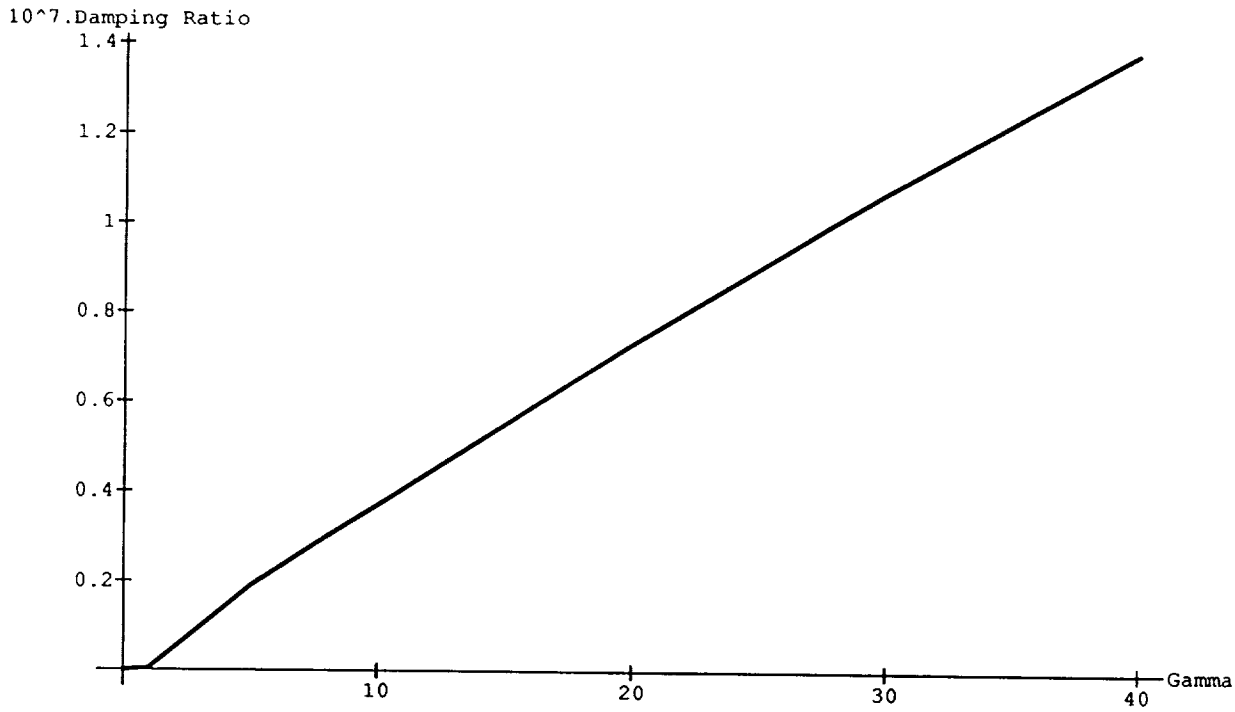

Figure 4. Damping ratio vs. damping parameter γ: mode angular frequency 314; $N = 30$.

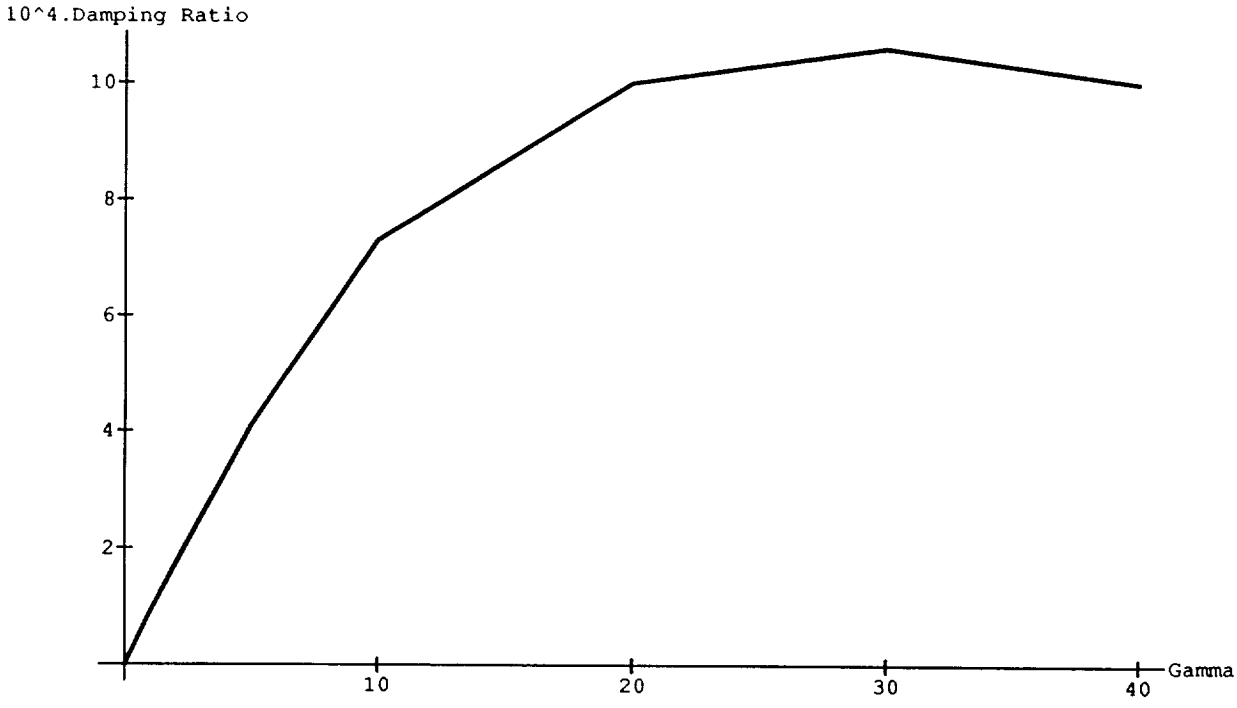

Figure 5. Damping ratio vs. damping parameter γ: mode angular frequency 106; $N = 30$.

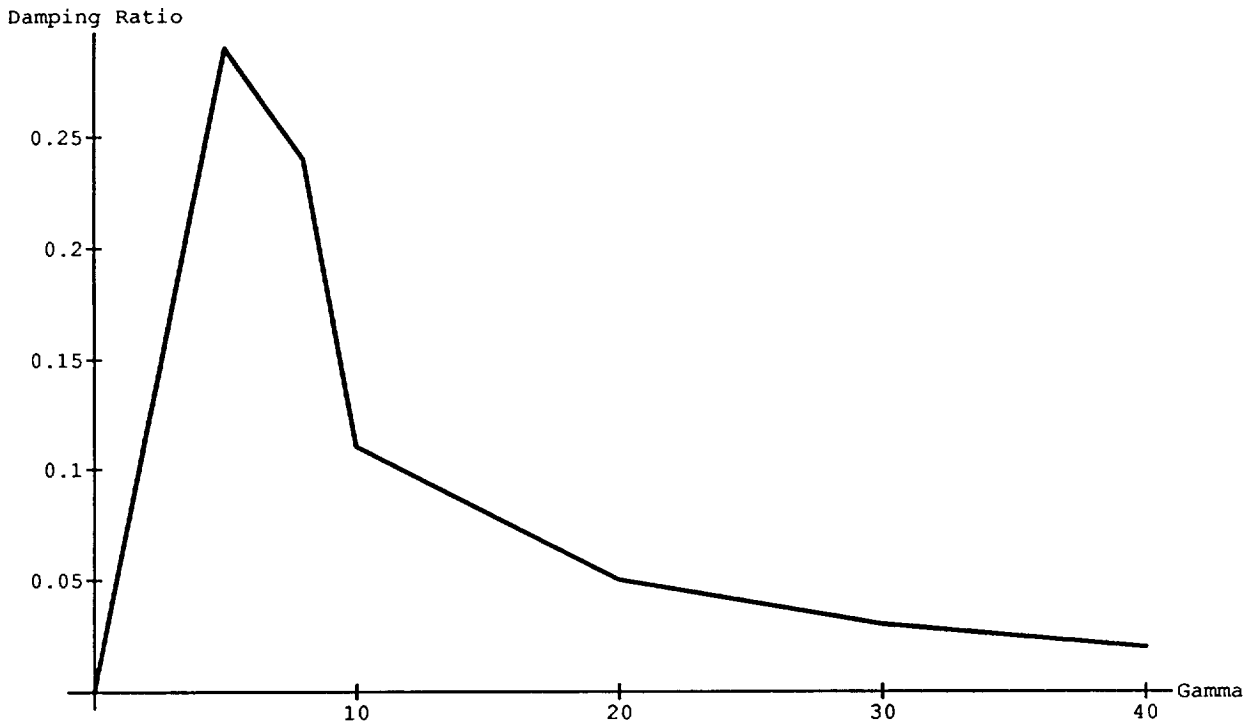

Figure 6. Damping ratio vs. damping parameter γ: mode angular frequency 9.25; $N = 30$.

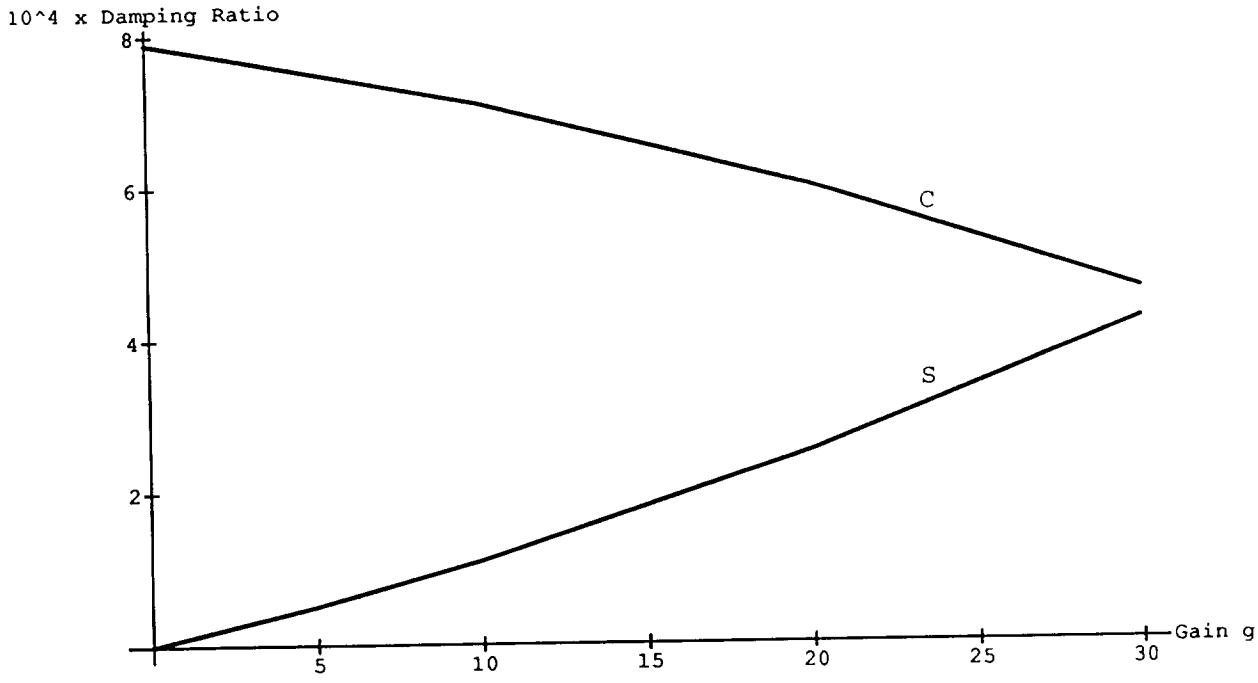

Figure 7. Damping ratio vs. g: mode frequency 21.49 r/s; $N = 86$; $\gamma = 10$; C: control; S: structure

Angular Frequency	Damping Ratio
.17106E+01	.48814E+00
.25233E+01	.42349E+00
.38285E+01	.18903E+00
.40291E+01	.53048E+00
.50981E+01	.53701E-01
.55010E+01	.27800E+00
.62846E+01	.48991E+00
.65389E+01	.15363E+00
.73598E+01	.25791E+00
.88473E+01	.28576E+00
.96096E+01	.23182E+00
.98633E+01	.46814E-01
.14333E+02	.26440E-02
.14370E+02	.13551E-01
.15912E+02	.94853E-03
.15918E+02	.12789E-03
.16858E+02	.34110E+00
.17438E+02	.15497E-01
.17615E+02	.36468E-02
.18676E+02	.27518E+00
.21478E+02	.26988E-03
.21491E+02	.25982E-03
.21897E+02	.29663E-03
.21913E+02	.24238E-03
.22536E+02	.20344E-03
.22544E+02	.20967E-03
.23354E+02	.22881E+00
.23666E+02	.31516E-01
.25234E+02	.10998E-02
.25241E+02	.24057E-03
.25492E+02	.34385E-01
.26321E+02	.16274E-02
.26361E+02	.82509E-03
.27975E+02	.10362E+00
.30735E+02	.22514E+00
.30903E+02	.16990E+00
.31554E+02	.10862E-02
.31573E+02	.34084E-02
.31601E+02	.36615E-05
.31601E+02	.60475E-05
.33265E+02	.29600E-01
.35339E+02	.12758E-01
.36245E+02	.22248E-01
.38097E+02	.15841E-01
.39485E+02	.23587E-01
.39715E+02	.64462E-02
.40253E+02	.96291E-02
.42723E+02	.40264E-01
.47595E+02	.20357E+00
.49116E+02	.37251E-01
.50628E+02	.74785E-01
.52567E+02	.48805E-03
.52612E+02	.36127E-03
.52923E+02	.23978E-01
.53030E+02	.65234E-03
.53116E+02	.39229E-02
.55388E+02	.51163E-03
.55476E+02	.11573E-02
.55627E+02	.47474E-01
.55777E+02	.20228E+00
.56012E+02	.50958E-03
.56120E+02	.32213E-02
.57973E+02	.33939E-03
.58058E+02	.22112E-02
.59857E+02	.16844E-04
.59860E+02	.10358E-03
.61950E+02	.10323E+00
.62123E+02	.77622E-03
.62301E+02	.15341E-02
.77219E+02	.89300E-02
.79869E+02	.16028E-01
.85536E+02	.45737E-04
.85554E+02	.13440E-03
.89610E+02	.18167E-02
.90357E+02	.56712E-02
.92127E+02	.21810E-02
.92875E+02	.35775E-02
.99737E+02	.42099E-03
.99912E+02	.10766E-02
.10474E+03	.62417E-02
.10629E+03	.21788E-02
.10703E+03	.53890E-02
.10757E+03	.10741E-01
.11586E+03	.14946E-02
.11648E+03	.24414E-02
.12059E+03	.22062E-04
.12059E+03	.32178E-04
.13306E+03	.38080E-03
.13322E+03	.42566E-03
.13759E+03	.12103E-02
.13809E+03	.12406E-02
.13957E+03	.39718E-05
.13957E+03	.50153E-05
.14684E+03	.17338E-02
.14771E+03	.22478E-02

Table II. Damping Ratio Vs. Angular Frequency: $N = 86$; $g = 20$; $\gamma = 5$

Angular Frequency	Damping Ratio
.17111E+01	.48787E+00
.25240E+01	.42289E+00
.38283E+01	.18850E+00
.40268E+01	.53155E+00
.50982E+01	.53764E-01
.55074E+01	.27646E+00
.62704E+01	.49202E+00
.65413E+01	.15327E+00
.73966E+01	.25589E+00
.88395E+01	.28765E+00
.96114E+01	.24204E+00
.98657E+01	.46669E-01
.14333E+02	.26268E-02
.14371E+02	.13622E-01
.15912E+02	.94628E-03
.15918E+02	.12646E-03
.16873E+02	.34829E+00
.17439E+02	.15483E-01
.17615E+02	.36319E-02
.18473E+02	.29242E+00
.21478E+02	.26755E-03
.21491E+02	.26123E-03
.21897E+02	.29369E-03
.21913E+02	.24459E-03
.22536E+02	.19617E-03
.22544E+02	.21245E-03
.23367E+02	.23050E+00
.23680E+02	.29890E-01
.25234E+02	.11092E-02
.25241E+02	.24125E-03
.25495E+02	.33946E-01
.26323E+02	.16797E-02
.26362E+02	.80854E-03
.27681E+02	.10975E+00
.30664E+02	.22748E+00
.30908E+02	.16861E+00
.31554E+02	.10567E-02
.31573E+02	.34060E-02
.31601E+02	.36214E-05
.31601E+02	.60906E-05
.33268E+02	.29376E-01
.35300E+02	.13261E-01
.36246E+02	.21919E-01
.38090E+02	.15162E-01
.39472E+02	.24008E-01
.39716E+02	.61748E-02
.40247E+02	.98628E-02
.42747E+02	.38763E-01
.47582E+02	.20393E+00
.49299E+02	.30838E-01
.50456E+02	.78217E-01
.52567E+02	.50746E-03
.52615E+02	.32023E-03
.53031E+02	.60754E-03
.53108E+02	.36922E-02
.55446E+02	.30132E-03
.55694E+02	.20493E+00
.55773E+02	.44503E-01
.56112E+02	.13185E-02
.58052E+02	.72573E-03
.58417E+02	.24337E-01
.59861E+02	.78116E-04
.62235E+02	.19700E-03
.78798E+02	.19928E-02
.85547E+02	.18896E-04
.90088E+02	.74096E-03
.92550E+02	.19914E-03
.99846E+02	.13752E-03
.10612E+03	.41269E-03
.10689E+03	.23571E-03
.11618E+03	.42708E-04
.12059E+03	.81852E-06
.13315E+03	.42638E-05
.13785E+03	.64145E-05
.13957E+03	.88491E-07
.14728E+03	.89389E-05

Table III. Damping Ratio vs. Angular Frequency: $N = 30$; $g = 20$; $\gamma = 5$

Angular Frequency	Damping Ratio
.45872E+01	.00000E+00
.46986E+01	.00000E+00
.53549E+01	.10629E+00
.54914E+01	.00000E+00
.89044E+01	.84249E-01
.92581E+01	.00000E+00
.10921E+02	.00000E+00
.11831E+02	.00000E+00
.13632E+02	.17079E+01
.14263E+02	.77629E-02
.14460E+02	.00000E+00
.15914E+02	.28005E-03
.15926E+02	.00000E+00
.17552E+02	.82357E-02
.17835E+02	.00000E+00
.21485E+02	.00000E+00
.21487E+02	.78458E-03
.21905E+02	.00000E+00
.21907E+02	.90374E-03
.22375E+02	.13007E+00
.22540E+02	.00000E+00
.22541E+02	.24691E-03
.24459E+02	.13332E+00
.25225E+02	.00000E+00
.25243E+02	.45734E-03
.25335E+02	.00000E+00
.26335E+02	.13181E-02
.26425E+02	.00000E+00
.27595E+02	.00000E+00
.30456E+02	.13725E+00
.31563E+02	.30544E-02
.31601E+02	.00000E+00
.31601E+02	.11152E-04
.31629E+02	.00000E+00
.34566E+02	.00000E+00
.35259E+02	.24327E-01
.38762E+02	.32907E-01
.38827E+02	.00000E+00
.39149E+02	.00000E+00
.39744E+02	.22024E-01
.40658E+02	.00000E+00
.41118E+02	.24327E+00
.41908E+02	.00000E+00
.46322E+02	.00000E+00
.46630E+02	.20336E+00
.50739E+02	.80977E-01
.52108E+02	.00000E+00
.52588E+02	.42582E-03
.52838E+02	.00000E+00
.52988E+02	.21608E-02
.53132E+02	.00000E+00
.55387E+02	.22200E-02
.55441E+02	.00000E+00
.55964E+02	.17243E-02
.56086E+02	.00000E+00
.56337E+02	.00000E+00
.57938E+02	.11515E-02
.58024E+02	.00000E+00
.59855E+02	.51996E-04
.59860E+02	.00000E+00
.62125E+02	.34738E-02
.62211E+02	.00000E+00
.77305E+02	.39799E-01
.78451E+02	.00000E+00
.85533E+02	.19002E-03
.85544E+02	.00000E+00
.89479E+02	.73662E-02
.89944E+02	.00000E+00
.92185E+02	.99239E-02
.92478E+02	.00000E+00
.99727E+02	.17443E-02
.99817E+02	.00000E+00
.10466E+03	.29513E-01
.10589E+03	.00000E+00
.10616E+03	.92339E-02
.10677E+03	.00000E+00
.11595E+03	.63634E-02
.11615E+03	.00000E+00
.12059E+03	.97457E-04
.12059E+03	.00000E+00
.13312E+03	.15997E-02
.13314E+03	.00000E+00
.13783E+03	.49739E-02
.13784E+03	.00000E+00
.13957E+03	.16752E-04
.13957E+03	.00000E+00
.14705E+03	.77790E-02
.14726E+03	.00000E+00

Table IV. Damping: Zero Gain: $N = 86$; $\gamma = 10$

7. CONCLUSIONS

A class of compensators in explicit form (not requiring computer calculations) has been presented for stabilizing flexibility structures with collocated rate sensors. They are optimized for the LQG criterion for minimizing the mean square rate and hence have inherently good noise response features. They are robust with respect to system stability, can be instrumented in state space form suitable for digital control and above all can be specified to any complexity desired directly from the structure modes and mode signatures at the sensor sites. Simulation results are presented for the modal model of the NASA LaRC Phase Zero Evolutionary Model — mainly damping ratios attainable and their dependence on compensator design parameters and complexity. The damping ratios compare favorably with those reported in [5, 6], but any detailed comparative evaluation of course is possible only after further study.

REFERENCES

1. Balakrishnan, A. V.: Compensator Design for Stability Enhancement with Collocated Controllers," *IEEE Transactions on Automatic Control*, vol. 36, no. 9, September 1991, pp. 994-1007.
2. Balakrishnan, A. V.: Modes of Interconnected Lattice Trusses Using Continuum Models, Part 1, NASA CR 189568, December 1991.

3. Balakrishnan, A. V.: Compensator Design for Stability Enhancement with Collocated Controllers: Explicit Solutions. *IEEE Transactions on Automatic Control,* vol. 37, no. 1, January 1993.
4. Belvin, W. K.; Horta, L. G.; and Elliott, K. E.: The LaRC CSI Phase-0 Evolutionary Model Test Bed: Design and Experimental Results. Paper presented at the 4th Annual NASA-DOD Conference on CSI Technology, November 5-7, 1990, Orlando, Florida.
5. Lim, K. B.; Maghami, P. G.; and Joshi, S. M.: A comparison of controller designs for an experimental flexible structure. Paper presented at the 1991 American Control Conference, June 1991, Boston, Massachusetts.
6. Joshi, S. M.; Maghami, P. G.; and Kelkar, A. G.: Dynamic Dissipative Compensator Design for Large Space Structures." AIAA-91-2650, August 1991.

A Synopsis of Test Results and Knowledge Gained From the Phase-0 CSI Evolutionary Model

W. Keith Belvin, Kenny B. Elliott and Lucas G. Horta

Abstract

The Phase-0 CSI Evolutionary Model (CEM) is a testbed for the study of space platform global line-of-sight (LOS) pointing. Now that the tests have been completed, a summary of hardware and closed-loop test experiences is necessary to insure a timely dissemination of the knowledge gained. The testbed is described and modeling experiences are presented followed by a summary of the research performed by various investigators. Some early lessons on implementing the closed-loop controllers are described with particular emphasis on real-time computing requirements. A summary of closed-loop studies and a synopsis of test results are presented. Plans for evolving the CEM from phase 0 to phases 1 and 2 are also described. Subsequently, a summary of knowledge gained from the design and testing of the Phase-0 CEM is made.

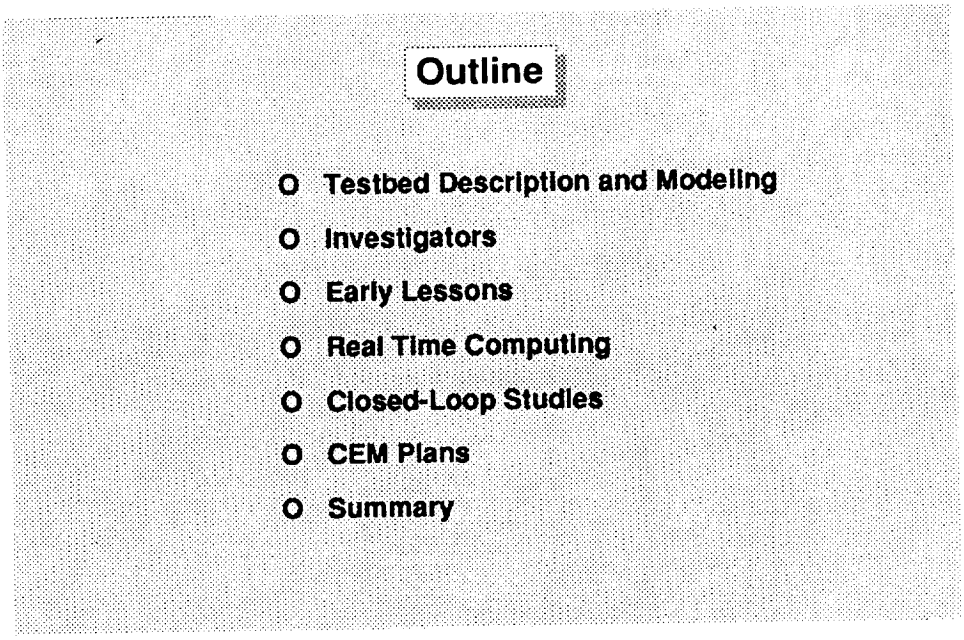

Introduction

The Phase-0 CSI Evolutionary Model (CEM) testbed design was driven by the interaction of flexible body dynamics and active pointing control systems expected on future space platforms. The testbed structure, shown below, consists of a 55' long aluminum truss with several appendages. A laser, mounted to one appendage, is used to illuminate an optical path from the laser source to a 16' diameter reflector. The optical path continues from the reflector to an LOS scoring detector mounted inertially on the ceiling of the test facility. The structure, instrumentation and data acquisition and control computers are described in detail in Refs. [1-3].

This paper summarizes the types of tests and experimental results obtained using the CEM testbed. Hardware experiences are described in terms of gravity influences and modeling requirements. System identification tests and results are presented to show the accuracy of pre-test and post-test finite element modeling procedures. Results of dissipative controller tests are compared to model based controllers in terms of stability and performance. It is shown with the level of uncertainty that exists in the CEM analytic models, a combination of dissipative and model based controllers give the best performance. The implementation of digital controllers is also discussed in terms of the effects of time delay. Plans for evolving the testbed are also presented.

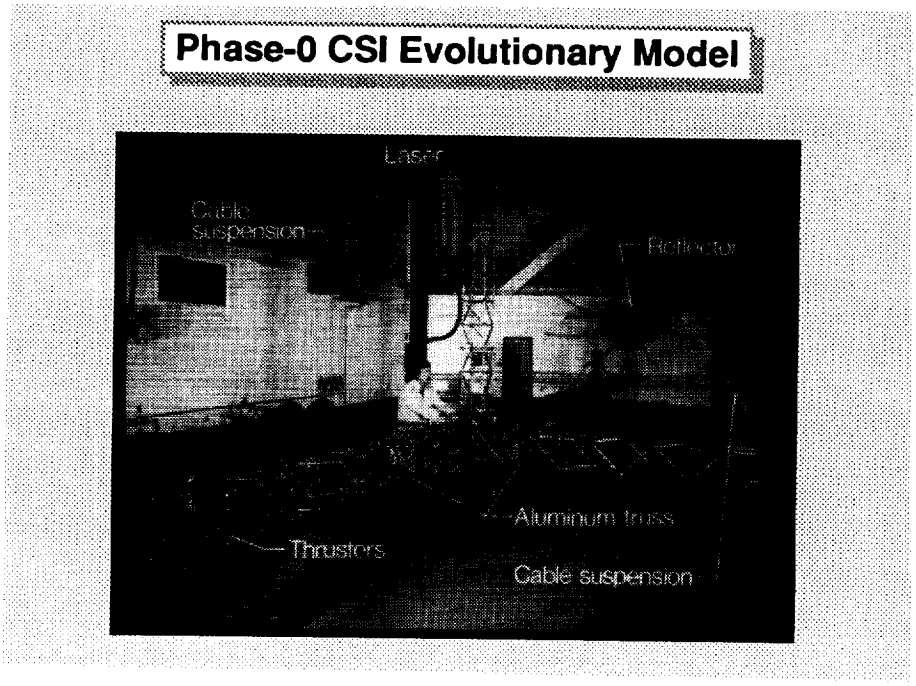

Phase-0 CEM Actuators/Sensor Pairs

Acceleration sensors have been used as the primary control sensor in conjunction with linear bi-directional thrusters. The actuators and sensors were spatially collocated at the 8 locations shown below. The low frequency nature of the testbed requires sensors with a bandwidth down to 0 Hz. As such, the accelerometers detect the acceleration due to gravity. This poses a classic ground-based measurement problem whereby the acceleration of the "pendulum" suspension modes is nearly exactly canceled by the change in the gravity acceleration vector. For the Phase 0 CEM, this phenomenon only occurs in mode 2. Hence the measured acceleration of mode 2 differs significantly from that predicted by linear (small angle) analysis. Another experience with low frequency accelerometers is DC drift and/or biases which require special considerations when integrating the measured acceleration particularly if the controller has a DC gain.

The thrusters [4] have proved to be reliable control effectors with minimal dynamics in the 0 to 10 Hz bandwidth. Eight pairs of thrusters were mounted such that a net force was applied to the model at the 8 locations shown below. Although pure collocation of the sensors and actuators was attempted, results, shown herein, indicate limited success was achieved.

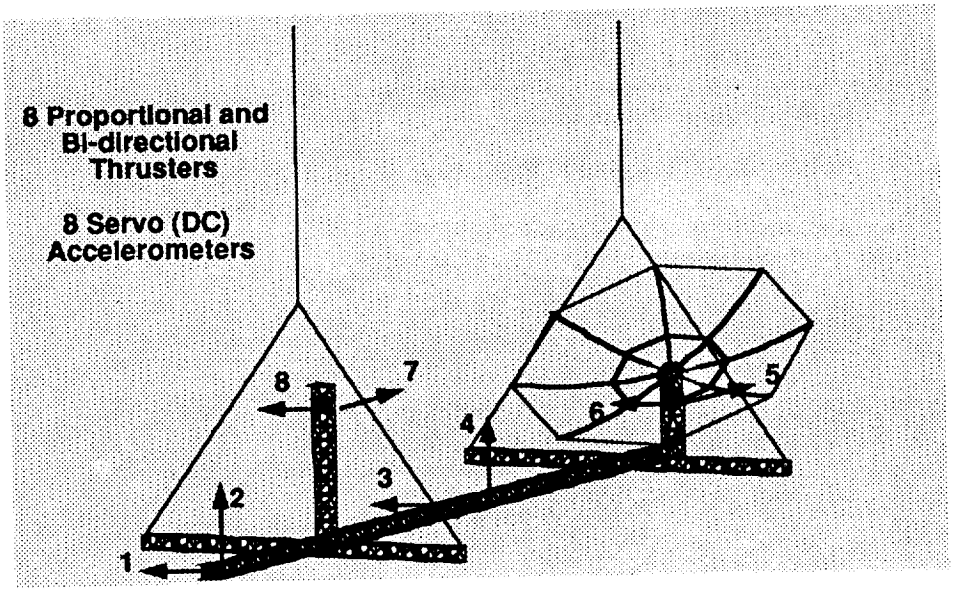

Structural and Line-Of-Sight Modeling

The Phase-0 CEM truss structure was designed to simulate the generic dynamic behavior of space platforms with 1 to 2 Hz global vibration modes coupled with higher-frequency, localized or appendage vibration modes. For ground testing, a structural suspension system was designed to permit all 6 "rigid-body" modes while not overstressing the truss struts due to gravitational preload. The resulting structural system, including the suspension, was modeled by the NASTRAN finite element program. The inclusion of nonlinear differential stiffness was required to predict the "rigid" body modes and the effect of the suspension on the flexible body modes.

As indicated below, the NASTRAN model was used to compute an eigen basis for control design and simulation using the MATLAB program. Various levels of model reduction were performed. Typically a 40 mode "truth" model was used for simulation of the closed-loop response of the Phase-0 testbed.

Once a time history of the modal states was computed, a linear transformation of the response was performed to predict the line-of-sight pointing performance [5].

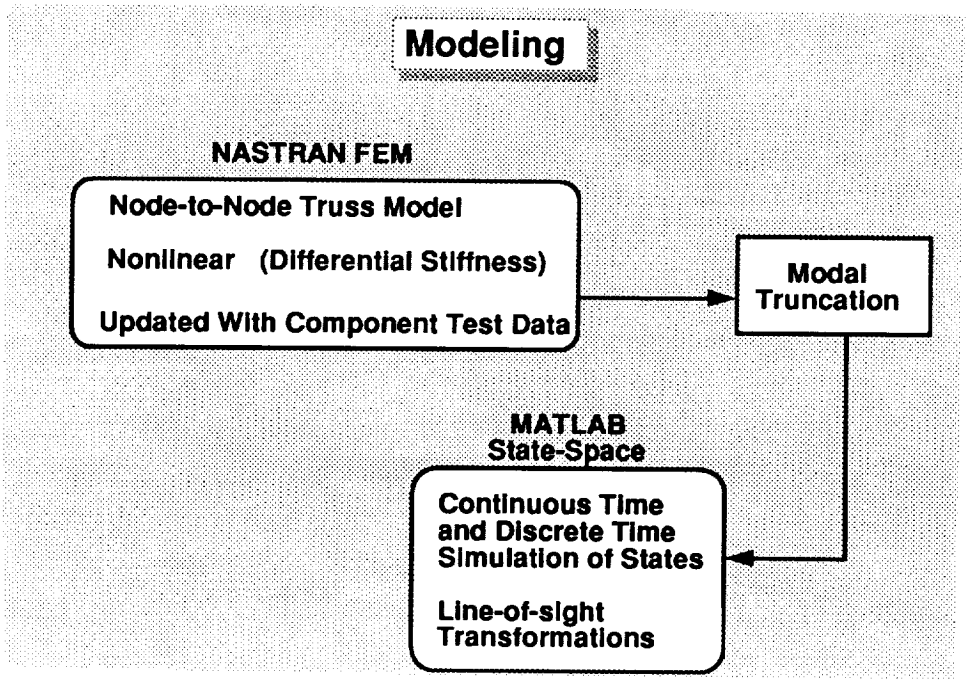

Test and Analysis Frequency Correlation

Modal vibration tests of the CEM have been performed using 24 servo and 195 piezo channels of accelerometer data. Multi-input, multi-output (MIMO) tests were performed to measure the frequency response functions between the acceleration output to the force input from each of the 8 thrusters. The data below show the experimental frequencies as identified from the frequency response functions using the Polyreference method of data reduction. The mode numbers are based on the order of the analytical mode shapes. It is interesting to note the measured damping decreases with increasing mode number.

The frequency error between test and analysis is also shown. Two values of error are shown, one for the original finite element model (FEM) and one for an updated FEM using measured thruster air hose stiffness and component test data from the Phase-0 truss. The refined model was much more accurate in predicting the modes up to 2.5 Hz; however, considerable error still remained in the prediction of modes involving the reflector appendage.

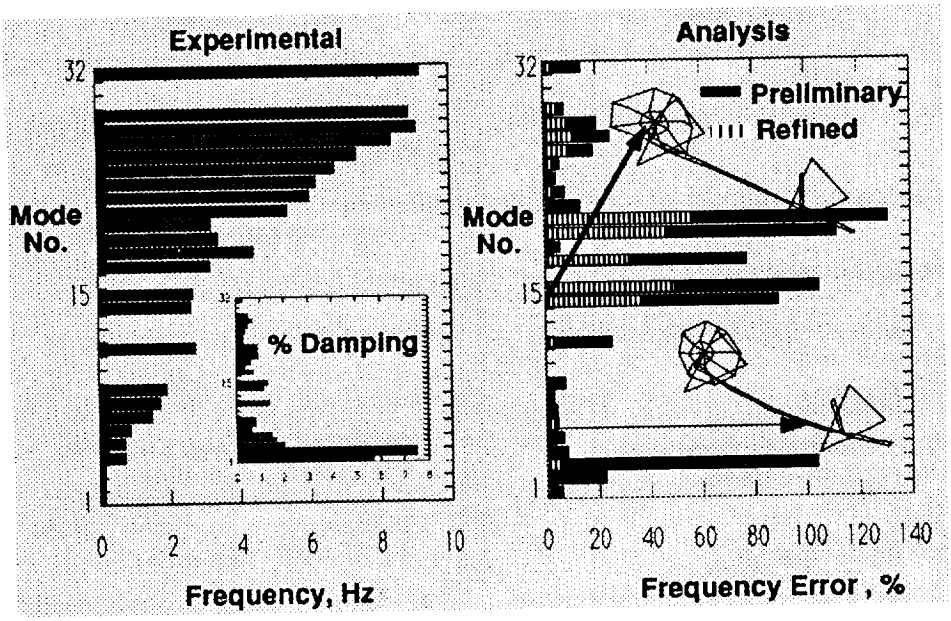

Phase-0 CEM Investigators

A wide variety of research was performed on the Phase-0 CEM. The table below shows the investigators and their major area of research. Two teams at Langley performed most of the system studies. Within the Spacecraft Dynamics Branch, the CSI Ground Test Methods team performed hardware implementation and HAC/LAC control studies. The CSI Analytical Design Methods Team of the Spacecraft Controls Branch performed much research on advanced controllers and integrated controls/structures design.

A number of guest investigators (external to NASA LaRC) pursued CSI technology development using the Phase-0 testbed. The work by JPL is of particular merit and will be described later.

It must be stated that each of the investigators were supported by a large contingent of NASA LaRC and Lockheed Engineering and Sciences Corporation employees. Without this technical support, only a fraction of the studies could have been completed during the Phase-0 CEM operational period (May 21, 1991 to September 5, 1992).

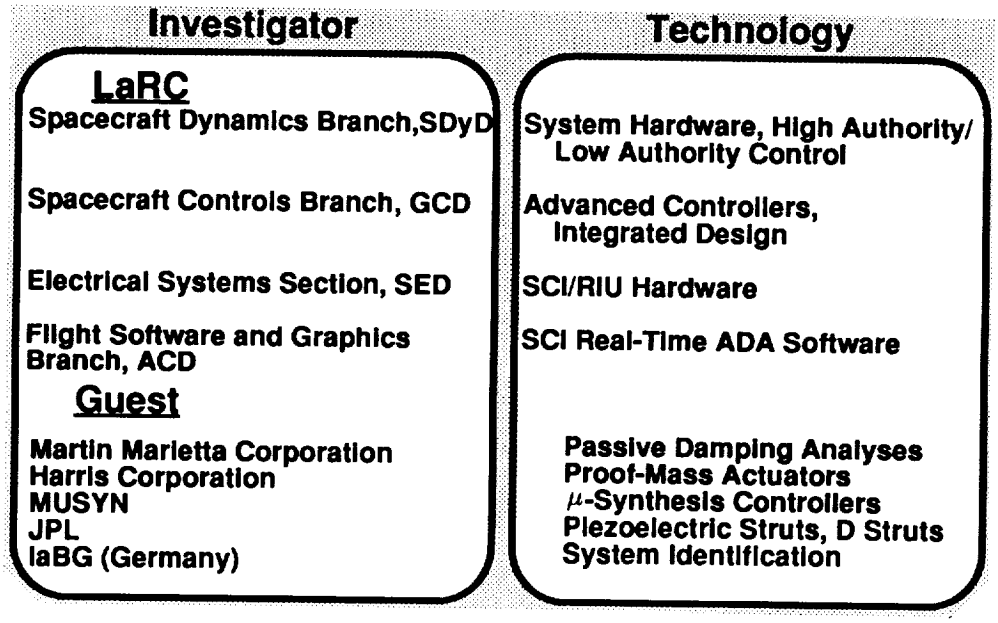

Controller Delay and Non-Collocation Effects

Among the first closed-loop controllers that was executed on the testbed was a dissipative controller with "guaranteed stability" if actuator and sensor collocation was realized. The figure below shows neither spatial nor temporal collocation was realized in the initial experiments.

The time delay introduced by digital implementation of the controllers can result in instabilities. The real-time controller update rate was set to 80 Hz for the first experiment which is more than an order of magnitude greater than the controller bandwidth. Nevertheless, a 7 Hz mode was being destabilized. By simply increasing the controller update rate to 350 Hz, the decrease in time delay stabilized the response. This early lesson indicated that the controller update rates should approach two orders of magnitude higher than the controller bandwidth when trying to implement a continuous time controller with discrete computations.

It was also learned that the original accelerometer mounting violated spatial collocation. The original non-spatial collocation of sensors and actuators involved coupling of bending and torsion vibrations. The figure on the right shows the response with the original accelerometer installation (on the corner of the truss). The accelerometer detected torsional vibration which was fed-back to a thruster pair which could only produce bending. Hence, significant performance degradation was observed. By moving the accelerometers to prevent the torsion/bending coupling, good closed-loop performance was obtained.

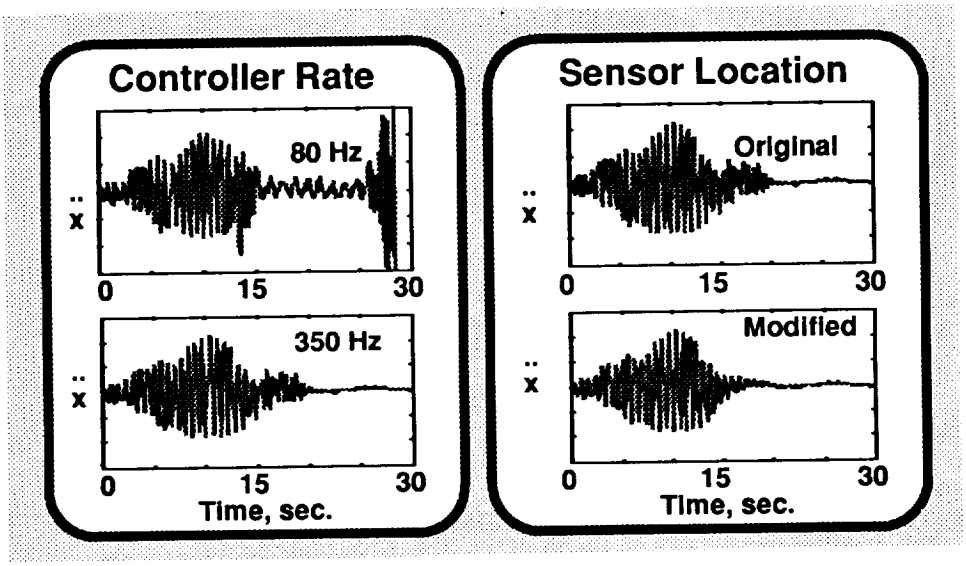

Real-Time Computing

To implement the control laws in digital (discrete) form, several real-time computing systems have been developed. The figure below highlights a flight like SCI computer system, programmed in ADA and implemented using a flight qualified 1553B bus structure. The system software for implementation of general control laws and digital filtering was successfully demonstrated using the Phase 0 testbed.

The controller update rates, which have already been shown to influence stability, are one of the key parameters to assess the adequacy of a real-time computer for closed-loop testing. The data below show the SCI computer can achieve rates exceeding 200 Hz for an 8 input-8 output controller. However, the remote interface unit (RIU) is limited to 200 Hz. This 200 Hz rate proved adequate for most of the Phase-0 experiments. Test results and development documentation for the SCI/RIU system can be found in Ref. [6].

It is noted the primary controller for the Phase-0 testbed was a VAX 3200. The enhanced version of this computer, coupled with tridiagonalization of the controller A matrix could achieve 280 Hz rates for a 40 state controller with 8 inputs and 8 outputs. The VAX based primary control system development is described in Ref. [7].

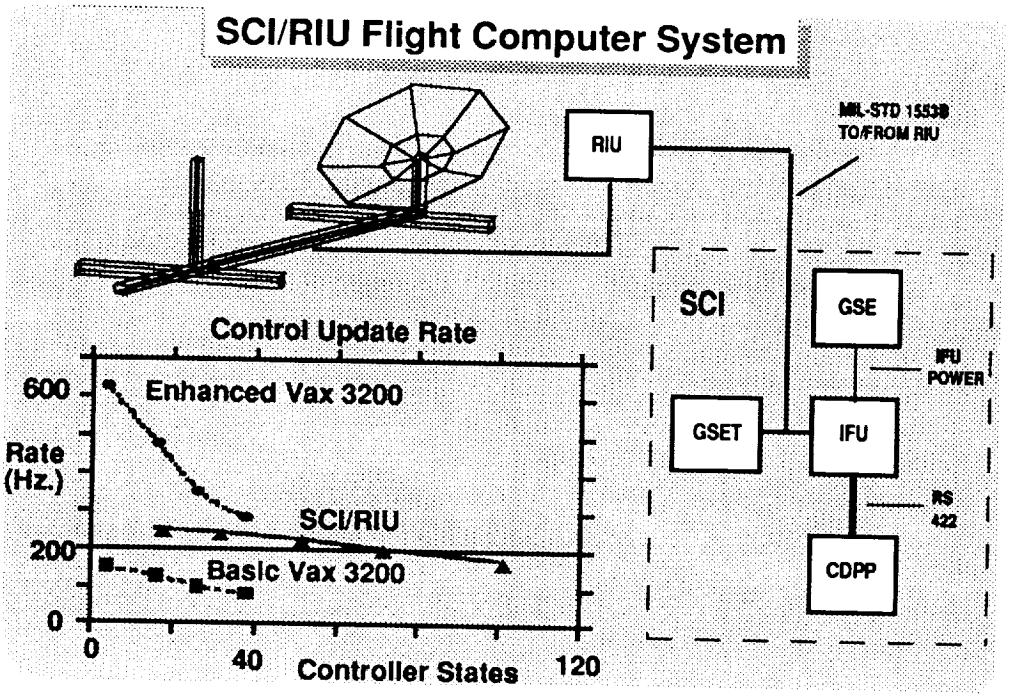

Closed-Loop Studies

A number of controllers have been designed for the Phase-0 CEM using both model independent and model based approaches as indicated below. The performance goals have been to add damping to prescribed modes and to minimize LOS pointing errors due to applied disturbances. Stability determination of the controllers was based on experimental transient response data.

Among the dissipative controllers that were tested, an active vibration absorber (AVA) concept [8, 9] has been used to dissipate energy from the first nine modes of the Phase-0 CEM. The AVA controller is guaranteed to be stable for collocated actuators and sensors. LQG and H-infinity model based controllers have been designed for the Phase-0 CEM. The LQG controllers usually result in instabilities due to controller spillover in higher-frequency, unmodeled modes when high performance is desired. Results from H-infinity controller testing show that to maintain stability with the model error that existed in the FEM, relatively low gain (low performance) controllers were obtained. H-infinity and μ synthesis controller results are also described in Refs. [10, 11].

The AVA controller and a combination LQG/AVA (HAC/LAC) controller will be described and compared in the next few pages. In addition, a novel second-order observer for use with acceleration measurements will be described. Closed-loop LOS pointing results are presented and stability enhancement using strut actuators will be demonstrated.

- **Dissipative Controllers**
  - Active Vibration Absorber (AVA)
- **Controller Merit Index**
  - Compare AVA, LQG and HAC/LAC
- **Model Based Controllers**
  - HAC/LAC
  - Second-Order Observer
- **Line-Of-Sight Pointing**
  - Closed-Loop Performance
  - Predictive Accuracy
- **Stability**
  - HAC/LAC Stability
  - Piezoelectric Strut Appendage Control

Active Vibration Absorber (AVA)

Several collocated controllers have been tested to verify stability and performance. An active vibration absorber (AVA) concept [8, 9] has been used to dissipate energy from the first nine modes of the Phase-0 CEM. The AVA controller is guaranteed stable for collocated actuators and sensors; however, as already shown collocation is only approximated on the Phase-0 testbed.

As shown below, the AVA controller emulates a spring-mass-damper system by using acceleration feedback and a second-order control law. An added advantage of the AVA controller is that the control law gains can be synthesized on a mode by mode basis since the only stability constraint is that positive definite controller mass, damping, and stiffness matrices be used.

Tests of this controller on the Phase-0 testbed have shown good performance and high stability as long as the thruster and accelerometer pairs are "nearly" collocated. The combination of actuator dynamics and computational delay limited the use of the AVA controllers to a bandwidth of 0 to 10 Hz.

- Emulates a mass-spring-damper attached to the structure
- The second-order controller is of the form:

$$M_c\ddot{x}_r + D_c\dot{x}_r + K_c x_r = -M_c H\ddot{y}$$

$$u = D_c\dot{x}_r + K_c x_r \qquad x_r = x_c - Hy$$

- Guaranteed Stable for Thruster/Accelerometer Collocation
- Gain synthesis on a mode by mode basis

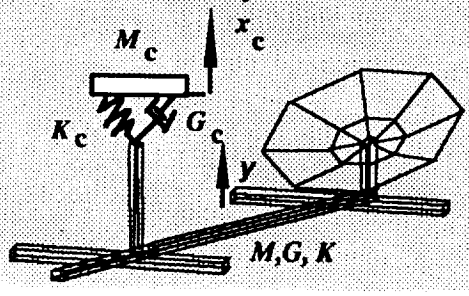

HAC/LAC Control

The HAC/LAC controller developed for the Phase-0 testbed was formed by using the LQG controller for performance (high authority) and designing AVA controllers for stability (low authority); i. e. AVA control of those modes being destabilized by the LQG controller. In the figure below, the HAC and LAC loops are shown to operate in parallel. It is noted that the LAC loop does not appreciably add to the amount of force produced by the thrusters. The low authority "stability" modes require very little energy to control. The HAC/LAC controller, with the first nine modes of the testbed controlled by the LGQ loop and six modes in the AVA loop, was the primary controller used for LOS pointing demonstrations.

An alternative approach to stabilize the LQG controller, by decreasing the LQG gains for gain stabilization and adding damping with an AVA controller to the same modes to recover performance, was met with limited success. A third approach to improve the stability of implementing LQR (model based) gains was through the use of a second-order observer in place of the Kalman Filter. This new observer is described next.

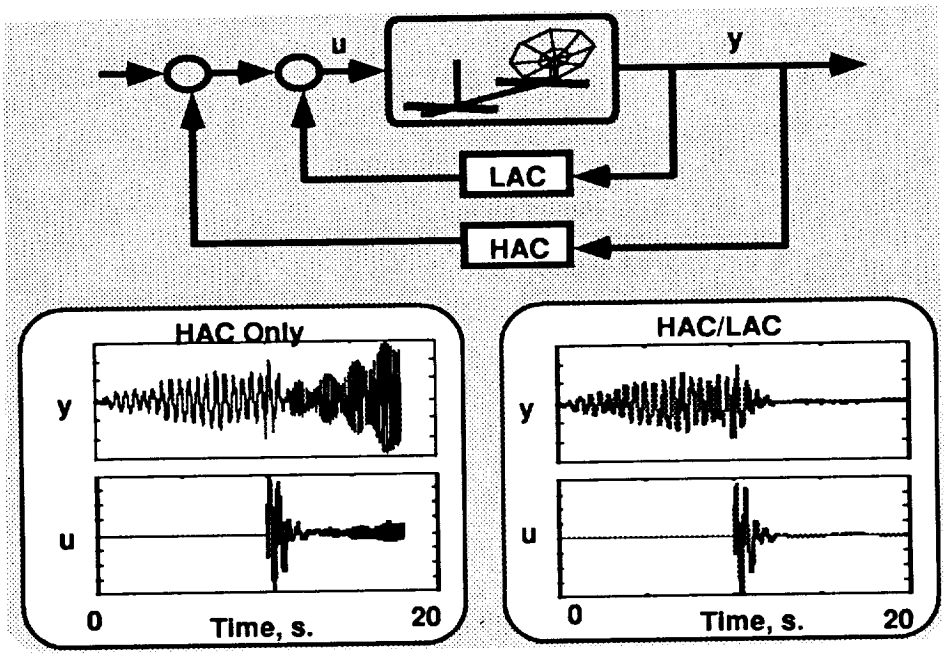

Second-Order State Estimation Using Acceleration Measurements

A second-order observer has been developed and applied to the Phase-0 testbed for state estimation with direct feedback of acceleration measurements. The observer uses the concept of the AVA controller as applied to the observer model error equation. Hence the model independent stability and mode-by-mode gain synthesis properties of the AVA controller also apply.

To verify the second-order observer performance and stability, LQR gains were synthesized and used with both the Kalman Filter and the second-order (AVA) observer. The figures below show the experimental response of the structure at accelerometer location 2. The data for the LQG shows an instability which required the actuators to be disabled at t=16.6 sec. This instability of a mode near 7 Hz is due to unmodeled dynamics since a nine mode model with frequencies less than 2 Hz was used in the LQR and Kalman filter gain synthesis. Although the AVA observer used the same nine-mode control gain, the AVA observer produced a stable closed-loop response. Hence, the second-order (AVA) observer is useful in reducing observation spillover instabilities. Details of this work are found in Ref. [12].

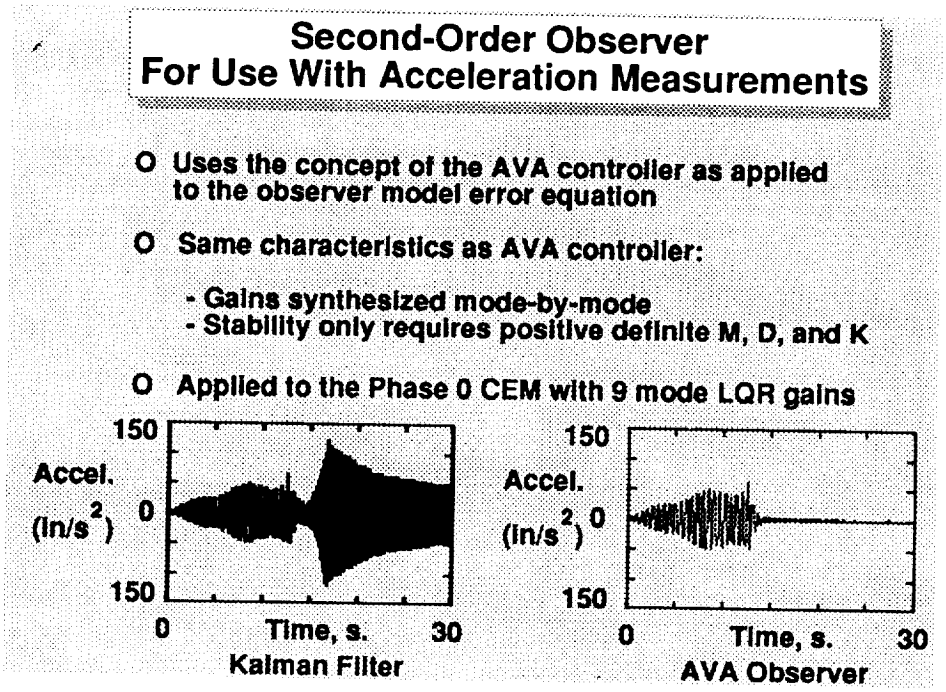

Line-Of-Sight Pointing Results

Using the HAC/LAC controller described previously, the LOS pointing performance has been measured and simulated using the reduced order state space models. Typical tests consisted of 10 seconds of excitation followed by either free-decay or closed-loop control.

As indicated in the figures below, the test and simulated LOS pointing is qualitatively in very good agreement, although some quantitative differences are apparent. This indicates that control law design for flexible structures using finite element derived design models is quite viable.

The performance of the HAC/LAC controller can be described in terms of the LOS pointing error decay rates. The damping is increased from less than 1% to more than 10% between open- and closed-loop, respectively. While this limitation was partially due to actuator saturation, the stability margin of the high-gain HAC/LAC controller limited performance as described next.

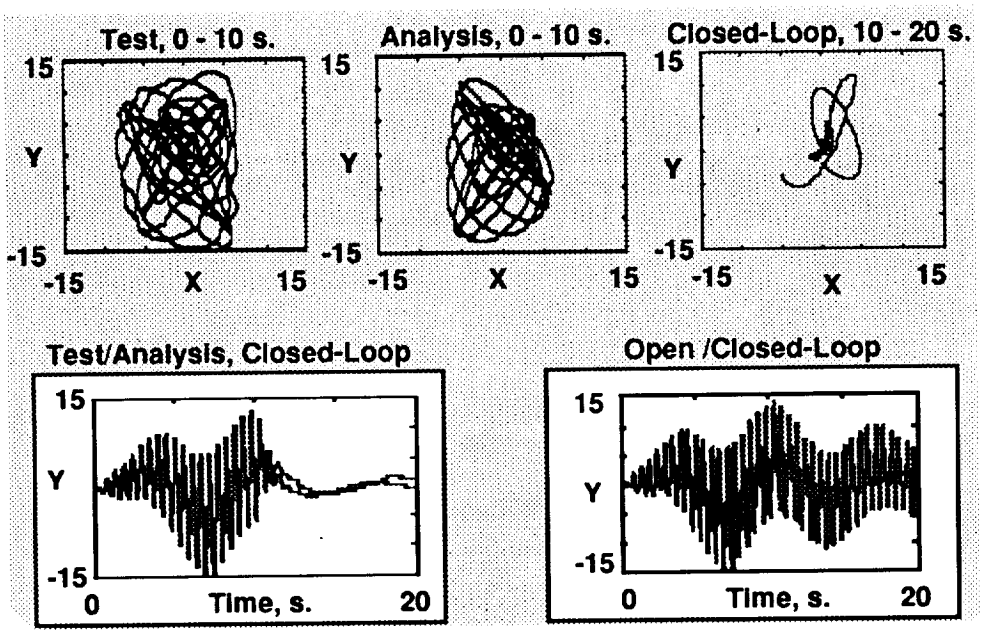

Controller Merit

To assess the performance of various controllers, a merit index was used that measures the RMS LOS error and the RMS energy used by the controller. The lower the merit index, the "better" the controller. As shown below, the HAC/LAC controller merit was among the best tested. The HAC/LAC controller was formed by using the LQG controller for good performance and designing AVA controllers for those modes being destabilized by the LQG control.

The LQG controller was found to have the best merit index if stability could be maintained. In the data below, a 7 Hz mode is destabilized by the LQG controller as shown in the LOS pointing error. The AVA controller was stable but produced a poor merit index. By combining the two controllers as described above, good stability and a reasonable controller merit index were obtained. The next page further describes the HAC/LAC controller.

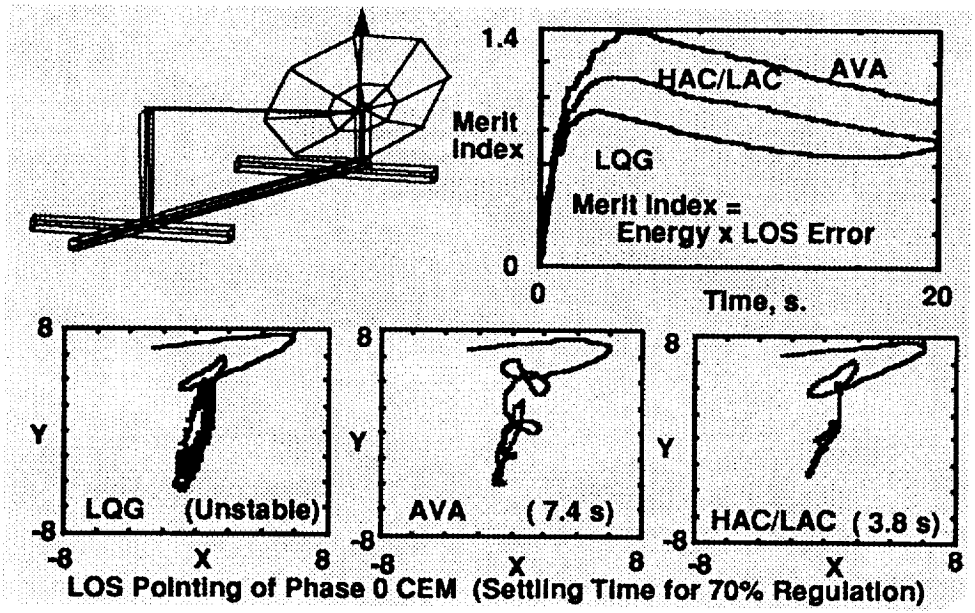

Controller Stability

The high-gain HAC/LAC controller used to produce the closed-loop line-of-sight pointing results shown on the previous page shows lower stability than desired. The figure below shows the open-loop and closed-loop frequency response for the acceleration magnitude at location 8 to a force input at location 1. This particular HAC/LAC controller consisted of an LQG design for the first 9 modes (modes below 2 Hz) and 6 single mode AVA controllers. The AVA controllers were designed to enhance stability of the HAC (LQG) controller in the 6 to 10 Hz frequency range. Nevertheless, there remained a laser tower bending mode which showed very low stability at a frequency near 7 Hz as noted by higher vibration magnitudes in closed-loop than in open-loop!

To enhance the stability of the HAC/LAC controller the use of induced strain actuators at the base of the laser tower was proposed. The next page describes the implementation of two JPL piezoelectric struts and four viscous damped struts to augment the HAC/LAC controller stability.

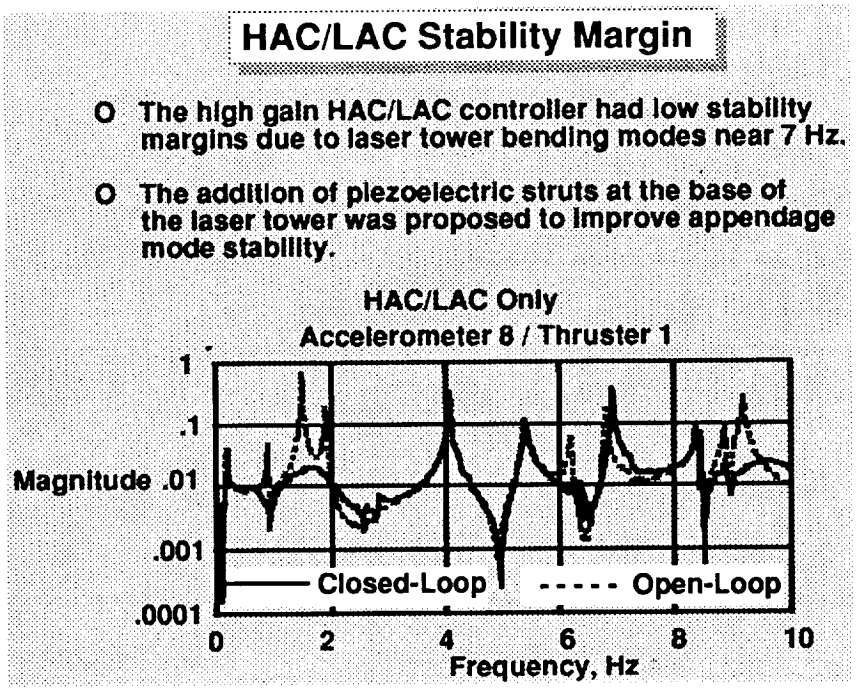

Appendage Control With Strut Actuators

Two active struts and four passive struts were incorporated in the Phase-0 CEM testbed to augment the damping of modes in the frequency range of 5 to 8 Hz. The active struts, which replaced two longerons at the base of the laser tower, were developed at JPL and are described in Ref. [13]. The passive struts, used to replace four existing diagonal truss members, were jointly developed at Honeywell and JPL as described in Ref [14].

The figures below show the effects of the active and passive struts on the frequency response magnitude function shown previously. Modes in the range of 5 to 8 Hz were successfully attenuated. The figure on the right shows that the combination of the HAC/LAC controller and the decentralized appendage controller using strut actuators. It is shown that the laser tower appendage mode no longer poses a stability concern.

From these results it is shown that the addition of actuators and sensors to control appendage vibrations can be successfully achieved using strut actuators. The ability to implement the appendage controllers in a decentralized manner helps to reduce the complexity of the centralized platform controllers. These results are more fully documented in Ref. [15].

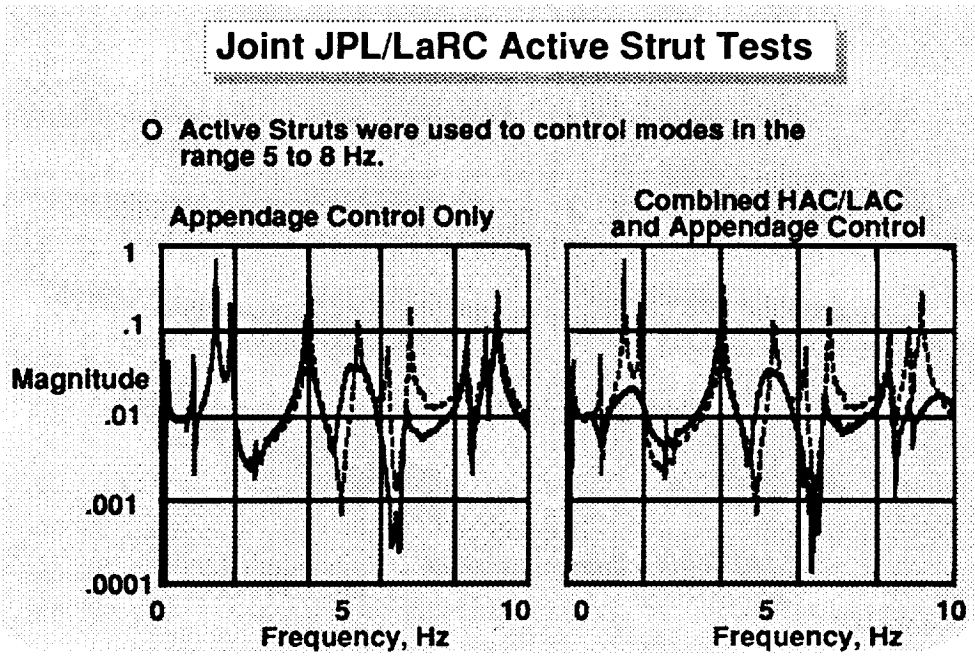

Evolution Of The CEM Testbed

Tests on the Phase-0 CEM were successfully concluded on September 5, 1991.

The Phase-1 testbed will be built based on an integrated design [16] of 21 different strut stiffness/mass properties and a static dissipative controller. The Phase-1 CEM will have the same geometry as the Phase-0 testbed. Tests of the Phase-1 CEM are planned for the spring and summer of 1992.

The Phase-2 CEM will entail a modification of the Phase-1 geometry and suspension. Moreover, Phase-2 will also include three two-axis gimbals and advanced scoring systems to simulate pointing of multiple science instruments. The Phase-2 CEM will permit 2.5 arc-sec pointing using piezo struts for flexible body control. Phase-2 also enables the study of multiple-payload platforms whereby a combination of centralized, hierarchical and/or distributed control schemes may be evaluated. Initial capabilities of the Phase-2 CEM should be operational in the late fall of 1992.

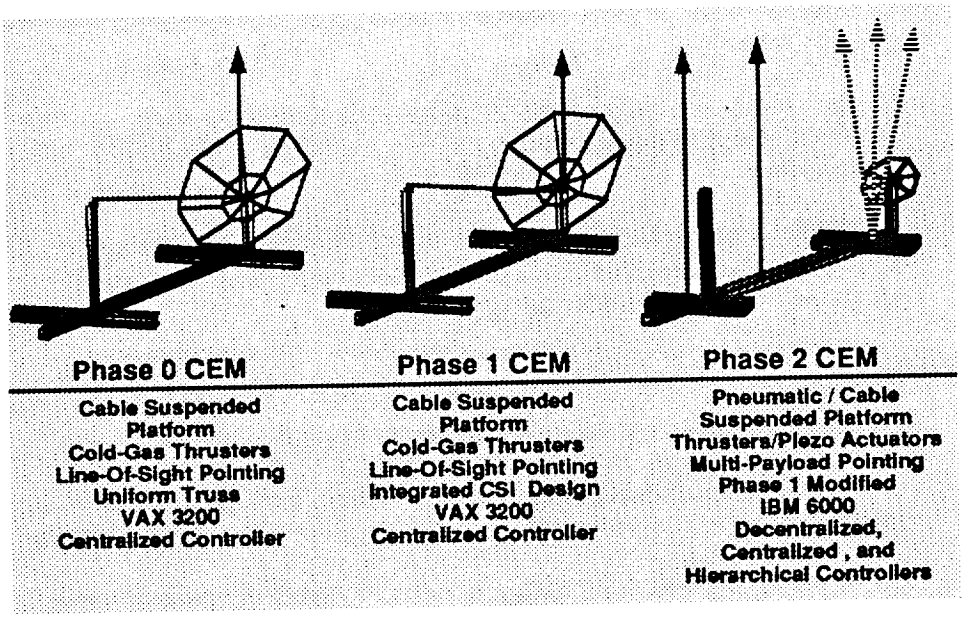

Summary

The Phase-0 CEM has been a very fruitful testbed for the study of global LOS pointing and active vibration suppression. The testbed dynamic behavior was sufficiently rich that spillover instabilities were common in model based controllers. The Phase-0 testbed has proved to be very valuable in advancing flexible body control technology, training researchers, and building a knowledge base for future testbeds with similar objectives. Some important findings are offered below:

Design And Modeling

O Integrated suspension and structural design is needed to allow low-frequency dynamic behavior without violating static stress constraints.

O Finite element models should be based on component (and perhaps subassembly) tests to obtain sufficient accuracy for controller design models.

O Although differential stiffness (due to gravity preload) may not significantly affect flexible body vibrations, it must be included in the analysis to predict suspension cable effects.

Hardware

O Truss joints fabricated to carry 1600 lbs of load have typically produced 0.1 - 0.3 % critical damping in the flexible body modes of vibration.

O Linear bi-directional thrusters can be used for laboratory control of flexible structures.

O Servo accelerometers can be used, in conjunction with software bias removal, for feedback control of low frequency (0.15 Hz) structural vibrations.

O Digital implementation of continuous time controllers requires nearly two orders of magnitude faster update rates than the highest mode frequency in the controller design model.

Control

O Dissipative (static and dynamic) controllers are highly stable provided both spatial and temporal collocation can be approximated.

O Model based controllers, when stable, are usually more energy efficient for the same level of performance than dissipative controllers.

O Appendage control, using a decentralized control approach, can enhance stability and simplify the centralized platform controller.

Acknowledgements

The authors wish to thank the entire CSI Ground Test Methods Team at the LaRC for excellent support of the Phase-0 CEM tests. We further wish to recognize Brantley Hanks of the Spacecraft Dynamics Branch, Structural Dynamics Division, and Jerry Newsom of the CSI Office, Guidance and Controls Division, for managing the CEM testbed activities.

References

1. Belvin , W. K., Horta, L. G., Elliott, K. B., Bruner, A. and Sulla, J.: "The LaRC CSI Phase-0 Evolutionary Model Testbed: Design and Experimental Results," WL-TR-91-3013, Fourth NASA/DOD CSI Conference, Orlando FL, Nov., 1990, pp. 594-613.

2. Reaves, M. C., Belvin, W. K., and Bailey, J.: "Finite Element Analysis and Ground Testing of the CSI Evolutionary Model Reflector," NASA TM 4293, July 1991.

3. Belvin, W. K., Elliott, K. B., Horta, L. G., Bailey, J., Bruner, A., Sulla, J., Won, J. and Ugoletti, R.:"Langley's CSI Evolutionary Model: Phase 0," NASA TM 104165, August 1991.

4. Jacot, A. D., Bushnell, G. S. and Anderson, T. M.: "Bi-Directional Thruster Development and Test Report," NASA CR 182013, Feb. 1990.

5. Lim, K. B. and Horta, L. G., "A Line-Of-Sight Performance Criterion for Controller Design of a Proposed Laboratory Model, " AIAA no. 90-1226, AIAA Dynamics Specialist Conference, Long Beach, CA, April 1990.

6. Sparks, D. W. Jr., Peri, F. Jr., and Schuler, M. P.: "CSI Flight Computer System and Experimental Test Results," Fifth NASA/DOD CSI Technology Conference, NASA CP-3177, Lake Tahoe, NV, March, 1992.

7. Elliott, K. B., Ugoletti, R. and Sulla, J.: "Computer Optimization Techniques for NASA Langley's CSI Evolutionary Model's Real-Time Control System," 38th International Instrumentation Symposium, Las Vegas, NV, April 1992.

8. Juang, J-N., and Phan, M., "Robust Controller Designs for Second-Order Dynamic Systems: A Virtual Passive Approach," NASA TM-102666, May, 1990.

9. Bruner, A. M., Belvin, W. K., Horta, L. G. and Juang, J-N.: "Active Vibration Absorber for CSI Evolutionary Model: Design and Experimental Results," 32nd Structures, Dynamics, and Materials Conference, Baltimore, Md, April, 1991.

10. Lim, K. B., Maghami, P. G. and Joshi, S. M.: "A Comparison of Controller Designs for an Experimental Flexible Structure," Presented at the 1991 ACC Conference, June, 1991, Boston, MA.

11. Lim, K. B. and Balas, G. J.: "Line-Of-Sight Control of the CSI Evolutionary Model: μ Control," American Control Conference, Chicago, IL, June, 1992.

12. Belvin, W. K.: "Second-Order State Estimation Experiments Using Acceleration Measurements," AIAA Paper no. 92-2093, Dynamics Specialist Conference, Dallas, TX, April 1992.

13. Anderson, E. H., Moore, D. M., Fanson, J. L. and Ealey, M. A.: "Development of an Active Member Using Piezoelectric and Electrostrictive Actuation for Control of Precision Structures," AIAA Paper No. 90-1085-CP, 31st Structures, Dynamics, and Materials Conference, Long Beach, CA, April 1990.

14. Anderson, E., Laskin, B. O'Neal, M. Davis, P. and Ginter, S.: "The D-Strut: A Viscous Passive Damper for Use in Precision Truss Structures," WL-TR-91-3013, Fourth NASA/DOD CSI Technology Conference, Orlando, FL, Nov. 1990, pp. 41-52.

15. Neat, G., Lurie, B., O'Brien, J., Garnica, A., Belvin, K., Sulla, J. and Won, J.: "Joint Langley Research Center/Jet Propulsion Laboratory CSI Experiment," AAS Guidance and Control Conference, Keystone, CO, Feb. 1992.

16. Maghami, P. G., Joshi, S. M., Walz, J. E. and Elliott, K. B.: "Integrated Design of the CSI Evolutionary Structure: A Verification of the Design Methodology," Fifth NASA/DOD CSI Technology Conference, NASA CP-3177 Lake Tahoe, NV, March 1992.

N93-18934

CONTROLS-STRUCTURES-INTERACTION DYNAMICS DURING RCS CONTROL OF THE ORBITER/SRMS/SSF CONFIGURATION

J. A. Schliesing
NASA Johnson Space Center
Houston, Texas 77058

L. S. Shieh
Department of Electrical Engineering
University of Houston–University Park
Houston, Texas 77204

ABSTRACT

During the assembly flights of the Space Station Freedom (SSF), the Orbiter will either dock with the SSF and retract to the final berthed position, or will grapple the SSF using the Shuttle Remote Manipulator System (SRMS) and maneuver the SRMS coupled vehicles to their final berthed position. The SRMS method is expected to take approximately one to one and a half hours to complete and require periodic attitude corrections by either the Orbiter or the SSF reaction control system (RCS) or continuous control by a control moment gyro (CMG) system with RCS desaturation as required. Free drift of the attached vehicles is not currently thought to be acceptable because the desired system attitude will quickly deteriorate due to unbalanced gravity gradient and aerodynamic torques resulting in power generation problems, thermodynamic control problems, and communications problems. This paper deals with the simulation and control of the SRMS during trunnion/latch interaction dynamics and during RCS maneuvers. The SRMS servo drive joints have highly non-linear elastic characteristics which tend to degrade sensitive control strategies. In addition the system natural frequencies are extremely low and depend on the drive joint deflections and SRMS geometric position. The lowest mean period of oscillation for the Orbiter/SRMS/SSF(MB6) system in brakes hold mode positioned near the final berthed position is approximately 120 seconds. A detailed finite element model of the SRMS has been developed and used in a newly developed SRMS systems dynamics simulation to investigate the non-linear transient response dynamics of the Orbiter/SRMS/SSF systems. The present SRMS control strategy of brakes only recommended by the Charles Draper Labs is contrasted with a robust controller developed by the authors. The robust controller uses an optimal linear quadratic regulator (LQR) to optimally place the closed–loop poles of a multivariable continuous-time system within the common region of an open sector with the sector angle $\pm 45°$ from the negative real axis, and the left-hand side of a line parallel to the imaginary axis in the complex s-plane. This guarantees that the critical damping ratio for the desired control modes is equal to or in excess of 0.707. The matrix sign function is used for solving the Riccati equations which appear in the controller design procedure. Fast and stable algorithms have recently been developed for the computation of the matrix sign function (ref. 1). Simulation results are given which

demonstrate the potential CSI involvement for the current SRMS control system and the proposed control system.

INTRODUCTION

The Space Station Freedom (SSF) will be assembled and supplied by the Orbiter. Each visit to the SSF will require a rigid structural attachment between the vehicles in order to assemble the mission build (MB) segments, and/or to resupply and exchange crew members. During the assembly flights of the SSF, the Orbiter will either dock to the SSF and retract to form a rigid and stable structural connection between the docking vehicles, or an Orbiter crew member will grapple the SSF using the SRMS and maneuver (see figure 1) to the berthed position. An intensive engineering study involving many Johnson Spacecraft Center (JSC) divisions, their subcontractors, together with the Canadian SPAR Aerospace Limited, is being conducted to determine the viability of the SRMS berthing approach for attaching the large space structures. The viability of the docking approach to mating vehicles with similar weight properties has been established in previous NASA projects.

The SRMS attachment method for MB2 through MB6 is expected to take from one to one and a half hours to complete and requires the Orbiter to maneuver the SRMS attached system from the initial grapple attitude to the combined vehicle torque equilibrium attitude (TEA). Free drift of the attached vehicles at this point in the mission is not thought to be acceptable because the desired system TEA will quickly deteriorate to large attitude excursions due to the unbalanced gravity gradient and aerodynamic torques acting on the system. This will result in power supply problems, thermodynamic control problems, and communication problems. Alleviating these problems requires periodic attitude corrections by the Orbiter Reaction Control System (RCS), or the SSF RCS, or continuous control by the Control Moment Gyro (CMG) system with RCS desaturation as required. Where possible, the CMG system will be employed to maintain the TEA since its control is less likely to move the SRMS joints significantly. However, during the SRMS retraction while using the CMG's it may be necessary to desaturate the moment build up of the CMG's using either the Orbiter or the SSF RCS jets. The SRMS must not allow the berthing vehicles to contact each other with sufficient relative kinetic energy to damage any part of either structure. Thus for the SRMS attachment system to be viable, with regards to a structural loads standpoint, it must be able to withstand some form of attitude maneuvers using RCS jets, and be able to control and limit the relative contact kinetic energy and the constrained motion loading at the structural latch interfaces.

The SRMS servo drive joints have highly nonlinear elastic characteristics due to the anti-backlash mechanisms in their gear boxes which tend to degrade sensitive control strategies. In addition the natural frequencies of the combined system are extremely low and nonlinear, depending on the drive joint deflections, the SRMS geometric position, and the control system gains if the brakes are not applied. The lowest mean period of oscillation for the Orbiter/SRMS/MB6 system during the SSF trunnion insertion into the

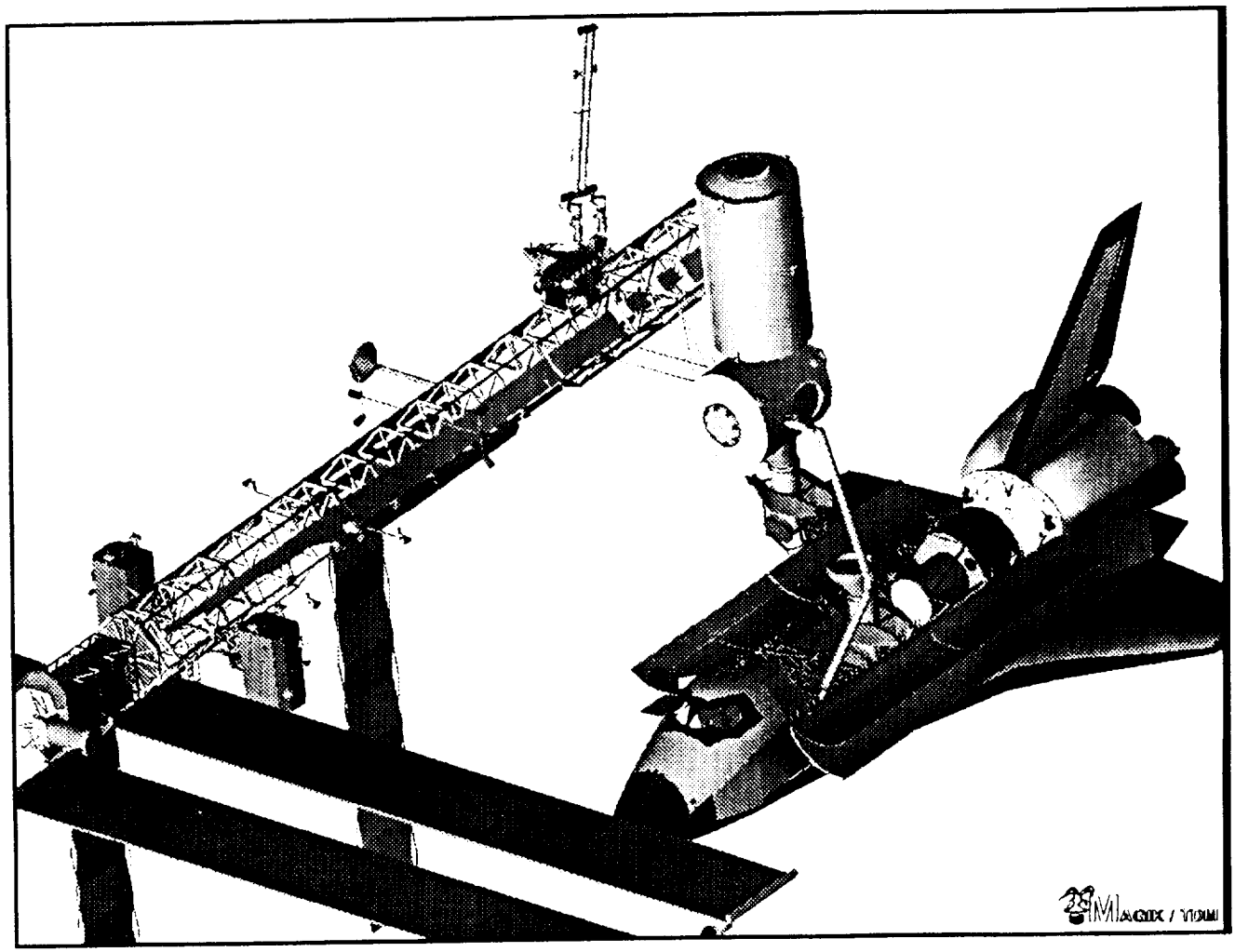

Figure 1. Orbiter/SRMS/MB6 berthing orientation.

Payload Retention Latch Assembly's (PRLA's), a relatively stiff SRMS position, is around 120 seconds with the brakes on. The current SRMS system responds to external loads with non–commanded motion and long transient response oscillations which add critically needed time to the retraction maneuver task. Evidence of this effect has been noted by crew members on past shuttle flights where crew members waited for the oscillation to decay before issuing new maneuver commands. The extremely low frequency response of the heavy Orbiter/SRMS/SSF system will only aggravate this aspect of the control task. A disturbance rejection methodology will greatly enhance SRMS operations.

In order to accurately represent the structural dynamics of the entire coupled system and because of the complex nature of the SSF finite element component structures, a detailed finite element model of the SRMS with nonlinear joints was developed by the authors. This model has been coupled to the Orbiter and the finite element model of the MB6. The MB stage modal models are contractually furnished by the McDonnell Douglas Space System Company for the Space Station Freedom Loads and Dynamic Working

Group. Modal frequencies to 50 Hertz are retained for the analysis to accurately form a mathematical basis for the SRMS flexible body dynamics coupled with the joint servomotor dynamics. The requirements for loads convergence during trunnion to PRLA contact require modal frequencies to 25 Hertz. The coupled modal approach efficiently represents the arm segment to arm segment interaction since it is included in the basic finite element model with the correct boundary conditions. The modal model is then used in a newly developed SRMS systems dynamics simulation program, Manipulator Docking Dynamics Program (MDDP), to investigate the non-linear transient response dynamics of the Orbiter/SRMS/SSF systems during attitude control maneuvers and during interface trunnion/latch interaction dynamics. This approach has the advantage of accurately representing the entire SRMS flexural dynamics coupled with the flexible body dynamics of the attached vehicles.

The present brakes on control system response of the SRMS has been simulated for a representative Orbiter PRCS jet firing. A single .080 second pulse dual jet +pitch maneuver was executed and the system was allowed to ring out for 100 seconds. Next a similar case was simulated with the optimum robust controller developed by the authors. The robust controller uses a linear optimal quadratic regulator to optimally place the closed-loop poles of a multivariable continuous-time system within the common region of an open sector, and the left-hand side of a line parallel to the imaginary axis in the complex s-plane. The open sector, see figure 2, is defined by a sector angle of $\pm 45°$ from the negative real axis. This guarantees that the damping ratios for the desired control modes are in excess of 0.707 percent of critical. The matrix sign function (ref. 1) is used for solving the Riccati equations which appear in the controller design procedure.

In summary, this paper deals with (1) the development and capability of the analytical test bed MDDP used to simulate the systems dynamics and resulting transient structural dynamics, (2) the theoretical basis for an optimal quadratic regulator with pole placement controller developed by the authors and used as an optional control method in the SRMS, and (3) the simulation results of controlling the SRMS with two different controllers during the transient dynamics occurring when the PRCS fires jets to begin a maneuver.

SIMULATION DESCRIPTION

A detailed finite element model of the SRMS has been developed to support the decision to study berthing the MB elements of SSF to the Orbiter using the SRMS. This model is intended to serve as a test bed in investigating the overall system dynamics during attitude control firing transients and during the interaction dynamics of the berthing vehicles as the SSF trunnions contact the Orbiter PRLA's. The interaction contact dynamics have been correlated with result from a NASTRAN simulation. The NASTRAN run simulated an initial impact velocity between the left front PRLA and the corresponding SSF trunnion. The interface between the trunnion and PRLA was elastically represented with a high stiffness spring perpendicular to the PRLA latch surface and with weak springs orthogonal to the load direction. Only the first compression loading segment of the

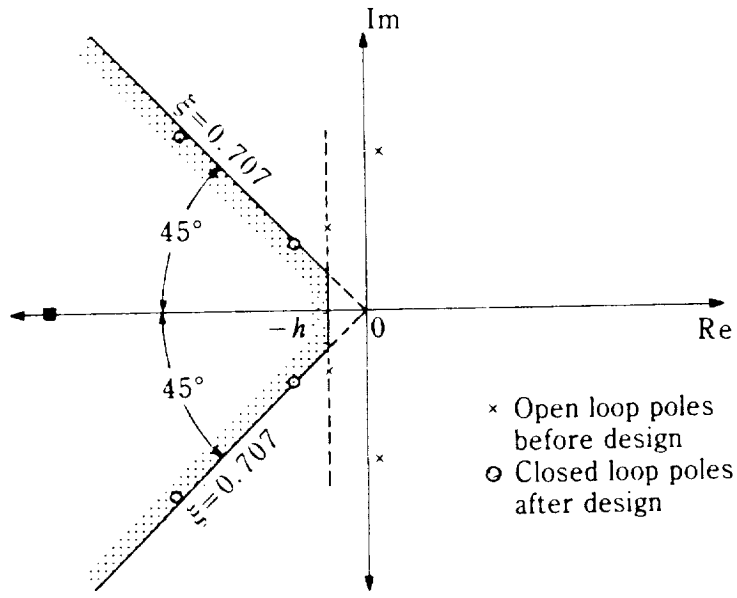

Figure 2. The region of interest in the continuous-time s-plane.

NASTRAN response simulation is applicable for correlation of impact and bounce from the surface. The MDDP has the simulation capability to bounce from surface contact to surface contact while dynamically coupled with the SRMS system. Surface contact is maintained as long as there is a compressive load on the surface. Figures 3 and 4 give the resulting load history for the case of impacting the systems with a relative z_o velocity of 0.1 fps. In figure 3, the NASTRAN load is perpendicular to the surface, while in figure 4 the MDDP load is given in component form. The bouncing characteristics predicted by MDDP are shown in figures 5 and 6 for a case where the trunnion first impacts near the apex of the latch then bounces from surface to surface. The load history is given in figure 5, and the motion history is given in figure 6. The MDDP simulation will also be used to study the interaction dynamics of pre–integrated truss (PIT) to PIT berthing dynamics. The detailed transient load histories will be processed in load indicator subroutines to determine design limit loads for the SSF. The finite element model of the SRMS is coupled with a rigid body Orbiter and a finite element model of the SSF-MB6. The MDDP simulation of the SRMS includes the following capabilities:

- Physical and dynamical properties
  - High frequency arm flexural dynamics (162 degrees of freedom).
  - SRMS joint servo control model adapted from the JSC Shuttle Engineering Simulator (SES), correlation in progress.

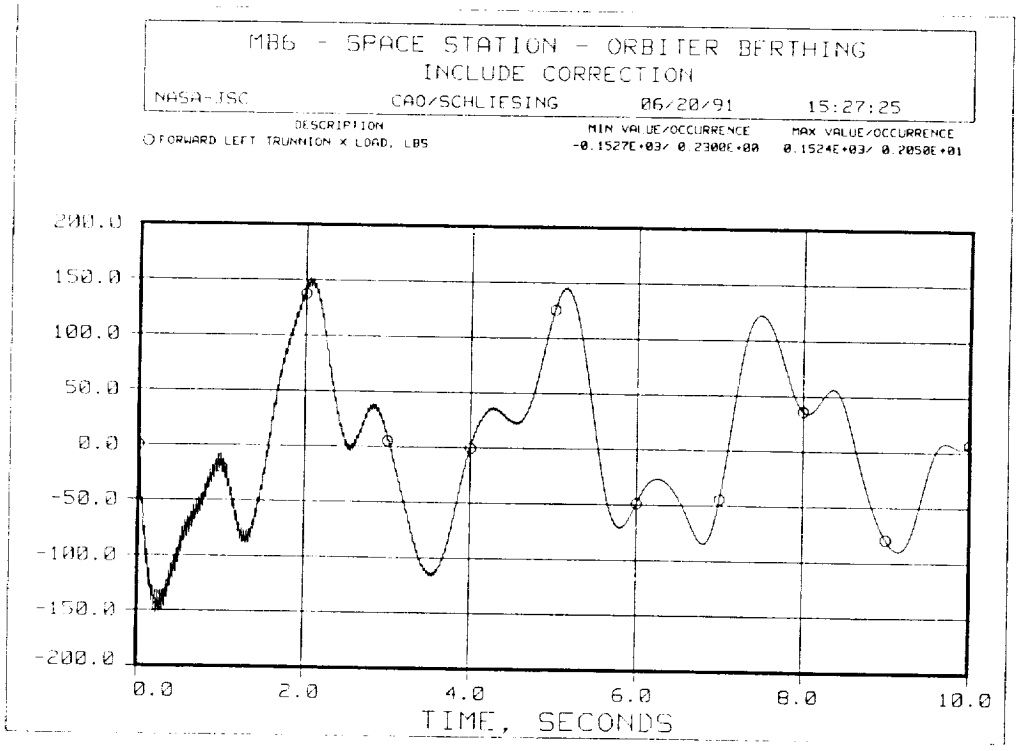

Figure 3. Interaction loads history for trunnion/PRLA contact computed by NASTRAN.

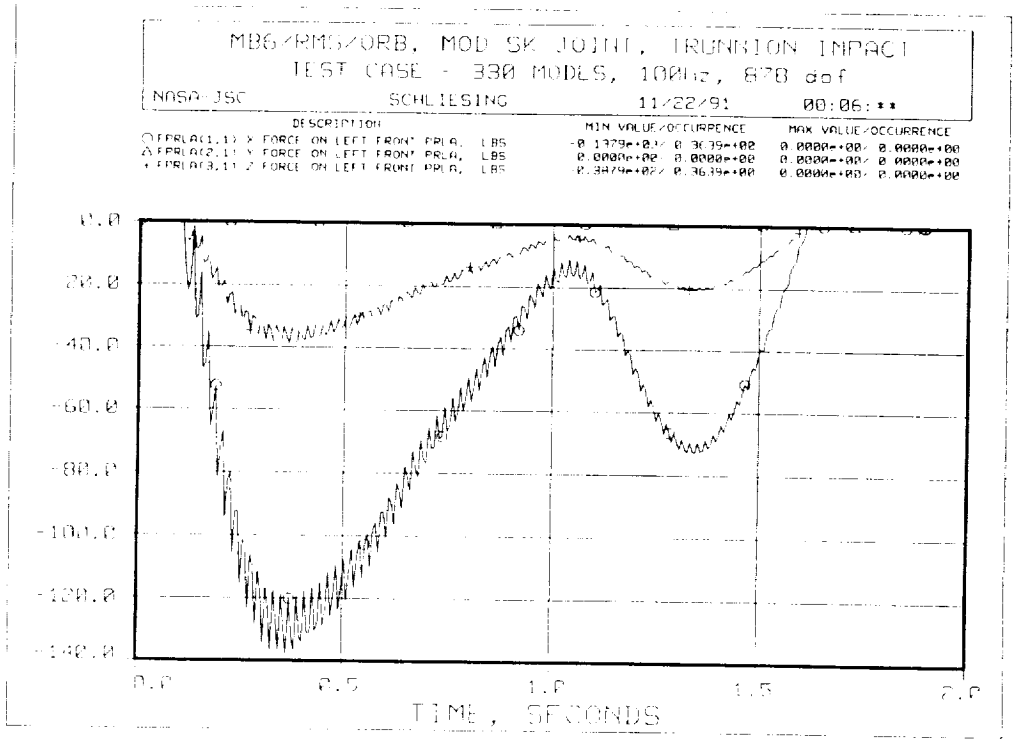

Figure 4. Interaction loads history for trunnion/PRLA contact computed by MDDP.

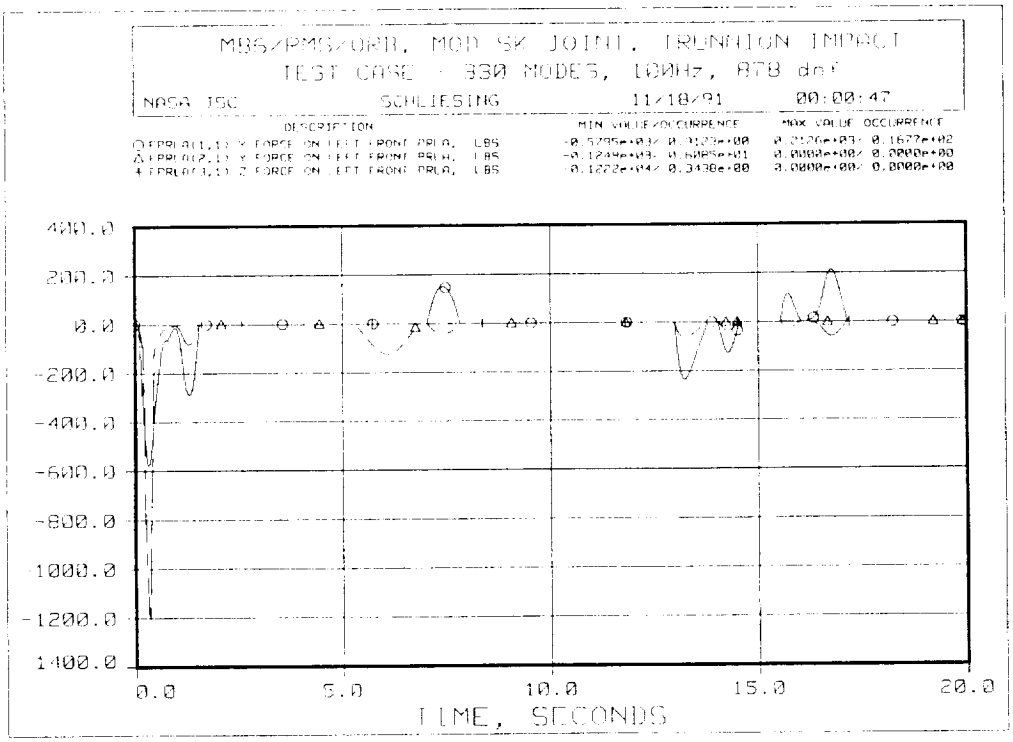

Figure 5. Interaction loads history for trunnion/PRLA contact computed by MDDP.

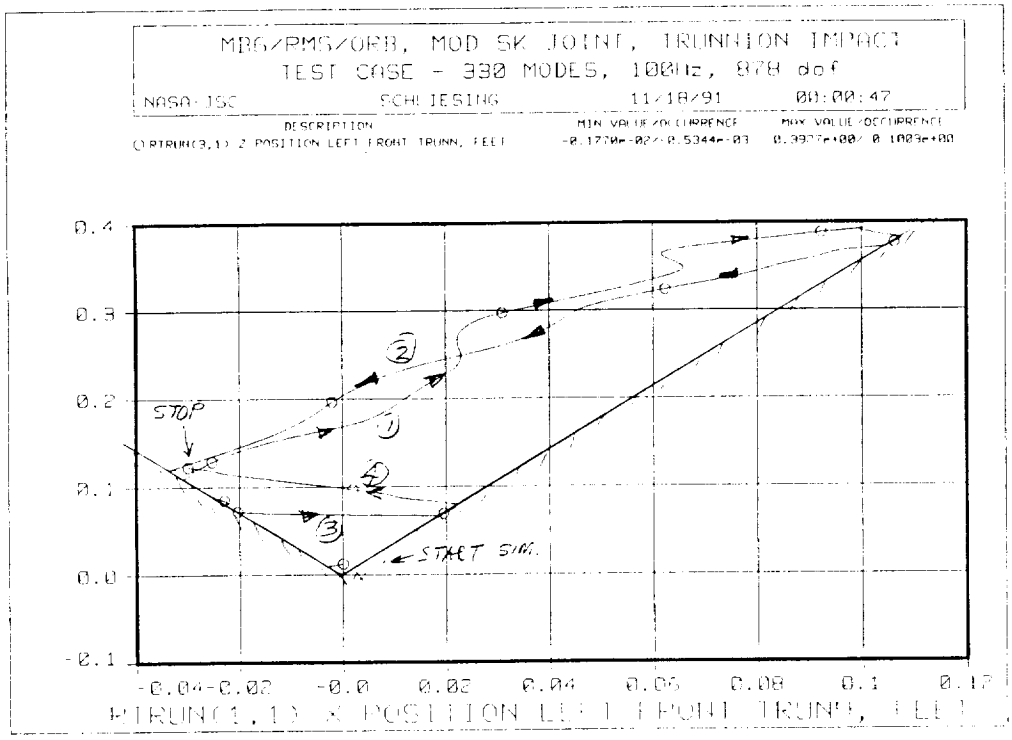

Figure 6. Interaction x_o–y_o motion for trunnion/PRLA contact.

- Nonlinear hysteresis SRMS joints.
- Second order servomotor dynamics.
- SRMS brake dynamics including motor friction.
- Locked or bottomed SRMS servo joints.
- Flexible body payloads (716 degree of freedom for MB6).

- Control Modes
  - Manual single joint drive with remaining joints in position hold.
  - Direct drive mode with remaining joints in brakes hold.
  - Position hold submode.
  - Optimal linear quadratic regulator with pole placement control system.

The RCS attitude control systems for the Orbiter and the SSF are under development. The current program has the capability to apply a predetermined RCS pulse history to either vehicle for testing maneuver disturbances.

The equations of motion for MDDP are linearized about the initial unstressed position geometry. For geometry changes greater than some ϵ, the modes and frequencies of the system equations for the SRMS will be recomputed and the new modal state initialized such that the physical states of the total system match at the transition. For a fifty foot SRMS, a 5 percent geometry change would correspond to end deflections of 2.5 feet. Practically, modal recomputations do not occur very often for the type of studies that the MDDP is designed to handle. The relative motion interaction dynamics between the trunnions and PRLA's are constrained by the latch geometry, thus limited to less than ± 3 inches in the Orbiter x_o and y_o directions. The Orbiter $+z_o$ direction is unlimited; however, the bottom of the PRLA latch limits the $-z_o$ motion direction. The top of the PRLA guides are a maximum of 24 inches tall. For the case of RCS excitement, a 2.5 foot change in geometry indicates that the system is not performing very well in its position hold capability.

The flexible body model of the SSF was constructed by a component mode synthesis method using the Craig–Bampton (ref. 2) constrained boundary component mode reduction technique. This dynamic reduction technique was used in both MSC/NASTRAN internally defined superelements and external superelements supplied by the different Space Station Work Package contractors and by the international partners.

The simulation is written in the FORTRAN 77 language and is computer based in the Engineering Computation Facility (ECF) at JSC. The ECF consists of a Cray X-MP EA/464 high speed vector processor (HVSP) and an Amdahl 5990-500 scalar processor, both operating under the UNIX operating environment. The simulation program is typically submitted from the Amdahl front end to the Cray in batch form.

In the following section, the optimal quadratic-pole placement technique used in this study will be presented together with an adaptation to the SRMS control system.

OPTIMAL QUADRATIC REGULATOR WITH POLE PLACEMENT

This section presents the mathematical basis for the optimal quadratic regulator as developed by the authors, and the adaptation to the SRMS system. The flexible body system equations of motion for the Orbiter/SRMS/SSF structure can be represented by

$$\mathbf{M}\ddot{\mathbf{x}} + \mathbf{D}\dot{\mathbf{x}} + \mathbf{K}\mathbf{x} = \mathbf{C}\mathbf{u}; \qquad \mathbf{x}(0), \dot{\mathbf{x}}(0) \tag{1}$$

where $\mathbf{x}$ and $\mathbf{u}$ are an $n \times 1$ physical vector and an $m \times 1$ control input vector, respectively, and $\mathbf{M}$, $\mathbf{D}$, $\mathbf{K}$ and $\mathbf{C}$ are of appropriate dimensions and represent the structural mass matrix, the damping matrix, the stiffness matrix, and the control distribution matrix, respectively.

Next we employ modal analysis to Eq. (1) to decouple and reduce the order of the problem to a smaller size based on the dominate modes. The physical to modal transformation is given by

$$\mathbf{x} = \boldsymbol{\phi}\mathbf{y}, \tag{2}$$

where $\boldsymbol{\phi}$ is the $n \times n$ mode shape matrix and $\mathbf{y}$ is the $n \times 1$ modal vector. Using Eq. (2) in Eq. (1) yields the decoupled modal equation (ref. 3) given by

$$\mathbf{I}\ddot{\mathbf{y}} + 2\xi\boldsymbol{\omega}\dot{\mathbf{y}} + \boldsymbol{\omega}^2\mathbf{y} = \boldsymbol{\phi}^T\mathbf{C}\mathbf{u}. \tag{3}$$

where $\mathbf{I} = \boldsymbol{\phi}^T\mathbf{M}\boldsymbol{\phi}$; $2\xi\boldsymbol{\omega} = \boldsymbol{\phi}^T\mathbf{D}\boldsymbol{\phi}$; and $\boldsymbol{\omega}^2 = \boldsymbol{\phi}^T\mathbf{K}\boldsymbol{\phi}$. The superscript T denotes the transpose of a matrix.

We reorder our modal matrices to retain the elements we wish to design in the optimal control section in the following manner

$$\mathbf{y} = \begin{bmatrix} \mathbf{z}_r \\ \mathbf{z}_o \end{bmatrix} \tag{4}$$

where $\mathbf{z}_r$ are the regulated modal variables to be designed and $\mathbf{z}_o$ are the omitted modal variables. We then obtain the following

$$\begin{bmatrix} \ddot{\mathbf{z}}_r \\ \ddot{\mathbf{z}}_o \end{bmatrix} + \begin{bmatrix} 2\xi_r\boldsymbol{\omega}_r & \mathbf{0} \\ \mathbf{0} & 2\xi_o\boldsymbol{\omega}_o \end{bmatrix} \begin{bmatrix} \dot{\mathbf{z}}_r \\ \dot{\mathbf{z}}_o \end{bmatrix} + \begin{bmatrix} \boldsymbol{\omega}_r^2 & \mathbf{0} \\ \mathbf{0} & \boldsymbol{\omega}_o^2 \end{bmatrix} \begin{bmatrix} \mathbf{z}_r \\ \mathbf{z}_o \end{bmatrix} = \begin{bmatrix} \mathbf{C}_r \\ \mathbf{C}_o \end{bmatrix} \mathbf{u} \tag{5}$$

where $\mathbf{z}_r$ is an $n_r \times 1$ vector, with appropriate dimensions for the remaining terms. The equations to design by optimal controller can be separated from Eq. (5) as

$$\ddot{\mathbf{z}}_r + 2\xi_r\boldsymbol{\omega}_r\dot{\mathbf{z}}_r + \boldsymbol{\omega}_r^2\mathbf{z}_r = \mathbf{C}_r\mathbf{u}. \tag{6}$$

Next we can express Eq. (6) in the first order state space form in terms of a new vector $\mathbf{w}$ as

$$\begin{bmatrix} \dot{\mathbf{w}}_1 \\ \dot{\mathbf{w}}_2 \end{bmatrix} = \begin{bmatrix} \mathbf{0} & \mathbf{I} \\ -\boldsymbol{\omega}_r^2 & -2\xi_r\boldsymbol{\omega}_r \end{bmatrix} \begin{bmatrix} \mathbf{w}_1 \\ \mathbf{w}_2 \end{bmatrix} + \begin{bmatrix} \mathbf{0} \\ \mathbf{C}_r \end{bmatrix} \mathbf{u}. \tag{7}$$

Equation (7) in compact notation becomes the linear controllable continuous-time system described by

$$\dot{\mathbf{w}} = \mathbf{A}\mathbf{w} + \mathbf{B}\mathbf{u}, \qquad \mathbf{w}(0) \tag{8}$$

where $\mathbf{w}$ and $\mathbf{u}$ are $2n_r \times 1$ and $m \times 1$ respectively. $\mathbf{A}$ and $\mathbf{B}$ follow from Eq. (7) and are constant matrices of appropriate dimensions. Let the quadratic cost function for the system in Eq. (8) be

$$\mathbf{J} = \int_0^{+\infty} [\mathbf{w}^T\mathbf{Q}\mathbf{w} + \mathbf{u}^T\mathbf{R}\mathbf{u}]dt, \tag{9}$$

where the weighting matrices $\mathbf{Q}$ and $\mathbf{R}$ are $2n_r \times 2n_r$ non-negative definite and $m \times m$ positive definite symmetric matrices, respectively. The feedback control law that minimizes the performance index $\mathbf{J}$ in Eq. (9) is given by (ref. 4) :

$$\mathbf{u} = -\mathbf{K}\mathbf{w} + \mathbf{E}\mathbf{r} = -\mathbf{R}^{-1}\mathbf{B}^T\mathbf{P}\mathbf{w} + \mathbf{E}\mathbf{r} \tag{10}$$

where $\mathbf{K}$ is an $m \times 2n_r$ feedback gain; $\mathbf{E}$ is an $m \times m$ forward gain; $\mathbf{r}$ is an $m \times 1$ reference input; and $\mathbf{P}$, an $2n_r \times 2n_r$ non-negative definite symmetric matrix, is the solution of the Riccati equation,

$$\mathbf{P}\mathbf{B}\mathbf{R}^{-1}\mathbf{B}^T\mathbf{P} - \mathbf{P}\mathbf{A} - \mathbf{A}^T\mathbf{P} - \mathbf{Q} = \mathbf{0} \tag{11}$$

with $(\mathbf{A},\ \mathbf{Q})$ detectable. Thus the resulting closed-loop system becomes

$$\dot{\mathbf{w}} = (\mathbf{A} - \mathbf{B}\mathbf{K})\mathbf{w} + \mathbf{B}\mathbf{E}\mathbf{r} \tag{12}$$

The eigenvalues of $(\mathbf{A} - \mathbf{B}\mathbf{K})$, denoted by $\sigma(\mathbf{A} - \mathbf{B}\mathbf{K})$, lie in the open left-half plane of the complex s plane. Our objective given a suitable $\mathbf{R}$ is to determine $\mathbf{Q}$, $\mathbf{P}$, and $\mathbf{K}$ so that the closed-loop system in Eq. (12) has its eigenvalues on or within a specified sector region shown in figure 2. The important results to achieve the desired design are presented in the following.

Lemma 1. : (refs. 4 and 5) Let $(\mathbf{A},\ \mathbf{B})$ be the pair of the given open-loop system in Eq. (8) with the quadratic cost function in Eq. (9). Also let $h \geq 0$ represent the prescribed degrees of relative stability. Then the eigenvalues of the closed-loop system $(\mathbf{A} - \mathbf{B}\mathbf{K})$ consist of the invariant eigenvalues of $\mathbf{A}$ lying to the left of the $-h$ vertical line with the matrix $\mathbf{P}$ being the solution of the Riccati equation:

$$\mathbf{P}\mathbf{B}\mathbf{R}^{-1}\mathbf{B}^T\mathbf{P} - \mathbf{P}(\mathbf{A} + h\mathbf{I}) - (\mathbf{A} + h\mathbf{I})^T\mathbf{P} = \mathbf{0} \tag{13}$$

Theorem 1 : (ref. 6) Let the given stable system matrix $\mathbf{A} \in \Re^{n\times n}$ have eigenvalues $\hat{\sigma}_i^-(i = 1, 2, \ldots, n^-)$ lying in the open sector of figure 2 with the sector angle $\pm 45°$ from the negative real axis and the eigenvalues $\hat{\sigma}_i^+(i = 1, 2, \ldots, n^+)$ outside that sector, with $n = n^- + n^+$. Now, consider the two Riccati equations,

$$\hat{\mathbf{Q}}\mathbf{B}\mathbf{R}^{-1}\mathbf{B}^T\hat{\mathbf{Q}} - \hat{\mathbf{Q}}(-\mathbf{A}^2) - (\mathbf{A}^2)^T\hat{\mathbf{Q}} = \mathbf{0} \tag{14a}$$

and

$$\mathbf{P}\mathbf{B}\mathbf{R}^{-1}\mathbf{B}^T\mathbf{P} - \mathbf{P}\mathbf{A} - \mathbf{A}^T\mathbf{P} - \hat{\mathbf{Q}} = \mathbf{0} \tag{14b}$$

Then, the closed–loop system,

$$\mathbf{A}_c = \mathbf{A} - \gamma \mathbf{B}\mathbf{K} = \mathbf{A} - \gamma \mathbf{B}\mathbf{R}^{-1}\mathbf{B}^T\mathbf{P}, \tag{15}$$

will enclose the invariant eigenvalues $\hat{\sigma}^-(i = 1, \ldots, n^-)$ and at least one additional pair of complex conjugate eigenvalues lying in the open sector of figure 2, for the constant gain γ in Eq. (15) satisfying

$$\gamma \geq max\{\frac{1}{2}, \frac{b + \sqrt{b^2 + ac}}{a}\} \tag{16}$$

where $a = tr[(\mathbf{B}\mathbf{R}^{-1}\mathbf{B}^T\mathbf{P})^2]$, $b = tr[\mathbf{B}\mathbf{R}^{-1}\mathbf{B}^T\mathbf{P}\mathbf{A}]$, and $c = (1/2)tr[\mathbf{B}\mathbf{R}^{-1}\mathbf{B}^T\hat{\mathbf{Q}}]$.

Remark 1 : The steady state solutions of the Riccati equations in Eqs. (11 and 14) can be found using the matrix sign function techniques (refs. 7, 8).

The steps to optimally place all the closed–loop eigenvalues in the hatched region of figure 2 are described as follows.

Step 1 : Let the given continuous time system be as in Eq. (8). Specify h so that the $-h$ vertical line on the negative real axis would represent the line beyond which the eigenvalues have to be placed in the cross hatched sector of figure 2. Also, assign $\mathbf{A}_0 = \mathbf{A}$ and the positive definite matrix $\mathbf{R} = \mathbf{I}$. Set $i = 1$. If the system is unstable, then solve Eq. (13) to obtain $\mathbf{P}_o$ and the closed–loop system $\mathbf{A}_1 = \mathbf{A} - \gamma_0\mathbf{B}\mathbf{R}^{-1}\mathbf{B}^T\mathbf{P}_0 = \mathbf{A} - \gamma_0\mathbf{B}\mathbf{K}_0$, with $\gamma_0 = 1$; else (stable system) go to Step 2 with $\mathbf{A}_1 = \mathbf{A}, \mathbf{P}_0 = \mathbf{0}$ and $\gamma_0 = 0$.

Step 2 : Solve Eq. (14a) for $\hat{\mathbf{Q}}_i$ with $\mathbf{A} := \mathbf{A}_i$. Check if $(1/2)tr[\mathbf{B}\mathbf{R}^{-1}\mathbf{B}^T\hat{\mathbf{Q}}_i]$ is zero. If it is equal to zero, go to Step 4 with j=i; else, continue and go to Step 3. Note that, when $(1/2)tr[\mathbf{B}\mathbf{R}^{-1}\mathbf{B}^T\hat{\mathbf{Q}}_i] = 0$, all eigenvalues of the matrix $\mathbf{A}_i$ lie on or within the open sector of figure 2.

Step 3 : Solve Eq. (14b) for $\mathbf{P}_i$ with $\mathbf{A} := \mathbf{A}_i$ and $\hat{\mathbf{Q}} := \hat{\mathbf{Q}}_i$. Then the constant gain γ_i can be evaluated using Eq. (16). The closed–loop system matrix is

$$\mathbf{A}_{i+1} = \mathbf{A}_i - \gamma_i\mathbf{B}\mathbf{R}^{-1}\mathbf{B}^T\mathbf{P}_i = \mathbf{A}_i - \gamma_i\mathbf{B}\mathbf{K}_i \tag{17a}$$

Set $i := i + 1$ and go to Step 2.

Step 4 : Check if $tr[(\mathbf{A}_j + h\mathbf{I})]^+$ (sum of the eigenvalues to the right of the vertical line at $-h$) is zero. If it is equal to zero, go to Step 5 with $\mathbf{P}_{j+1} = \mathbf{0}$ and $\gamma_{j+1} = 0$; else, solve Eq.

(13) for $\mathbf{P}_{j+1}$ with $\mathbf{A} := \mathbf{A}_j$ and obtain the closed-loop system $\mathbf{A}_j - \gamma_{j+1}\mathbf{B}\mathbf{R}^{-1}\mathbf{B}^T\mathbf{P}_{j+1} = \mathbf{A}_j - \gamma_{j+1}\mathbf{B}\mathbf{K}_{j+1}$, with $\gamma_{j+1} = 1$ and $\mathbf{K}_{j+1} = \mathbf{R}^{-1}\mathbf{B}^T\mathbf{P}_{j+1}$.

Step 5 : The designed closed-loop system is

$$\mathbf{A}_0 - \mathbf{B}\mathbf{R}^{-1}\mathbf{B}^T \sum_{k=0}^{j+1} \gamma_k \mathbf{P}_k \tag{17b}$$

and its eigenvalues lie in the hatched region of figure 2. Note that the above system matrix in Eq. (17b) is equal to the system matrix in Eq. (12), with

$$\mathbf{Q} = 2h\mathbf{P}_0 + \sum_{i=1}^{j} (\hat{\mathbf{Q}}_i + \Delta\gamma_i \mathbf{P}_i \mathbf{B}\mathbf{R}^{-1}\mathbf{B}^T\mathbf{P}_i)\gamma_i \tag{18}$$

In the above equation, $\Delta\gamma_i = \gamma_i - 1$ and the matrix $\mathbf{R}$ is as originally assigned. Also, the optimal continuous time regulator can be given as

$$\mathbf{u} = -(\sum_{i=0}^{j+1} \gamma_i \mathbf{K}_i)\mathbf{w} + \mathbf{E}\mathbf{r} = -\mathbf{K}\mathbf{w} + \mathbf{E}\mathbf{r} \tag{19}$$

where $\mathbf{r}$ is any reference input and $\mathbf{K}$ is the desired state feedback gain matrix.

Next we transform back to the modal state $\mathbf{y}$ in order to apply our control gains back in our test bed simulation. Note that control input $\mathbf{u}$ becomes

$$\mathbf{u} = -\mathbf{K}\mathbf{w} = -[\mathbf{K}_{11} \quad \mathbf{K}_{12}] \begin{bmatrix} \mathbf{z}_r \\ \dot{\mathbf{z}}_r \end{bmatrix}, \tag{20}$$

and further rearrangement yields

$$\mathbf{u} = -[\mathbf{K}_{11} \quad \mathbf{0}] \begin{bmatrix} \mathbf{z}_r \\ \mathbf{z}_o \end{bmatrix} - [\mathbf{K}_{12} \quad \mathbf{0}] \begin{bmatrix} \dot{\mathbf{z}}_r \\ \dot{\mathbf{z}}_o \end{bmatrix}, \tag{21}$$

and using Eq. (4) we obtain the desired input

$$\mathbf{u} = -[\mathbf{K}_{11} \quad \mathbf{0}]\mathbf{y} - [\mathbf{K}_{12} \quad \mathbf{0}]\dot{\mathbf{y}}. \tag{22}$$

In the test bed we solve for **u** and substitute back into Eq. (3) and use a variable step fourth order Runge Kutta integrating method to propagate a time history of the system dynamics.

The control system feedback gain matrix, **K**, was obtained by following the above design steps for the case of the Orbiter SRMS handling the MB6 spacecraft. The complex frequencies for the dominate modes of the open loop system with soft torsional springs at each of the SRMS servo joints are $\{ -.000153 \pm j.00766; -.000235 \pm j.0112; -.000595 \pm j.0297; -.000923 \pm j.0461; -.00128 \pm j.0638; -.00535 \pm j.268 \}$. The value of $h = .004$ was chosen to place the closed loop poles in the phase plane such that the joint torque requirements **u** do not exceed the system capability for the given PRCS disturbance. The closed loop system eigenvalues $\sigma(\mathbf{A} - \mathbf{BK})$ after design are $\{ -.00785 \pm j.00766; -.0145 \pm j.118; -.054 \pm j.0468; -.103 \pm j.0937; -.166 \pm j.157; -1.594 \pm j1.594 \}$ all within the required stability sector given in figure 2. The feedback gain matrices for this design are given as

$$[\mathbf{K}_{11}] = \begin{bmatrix} -.2981e1 & +.2026e1 & -.5281e0 & +.3582e1 & +.2090e2 & -.8834e3 \\ +.1588e1 & +.1997e0 & -.2833e1 & -.3350e2 & -.8016e1 & -.1452e2 \\ -.2854e0 & -.5697e0 & +.1168e2 & +.1785e2 & +.5723e2 & +.1112e2 \\ +.1249e2 & -.4620e0 & -.2918e1 & +.6502e1 & -.5299e2 & -.1330e4 \\ -.2795e1 & +.2346e1 & +.1060e2 & -.5890e1 & -.4631e2 & +.4805e3 \\ +.5814e1 & -.5165e1 & +.6126e1 & -.8879e1 & +.1820e2 & -.1574e4 \end{bmatrix}$$

and

$$[\mathbf{K}_{12}] = \begin{bmatrix} +.3766e3 & +.2269e1 & -.4313e2 & +.1937e2 & +.1539e3 & -.5734e3 \\ +.3493e3 & -.1078e3 & -.1035e2 & -.3947e3 & -.4719e2 & -.1115e2 \\ -.3622e3 & +.4103e2 & +.1935e3 & +.1719e3 & +.4239e3 & +.1438e2 \\ +.2473e4 & -.6692e3 & +.2952e2 & +.1214e3 & -.3278e3 & -.8417e3 \\ +.7537e3 & +.7676e2 & +.3337e3 & -.3160e2 & -.2773e3 & +.3002e3 \\ -.1587e4 & -.1212e3 & +.1609e3 & -.9004e2 & +.1312e3 & -.9929e3 \end{bmatrix}$$

SIMULATION RESULTS

The SRMS was designed to handle payload weights up to 45,000 lbs. with the Orbiter attitude control system in a free drift mode. Current plans to grapple vehicles such as SSF-MB6, which weighs approximately 250,000 lbs., and to maneuver the combined spacecraft require a close engineering look at the systems and careful testing. The new alternative digital auto pilot (ALT DAP) control mode for the Orbiter, which wasn't available when the SRMS was originally designed, will greatly help reduce the dynamic excitation of the system. The ALT DAP allows both selectable burn times and delay times between firings, so conceivably the elastic response disturbances can have a chance to damp out between firings. With this in mind, a test case representing a .08 second Orbiter PRCS dual jet

pitch axis firing was simulated to determine the dynamic response motion between the Orbiter PRLA's and the MB6 trunnions.

The first case was simulated using an SRMS brakes hold mode for all servo joints with the arm geometry placing the pressurized berthing adapter (PBA) in the cargo bay of the Orbiter with the SSF trunnions inside the PRLA's. The interaction loads dynamics between the trunnions and the PRLA's was turned off in MDDP in order to see the unrestrained motion. The case was simulated for 100 seconds with the initial state of the system being zero. Shown in figures 7, 8, and 9 are the Orbiter's angular rate vector history together with the total system angular rate vector history, the velocity history of the left front trunnion with respect to the left front PRLA, and the motion of the left front trunnion with respect to the left front PRLA in a x_o,–y_o plane, respectively. Figure 7 shows that the system damps very slow after the brakes quit slipping. This represents a potential problem, since additional thrusting can easily reinforce the excitation level, causing additional slip of the motors and payloads. The relative velocities shown in figure 8 are less than .013 fps after 20 seconds. The relative motion shown in figure 9 did not exceed

The second case simulated used the optimal controller for 100 seconds of simulation time. The results shown in figures 10, 11, and 12 are for the same parameters as in the first case. The angular rate results shown in figure 10 exhibit the optimal characteristic of a slight dynamic overshoot of approximately 0.008 dps for the Orbiter roll axis, and remain below this value after about 17 seconds as the controller brings the Orbiter rates to match with the overall system rates. The relative velocities between the trunnion and PRLA in figure 11 stay below 0.005 fps after 12 seconds from the initial transient PRCS firing. Very small amplitude modal coupling can be seen in the results for the optimal controller as compared to the coupling seen in previous cases. The optimal controller quickly rejects the PRCS disturbance, reducing the system state to a level where additional firings can be made. The motion of the trunnion with respect to the Orbiter shown in figure 12 was very smooth and peaked at 0.26 feet, slightly more than for the case with applied brakes.

CONCLUSIONS

This paper has presented a description of MDDP, a high fidelity finite element model simulation of the SRMS specifically designed to study SRMS structural transient responses while connected to a flexible body payload. Of particular interest to structural engineers are the interaction dynamics computed between structural elements in the simulation and also the familiar finite element form of the equations. The simulation addresses two specific dynamics events, (1) constrained motion transient dynamics and the resulting structural loads occurring during interface contact, and (2) system transient dynamics resulting from the firing of RCS jets. The constrained motion loading relies entirely on the finite element representation of the contacting structures since no attenuation mechanism has been allocated for this interface. A new optimal LQR control method has been presented and shown to be very effective for rejecting the transient responses caused by the firing of the Orbiter PRCS. Future work will test the optimal LQR controller during the interaction dynamics

contact phase. The multivariable state-space optimal controller is stable and has good robustness properties. The state-space approach mathematically decouples the actuators from each other thereby greatly reducing the unwanted dynamic motion typically seen in the SRMS transient response.

REFERENCES

1. Shieh, L. S.; Lian., S. R.; and Mc Innis, B. C.: Fast and stable algorthims for computing the principle square root of a complex matrix. *IEEE Trans. Autom. Control*, AC-32, 1987, pp.820–822.

2. Craig, Roy R.; and Bampton, Mervyn C.C.: Coupling of Substructures for Dynamic Analysis. AIAA Journal, Vol. 6, no.7, July 1968.

3. Meirovitch, Leonard: *Linear Optimal Control*, Prentice -Hall, Englewood, 1967.

4. Anderson, B.D.O.; and Moore, J.B.: *Linear Optimal Control*, Prentice–Hall, Englewood Cliffs, New Jersey, 1971.

5. Shieh, L. S.; Dib, H.M.; and McInnis, B.C.: Linear quadratic regulators with eigenvalue placement in a horizontal strip. *IEEE Trans. Autom. Contr.*, AC–31, 1986, pp. 241–243.

6. Shieh, L.S.; Dib, H.M.; and Ganesan, S.: Continuous–time quadratic regulators and pseudo–continuous–time quadratic regulators with pole placement in a specific region. *IEE Proc.*, Vol. 134, Pt. D, 1987, pp. 338–346.

7. Shieh, L.S.; Tsay, Y.T.; Lin, S.W.; and Coleman, N.P.: Block–diagonalization and block–triangularization of a matrix via the matrix sign function. *Int. J. Syst. Sci.*, Vol. 15, 1984, pp. 1203–1220.

8. Bierman, G.J.: Computational aspects of the matrix sign function solution to the ARE., *Proc. 23rd Conf. Decision Contr.*, 1984, pp. 514–519.

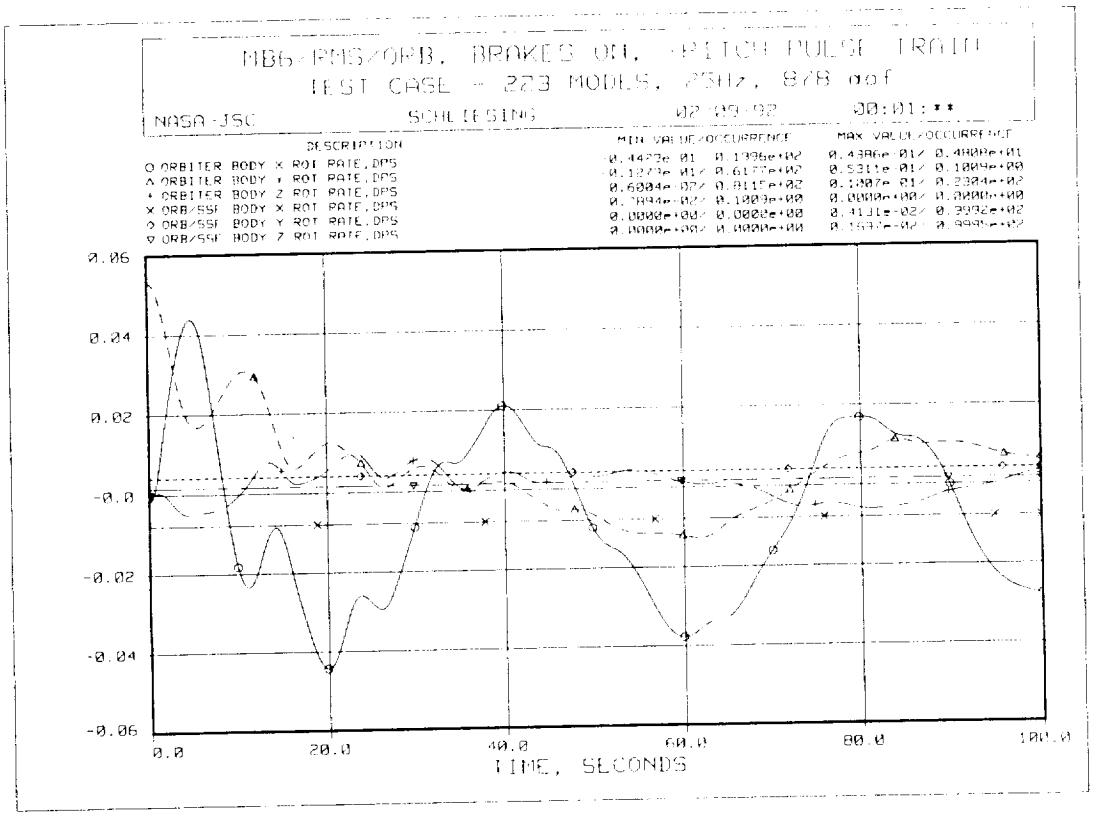

Figure 7. Orbiter and Orbiter/SRMS/MB6 angular rate history for brake hold.

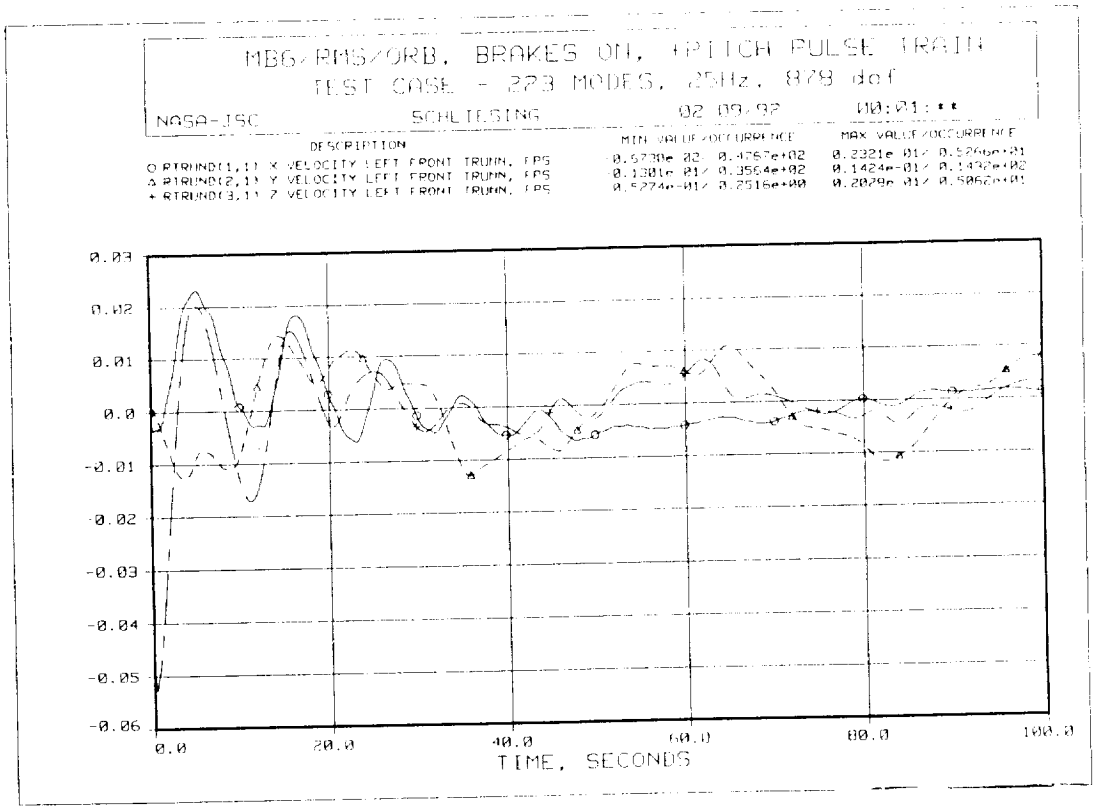

Figure 8. Relative velocity history of the left front trunnion for brake hold.

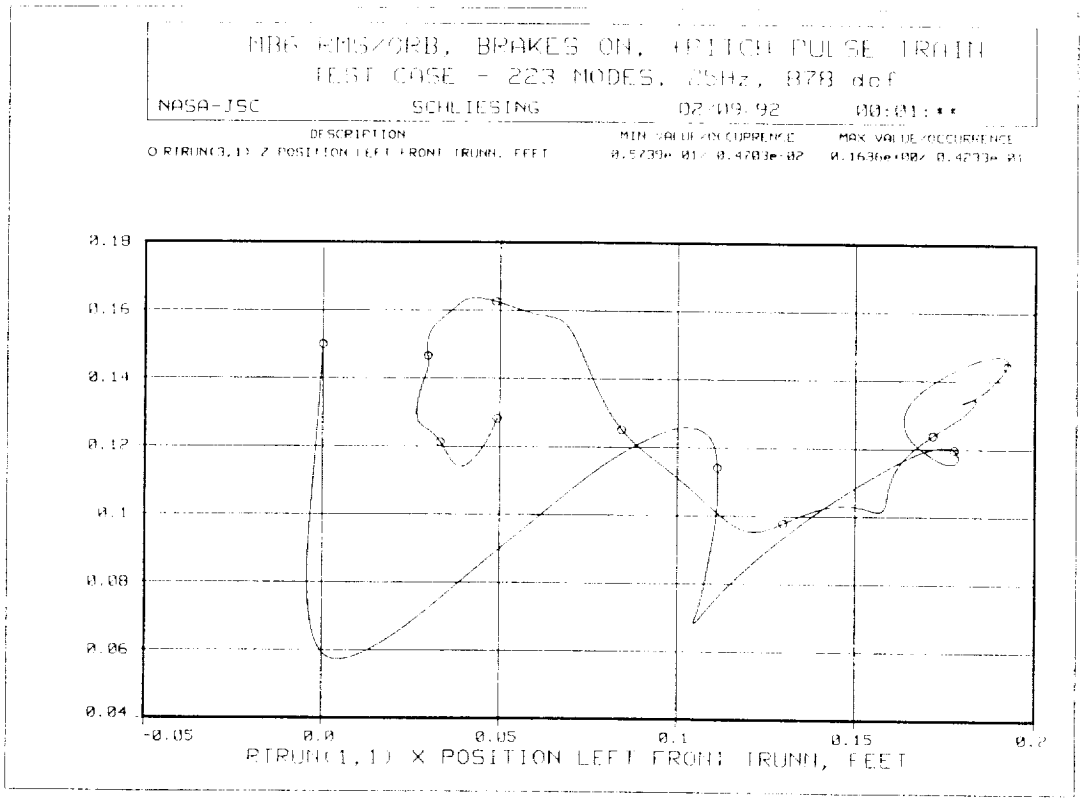

Figure 9. Trunnion motion in the xo–zo plane with respect to the PRLA for brake hold.

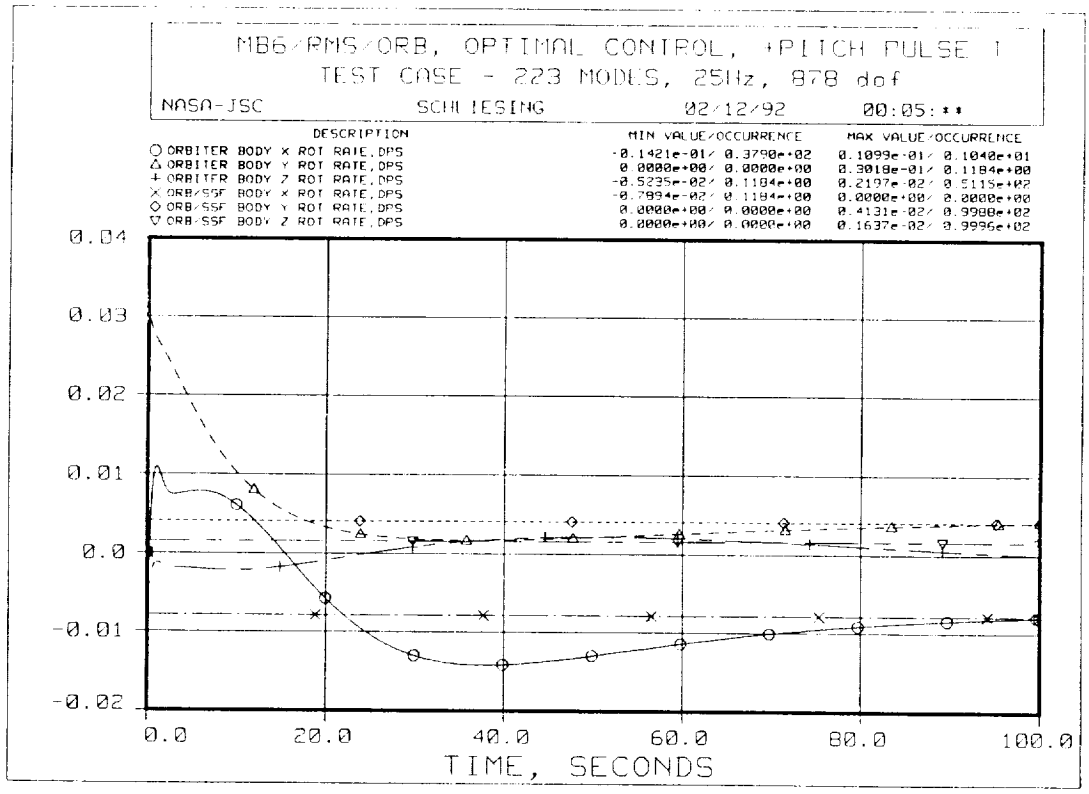

Figure 10. Orbiter and Orbiter/SRMS/MB6 angular rate history for optimal control.

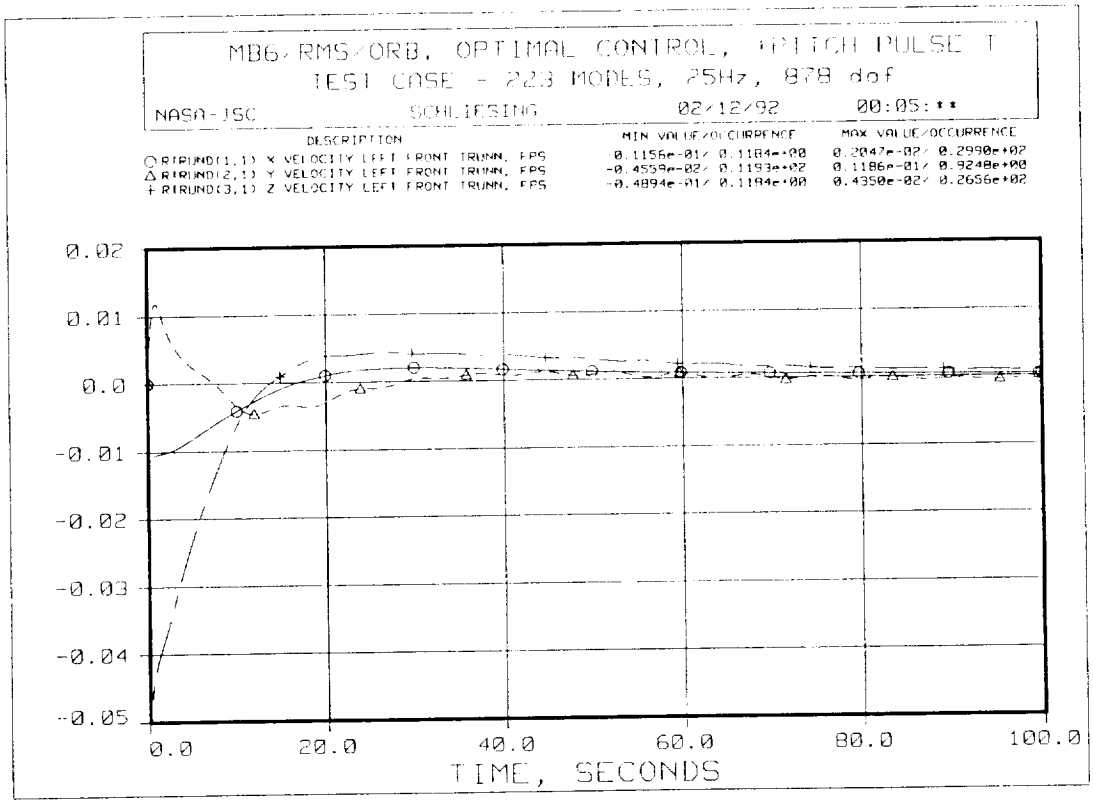

Figure 11. Relative velocity history of the left front trunnion for optimal control.

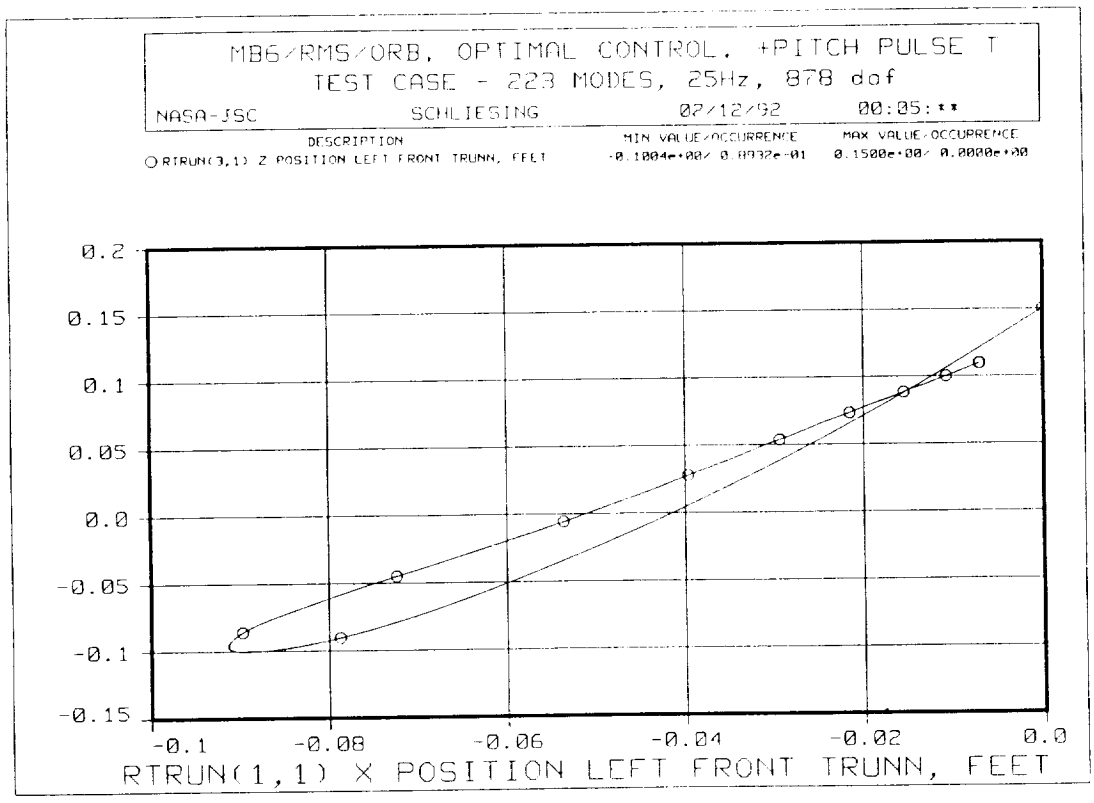

Figure 12. Trunnion motion in the xo–zo plane with respect to the PRLA for optimal control.

MODEL REDUCTION IN INTEGRATED CONTROLS-STRUCTURES DESIGN

P. G. Maghami and S. P. Kenny
Spacecraft Controls Branch
NASA Langley Research Center
Hampton, VA 23665

It is the objective of this paper to present a model reduction technique developed for the integrated controls-structures design of flexible structures. Integrated controls-structures design problems are typically posed as nonlinear mathematical programming problems, where the design variables consist of both structural and control parameters. In the solution process, both structural and control design variables are constantly changing; therefore, the dynamic characteristics of the structure are also changing. This presents a problem in obtaining a reduced-order model for active control design and analysis which will be valid for all design points within the design space. In other words, the frequency and number of the significant modes of the structure (modes that should be included) may vary considerably throughout the design process [1,2]. This is also true as the locations and/or masses of the sensors and actuators change. Moreover, since the number of design evaluations in the integrated design process could easily run into thousands, any feasible order-reduction method should not require model reduction analysis at every design iteration. In this paper a novel and efficient technique for model reduction in the integrated controls-structures design process, which addresses these issues, is presented.

OBJECTIVE

- Develop a model reduction technique for use in the integrated controls-structures design.

  —>Address the problem of a changing structure: the number and frequency of the significant modes may vary.

  —>Address the problem of control system implementation: sensor and actuator locations and masses.

  —>Address computational efficiency issues.

The approach presented in this paper is first to use a first-order Taylor's Series approximation of the open-loop eigenvalues and eigenvectors with the aid of their respective analytical derivatives with respect to both the structural and control design variables. Then, evaluating the significance of each mode through cost measures related to its controllability and observability [3], the number and frequency of the significant modes at the nominal design point, as well as the number and frequency of modes that might become significant in a prescribed neighborhood of the nominal point, are determined using a worst-case scenario approach. If the current design is within the prescribed neighborhood of the nominal design, the modes identified in the above are used in the control design and analysis. However, if the current design is outside the neighborhood, a single-point order reduction is performed.

APPROACH

- Evaluate the significance of each mode through its controllability and observability cost measures.

- Use a first-order Taylor's Series approximation of the open-loop eigenvalues and eigenvectors in a prescribed "linear" neighborhood about a nominal design.

- Identify the number and frequency of modes that may become significant within a neighborhood of a nominal design using a worst-case scenario approach.

- Perform "single-point" model reduction for design points outside the "linear" neighborhood.

The equations of motion for a flexible structure, in state-space form, are shown below, where A, B, and C are the plant, the actuator influence, and the sensor influence matrices, respectively. The plant matrix, in general, is nonsymmetric and fully populated. For a large flexible structure, the order of the initial model can be in the thousands, which makes it unsuitable for design and analysis. The classical approach for reducing the size of the problem is to introduce a model reduction method to eliminate dynamics characteristics that are outside the bandwidth of interest, hence reducing the computational burden. This naturally leads to the question whether the problem can be reduced even further, i.e., are there modes within the bandwidth that do not contribute much to the dynamic response? In order to distinguish a significant mode from an insignificant mode, a measure of modal significance must be adopted and compared. In this paper, the controllability and observability cost measures presented in [3] are used.

CONTROLLABILITY AND OBSERVABILITY COST MEASURES

The equations of motion, in state-space form, are given as:

$$\dot{q} = Aq + Bu$$

$$y = Cq$$

A measure of controllability and observability may be defined as:

$$\alpha_{ci} = \frac{\phi_i^H W_c \phi_i}{\phi_i^H \phi_i}$$

$$\alpha_{oi} = \frac{\phi_i^H W_o \phi_i}{\phi_i^H \phi_i}$$

Where α_{ci} and α_{oi} are measures of the closeness of the i^{th} mode w.r.t. the controllable (observable) range spaces, defined by $\Re(W_c)$ $(\Re(W_o))$.

Transforming the equations of motion from physical coordinates to modal coordinates results in a plant matrix that is block diagonal. Normalizing the modes of the structure for unity modal mass results in 2 × 2 blocks of the form shown below. Due to this particular block-diagonal nature of A, its eigenvectors have a special form as well, such that there are complex conjugate vector pairs associated with each 2 × 2 block. This considerably simplifies the expressions for controllability and observability cost measures.

CONTROLLABILITY AND OBSERVABILITY COST MEASURES (CONT'D)

- If the modes of the structure are normalized to produce unity modal mass, i.e.,

$$X_i^T M X_j = \begin{cases} 0 & i \neq j \\ 1 & i = j \end{cases}$$

- The plant matrix can be written in modal form as:

$$A = \begin{bmatrix} A_1 & 0 & 0 \\ 0 & \ddots & 0 \\ 0 & 0 & A_n \end{bmatrix}$$

- A_i's have a 2x2 diagonal block form:

$$A_i = \begin{bmatrix} 0 & 1 \\ -\omega_i^2 & -2\xi_i\omega_i \end{bmatrix}$$

Because of this special form of the eigenvectors of A, it becomes apparent that the controllability and observability cost measures do not require full multiplication of the matrices and vectors, but rather may be reduced to a series of 2×1 vector and 2×2 matrix multiplications. The components of the 2×1 vector are the two nonzero components of the eigenvectors of A, and the 2×2 matrices are block diagonal components of the controllability and observability grammians. In other words, the modal controllability and observability cost measures decouple, i.e., they depend only on the corresponding modal parameters.

CONTROLLABILITY AND OBSERVABILITY COST MEASURES (CONT'D)

- Simplified expressions for the controllability and observability cost measures are given as:

$$\alpha_{ci} = \frac{1}{1+\omega_i^2} \begin{Bmatrix} 1 \\ \xi_i\omega_i + \omega_i\sqrt{1-\xi_i^2}\ \underline{j} \end{Bmatrix}^H W_{ci} \begin{Bmatrix} 1 \\ \xi_i\omega_i + \omega_i\sqrt{1-\xi_i^2}\ \underline{j} \end{Bmatrix}$$

$$\alpha_{oi} = \frac{1}{1+\omega_i^2} \begin{Bmatrix} 1 \\ \xi_i\omega_i + \omega_i\sqrt{1-\xi_i^2}\ \underline{j} \end{Bmatrix}^H W_{oi} \begin{Bmatrix} 1 \\ \xi_i\omega_i + \omega_i\sqrt{1-\xi_i^2}\ \underline{j} \end{Bmatrix}$$

- W_{ci} and W_{oi} represent the i^{th} 2x2 block on the diagonal of the grammians W_c and W_o, respectively.

The 2×2 block diagonal elements of the controllability and observability grammians may be obtained analytically. Here, the vectors ψ_i, γ_{di}, and γ_{ri} represent the input, displacement output, and rate output influence coefficients, respectively. These solutions may then be combined with the reduced expressions for the controllability and observability cost measures yielding simplified modal cost measures, α_{ci} and α_{oi}, as shown below.

CONTROLLABILITY AND OBSERVABILITY COST MEASURES (CONT'D)

- Simplified controllability and observability grammians:

$$W_{ci} = \begin{bmatrix} \frac{1}{4\xi_i\omega_i^3} & 0 \\ 0 & \frac{1}{4\xi_i\omega_i} \end{bmatrix} \psi_i^T \psi_i$$

$$W_{oi} = \begin{bmatrix} \frac{1+4\xi_i^2}{4\xi_i\omega_i^3}\gamma_{di}^T\gamma_{di} + \frac{\omega_i}{4\xi_i}\gamma_{ri}^T\gamma_{ri} & \frac{1}{2\omega_i^2}\gamma_{di}^T\gamma_{di} \\ \frac{1}{2\omega_i^2}\gamma_{di}^T\gamma_{di} & \frac{1}{4\xi_i\omega_i}\gamma_{ri}^T\gamma_{ri} + \frac{1}{4\xi_i\omega_i^3}\gamma_{di}^T\gamma_{di} \end{bmatrix}$$

- Simplified modal controllability and observability cost measures:

$$\alpha_{ci} = \frac{1}{4\left(1+\omega_i^2\right)\xi_i}\left\{\frac{1}{\omega_i^3} + \omega_i\right\}\psi_i^T\psi_i$$

$$\alpha_{oi} = \frac{1}{2\left(1+\omega_i^2\right)\xi_i}\left\{\frac{1+4\xi_i^2}{\omega_i}\gamma_{di}^T\gamma_{di} + \omega_i\gamma_{ri}^T\gamma_{ri}\right\}$$

The model reduction algorithm computes the sensitivity of the open-loop eigenvalues and eigenvectors each time that the optimization requests gradient information (gradient of the objectives and constraints with respect to the design variables). Then, upper bound values for the modal controllability and observability cost measures α_{ci}^{U} and α_{oi}^{U} are computed and compared with preset threshold values in order to identify the significant modes for designs within the prescribed neighborhood of the nominal design. Now, if an upcoming design is within this neighborhood, these identified modes are used to form a design model for control synthesis. However, if an upcoming design is outside this neighborhood, a single-point model reduction is performed to identify the significant modes for control design. This process is repeated until the integrated design optimization converges.

MODEL REDUCTION ALGORITHM

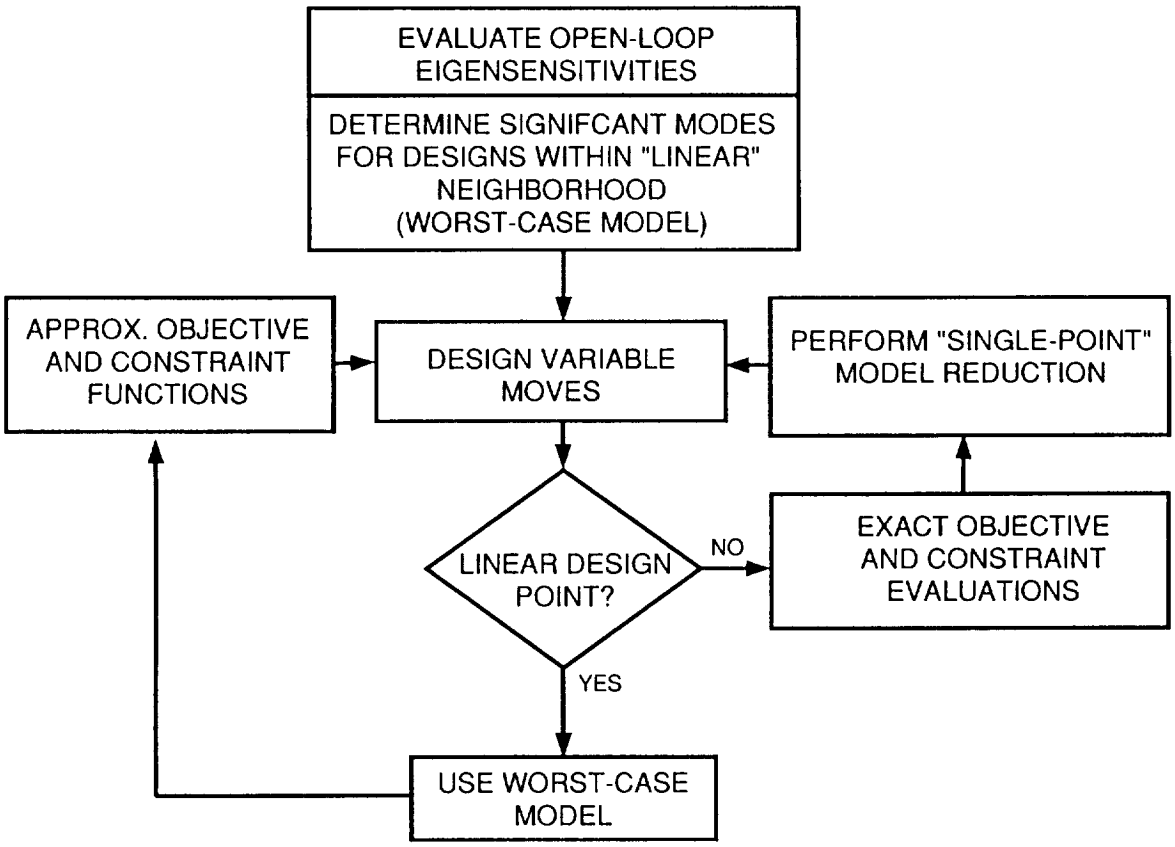

Consider the real symmetric structural eigenvalue problem, as stated below, where K and M are symmetric positive semi-definite stiffness and symmetric positive-definite mass matrices, respectively. Differentiating the defining eigenvalue problem with respect to a structural design variable, ρ_j, gives expressions for both the eigenvalue and eigenvector derivatives. Premultiplying by the eigenvector yields a simple expression for the eigenvalue derivative. However, due to the rank deficiency of the defining eigenvalue problem, the eigenvector derivative cannot be uniquely determined from this expression.

STRUCTURAL EIGENSYSTEM (OPEN-LOOP) SENSITIVITY ANALYSIS

- Structural Eigenvalue Problem: $(K - \lambda_i M)X_i = 0$
- Eigenvalue Derivative: $\frac{\partial \lambda_i}{\partial \rho_j} = X_i^T \left(\frac{\partial K}{\partial \rho_j} - \lambda_i \frac{\partial M}{\partial \rho_j} \right) X_i$
- Eigenvector Derivative:

$$(K - \lambda_i M)\frac{\partial X_i}{\partial \rho_j} = \frac{\partial \lambda_i}{\partial \rho_j} M X_i - \left(\frac{\partial K}{\partial \rho_j} - \lambda_i \frac{\partial M}{\partial \rho_j} \right) X_i$$

Note that $(K - \lambda_i M)$ is rank deficient.

Expressing the eigenvector derivative as a linear combination of all the eigenvectors and substituting it into the defining eigenvector derivative equation gives an expression for the particular solution, V_{ij}. Noting that the particular solution is mass-orthogonal with respect to the eigenvector provides a set of linear constraints that may be used to eliminate the singularity problems of the unconstrained expression. The constant, C_{ij}, may be obtained by differentiating the eigenvector normalization condition $X_i^T M X_i = 1$. For a detailed development of the eigensystem sensitivity equations, see [4].

STRUCTURAL EIGENSYSTEM SENSITIVITY ANALYSIS (CONT'D)

A solution for the eigenvector derivative may be obtained by expressing it as a linear combination of all of the eigenvectors

$$\frac{\partial X_i}{\partial \rho_j} = \sum_{\substack{k=1 \\ k \neq i}}^{n} C_{kj} X_k + C_{ij} X_i = V_{ij} + C_{ij} X_i$$

Where V_{ij} and C_{ij} are defined as follows:

$$\begin{bmatrix} (K - \lambda_i M) & M X_i \\ X_i^T M & 0 \end{bmatrix} \begin{Bmatrix} V_{ij} \\ \frac{\partial \lambda_i}{\partial \rho_j} \end{Bmatrix} = \begin{Bmatrix} -\left(\frac{\partial K}{\partial \rho_j} - \lambda_i \frac{\partial M}{\partial \rho_j} \right) X_i \\ 0 \end{Bmatrix}$$

$$C_{ij} = -\frac{1}{2} X_i^T \frac{\partial M}{\partial \rho_j} X_i$$

Both modal controllability and observability cost measures, α_{ci} and α_{oi}, are functions of the design variables ρ. As the current design moves away from the nominal design point, the number and frequency of the significant modes measured by α_{ci} and α_{oi} might change. Consequently, if upper bound values, α_{ci}^U and α_{oi}^U, can be established for the modal controllability and observability cost measures for design points within a prescribed neighborhood of a nominal design, they may be used to identify the modes that are currently significant and modes that might become significant as the design optimization progresses.

MODAL COST APPROXIMATIONS

- Compute upper bound values for the controllability and observability cost measures if the new design is within the neighborhood of the nominal design:

—>Find an upper bound value for the controllability cost measure:

$$\max_{\rho} \left\{ \alpha_{ci}(\rho) = \frac{1}{4(1+\omega_i^2(\rho))\xi_i} \left\{ \frac{1}{\omega_i^3(\rho)} + \omega_i(\rho) \right\} \psi_i^T(\rho)\psi_i(\rho) \right\}$$

—>Find an upper bound value for the observability cost measure:

$$\max_{\rho} \left\{ \alpha_{oi}(\rho) = \frac{1}{2(1+\omega_i^2(\rho))\xi_i} \left[\frac{1+4\xi_i^2}{\omega_i(\rho)} \gamma_{di}^T(\rho)\gamma_{di}(\rho) + \omega_i(\rho)\gamma_{ri}^T(\rho)\gamma_{ri}(\rho) \right] \right\}$$

Upper bound values for the modal controllability and observability cost measures may be established by using a worst-case scenario approach, wherein the maximum possible contribution from each term is used in the computations. These terms involve functions of the open-loop eigenvalues and the input and the output influence vectors which are approximated by a first-order Taylor's Series expansion.

MODAL COST APPROXIMATION (CONT'D)

- Obtain upper bound values for the modal controllability and observability cost measures

$$\alpha_{ci}(\rho) \leq 1/(4\xi_i)\left[\max_{\rho}\left\{1/\omega_i^3(\rho)\left(1+\omega_i^2(\rho)\right)\right\} + \max_{\rho}\left\{\omega_i(\rho)/\left(1+\omega_i^2(\rho)\right)\right\}\right] \cdot \max_{\rho}\left\{\psi_i^T(\rho)\psi_i(\rho)\right\} \equiv \alpha_{ci}^U$$

$$\alpha_{io}(\rho) \leq \left[\left(4\xi_i^2+1\right)/(2\xi_i)\right]\left\{\left\{\max_{\rho}\left[1/\omega_i(\rho)\left(1+\omega_i^2(\rho)\right)\right]\max_{\rho}\left\{\gamma_{di}^T(\rho)\gamma_{di}(\rho)\right\}\right\}\right\} + [1/(2\xi_i)]\left\{\left\{\max_{\rho}\left[\omega_i(\rho)/\left(1+\omega_i^2(\rho)\right)\right]\max_{\rho}\left\{\gamma_{ri}^T(\rho)\gamma_{ri}(\rho)\right\}\right\}\right\} \equiv \alpha_{oi}^U$$

- Use a first-order Taylor's Series approximation for the open-loop eigenvalues and the influence coefficients

$$\omega_i(\rho) \approx \omega_i(\rho_o) + \sum_{j=1}^{n_d} \left.\frac{\partial \omega_i}{\partial \rho_j}\right|_{\rho_{oj}} (\rho_j - \rho_{oj})$$

$$\psi_i(\rho) \approx \psi_i(\rho_o) + \sum_{j=1}^{n_d} \left.\frac{\partial \psi_i}{\partial \rho_j}\right|_{\rho_{oj}} (\rho_j - \rho_{oj})$$

Upper bound values for terms in the modal controllability and observability cost measures that involve the influence vectors ψ_i, γ_{di}, and γ_{ri} may be obtained by evaluating these terms at a design point in the direction of the steepest ascent and at the boundary of the neighborhood. Here, it is assumed that the coupling between the influence vectors corresponding to different modes is small. The remaining terms in the cost measures involve functions of the open-loop eigenvalues. All but one of these functions of ω_i have no maximum. Only the function $f^* = \omega_i(\rho)/\left(1+\omega_i^2(\rho)\right)$ has a maximum at $\omega_i(\rho) = 1$. Consequently, upper bound values for all these functions except f^* can be obtained by computing the maximum value of these functions at the smallest and the largest possible values of ω_i (ω_i^L *and* ω_i^U) within the prescribed neighborhood. As for f^*, if $\omega_i(\rho) = 1$ is within the prescribed neighborhood, then $f^*_{max} = 1/2$. Otherwise, the same procedure as for other functions is used.

MODAL COST APPROXIMATION (CONT'D)

- Upper bound value for the influence coefficient terms:

$$\max_{\rho}\left\{\psi_i^T(\rho)\psi_i(\rho)\right\} \approx \psi_i^T(\rho_o)\psi_i(\rho_o) + 2\sum_{j=1}^{n_d}\psi_i^T(\rho_o)[\partial\psi_i/\partial\rho_j]\,sgn\left\{\psi_i^T(\rho_o)[\partial\psi_i/\partial\rho_j]\right\}\rho_{oj}\epsilon +$$
$$\sum_{j=1}^{n_d}\sum_{k=1}^{n_d}[\partial\psi_i/\partial\rho_j]^T[\partial\psi_i/\partial\rho_k]\,sgn\left\{\psi_i^T(\rho_o)[\partial\psi_i/\partial\rho_j]\right\}sgn\left\{\psi_i^T(\rho_o)[\partial\psi_i/\partial\rho_k]\right\}\rho_{oj}\rho_{ok}\epsilon^2$$

- Upper bound values for the scalar functions of ω_i may be obtained by computing these functions at ω_i^U and ω_i^L.

$$\omega_i^L(\rho) = \omega_i(\rho_o) - \sum_{j=1}^{n_d}|\partial\omega_i/\partial\rho_j|\rho_{oj}\epsilon$$

$$\omega_i^U(\rho) = \omega_i(\rho_o) + \sum_{j=1}^{n_d}|\partial\omega_i/\partial\rho_j|\rho_{oj}\epsilon$$

The CSI Evolutionary Model is a laboratory testbed designed and constructed at the NASA Langley Research Center for experimental validation of the control design methods and the integrated design methodology [5]. The Phase-Zero Evolutionary Model, shown in the figure, consists of a 62-bay central truss, with each bay 10 inches long, two vertical towers, and two horizontal booms. The structure is suspended using two cables as shown. A laser source is mounted at the top of one of the towers, and a reflector with a mirrored surface is mounted on the other tower. The laser beam is reflected by the mirrored surface onto a detector surface 660 inches above the reflector. Eight proportional, bi-directional, gas thrusters provide the input actuation, while collocated servo accelerometers provide output measurements. An integrated controls-structures design of this test article is sought.

To perform the integrated design, the structure was divided into seven sections, three sections in the main bus, and one section each for the two horizontal booms and two vertical towers. Three structural design variables were used in each section, namely, effective cross-sectional area of the longerons, the battens, and the diagonals, making a total of 21 structural design variables.

STRUCTURAL DESIGN VARIABLES

- Structure is divided into seven sections
- The effective cross-sectional areas of longerons, battens and diagonals are chosen as design variables
- Total of 21 structural design variables

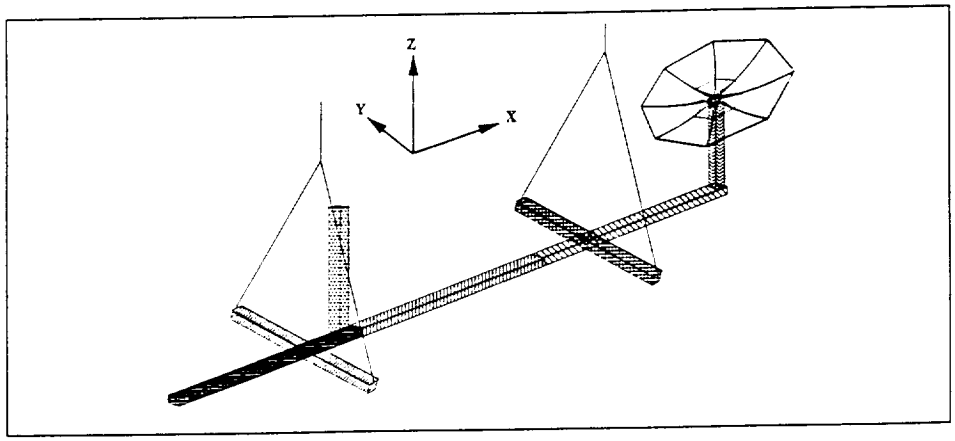

The static (or constant-gain) dissipative controller which employs collocated and compatible actuators and sensors, and consists of feedbacks of the measured attitude vector y_p and the attitude rate vector y_r using constant, positive-definite gain matrices G_p and G_r, is used for feedback control. This controller is robust in the presence of parametric uncertainties, unmodelled dynamics, and certain types of actuator and sensor nonlinearities [6]. However, the performance of such controllers is inherently limited because of their structure. Here, two of the eight available actuators were used to generate persistent white-noise disturbances, while the remaining six actuators were used for feedback control. The static dissipative controller uses a 6 x 6 diagonal rate-gain matrix with no position feedback (since this system has no zero-frequency eigenvalues, position feedback is not necessary for asymptotic stability). Thus, in the integrated design with the static dissipative controller, the total number of design variables was 27 (21 structural plus 6 control design variables).

CANDIDATE CONTROLLERS

Static Dissipative Controllers

$$u = -G_r y_r$$

- Collocated sensors and actuators
- Positive definite gain matrices
- Robust in presence of model uncertainties
- May have limited performance
- Elements of the Cholesky-factor matrix of the rate gain matrix are used as control design variables (no position feedback)

$$G_r = L_r L_r^T$$

An integrated controls-structures design was obtained by minimizing the steady-state average control power in the presence of white-noise input disturbances with unit intensity (i.e., standard deviation intensity = 1 lbf.) at actuators No. 1 and 2 (located at the end of the main bus nearest to the laser tower). A constraint was placed on the steady-state rms position error at the laser detector (above the structure) for reasonable steady-state pointing performance. Additionally, the total mass of the structure was constrained to facilitate a fair comparison with the phase-0 design. The six remaining actuators were used in the control design, along with velocity signals (required for feedback by the dissipative controllers) obtained by processing the accelerometer outputs. Side constraints were also placed on the structural design variables for safety and practicality concerns. Lower bound values were placed on these variables to satisfy structural integrity requirements against buckling and stress failures. On the other hand, upper bound values were placed on these variables to accommodate design and fabrication limitations.

DESIGN PROBLEM

- Pose the integrated controls-structures design as a simultaneous optimization problem
- Minimize the average control power

$$J \equiv Trace\left\{E\left\{uu^T\right\}\right\}$$

subject to

$$Trace\left\{E\left\{y_{los}y_{los}^T\right\}\right\} \leq \epsilon$$

$$M_{tot} \leq M_{budget}$$

- Side constraints on the structural design variables to accommodate safety, reliability, and fabrication issues

The controls-structures integrated design results are shown below. The results indicate that the evaluation (fifty-mode) model and reduced-order model converged to essentially the same final design. This is a clear indication that the model reduction method presented in this paper can handle possible discontinuities associated with the changing dynamic characteristics of the evolving structure.

The controls-structures integrated design results were obtained using the Automatic Design Synthesis (ADS) software package [7]. All solutions were computed using an interior penalty function method with a Broyden-Fletcher-Goldfarb-Shanno method for the unconstrained subproblem.

INTEGRATED DESIGN RESULTS

	CONTROL POWER	RMS POINTING	TOTAL MASS
EVAL. MODEL	2.64	2.999	1.896
REDUCED-ORDER MODEL	2.57	2.998	1.918

The table below presents a computational performance comparison of the evaluation model and reduced-order model. The results indicate that the model reduction scheme yielded approximately a 49 percent reduction in CPU time. This increased performance can be attributed to CPU time reductions in both the closed-loop analysis, as well as those gained by introducing open-loop eigenvalue/vector approximations. It should also be noted that the model reduction method required 8 percent more function evaluations to obtain an optimal design. This may be attributed to inaccuracies induced by the open-loop eigensystem approximations.

COMPUTATIONAL REQUIREMENTS

	CPU TIME * (TOTAL)	CPU TIME (AVG. PER EVALUATION)
EVAL. MODEL	28 hrs. 19 min.	82.7 sec.
REDUCED-ORDER MODEL	14 hrs. 30 min.	38.9 sec.

* SUN SPARC 2 workstation.

The bar charts shown below present the resulting structural design variables for both the full model and the reduced-order model in terms of initial versus final design. The results indicate that the two methods converged to basically the same final design.

STRUCTURAL DESIGN VARIABLES

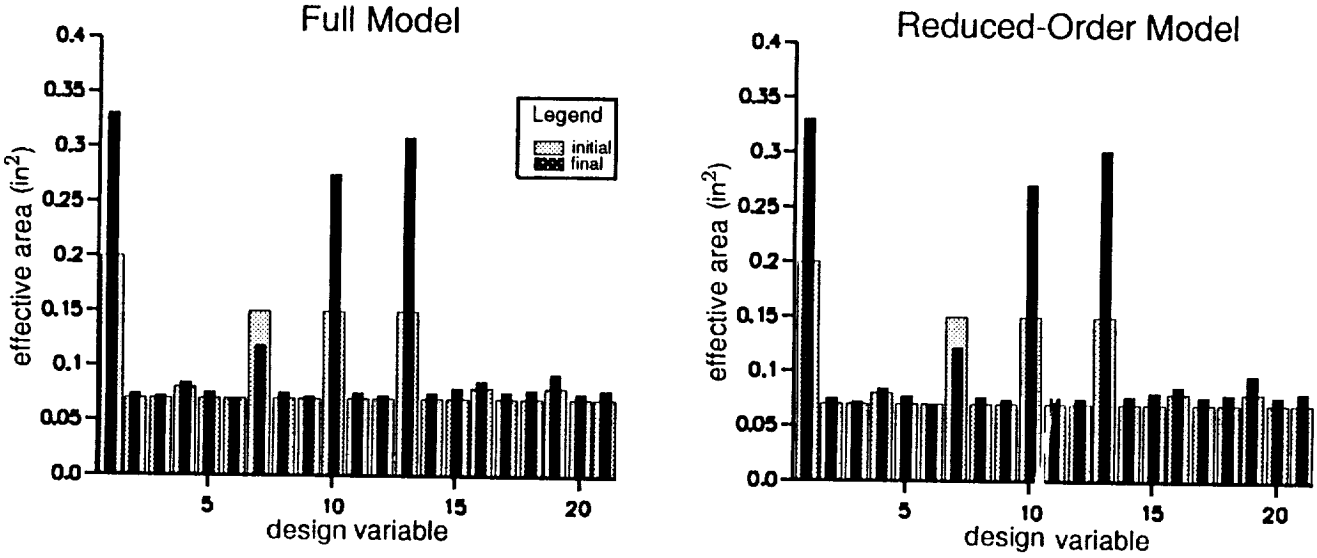

In the bar charts below, controllability and observability cost measures for the first 20 modes are listed. The controllability and observability cost measures are for a nominal point and the worst-case values within a 5 percent perturbation from the nominal. Using the worst-case scenario approach described earlier, the number of modes retained for closed-loop analysis was increased from 36 to 38. This chart also indicates the relative sensitivity of α_{ci} and α_{oi} with respect to changes in the structural design variables. It can be observed that the first three suspension modes (1–3) are the most controllable and observable modes. However, the last two modes (5 and 6) along with the first three flexible modes (7–9) are quite controllable and observable as well. Moreover, it can be seen that modes that are not significant at the nominal design point (modes 17 and 19) are as sensitive to design perturbations as lower frequency modes, and, therefore, might become significant as the design optimization progresses. Although not shown, the same level of sensitivity was found in modes 21 through 50. It should be noted that in this design problem the sensors and actuators are collocated, thereby producing values for the controllability and observability cost measures which are similar, but different in scaling.

CONTROLLABILITY AND
OBSERVABILITY COST MEASURES

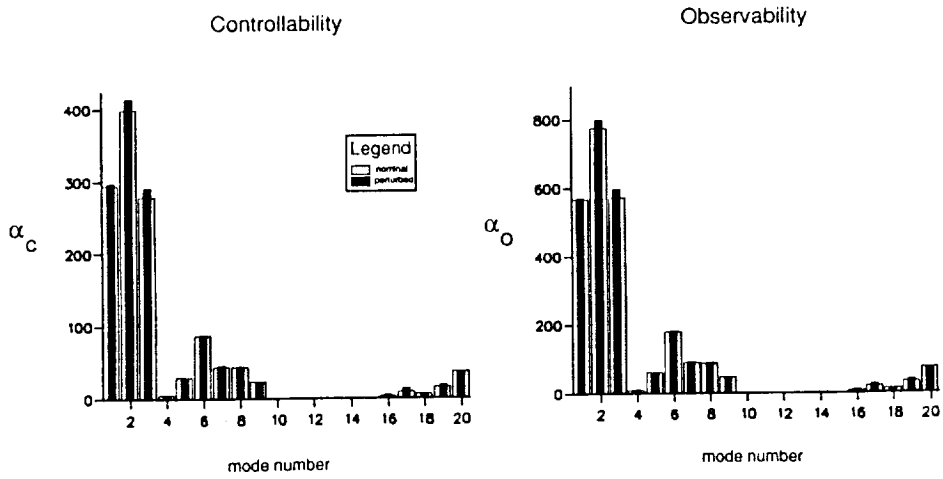

A novel and efficient method for model order reduction in the integrated controls-structures design process has been developed. The method uses a linear approximation of the open-loop eigenvalues and eigenvectors and identifies, through a worst-case scenario, the structural modes that are significant at a nominal design point along with modes that might become significant as the optimization moves the structural design variables within a prescribed neighborhood of the nominal design point. Consequently, this approach can handle the discontinuities that may hamper the integrated design optimization process because of the evolving structure, i.e., the frequency and number of significant structural modes can change at each design iteration. Although in this paper modal controllability and observability cost measures were used to evaluate the significance of each mode for inclusion in the control design model, the approach of linear approximation and worst-case analysis can be used in conjunction with other modal cost measures as well. Finally, further research is required to identify proper threshold levels for controllability and observability cost measures as well as to choose the size of the prescribed neighborhood used in the linear approximation.

CONCLUDING REMARKS

- A new and efficient method for model order reduction in the integrated controls-structures design has been developed.

  —>The method can handle the discontinuity problems that may hamper the optimization process.

  —>The method can be used in conjunction with other model reduction techniques.

- Further research is required in choosing the threshold levels for controllability and observability, as well as the size of the neighborhood for linear approximation.

REFERENCES

1. Maghami, P. G., Joshi, S. M., Armstrong, E. S., and Walz, J. E., "Integrated Controls-Structures Design Methodology Development for a Class of Flexible Spacecraft," Proceedings of the Third Air Force/NASA Symposium on Recent Advances in Multidisciplinary Analysis and Optimization, San Francisco, California, Sept. 24–26, 1990.
2. Maghami, P. G., Joshi, S. M., and Lim, K. B., "Integrated Controls-Structures Design: A Practical Tool for Modern Spacecraft," Proceedings of the 1991 American Control Conf., Boston, Massachusetts, June 26–28, 1991.
3. Lim, K. B., "A Method for Optimal Actuator and Sensor Placement for Large Flexible Structures," Presented at the AIAA Guidance, Navigation and Control Conference, August 1990, Portland, Oregon, Paper No.: 90–3466.
4. Kenny, S. P., "Eigensensitivity Analysis for Space Structures with Applications in Design Optimization," Master's Thesis, Old Dominion University, May 1990.
5. Belvin, W. K., Horta, L. G., and Elliot, K. E., "The LaRC CSI Phase-0 Evolutionary Model Testbed: Design and Experimental Results," Proceedings of the Fourth NASA/DOD Controls/Structures Interaction Technology Conf., Orlando, Florida, Nov. 5–7, 1990.
6. Joshi, S. M., "Control of Large Flexible Space Structures," Berlin Springer-Verlag, Vol. 131, Lecture Notes in Control and Info. Sciences, 1989.
7. Vanderplaats, G. N., "ADS- A Fortran Program for Automated Design Synthesis - Version 1.10," NASA Contractor Report 177985, September 1985.

THE MIDDECK ACTIVE CONTROL EXPERIMENT (MACE)

David W. Miller[1], Raymond B. Sepe[2], Daniel Rey[3], Erik Saarmaa[4], Edward F. Crawley[5]
Space Engineering Research Center
Massachusetts Institute of Technology
Cambridge, Massachusetts

ABSTRACT

The Middeck Active Control Experiment (MACE) is a NASA In-Step and Control Structure Interaction (CSI) Office funded Shuttle middeck experiment. The objective is to investigate the extent to which closed-loop behavior of flexible spacecraft in zero gravity (0-g) can be predicted. This prediction becomes particularly difficult when dynamic behavior during ground testing exhibits extensive suspension and direct gravity coupling. On-orbit system identification and control reconfiguration is investigated to improve performance which would otherwise be limited due to errors in prediction. The program is presently in its preliminary design phase with launch expected in the summer of 1994.

The MACE test article consists of three attitude control torque wheels, a two axis gimballing payload, inertial sensors and a flexible support structure. With the acquisition of a second payload, this will represent a multiple payload platform with significant structural flexibility. This paper presents on-going work in the areas of modelling and control of the MACE test article in the zero and one-gravity environments. Finite element models, which include suspension and gravity effects, and measurement models, derived from experimental data, are used as the basis for Linear Quadratic Gaussian controller designs. Finite element based controllers are analytically used to study the differences in closed-loop performance as the test article transitions between the 0-g and 1-g environments. Measurement based controllers are experimentally applied to the MACE test article in the 1-g environment and achieve over an order of magnitude improvement in payload pointing accuracy when disturbed by a broadband torque disturbance. The various aspects of the flight portion of the experiment are also discussed.

INTRODUCTION

Objective and Rationale

The objective of the Middeck Active Control Experiment (MACE) is to develop a qualification procedure for flexible, precision spacecraft. For future vehicles which cannot be dynamically tested on the ground in a sufficiently realistic zero-gravity simulation, this procedure will increase confidence in the eventual orbital performance of such spacecraft (refs. 1 and 2). Confidence is developed through analysis and extensive ground testing. Analytical models, such as finite elements, require extensive refinement in order to achieve the accuracy required of high authority control (ref. 3). This refinement is enabled by modal identification (ref. 4). If suspension and gravity effects couple with the flexible behavior during ground testing, the analytical model must include these effects to ensure that the model is properly refined. However, the model will no longer accurately represent 0-g behavior.

An alternative to analytical models for control design is the development of measurement models (refs. 5 and 6). Transfer functions measured through the control hardware are fitted using an assortment of poles, zeros, gains and time delays. These models can provide high accuracy. However, if suspension and gravity effects are present in the measurements, the resulting control will be inappropriate for 0-g operation.

Therefore, the MACE program attempts to determine how a spacecraft designer might acquire confidence in the eventual on-orbit performance of a flexible spacecraft when the analytical 0-g predictions are inaccurate and the 1-g measurement models are inappropriate. To achieve this, the program follows the evolution of a 'CSI spacecraft' from analysis and ground testing through on-orbit system identification and control on board the middeck of the Shuttle. The test article is designed to couple suspension and direct gravity effects with the flexible behavior during ground testing (refs. 7 and 8).

[1] Principal Research Scientist, Member AIAA, ASME
[2] Postdoctoral Associate, Member IEEE
[3] Research Assistant
[4] Project Engineer
[5] Professor, Aeronautics and Astronautics, Member AIAA, ASME

Development Model Hardware Description

The Development Model (DM) is the first of three sets of hardware to be developed under the MACE program. As shown in Figure 1, the DM is composed of a three-axis torque wheel assembly, a two-axis gimballing payload, and a dummy mass which will be replaced by a second gimbal in the near future. When these components are connected by a flexible structural bus, the fundamental bending mode is 1.7 Hz.

The DM is instrumented with two angle encoders on the gimbal axes, two three axis rate gyro platforms, and other assorted sensors. One rate gyro platform is mounted in the payload while the other is mounted under the torque wheel assembly. The bus is composed of flexible Lexan™ struts interconnected by aluminum nodes. The torque wheel assembly is comprised of three orthogonally mounted DC servo motors with an aluminum inertia wheel mounted to each. Two-axis gimbal rotation is excited about the x and z axes via two DC torque motors.

The hardware components that serve as support equipment for the test article are a pneumatic/electric low-frequency suspension system (ref. 9), a real-time control computer (ref. 10), a Fourier analyzer, and various signal conditioning and power amplification electronics for the sensors and actuators, respectively.

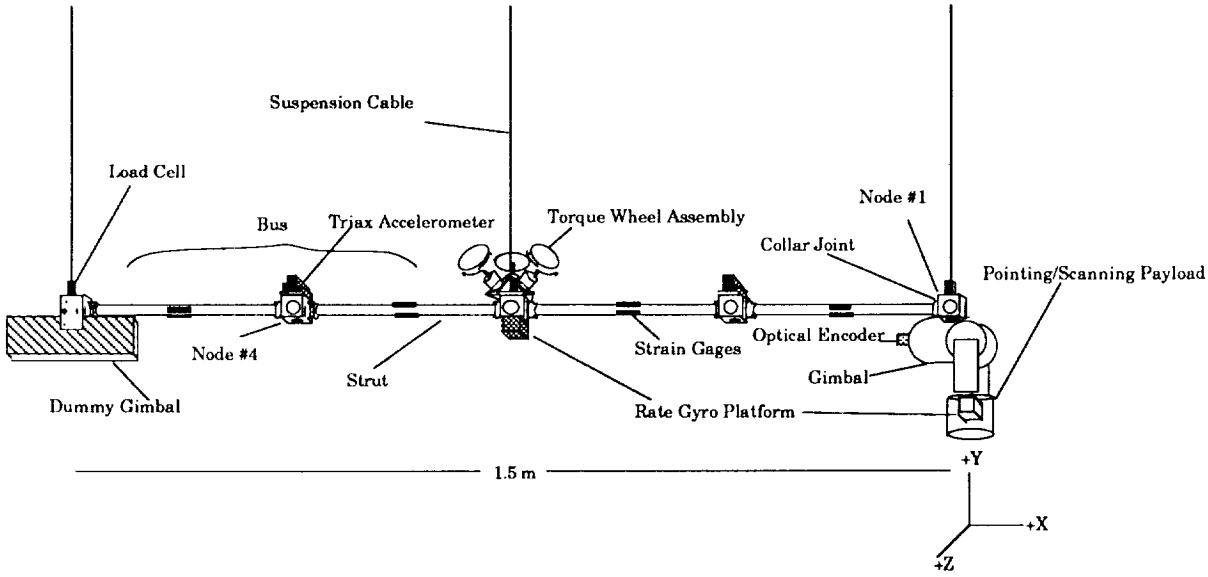

Figure 1. Development Model test article.

Science Approach

In the 1-g and 0-g control design for MACE, analytical finite element and measurement models are used in concert. This paper presents current progress along both avenues. Analytical models are useful in that they enable design work to be conducted prior to the acquisition of data or, for that matter, the test article itself. They also provide the crucial ability to predict on-orbit performance of flexible spacecraft. On the other hand, measurement models provide high accuracy and are essential for the design of high performance control.

Figure 2 illustrates how analytical model and measurement based control will be used in the MACE program to predict and develop high performance 0-g control. The figure represents open-loop identification and closed-loop control in two arenas: ground (1-g) and on orbit (0-g). The approach starts with the formulation of a 1-g finite element model. This model includes direct gravity and suspension effects in addition to the inertia, dissipation and elastic properties of the structure. The purpose of this model is to achieve as accurate a representation of 1-g behavior as possible. Finite element model accuracy is achieved through modal identification to correlate open-loop behavior and 1-g control implementation, and to identify critical dynamics which have been poorly modeled. By observing the degree to which this model is useful in the design of 1-g control, a sense for the limitations of 0-g predictions is obtained.

In parallel with the finite element modelling, measurement models are developed by fitting poles, zeros, gains and time delays to pertinent transfer functions through the control hardware. These models are used to derive control and can be refined based upon closed-loop results. Measurement models will generally provide higher accuracy than finite element models when low noise devices are used. Therefore, the closed-loop results reveal the practical limitations in performance improvement that can be obtained given a particular form of control formulation and architecture. By comparing this performance with that achieved using finite element based control, the designer can understand the cost-benefit of further finite element model refinement.

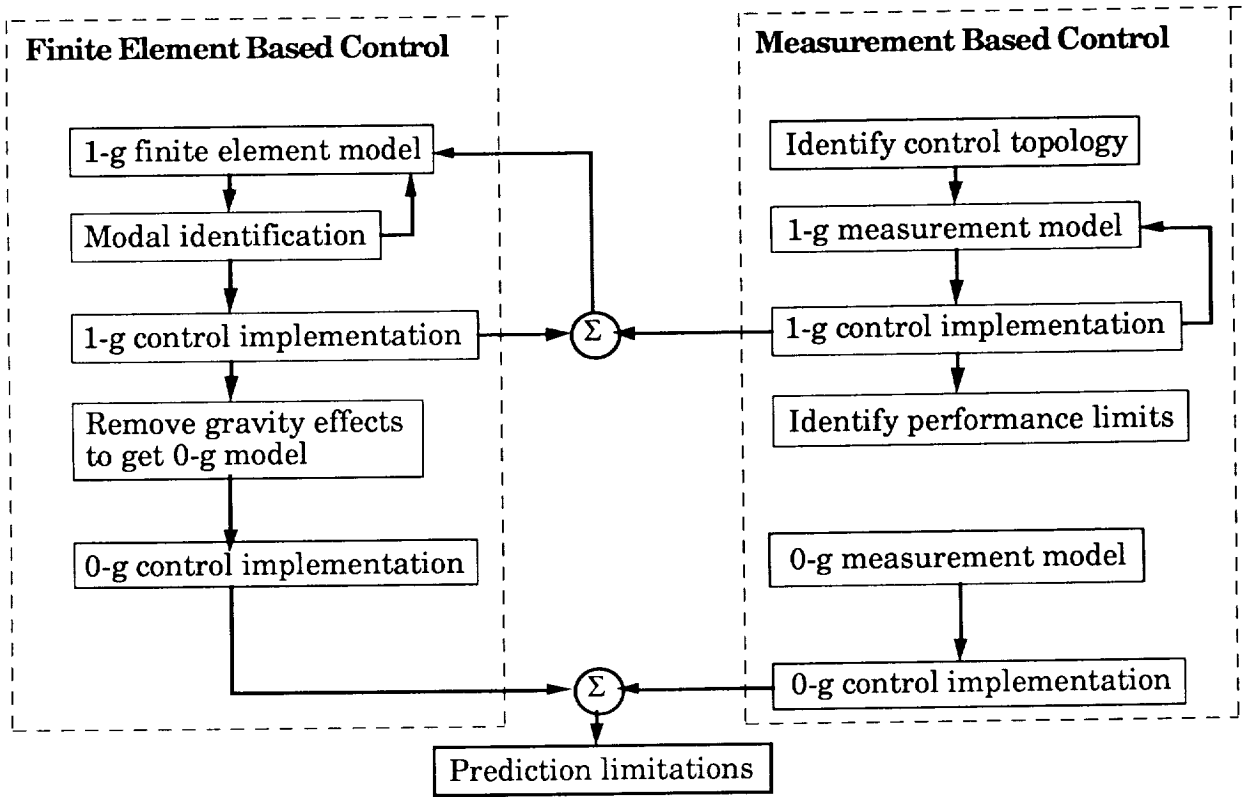

Figure 2. Science approach.

Once the finite element model has been sufficiently refined based upon ground testing, the gravity and suspension effects can be removed to yield a 0-g model. This model is then used to derive control for implementation on orbit. The accuracy of the 0-g finite element model can be assessed in open-loop by comparing predicted dynamics with 0-g system identification measurements acquired on orbit. It can also be assessed in closed-loop by comparing performance with both finite element predictions and 0-g measurement based control.

This science approach implies that on-orbit science operations will involve three phases. In the first phase, system identification will be performed to obtain measurement data for judging finite element model accuracy and deriving a 0-g measurement model. The second phase will involve the implementation of control algorithms based on the 0-g finite element model. During the third phase, control algorithms derived using the 0-g measurement model, developed using the system identification data, will be implemented.

This paper details some preliminary open and closed-loop results that have been obtained through analysis and ground testing. The next section develops both the 1-g and 0-g finite element models and analyzes the implications of testing the MACE test article in a 1-g environment when the control has been derived using a model of 0-g behavior. Such a scenario would be typical of preflight qualification testing for a flexible spacecraft. The following section discusses the use of 1-g measurement models to derive and exercise real time Linear Quadratic Gaussian (ref. 11) control on the MACE test article. This is followed by a brief description of the flight portion of the MACE program.

Suspension and Direct Gravity Effects

Ground-based test articles for research and qualification of precision spacecraft must be suspended in an effort to simulate the free-free boundary conditions of their operational environment. Under these conditions it is possible to group the perturbation effects of gravity on the dynamics of the controlled structure into five classes:

1) Suspension effects: The suspension system establishes the boundary conditions which affect the test article dynamics. All of the test article rigid-body modes are stiffened and the flexible modes couple to varying degrees with the suspension system dynamics.

2) Non-linear effects: This category encompasses all changes to the structural behavior due to gravity loading which must be modelled in a nonlinear fashion; e.g. loading of joints that have a deadband, gravity induced friction in articulations and devices, etc.

3) Stiffness Effects: The constant initial stress of the suspended structure due to gravity loading has the net effect of altering the structure's stiffness. This effect is a perturbation to the linear system model but can only be determined by taking into account the second order or quadratic strain terms in the equilibrium principle. Captured are the gravity stiffening and destiffening of the structural and suspension modes.

4) Static Pre-deformations: Given discrete suspension attach point locations, gravity loading will deform the structure and change the reference equilibrium about which the system dynamics are defined. Even slight deformations can couple otherwise decoupled modes.

5) Direct Sensor and Actuator Effects: The behavior of accelerometers and proof-mass actuators is directly affected by gravity when they are subject to harmonic orientation changes in a gravity field (ref. 12). The perturbation is additive and can result in amplifications, attenuations and even phase reversals of the device input or output.

The specific objective of the Middeck 0-gravity Dynamics Experiment (MODE) (ref. 13) was the study of the first two gravity influences with a particular focus on the non-linear gravity effects given the presence of a scaled space station alpha joint, tensioning cables which can slacken and numerous deployment hinges. MACE, the successor to the MODE experiment, is designed to investigate the first, third and fourth types of gravity effects on the dynamics of a flexible articulating multi-body test article in both open and closed-loop configurations.

Gravity Effect Modelling Procedure

The first step in including gravity effects into a finite element model of the MACE test article is the incorporation of the suspension system. Once this step is accomplished it is then possible to introduce the mass proportional gravity loading on the entire system and determine not only the static pre-deformations but also the gravity stiffening effects. This latter computation is the key to properly describing the system behavior in a gravity field.

Given a known internal stress state, it is possible to solve for a geometric or differential stress stiffness matrix which is a linear function of the loading. The static deformations are proportional to the loading and inversely proportional to the system stiffness matrix. However, the system stiffness matrix is itself a function of the loading and the system deformations. Therefore, it is necessary to iterate to solve for the static deformations.

The ADINA (Automatic Dynamic Incremental Nonlinear Analysis) (ref. 14) finite element modelling package was used to model both the MODE (ref. 15) and MACE test articles and as a research tool in the study of sample problems for the identification of gravity and suspension effects. Modelling gravity effects in ADINA is a multi-step procedure. If suspension system bounce frequency tuning is required to achieve mass proportional stiffnesses in the suspension devices, as was the case with the MACE pneumatic/electric suspension devices, it is necessary to initially perform a static reaction force analysis with the structure pinned at the attachment points. The suspension spring stiffnesses are then prescribed given a known bounce frequency and the loads on each suspension cable. The next step consists of performing a nonlinear large displacement analysis with incremental loading and stiffness reformations at every step. The initial condition typically has the suspension springs unstretched with concentrated damping elements to damp the

system response. The iterations are performed until the structure reaches equilibrium under actual loading conditions. The end result of this step is a linear model of the statically deformed structure with geometric stiffening effects included. The third and final step is the eigensolution for infinitesimal displacements about the statically deformed configuration with the concentrated nodal damping elements removed.

Typical Results

Both 0-g and 1-g models were derived for the simple structure portrayed in Figure 3 with the primary payload rotated 45 degrees out of the vertical plane. The eigenfrequency shifts from the 0-g model to the 1-g model are shown in Figure 4. The rigid-body modes are all stiffened as they are replaced by bounce, tilt and pendular type modes while the flexible modes are variably stiffened and destiffened. Figure 5 shows two views of the modal cross-orthogonality mesh between the 0-g and 1-g eigenvectors. If the gravity effects were nil, the mesh would appear as a perfect diagonal due to orthogonality of modes. Clearly the rigid-body modes (low freq.) are perturbed the most resulting in a highly coupled subspace while flexible mode (high freq.) perturbations are largely limited to couplings between pairs of modes.

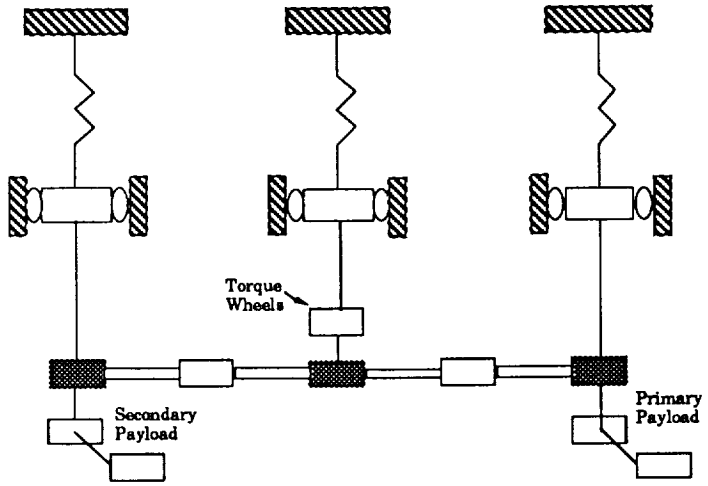

Figure 3. Simple analytical model for study of suspension and gravity effects.

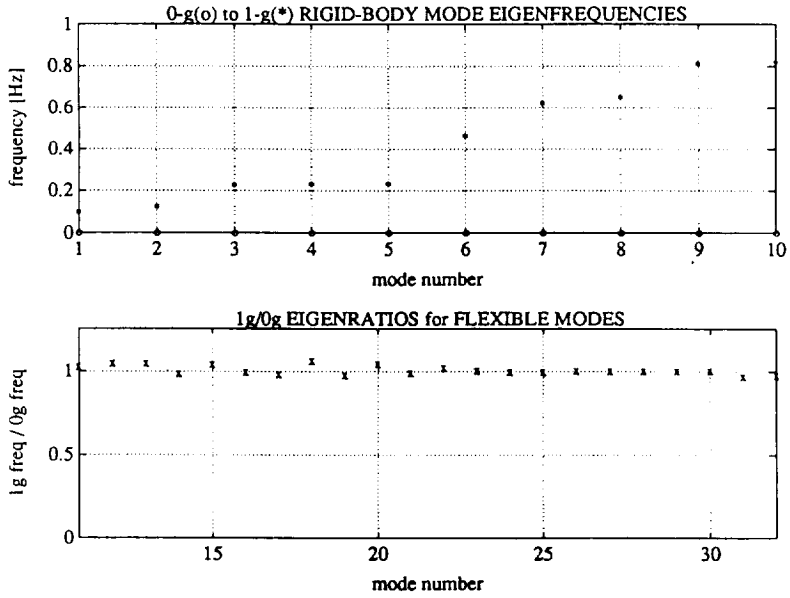

Figure 4. Eigenfrequencies for suspension modes and eigenratios for flexible modes.

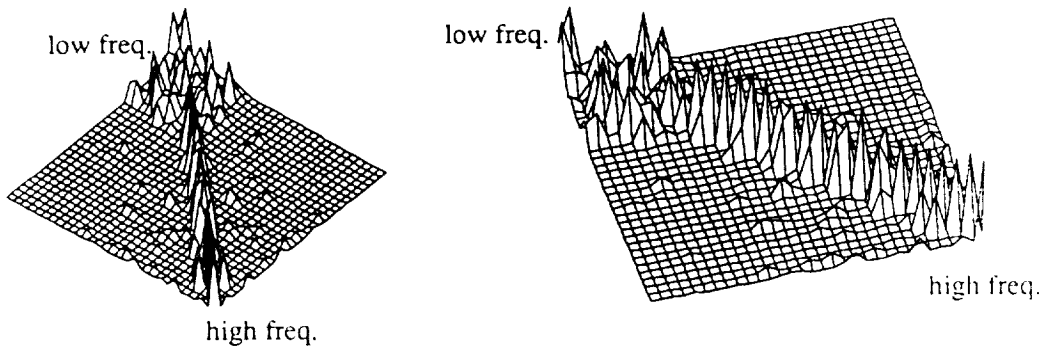

Figure 5. Modal cross-orthogonality mesh for 0-g and 1-g mode shapes.

Application to the MACE Development Model

An alternative means of visualizing the effects of suspension and gravity is to observe the perturbations to particular transfer functions through the structure. For this purpose, gravity effects were placed into a 0-g finite element model of the existing MACE DM hardware as shown in Figure 1. Figures 6a and 6b show the overlay of transfer functions from z-axis gimbal torque to the z-axis inertial angular rate of both the payload and the torque wheel assembly, respectively. The three transfer functions in each figure are from the 0-g model, 1-g model and measured data.

Notice at frequencies below 2 Hz that the 1-g model captures the payload pendulum and suspension

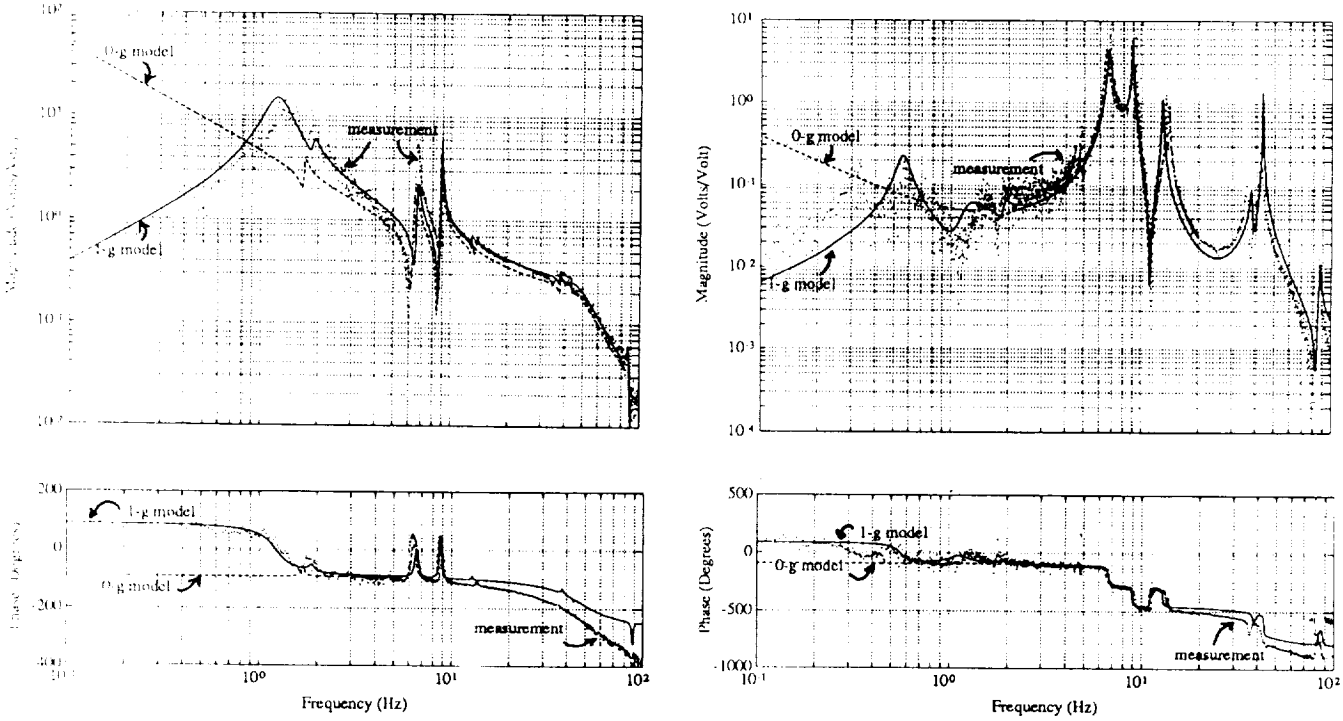

a) b)

Figure 6. Overlay of transfer functions from gimbal z-axis torque to a) payload z-axis inertial angular rate and b) bus inertial angular rate at the torque wheel location. Transfer functions are derived from measurements, the 1-g model and the 0-g model.

plunge modes while the 0-g model exhibits rigid body behavior. At higher frequencies, the 1-g model exhibits generally stiffer flexible modes than the 0-g model. This stiffening trend, caused by the gravity and suspension effects, appears to improve the agreement between the model and 1-g data as expected. Unmodelled time delays in the measurement devices could account for the deviation in modelled and measured phase behavior at higher frequencies.

Closed-Loop Control Analysis

With the 1-g and 0-g finite element models developed, one can now analyze the implications of testing the MACE test article in a 1-g environment when the control has been derived using a model of 0-g behavior. The model in Figure 3 was used for this analysis. For 0-g modelling, the suspension system is removed. The inertial angles of the primary payload and the inertial angles of the bus at the torque wheel location combine to form the performance metric. The gimbal motors in the secondary payload are used to generate torque disturbances on the structure. Both payloads are free to vary about their nominal positions.

The inputs to the plant are five torque actuators: three torque wheels for attitude control of the bus and two gimbal torque motors that rotate the primary payload about the relative x and z-axes. The physical outputs are taken to be 14 measurements: three inertial angles at the torque wheel assembly, two inertial angles at the primary payload, two relative gimbal angles, and the 7 corresponding angular velocities.

The 10 rigid body modes in the 0-g model are composed of three translations and three rotations of the bus, two rotations of the primary payload, and two rotations of the secondary payload. In the 1-g model, the presence of the suspension system results in no rigid body modes. All flexible modes are set to 1% damping. In the 1-g case, the 10 lowest frequency modes that correspond to pendulum-suspension modes are given 3% damping to account for the suspension system.

The presence of the 10 rigid body modes found in the 0-g structure are reflected in the complex frequency domain by the presence of 10 poles located at the origin. Thus, the rigid body modes are essentially pure integrators, which have infinite gain at DC. This presents a problem in the analysis in that any disturbance with low frequency content will be significantly amplified by the large low frequency gains of the rigid body modes. A two pronged approach is used to reduce the influence of the rigid body modes on the system. First, the performance of the closed-loop plant is evaluated using white noise bandlimited between 0.1 Hz and 60 Hz. This reduces the low frequency content of the disturbance. Second, the rigid body modes are stabilized using local proportional-differential (PD) feedback loops. The bus inertial angles and angular rates are fed to the torque wheels for rudimentary attitude control while the relative gimbal angles and angular rates are fed to the gimbal motors for coarse payload pointing.

The LQG controller design is carried out on the PD controlled 0-g model and then impinged on the 0-g and 1-g models. Behavioral differences are illustrated by plotting the performance versus increasing LQG control authority for both the 0-g and 1-g models. The intensity of the torque disturbance used to stimulate the PD controlled 0-g structure is adjusted to produce a 3σ performance (performance metric defined below) of 1 degree at low levels of LQG control authority. At high levels of control authority, it is desired that the LQG controlled 0-g system will exhibit a performance improvement of 40 db over the very low authority 0-g system. For the purposes of the design, the noise inputs are considered to be white. These assumptions avoid adding considerably more complexity to the design process and controller implementation. Although the assumption of white noise inputs will be made during the design process, the evaluation of the controller performance will take place using the closed-loop system with bandlimited noise.

The performance metric is chosen to be the weighted sum of the two payload inertial angles and the three bus inertial angles. This measure of performance emphasizes the inertial angular position of the primary payload while still recognizing that the inertial angular position of the bus must be bounded. The performance metric as a function of control authority for the total closed-loop system is shown in Figure 7a. Note that a new LQG design is performed for each level of control effort. The 0-g model shows a performance improvement of 36 db (40 db was the target) as the control authority is increased. For low control authority, the PD control stabilizes the rigid body modes of the 0-g system. The 1-g system has superior performance at low control authority due to the added damping and stiffness of the suspension system. However, as the control authority is increased on the 1-g system, its performance quickly deteriorates. An eigenvalue analysis indicates that a single closed-loop mode is driven unstable when the

control authority is increased. A participation factor analysis reveals that a suspension mode is the significant contributor to this instability.

Further evidence supporting this conclusion is obtained by subdividing both the 0-g and the 1-g models into flexible and nonflexible submodels. The closed-loop controller design procedure is then repeated. The submodel without any flexibility gives nearly identical performance to the model that included both flexible and nonflexible modes (Figure 7a). On the other hand, Figure 7b indicates that the performance of the flexible submodels for 0-g and 1-g begin to significantly distinguish themselves at a much higher level of control authority than the nonflexible submodels. This is an important result. In the 1-g environment, any potential instabilities of the flexible system that might occur at a high level of control authority are masked out by the deterioration in performance that occurs when the suspension modes are driven unstable at a relatively low level of control authority.

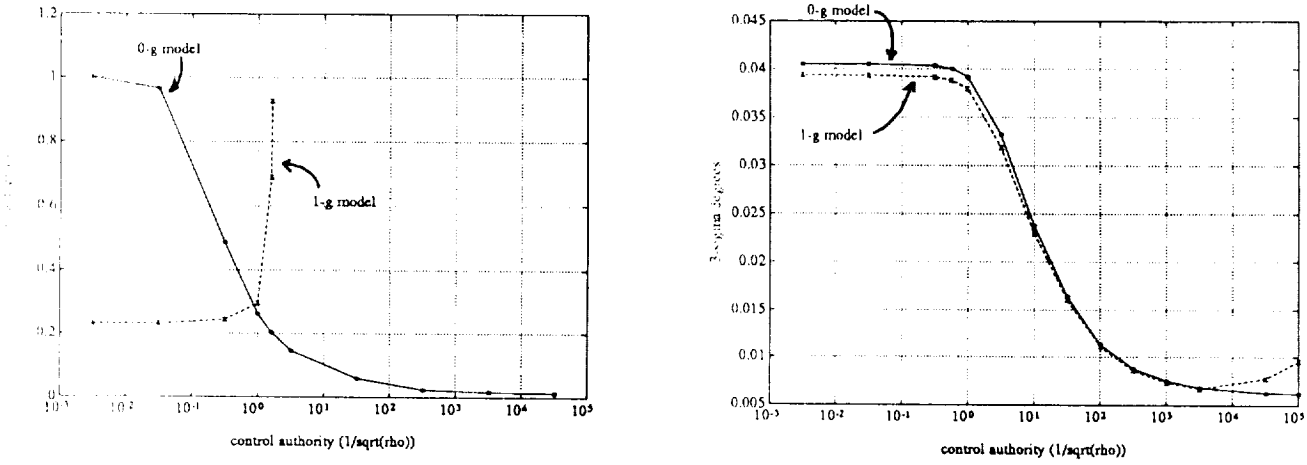

a) Total system

b) Flexible modes only

Figure 7. Closed-loop performance versus control authority for controller designed with 0-g model and impinged on 0-g and 1-g models.

MEASUREMENT BASED CONTROL

Control Objectives

In parallel with the finite element analysis, experimental measurement based control was performed. The objective was to inertially point one axis of the payload while a band-limited white noise disturbance was introduced through the gimbal torque motor. The control problem was posed to primarily involve control of flexible response in the x-y plane as shown in Figure 8. Therefore, all measured angles and actuated torques in the experiments were about the z-axis. Two different feedback architectures were used.

In the first architecture, the inertial angle of the payload was fed through a dynamic feedback compensator to drive the gimbal motor (Figure 8a). This resulted in a control problem where both the feedback sensor (**y**) and performance metric (**z**) were the inertial angle of the payload and the disturbance (**w**) and control signals (**u**) both entered the structure through the gimbal motor. This is referred to as the single-input, single-output (**SISO**) control problem.

In the second architecture, the feedback sensors were the the inertial angle of the torque wheels (**y**) and the relative gimbal angle as measured by the optical encoder (**y**) (Figure 8b). Along with a model of the intervening flexibility, the control formulation could employ the inertial bus and relative gimbal angles to make the inertial angle of the payload observable. Again, the gimbal torque motor acted as both the disturbance source (**w**) and control actuator (**u**). This resulted in a single-input, two-output (**SITO**) feedback architecture. A SITO controller was first formulated for the performance metric discussed above (**z** in Figure 8b). Then this metric was augmented by the addition of the bus inertial angle (**z** in Fig. 8c). This combined metric forced the control to attenuate flexible motion of the bus in addition to isolating the payload.

In total, three sets of experiments were conducted: **1)** SISO control to minimize payload pointing

error; 2) SITO control to minimize payload pointing error; and 3) SITO control to minimize a combination of payload pointing error and bus attitude. For each experiment, measurements of the pertinent transfer functions through the hardware were used to formulate a measurement model. The pertinent transfer functions were from the disturbances and actuators to both the feedback sensors and performance metric. These functions were fitted using poles, zeros, a gain and a time delay. Once the poles and residues of these transfer functions were placed in state-space form, Linear Quadratic Gaussian (LQG) control was derived. While the resulting dynamic compensators were implemented on an AC-100 real time control computer, the transfer functions from the disturbance to the performance metric were measured. These measurements were finally used to evaluate performance. The following two sub-sections present the evolution from modelling to closed-loop results for the SISO and SITO control architectures.

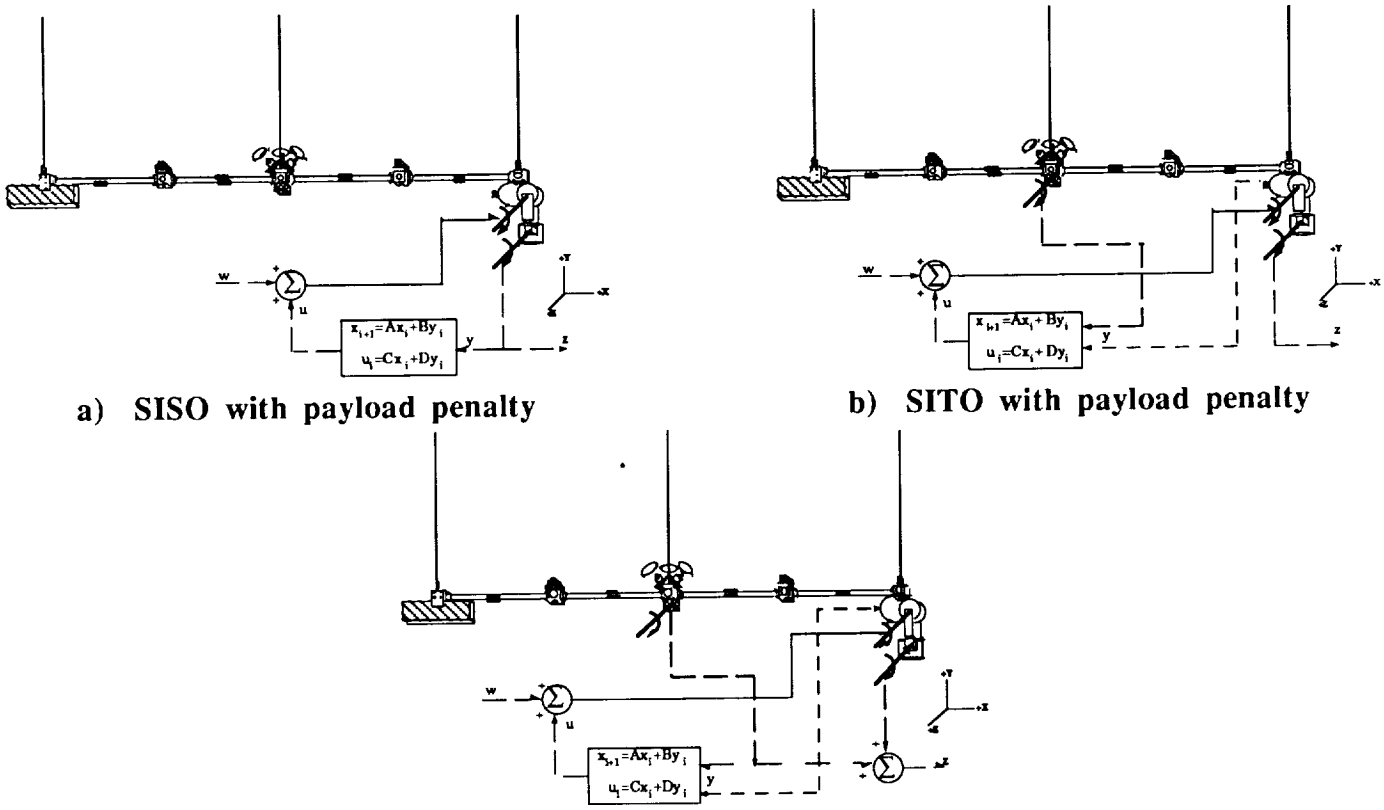

a) SISO with payload penalty

b) SITO with payload penalty

c) SITO with payload and bus penalty

Figure 8. Disturbance, performance metric and feedback architectures for the experiments.

Single-Input, Single-Output Control Architecture

A measurement model of the DM was obtained by measuring the transfer function from the gimbal torque to the payload inertial angle. This SISO transfer function was fit using poles, zeros, a static gain and a time delay which were then placed into continuous state-space form. Figure 9a overlays the measured transfer function (Data) with that calculated using the fitted parameters (Fit). The two resonances between one and two Hertz represent the pendulum mode of the gimbal and the first bending mode of the bus. Additional flexible modes occur near 7 and 9 Hz. The model contained 10 structural states and a third order Pade approximation to the time delay to yield a 13 state control design model.

Figure 9b overlays the open-loop (OL) and several closed-loop transfer functions from the gimbal disturbance to the inertial angle of the payload. The prediction of the closed-loop transfer function and the actual measurement were in very close agreement. This was made possible by the accuracy of the nonlinear fit. At low levels of control authority, the control reduced the static, pendulum and first bending mode

responses (CL1). The plant inverting dynamics in the compensator left the higher frequency modes almost unaffected. As authority was increased, the second bending mode near 7 Hz started to be suppressed. Eventually, all of the flexible dynamics visible in Figure 9b were suppressed (CL2). The closed-loop improvement in the RMS inertial payload angle was over one order of magnitude.

The same compensators were implemented several weeks later. A shift in the frequencies of the modes near 9 Hz caused instability when the compensator corresponding to CL2 was implemented. The highest level of control authority that was stable at this later date corresponds to CL1. Since the compensator performs plant inversion of the 9 Hz dynamics, stability is highly sensitive to slight shifts in these dynamics over time. To reduce this sensitivity, a multimodel technique (ref. 16) was used to derive the control. Control was designed to yield a given level of performance when applied to either model. The two chosen models differed by slight shifts in the frequencies of the dynamics near 9 Hz. The closed-loop response (CL3 in Figure 9b) using this new compensator was stable and exhibited adequate gain and phase margin despite the fact that the two models were based upon several week old data.

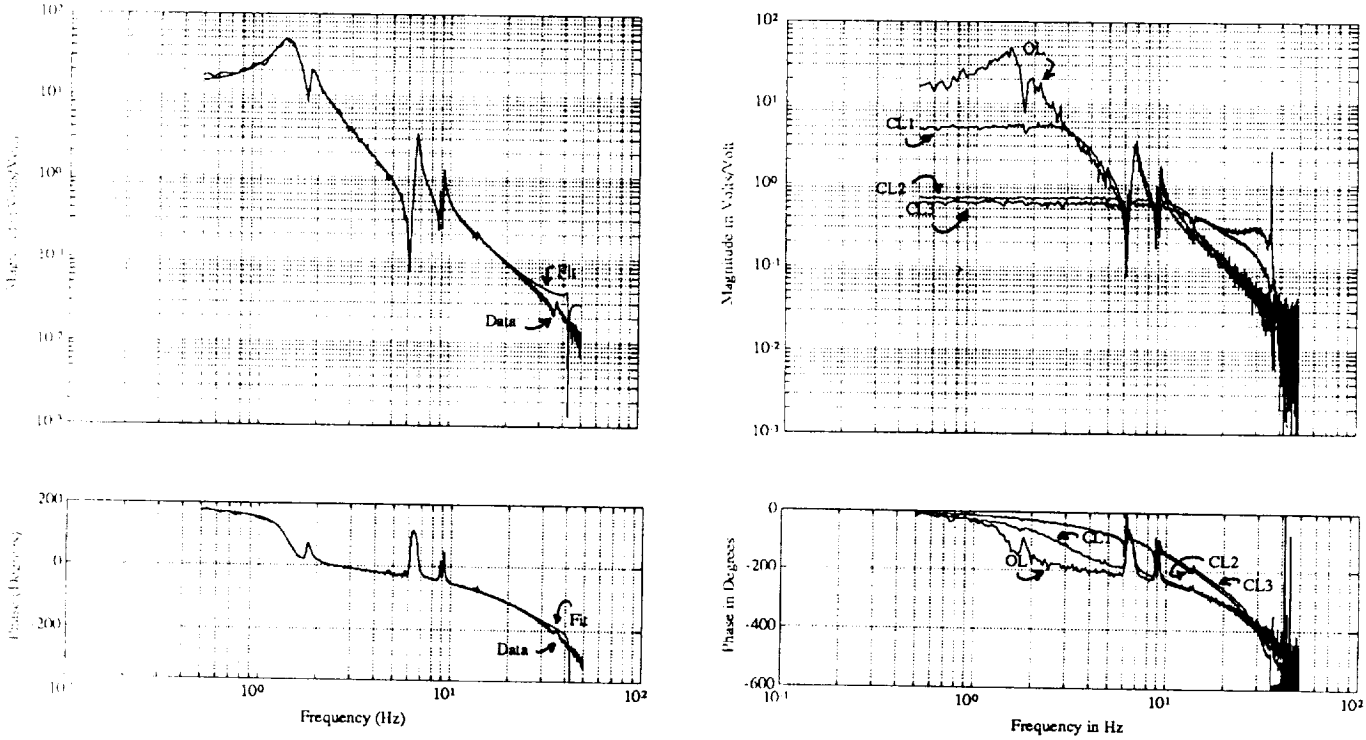

a) b)

Figure 9. a) **Data and pole-zero fit to the transfer function from z-axis gimbal torque to payload inertial angle.**

b) **Measured open and closed-loop transfer functions from gimbal disturbance to payload inertial angle.**

Single-Input, Two-Output Control Architecture

Three transfer functions were measured for this model. The first transfer function is shown in Figure 9a and represents the transfer function from both the disturbance and control actuator (gimbal) to the performance metric (payload inertial angle). The second transfer function was from gimbal torque command to relative gimbal angle as measured by an optical encoder (Figure 10a). The third transfer function was from gimbal torque to the bus inertial angle (Figure 10b). These last two measurements corresponded to the

transfer functions from the actuator to the feedback sensors.

The next step in the model development used a nonlinear fit routine to fit left half plane complex pairs of poles and zeros along with gains and time delays to these three transfer functions. Nonminimum phase zeros were required to achieve the fit to the noncolocated transfer function shown in Fig. 10b (Fit). The next step involved placing the poles, zeros, gains and time delays into state-space form.

Figure 11 overlays the open and highest authority closed-loop transfer functions from the gimbal disturbance to the payload inertial angle for SITO control with payload penalty (Fig. 8b). As in the SISO results, the control first reduced the 1.0 to 2.0 Hz response composed of the payload pendulum and first bending modes and then started to reduce second bending near 7 Hz. At low levels of control authority, the modes near 9 Hz were destabilized due to inaccuracies in the plant inversion being attempted by the compensator. To correct this, a lead compensator was added by placing a lightly damped pair of zeros just below the two modes near 9 Hz followed by a lightly damped pair of poles just above these modes. The increase in gain and phase margin allowed the control authority to be increased to the level which was used to obtain the result shown in Fig. 11.

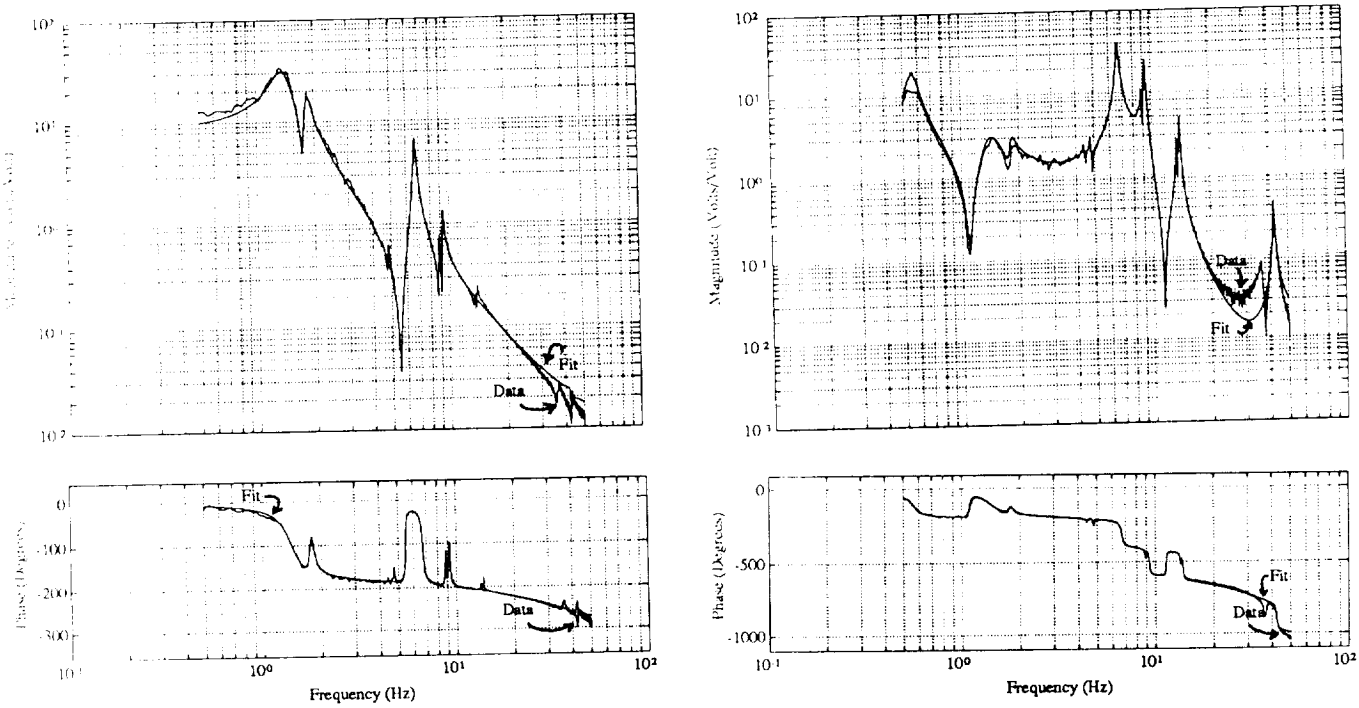

Figure 10. Data and pole-zero fit to the transfer function from z-axis gimbal torque to a) encoder angle and b) bus inertial angle.

As might be expected by observing Figures 10b, the addition of bus angle to the performance metric will cause the control to concentrate more on reducing flexible motion. The control will not only focus on reducing the payload pendulum and first bending modes, which dominate response in Fig. 9a, but to also suppress the flexible modes at 7 and 9 Hz, which dominate the response in Fig. 10b. As expected, the payload pendulum and first bending modes observed in the gimbal to payload inertial angle transfer function were suppressed (Figure 12a). Figures 12a and 12b show that the flexible modes near 7 and 9 Hz were also suppressed. In fact, the response in this frequency regime is reduced by an order of magnitude more than the level in Figures 9b and 11. Notice that the response is increased at frequencies above 10 Hz as a sacrifice for the dramatic reduction at low frequencies. In general, all of the closed-loop ground experiments achieved over an order of magnitude reduction in payload pointing error.

FLIGHT EXPERIMENT

The on-orbit science operations are designed to compliment the ground test program as shown in Figure 2. The on-orbit experiment exploits the unique shirt sleeve environment of the Shuttle middeck. Figure 13 shows the test article in the Shuttle middeck. The basic hardware and operations will mimic that of the Middeck 0-Gravity Dynamics Experiment (MODE) which flew on Discovery during the STS-48 mission in September, 1991 (ref. 13). In total, the MACE experiment will require three 8-hour days of one crew member. The assistance of a second crew member will be necessary periodically. The test article, data storage disks, and other support equipment will be stored in a disassembled fashion in three middeck lockers. A fourth locker will contain the Experiment Support Module (ESM). This package contains the experiment control computer, the real time control computer, data acquisition and storage, signal conditioning and power amplification electronics. A hand held keypad and display will enable the crew member to control the experiment and a digital interface to a portable computer will give access data analysis software and STS downlink channels.

The first on-orbit experiment in the summer of 1994 will involve open-loop system identification. Time response data will be measured from the disturbance source and control actuators to the feedback sensors and performance metric and stored in the ESM. Depending upon the final form of downlink available, either time or frequency domain data will be downlinked to the ground. This data will first be used to possibly restructure the sequence of pre-programmed control protocols. In addition, a measurement model will be developed for use in formulating 0-g measurement based control. Additional open-loop identifications will be conducted at the beginning of every science operations day.

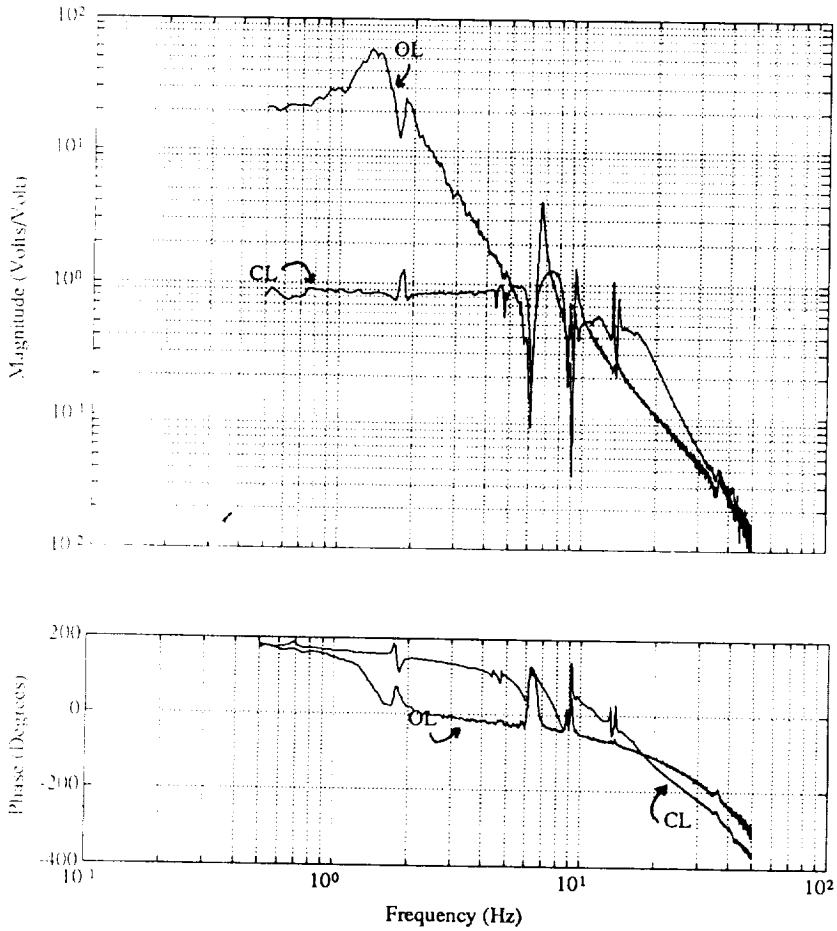

Figure 11. Measured open and closed-loop transfer functions from disturbance to payload angle for SITO control with payload penalty.

The on-orbit closed-loop tests will involve two classes of controllers. The first class will be derived using the analytical predictions of 0-g behavior. The finite element model, which will have undergone refinement through ground testing and analysis, will have the gravity effects removed. This 0-g model will then be used to formulate controllers. The on-orbit performance of these controllers, at various levels of control authority, will be compared to finite element predictions. As the 0-g results and 1-g predictions diverge, a feel for predictive accuracy achieved through analysis and ground testing will be obtained.

The second class will use system identification data, downlinked from the Orbiter, to develop a measurement model. The resulting controllers will be uplinked several days later for implementation. This class of controller investigates the performance improvements that are achievable through on-orbit identification and control reconfiguration.

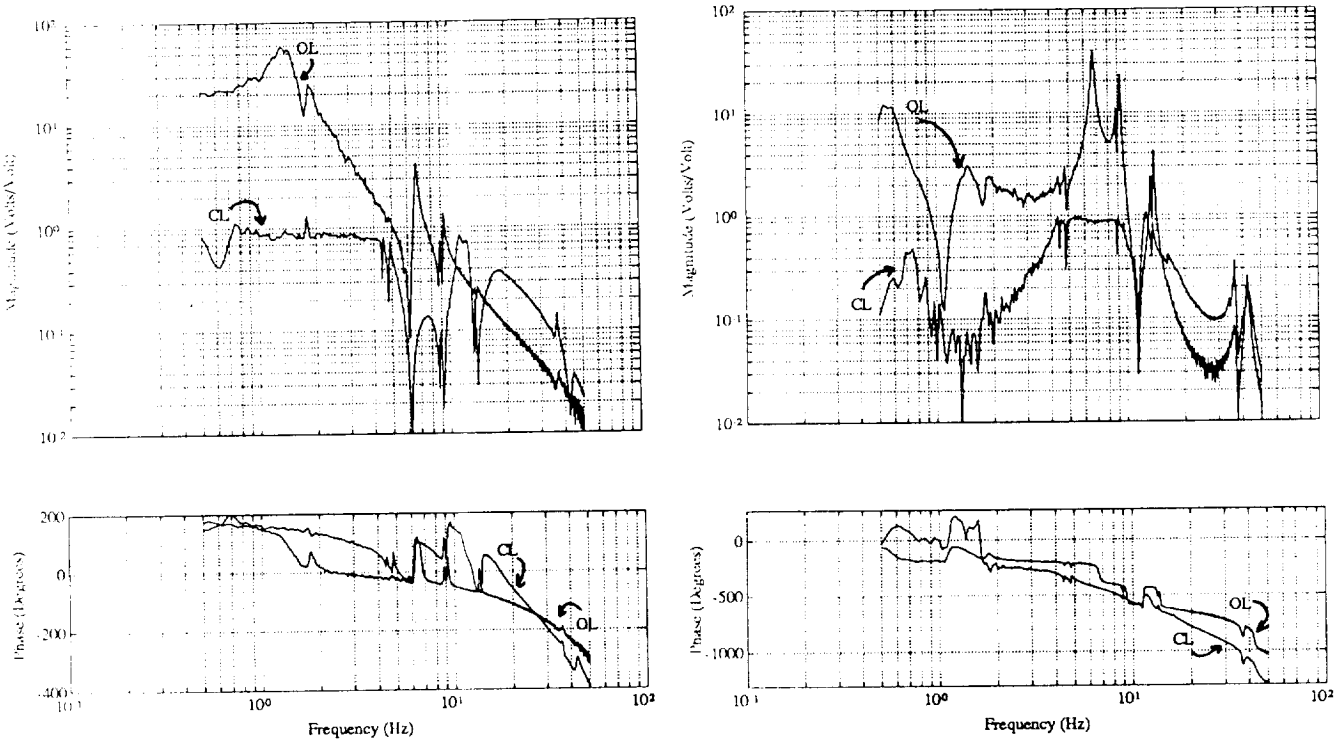

a) b)

Figure 12. Measured open and closed-loop transfer functions from disturbance to a) payload angle and b) bus inertial angle for SITO control with payload and bus penalty.

SUMMARY

The Middeck Active Control Experiment (MACE) is designed to study the ability to predict and tune on-orbit control performance given analysis, ground testing, and 0-g system identification. The science approach for MACE exploits both analytical and measurement models to generate predictions of on-orbit performance.

Analytical models developed using finite element analysis incorporate suspension effects, stiffness effects and static pre-deformations. The use of these effects improves the agreement between model predictions and ground test data. Further refinement is achieved through open and closed-loop ground testing of the hardware. The gravity and suspension effects are removed from the analytical model for the formulation of controllers for tests on orbit.

Analytical modelling of the MACE test article showed that a low fundamental frequency, multiple payload device exhibits significant suspension and gravity coupling. Linear Quadratic Gaussian controllers designed for on-orbit operation, but subjected to these effects on the ground, were shown capable of first

destabilizing suspension modes and then flexible modes at higher levels of control authority. This makes ground testing of candidate on-orbit controllers difficult. Therefore, the accuracy of on-orbit predictions would be unknown. In order to improve on-orbit performance limited by prediction error, 0-g system identification data will be used to develop a measurement model for tuning the control on orbit.

Measurement models have been developed and Linear Quadratic Gaussian controllers have been implemented in the laboratory. In general, Linear Quadratic Gaussian control proved to be very effective at achieving significant performance improvements under broadband disturbance. Over an order of magnitude reduction in pointing error was achieved. However, the plant inversion that LQG employs cannot tolerate changes in test article dynamics. Both multimodel and classical design techniques were used to make the control more robust.

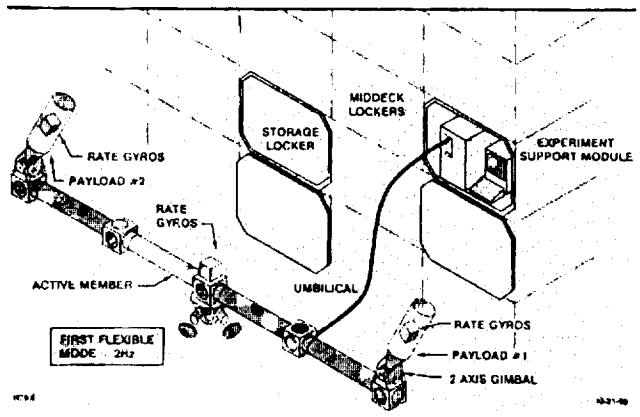

Figure 13. Test article deployed on the middeck.

ACKNOWLEDGEMENTS

This work is supported by the NASA In-Step and CSI Offices with Mr. Anthony Fontana as technical monitor. Special thanks to Mr. Douglas MacMartin and Mr. Jonathan How for their invaluable assistance in the control design.

REFERENCES

1. Experiment Requirements Document, MACE Document No. MACE-1-101, M.I.T. Space Engineering Research Center, Oct. 1991.
2. Miller, D. W.; de Luis, J.; Crawley, E. F.: Dynamics and Control of Multipayload Platforms: The Middeck Active Control Experiment (MACE). Proceedings of the 41st International Astronautical Federation Congress, Dresden, GDR, paper No. IAF-90-292, Vol. 24 of Acta Astronautica, Oct 6-12, 1990.
3. Wada, B. K.: Adaptive Structures. 89-1160-CP, presented at the 30th Structures, Structural Dynamics and Materials Conference, Part 1, Mobile, AL, 1989, pp. 1-11.
4. Chen, J-C; Fanson, J. L.: System Identification Test Using Active Members. AIAA 89-1290, presented at the 30th Structures, Structural Dynamics and Materials Conference, Mobile, AL, April, 1989, pp. 1154-1163.
5. Gilpin, K.; Athans, M.; Bokor, J.: Identification of a Lightly Damped Structure for Control-Structure Interaction. M.I.T. SERC #11-91, August, 1991.
6. Sidman, M. D.; DeAngelis, F. E.; Verghese, G. C.: Parametric System Identification on Logarithmic Frequency Response Data. IEEE Transactions on Automatic Control, Vol. 36, No. 9, September, 1991, pp. 1065-1070.

7. Crawley, E. F.; de Luis, J.; Miller, D. W.: Middeck Active Control Experiment: Phase A Final Report. MIT-SSL Report #7-89, 1989.
8. Rey, D. A.; Crawley, E. F.; Alexander, H.: The Direct Effects of Gravity on the Control and Output Matrices of Controlled Structure Models. AIAA 92-2094, presented at the AIAA Dynamics Specialist Conference, Dallas, TX, April 1992.
9. Kienholz, D. A.: A Pneumatic/Electric Suspension System for Simulating On-Orbit Conditions. 90-WA/Aero-8, presented at the Winter Annual Meeting of the American Society of Mechanical Engineers, Dallas, TX, November, 1990.
10. Using the AC-100: AC-100 User's Guide v2.4.03A. Integrated Systems Inc., November, 1990.
11. Kwakernaak, H.; Sivan, R.: *Linear Optimal Control Systems*. Wiley-Interscience, John Wiley & Sons, Inc., 1972.
12. Rey, D.A.: The Direct Effects of Gravity on the Control and Output Matrices of Controlled Structure Models. AIAA Paper No. 92-2094, 33rd AIAA Dynamics Specialist Conference, Dallas, April 1992.
13. Crawley, E. F.; Miller, D. W.; van Schoor, M.; de Luis, J.: Middeck 0-Gravity Dynamics Experiment: Project Plan. MIT-SSL Report 9-89, 1989.
14. ADINA User's Manual. ADINA R&D, Watertown, MA, 1987.
15. Crawley, E.F.; Barlow, M.S.; vanSchoor, M.C.; Bicos, A.: Variation in the Modal Parameters of Space Structures. Presented at the 33rd Structural Dynamics and Materials Conference, Dallas, April 1992.
16. MacMartin, D. G.; Hall, S. R.; Bernstein, D. S.: Fixed-Order Multi-Model Estimation and Control. Presented at the 1991 American Control Conference, Boston, MA.

SESSION V

Chairman: Brantley R. Hanks
NASA Langley Research Center
Hampton, Virginia

Co-Chairman: Capt. Chuck Sherwin
Phillips Laboratory
Edwards AFB, California

CSI/MMC Studies for Improving Jitter Performance for Large Multi-Payload Platforms

FINAL REPORT

JOHN CHIONCHIO
MICHAEL GARNEK

MIRROR MOTION COMPENSATION

AGENDA

- INTRODUCTION TO MIRROR MOTION COMPENSATION
- EOS PLATFORM MODEL AND DISTURBANCE DEFINITION
- INSTRUMENT JITTER RESPONSE
- MODELING UNCERTAINTIES
  - FREQUENCY
  - DAMPING
  - LAG FILTER
  - MIRROR INERTIA
- MULTIPLE DISTURBANCES
- FEEDBACK
- SUMMARY

ACKNOWLEDGEMENTS

This study was performed under NASA contract number NAS5-32500, task assignment 003, Development of Dynamic Spacecraft Models, under the direction of William Grantham, Deputy Head CSIO, NASA Langley Research Center.

Original members of the GE Astro Space team who made significant contributions to the study are Dennis Hill and David Breskman.

INTRODUCTION

The objective of the study was to demonstrate the feasibility of the Mirror Motion Compensation (MMC) technique for the reduction or suppression of instrument on-orbit jitter. Future remote sensing spacecraft consisting of large platforms with multiple payloads will be required to meet tight jitter constraints, typically less than 0.1 arc seconds. Mirror Motion Compensation provides a method which may prove useful in meeting these future requirements. The MMC technique features a central compensation logic which predicts instrument response to known disturbances and modifies the line of sight of the affected instruments accordingly to compensate for the disturbance.

MIRROR MOTION COMPENSATION

- **OBJECTIVES**

  1. **DEMONSTRATE FEASIBILITY OF MMC TECHNIQUE TO REDUCE ON - ORBIT INSTRUMENT JITTER**

  2. **INVESTIGATE THE USE OF SPACECRAFT FLEXIBLE MODES**

  3. **INVESTIGATE THE SENSITIVITY OF MMC TECHNIQUE TO MODELING ERRORS**

INTRODUCTION

Instrument jitter, or the rotational response of an instrument to a disturbance, must be controlled if maximum instrument performance is to be expected. Control and suppression of jitter effects have become increasingly important for the following reasons:

1. Increased pointing accuracy requirements on instruments.

2. Multiple disturbance sources, in the form of slewing sensors and internal instrument disturbances (cryo-coolers), present on the same platform.

3. Trends toward large, flexible orbiting platforms subject to significant response from both rigid body motion and flexible modes of vibration.

The approach used in the study featured the application of the MMC technique to instruments on-board the EOS A-1 platform. The EOS A-1 spacecraft was an appropriate choice since it represents the class of large flexible space platforms mounting multiple instruments with stringent pointing requirements subject to multiple vibration disturbance sources.

- **WHY USE MMC?**

  SUPPRESSION OF JITTER HAS BECOME INCREASINGLY IMPORTANT FOR THE FOLLOWING REASONS:

  1. **INSTRUMENTS WITH MORE STRINGENT POINTING REQUIREMENTS.**
  2. **TRENDS TOWARD LARGER PLATFORMS WITH MULTIPLE DISTURBANCE SOURCES.**
  3. **TRENDS TOWARD SPACECRAFT WITH LARGE FLEXIBLE APPENDAGES.**

- **APPROACH**

  EOS A-1 DYNAMIC MODEL WITH INTEGRAL ACS CONTROLLER USED AS A GENERIC LARGE SPACE STRUCTURE.

SPACECRAFT FEEDBACK CONTROL VERSUS OPEN LOOP MMC

The MMC technique features a centralized compensation logic which simulates the response of the platform to a disturbance (or multiple disturbances) in real time and modifies the lines of sight of the affected instruments. The disturbance torques, platform dynamics, and sensor dynamics must be known. This knowledge is used by the compensation logic program to predict the response of a given sensor to a disturbance. The compensation logic uses the response predictions to issue sensor motion commands which counteract the disturbance response and suppress instrument jitter. Note that there is no feedback from the controlled instrument to the compensation logic program. This is a salient feature of the MMC system which distinguishes it from more traditional control approaches. The advantage is that if no feedback is employed then the feedback sensors are unnecessary, thus saving cost, weight, and providing a simpler control system.

Clearly, the MMC system is best applied in cases where the disturbances are deterministic and the spacecraft dynamic characteristics are well known and accurately modeled.

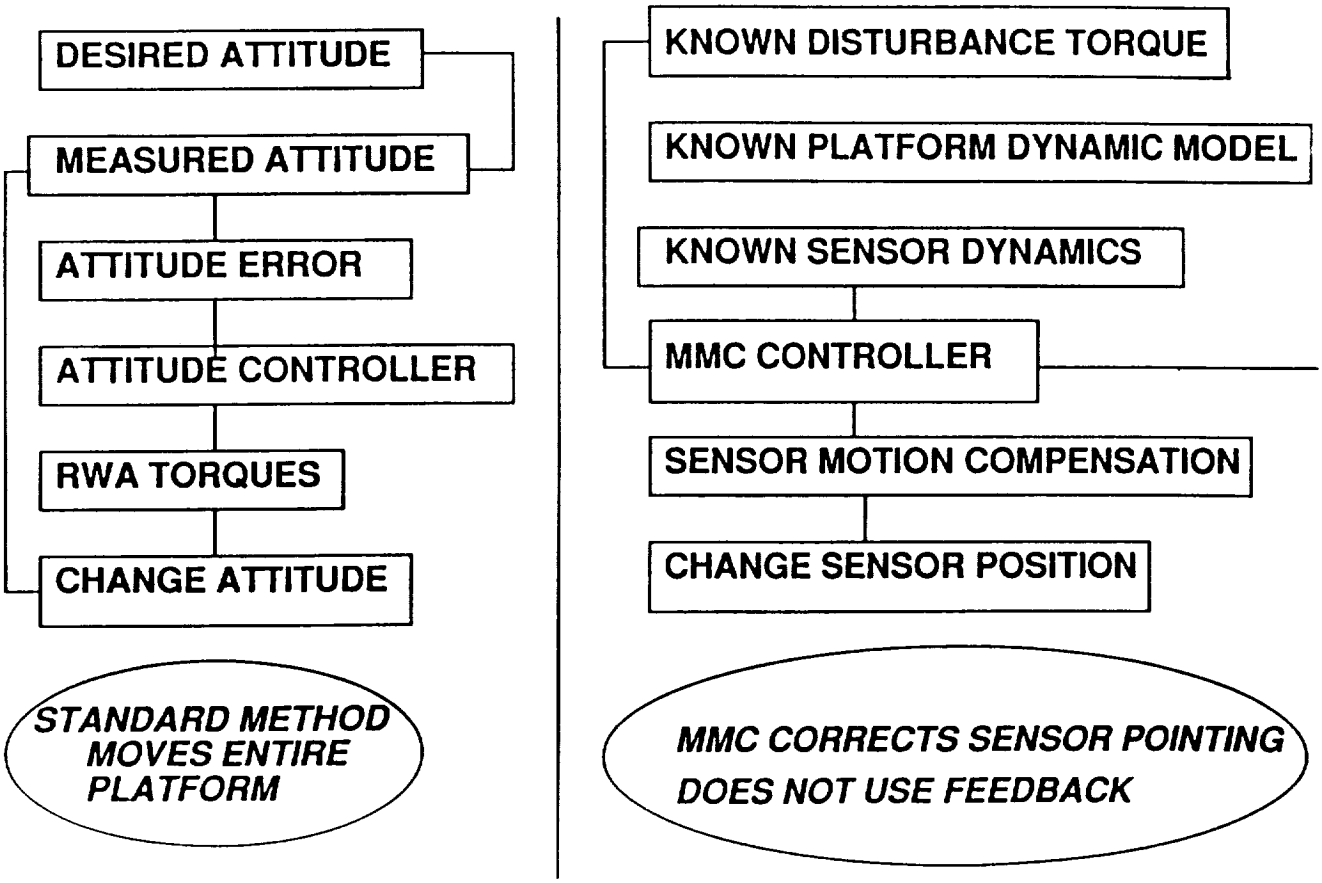

AMSU DISTURBANCE

Of significantly higher frequency, the AMSU disturbance is also a roll axis torque disturbance. The significant action for this disturbance occurs over approximately 8 seconds, as contrasted with the MODIS-T, which requires almost 400 seconds to complete its cycle. The disturbance profile is analytically determined and provided by the instrumenter.

The AMSU instrument module contains three mirrors which rotate continuously in one direction about a line parallel to the spacecraft roll axis. The AMSU A-1 has 2 of the scan mirrors and its scan profile, shown on the facing page, represents the disturbance due to both mirrors combined. All mirrors have a scan cycle (360 degree rotation) period of 8 seconds during which time their angular speed varies. For all mirrors, a scan cycle starts with an Earth scan whereby they are stepped 30 times to cover 99.9 degrees with NADIR in the middle. This is followed by cold and hot calibrations at constant angular speed in between which are accelerations and decelerations. These calibration torques move the mirrors the remaining 260.1 degrees, returning them to their original position. This entire scan pattern is repeated every 8 seconds.

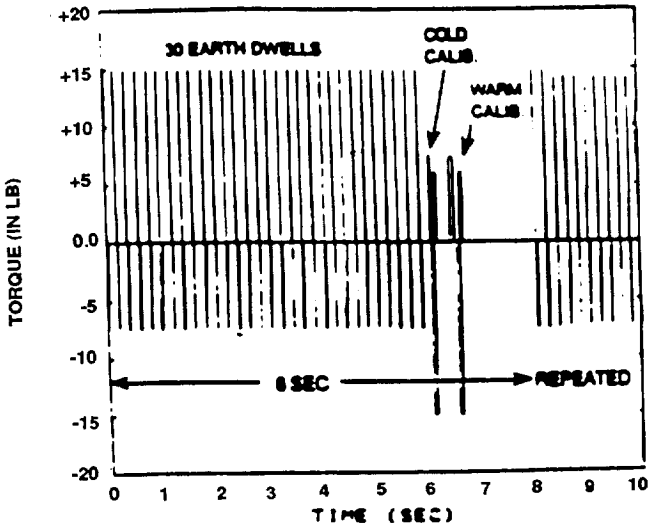

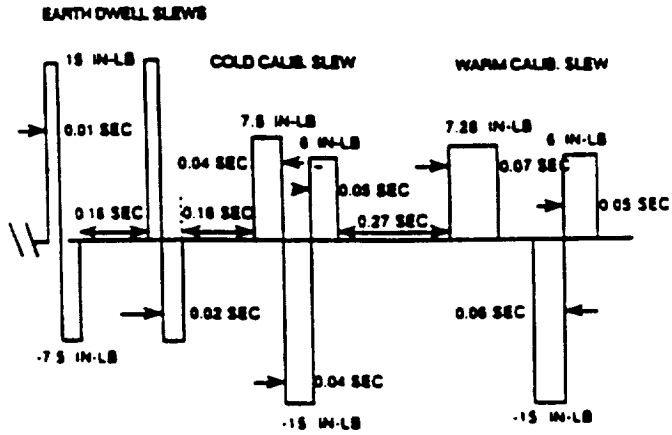

EOS SPACECRAFT

The illustration depicts the EOS A-1 spacecraft and the reference coordinate axes defining the roll, pitch, and yaw degrees of freedom. The EOS A-1 is a large platform, 38 feet long, 10 feet in diameter, and weighing 33,000 lbs. Originally designed for launch on the Titan booster, the design features a truss structure with graphite-epoxy tubes connected via titanium cluster fittings at the truss joints. Precision mounting platforms consisting of plates of lightweight aluminum honeycomb core with graphite-epoxy skins span the truss and provide surfaces for instrument mounting as shown. Of particular interest in this study are the AMSU, MODIS-T, and CERES instruments. The study focuses on the roll and yaw axis jitter of the CERES subject to vibration disturbance from both the AMSU and MODIS-T.

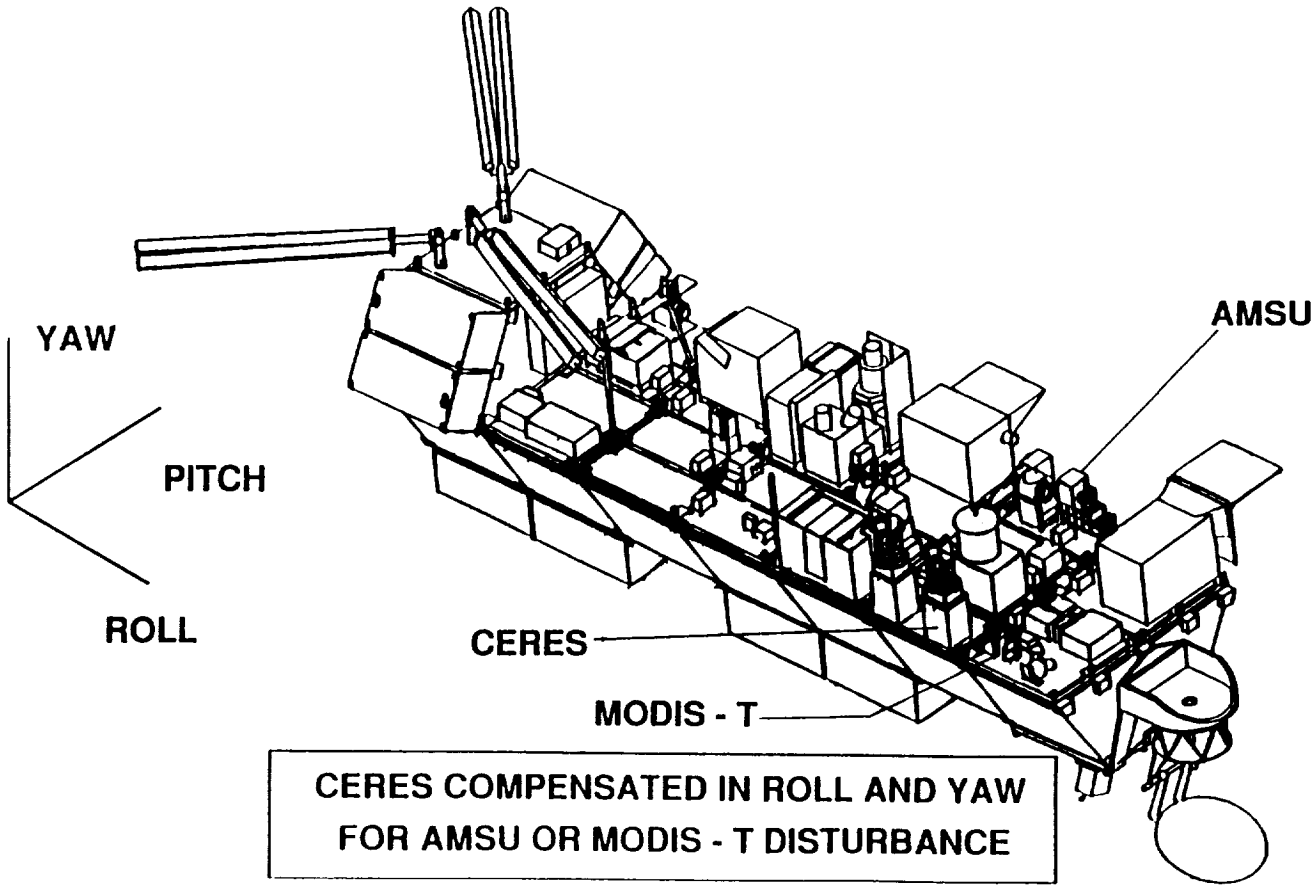

DISTURBANCE AND RESPONSE

Criteria were established for both the subject instrument and the disturbance sources in this study. Disturbance criteria focused on spacecraft components which produce significant vibration which is then transmitted to other instruments through the spacecraft structure. In addition to being major sources of jitter, the disturbance sources should represent a broad spectrum of vibration frequency components. MODIS-T and AMSU were found in combination to fulfill these requirements. Both are scanning instruments which produce significant vibration. The MODIS-T vibration provides the low frequency components and AMSU is responsible for the higher frequencies.

The CERES was chosen as the subject instrument for jitter compensation since it completely satisfied the criteria, which required an instrument which suffered from significant jitter and had a 2 axis gimbal at which the compensation could be applied to suppress the jitter. The CERES degrees of freedom corresponding to the 2 axis gimbal are about the spacecraft roll and yaw axes previously depicted.

DISTURBANCE CRITERIA

- CHOOSE COMPONENTS WHICH ARE MAJOR DISTURBERS
- CAPTURE BOTH HIGH AND LOW FREQUENCY INPUTS

RESPONSE CRITERIA

- CHOOSE INSTRUMENT WITH SIGNIFICANT JITTER
- CHOOSE INSTRUMENT WITH 2 AXIS GIMBAL

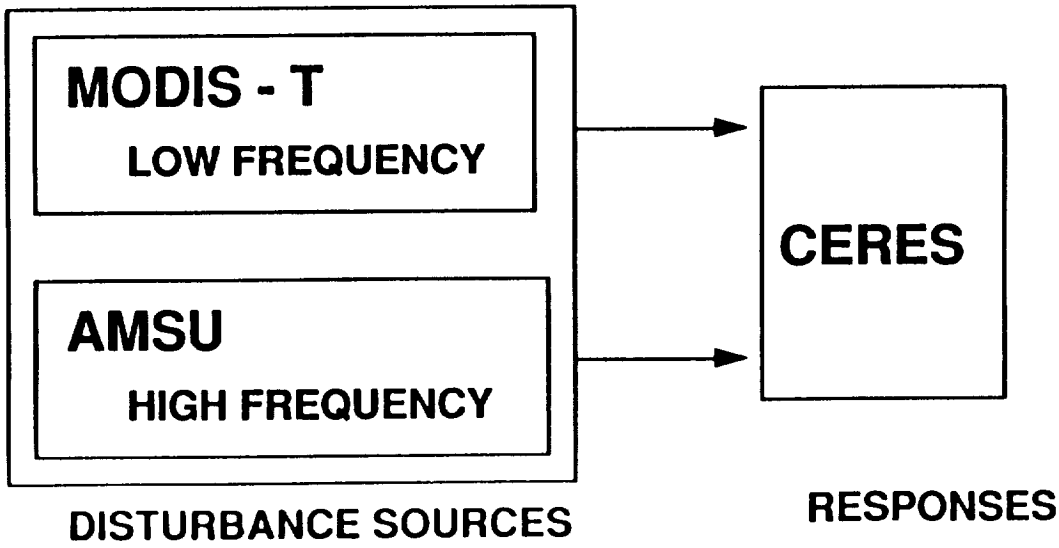

EOS A-1 FINITE ELEMENT MODEL

A large and detailed structural finite element model of the EOS A-1 was available from previous EOS jitter studies. The model contains 11900 nodes and 14400 elements, and simulates the spacecraft in the on orbit configuration with the solar array deployed and oriented as shown. Normal modes analysis yields 655 modes up to a frequency of 150 Hertz.

A dynamic modal model consisting of 172 modal degrees of freedom and 655 mass normalized modes was obtained from the structural finite element model. The 172 modal degrees of freedom constitute the points of interest, such as instrument locations, reaction wheel locations, and spacecraft center of gravity, relevant to the problem. This dynamic model was designated EOS 5.

The modal model describes the dynamic relationships between the disturbance sources and the affected instruments, spacecraft structure, and control sensors and actuators via the chosen degrees of freedom and the associated normal mode shapes. Solar array modes were retained up to 3 Hertz and spacecraft primary structure modes were retained up to 150 Hertz in order to obtain acceptable dynamic fidelity up to 120 Hertz, the highest significant component of the Stirling-cycle cyro-cooler.

The 655 mass normalized modes include 6 rigid body modes of the unconstrained spacecraft structure as well as 11 so called gimbal modes (only 2 were used in this study). The gimbal modes represent the displacement of the instrument scanning element degree of freedom relative to the spacecraft. Since the scanning elements must be free to rotate relative to the spacecraft in order to compensate for the spacecraft rotation, these degrees of freedom yield a zero frequency mode for each free axis of rotation. Certain instruments, such as CERES, have 2 axis gimbals and thus produce 2 gimbal modes. Other instruments rotate about a single axis and contribute only one mode to the gimbal mode set.

- FEM COMPOSED OF 11900 NODES AND 14400 ELEMENTS
- NORMAL MODES ANALYSIS YIELDS 655 MODES UP TO 150 HERTZ

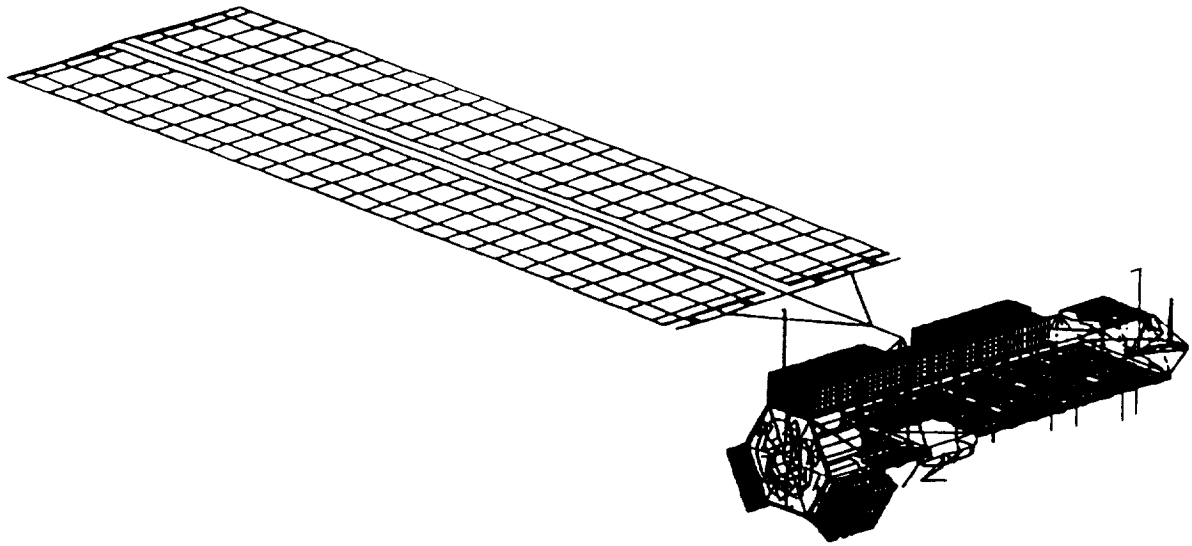

LARGE FEM NEEDED TO OBTAIN HIGH FREQUENCY MODES FOR EOS STIRLING COOLER STUDY

FUNDAMENTAL SOLAR ARRAY MODE

The remaining 638 modes are flexible structural modes divided between the solar array (109 modes) and the primary structure (529 modes). Of these modes a subset was found, by a modal significance survey, to be important for the jitter predictions. The fundamental solar array mode, shown in the illustration, occurred at a frequency of .208 Hertz. As can be clearly seen in the mode shape plot, this mode would naturally contribute significantly to instrument roll axis jitter. This mode was in fact the only significant mode for the lower frequency MODIS-T disturbance, and accurate predictions of jitter were possible using only this mode and the 17 rigid body and gimbal modes in the dynamic simulation. The AMSU disturbance, however, required that 5 flexible modes be retained to ensure dynamic fidelity. The AMSU mode set included the fundamental solar array mode, as well as several higher flexible modes, reflecting the higher frequency content of this disturbance.

The complete dynamic model includes the modal model generated from the FEM and the algorithms to control the attitude of the EOS-A1. The ACS controller features a proportional double integral derivative controller with a 4th order structural filter and results in a closed loop bandwidth of 0.03 Hertz, originally chosen to be about one tenth of the fundamental solar array frequency. The ACS controller is implemented in a state-space formulation, and accepts outputs from gyroscopic sensors and generates torque commands to reaction wheels.

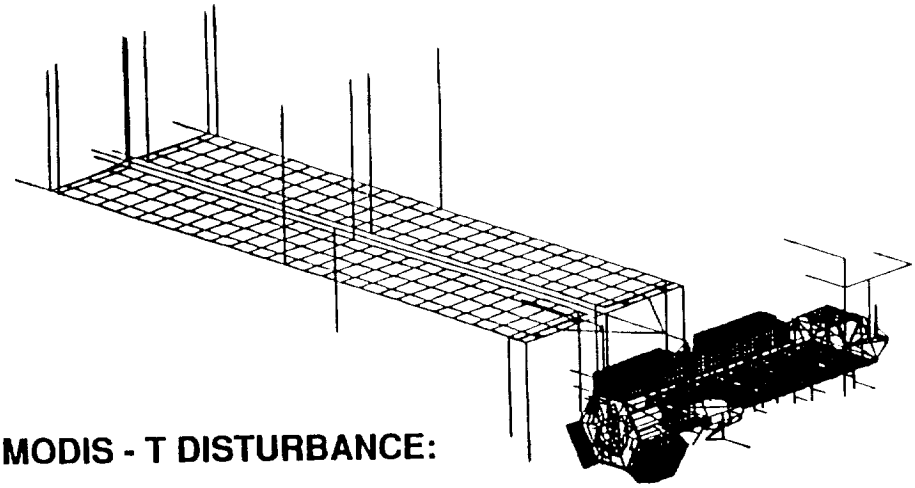

FOR MODIS - T DISTURBANCE:

FUNDAMENTAL SOLAR ARRAY MODE AT 0.208 HERTZ DOMINANT FOR ROLL RESPONSE

FOR AMSU DISTURBANCE:

MODES 22 (0.208 HZ), 42 (1.0 HZ), 150 (31.6 HZ), 153 (33.6 HZ) AND 155 (36.1 HZ) DOMINANT FOR ROLL RESPONSE

As previously stated, the MMC technique is best suited to cases where the disturbances are deterministic. In this case, the MODIS-T disturbance is well known and regular. The result of a scanning mirror slew, the disturbance inputs roll axis torque disturbances as shown. The disturbance profile is analytically determined and provided by the instrumenter.

The diffuser mechanism within the MODIS-T instrument rotates back and forth about a line parallel to the spacecraft roll axis. The instrument takes data for about 40 % of a full orbit and only on the day side of the orbit. There is a calibration deployment over the equator lasting 3 minutes.

The disturbance torque, which is shown on the facing page, moves the MODIS-T diffuser mechanism 180 degrees in 90 seconds to its deployed position and remains in this position for 3 minutes over the equator for solar calibration. The disturbance torque is then applied again with the sign reversed to return the MODIS-T to its original position. This procedure may occur as often as once per orbit, or only once per solar day.

MODIS - T DIFFUSER MECHANISM TORQUE PROFILE

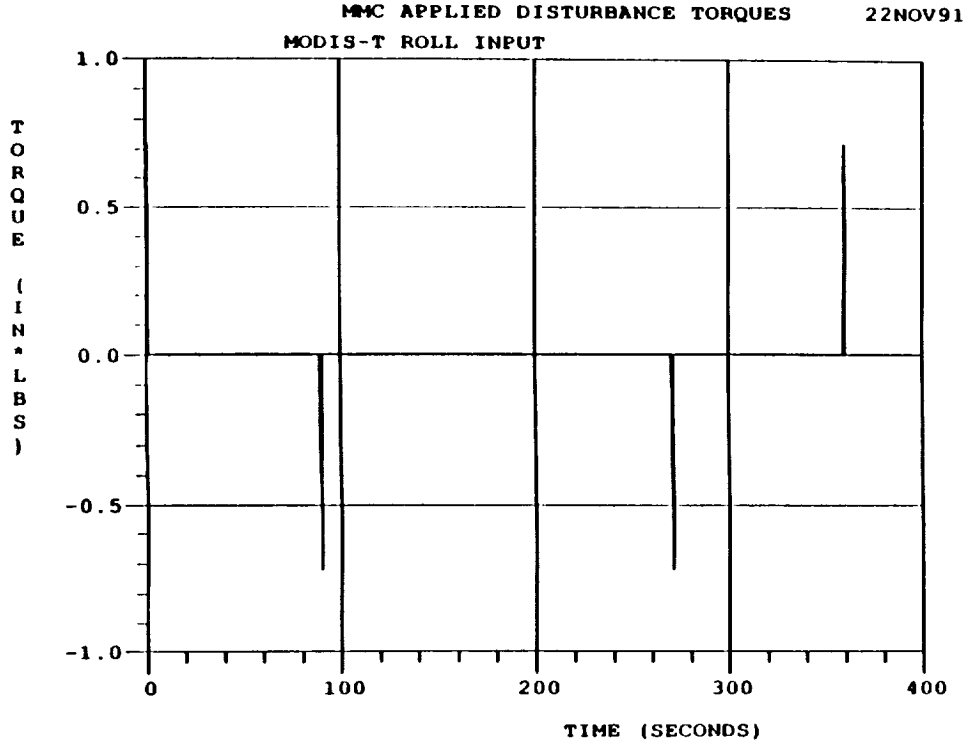

UNCOMPENSATED CERES RESPONSE TO MODIS-T INPUT

The dynamic model specified by the mode shapes and associated frequencies was input to the dynamic software simulator. The simulator is based on standard GE software packages of FORTRAN subroutines for the manipulation of large matrices and the solution of the equations of motion for a many degree of freedom system. The solution technique relies on an exact inverse Laplace transform method and is performed in the modal space on mass normalized modes, thereby taking advantage of the decoupling afforded by this technique. The disturbance is converted into a modal admittance and applied to the equations, the solution of which yields the modal acceleration, velocity, and position as a function of time. The modal coordinates are transformed to the appropriate physical coordinates and plotted as shown on the facing figure.

The time history plot predicts the response of the dynamic model degree of freedom representing the CERES roll displacement subject to the MODIS-T disturbance. This is the baseline response representing the jitter which would occur without any compensation applied. It can be observed that the response consists of a rigid body displacement with flexible modes superposed. In fact, detailed analysis reveals that the fundamental solar array mode is responsible for almost all of the flexible component of the response. The spacecraft navigation and guidance controller effect is evident as the rigid body portion of the response is seen to decay and by approximately 600 seconds only the flexible response remains.

UNCOMPENSATED CERES RESPONSE TO MODIS - T DISTURBANCE

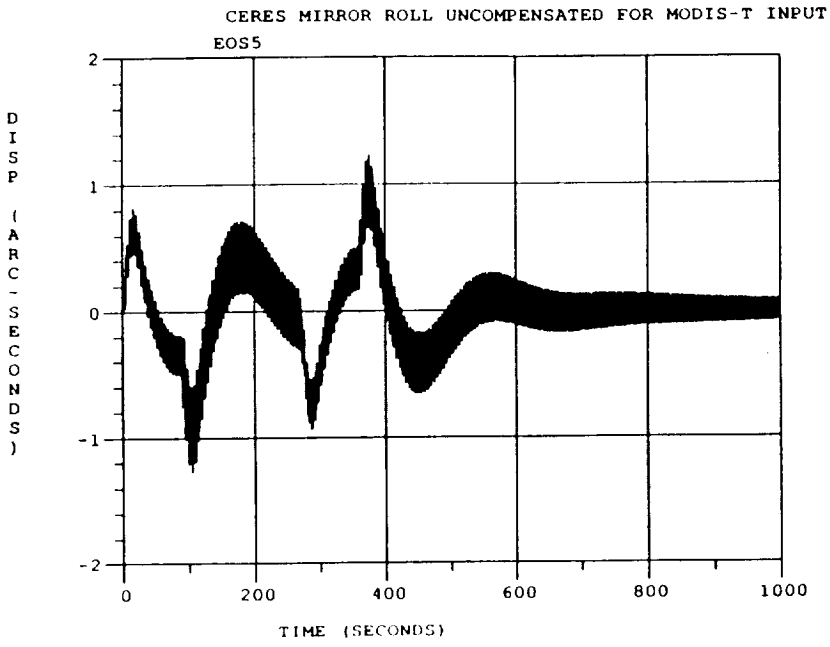

MODIS - T DISTURBANCE EXCITES LOW FREQUENCY SOLAR ARRAY MODE

MODIS-T AND AMSU COMPARED

To further illustrate the contrast between the two disturbances, both profiles were plotted on the same time and magnitude axes. One "spike" of the MODIS-T disturbance is represented by the dotted line, which can be seen overlapping 5 "spikes" of the significantly larger AMSU disturbance. The high frequency nature of the AMSU disturbance is readily apparent.

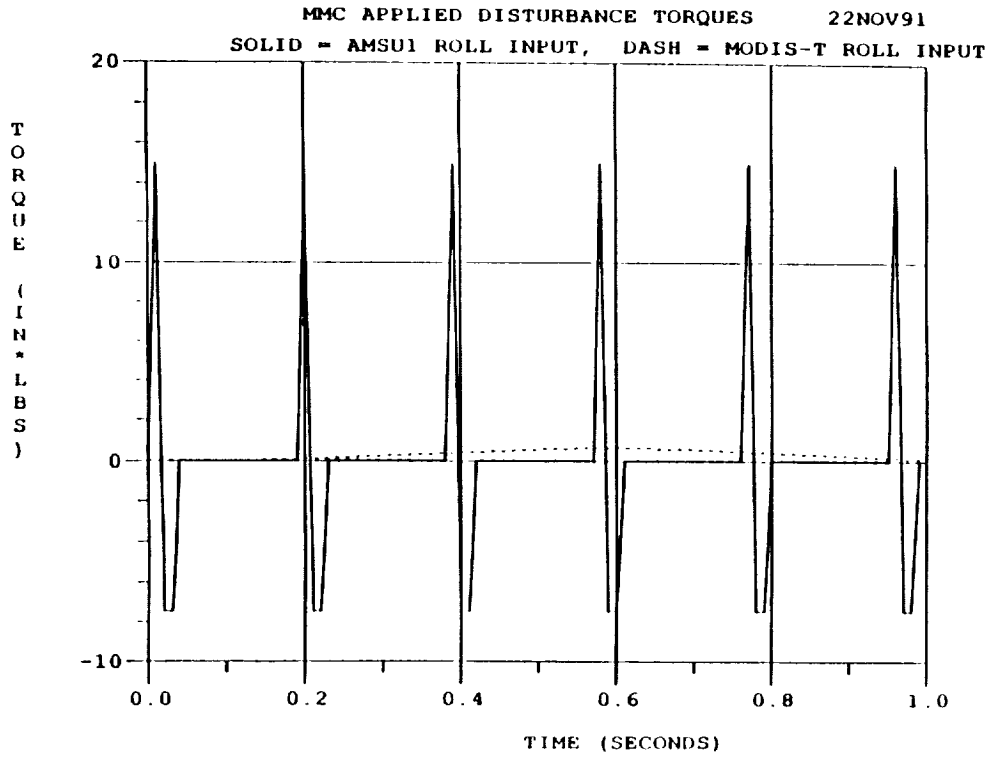

C-3

COMPENSATED CERES RESPONSE TO MODIS-T DISTURBANCE
RIGID BODY MODES ONLY

The application of mirror motion compensation proceeds differently from the simple uncompensated run. First a "predictor" dynamic model is solved for the time history of the degree of freedom in question (in this case, the CERES response to the MODIS-T disturbance). This predictor model is not necessarily the full 655 mode dynamic model of the baseline run, but can be a subset of it. The predictor model simulates the MMC centralized compensation logic. The solution of the predictor model provides the rotational acceleration of the degrees of freedom in question. These accelerations are combined with the known sensor dynamics to calculate a torque function of time. The torque function is stored and the full 655 modes "truth" model is then run through the simulator. The torques from the predictor model are applied to the appropriate sensor gimbal degrees of freedom in the truth model, but in the opposite sense. The gimbal degrees of freedom are free to rotate under the action of the torques in this model (unlike the predictor model where they are locked), thus the ensuing motion of the sensor compensates for the motion of the spacecraft caused by the disturbance. The modal displacements of the truth model are calculated and converted to physical displacements and plotted as shown.

In this case, the predictor model consisted of only the spacecraft and gimbal rigid body modes. The compensating torques derived from the predictor model thus can only, at best, null out the rigid body portion of the disturbance. This is in fact what occurs as demonstrated in the plot of the CERES roll response to MODIS-T disturbance as predicted by the truth model. Note that the rigid body component is effectively eliminated when compared with the baseline response. The flexible component decays slowly, due to the light damping of 0.15% critical. The damping is applied as modal damping, with all modes having the same damping value.

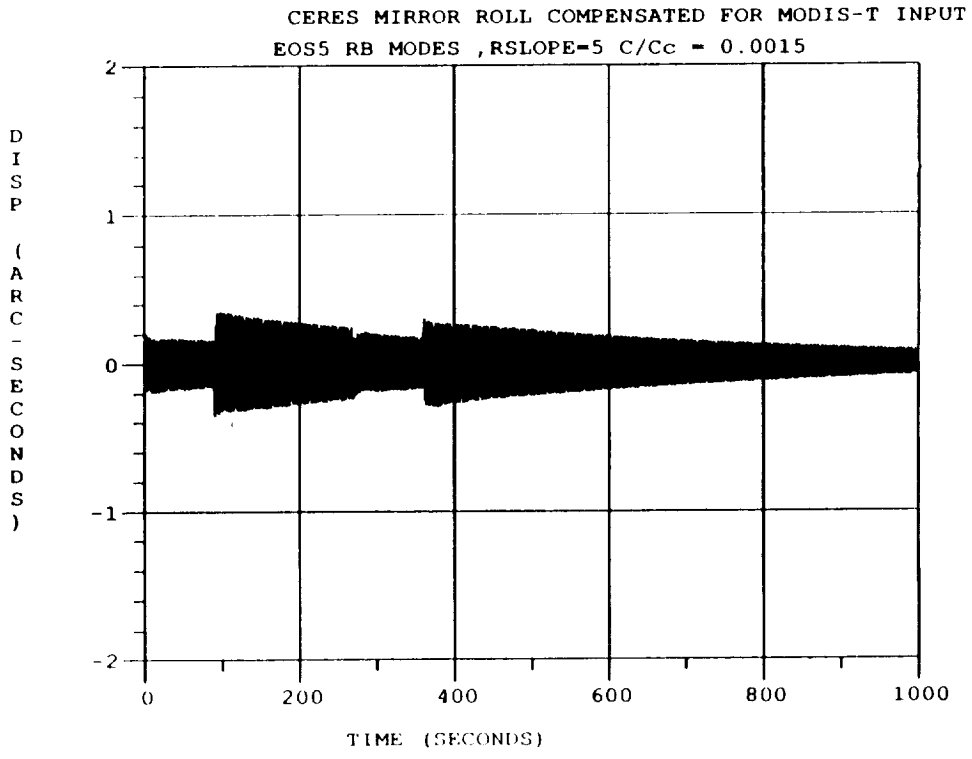

RIGID BODY MODES EFFECTIVELY COMPENSATED

COMPENSATED CERES RESPONSE TO MODIS-T DISTURBANCE
RIGID BODY PLUS FLEXIBLE MODE 22(.208HZ)

The sophistication of the predictor model was increased by adding the fundamental solar array mode. The motion predicted now includes information about the flexible component of the response and the compensating torques are dramatically effective at reducing jitter when applied in the truth model. This dramatic decrease in response is due to perfect knowledge of the platform and sensor dynamics. The reason for the small residual error is due to the effects of gimbal motor rise time and the secondary torque effects on the platform, which are discussed in more detail in the next chart.

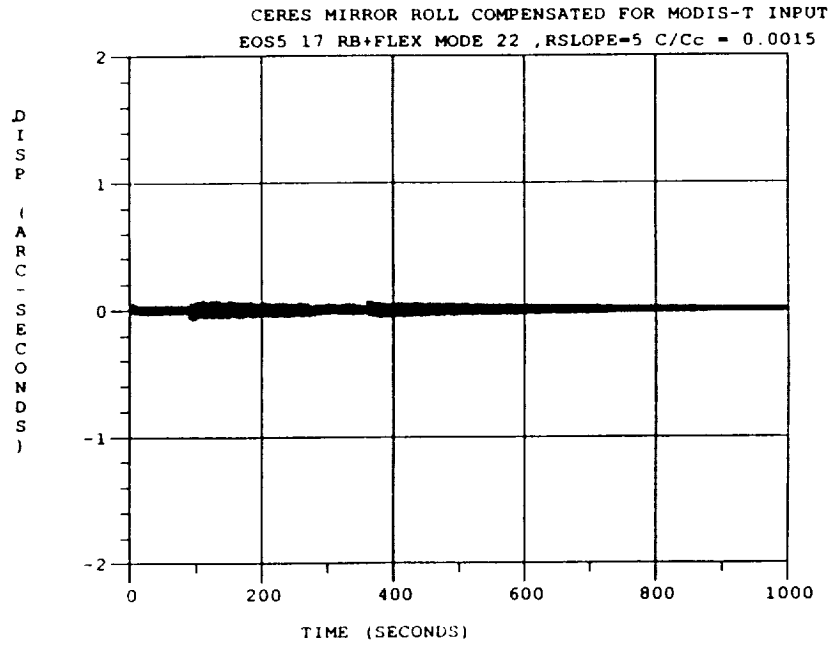

LARGE REDUCTION IN JITTER WITH ONE FLEXIBLE MODE COMPENSATED

COMPENSATED CERES RESPONSE TO MODIS-T DISTURBANCE
RIGID BODY PLUS ALL FLEXIBLE MODES

The predictor model now uses all of the modes and is identical to the truth model. Only slight jitter reduction improvement is obtained. We can conclude that the fundamental solar array mode is the dominant mode with regard to the CERES - MODIS-T disturbance relation. Jitter is still present despite the fact that the predictor and truth models are identical. The jitter results from two sources. The compensation motion of the mirrors affects the spacecraft as another disturbance source of both rigid body and flexible motion. This source is not accounted for in the predictor model. A second source of errors occurs due to the finite rise time of the motors that move the mirrors. Since the torques in reality cannot be applied instantaneously, a lag filter is used in the simulation to model these effects. The torque commands must pass through this lag filter before they are applied to the gimbal degrees of freedom in the truth model. The lag filter has a time constant, represented by the RSLOPE value, and attenuates the torque to simulate actual motor behavior. The time constant is set at 200 milliseconds baseline, corresponding to an RSLOPE value of 5 as noted on the plot. The predictor model does not account for the lag filter.

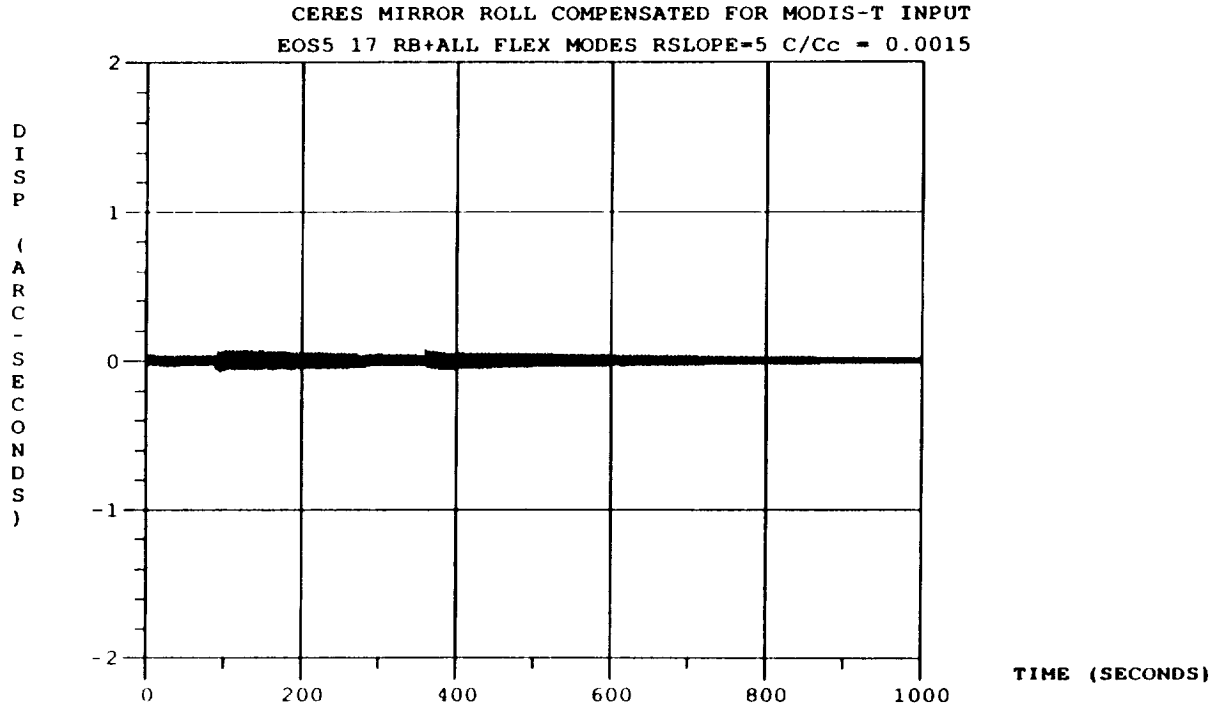

MARGINAL IMPROVEMENT WITH ALL FLEXIBLE MODES

MODE 22 DOMINANT

SUMMARY TABLE OF CERES RESPONSE TO MODIS-T DISTURBANCE

Tabular data is provided to more readily ascertain the effectiveness of the MMC scheme. For a moving sample window 1 second wide the jitter was reduced by a factor greater than 5 for a predictor model with all rigid body and the fundamental solar array modes. Longer duration windows describe the stability of the system, and an improvement can be seen for stability by a factor of 17.

MODEL	JITTER IN ARC SECONDS WINDOW SIZE (SECONDS)			
	1.0	9.0	60.0	1000.0
UNCOMPENSATED	0.4698	1.0047	1.9449	2.4977
RIGID BODY MODES	0.4159	0.6960	0.6984	0.6984
RB + MODE 22	0.0866	0.1438	0.1492	0.1492
RB + ALL MODES	0.0842	0.1421	0.1458	0.1458

MMC TECHNIQUE REDUCES JITTER AND IMPROVES STABILITY

UNCOMPENSATED CERES RESPONSE TO AMSU DISTURBANCE

Baseline plot of the CERES roll response to the AMSU disturbance as predicted by the truth model again shows the effect of superimposed flexible and rigid body modes. The response shows the fundamental solar array mode at 0.208 Hz as well as higher frequency modes. The response is significantly smaller than that due to the MODIS-T disturbance, but higher in frequency.

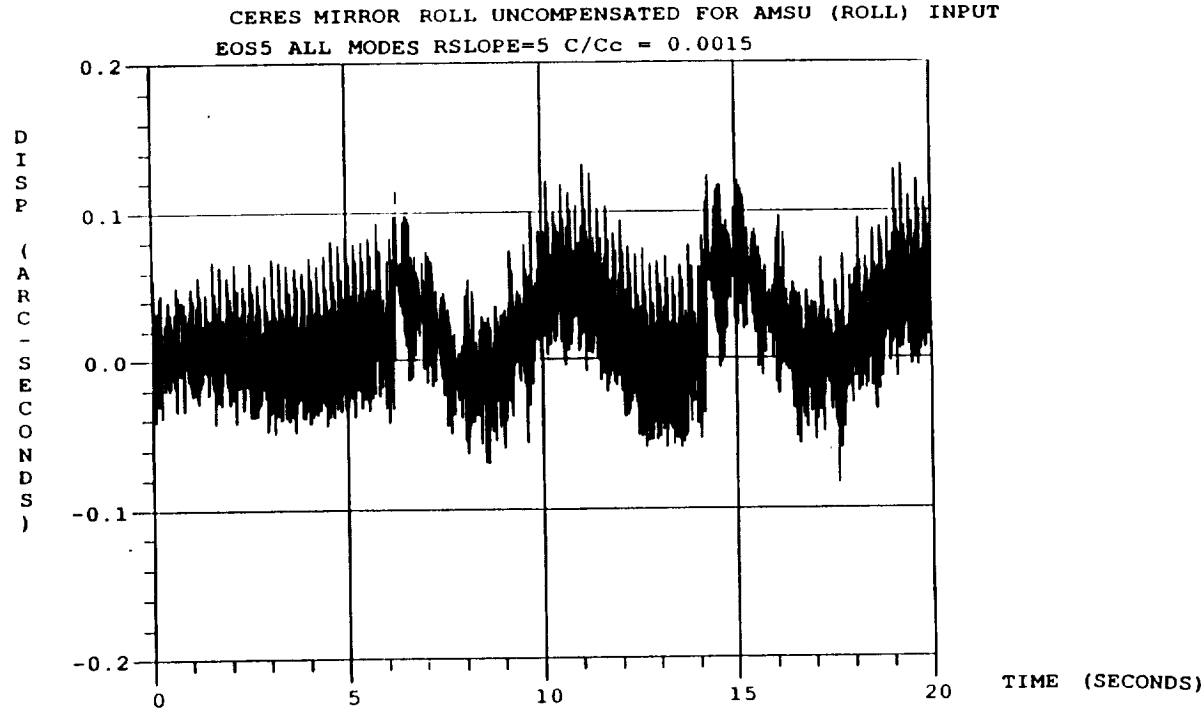

AMSU DISTURBANCE EXCITES HIGH FREQUENCY MODES

COMPENSATED CERES RESPONSE TO AMSU DISTURBANCE
RIGID BODY MODES ONLY

The jitter values are essentially the same as the baseline (uncompensated) case.. Careful observation will discern the fundamental solar array mode at approximately 0.2 Hertz (5 second period) with higher frequency components superimposed. Jitter suppression is not effective for the rigid body predictor model.

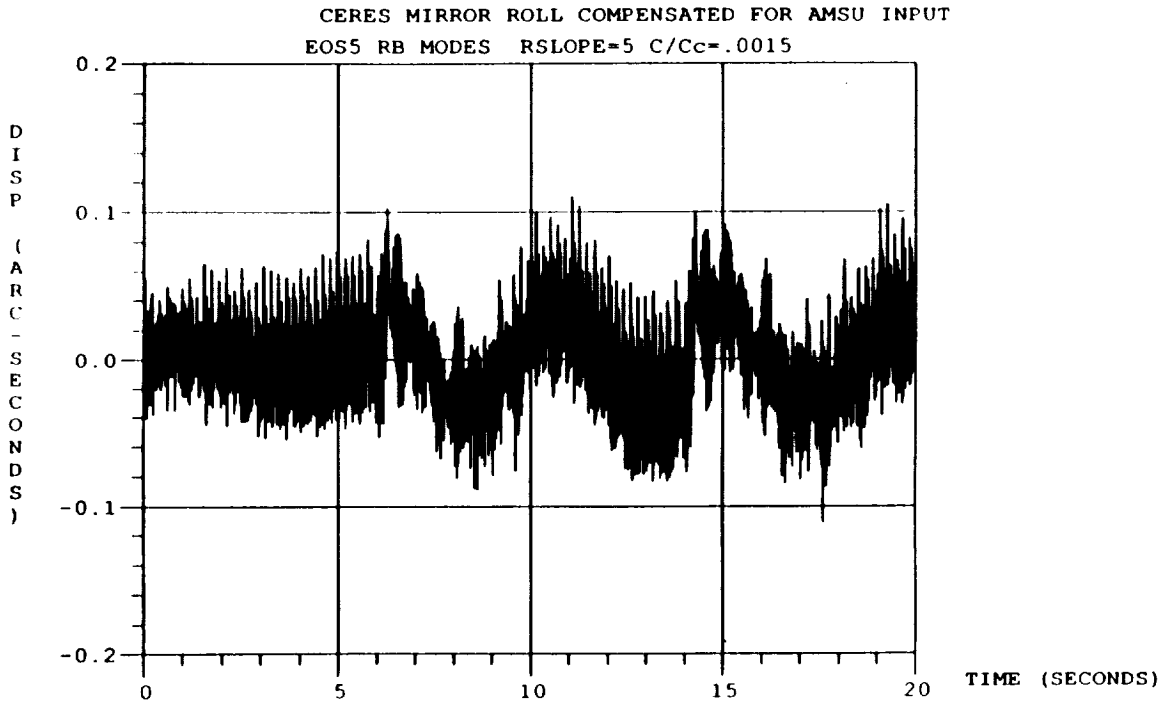

MMC WITH RIGID BODY MODES DOES NOT CONTROL JITTER

HIGH FREQUENCIES CONTRIBUTE TO JITTER

COMPENSATED CERES RESPONSE TO AMSU DISTURBANCE
RIGID BODY PLUS FLEXIBLE MODES 22, 42, 150, 153, 155

Based on a modal significance study modes 22 (at 0.208 Hz), 42 (at 1.009 Hz), 150 (at 31.629 Hz), 153 (at 33.613 Hz), and 155 (at 36.123 Hz) were seen to be significant for the AMSU - CERES interaction. These modes were included in the predictor model and resulted in some jitter reduction. The response plot on the facing page shows that the response attributable to the fundamental solar array mode has been suppressed. It is obvious, however, that the MMC technique is not as effective in reducing jitter from AMSU as compared with the reduction from the MODIS-T disturbance. The AMSU disturbs high frequency modes which are more difficult to compensate.

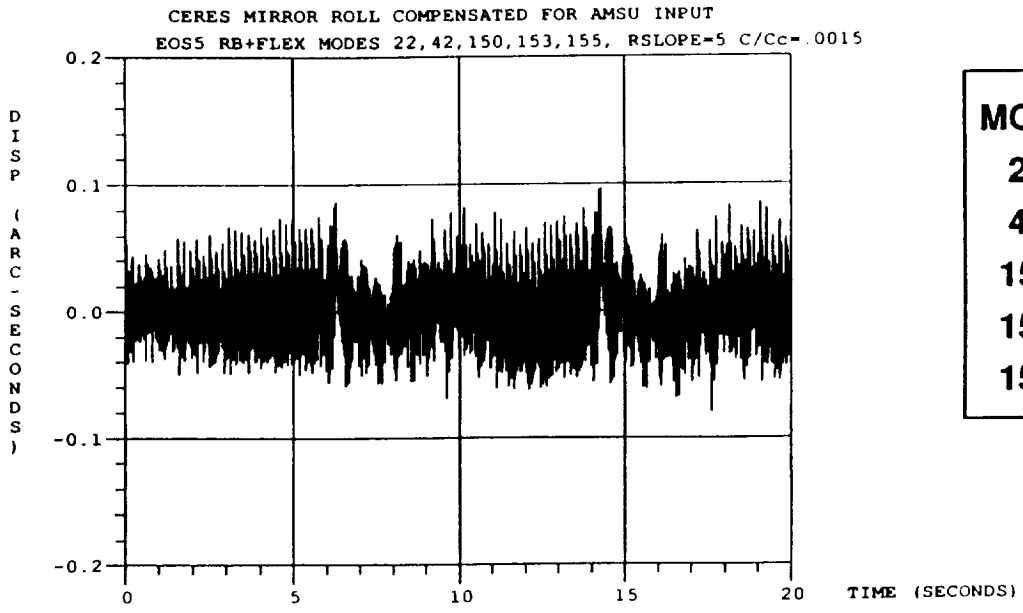

MODE	f (Hz)
22	0.208
42	1.009
150	31.629
153	33.613
155	36.123

PERFORMANCE IMPROVES WITH SUPPRESSION OF HIGHER MODES

SUMMARY TABLE OF CERES RESPONSE TO AMSU INPUT

The summary table demonstrates the less effective performance of MMC for the high frequency AMSU disturbance. Only marginal jitter reduction was achieved (a factor of 1.2) for the most sophisticated predictor model (all modes). The main reason for the poorer MMC performance can be traced to the high frequency nature of the AMSU disturbance. Further, the lag filter becomes more of a factor as the required response frequencies increase.

MODEL	JITTER IN ARC SECONDS WINDOW SIZE (SECONDS)			
	1.0	9.0	60.0	1000.0
UNCOMPENSATED	0.1928	0.2354	0.2512	0.2512
RIGID BODY MODES	0.1935	0.2311	0.2311	0.2311
RB + MODES 22 ,42,150, 153,155	0.1633	0.1766	0.1815	0.1815
RB + ALL MODES	0.1600	0.1767	0.1811	0.1811

MMC TECHNIQUE LESS EFFECTIVE FOR HIGH FREQUENCY EXCITATION

LAG FILTER SIMULATING MOTOR LAG LIMITS EFFECTIVENESS

LAG FILTER

The lag filter is present in the truth model to provide a variable and controllable source of error in the simulation. It simulates the physical behavior of an electric motor which, when given a torque command, takes some finite time to achieve the full torque value. For any time step, the relationship between the required torque and the available torque is given by Ta=Tr*(1-e**(-at)) where Ta is the torque available, Tr is the torque required (for perfect nulling), a is the time constant, and t is the time variable. The plot shows the effect of the lag filter on a step pulse. The parameter RSLOPE was varied from 1 to 5 to 10 to demonstrate the effect of this parameter on the applied torque. The RSLOPE parameter controls the rise time of the torque pulse. As the value of RSLOPE decreases the rise time increases.

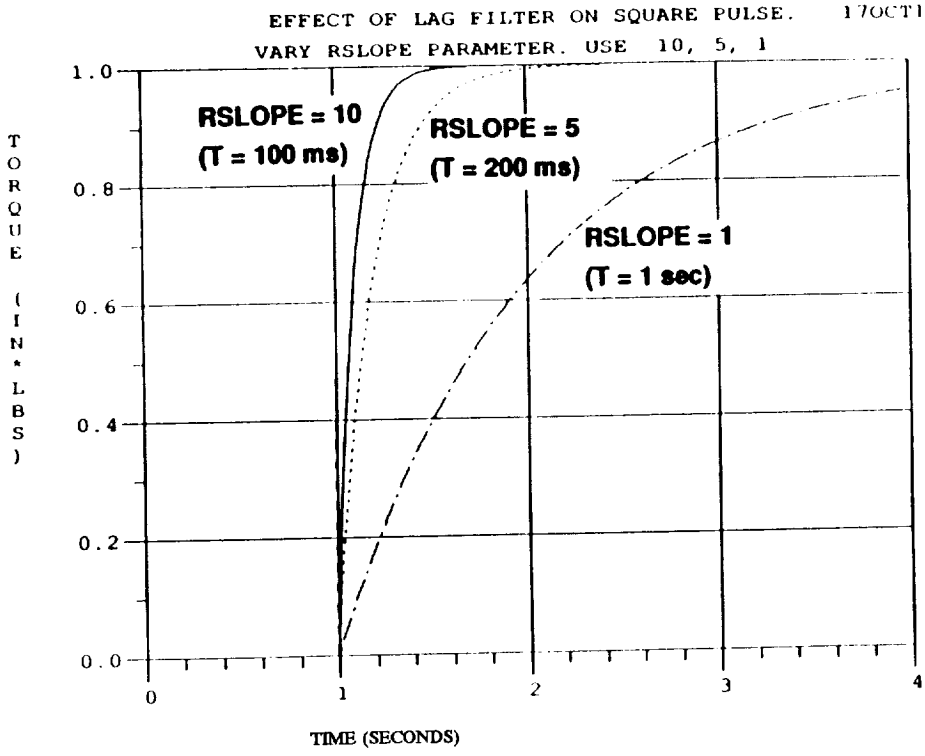

T = RISE TIME

LAG FILTER
EFFECT OF LAG FILTER VARIATION ON JITTER

If the lag filter is effectively eliminated by specifying a very short time constant the jitter suppression for the AMSU disturbance will improve from a factor of 1.2 to almost 2. This is still not as good as that obtained for the MODIS-T. A full modes predictor model was run with the AMSU disturbance with the effect of the lag filter eliminated. Jitter values less than 0.1 arc seconds were obtained. Note that other sources of jitter are still present, such as compensating torque reactions.

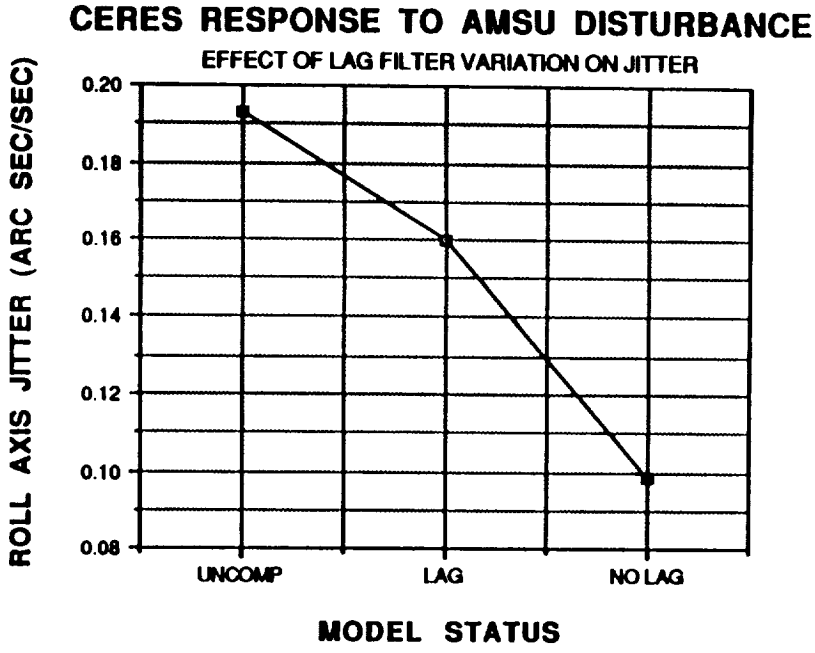

LAG PHENOMENON ADVERSELY AFFECTS JITTER COMPENSATION

MODELING UNCERTAINTIES

Although impressive jitter suppression results are predicted for the MMC technique, the question of the system's robustness remains to be explored. The results thus far have assumed a priori perfect knowledge of the important system parameters - structure natural frequencies and mode shapes, disturbance torque profiles, structural damping, sensor dynamics, and the phase relationship between the disturbance and the compensation motion. In an attempt to ascertain the effect of uncertainty of these parameters on MMC system performance a series of parametric studies was conducted.

- COMPENSATION IS EFFECTIVE WITH "PERFECT" KNOWLEDGE
- EVALUATION OF EFFECTIVENESS OF MMC SYSTEM WITH UNCERTAINTIES:
  - STRUCTURAL DYNAMIC PROPERTIES
    - FREQUENCY
    - DAMPING
  - ACTUATOR RESPONSE UNCERTAINTIES
    - LAG

FREQUENCY SENSITIVITY
COMPENSATED CERES RESPONSE TO MODIS-T INPUT

There is an inherent limit in the accuracy to which structural normal modes can be predicted. The uncertainties in natural frequency between the predicted and actual values will affect MMC system performance. The nature of this MMC simulation allows us to explore the effect resonant frequency uncertainty will have by using a different natural frequency in the predictor model from that used in the truth model.

The plot shows the effect on the CERES response to MODIS-T disturbance of varying the predicted natural frequency of the fundamental solar array mode from its nominal value (used in the truth model) of 0.208 Hertz. The plot shows that for a +/-10 % variation (0.187 Hertz to 0.229 Hertz) the compensated jitter performance is substantially worse than if no compensation system were present. This is due to the phasing of the input and the response, which, for slight differences in frequency between the truth and predictor model, will result in the well known beating phenomenon as the input and response move in an out of phase, alternately adding constructively and destructively. In fact, the plot indicates that the MMC performance is extremely sensitive to variations in frequency between the predictor model and the truth model. Even a +/- 1 % variation is inadequate. This betrays a serious weakness in the system, since structural modes are predicted, at best, to within 5 %. Thus we conclude that, for cases where the flexible response is large, the feasibility of the MMC system depends heavily upon our knowledge of the structural natural frequencies which must be known exactly if any benefit is to be realized from this technique.

The effect of frequency uncertainty on stability is also demonstrated in this plot. The curve for stability displays the same behavior as the jitter curve, but is always below the uncompensated value; thus stability is always improved by the action of the MMC system regardless of reasonable frequency error.

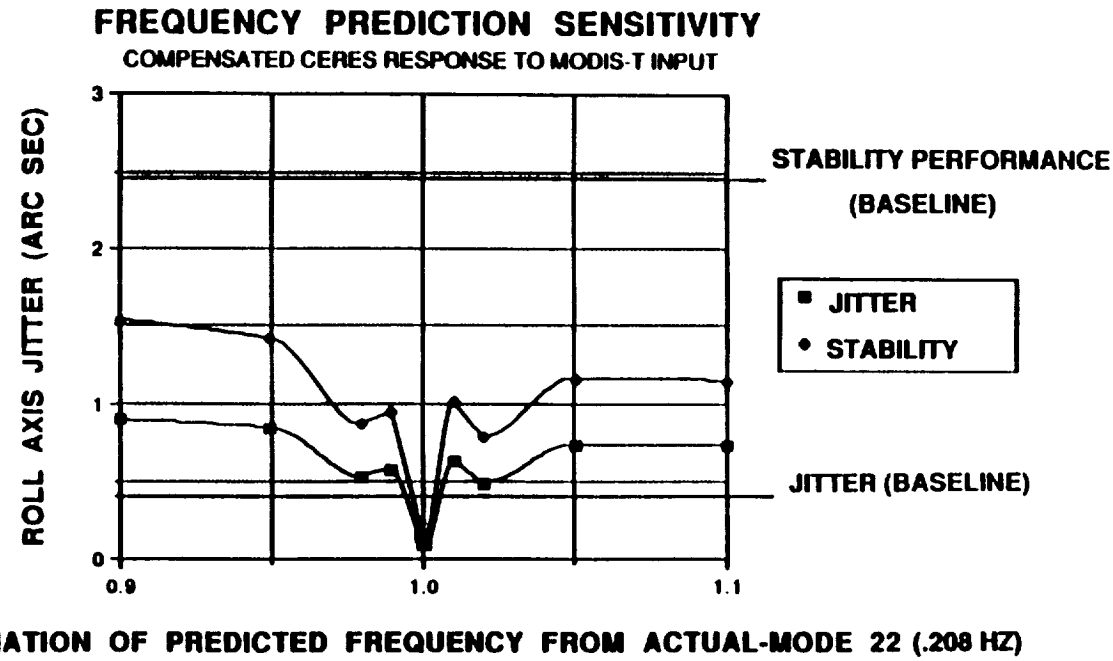

- EFFECTIVENESS OF JITTER COMPENSATION SENSITIVE TO FREQUENCY KNOWLEDGE
- STABILITY PERFORMANCE IMPROVEMENT ACHIEVABLE WITH FREQUENCY ERRORS

FREQUENCY SENSITIVITY
COMPENSATED CERES RESPONSE TO AMSU INPUT

The plot further explores the sensitivity of the MMC technique to the structural natural frequency parameter. A +/- 10 % variation of predicted natural frequency is again evaluated, this time on those modes significant to the CERES response to the AMSU input (modes 22 (at 0.208 Hz), 42 (at 1.009 Hz), 150 (at 31.629 Hz), 153 (at 33.613 Hz), and 155 (at 36.123 Hz)). The variation was imposed on all five significant modes simultaneously.

We note immediately that the curve is broader in the region of interest about the nominal frequencies, thus indicating less sensitivity to frequency uncertainty. The high frequency nature of the AMSU disturbance is largely responsible for this behavior. At the higher frequencies the damping present has more effect and damps out the higher modes proportionally more rapidly since it operates on more cycles over a shorter period of time. The broadening of the sensitivity curve is analogous to the broadening of a response curve with increasing damping of a single degree of freedom harmonic oscillator around resonance.

Stability again is generally improved for all reasonable values of frequency, but is marginal at differences greater than 5%.

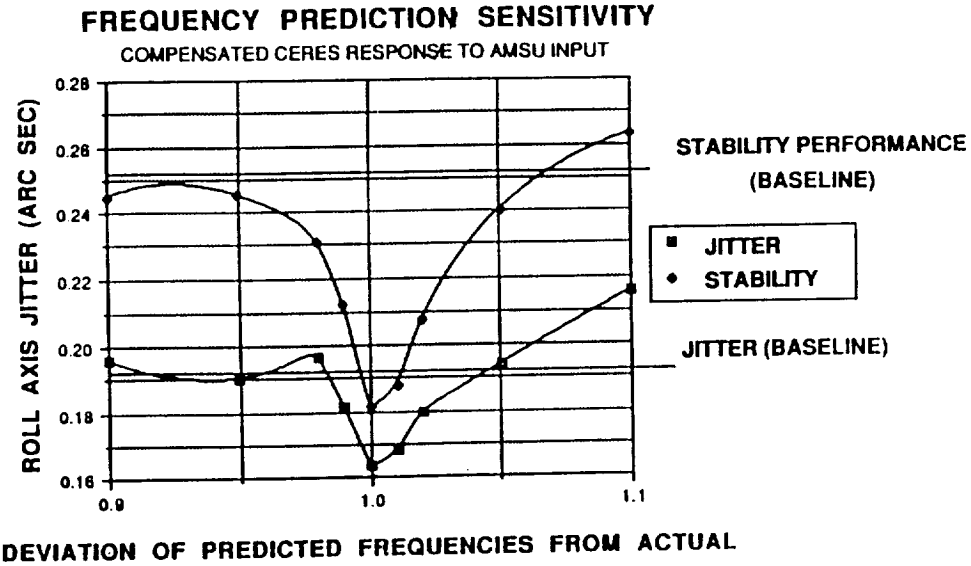

- JITTER REDUCTION NOT AS EFFECTIVE FOR AMSU
- JITTER COMPENSATION NOT AS SENSITIVE TO FREQUENCY ERROR

DAMPING PARAMETRIC STUDY

The damping is another parameter which affects MMC performance and is difficult to predict. Thus it was necessary to characterize the behavior of the system with variations in damping, first in its effect on the frequency study previously described.

The damping in both the predictor model and truth model, applied as modal damping, identical for all modes, was varied from the baseline value of 0.0015 C/Cc through 0.005, 0.015, and 0.03 C/Cc. Simultaneously, the frequency of the fundamental solar array mode was varied in the predictor model while held constant in the truth model as in the previous analysis. The family of curves which resulted is shown for the CERES response to the MODIS-T disturbance.

We immediately recognize the baseline run, representing light damping at 0.0015 C/Cc, with its characteristic narrow band and poor jitter compensation with any frequency error. As the system damping increases we note the broadening of the curves as expected, indicating less sensitivity to frequency error with increasing damping. In addition, the overall jitter level decreases dramatically with increasing damping, until, at the heavily damped level of 0.03 C/Cc, the jitter performance is superior to the uncompensated baseline response over the entire +/- 10 % range variation. This is also true for the damping value of 0.015 C/Cc.

Thus we see dramatically the advantage obtained by increased damping, indicating that it would be worthwhile to include passive damping in the system to enhance system performance and further suppress jitter effects.

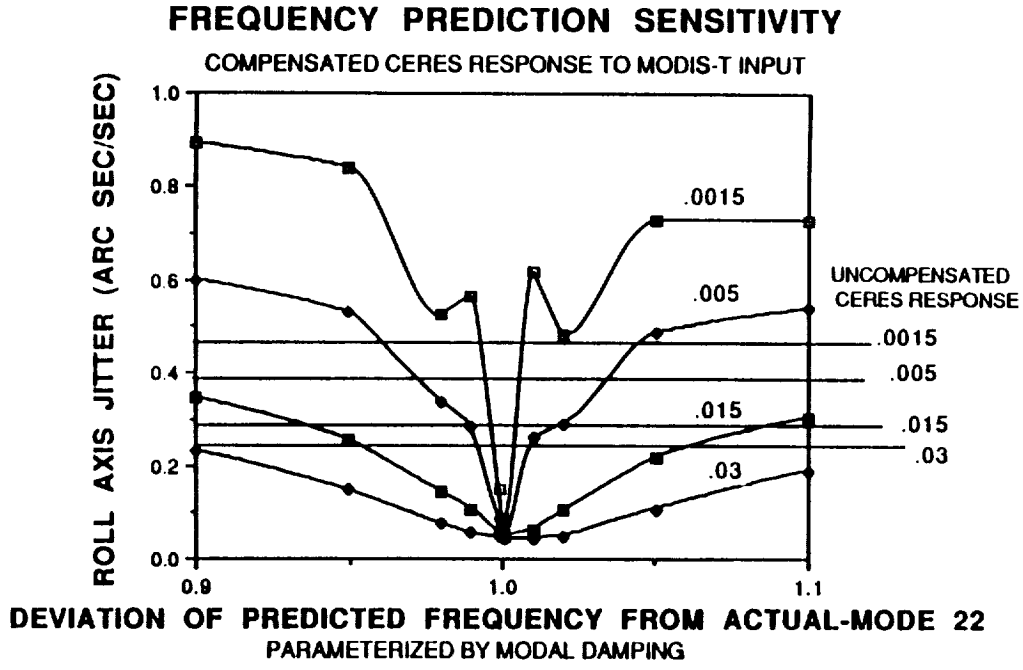

- DAMPING REDUCES ERROR SENSITIVITY
- DAMPING EFFECTIVELY SUPPRESSES JITTER

DAMPING SENSITIVITY

Further damping studies explored the effect of predicted damping differing from actual damping. The effect was evaluated by varying the damping in the predictor model from the value used in the truth model. This was performed for three different damping baseline values producing the family of curves shown in the plot below.

Each curve represents a different baseline modal damping value used in the truth model, as indicated by the curve label of 0.0015, 0.005, 0.015 C/Cc. The curves were generated by varying the predictor model damping among the values 0.0015, 0.005, 0.015, and 0.03 C/Cc and plotting the maximum jitter.

Trends revealed by the exercise show the expected jitter decrease with increasing damping, consistent with previous work. Note that as we under-predict or over-predict the damping the jitter control performance degrades although not as severely as with frequency variation. The predicted jitter is below the uncompensated baseline values for all reasonable damping variations, indicating the less critical nature of the damping parameter with regard to jitter performance.

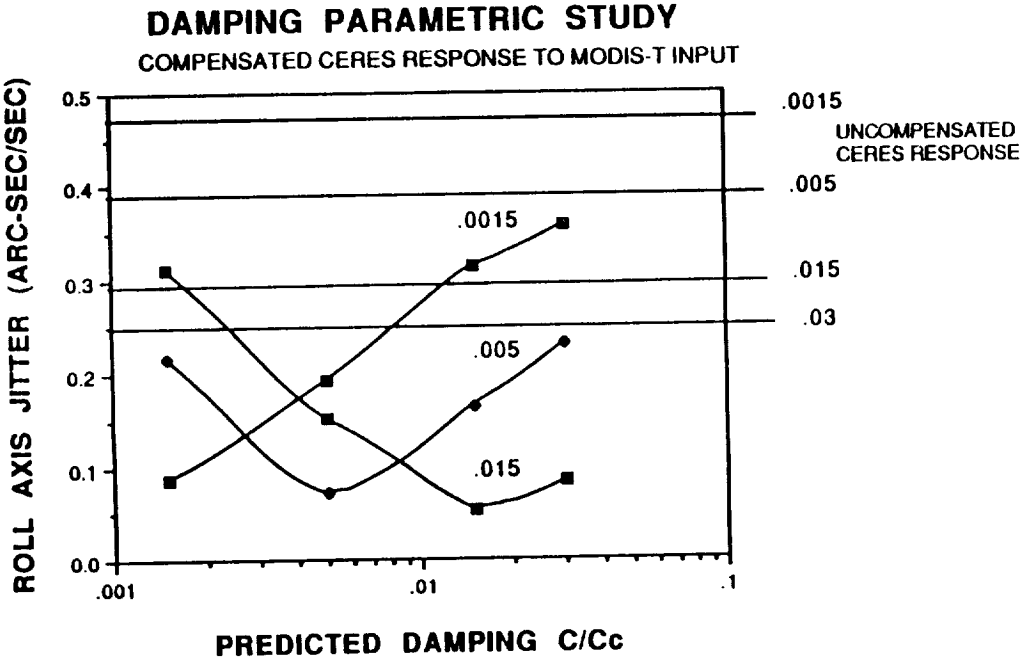

MMC EFFECTIVENESS NOT AS SENSITIVE TO DAMPING PREDICTION ERRORS

JITTER SENSITIVITY TO LAG FILTER

As described previously, a lag filter was incorporated in the truth model to provide a source of variable, controllable error. The lag filter simulates the actual response of a motor actuator by attenuating the torque required to provide perfect compensation of the subject mirror sensor.

In this sensitivity study the lag filter time constant was varied from 2 seconds through 67 milliseconds, simulating a decreasing motor response time. The resulting curve depicts the effect of lag filter variation on roll axis jitter of the CERES response to the AMSU disturbance. Note that the jitter approaches a limiting value as the response time of the motor decreases, indicating other sources of error as described before. Note that the predictor model is the AMSU significant mode subset of modes 22, 42, 150, 153, and 155. This is no doubt a partial cause for the limited jitter reduction seen in the plot.

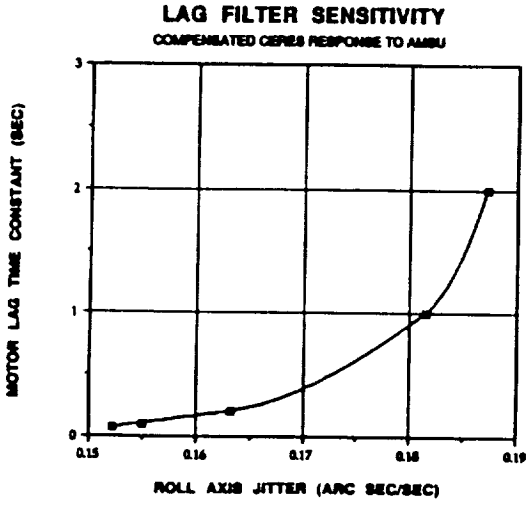

INCREASING LAG CONSTANT CORRESPONDS TO DECREASING RESPONSE TIME

JITTER APPROACHES LIMITING VALUE AS LAG CONSTANT INCREASES

MIRROR INERTIA STUDY

Of interest to the study was the effect of larger mirrors on MMC system performance. The effect of larger mirrors was explored by examining the CERES response to both MODIS-T and AMSU inputs for increasing CERES mirror roll axis mass moment of inertia.

The baseline inertia was varied by factors of 2x, 5x, 10x, 20x, and 50x in a series of runs where maximum jitter was calculated for each disturbance source. As the mirror inertia is increased, the larger secondary torques required for the MMC correction eventually override the baseline disturbances. For MODIS-T this is seen to happen when the mirror inertia is increased by a factor greater than 2. This is demonstrated in the plot below.

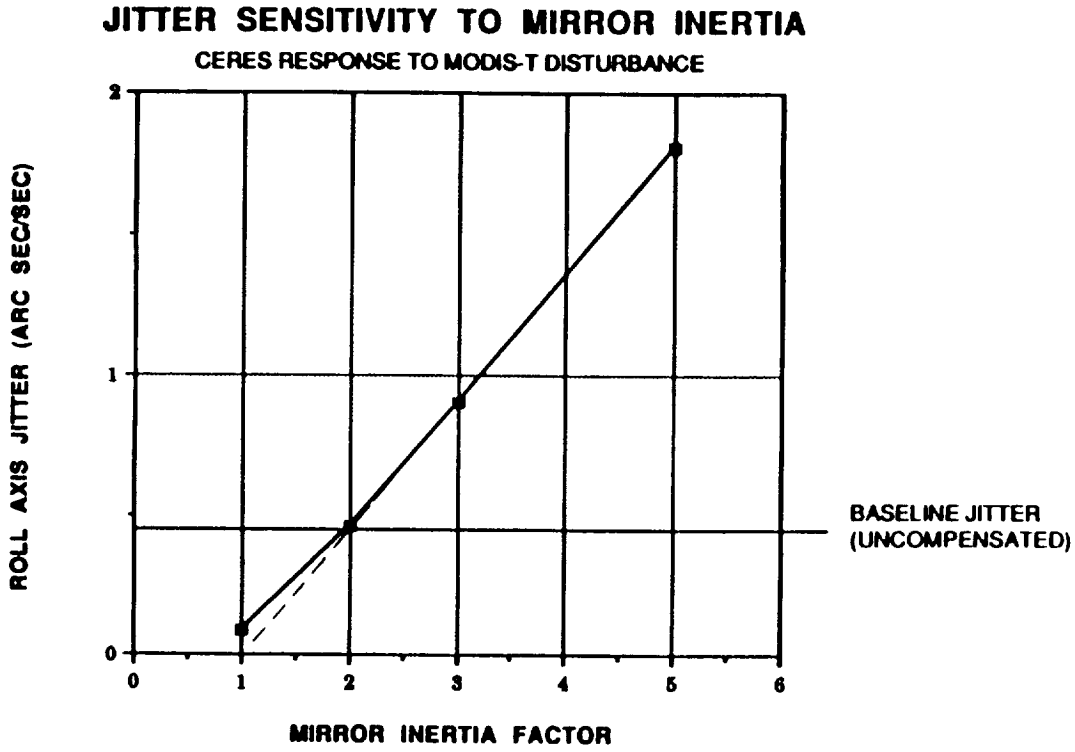

JITTER INCREASES WITH MIRROR INERTIA

MIRROR INERTIA STUDY
SUMMARY TABLE OF CERES RESPONSE TO AMSU INPUT

The summary table displays the information obtained in the mirror inertia study for jitter and stability behavior of the CERES for the AMSU disturbance.

MODEL	JITTER IN ARC SECONDS WINDOW SIZE (SECONDS)			
	1.0	9.0	60.0	1000.0
BASELINE AMSU	.1633	.1766	.1815	.1815
2 X INERTIA	.1973	.2202	.2355	.2371
5 X INERTIA	.3627	.4348	.5585	.5698
10 X INERTIA	.6595	.8127	1.115	1.136
20 X INERTIA	1.241	1.585	2.231	2.269
50 X INERTIA	3.061	3.937	5.616	5.735

MIRROR INERTIA STUDY
SUMMARY TABLE OF CERES RESPONSE TO MODIS-T INPUT

The summary table of complete CERES response to the MODIS-T disturbance for the mirror inertia study, including both jitter and stability data in tabular format.

MODEL	JITTER IN ARC SECONDS WINDOW SIZE (SECONDS)			
	1.0	9.0	60.0	1000.0
BASELINE MODIS-T	.0866	.1438	.1492	.1492
2 X INERTIA	.4613	.9755	1.911	2.467
5 X INERTIA	1.809	3.903	7.658	9.865
10 X INERTIA	4.066	8.796	17.25	22.21
20 X INERTIA	8.594	18.59	36.44	46.89
50 X INERTIA	22.17	47.97	94.00	>100

MULTIPLE DISTURBANCES
UNCOMPENSATED CERES RESPONSE TO AMSU AND MODIS-T DISTURBANCE

Time history plot showing the CERES response to AMSU and MODIS-T disturbances occurring simultaneously. The combined response is the superposition of the individual responses, as can be readily observed in the plots below.

UNCOMPENSATED RESPONSE TO AMSU AND MODIS-T DISTURBANCE

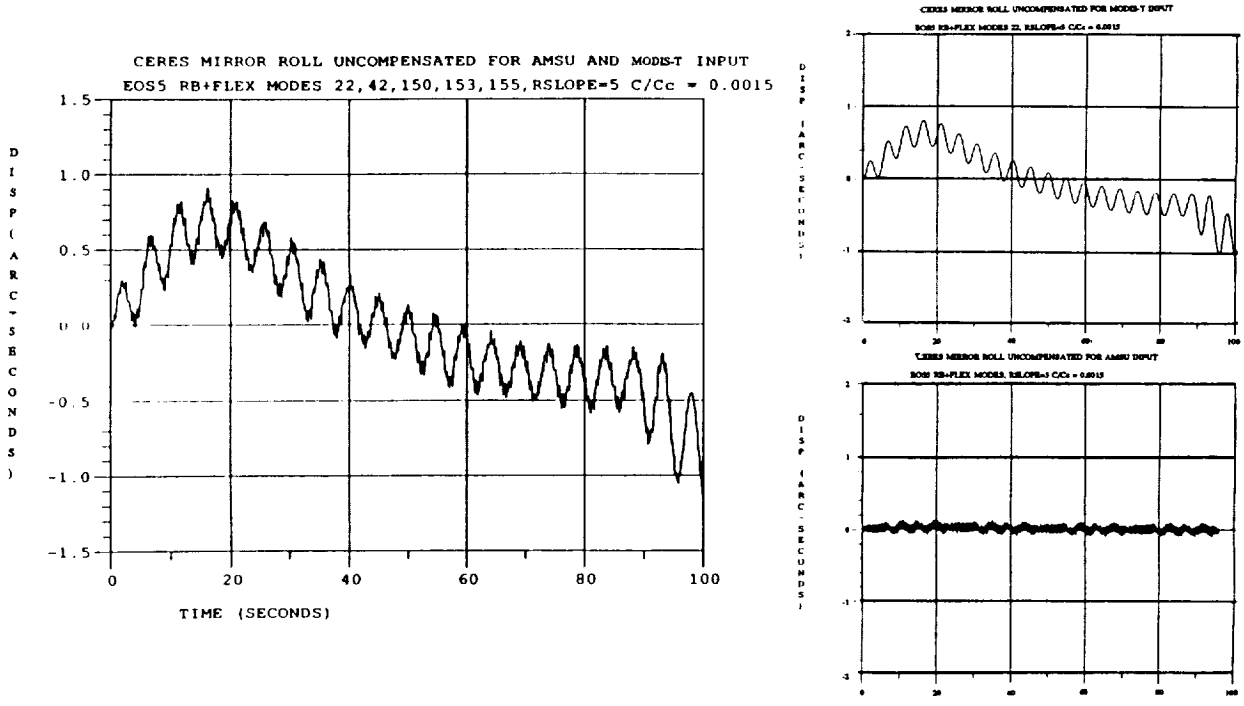

COMBINED RESPONSE IS SUPERPOSITION OF INDIVIDUAL RESPONSES

MULTIPLE DISTURBANCES
COMPENSATED CERES RESPONSE TO AMSU AND MODIS-T DISTURBANCE

As seen in the plots below, the MMC logic works effectively for the case when both disturbance sources are applied at the same time. The residual jitter value for combined torques with compensation is somewhat lower than the two individual compensated responses.

COMPENSATED RESPONSE TO AMSU AND MODIS-T DISTURBANCE

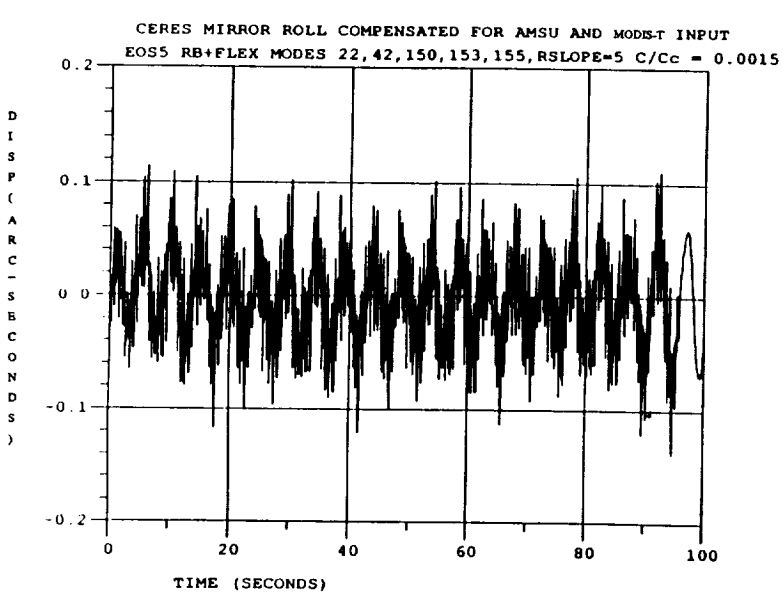

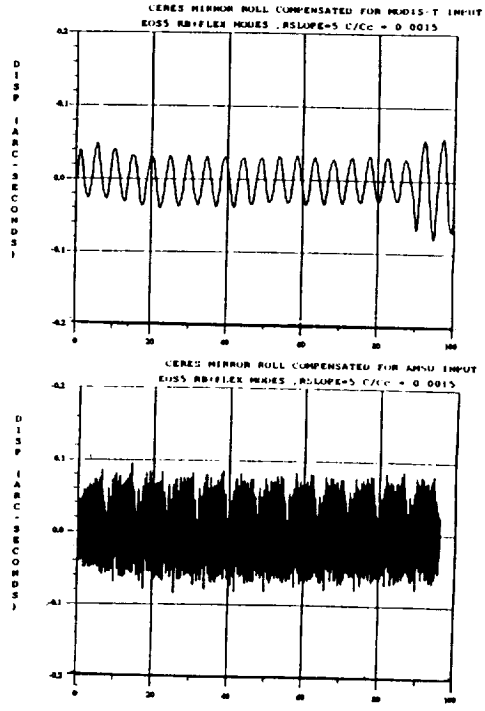

SUPERPOSITION OF COMPENSATED RESPONSE TO TWO DIFFERENT SOURCES

Graphic display of CERES roll axis jitter response due to multiple simultaneous sources (AMSU plus MODIS-T) shows that the jitter is not the sum of the individual jitter values. This is because the maximum jitter value does not occur at the same time for each disturbance response. Note that the jitter is calculated by a sampling window which moves along the time axis taking the maximum peak to peak difference between the response values within the window. The first three bars of the plot below compare the uncompensated response for AMSU disturbance alone, the combination of AMSU and MODIS-T, and the response to MODIS-T alone. The next three bars display the same information for the compensated CERES response (the MMC system active).

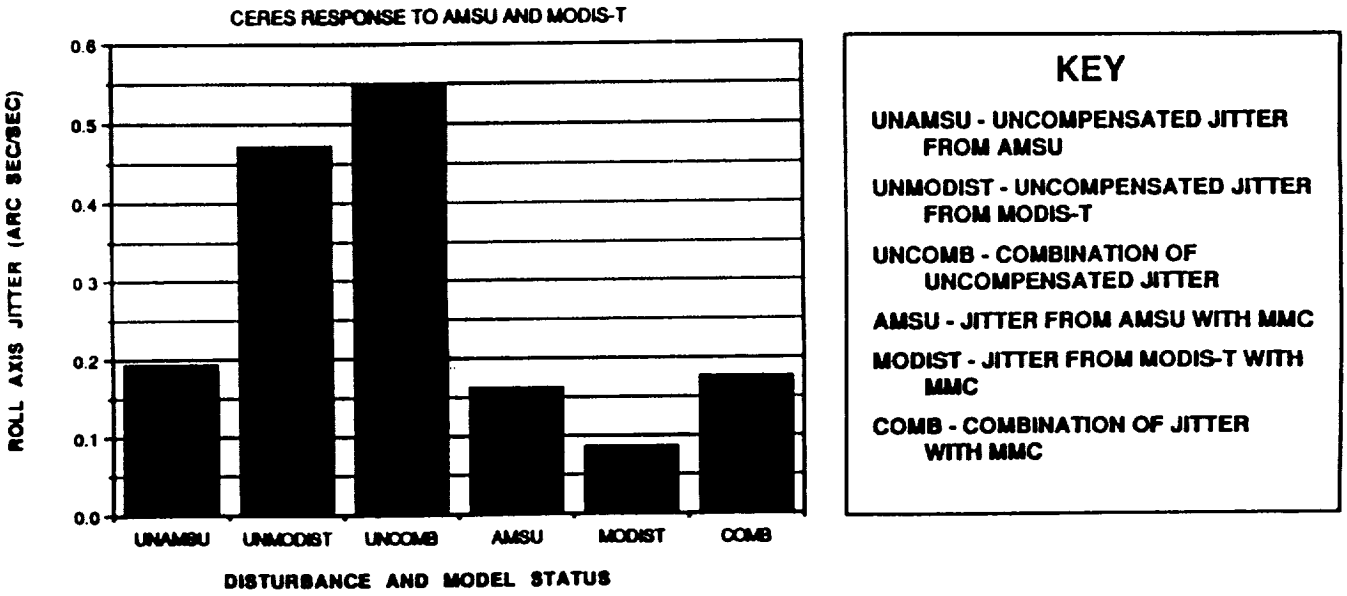

MMC LOGIC EFFECTIVE FOR MULTIPLE DISTURBANCES

MLS SCAN 3 DISTURBANCE TORQUE PROFILE

The MMC technique was applied to suppress disturbances from the MLS instrument, which is currently on the UARS, and is well known as a pernicious source of jitter.

The torque profile is displayed below, and consists of a number of forward torque pulses, each of which rotates a scanning mirror about the spacecraft roll axis 0.05 degrees. Two return pulses follow the forward pulse train. The return profile was split into two identical parts as a result of a previous UARS disturbance torque analysis which showed high amplitude residual vibrations at the completion of each MLS scan due to return pulse excitation of the UARS solar array. The second pulse is timed to cancel the UARS solar array excitation, which yielded a 75 % reduction in the solar array free vibration when compared with the effects of a single return pulse. The MLS torque profile was applied to the EOS in this study without consideration to the EOS solar array mode.

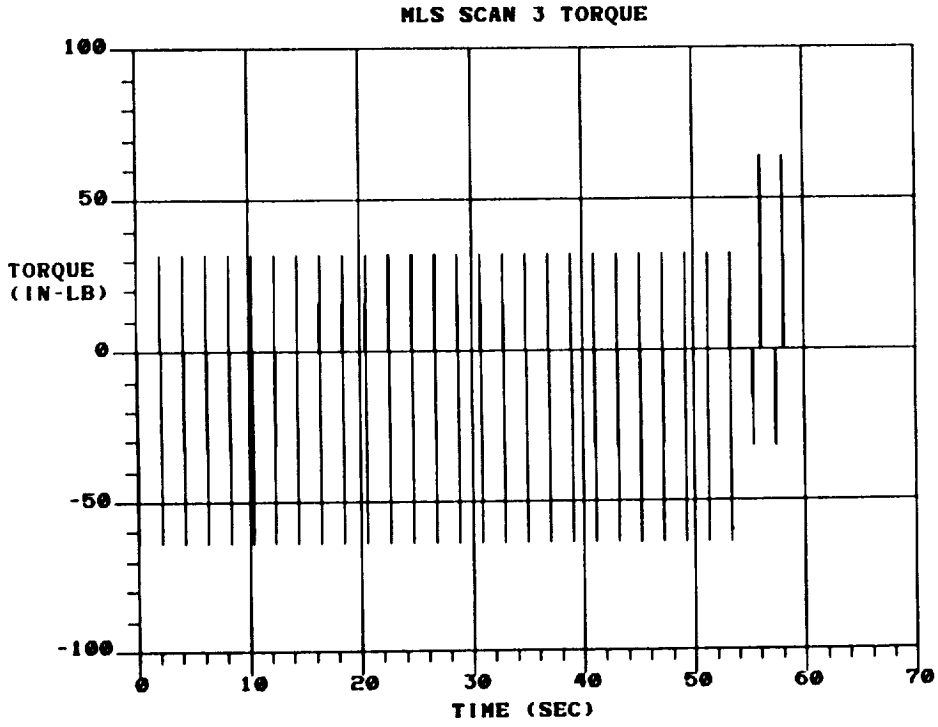

DOUBLE RETURN PULSE IMPLEMENTED TO REDUCE LARGE JITTER RESPONSE

UNCOMPENSATED CERES BASELINE RESPONSE TO MLS

The MLS disturbance excites both high and low frequency responses, as evidenced in the plot below. The forward pulse train excites the high frequency components, as seen in the plot from time zero to approximately 55 seconds, at which point the double return pulse excites the lower frequency modes, especially the fundamental solar array mode. Significant jitter results from the MLS disturbance.

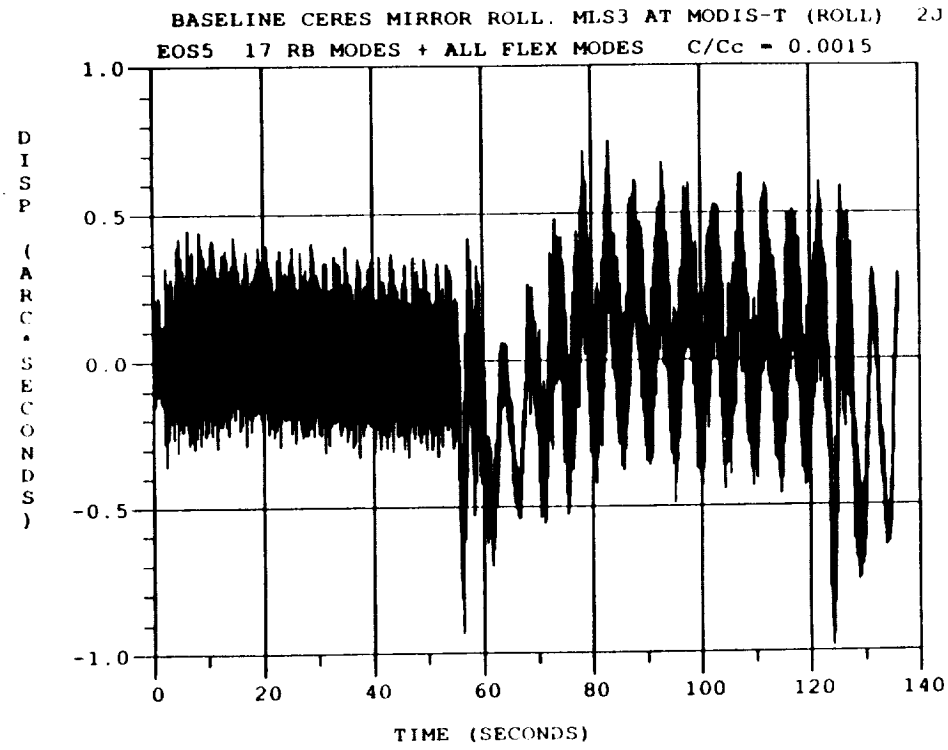

MLS EXCITES BOTH LOW AND HIGH FREQUENCY MODES

COMPENSATED CERES RESPONSE WITH RIGID BODY MODES ONLY IN PREDICTOR MODEL

Application of MMC with a primitive predictor model consisting only of the rigid body and gimbal modes proved ineffective at jitter reduction, as seen below. Jitter values actually increased slightly, due to lag filter and reverse torque error effects. Clearly a more sophisticated predictor model is required for effective jitter suppression.

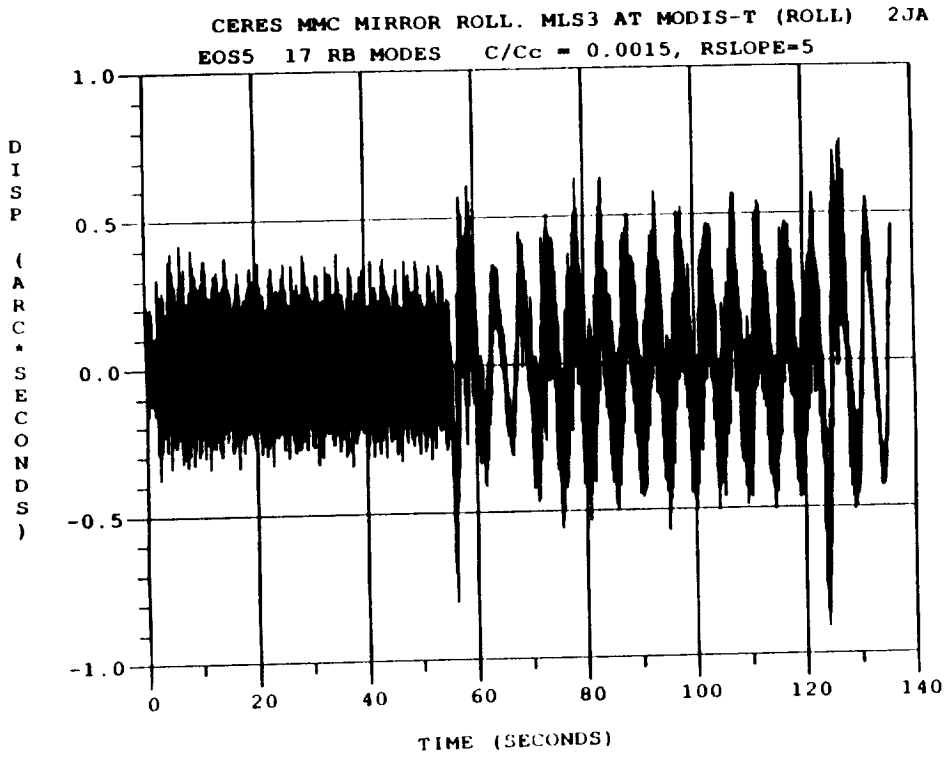

RIGID BODY PREDICTOR MODEL NOT EFFECTIVE FOR JITTER SUPPRESSION

COMPENSATED CERES RESPONSE
WITH RIGID BODY MODES PLUS FUNDAMENTAL SOLAR ARRAY MODE
IN PREDICTOR MODEL

The degree of sophistication of the MMC predictor model was increased by including the fundamental solar array mode along with the rigid body modes. The response plot below shows some jitter reduction with especially effective elimination of the solar array response as expected. The actual reduction factor for jitter is 1.5 for this model.

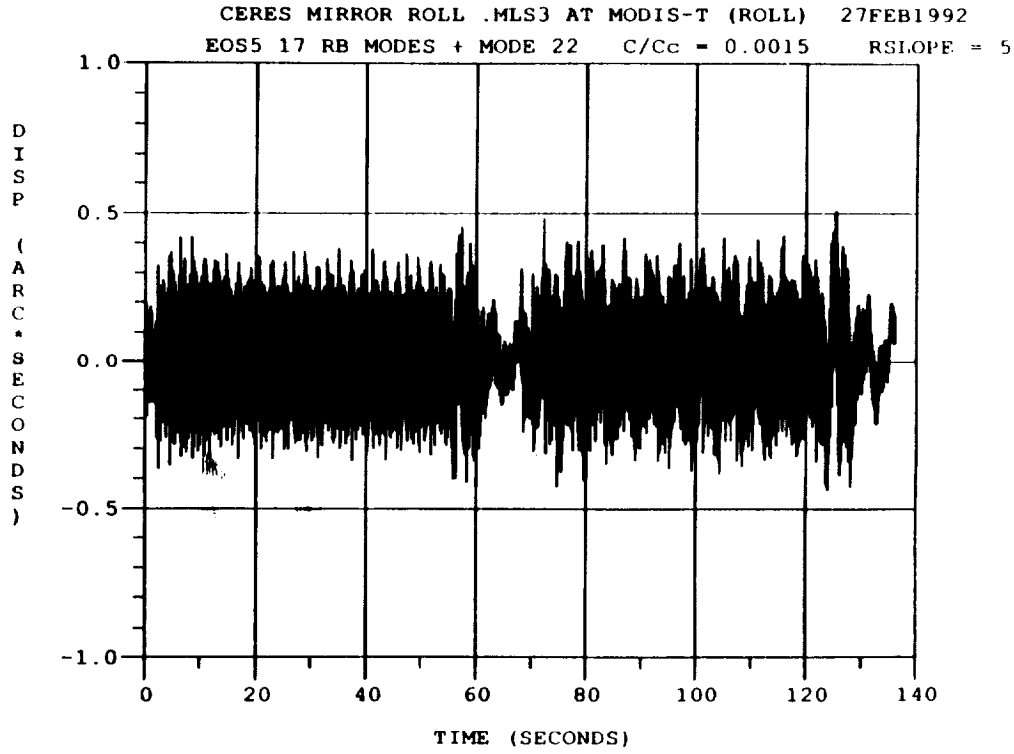

MMC EFFECTIVENESS IMPROVES WITH ADDITION OF FLEXIBLE MODE

COMPENSATED CERES RESPONSE WITH ALL FLEXIBLE MODES

The use of all flexible modes with the rigid body modes in the predictor model shows marginal improvement over the previous model with the fundamental solar array mode as the only flexible mode. A jitter reduction factor of 1.6 was achieved. No doubt a modal significance study would reveal a subset of flexible modes which would produce an equivalent jitter reduction to that achieved by the use of all the flexible modes, as seen previously in the AMSU disturbance case. Again, high frequency disturbances prove difficult for the MMC to suppress effectively given the limitations and assumptions of the study with regard to lag and reverse torque error.

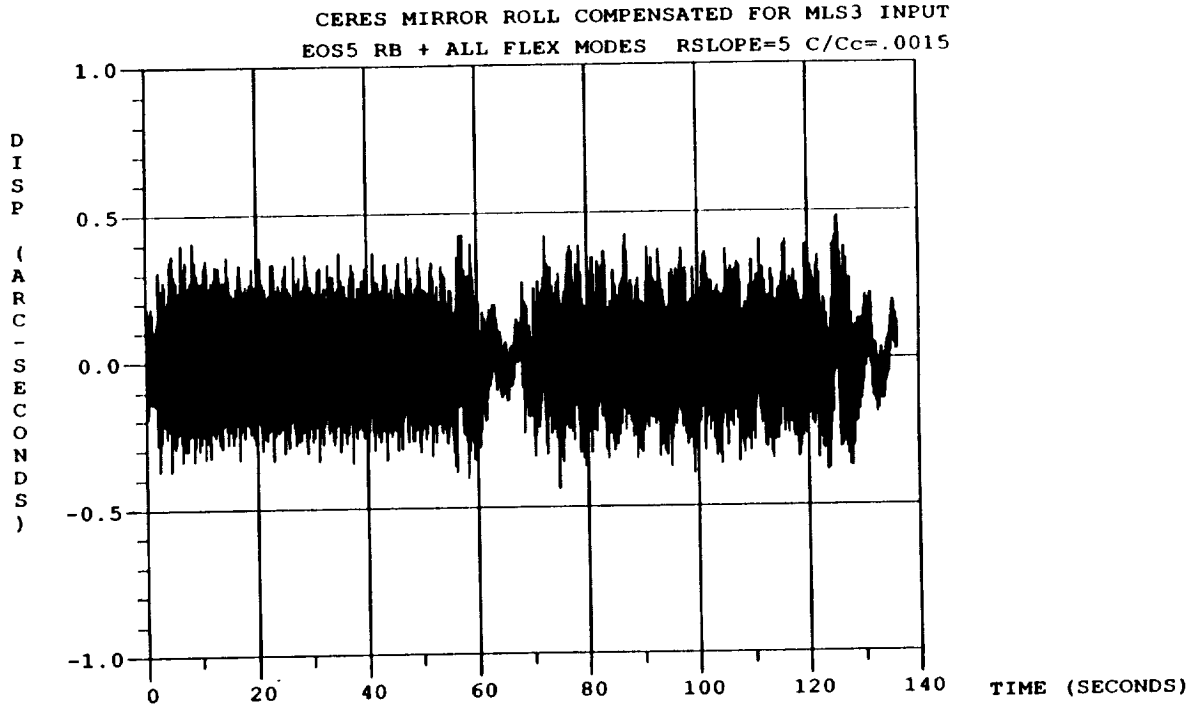

BEST MMC PERFORMANCE ACHIEVED WITH ALL FLEXIBLE MODES

COMPENSATED CERES RESPONSE WITH ALL FLEXIBLE MODES
NO LAG

As expected, when the error due to motor lag is removed the MMC performance improves and the jitter is further reduced. Note particular improvement in the response caused by the return pulse.

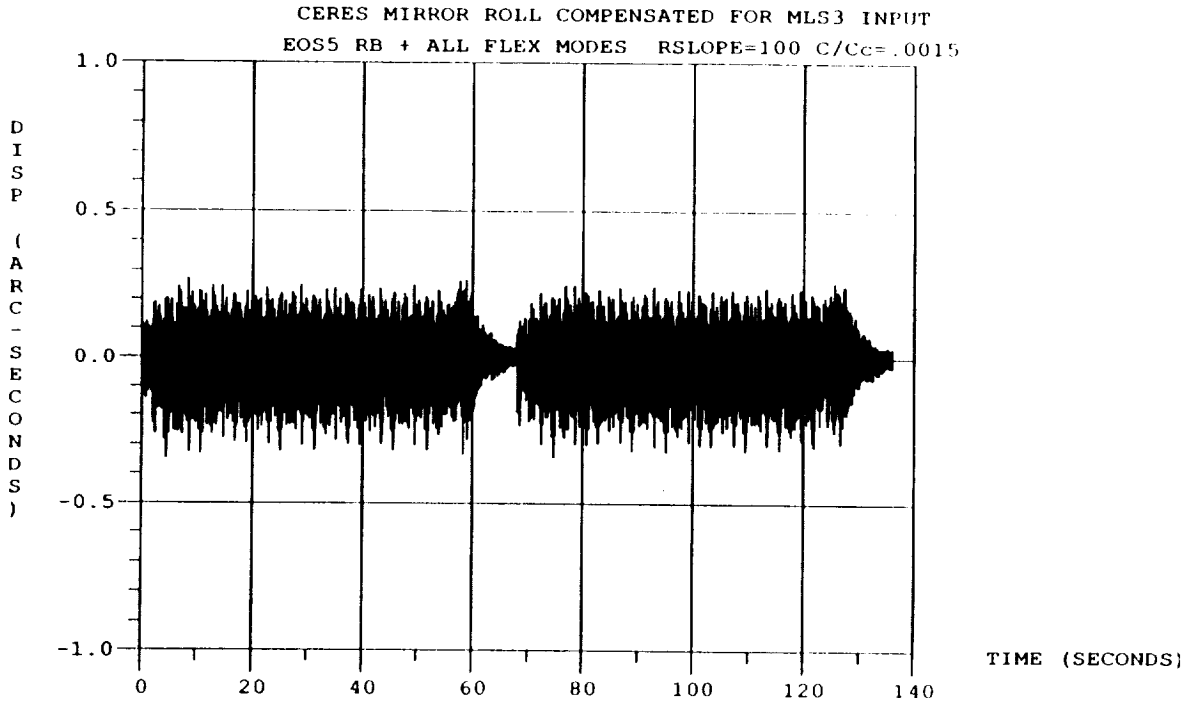

RESPONSE WITH NO LAG PROVIDES IDEALIZED COMPARISON

SUMMARY TABLE OF CERES RESPONSE TO MLS DISTURBANCE

The chart below summarizes the jitter reduction and stability performance for the CERES response to the MLS disturbance for various predictor models. Comparison with the baseline predictions shows modest jitter reduction, with a maximum factor of 1.6 realized. Stability results are also lackluster, with a maximum reduction factor of 1.87 seen.

MODEL STATUS	JITTER IN ARC SECONDS WINDOW SIZE (SECONDS)			
	1.0	9.0	60.0	1000.0
UNCOMPENSATED	1.367	1.588	1.731	1.731
RIGID BODY MODES	1.387	1.663	1.663	1.663
RB + FUNDAMENTAL S/A	0.901	0.951	0.951	0.951
RB + ALL FLEX MODES	0.835	0.868	0.925	0.925
RB + FLEX MODES NO LAG	0.601	0.619	0.619	0.619

HIGH FREQUENCY CONTENT OF MLS DISTURBANCE LIMITS EFFECTIVENESS OF JITTER SUPPRESSION TO A FACTOR OF 1.6

In order to explore the possibility of utilizing a feedback control scheme as opposed to the MMC system thus far described, a simplified feedback control concept was studied.

Although there is no doubt that a classic sophisticated feedback control system could be developed to suppress instrument jitter, the intent of this study is to explore less costly alternatives which could prove effective in jitter control and suppression. Thus a feedback control system using information from sensors already on the platform for other purposes was proposed.

In this highly idealized approach it is assumed that gyros at the NAVBASE can provide rotational acceleration data about all three axes. The signals from these gyros is assumed to be free of noise, furthermore, no sampling rate limits are present.

The chart below displays a diagram of the logic steps which are followed in this NAV BASE feedback algorithm.

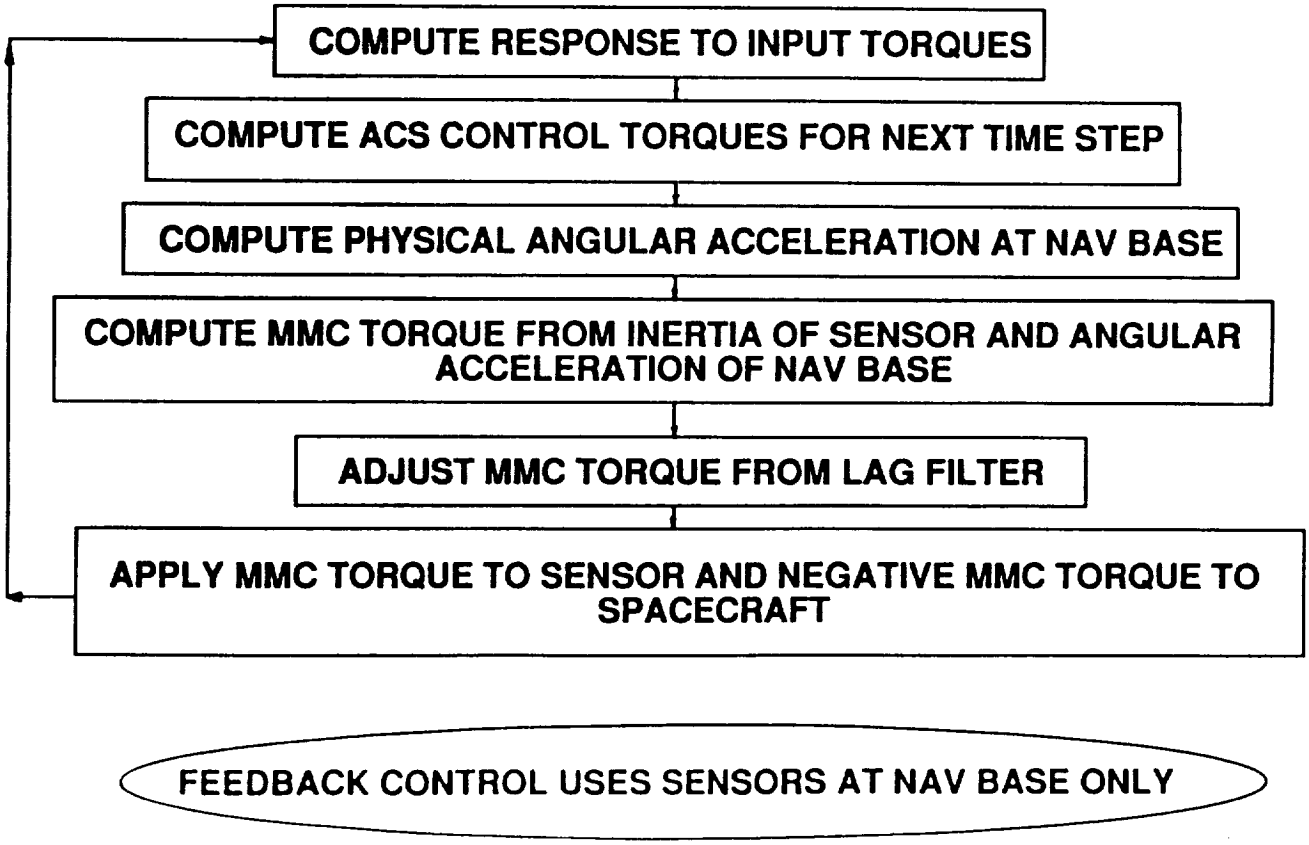

In order to provide a fair comparison between the MMC technique considered in this study and the NAV BASE feedback system, the compensated jitter response of the CERES to the MODIS-T input was calculated with the MMC technique. The MMC technique is employed in an ideal case eliminating error sources due to frequency and damping, and matching the lag effects between it and the NAV BASE system. The secondary reaction torques are present as an error source, however, since the MMC system does not take these into account when it makes its response predictions.

The chart below shows the jitter time history of the compensated CERES response to the MODIS-T disturbance calculated via the MMC technique. This plot forms the baseline for comparison with the NAV BASE feedback system, shown on the next viewgraph. The predictor model consists of 17 rigid body and gimbal modes plus the fundamental solar array mode. It must be emphasized that this is an unrealistically ideal case presented for comparison purposes only.

BASELINE MMC FOR COMPARISON WITH FEEDBACK COMPENSATED CERES RESPONSE TO MODIS-T INPUT 17 RIGID BODY MODES PLUS FUNDAMENTAL SOLAR ARRAY MODE

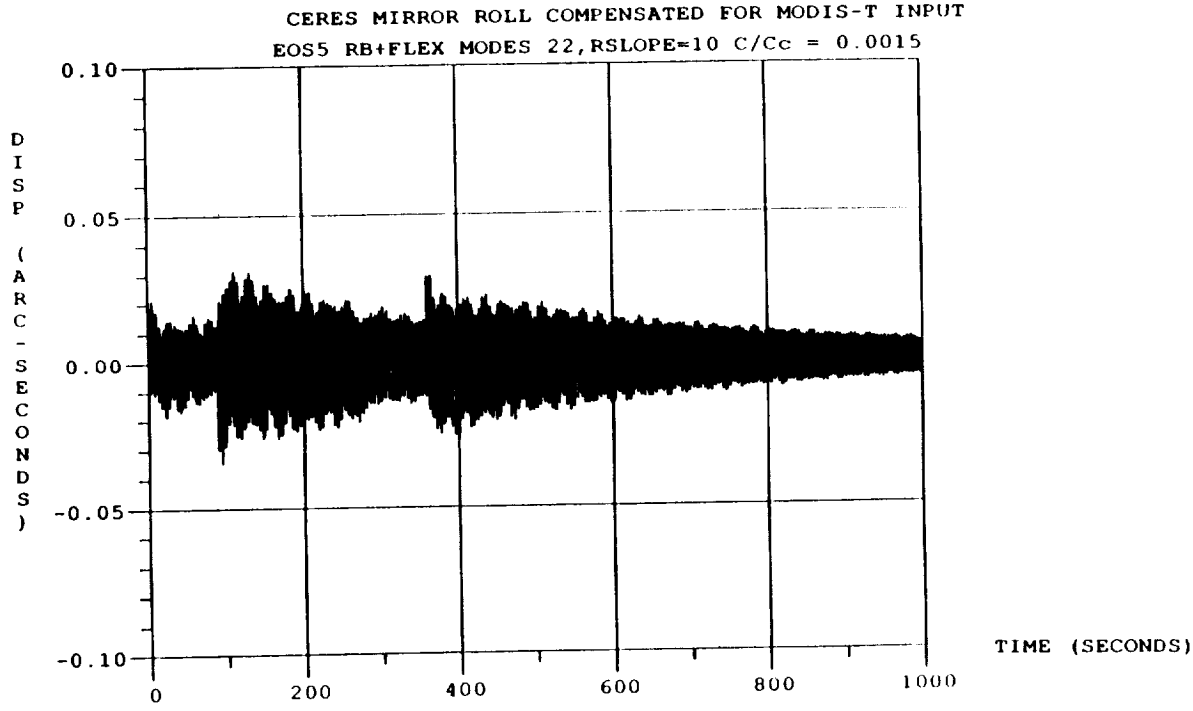

EFFECTIVE JITTER COMPENSATION WITH PERFECT KNOWLEDGE

The chart below shows the effectiveness of the NAV BASE feedback system for mirror motion compensation. The jitter for the CERES response to the MODIS-T input is displayed. Note that the models for the MMC system and NAV BASE feedback system are of the same degree of sophistication, both featuring 17 rigid body and gimbal modes plus the fundamental solar array mode. In addition, roughly the same error due to lag is present in both models. Further equivalent idealizations were made for both models as outlined previously.

Under these ideal conditions the NAV BASE feedback system is effective in jitter control, showing a substantial jitter reduction over the uncompensated baseline. The MMC system shows very similar effectiveness.

COMPENSATED CERES RESPONSE TO MODIS-T DISTURBANCE NAV BASE FEEDBACK SYSTEM WITH SOLAR ARRAY MODE

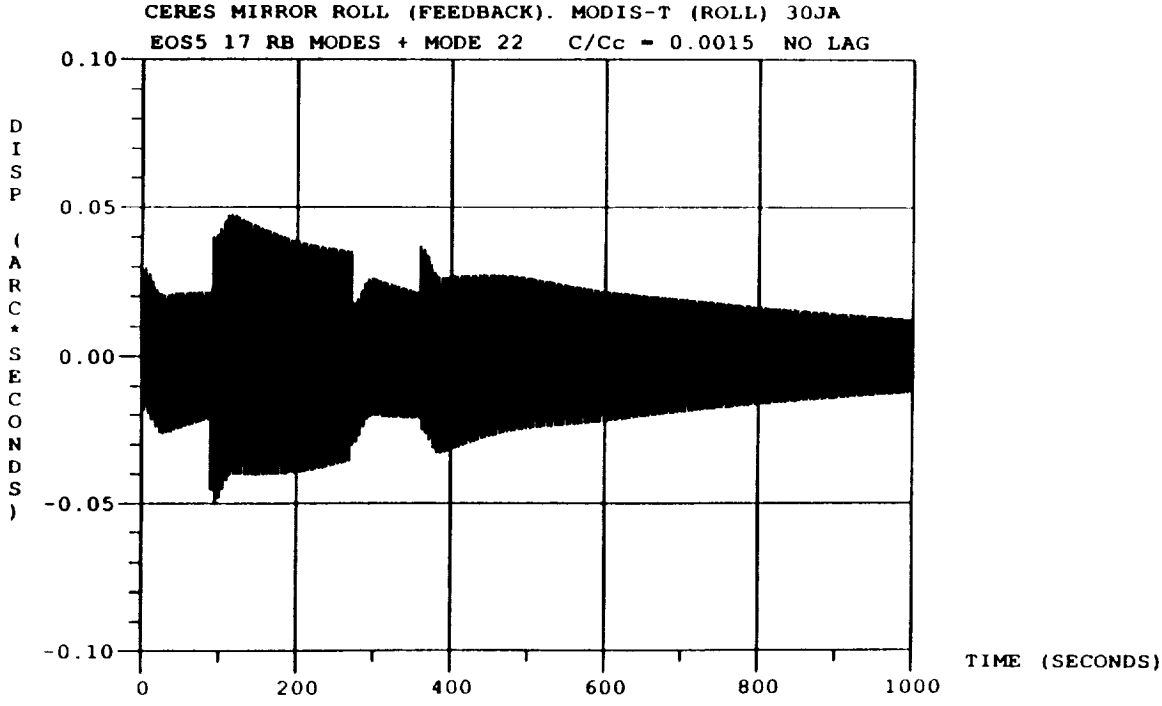

EFFECTIVE COMPENSATION POSSIBLE SIMILAR TO MMC

The chart below provides direct numerical comparison between the uncompensated jitter, the jitter with MMC for a lag constant of 10, and the jitter for the idealized NAV BASE feedback system. All jitter values refer to CERES roll response due to MODIS-T disturbance. Stability values are presented as well. Again, the numbers show that the NAV BASE feedback system provides effective jitter control compared to the uncompensated baseline, on the same order as the MMC system for similar idealized assumptions.

SUMMARY TABLE COMPARING MMC WITH NAV BASE FEEDBACK

MODEL	JITTER IN ARC SECONDS WINDOW SIZE (SECONDS)			
	1.0	9.0	60.0	1000.0
UNCOMPENSATED	.4698	1.005	1.945	2.498
MMC LAG = 10	.0399	.0603	.0658	.0659
NAV BASE FEEDBACK	.0556	.0939	.0981	.0981

BOTH MMC AND NAV BASE FEEDBACK SHOW SIGNIFICANT IMPROVEMENT OVER UNCOMPENSATED BASELINE JITTER AND STABILITY

SUMMARY

The salient points of the study are outlined on the summary chart below. As predicted in previous studies, the MMC technique is extremely effective at nulling jitter from rigid body motion. Excellent jitter compensation is theoretically possible for flexible modes as well. The study predicts jitter reduction factors of 5.4 for low frequency sources and 1.2 for high frequency sources. Stability reduction is even more dramatic, with factors as high as 17 predicted. However, it must be emphasized that extreme frequency sensitivity is characteristic of the MMC technique, limiting its use to linear systems which are empirically modeled to extreme fidelity. State of the art prediction techniques (finite element model normal modes analysis) for the modal parameters are insufficient to ensure acceptable performance.

The study also demonstrated the effectiveness of increased damping on jitter suppression, and its associated lessening of MMC frequency sensitivity with increased damping. It was also observed that errors in predicted damping had less adverse effects than similar errors in predicted frequency.

Multiple disturbances were explored and the MMC technique was seen to be effective here as well.

Finally, the MMC technique was compared to a primitive feedback system, and was seen to have similar limitations and effectiveness.

- **RIGID BODY MOTION EFFECTIVELY NULLED**

- **FOR FLEXIBLE MODES:**
  - **LOW FREQUENCY RESPONSES CAN BE READILY SUPPRESSED**
  - **HIGH FREQUENCY RESPONSES MORE DIFFICULT TO CONTROL**

HOWEVER:

ACCURATE DYNAMIC MODEL VITAL TO MMC EFFECTIVENESS FOR FLEXIBLE MODES

MMC HAS POTENTIAL APPLICATION FOR JITTER REDUCTION FOR NEXT GENERATION REMOTE SENSING SPACECRAFT

RECOMMENDATION

Due to the extreme frequency sensitivity displayed by the MMC technique, it is imperative that the system modal parameters be characterized with great accuracy. This necessitates the use of on-board measured data to characterize the dynamic behavior of the spacecraft. It is not possible to predict a priori the modal parameters to sufficient accuracy for the MMC technique to be effective.

USE ONBOARD MEASUREMENTS TO EXTRACT MODAL PARAMETERS

IMPLEMENT MMC USING MEASURED DATA TO SUPPRESS INSTRUMENT JITTER

USE GROUND DEMONSTRATION MODEL TO EVALUATE EFFECTIVENESS OF MMC TECHNIQUE

EXPERIMENTAL VALIDATION IS REQUIRED TO DEMONSTRATE FEASIBILITY OF MMC

Precision Slew/Settle Technologies for Flexible Spacecraft

R. A. Manning[1],V. A. Spector[2]
TRW Space and Technology Group

Abstract

Many spacecraft missions in the next decade will require both a high degree of agility and precision pointing. Agility includes both rotational maneuvering for retargeting and translational motion for orbit adjustment and threat avoidance. The major challenge associated with such missions is the need for control over a wide range of amplitudes and frequencies, ranging from tens of degrees at less than 1 Hz to a few μradians at hundreds of Hz. TRW's internally funded Precision Control of Agile Spacecraft (PCAS) project is concerned with developing and validating in hardware the tools necessary to successfuly complete the combined agile maneuvering/precision pointing missions.

Development has been undertaken on a number of fronts for quietly slewing flexible structures. Various methods for designing slew torque profiles have been investigated. Prime candidates for rapid slew/settle scenarios include Inverse Dynamics and Parameterized Function Space. Joint work with Professor Bayo at the University of California, Santa Barbara and Professor Flashner at the University of Southern California has led to promising torque profile design methods. Active and passive vibration suppression techniques also play a key role for rapid slew/settle mission scenarios. Active members with local control loops and passive members with high loss factor viscoelastic material have been selected for hardware verification. Progress in each of these areas produces large gains in the quiet slewing of flexible spacecraft.

The main thrust of the effort to date has been the development of a modular testbed for hardware validation of the precision control concepts. The testbed is a slewing eighteen foot long flexible truss. Active and passive members can be interchanged with the baseline aluminum members to augment the inherent damping in the system. For precision control the active members utilize control laws running on a high speed digital structural control processor. Tip and midpsan motions of the truss are determined using optical sensors while accelerometers can be used to monitor the motions of other points of interest.

Preliminary results indicate that a mix of technologies produces the greatest benefit. For example, shaping the torque profile produces large improvements in slew/settle performance, but without added damping settling times may still be excessive. With the introduction of moderate amounts of damping, slew/settle performance is vastly improved. On the other hand, introducing damping without shaping the torque profile may not yield the desired level of performance.

[1] Staff Engineer, AIAA Member, ASME Member
[2] PCAS Principal Investigator, IEEE Member

Introduction

In the past, slew and/or reorientation maneuvers of flexible spacecraft have been performed over long periods of time so that no significant energy is imparted to the structure's flexible modes. Reorientation of the spacecraft was accomplished by pumping energy into the rigid body modes and rolling off the control system before the frequencies at which the flexible modes occurred. Separation of the control system bandwidth and the flexible mode frequencies allowed this technique to work.

Many of the future space missions will not have the advantage of a separation in control system bandwidth and flexible mode frequencies. The separation becomes blurry, and even overlapping, when the structure begins to get large in size or the control system bandwidth increases. The former significantly reduces the flexible frequencies of the system while the latter represents the case of a very rapid slew or reorientation maneuver. For such systems, attempts to quietly reorient the structure using these older methods for generating slew torque profiles are doomed to failure. New torque profile design techniques are required which take into account the overlapping control system bandwidth and flexible modes. In addition, designing in damping relaxes the requirements on the bandwidth of the slew controller and increases the robustness of the system to parameter uncertainty.

When new slew torque profile design methodologies and damping techniques are discovered, they have to be demonstrated in hardware. This allows the effects of hardware limitations on the performance of the slewing system to be documented. Furthermore the robustness of the slew and damping techniques in a scaleable/traceable testbed can be demonstrated.

Relation to Previous Work

Large angle quiet maneuvers have been an active area of research over the past 10-15 years. A survey of ground-based test facilities for such demonstrations is given by Das [1]. He focuses on space structures with both large angle reorientation maneuvers and vibration suppression for rapid slew/settle mission scenarios. The early work focused on accomplishing the slew/reorientation maneuver in minimum time using gas thrusters. As such, predominantly bang-bang controllers were used to accomplish the maneuver [2]. Improvements to the slew methodologies improved the performance that could be obtained using bang-bang actuators [3], but performance was not at a level that would be required for some proposed space missions.

Theoretically, a significant amount of work has posed the rapid slew/settle problem as a two point boundary value problem and solved for the torque profiles using standard optimal control solution procedures. Breakwell [4] posed such a solution using standard fixed-time linear quadratic Gaussian regulator control theory with a modal decomposition of the flexible body. A suggested improvement by Junkins [5] "smooths" Breakwell's torque profiles, thus somewhat reducing the bandwidth requirement on the reorientation actuators. The methods based on optimal control theory, though performing very well for the nominal system, are sensitive to uncertainties in the plant, the environment, or the specific hardware being used.

Robotics reorientation goals are similar to those of slewing/reorienting a flexible spacecraft. A fixed maneuver is to be accomplished with minimal residual vibrations at the conclusion of the maneuver. As such, some of the inverse dynamics design methods [6,7] for generating slew torque profiles have shown promise for quickly and quietly reorienting flexible manipulators. Furthermore, preliminary studies have shown that the inverse dynamics methods are less sensitive to parameter uncertainties than the optimal control methods.

Regarding vibration suppression during and following the reorientation maneuver, internal sensing and actuating devices are required so that the flexible modes can be damped without affecting the rigid body modes. In this manner, a separation in topology between the slew controller and vibration controller can be drawn, though the bandwidths of the controllers may still overlap. Fanson et al [8] have shown the types of vibration suppression performance that can be obtained in fixed position static trusses. Their work utilized piezoceramic stack actuators and internal force measurements to achieve 25-35 dB attenuation of peak vibrations. Improvements in materials processing at TRW [9,10] have led to the piezoceramic sensors and actuators being embedded within the layup of graphite composite members.

Applicable Space Missions/Typical Mission Scenarios

A number of proposed space missions contain operational scenarios which require reorientation and target acquisition. Of these missions, some have extremely rapid reorientation rate goals, fast slew/settle times, and/or precision pointing/alignment needs.

Typical of the large agile space missions are scanning surveillance spacecraft such as Space Based Radar/Space Based Wide Area Surveillance (SBR/SBWAS) missions. These spacecraft must be large to maintain suitable signal strengths and be agile during scan maneuvers. During a typical raster scan maneuver, minimizing the time spent in the turnaround and settle phase of the scan will increase the duty cycle of the mission. Due to their large size, structural modes will lie within the bandwidth of the attitude control system. Harmful controls/structure interactions will be present which jeopardize the settle/pointing performance of the spacecraft. SBR/SBWAS missions would significantly benefit from the technology presented in this paper. The combined quiet slew torque profile design methodology and active/passive damping would increase SBR/SBWAS turnaround and settle performance as well as increase critical component pointing accuracy.

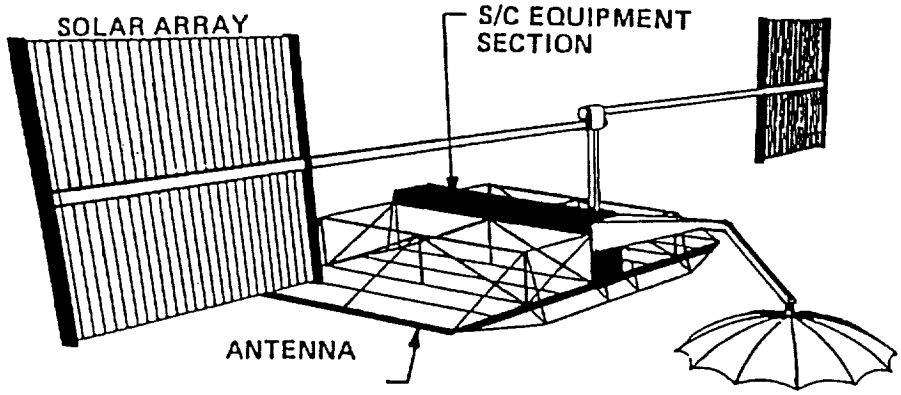

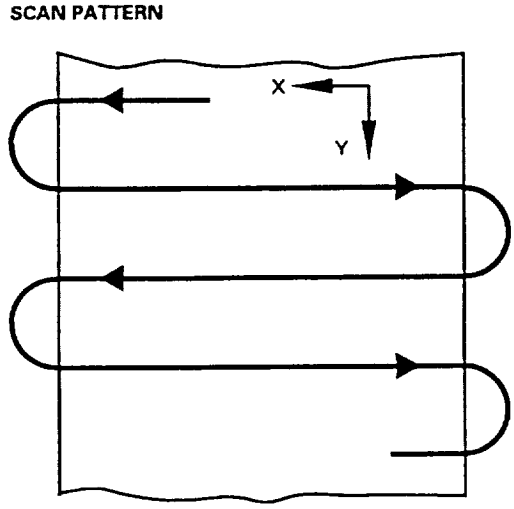

Applicable Space Missions/Typical Mission Scenarios (Cont.)

Spacecraft which must be quieted from the effects of internal and external disturbances would benefit from the active and passive damping presented herein. Such spacecraft are proposed large optical interferometers, Defense Support Program (DSP) satellites, Defense Meteorological Satellite Program (DMSP) satellites, and Lightsats. In each of these instances, onboard disturbances and thermal/environmental disturbances threaten the operational mission. Active and/or passive vibration suppression and isolation could eliminate the harmful effects of the disturbances and restore mission integrity.

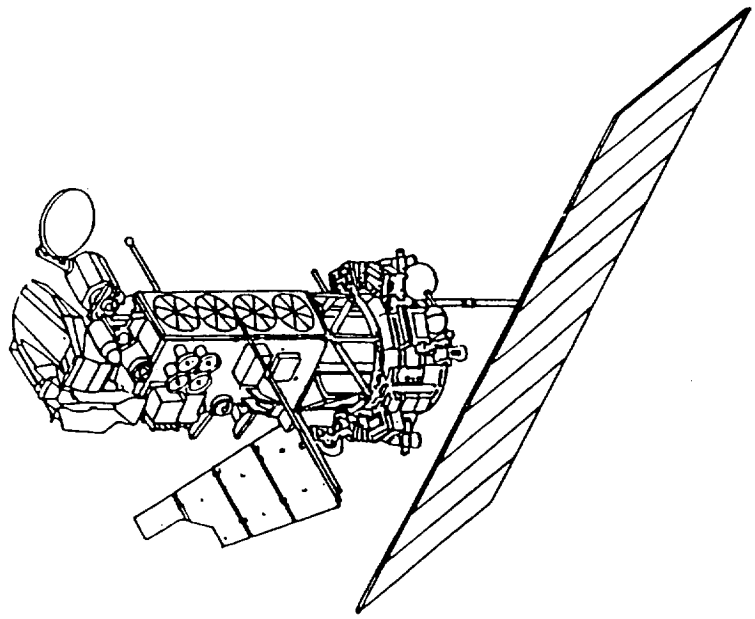

Testbed Overview

A nine bay, eighteen foot long slewing truss has been developed at TRW for use as a quiet slewing testbed. The baseline truss consists of threaded hub joints and aluminum truss members. All of the hubs and members are threaded so that any members can be replaced with active and or passive composite members without disassembling the complete structure. A stiff aluminum backing structure serves to counterbalance the structure over the simulated control moment gyro (CMG) and to provide a dragless mounting platform for optical sensor cameras and cables. (All performance sensors and actuators are described on the following pages.) The total weight of the truss is approximately 90 pounds, with the hubs accounting for 60 pounds and the truss members accounting for the remaining 30 pounds. The simulated CMG is mounted on a pedestal which also serves to keep the truss near eye level and to mount cables and slew limit switches/stops.

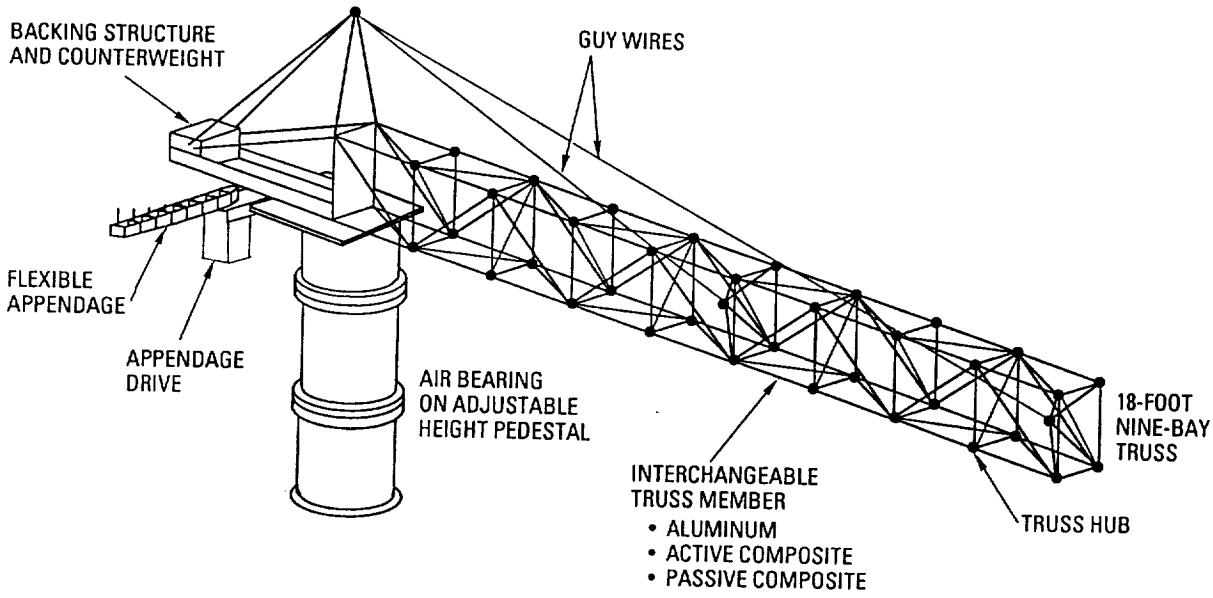

Sensor and Actuator Layouts

A combined air bearing/slew torque motor simulates typical CMGs for reorienting the structure. The air bearing has the capability to support 500 pounds (i.e., truss, backing structure, and equipment) and can withstand 100 inch pounds of overturning moment. The motor used to slew the truss/backing structure can supply up to 40 ft-lbs of torque. Maximum angular accelerations of greater than 4 deg/sec^2 can be produced with the testbed in its current configuration. An optical encoder is integral with the slew torque motor and provides angular position measurements for the base of the truss.

Optical sensors and accelerometers provide performance data during and after the slew. TRW's Surface Accuracy Measurement Sensors (SAMS) provide vertical and horizontal displacement measurements at the tip and midspan of the truss. The receivers of the SAMS sensors are mounted on the backing structure of the truss and rotate with the truss. Thus these sensors provide information concerning the flexible motion of the truss. A laser interferometer retroreflector is mounted at the tip of the truss and is used to provide absolute motion (i.e., rigid plus flexible mode motion) measurements. The interferometer itself has resolution down to 10 nanometers and is mounted on an optical bench.

Additional measurements on the performance of the truss are obtained using four accelerometers. Three of the accelerometers are mounted at the eighth bay of the truss and oriented such that vertical, horizontal, and torsional motions at that station can be obtained. A fourth accelerometer is mounted at the second bay of the truss and provides horizontal motion information during and after the slew maneuvers.

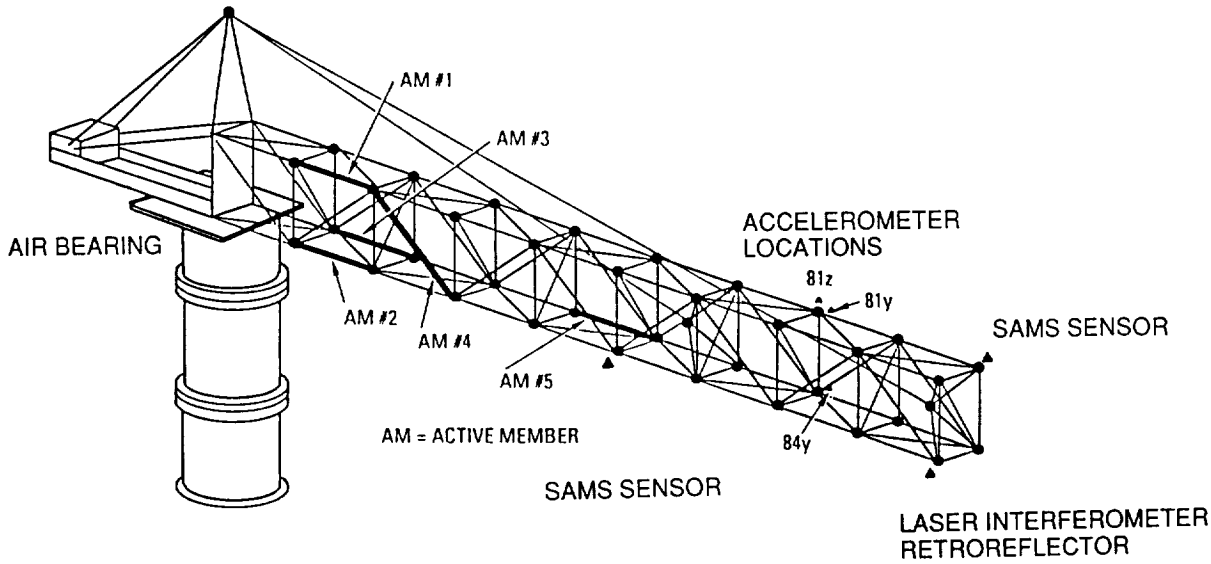

Typical Modal Content

A summary of the first few modes of the slewing testbed is given in the table below. Though the modes are not necessarily closely spaced, they are not widely separated either. The separation is approximately typical of those expected for primary structure modes for some future space missions. The mode at 1.8 Hz is a quasi-rigid body mode caused by the interaction of the truss/backing structure inertia and the electronic stiffness in the air bearing/motor drive electronics. The primary horizontal bending mode (i.e., slew plane bending mode) at 6.3 Hz has a moderate amount of damping due to the electromagnetic damping in the air bearing/motor assembly. All of the remaining modes have levels of damping expected from a threaded joint type structure.

Table 1: **Slewing Testbed Modal Content**

Mode	Description	Frequency (Hz)	Damping (ζ)
1	Rigid Body Slew Mode	0.0	
2	Motor Electronics Mode	1.8	
3	Vertical Bending Mode	4.7	0.7
4	Horizontal Bending Mode	6.3	2.0
5	Torsional Mode	12.9	0.2
6	2nd Horizontal Bending	26.3	0.8
7	2nd Vertical Bending	34.1	2.7
8	2nd Torsion	41.6	0.4

Test Facilities

The test facilities containing the slewing testbed were designed and built with precision, quiet measurements in mind. A seismically isolated pad supports the pedestal/testbed and the optical bench which contains the interferometer. In this manner, disturbances such as nearby foot traffic, automobile traffic, and ocean wave motion will not upset tests in progress. Both the ceilings and the walls of the facility are covered with sound and light absorbing material to minimize stray vibrations and light reflections. A special quiet air conditioning system was installed that can be turned off during precision tests and turned back on for user comfort.

Various secondary tests have been conducted in the test facility. A number of passive damping applications have been tested using a modal survey system. These applications include printed circuit boards, reaction wheel assembly isolators, and passive member component development tests. Other active member tests and demonstrations have also utilized the PCAS test facility. These range from optical level pointing and resolution tests to eye-witness damping demonstrations.

Passive Member Description and Component Testing

Passive composite members with cocured viscoelastic material (VEM) were designed, fabricated, and tested for use in the slewing testbed. The members were constructured in a manner similar to those presented in [11] and shown in the figure below.

The idea is to weave the dynamic load from the stiff graphite constraining layer through the VEM to the opposite stiff graphite constraining layer. In this manner, dynamic shear loads are routed through the high loss VEM. The fiberglass which runs continuously along the length of the tube provides a parallel elastic load path to prevent creep of the VEM under static loads.

Initial tests yielded a disappointing 2-6% damping with the additional drawback that the members were difficult and labor intensive to build. A retrofit VEM/graphite constraining layer bridge was added (see middle diagram of figure) which yielded damping levels up to 18%. A typical time history for the cantilever impact test is shown below. Due to time constraints, the passive members were not incorporated into the slewing testbed. System level slew and damping performance on the testbed will be reported when they become available.

Future members will utilize the VEM/graphite constraining layers and VEM/graphite constraining layer bridges only on the outside of the tube in order to simplify the fabrication procedure. (See right side diagram in the figure below.)

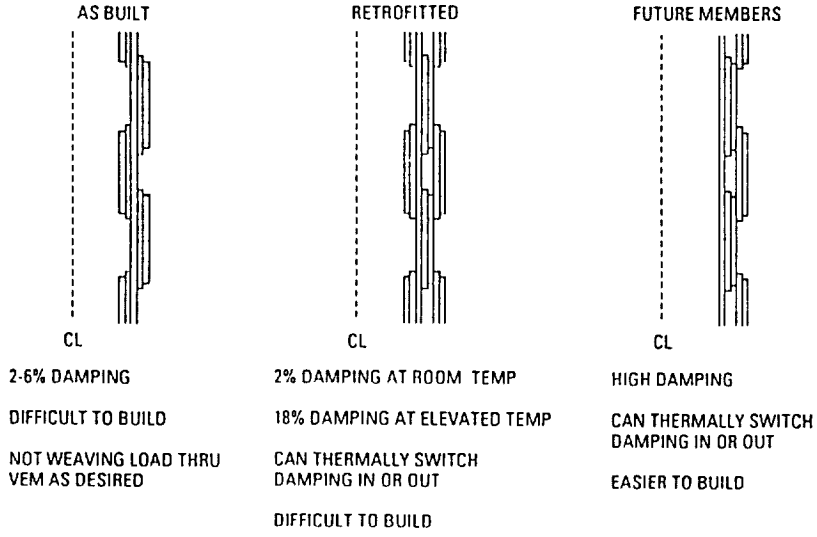

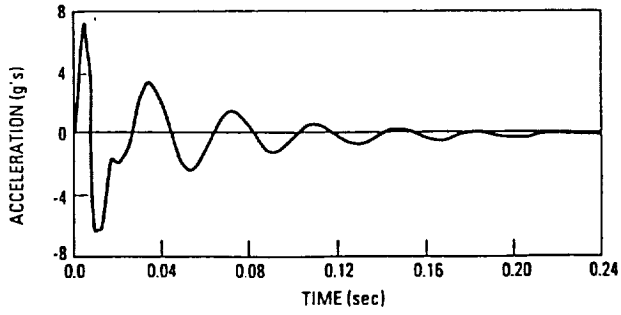

Active Member Description

Active composite members for vibration suppression during and following the slew were designed, fabricated, and integrated with the slewing testbed. The active members utilize separate piezoceramic wafers for the sensors and the actuators. Each side of the square truss members has one actuator string and two sensors. One of the sensors is colocated with the actuator string while the other is nearly colocated. By averaging these two sensor measurements, the transfer functions that the active members "see" can be tailored to be advantageous for the local control loop design task. The layup of the composite host material for the active members was arrived at by matching the stiffness of the members that are to be replaced and by maximizing the actuation capability of the resulting strut.

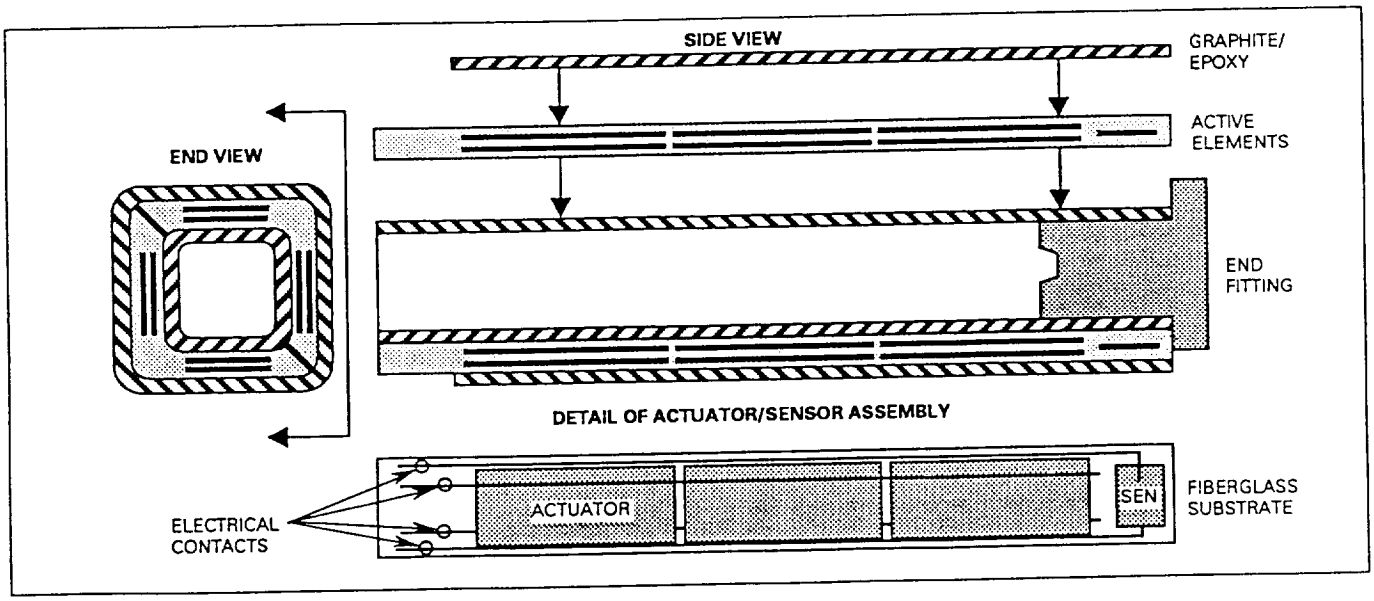

Active Member Characterization Testing

A number of component level tests were done on the active members to characterize their actuation characteristics. A creep test was performed by clamping one end of the strut, applying a step voltage, and measuring the resulting tip displacement. Three different levels of applied voltage were used in order to calculate the linearity of the actuation with applied voltage. The numerically filtered results of these tests are shown in the figure and table below. (The data was numerically filtered to eliminate the undamped oscillations and give a quasi-steady state result.) The free end of the active member achieves 98% of the steady state level in 0.2-0.3 seconds and total creep levels for all cases are less than 2.0%. Even when applying voltages greater than the recommended maximum field strengths (i.e., greater than 700 V/mm) the strut behaves very well and shows very little creep or nonlinear behavior. These results compare favorably with those reported in [12] where a piezoelectric stack was used for the actuator.

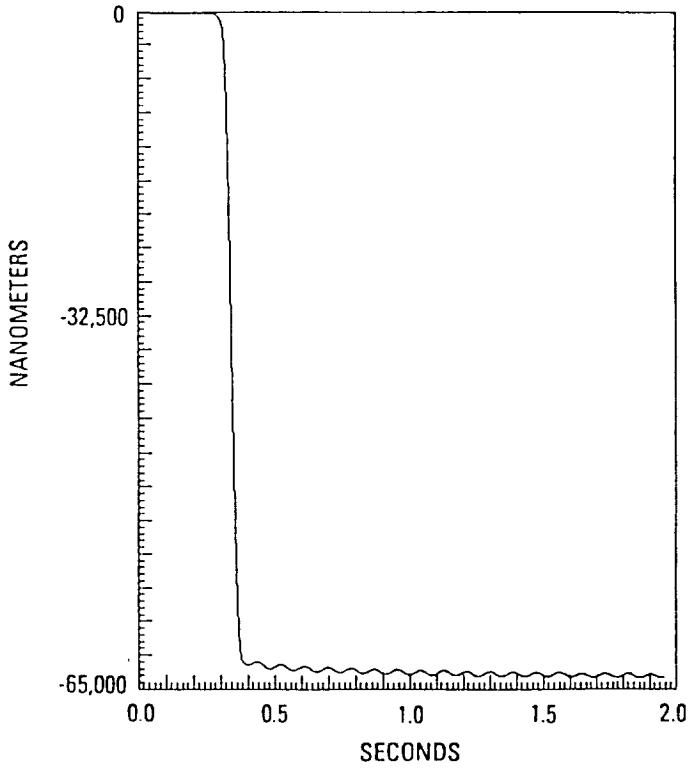

Active Member Characterization Testing (Cont.)

Parameter	TRW Active Member with Embedded Actuators			JPL PZT Actuator*
Field Strength Change	210 V/mm	528 V/mm	788 V/mm	700 V/mm
Bias Voltage	0 V	0 V	0 V	350 V
Time to 95% of Step	<0.1 sec	<0.1 sec	<0.1 sec	6 sec
Time to 98% of Step	0.2 sec	0.2 sec	0.3 sec	>50 sec
Total Creep	1.0%	1.5%	2.0%	8%

*Piezoceramic stack design

Active Member Characterization Testing (Cont.)

A second component level test was run in order to verify the active members' capability for performing microdynamic shape and vibration control. In this case, very low level sinusoidal voltages were applied to the actuators and the resulting free end tip displacement monitored with a laser interferometer. The results of this test are shown in the figure below. The sinusoidal pattern is still visible down to the 10 nanometer resolution of the laser interferometer. With the delivery of an enhanced laser interferometer (e.g., resolution down to 2.5 nanometers), the limit of the active members' microdynamic control capability will be explored.

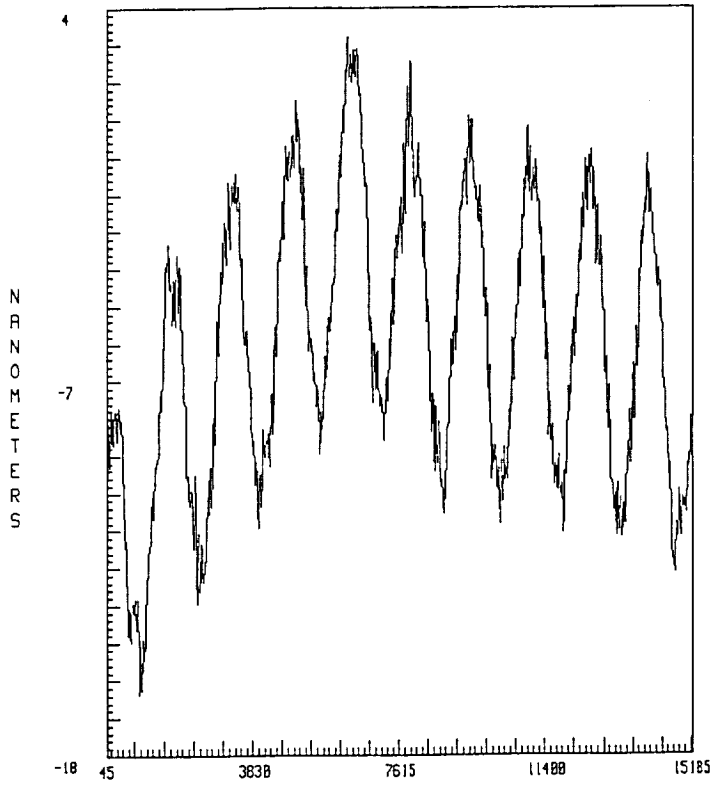

Structural Control Processor

Control loops around the active members are implemented using a flight-qualifiable high speed digital processor. A schematic of the processor is shown in the figure below. Two boards allow the implementation of 12 digital filters with a maximum order of 9 zeros and 10 poles each. In its current configuration, each of these filters can take measurements from all of the 24 sensor measurements and drive a single active member. (Thus the Structural Control Processor can drive a total of 12 active members.) For the results of multimode damping on the slewing truss testbed to date, each digital filter runs at 2.8 kHz. On benchmark tests of the processor itself, a throughput rate of 10.0 kHz per 10th order digital filter is achievable. A recent upgrade allows the filter parameters and gains to be adjusted in real time, lending the Structural Control Processor to adaptive control algorithm development and verification.

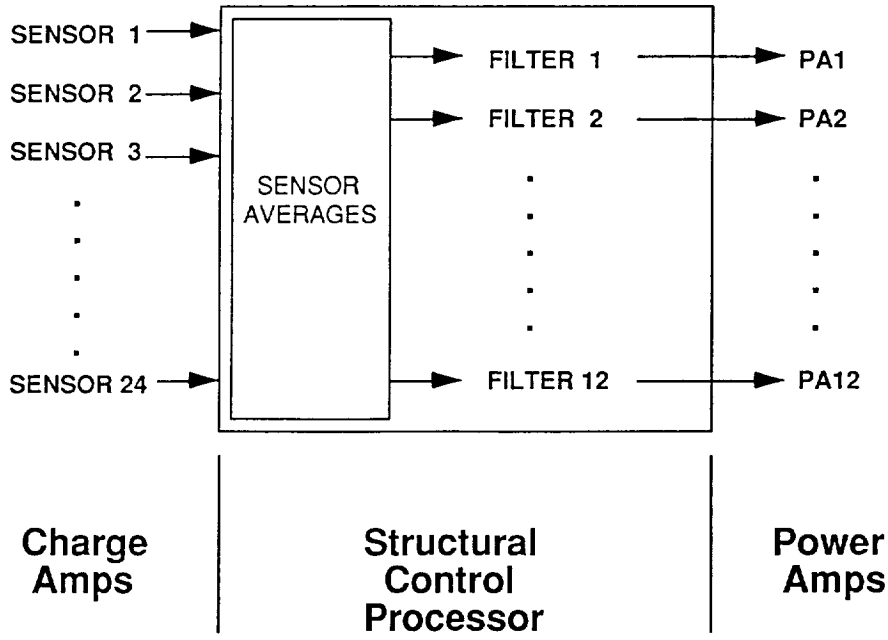

Active Damping Performance

The open and closed loop active damping performance of the slewing testbed is shown in the following figures. Five active members were placed at strategic locations within the truss. Four of these members were used for control purposes while a fifth was used to provide a white noise disturbance source. Accelerometers monitored the open and closed loop performance of the truss. Second order Positive Position Feedback (PPF) loops were used local to each member in generating the closed loop results.

Undamped and damped horizontal plane motions (i.e., slew plane motions) are shown in the figure below. In the undamped case, maximum horizontal motions are obtained in the primary vertical, horizontal, and torsional modes. With the loops closed, the vertical mode at 4.7 Hz is attenuated down to the threshold of the accelerometers, the horizontal mode has been significantly reduced, and the torsional mode has been attenuated by 30 dB. None of the higher modes have been affected, indicating no harmful control spillover effects. The higher modes could be damped if they significantly affect the slew performance and if a higher order control law is used.

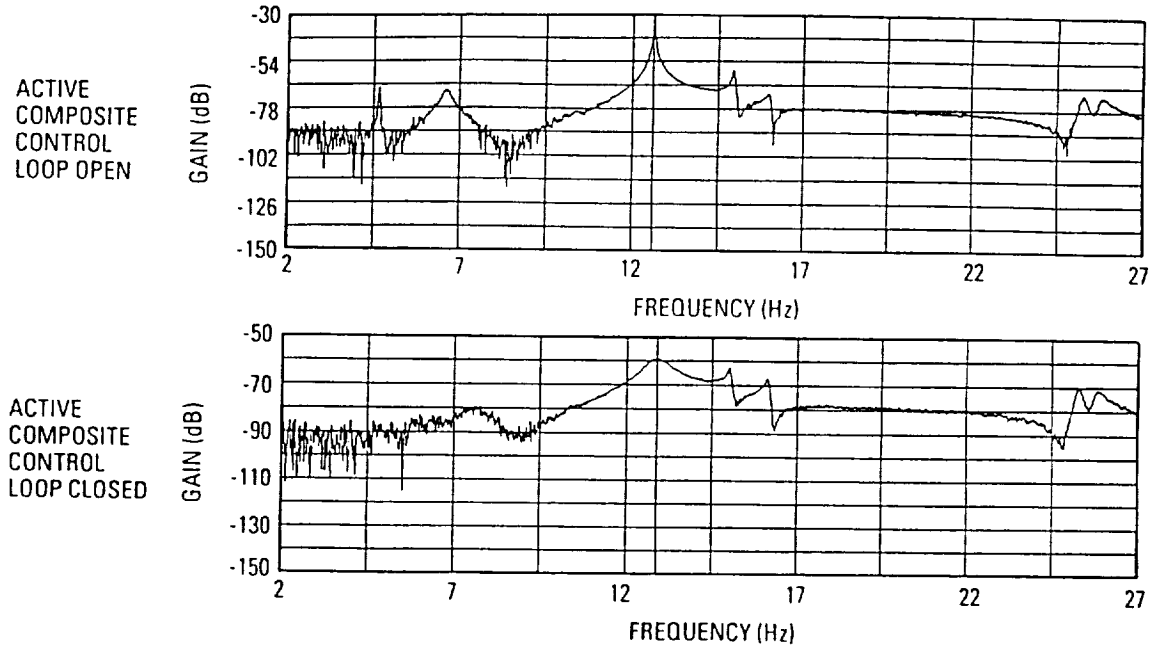

HORIZONTAL RESPONSE

Active Damping Performance (Cont.)

Undamped and damped vertical motions are shown in the following figure. Again the primary vertical, horizontal, and torsional modes have been attenuated to a significant degree. These results were generated using approximately 40 volts maximum drive to the active members and using less than 4 Watts of power consumption in both the active members and the electronics that drive them. These results demonstrate that significant amounts of system level damping can be achieved with the active members using very few struts, very little power, low voltage drive, and low order local compensators.

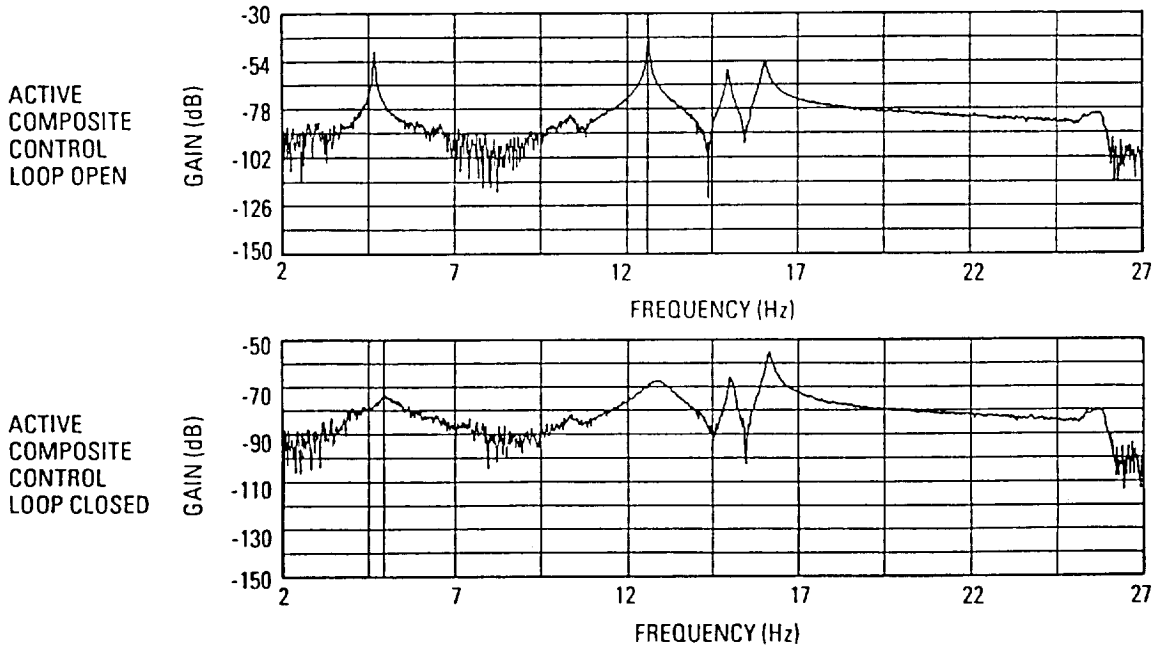

VERTICAL RESPONSE

Typical Slew Results (Open Loop)

Open loop slew results for the testbed are shown in the figure below. The figure shows the tip displacement time history during and after the maneuver. In this case, a bang-bang slew torque profile was used to generate a 16° slew. Note that the first horizontal plane mode at 6.3 Hz is excited during the slew maneuver. At the conclusion of the slew, the 1.8 Hz motor electromagnetic mode dominates the response. This performance is typical of an initial spacecraft design where rigid body modes, flexible modes, and electronic modes are present in the system. Without careful and systematic identification of the system (including the electronics drivers), the performance of the system may be far below the requirements.

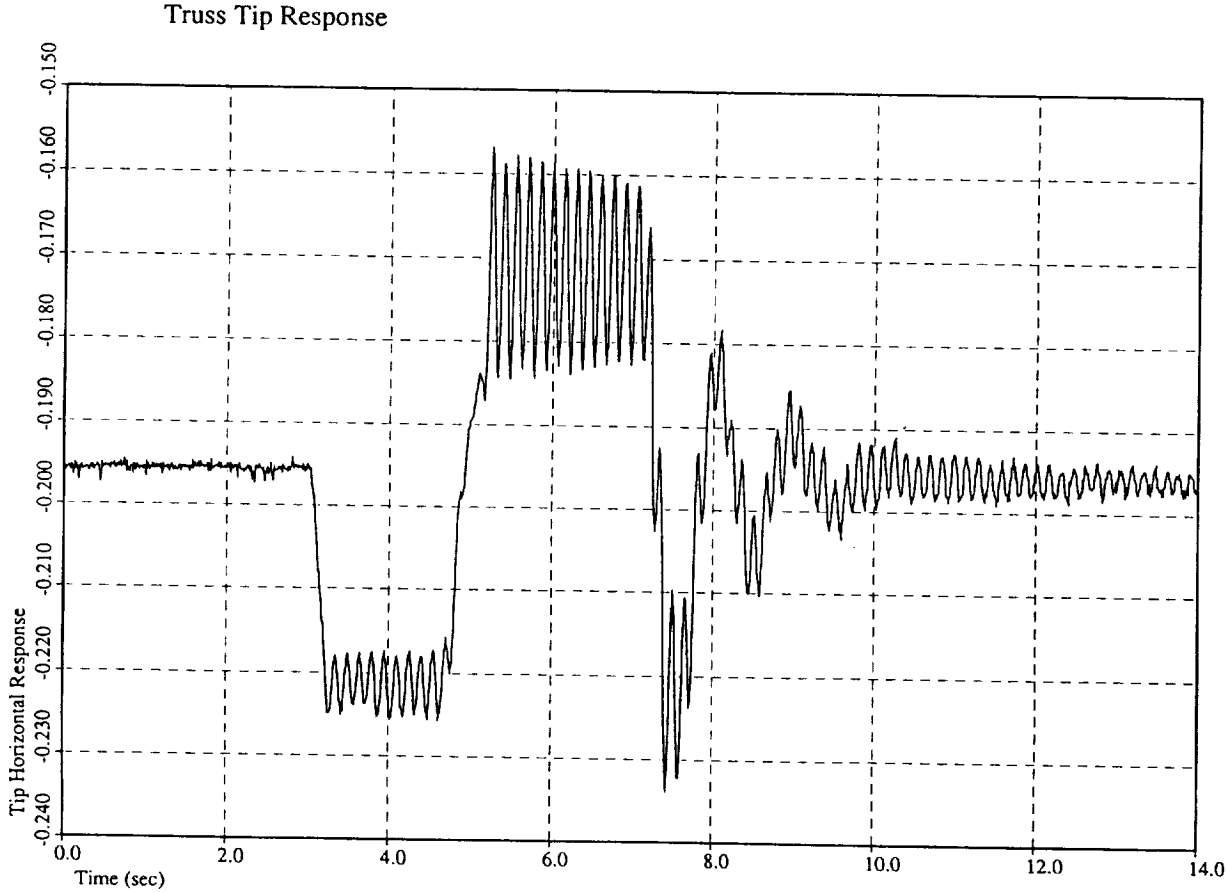

Typical Slew Results (Closed Loop)

The figure below shows the same 16° slew maneuver but with the active members running closed loop. In this case, three active members were used to damp out the first two flexible modes (i.e., the vertical bending and horizontal bending). The flexibility of the Structural Control Processor was utilized to average a number of sensors from the active members so as to separate the two modes. As a result, a moderately aggressive control system was used without destabilizing the system. The slew results show that the horizontal bending mode at 6.3 Hz is moderately damped both during and after the slew. At the conclusion of the slew, the 1.8 Hz electromagnetic mode, rather than the 6.3 Hz flexible mode, dominates the response. The participation of the 1.8 Hz mode in the settling time could be attenuated using the Inverse Dynamics torque profile design method. These results point out that the active members can run closed loop during the extreme loading of the slew maneuver and contribute to significant slew/settle performance improvements without destabilizing the system.

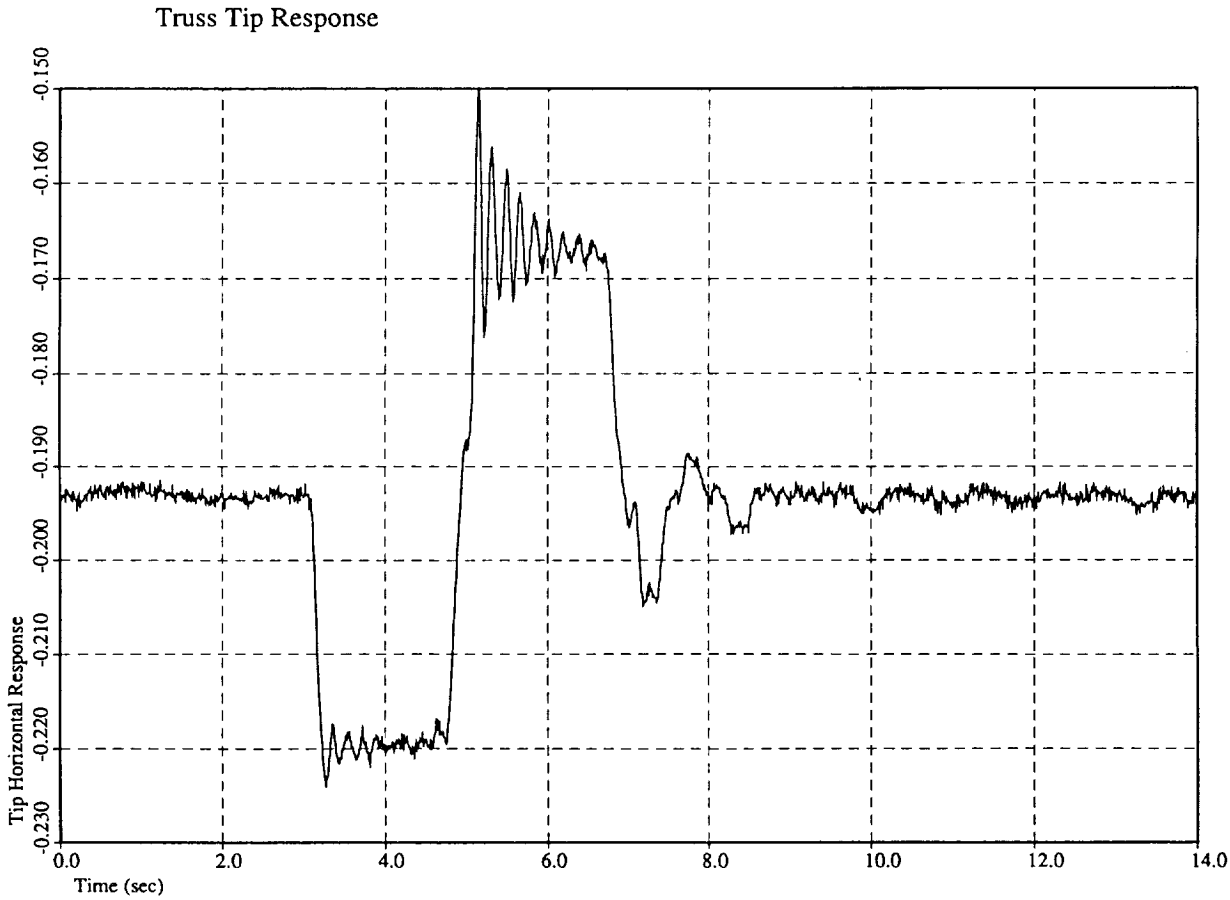

Conclusions

Both a systems and a component level approach to making flexible spacecraft more agile and precise has been presented. The systems level approach dealt with designing the slew torque profile, placing the active members in strategic locations on the truss, and with designing the overlapping bandwidth control systems. The approach at the component level dealt with active and passive members for precision damping and shape control.

The experimental results presented here have shown that significant amounts of system level damping can be achieved with the active members using very few struts, very little power, low voltage drive, and low order compensators. The performance improvements for the slew/settle problem of using the active members during and after the slew were experimentally demonstrated. All of the technologies discussed in this paper, slew torque profile design, active/passive damping, and the high speed digital processor, are mission enabling technologies for many of the next generation of precision agile spacecraft.

References

[1] Das, A. "Large Angle Maneuver Experiments in Ground-Based Laboratories", *Proceedings of the AIAA Dynamics Specialists Conference*, Long Beach, California, April 5-6, 1990, pp. 431-442.

[2] Floyd, M.A. and Vander Velde, W.E., "Verification of RCS Controller Methods for Flexible Spacecraft", Vol I & II, Air Force Rocket Propulsion Lab., Edwards AFB, California, AFRPL TR-84-092, Dec. 1984.

[3] Vander Velde, W.E. and He J., "Optimal Control of Large Space Structures Using On-Off Thrusters", *Journal of Guidance, Control, and Dynamics*, Vol. 6, No. 1, Jan-Feb, 1983., pp. 53-60.

[4] Breakwell, J.A., "Optimal Feedback Slewing of Flexible Spacecraft", *Journal of Guidance and Control*, Vol. 4, No. 5, September-October, 1981, pp. 472-479.

[5] Junkins, J.L., "Comment on Optimal Feedback Slewing of Flexible Spacecraft", *Journal of Guidance and Control*, Vol. 5, No. 3, May-June, 1982., p. 318.

[6] Bayo, E., Movaghar, R., and Medus, M., "Inverse Dynamics of a Single-Link Flexible Robot. Analytical and Experimental Results", *International Journal of Robotics and Automation*, Vol. 3, No. 3, 1988, pp. 150-157.

[7] Bayo, E., Serna, M., Papadopoulos, P., and Stubbe, J., "Inverse Dynamics and Kinematics of Multi-Link Elastic Robots. An Iterative Frequency Domain Approach", Report #UCSB-ME-87-7, Mechanical Engineering Department, University of California, Santa Barbara, Dec. 1987.

[8] Fanson, J.L., Blackwood, G.H., and Chu, C-C., "Active-Member Control of Precision Structures", *Proceedings of the AIAA/ASME/ASCE/AHS/ASC 30th Structures, Structural Dynamics, and Materials Conference*, Mobile, Alabama, April 3-5, 1989, pp. 1480-1494.

[9] Bronowicki, A.J., Mendenhall, T.L., and Manning, R.A., "Advanced Composites with Embedded Sensors and Actuators", Interim Technical Report, AL-TR-89-086, March, 1990.

[10] Betros, R. S. and Dvorsky, G. R., "Encapsulation Technique to Enhance Actuator Performance in Composite Beams", presented at the Fourth NASA/DoD Controls-Structures Interaction Technology Conference, Orlando, Florida, November 5-7, 1990.

[11] Bronowicki, A.J. and Diaz, H.P., "Analysis, Optimization, Fabrication and Test of Composite Shells with Embedded Viscoelastic Layers", *Proceedings of Damping '89*, West Palm Beach, Florida, February 8-10, 1989, pp. GCA-1-GCA-21.

[12] Anderson, E.H., Moore, D.M., Fanson, J.L., and Ealey, M.A., "Development of an Active Member Using Piezoelectric and Electrostrictive Actuation for Control of Precision Structures", *Proceedings of the AIAA/ASME/ASCE/AHS/ASC 31st Structures, Structural Dynamics, and Materials Conference*, Long Beach, California, April 2-4, 1990, pp. 2221-2233.

Average-Cost Based Robust Structural Control

Nesbitt W. Hagood *
Massachusetts Institute of Technology
Cambridge, MA 02139

Abstract

A method is presented for the synthesis of robust controllers for linear time invariant structural systems with parameterized uncertainty. The method involves minimizing quantities related to the quadratic cost ($\mathcal{H}_2$-norm) averaged over a set of systems described by real parameters such as natural frequencies and modal residues. Bounded average cost is shown to imply stability over the set of systems. Approximations for the exact average are derived and proposed as cost functionals. The properties of these approximate average cost functionals are established. The exact average and approximate average cost functionals are used to derive dynamic controllers which can provide stability robustness. The robustness properties of these controllers are demonstrated in illustrative numerical examples and tested in a simple SISO experiment on the MIT multi-point alignment testbed.

1 Introduction

The problems of stability and performance robustness in the presence of uncertain model parameters is of particular interest in the area of control of flexible structures. Uncertain stiffness, natural frequencies, damping, and actuator effectiveness all enter the model as variable parameters in the system matrices. The present work will attempt to address the robustness issues for parameterized plants by examining the properties of the quadratic ($\mathcal{H}_2$) performance of the system averaged over the set of plants given by the parameterization.

In the past, the average cost of a finite set of systems has been used to design for robustness in the face of parametric uncertainty [1], high frequency uncertainty [2], or variable flight regimes [3]. The goal is to design controllers that stabilize each model in a finite collection of plant models. This problem is called the simultaneous stabilization problem and has been treated previously in Refs. [4,5]. The cost averaged over a finite set of plants has also been used to derive full state feedback [6] and dynamic output feedback [7] compensators using parameter optimization to determine fixed-form compensator gains.

The present paper considers a quadratic performance criterion (formulated as the $\mathcal{H}_2$ system norm) averaged over a continuously parameterized set of plants controlled by a single feedback compensator. The model set is thus based on a continuous rather than discrete parameterization. This type of parameterization avoids ad hoc selection of plants to be represented in the control design and well represents the type of uncertain parameter dependence common in flexible structures. Typically

*Assistant Professor, Department of Aeronautics and Astronautics, Rm. 33-313 Tel. (617) 253-2738.

an uncertain parameter is specified by a range rather than a finite number of possible values. In addition, by considering this type of uncertainty, a link can be established between bounded average cost and simultaneous stability over the set of systems. The necessary conditions for minimization of a quadratic cost averaged over a continuously parameterized set of systems were previously derived for the static output feedback case in Ref. [8], and are here extended to the case of dynamic output feedback.

In the first section of this paper, the continuously parameterized model set and properties of the exact average cost are established. It will be shown that bounded average cost implies stability over the model set. Since it is difficult to compute the exact average cost, two approximations to it will be presented in the next section. The first approximation is based on a perturbation expansion about the nominal solution, while the second is derived from an approximation commonly used in the field of wave propagation in random media. Their properties and computation will be addressed. The derivation of these approximations to the average cost is based on operator decomposition methods which are presented in Ref. [9,10].

The second half of the paper concerns the design of controllers based on exact and approximate average cost minimization. The approach taken involves fixing the order of the compensator and optimizing over the feedback gains. This fixed-structure approach is a direct extension of the technique utilized in [6,7,11]. The controllers derived from the exact and approximate average minimization will be compared in numerical examples. In addition, an average-cost based controller will be compared to traditional LQG designs in an experimental application of the methods to control a precision optical path on the MIT multipoint alignment testbed.

2 The Average Cost

In the following sections, the average cost will be examined as a cost functional for control design. The first step in this process is to define the set of systems over which the quadratic cost ($\mathcal{H}_2$-norm) of the system is averaged. The next step is to examine the average cost for properties which will be useful in the design of stabilizing compensators.

2.1 The General Set of Systems

The concept of the model set, a set of plants parameterized in terms of real parameters, will now be introduced. Throughout the rest of this work, the standard system notation in Ref. [12] will be used. The set $\mathcal{G}_g$ of systems is parameterized as follows

$$\mathcal{G}_g = \{G_g(\alpha) \,\forall\, \alpha \in \Omega\} \tag{1}$$

where $\Omega \in \mathbb{R}^r$ is a compact region over which a distribution function, $\mu(\alpha)$, is defined. Each system is described in the state space as

$$G_g(\alpha) = \left[\begin{array}{c|cc} A(\alpha) & B_1(\alpha) & B_2(\alpha) \\ \hline C_1(\alpha) & 0 & D_{12}(\alpha) \\ C_2(\alpha) & D_{21}(\alpha) & 0 \end{array}\right] \tag{2}$$

where $A(\alpha) \in \mathbb{R}^{n\times n}$, $B_2(\alpha) \in \mathbb{R}^{n\times m}$, $C_2(\alpha) \in \mathbb{R}^{l\times n}$, $B_1(\alpha) \in \mathbb{R}^{n\times p}$, $C_1(\alpha) \in \mathbb{R}^{q\times n}$, $\alpha \in \Omega$ and the D matrices are partitioned conformally.

In addition to the assumptions implicit in the set definition, the following assumptions will be made on the system.

(i) For each $\alpha \in \Omega, (A(\alpha), B_1(\alpha))$ is stabilizable, $(C_1(\alpha), A(\alpha))$ is detectable.

(ii) For each $\alpha \in \Omega, (A(\alpha), B_2(\alpha))$ is stabilizable, $(C_2(\alpha), A(\alpha))$ is detectable.

(iii) $D_{12}^T(\alpha) \begin{bmatrix} C_1(\alpha) & D_{12}(\alpha) \end{bmatrix} = \begin{bmatrix} 0 & R(\alpha) \end{bmatrix}$, $R(\alpha) > 0 \; \forall \, \alpha \in \Omega$

(iv) $D_{21}(\alpha) \begin{bmatrix} B_1^T(\alpha) & D_{21}^T(\alpha) \end{bmatrix} = \begin{bmatrix} 0 & V(\alpha) \end{bmatrix}$, $V(\alpha) > 0 \; \forall \, \alpha \in \Omega$

(v) The set of systems, $\mathcal{G}_g$, must be simultaneously stabilizable. The conditions for simultaneously stabilizable sets of systems have been considered in Ref. [4,5].

Assumptions (i) and (ii) are made to ensure the observability and controllability of unstable modes from the controller and the disturbability and measurability of the unstable modes in the performance. Assumption (iii) implies that $C_1 x$ and $D_{12} u$ are orthogonal so that there is no cross weighting between the output and control. R is positive definite so that the weighting on z includes a nonsingular weighting on the control. Assumption (iv) is dual to (iii) and ensures the noncorrelation of the plant and sensor noise. It is equivalent to the standard conditions assumed for the Kalman filter. Assumption (v) is made to guarantee existence of the controllers derived in the next section.

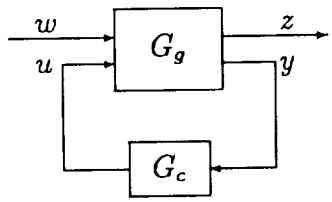

Figure 1: The Control Problem for Dynamic Output Feedback

It is useful at this point to consider the set of closed-loop systems. The control problem for each element of the model set can be illustrated by the standard block diagram shown in Figure 1. Given the set $\mathcal{G}_g$ of open loop systems and the compensator of order, n_c, with

$$G_c = \left[\begin{array}{c|c} A_c & B_c \\ \hline C_c & 0 \end{array}\right] \tag{3}$$

with input y and output u, the set of closed-loop transfer functions from w to z, $\mathcal{G}_{zw}$, can be defined. Each element of $\mathcal{G}_{zw}$ can be expressed in state space form for dynamic output feedback as:

$$\begin{aligned} G_{zw}(\alpha) &= \left[\begin{array}{cc|c} A(\alpha) & B_2(\alpha)C_c & B_1(\alpha) \\ B_cC_2(\alpha) & A_c & B_cD_{21}(\alpha) \\ \hline C_1(\alpha) & D_{12}(\alpha)C_c & 0 \end{array}\right] \\ &= \left[\begin{array}{c|c} \tilde{A}(\alpha) & \tilde{B}(\alpha) \\ \hline \tilde{C}(\alpha) & 0 \end{array}\right] \end{aligned} \tag{4}$$

where $\tilde{A}(\alpha) \in \mathbb{R}^{\tilde{n} \times \tilde{n}}$, $\tilde{B}(\alpha) \in \mathbb{R}^{\tilde{n} \times p}$, $\tilde{C}(\alpha) \in \mathbb{R}^{q \times \tilde{n}}$ are the closed-loop system matrices of order $\tilde{n} = n + n_c$.

2.2 The Average $\mathcal{H}_2$-norm as a Cost Functional

Having defined a parameterized set of systems, it is now possible to define a cost which will reflect the system parameter uncertainty. One possible approach is to look at the quadratic cost (system

$\mathcal{H}_2$-norm) averaged over set of possible systems. In this section this average cost will be defined and discussed in the context of computing the average performance of a linear time invariant system. We will start by considering the definition and properties of the exact average cost. The exact average cost is defined as the closed-loop system $\mathcal{H}_2$-norm averaged (integrated) over the model set.

$$J(G_c) = \int_\Omega \|G_{zw}(\alpha)\|_2^2 \, d\mu(\alpha) = \left\langle \|G_{zw}(\alpha)\|_2^2 \right\rangle \tag{5}$$

where $\int_\Omega \cdot \, d\mu(\alpha) = \langle \cdot \rangle$ is the averaging function.

The first property of interest is the relationship between simultaneous stability and bounded average $\mathcal{H}_2$-norm. If the exact averaged cost, Eq. (5), over the set $\mathcal{G}_{zw}$ is bounded

$$J(G_c) = \left\langle \|G_{zw}(\alpha)\|_2^2 \right\rangle < \infty \tag{6}$$

then all the parameterized closed-loop systems, $G_{zw}(\alpha)$, are asymptotically stable except for the possibility of having an isolated plant in the set with poles on the imaginary axis. In general, no system in $\mathcal{G}_{zw}$ can have eigenvalues with positive real parts.

This result provides the motivation for examining the average cost since controllers designed by minimizing the average cost will be guaranteed stable over the model set. Since at each value of α the cost is given by the solution of a Lyapunov equation, the next step in the development is to relate the averaged $\mathcal{H}_2$-norm to the averaged solution of a parameterized Lyapunov equation. This gives a possible method of calculating the average cost by calculating the average solution to a linear Lyapunov equation.

Given a specified compensator, G_c, if the parameterized closed-loop systems, $G_{zw}(\alpha)$, are stable for almost all $\alpha \in \Omega$ then

$$J(G_c) = \mathrm{tr}\left\{ \left\langle \tilde{Q}(\alpha)\tilde{C}^T(\alpha)\tilde{C}(\alpha) \right\rangle \right\} \tag{7}$$

where for each $\alpha \in \Omega$, $\tilde{Q}(\alpha)$ is the unique positive definite solution to

$$0 = \tilde{A}(\alpha)\tilde{Q}(\alpha) + \tilde{Q}(\alpha)\tilde{A}^T(\alpha) + \tilde{B}(\alpha)\tilde{B}^T(\alpha) \tag{8}$$

The exact averaged cost is difficult to calculate because of the difficulty of averaging the solution to the Lyapunov equation, Eq. (8). In most instances the solution to Eq. (8) can be obtained explicitly as a function of α, and then averaged either numerically of symbolically. There are also numerous numerical techniques for approximating the average solution such a Monte-Carlo or direct numerical integration. The computational issues will be discussed in a latter section.

3 Approximate Average Costs

In this section, explicit equations for the calculation of approximate average costs will be derived. Two types of approximations will be discussed. The first is derived from a truncation of the perturbation expansion of the solution of the parameterized Lyapunov equation, Eq. (8), about the nominal solution. The second is a more sophisticated approximation for the solution of parameterized linear operators which has been widely used in the fields of wave propagation in random media [13], and turbulence modelling. A brief presentation of the relevant work in parameterized linear operators is presented in Appendix A of reference 10.

3.1 The Structured Set of Systems

It will prove useful to define a different set of systems with more restrictive assumptions on the functional form of the parameter dependence of the system matrices. The first assumption is that only parameter uncertainties entering into the closed-loop $\tilde{A}$ matrix will be considered. This amounts to restricting the $\tilde{B}$ and $\tilde{C}$ matrices to being parameter independent. This assumption is not overly restrictive for stability robustness considerations since only uncertainties in the closed-loop A matrix affect stability. The uncertainties in the $\tilde{B}$ and $\tilde{C}$ matrices would however affect average performance. This uncertainty restriction is made primarily to enable derivation of approximations to the average cost.

The general uncertain set of systems in (2) can be specialized to a more structured set which allows less general parameter dependence. The structured set, Ω_s, of parameter vectors, α, is defined

$$\Omega = \left\{\alpha \ : \alpha \in \mathbb{R}^r, \delta_i^L \leq \alpha_i \leq \delta_i^U \ \ i = 1, \cdots, r\right\} \tag{9}$$

where δ_i^L and δ_i^U are the lower and upper bounds for the i^{th} uncertain parameter. In addition, the parameter dependence of the elements of the remaining matrices will be assumed to be linear functions of the parameters. This is a very restrictive assumption but necessary if computable approximations for the average are to be derived. If they are in fact not linear functions, then the matrices must be linearized about the nominal values of the parameters.

Once the parameter dependence has been made linear a more structured set, $\mathcal{G}_s$, of systems can be defined

$$\mathcal{G}_s = \{G_s(\alpha) \ : \alpha \in \Omega_s\} \tag{10}$$

where Ω_s is the structured set of parameter vectors and each element of $\mathcal{G}_s$ is described in the state space as

$$G_s(\alpha) = \left[\begin{array}{c|cc} A_0 + \sum_{i=1}^{r}\alpha_i A_i & B_1 & B_{2_0} + \sum_{i=1}^{r}\alpha_i B_{2_i} \\ \hline C_1 & 0 & D_{12} \\ C_{2_0} + \sum_{i=1}^{r}\alpha_i C_{2_i} & D_{21} & 0 \end{array}\right] \tag{11}$$

where for $i = 0, \ldots, r$; $A_i \in \mathbb{R}^{n\times n}, B_{2_i} \in \mathbb{R}^{n\times m}, C_{2_i} \in \mathbb{R}^{l\times n}$, and $B_1 \in \mathbb{R}^{n\times p} C_1 \in \mathbb{R}^{q\times n}$.

Just as for the general set of systems, a set of closed-loop transfer functions, denoted $\mathcal{G}_{zw}$, can be generated using the structured set of systems. This closed-loop set can be expressed is state space form for dynamic output feedback as

$$\begin{aligned} G_{zw}(\alpha) &= \left[\begin{array}{cc|c} A_0 + \sum_{i=1}^{r}\alpha_i A_i & B_{2_0}C_c + \sum_{i=1}^{r}\alpha_i B_{2_i} C_c & B_1 \\ B_c C_{2_0} + \sum_{i=1}^{r}\alpha_i B_c C_{2_i} & A_c & B_c D_{21} \\ \hline C_1 & D_{12}C_c & 0 \end{array}\right] \\ &= \left[\begin{array}{c|c} \tilde{A}_0 + \sum_{i=1}^{r}\alpha_i \tilde{A}_i & \tilde{B} \\ \hline \tilde{C} & 0 \end{array}\right] \end{aligned} \tag{12}$$

Because of the form assumed for the uncertainty, only the resulting closed-loop A matrix, $\tilde{A}(\alpha) \in \mathbb{R}^{\tilde{n}\times\tilde{n}}$, is parameter dependent and the closed-loop system is strictly proper.

3.2 Perturbation Expansion Approximation

At this point, we can begin our exposition on the perturbation expansion approximation to the exact average cost. Given a specified compensator, G_c, the perturbation approximation to the exact average cost is given by:

$$J^P(G_c) = \mathrm{tr}\left\{\left(\tilde{Q}^0 + \tilde{Q}^P\right)\tilde{C}^T\tilde{C}\right\} \tag{13}$$

where the nominal cost, $\tilde{Q}^0$, and the parameter dependent cost, $\tilde{Q}^P$, are the unique positive definite solutions to the following system of Lyapunov equations

$$0 = \tilde{A}_0\tilde{Q}^0 + \tilde{Q}^0\tilde{A}_0^T + \tilde{B}\tilde{B}^T \tag{14}$$

$$0 = \tilde{A}_0\tilde{Q}^i + \tilde{Q}^i\tilde{A}_0^T + \sigma_i\left(\tilde{A}_i\tilde{Q}^0 + \tilde{Q}^0\tilde{A}_i^T\right) \quad i = 1,\ldots,r \tag{15}$$

$$0 = \tilde{A}_0\tilde{Q}^P + \tilde{Q}^P\tilde{A}_0^T + \sum_{i=1}^{r}\sigma_i\left(\tilde{A}_i\tilde{Q}^i + \tilde{Q}^i\tilde{A}_i^T\right) \tag{16}$$

where σ_i is defined

$$\sigma_i^2 = \left\langle \alpha_i^2 \right\rangle \tag{17}$$

A detailed derivation of the perturbation expansion approximation is available in Ref. [9]. It is interesting to note that the system of Lyapunov equations presented in Eqs. (14-16) are coupled hierarchically. The nominal solution, $\tilde{Q}^0$, can first be solved using Eq. (14) and the solution substituted into each of the i equations represented by Eq. (15). The solutions for these equations, $\tilde{Q}^i$, can then be used to solve for $\tilde{Q}^P$ using Eq. (16).

The system of equations presented in Eqs. (14-16) are related to those inherent in the sensitivity system design methodology presented in Appendix A from Ref. [15]. This can be seen clearly by putting the equations for the component cost analysis in the notation used here.

$$0 = \tilde{A}_0\tilde{Q}^0 + \tilde{Q}^0\tilde{A}_0^T + \tilde{B}\tilde{B}^T \tag{18}$$

$$0 = \tilde{A}_0\tilde{Q}^i + \tilde{Q}^i\tilde{A}_0^T + \sigma_i\left(\tilde{Q}^0\tilde{A}_i^T\right) \quad i = 1,\ldots,r \tag{19}$$

$$0 = \tilde{A}_0\tilde{Q}^P + \tilde{Q}^P\tilde{A}_0^T + \sum_{i=1}^{r}\sigma_i\left(\tilde{A}_i\tilde{Q}^i + \tilde{Q}^{i^T}\tilde{A}_i^T\right) \tag{20}$$

Essentially there is only a single term omitted from (19) which is in (15).

This validates the assertion made in Ref. [15] that the sensitivity system cost is an approximation to the quadratic cost averaged over the uncertain parameters. The sensitivity system cost is essentially the average of the first three terms of a Taylor series expansion of the cost in powers of the uncertain parameters.

3.3 Bourret Approximation

An alternate approximation for the average cost can be derived based on series manipulation techniques presented in Refs. [9] and [14]. If the parameterized closed-loop systems, $G_{zw}(\alpha)$, are stable for almost all $\alpha \in \Omega$ then

$$J(G_c) \cong \mathrm{tr}\left\{\tilde{Q}^B\tilde{C}^T\tilde{C}\right\} \tag{21}$$

where $\tilde{Q}^B$ is the unique positive definite solution to the following coupled system of Lyapunov equations

$$0 = \tilde{A}_0\tilde{Q}^B + \tilde{Q}^B\tilde{A}_0^T + \tilde{B}\tilde{B}^T + \sum_{i=1}^{r}\sigma_i\left(\tilde{A}_i\tilde{Q}^i + \tilde{Q}^i\tilde{A}_i^T\right) \tag{22}$$

$$0 = \tilde{A}_0\tilde{Q}^i + \tilde{Q}^i\tilde{A}_0^T + \sigma_i\left(\tilde{A}_i\tilde{Q}^B + \tilde{Q}^B\tilde{A}_i^T\right) \quad i = 1,\ldots,r \tag{23}$$

where σ_i is defined from Eq. (17).

The system of Lyapunov equations presented in Eqs. (22-23) is very similar to the system generated by the perturbation expansion approximation. There is additional coupling occurring in Eq. (23). Instead of depending only on the nominal solution, $\tilde{Q}^0$, these equations depend on the total Bourret approximate average solution, $\tilde{Q}^B$. This coupling complicates the solution procedure but leads to a more accurate approximation.

The system of Lyapunov equations represented by Eqs. (22-23) can be solved iteratively for the Bourret approximate average, $\tilde{Q}^B$, using the nominal solution, $\tilde{Q}^0$, as the initial guess in Eq. (23). Equation (23) is then solved for $\tilde{Q}^i$ which is used in Eq. (22) to obtain a new value for $\tilde{Q}^B$. Equations (22) and (23) can also be solved using Kronecker math techniques as described in Ref. [9].

These two approximations, the perturbation expansion and the Bourret, will be used to generate robustifying controllers in the sections to come. Because they are approximations, however, controllers derived using these approximations will not necessarily guarantee stability over the design set. Thus *a priori* guaranteed stability is sacrificed when using the approximations. The approximations are however much easier to calculate than the exact average cost, especially for systems with large numbers of uncertainties or high order. For such systems, the exact average cost is essentially uncomputable and the approximations must be used to derive controllers which increase robustness to parameter variations. These cost equations will now be used to develop parameter robust control strategies.

4 Dynamic Compensation

In this section three dynamic output feedback problems will be investigated. The first is the minimization of the exact average $\mathcal{H}_2$-norm; the second is the minimization of the perturbation expansion approximization to the exact average; and the third is the minimization of the Bourret approximation to the exact average. The general technique will be to find the controller parameters which minimize quantities related to the exact average cost of the closed loop systems. This will be accomplished by first deriving necessary conditions of optimality and then using these in a numerical minimization scheme on the controller parameters. The derivations will begin with the exact average cost minimization since it is the basis of the approximation based cost minimization problems.

4.1 Exact Average Cost Minimization

In this section the formulation of the necessary conditions for the minimization of the exact average cost will be presented. The first step is to define the minimization problem for the exact average cost.

Problem 4.1 (Exact Average Cost Minimization Problem) *Given a set $\mathcal{G}_g$ or $\mathcal{G}_s$ of systems, determine the dynamic compensator or order, n_c,*

$$G_c = \left[\begin{array}{c|c} A_c & B_c \\ \hline C_c & 0 \end{array}\right] \tag{24}$$

which minimizes the the closed-loop $\mathcal{H}_2$-norm averaged over the model set.

$$J(G_c) = \left\langle \|G_{zw}(\alpha)\|_2^2 \right\rangle \tag{25}$$

In Section 2.2 the exact average cost was shown to be equivalent to

$$\mathcal{J}^E(G_c) = \mathrm{tr}\left\{ \left\langle \tilde{Q}(\alpha)\tilde{C}^T(\alpha)\tilde{C}(\alpha) \right\rangle \right\} = J(G_c) \tag{26}$$

where $\tilde{Q}(\alpha)$ is given by the solution of

$$0 = \tilde{A}(\alpha)\tilde{Q}(\alpha) + \tilde{Q}(\alpha)\tilde{A}^T(\alpha) + \tilde{B}(\alpha)\tilde{B}^T(\alpha) \tag{27}$$

for each $\alpha \in \Omega$.

The first step in deriving necessary conditions is to append Eq. (27) to the cost using a parameter dependent, symmetric matrix of Lagrange multipliers, $\tilde{P}(\alpha) \in \mathbb{R}^{\tilde{n}\times\tilde{n}}$. The matrix of Lagrange multipliers must be parameter dependent because the appended equations are parameter dependent. The appended cost becomes

$$\begin{aligned} \mathcal{J}^E(G_c) &= \mathrm{tr}\left\{ \left\langle \tilde{Q}(\alpha)\tilde{C}^T(\alpha)\tilde{C}(\alpha) \right\rangle \right\} \\ &+ \mathrm{tr}\left\{ \left\langle \left[\tilde{A}(\alpha)\tilde{Q}(\alpha) + \tilde{Q}(\alpha)\tilde{A}^T(\alpha) + \tilde{B}(\alpha)\tilde{B}^T(\alpha) \right] \tilde{P}(\alpha) \right\rangle \right\} \end{aligned} \tag{28}$$

where $\tilde{A}(\alpha)$, $\tilde{B}(\alpha)$, and $\tilde{C}(\alpha)$ are defined in Eq. (2). The necessary conditions for minimization of the exact average cost can now be stated by taking the derivatives with respect to G_c, $\tilde{P}(\alpha)$, and $\tilde{Q}(\alpha)$. An explanation of matrix derivatives can be found in Ref. [9] [16].

Suppose G_c, the dynamic compensator of order, n_c, defined in Eq. (24) solves the exact average cost minimization problem (4.1); then there exist matrices, $\tilde{Q}(\alpha)$ and $\tilde{P}(\alpha) \geq 0 \in \mathbb{R}^{\tilde{n}\times\tilde{n}}$ such that

$$0 = \left\langle \tilde{P}_{21}(\alpha)\tilde{Q}_{12}(\alpha) + \tilde{P}_{22}(\alpha)\tilde{Q}_{22}(\alpha) \right\rangle \tag{29}$$

$$\begin{aligned} 0 &= \left\langle \tilde{P}_{22}(\alpha)B_cD_{21}(\alpha)D_{21}^T(\alpha) \right\rangle \\ &+ \left\langle \tilde{P}_{21}(\alpha)\tilde{Q}_{11}(\alpha)C_2^T(\alpha) + \tilde{P}_{22}(\alpha)\tilde{Q}_{21}(\alpha)C_2^T(\alpha) \right\rangle \end{aligned} \tag{30}$$

$$\begin{aligned} 0 &= \left\langle D_{12}^T(\alpha)D_{12}(\alpha)C_c\tilde{Q}_{22}(\alpha) \right\rangle \\ &+ \left\langle B_2^T(\alpha)\tilde{P}_{11}(\alpha)\tilde{Q}_{12}(\alpha) + B_2^T(\alpha)\tilde{P}_{12}(\alpha)\tilde{Q}_{22}(\alpha) \right\rangle \end{aligned} \tag{31}$$

where $\tilde{Q}(\alpha)$ satisfies the parameterized Lyapunov equation

$$0 = \tilde{A}(\alpha)\tilde{Q}(\alpha) + \tilde{Q}(\alpha)\tilde{A}^T(\alpha) + \tilde{B}(\alpha)\tilde{B}^T(\alpha) \tag{32}$$

and $\tilde{P}(\alpha)$ satisfies the Adjoint Lyapunov equation

$$0 = \tilde{A}^T(\alpha)\tilde{P}(\alpha) + \tilde{P}(\alpha)\tilde{A}(\alpha) + \tilde{C}^T(\alpha)\tilde{C}(\alpha) \tag{33}$$

and $\tilde{Q}(\alpha)$ and $\tilde{P}(\alpha)$ are partitioned

$$\tilde{Q}(\alpha) = \begin{bmatrix} \tilde{Q}_{11}(\alpha) & \tilde{Q}_{12}(\alpha) \\ \tilde{Q}_{21}(\alpha) & \tilde{Q}_{22}(\alpha) \end{bmatrix}, \quad \tilde{P}(\alpha) = \begin{bmatrix} \tilde{P}_{11}(\alpha) & \tilde{P}_{12}(\alpha) \\ \tilde{P}_{21}(\alpha) & \tilde{P}_{22}(\alpha) \end{bmatrix} \tag{34}$$

with $\tilde{Q}_{11}$, $\tilde{P}_{11} \in \mathbb{R}^{n\times n}$, and $\tilde{Q}_{22}$, $\tilde{P}_{22} \in \mathbb{R}^{n_c\times n_c}$.

The result is a consequence of the differentiation of the cost, Eq. (28), with respect to A_c, B_c, C_c, $\tilde{P}(\alpha)$, and $\tilde{Q}(\alpha)$. Note that the necessary conditions that result from differentiation of the cost with respect to $\tilde{Q}(\alpha)$ and $\tilde{P}(\alpha)$, (32) and (33) respectively, are parameter dependent because $\tilde{Q}(\alpha)$ and $\tilde{P}(\alpha)$ are parameter dependent. The traditional LQG results are recovered in the case of no uncertainty and $n_c = n$.

The difficulty inherent in Eqs. (29)-(31) for the optimal gains is that that they involve the average of the product of the solution of two parameter dependent Lyapunov equations, $\tilde{Q}(\alpha)$ and $\tilde{P}(\alpha)$. These matrices are only given as implicit functions of α in Equations (32) and (33). Only in the simplest of cases can the average of the product be solved for exactly. The solution can be obtained numerically by Monte-Carlo techniques, averaged numerically, or the explicit α dependence can be found by symbolic manipulations and the expressions averaged numerically or symbolically. All of these techniques are computationally intensive. In the next sections, the Perturbation Expansion approximation and Bourret approximation to the average cost will be minimized in an attempt to approximate the optimal solution by minimizing approximate but calculable expressions for the cost.

4.2 Approximate Average Cost Minimization

In this section the formulation of the necessary conditions for the minimization of the perturbation expansion approximate cost and the Bourret approximate cost will be discussed. The procedure is essentially the same as for the exact average cost only for the approximate costs the averages can be performed explicitly. The first step is to define the minimization problem. For the perturbation expansion approximation, the problem is to determine the dynamic compensator of order, n_c, defined in Eq. (24), which minimizes

$$\mathcal{J}^P(G_c) = \mathrm{tr}\left\{\left(\tilde{Q}^0 + \tilde{Q}^P\right)\tilde{C}^T\tilde{C}\right\} \tag{35}$$

where the nominal cost, $\tilde{Q}^0$, and the parameter dependent cost, $\tilde{Q}^P$, are the unique positive definite solutions to the system of Lyapunov equations described in Eqs. (14)-(16).

As for the Exact Average, the first step in deriving the necessary conditions for the Minimization Problem is to append Eqs. (14)-(16) to the cost using parameter independent, symmetric matrices of Lagrange multipliers, $\tilde{P}^0$, $\tilde{P}^P$, and $\tilde{P}^i$, $i = 1 \ldots r \in \mathbb{R}^{2n\times 2n}$.

$$\mathcal{J}(G_c) = \mathrm{tr}\left\{\left(\tilde{Q}^0 + \tilde{Q}^P\right)\tilde{C}^T\tilde{C}\right\} \tag{36}$$

$$+\ \mathrm{tr}\left\{\left[\tilde{A}_0\tilde{Q}^0 + \tilde{Q}^0\tilde{A}_0^T + \tilde{B}\tilde{B}^T\right]\tilde{P}^0\right\} \tag{37}$$

$$+\ \mathrm{tr}\left\{\sum_{i=1}^{r}\left[\tilde{A}_0\tilde{Q}^i + \tilde{Q}^i\tilde{A}_0^T + \sigma_i\left(\tilde{A}_i\tilde{Q}^0 + \tilde{Q}^0\tilde{A}_i^T\right)\right]\tilde{P}^i\right\} \tag{38}$$

$$+\ \mathrm{tr}\left\{\left[\tilde{A}_0\tilde{Q}^P + \tilde{Q}^P\tilde{A}_0^T + \sum_{i=1}^{r}\sigma_i\left(\tilde{A}_i\tilde{Q}^i + \tilde{Q}^i\tilde{A}_i^T\right)\right]\tilde{P}^P\right\} \tag{39}$$

where $\tilde{A}$, $\tilde{B}$, and $\tilde{C}$ are defined in Eq. (12). Taking the derivatives with respect to $G_c, \tilde{P}^0$, $\tilde{P}^P$, $\tilde{P}^i$ and $\tilde{Q}^0$, $\tilde{Q}^P$, $\tilde{Q}^i$ gives the necessary conditions for minimization of the perturbation expansion approximation to the exact average cost. They can be found in Refs. [9] or [14]. The key difference

between these necessary conditions and those of the exact average cost minimization is that these equations are parameter independent (no longer parameterized) and thus easier to solve.

Similar to the perturbation expansion minimization, the problem for the Bourret approximate average cost compensator design is to determine the dynamic compensator of order, n_c, defined in Eq. (24), which minimizes

$$\mathcal{J}^B(G_c) = \mathrm{tr}\left\{\tilde{Q}^B \tilde{C}^T \tilde{C}\right\} \tag{40}$$

where $\tilde{Q}^B$ is the unique positive definite solution to the system of coupled Lyapunov equations described in Eqs. (22)-(23).

As before, the first step in deriving the necessary condition is to append Eqs. (22) and (23) to the cost using parameter independent, symmetric matrices of Lagrange multipliers, $\tilde{P}^B$ and $\tilde{P}^i$, $i = 1 \ldots r \in \mathbb{R}^{\tilde{n} \times \tilde{n}}$. The equations have a form similar to (36). Taking the derivatives with respect to $G_c, \tilde{P}^B$, $\tilde{P}^i$ and $\tilde{Q}^B$, $\tilde{Q}^i$ gives the necessary conditions for minimization of the Bourret approximation to the exact average. They can be found in Refs. [9] or [14]. These necesary conditions are used for gradient information in a numerical minimization scheme described in the next section.

5 Controller Computation

In this section the techniques used to compute controllers based on the three cost functionals will be presented. The general technique used for computing the minimum cost controllers is parameter optimization. Since the controllers are fixed-form, the optimal controller can be found by minimizing the cost with respect to each of the parameters in the controller matrices. It should be noted that the parameter minimization is non-convex and the resulting minima can only be considered local minima although in practice they appear to be global. The gradient of the cost with respect to the controller parameters is given by the necessary conditions derived in Refs. [9] or [14]. These gradients are used in a standard Quasi-Newton numerical optimization routine to find the optimal controllers.

Since the minimizations are non-convex, the solution can be a function of the initial guess used in the optimization. This initial guess must also be a stabilizing compensator. This can be difficult to find for large values of uncertainty. These problems are overcome by first assuming little or no uncertainty and using the resulting controller as a starting point for calculating controllers at successively larger values of uncertainty. Standard LQG techniques can be used to find stabilizing compensators for systems with no uncertainty. The amount of uncertainty used in the design is gradually increased until the desired amount is reached. This solution technique is known as homotopic continuation. The general algorithm used to compute the controllers can be written.

(i) **Initialize** the homotopy with a stabilizing compensator for the system with no uncertainty.

(ii) **Increase** the amount of the uncertainty used in the design.

(iii) **Minimize** the cost to derive a new compensator using a Broyden-Fletcher-Goldfarb-Shanno (BFGS) quasi-Newton scheme.

(iv) **Evaluate** the resulting compensator to check the homotopy termination conditions.

(v) **Iterate** on ii.

For dynamic full order compensation, the LQG compensator can be used. If the compensator is of reduced order, optimal projection or a heuristic compensator reduction procedure can be used to find stabilizing compensators. A small amount of uncertainty is then introduced into the problem

and a new controller is found by minimization starting from the initial guess. If the amount of uncertainty is increased too much in the step the initial guess will not be near the new optimal solution and may be difficult to locate. Taking too small of a step is computationally wasteful. If the compensator is optimal for a given amount of uncertainty, then the gradient is exactly zero since the necessary conditions are satisfied. As the uncertainty is increased, the previous optimal solution no longer satisfies the necessary conditions for the new problem and thus the magnitude of the gradient increases. A tolerance can be placed on how large the gradient is allowed to grow before the cost is reminimized. When the norm of the gradient exceeds the tolerance, the cost is reminimized to find a new compensator which satisfies the necessary conditions.

The minimization step is relatively straightforward. The appropriate cost is minimized with respect to the controller parameters using the necessary conditions for gradient information. The minimization technique used to derive the controllers presented in the next section was the popular BFGS quasi-Newton method with a modification to constrain the parameter minimization to the set of stabilizing compensators.

The computation of the cost and gradient is problem dependent. The cost is usually given by either the average value of a parameterized Lyapunov equation in the exact average case or by the solution of a set of coupled Lyapunov equations as for the approximation cost functionals. The gradient of the cost with respect to the compensator parameters is usually a function of the compensator parameters as well as the solution to a coupled set of Lyapunov equations.

The exact average cost is calculated by numerical integration over the parameter domain using a 32 point Gaussian quadrature. If more than three uncertain parameters must be retained in the design, then Monte-Carlo integration is the only feasible method of computing the averages needed for the cost and gradient calculations. The gradient functions also require averages of the product of the solutions of the parameterized Lyapunov equation and its adjoint. For speed, these averages can be computed at the same time as the average cost. The solution of the approximations functions are discussed in Refs. [9,10]. The perturbation expansion approximate average is computed by utilizing a standard Lyapunov solver and solving the equations hierarchically. The Bourret approximation is solved iteratively.

6 Numerical Examples

The three average-related cost functionals will be compared on some simple examples. To streamline discussion in these sections it is convenient to define a series of acronyms for the various designs.

EAM Exact Average Minimization

PEAM Perturbation Expansion Approximation Minimization

BAM Bourret Approximation Minimization

These acronyms will be used extensively in subsequent sections. It should be noted that the PEAM design is essentially equivalent the the sensitivity system cost minimization presented in [17]. To simplify discussion of the examples and compare with previous work, an LQG problem statement will be developed and shown to be equivalent to the system norm cost formalism.

6.1 LQG Problem Statement

To begin the comparison between the LQG problem statement and the system norm formalism, the system dynamics can be defined by

$$\dot{x}(t) = Ax(t) + Bu(t) + L\xi(t) \tag{41}$$

$$y(t) = Cx(t) + \theta(t) \tag{42}$$

where $x(t) \in \mathbb{R}^n$, $u(t) \in \mathbb{R}^m$, $y(t) \in \mathbb{R}^l$. The two noise input vectors, $\xi(t) \in \mathbb{R}^q$, the process noise, and $\theta(t) \in \mathbb{R}^p$, the sensor noise, are independent, zero mean, Gaussian white noise processes with constant intensity matrices, Ξ and Θ, respectively. The LQG cost functional which is to be minimized is defined by

$$J_{LQG} = E\left\{\lim_{T\to\infty}\left(\frac{1}{T}\int_0^T x^T(t)Qx(t) + u^T(t)Ru(t)\ dt\right)\right\} \tag{43}$$

which involves a positive semi-definite state weighting, $Q \in \mathbb{R}^{n\times n}$, and a positive definite control weighting, $R \in \mathbb{R}^{m\times m}$.

The system upon which the controller is evaluated is different from the system used in the controller design. The two systems can be called the *evaluation* and *design* systems, respectively. The design system is typically the evaluation system with weighted inputs and outputs. The evaluation model can be expressed in the standard system notation by first defining the output vector, z, and the disturbance vector, w, used in [12]. Let

$$w(t) = \begin{bmatrix} \xi(t) \\ \theta(t) \end{bmatrix} \quad z(t) = \begin{bmatrix} x(t) \\ u(t) \end{bmatrix} \tag{44}$$

The evaluation system can now be written

$$G_{eval} = \left[\begin{array}{c|cc} A & L & 0 & B \\ \hline \begin{bmatrix} I \\ 0 \end{bmatrix} & \begin{matrix} 0 & 0 \\ 0 & 0 \end{matrix} & & \begin{bmatrix} 0 \\ I \end{bmatrix} \\ C & 0 & I & 0 \end{array}\right] \tag{45}$$

To derive the design model, the relative magnitudes of the input disturbances and output variables are explicitly weighted using the noise intensities, Ξ and Θ, and the output weights, Q and R, used in the quadratic cost, (43). The design plant has the form:

$$G_{des} = \left[\begin{array}{c|cc} A & L\Xi^{1/2} & 0 & B \\ \hline \begin{bmatrix} Q^{1/2} \\ 0 \end{bmatrix} & \begin{matrix} 0 & 0 \\ 0 & 0 \end{matrix} & & \begin{bmatrix} 0 \\ R^{1/2} \end{bmatrix} \\ C & 0 & \Theta^{1/2} & 0 \end{array}\right] \tag{46}$$

Given this definition of the design plant, the $\mathcal{H}_2$-norm of the design system is equivalent to the quadratic cost; that is

$$\|G_{des}\|_2^2 = J_{LQG} \tag{47}$$

and thus the problems of finding the compensator, G_c, to minimize either the average $\mathcal{H}_2$-norm of the design plant or the average quadratic cost defined in (43) are equivalent.

6.2 The Robust-Control Benchmark Problem

In this section, dynamic output feedback compensators based on the techniques presented in the preceding sections will be designed for the robust-control benchmark problem presented in Ref. [18]. The problem considered is a two-mass/spring system shown in Figure 2, which is a generic model of an uncertain dynamic system with a noncolocated sensor and actuator. The uncertainty stems from an

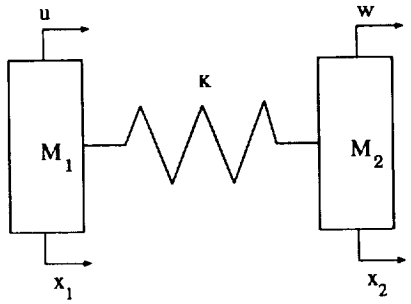

Figure 2: The Robust-Control Benchmark Problem

uncertain spring connecting the two masses. From Ref. [18] the system matrices can be represented in state space form using the notation presented in Section 6.1 as

$$\mathrm{A} = \begin{bmatrix} 0 & 0 & 1 & 0 \\ 0 & 0 & 0 & 1 \\ -k/m_1 & k/m_1 & 0 & 0 \\ k/m_2 & -k/m_2 & 0 & 0 \end{bmatrix} \quad \mathrm{B} = \begin{bmatrix} 0 \\ 0 \\ 1/m_1 \\ 0 \end{bmatrix} \quad \mathrm{L} = \begin{bmatrix} 0 \\ 0 \\ 0 \\ 1/m_2 \end{bmatrix} \tag{48}$$

$$C = \begin{bmatrix} 0 & 1 & 0 & 0 \end{bmatrix} \tag{49}$$

Within the system described in Eqs. (48)-(49), the uncertain spring, k, is decomposed into a nominal value and a bounded variable parameter

$$k = k_0 + \tilde{k}, \quad k_0 = 1.25, \quad |\tilde{k}| \leq \delta_k = 0.75 \tag{50}$$

Thus the parameter design bound, $\delta_k = 0.75$, allows the stiffness to vary in the range from 0.5 to 2. With this factorization the set of systems can be defined in the notation given for the structured set of systems, Eq. 11. In particular, only the A matrix is uncertain. It can be factored as

$$A(\tilde{k}, \tilde{c}) = A_0 + \tilde{k} A_k \tag{51}$$

$$A_0 = \begin{bmatrix} 0 & 0 & 1 & 0 \\ 0 & 0 & 0 & 1 \\ -1.25 & 1.25 & 0 & 0 \\ 1.25 & -1.25 & 0 & 0 \end{bmatrix} \quad A_k = \begin{bmatrix} 0 & 0 & 0 & 0 \\ 0 & 0 & 0 & 0 \\ -1 & 1 & 0 & 0 \\ 1 & -1 & 0 & 0 \end{bmatrix}$$

With this factorization, the robust control design methodologies presented in the previous sections can be applied. The LQG problem statement presented in Section 6.1 which is based on the standard LQG design weights will be adopted. In this method the designer selects the state weighting matrix, Q, the control weighting matrix, R, and the sensor and plant noise intensity matrices, Θ and Ξ, respectively. The evaluation plant is modified as in Eq. (46) to give the design plant. The control is designed on the design plant and implemented on the evaluation plant. The weighting values used in the design are

$$Q(2,2) = 1 \quad R = 0.0005 \tag{52}$$

Thus only the position of the second mass is penalized. The control weighting was chosen to be low to examine high performance designs which meet a settling time requirement of 15 seconds as specified in Ref. [18]. In addition to the state and control penalties, the plant noise and the plant noise intensity were assumed to be

$$\Xi = 1, \quad \Theta = 0.0005 \tag{53}$$

The signal noise intensity was chosen low to give a high gain Kalman filter in the LQG design.

Figure 3 compares the closed-loop $\mathcal{H}_2$-norm resulting from the various designs using $\delta_k = 0.4$ as a function of the deviation from the nominal spring constant, $\tilde{k}$. Thus the controllers were designed to accommodate a stiffness variation, $0.85 \leq k \leq 1.65$. Instability regions are indicated by an unbounded closed-loop $\mathcal{H}_2$-norm. The LQG results clearly indicate the well-known loss of robustness associated with high-gain LQG solutions. The LQG cost curve achieves a minimum at the nominal spring constant, $k = 1.25$, but tolerates almost no lower values of k. The stability region is increased by the PEAM and BAM designs at the cost of increasing the nominal system closed-loop $\mathcal{H}_2$-norm. Although both the PEAM and the BAM designs increase robustness they do not achieve stability throughout the whole design set, $-0.4 \leq \tilde{k} \leq 0.4$. Of the approximate methods, the Bourret approximation more nearly achieves stability throughout the set. The EAM design does achieve stability throughout the set as was indicated by the analysis. The cost of this stability guarantee is loss of nominal system performance.

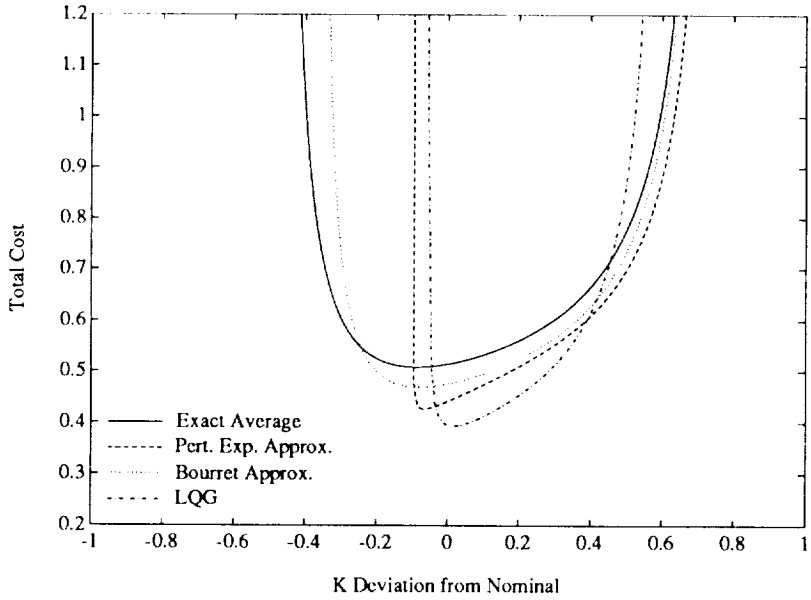

Figure 3: System Closed-Loop $\mathcal{H}_2$-norm (Quadratic Cost) as a Function of the Deviation about the Nominal Spring Constant, $\tilde{k}$, for Controllers Designed Using $\delta_k = 0.4$.

The actual range over which a given design is stable can be plotted as a function of the parameter range used in the design. The parameter range over which a particular design maintains stability is characterized by the *achieved bound* which is chosen to be the lower limit of the stability range. The parameter range actually considered in the design is characterized by the *design bound*, denoted δ_k, which specifies the upper and lower limit of $\tilde{k}$. Figure 4 shows the achieved lower $\tilde{k}$ stability bounds as a function of the design bound, δ_k. This plot is thus a measure of conservatism in the design. A conservative design would achieve stability over a much larger set of parameters actually used in its design. With no design uncertainty all five techniques converge to the stability range achieved by the standard LQG design ($|\tilde{k}| \leq 0.06$). As the uncertainty used in the design process is increased the achieved robustness is also increased. The EAM design always increases robustness enough to guarantee stability throughout the design set but the design is very nonconservative. The approximate cost minimization techniques don't provide this guarantee. The BAM design does come closer to guaranteeing stability than the PEAM design which does particularly poorly.

In Figure 5, the closed-loop $\mathcal{H}_2$-norm of the nominal plant ($k = 1.25$) is examined as a function

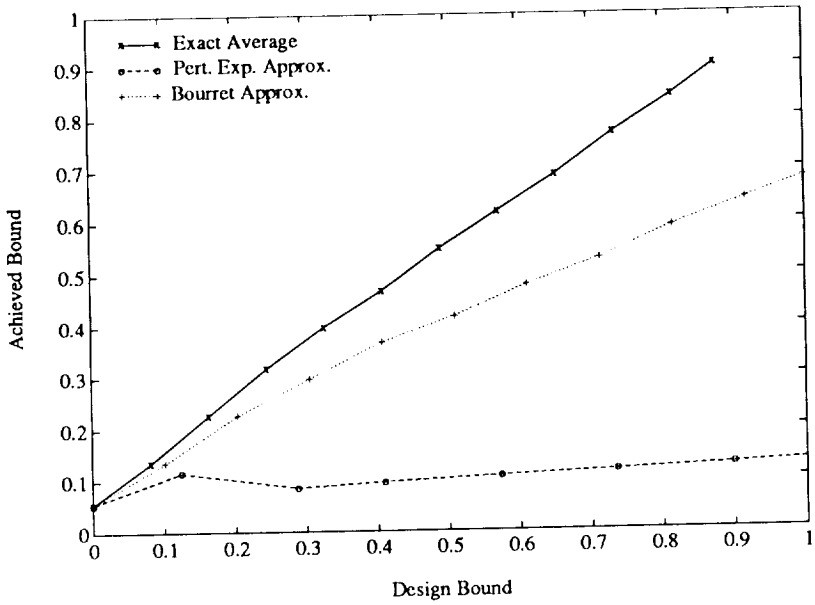

Figure 4: Achieved Closed-Loop Stability Bounds as a Function of the Design Bound, δ_k

of the achieved stability bound. A robust controller design methodology which sacrifices the least nominal performance for a given level of robustness can be called the most efficient. Figure 5 thus presents the relative efficiency of the three design techniques. The closed-loop cost ($\mathcal{H}_2$-norm) is also shown decomposed into the component associated with the output weighting, called the output cost, and the component associated with the control weighting, called the control cost. The EAM design achieves a given level of robustness with the least increase in the nominal cost and is therefore considered the most efficient design. The BAM design also has good efficiency, almost matching that of the EAM design. The PEAM design is clearly the least efficient of the three. It cannot achieve a stability bound of more than 0.2.

6.3 The Cannon-Rosenthal Problem

In this section, a four mass/spring/damper problem will be examined which was presented first in [19]. The layout of the system is shown in Fig. 6. The system consists of four masses connected by springs and viscous dampers. The uncertainty enters into the problem through a variable body-1 mass. The system can be represented in state space using the notation presented in Section 6.1 as

$$A = \begin{bmatrix} 0_{4\times4} & I_{4\times4} \\ A(k) & A(c) \end{bmatrix} \tag{54}$$

$$\mathrm{A(x)} = \begin{bmatrix} -x/m_1 & x/m_1 & 0 & 0 \\ x/m_2 & -2x/m_2 & x/m_2 & 0 \\ 0 & x/m_3 & -2x/m_3 & x/m_3 \\ 0 & 0 & x/m_4 & -x/m_4 \end{bmatrix} \tag{55}$$

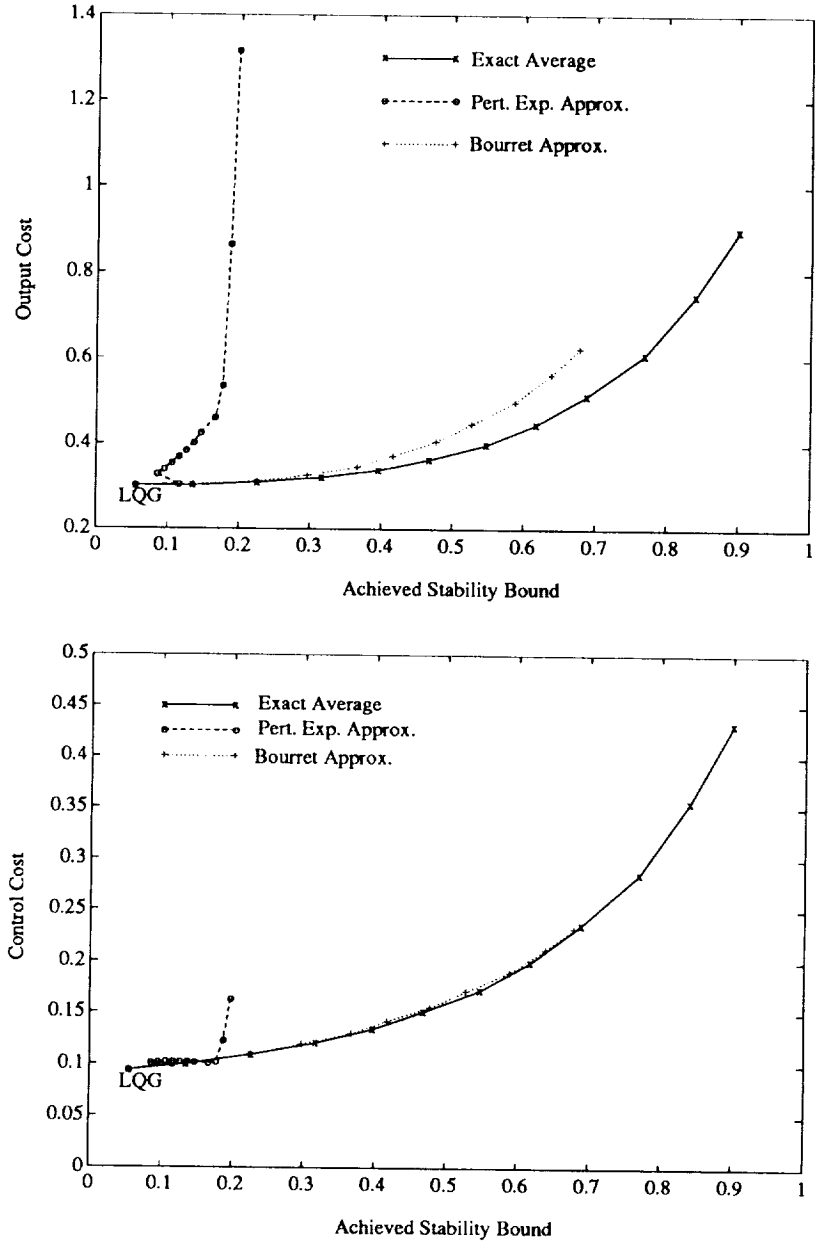

Figure 5: Output Cost and Control Cost as a Function of the Achieved Stability Bound.

$$\mathrm{L} = \begin{bmatrix} 0 \\ 0 \\ 0 \\ 0 \\ 0 \\ 0 \\ 0 \\ 1/m_4 \end{bmatrix}, \quad \mathrm{B} = \begin{bmatrix} 0 \\ 0 \\ 0 \\ 0 \\ 0 \\ 1/m_2 \\ 0 \\ 0 \end{bmatrix}, \quad \mathrm{C} = [\,0 \;\; 0 \;\; 0 \;\; 1 \;\; 0 \;\; 0 \;\; 0 \;\; 0\,] \tag{56}$$

For this problem the nominal values of the springs, dampers and masses were chosen to be $k = 1$, $c = .01$, $m_2 = m_3 = m_4 = 1$, and $m_1 = 0.5$. Within the system described in Eqs. (54)-(56), the

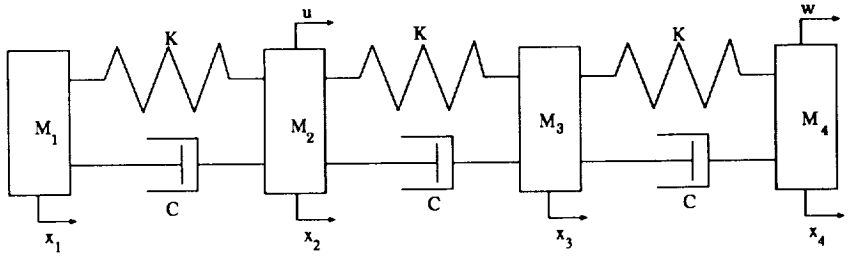

Figure 6: The Cannon-Rosenthal Problem

uncertain mass, m_1, enters into the equations through its inverse. The inverse of the mass will therefore be used as the uncertain parameter called $\tilde{m}$. If the nominal value of m_1 is 0.5, then the uncertainty can be represented as

$$1/m_1 = 1/m_{1_0} + \tilde{m}, \quad m_{1_0} = 0.5, \quad |\tilde{m}| \leq \delta_m \tag{57}$$

Thus m_1 varies from 1 to 0.25 as $\tilde{m}$ varies from -1 to 2. Only the A matrix is uncertain. It can be decomposed as

$$A(\tilde{m}) = A_0 + \tilde{m} A_m$$

in a manner analogous to the factorization for the uncertain spring in the robust-control benchmark problem. This problem was considered because of a pole-zero flip caused by the uncertain mass. In addition to changing the natural frequencies of all of the modes, as the mass is decreased from its nominal value of 0.5 to 0.25, an undamped zero between the first and second modes moves to between the second and third modes. This type of uncertainty is especially difficult to deal with since in effect the phase of the second mode can vary by ± 180 degrees between elements of the model set. This pole-zero flip makes the robust control design problem difficult. In addition if there is little damping, then the system effectively becomes uncontrollable or unobservable when the pole and zero cancel.

The robust control design methodologies presented in the previous sections can be applied to this problem. Just as in the Robust Control Benchmark Problem, the method of weighting the system that was presented in Section 6.1 which is based on the standard LQG design weights will be used for the control design. The evaluation plant given in Eqs. (54)-(56) is modified as in Eq. (46) to give the design plant. The control is designed on the design plant and implemented on the evaluation plant. Only the position of the fourth mass was penalized. The weighting values used in the design are

$$Q(4,4) = 1, \quad R = 0.05 \tag{58}$$

In addition to the state and control penalties, the plant noise and the plant noise intensity were assumed to be

$$\Xi = 1, \quad \Theta = 0.05 \tag{59}$$

This choice of penalties makes the LQG controller very sensitive to m_1 variation and thus presents a challenging robustness problem for the average-based methods.

The robustness properties of the control designs are compared to those of the standard LQG design in following discussions. Figure 7 compares the closed-loop $\mathcal{H}_2$-norm resulting from the various designs using $\delta_m = 0.1$ as a function of the deviation, $\tilde{m}$, from the nominal system mass. Thus as $\tilde{m}$ varies in the range, $-0.1 \leq \tilde{m} \leq 0.1$, m_1 varies in the range, $2.5 \geq m_1 \geq 1.6$. Instability regions are indicated by unbounded closed-loop $\mathcal{H}_2$-norm. The designs can thus be considered stable inside the region described by the upper and lower asymptotes. These asymptotes will be called the upper and lower achieved stability bounds for the particular problem.

The LQG results clearly indicate the well-known loss of robustness associated with high-gain LQG solutions. The LQG cost curve achieves a minimum at the nominal mass value, $\tilde{m} = 0$, but tolerates almost no variation in $\tilde{m}$. The stability region is increased by the PEAM and BAM designs at the cost of increasing nominal system closed-loop $\mathcal{H}_2$-norm. The PEAM design increases robustness, but it does not achieve stability throughout the whole design set. The Bourret approximation does achieve stability throughout the set. The EAM design also achieves stability throughout the set as was indicated by the analysis. The cost of this stability guarantee is loss of nominal system performance, although for this small amount of uncertainty the performance loss is negligible.

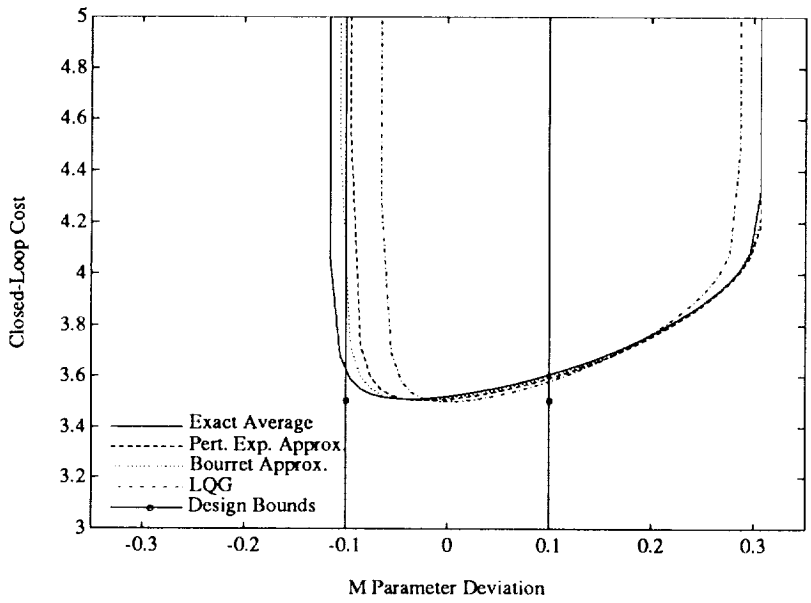

Figure 7: System Closed-Loop $\mathcal{H}_2$-norm as a Function of $\tilde{m}$, the Deviation about $1/m_1$, for Controllers Designed Using $\delta_m = 0.1$.

Figure 8 shows the lower values of $\tilde{m}$ beyond which the respective designs are unstable as a function of the bound on the parameter variation used in the design, δ_m. Figure 8 is thus a plot of the actual stability range achieved as a function of the parameter bound used in the design. The system is thus stable in the range

$$-\delta_a \leq \tilde{m} \leq \delta_a$$

where δ_a is the achieved lower stability bound. For the designs considered, the lower $\tilde{m}$ bound was always smaller than the upper indicating that the design procedures had more difficulty extending the stability range for negative $\tilde{m}$ (large mass) than for positive $\tilde{m}$ (smaller mass).

With no design uncertainty all five techniques converge to the stability bounds achieved by the standard LQG design ($|\tilde{m}| \leq 0.06$). Just as for the Robust-Control Benchmark Problem, as the uncertainty used in the design process is increased the achieved robustness is also increased. Again, the EAM design always increases robustness enough to guarantee stability throughout the design set, while the approximate cost minimization techniques don't provide this guarantee. Their curves lie below that of the EAM design. The EAM design curve has unity slope indicating that the EAM design achieves extremely nonconservative stability over the parameter set used in the design as was predicted by the analysis. The BAM design does come closer to guaranteeing stability than the PEAM design which has difficulty extending the stability range. In particular, for the PEAM design, increasing the design bound above $\delta_m = 0.5$ yields no increase in the achieved stability bound.

The design costs associated with the nominal system ($\tilde{m} = 0$) are plotted as a function of the

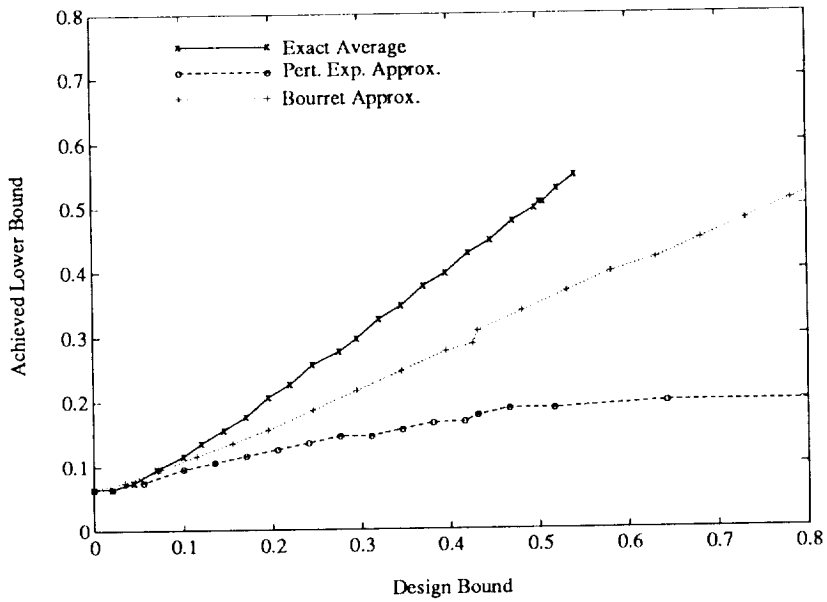

Figure 8: Achieved Lower Closed-Loop Stability Bounds as a Function of the Bound Used in the Design, δ_m.

achieved lower stability bound in Figure 9. Figure 9 is an indicator of the design efficiency of the robust design procedure. The EAM design is most efficient followed by the BAM design. In this problem the PEAM design exhibited much better relative efficiency than in the previous section. It cannot however yield controllers with stability bounds larger than 0.2. Increasing the design bound has no effect on the achieved bound. In essence the EAM design "stalls" out. This is possible because there are no stability guarantees associated with a given design bound.

The output costs are the chief contributors to the total cost as shown in Fig. 9. The control cost shown in Fig. 9 is lowered in all of the designs methods so as to increase the achieved stability robustness. Lowering the control cost is indicative of lower gain controllers. This is the opposite trend as the one observed in the benchmark problem where the control cost increased with greater achieved stability range. For the Cannon-Rosenthal Problem there are modes which cannot be phase stabilized due to the large phase uncertainty caused by the pole-zero flip. The only alternative left to the robust design procedure is gain stabilization as was employed.

7 Experimental Implementation

In this section, experiments on robust control of an optical pathlength on the MIT multipoint alignment testbed will be presented. The testbed was designed as a technology demonstrator for active control of precision structures with particular emphasis on technology necessary for very large baseline optical interferometry. In consideration of this purpose the stabilization of an optical pathlength using an active member within the structure was chosen as a characteristic problem. Detailed descriptions of the testbed hardware including the active member actuators, laser metrology systems, and real time control computer are available in Ref. [20] and will not be presented here. The particular problem considered is an SISO control loop from an active member located behind siderostat A to optical pathlength from siderostat A to the vertex at F, as shown in Figure 10. The problem is noncolocated and particulary difficult due to the inaccuracies of the model used for control design.

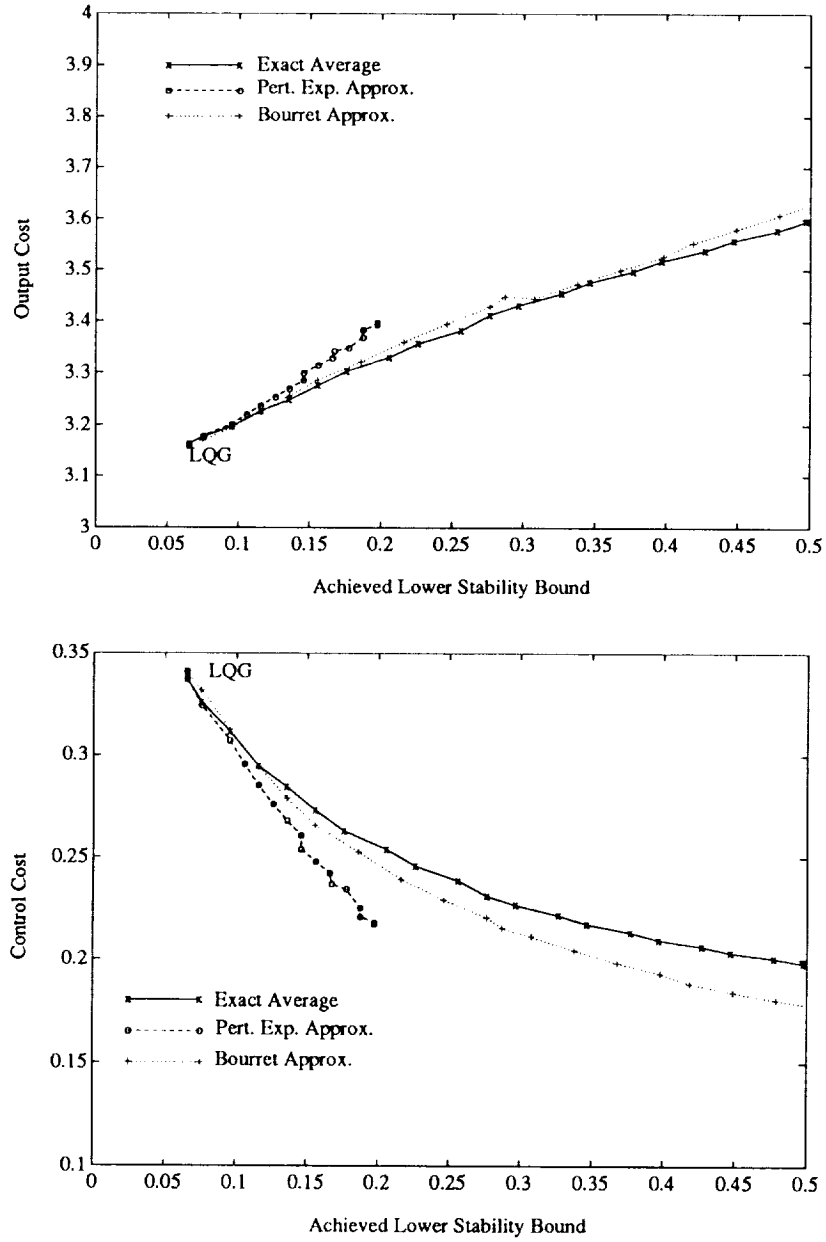

Figure 9: Output Cost and Control Cost as a Function of the Achieved Stability Bound.

All controllers designed in this section are based exclusively on the finite element model of the test-bed with the exception of DC gain information. The intent is to compare the achievable performance of an LQG compensator designed using the inaccurate model with that of a cost-averaging based compensator designed with explicit treatment of the model uncertainty. A comparison of the FEM and the measured transfer functions is shown in Figure 11. The modal frequencies of the FEM are an average of 5-10% in error and the damping ratios are as much as 100% in error. More importantly the modal residues and relative controllability and observability of the modes are in error especially in the region above 50 Hz. The plot of the magnitude of the error transfer function is shown in Figure 12. The additive error exceeds one at almost every mode. Small gain theory measures of robustness would require a compensator to roll-off significantly before the first mode. In addition to the modal

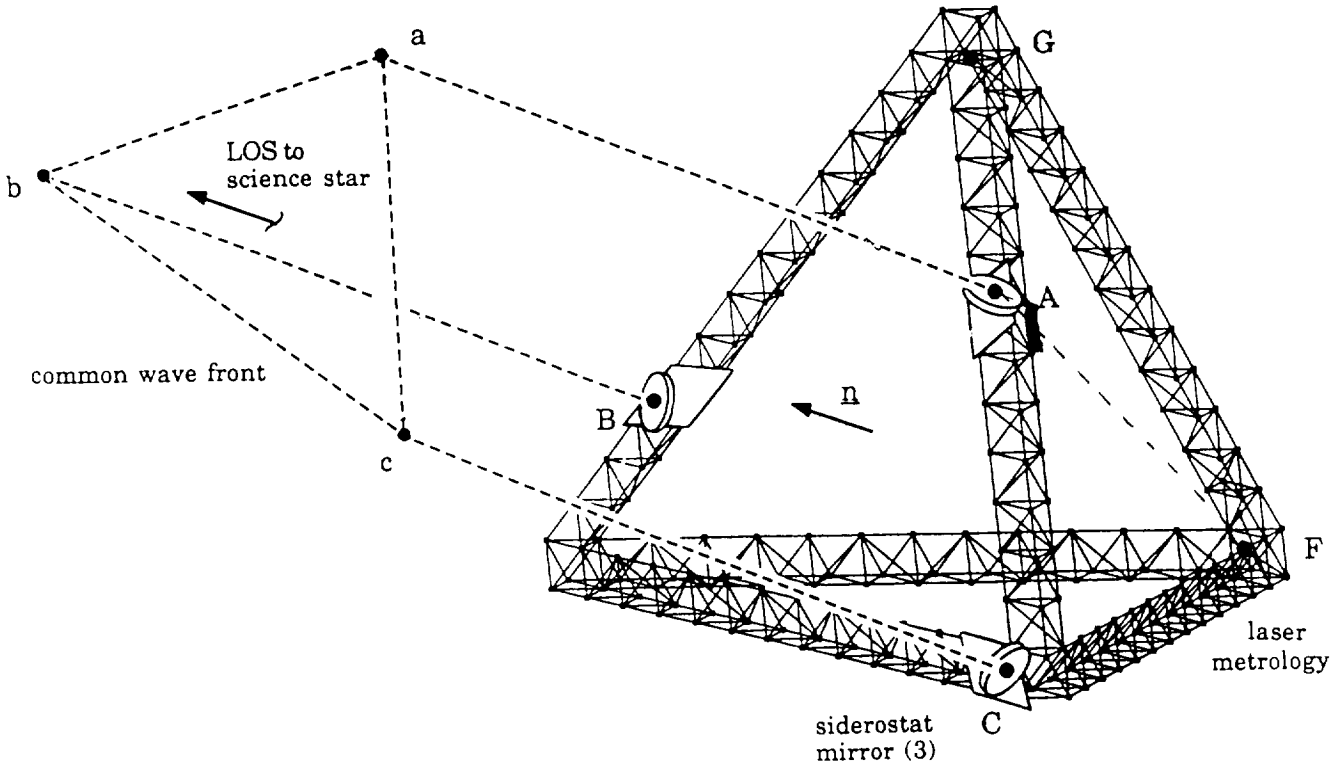

Figure 10: Schematic of the MIT multipoint alignment testbed showing controller optical path (A-F) and the active member control actuator (A).

errors there is phase drift caused by mismodelled time delay associated with the real time control computer.

The finite element model has 45 modes in the range from 0.3 (suspension) to 159.7 Hz. It was necessary to reduce the size of the model for control design. Initially, the model was truncated to retain only the 20 modes in the 10-100 Hz range. The model was further reduced by truncating a balanced realization of the system to the desired order. The controllers were then derived using the reduced system model. Initial experience with LQG controllers penalizing pathlength and control showed that there was no difference in achievable experimental performance when using either a 22 order compensator designed from the reduced FEM or a fourth order compensator designed from a further reduced model. The large uncertainties between the model and the plant limited performance to a gain level below that at which the compensator order effects became important. This fact, coupled with the severe model size limitations imposed by the computation of the averaged-cost based controllers, leads to the selection of a fourth order design plant shown in Figure 13. A mode was retained in the design model at 56 Hz to represent dynamics in the critical region of model uncertainty, those modes from 50-70 Hz.

Two types of controllers were designed and compared based on the fourth order design plant. The first was a LQG based design penalizing optical pathlength error as well as active member control voltage. The plant disturbance entered at the actuator, and the sensor noise entered in the optical pathlength. The pathlength error penalty and disturbance magnitude were normalized to unity while the effective compensator gain was changed by varying the control penalty and sensor noise intensity together. There is thus only a single variable weight used to generate the family of compensators presented.

In the LQG design the mode at 56 Hz was considered certain. In the average cost based design,

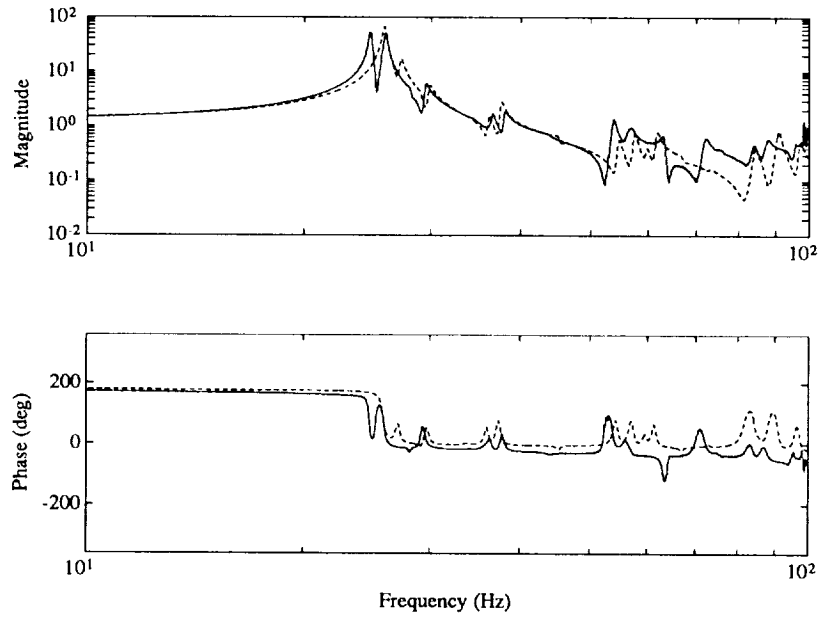

Figure 11: Magnitude and Phase of the Measured Transfer Function from Active Strut to Optical Pathlength (solid) to that Derived from the FEM (dashed).

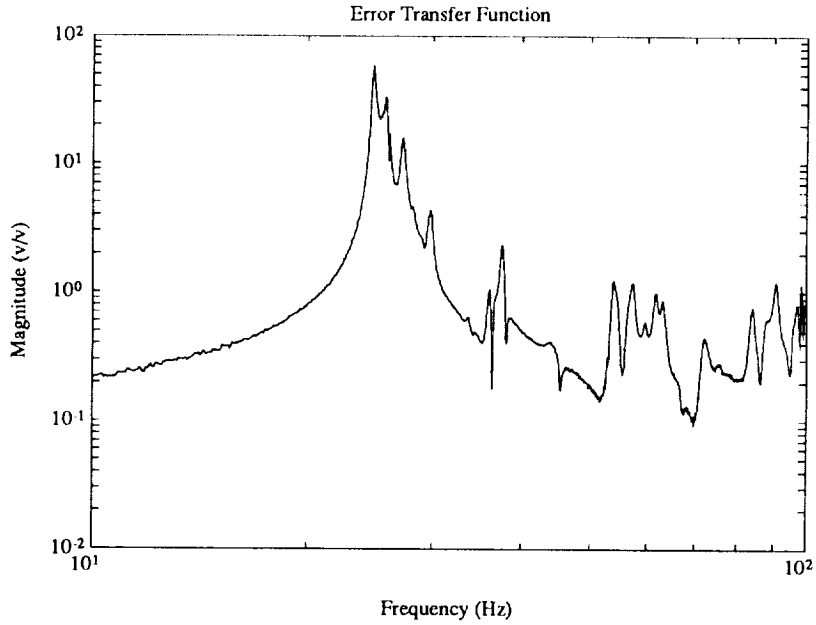

Figure 12: Magnitude of the Additive Error Between the Measured Plant Transfer Function and the FEM Derived Transfer Function.

this mode was assumed to have an uncertain natural frequency varying in the range of $\pm 30\%$ about the nominal. It was hoped that this natural frequency uncertainty would discourage the compensator from plant inversion in the highly uncertain region from 50-70 Hz. The Bourret approximate average cost design technique was chosen because of its superior performance in the analytical sample problems. The weightings used in the Bourret cost minimization were identical to those used in the LQG

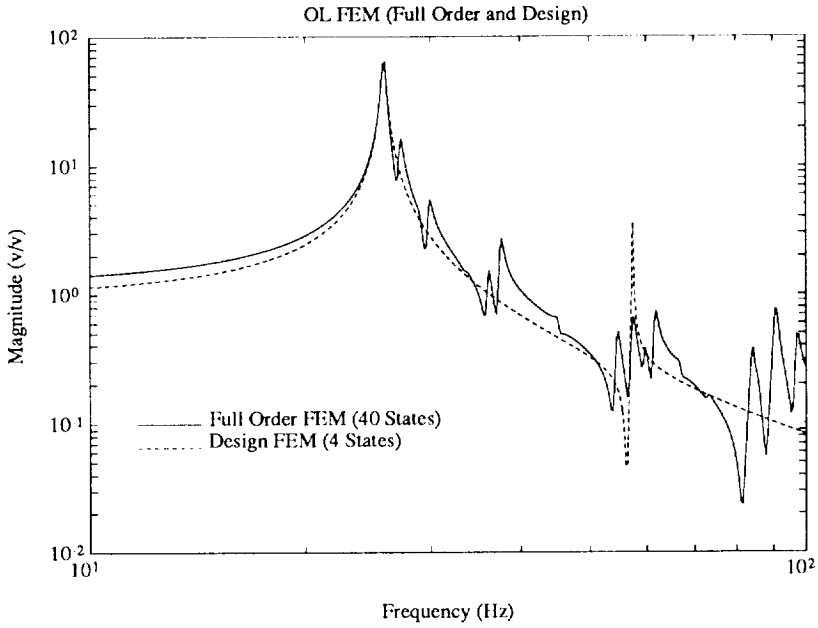

Figure 13: Magnitude of Full Order FEM compared to Fourth Order Design Model

problem.

The closed loop results for compensators based on the two design methods (LQG and Bourret) are presented in Figures 14 - 15. Figure 14 presents the tradeoff between achieved performance and controller effort expended. The performance is a measure of the rms pathlength error nondimensionalized by the open loop rms in the frequency range from 10-100 hz. The control effort is the rms control signal normalized by this same quantity. There is a clear performance improvement with the use of active control. As more control effort is expended, the rms pathlength error can be decreased to only 25% of its open loop value before the onset of instability. The achieved performance-control effort trade eventually diverges at high gain from that predicted when applying the compensators to the full order FEM. This divergence occurs when either controller has a bandwidth which encroaches on the highly uncertain modes in the range from 50-70 hz.

Both the LQG and the Bourret controllers go unstable at approximately the same level of gain. The best achieved experimental closed loops for the two controllers are shown in Figure 15. The robust controller was not able to add significantly to the achievable performance using the assumed single-mode uncertainty structure. As shown in Figure 15, it did change the actual mode which first goes unstable from one at 52 hz to one at 56 hz. Figure 16 shows the predicted performance of the compensators (LQG and Bourret) on the full order FEM. In contrast with the actual system, the modes from 50-70 hz in the FEM do not interact unstably with either compensator.

The poor modelling of the modes in the 50-70 hz region may require the use of multiple uncertain modes in the compensator design rather than the single mode used in the present robust control design. Since the present implementation of the Bourret controller design method is computationally intensive, these designs are effectively limited to accommodate only a few (1-3) uncertainties and a few modes. Practical application to this problem will require improved controller computational methods (more computer power) and/or better methods for selecting which uncertain modes and parameters should be retained in the design.

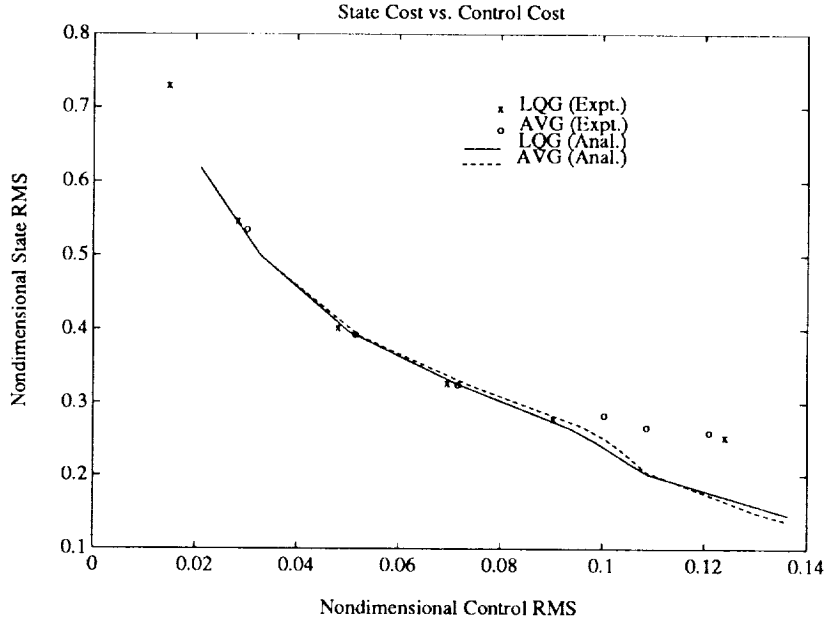

Figure 14: Nondimensional Closed Loop RMS Pathlength Error as a Function of the Nondimensional Control Effort.

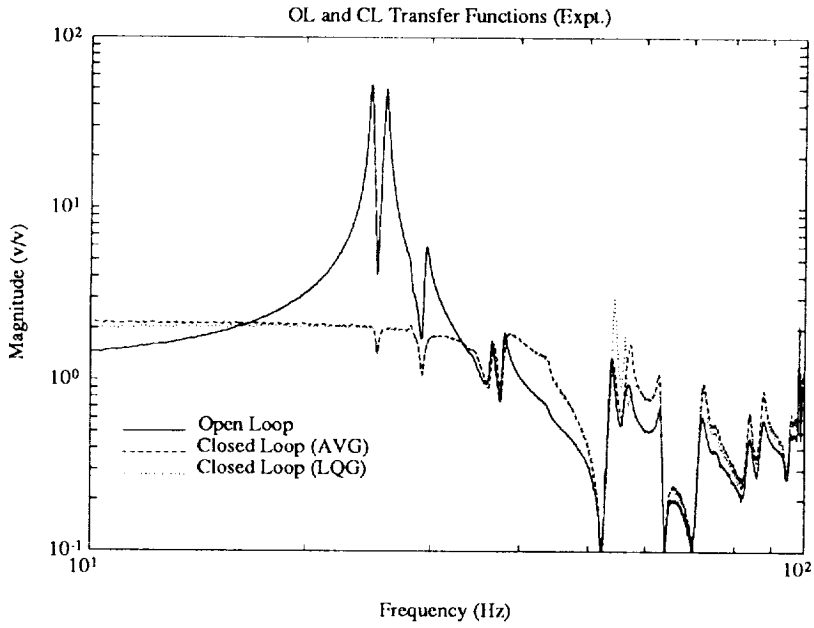

Figure 15: Experimental Open Loop (solid), Bourret Approximate Average Closed Loop (dashed), and LQG Closed Loop (dotted) Transfer Functions

8 Summary and Conclusions

The problem of computing the exact and approximate average $\mathcal{H}_2$-norm of a linear time invariant system has been addressed. This was motivated by showing that bounded average $\mathcal{H}_2$-norm implies stability throughout the model set. Therefore minimization of the average cost will guarantee stability

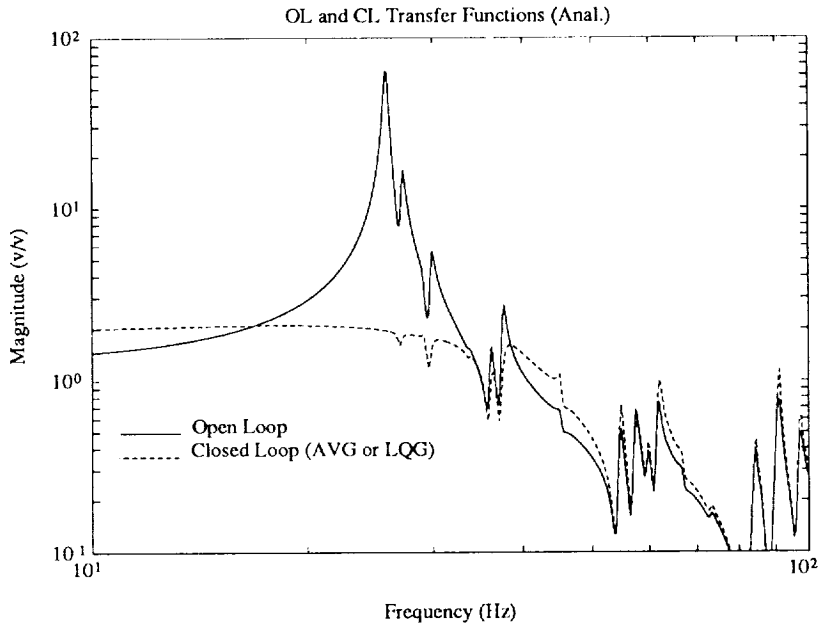

Figure 16: FEM based Analytical Open Loop (solid), Bourret Approximate Average Closed Loop (dashed), and LQG Closed Loop (dotted) Transfer Functions

without having to resort to worst case design techniques. Because the exact average cost is essentially uncomputable, two approximations were applied to the problem. The first approximation is based off of a perturbation expansion about the nominal Lyapunov equation solution, while the second is based on a more sophisticated technique widely used in the field of random wave propagation and turbulence modelling. Using these approximations, cost functionals were derived which are not parameterized and therefore suitable for control synthesis.

The average performance problem was formulated for dynamic output feedback. The cost minimized was represented by either the exact average, the perturbation expansion approximation, or the Bourret approximation to the average. Each cost minimization yields different necessary conditions and different properties for the resulting controllers. When the exact average cost is minimized they yield controllers which guarantee stability throughout the model set. Minimizing the approximations to the average increased robustness over the non-augmented cost minimization, (LQG), but did not necessarily guarantee stability throughout the model set. The numerical examples indicated that the Bourret approximation produced controllers whose properties more closely approximated those of the exact average based controllers. The Bourret approximate average minimization also resulted in less cost increase for a given stability range and can thus be considered a more efficient design methodology than the perturbation approximation minimization.

The experimental application of the method to pathlength control on the MIT multipoint alignment testbed revealed some weaknesses in the techniques. The controllers were calculated using an interative parameter optimization which was computationally intensive. The difficulties in controller calculation presently limit the methods applicability to robust control on large order systems with many uncertain parameters. The methods could however be profitably applied to the problem of uncertain model reduction where the computation requirements are not as great. Further work is underway in the area of uncertain model reduction and selection of appropriate uncertain parameters for retention in control design.

References

[1] Ashkenazi, A. and Bryson, A. E., "Control Logic for Parameter Insensitivity and Disturbance Attenuation," *AIAA J. of Guidance and Control*, Vol. 5, No. 4, 1982, pp. 383–388.

[2] Miyazawa, Y., "Robust Flight Control System Design with the Multiple Model Approach," *Proc. AIAA Guid. Nav. Contr. Conf.*, Portland OR, Aug. 1990, pp. 874–882.

[3] Gangsaas, D., Bruce, K. R., Blight, J. D., and Ly, U. "Application of Modern Synthesis to Aircraft Control," *IEEE Trans. Autom. Contr.*, Vol. AC–31, No. 11, Nov. 1986, pp. 995–1014.

[4] R. Saeks and J. J. Murray, "Fractional representation, algebraic geometry and the simultaneous stabilization problem," *IEEE Trans. Autom. Contr.*, Vol. AC–27, No. 4, Aug. 1982, pp. 895–903.

[5] B. K. Ghosh and C. I. Byrnes, "Simultaneous stabilization and simultaneous pole placement by non-switching dynamic compensation," *IEEE Trans. Autom. Contr.*, Vol. AC–28, No. 6, June 1983, pp. 735–741.

[6] P. M. Makila, **"On multiple criteria stationary linear quadratic control," IEEE Trans. Autom. Contr., Vol. 34, No. 12, Dec. 1989, pp. 1311–1313.**

[7] D. MacMartin, S. R. Hall, and D. S. Bernstein, "Fixed order Multi–Model Estimation and Control," Presented at the 1991 ACC Conference.

[8] Hopkins, W. E. Jr., "Optimal Control of Linear Systems with Parameter Uncertainty," *IEEE Trans. Autom. Contr.*, Vol. AC–31, No. 1, January 1986, pp. 72–74.

[9] Hagood, N. W., *Cost Averaging Techniques for Robust Control of Parametrically Uncertain Systems*, Phd Thesis, Massachusetts Institute of Technology, Department of Aeronautics and Astronautics, June 1991.

[10] Hagood, N. W.,"Cost Averaging Techniques for Robust Control of Parametrically Uncertain Systems," *Presented at the 1991 AIAA Guidance Navigation and Control Conference*, New Orleans,

[11] Hyland, D. C., and Bernstein, D. S., "The Optimal Projection Equations for Fixed-Order Dynamic Compensation," *IEEE Trans. Auto. Contr.*, Vol. AC–29, No. 11, Nov. 1985, pp. 1034-1037.

[12] Doyle, J. C., Glover, K., Khargonekar, P. P., Francis, B. A., "State Space Solutions to Standard $\mathcal{H}_2$and $\mathcal{H}_\infty$Control Problems" *IEEE Trans. Autom. Contr.*, Vol. AC–34, No. 8, August 1989, pp. 831–847.

[13] Frisch, U. "Wave Propagation in Random Media" *Probabilistic Methods in Applied Mathematics* Vol. 1, Edt. A. T. Bharuch-Reid, Academic Press, NY, 1968 ,pp 75-197.

[14] Yedavalli, R. K., and Skelton, R. E., "Determination of Critical Parameters in Large Flexible Space Structures with Uncertain Modal Data," *Journal of Dynamic Systems, Measurement, and Control*, Vol. 105, December 1983, pp. 238–244.

[15] Athans, M., "The Matrix Minimum Principle," *Inf. and Cntrl.* Vol. 11, 1968, pp. 592-606.

[16] Okada, K., Skelton, R. E., "Sensitivity Controller for Uncertain Systems," *AIAA Journal of Guidance, Control and Dynamics*, Vol. 13, No. 2, March–April 1990, pp. 321–329.

[17] Wie, B., and Bernstein, D. S., "Benchmark Problems for Robust Control Design," *Proc. 1991 ACC Conf.*, June, 1991.

[18] Cannon, R. H., Rosenthal, D. E., "Experiments in Control of Flexible Structures with Noncolocated Sensors and Actuators," *AIAA Journal of Guidance, Control, and Dynamics*, Vol. 7, No. 5, Sept.-Oct. 1984, pp. 546–553.

[19] Blackwood, G. H., Jacques, R. N., and Miller, D. W., "The MIT multipoint alignment testbed: technology development for optical interferometry," *Presented at the SPIE Conference on Active and Adaptive Optical Systems*, San Diego, CA 22-25 July, 1991 SPIE paper No. 1542-34.

MODAL CHARACTERIZATION OF THE ASCIE SEGMENTED OPTICS TEST BED: NEW ALGORITHMS AND EXPERIMENTAL RESULTS

Alain CARRIER, Jean-Noel AUBRUN
Lockheed Palo-Alto Research Laboratory, 1801 Page Mill Road,
Building 250, Organization 92-30, Palo-Alto, California, 94304-1211
Tel: (415) 354-5987 FAX (415) 354-5638

February 21, 1992

Abstract

New frequency response measurement procedures, on-line modal tuning techniques, and off-line modal identification algorithms are developed and applied to the modal identification of the Advanced Structures/Controls Integrated Experiment (ASCIE), a generic segmented optics telescope test-bed representative of future complex space structures.

The frequency response measurement procedure uses all the actuators simultaneously to excite the structure and all the sensors to measure the structural response so that all the transfer functions are measured simultaneously. Structural responses to sinusoidal excitations are measured and analyzed to calculate spectral responses. The spectral responses in turn are analyzed as the spectral data become available and, which is new, the results are used to maintain high quality measurements. Data acquisition, processing, and checking procedures are fully automated.

As the acquisition of the frequency response progresses, an on-line algorithm keeps track of the actuator force distribution that maximizes the structural response to automatically tune to a structural mode when approaching a resonant frequency. This tuning is insensitive to delays, ill-conditioning, and nonproportional damping. Experimental results show that it is useful for modal surveys even in high modal density regions.

For thorough modeling, a constructive procedure is proposed to identify the dynamics of a complex system from its frequency response with the minimization of a least-squares cost function as a desirable objective. This procedure relies on off-line modal separation algorithms to extract modal information and on least-squares parameter subset optimization to combine the modal results and globally fit the modal parameters to the measured data. The modal separation algorithms resolved modal density of 5 modes/Hz in the ASCIE experiment. They promise to be useful in many challenging applications.

Keywords: *modal characterization, system identification, flexible structures, segmented optics*

0 BACKGROUND

Active control for large flexible structures has been the object of 15 years of research, yet because of the lack of experimental demonstrations traceable to actual developments, it has not been im-

plemented in a single space mission. Much work has been done on not so large and not so complex flexible structures. As a result, numerically tractable and numerically robust procedures and algorithms for modeling and high performance control of truly large and complex systems are lacking. Precision segmented reflectors are major examples of systems where the size and the complexity issues arise. The Keck Ten Meter Telescope, soon to be operational on Mount Mauna Kea in Hawaii, is one of them. The Keck primary mirror is composed of 36 hexagonal segments. The control system uses 108 actuators and 162 sensors to maintain the segments optically aligned. The Keck structure has 150 modes below 50 Hz with a modal density as high as 25 modes/Hz. Regrettably, the Keck telescope will not benefit from structural control technology.

To address the challenges specific to the active control of precision segmented optics, and to the active control of complex flexible structures in general, the Lockheed Palo-Alto Research Laboratory designed and built the Advanced Structures/Controls Integrated Experiment (ASCIE). The ASCIE test-bed emulates a telescope with a segmented mirror. Its seven-hexagonal-segment primary mirror is mounted on a lightweight flexible truss structure. The six peripheral segments are actively controlled by 18 electromagnetic precision actuators. 24 position sensors measure the relative displacements between the segments. The ASCIE segmented optics and support structure have 50 modes below 50 Hz. The ASCIE control hardware [1] which has been designed to meet the strict requirements for precision control of segmented optics has demonstrated segment alignment performance down to 60 nanometers rms. Using a non validated Finite Element Model and worst case control design techniques, a factor of 3 to 5 improvement in segment alignment bandwidth was achieved over classical control techniques, and vibration attenuation in 25 out of 28 controlled modes was experimentally demonstrated.

The objective of the present work is to develop a dynamic model of ASCIE from experimental input output data. The objective is twofold. One objective is to test how accurately the dynamic behavior of complex systems like ASCIE can be predicted by Finite Element Analysis (one to one comparison between the Finite Element and the identified models requires careful system identification to extract all the natural modes of the system including those with relatively low response). The other is to develop a control design model. This model will be used to test how much improvement in segment alignment bandwidth and structural vibration suppression is achievable using an identified versus an FEM model. This paper reports on our work in modeling ASCIE.

1 INTRODUCTION

In this paper, a new modal characterization technique is developed. It identifies structural modes by applying the principles of gain (singular value) analysis during both the on-line data acquisition, and the off-line parametric identification processes.

The new characterization technique is applied to identify the dynamic model of the ASCIE segmented optics test bed. It coped successfully with the enormous task of estimating more than 2000 modal parameters. 50 modes were identified. The modes come primarily in two dense clusters: one cluster in a 5 Hz frequency band contains 18 modes; the other in an 8 Hz frequency band contains 12 modes. The ASCIE high modal density structure is representative of complex space structures.

For large flexible structures, present characterization techniques do not provide a reliable strategy to collect response data that have information about all of the dynamics of the test article, and

they become numerically untractable when it comes to extracting the dynamic information from the test data, particularly when the data is rich in modal information in some frequency bands [2].

To properly excite all of the dynamics of a large structure, wide-band random excitations, or impulse excitations requires levels of energy that would alter the integrity of the structure. Therefore, unless new excitations strategies are found, the Total Least Square [3] and the Eigenvalue Realization Algorithm [4] which are, at present, two popular identification techniques based on these types of test signals, as well as many other techniques, will only find limited engineering applications.

With system size blowing out the work space and the processing time requirements, and high modal density introducing numerical ill-conditioning, extracting the dynamic information from the test data for large structures is a computationally challenging task. The size, a function of the number of inputs, number of outputs, and number of modes, is a critical factor as the amount of data to be processed can exceed the work space of most current computers. On actual hardware, identification techniques have so far only been demonstrated on relatively small size systems [5], [6]. At present, no technique has addressed the computational complexity associated with high modal density structures.

When they do not require prohibitive testing time, classical sinusoidal or multitone excitations can be used to systematically excite all of the dynamics of a test article [7], [8], [9]. For these test signals, the characterization task is one of fitting a linear time invariant model to a measured non parametric complex admittance matrix. This is known to be a difficult task, and even the most recent single-input single-output, or single-input multiple-output fitting techniques exhibit serious numerical problems for relatively simple systems [10]. For high modal density structures, these techniques would be inappropriate because they would fail to differentiate natural vibration modes. The problem of modeling dynamic systems from their measured frequency responses has motivated some new efforts in rational interpolation theory [11], [12], [13], but whether these efforts effectively address the practical issues has still to be demonstrated.

Our work was to explore new excitation techniques for data acquisition using sinusoidal test signals, and new algorithms for extracting modal information from the non-parametric frequency response test data.

The data acquisition process we tested is classical, but the way we implemented it is not. Steady state responses to sinusoidal excitations were analyzed to determine the system admittance matrix at a given frequency, and frequency sweep was used to determine the full non parametric frequency dependent system admittance matrix. System non-linearities were handled via harmonic analysis. But, with what is new at each frequency, a system inversion was approximately realized to achieve good signal to noise ratio. In addition, the principal system admittance gains and associated input and output patterns were determined. This approach yields some important and inherently multivariable properties of the system being tested: namely, the modal frequencies, the modal dampings, what is new, and the mode shapes because, at a resonant frequency, the maximum system admittance gain is obtained when the actuator inputs are combined so as to excite a pure mode. Dwells in both spatial and frequency domains are performed which is critical to the modal identification of complex symmetric lightly damped structures, since for such structures tuning to the resonant frequency alone fails to isolate closely spaced modes.

When the acquisition process was completed, a parametric modal model was fitted to the full non parametric measured system admittance matrix, and new algorithms based on low rank matrix

approximation, or on convex and quadratic optimization techniques were used to carry one step further the identification of the modal parameters started during the data acquisition process. The algorithms are used repeatedly. Each time they are called, they extract one or several dominant natural modes from the non parametric response over a prespecified frequency range. To identify a mode, they use the modal information contained in the maximum system admittance gain and its associated input and output patterns, and the consistency of this modal information over any specified frequency range to give accurate modal parameters free to the extent possible from the contributions of the nearby modes.

The paper is organized as follows. Section 2 describes the ASCIE high modal density flexible structure that was used to demonstrate the new modeling techniques. In section 3, we discuss some of the issues involved in gathering a good set of input-output data for modeling complex flexible structures. In section 4, measured frequency response data are used to explore some of the difficulties associated with the modal characterization of the ASCIE segmented optics test-bed, and to define a sensible optimization criterion for parametric identification. In section 5, we discuss the choice of a model for flexible structures and modal testing under various assumptions. Section 6 addresses our work in data acquisition and on-line modal testing, and its application to the ASCIE experiment. Section 7 addresses our work in off-line modal analysis, in model refinement via parameter optimization, and its application to the modal identification of ASCIE.

2 ASCIE TEST-BED

The ASCIE emulates an f/1.25 Cassegrain telescope.* Its seven-hexagonal-segment primary mirror is mounted on a lightweight flexible truss structure. The six peripheral segments are actively controlled in three degrees of freedom by 18 linear electromagnetic precision actuators. 24 Kaman position sensors (4 per actively controlled segment) are used to measure the relative displacements between the segments and generate commands for the actuators to keep the segments optically aligned, the central segment acting as a reference.

Non Colocated sensing: The edge inductance sensors measure the relative positions of the primary mirror segments. The central segment, instead of the support structure which lacks dimensional stability, is used as a reference. The edge sensors have a 60 nanometer rms resolution below 5 Hz, and a large measurement range (± 1 mm) to accommodate the initially large segment misalignments. A laser optical system, not described, is used for initial calibration and system alignment. In future works, this system will also be useful for optical scoring.

Actuation: The actuators have been specially designed at Lockheed [1] to meet the strict resolution, dynamic range, smoothness of operation and bandwidth requirements for precision control of segmented optics. When driven in force mode, their bandwidth is 140 Hz. Each actuator is instrumented with an automatic system providing force offloading to reduce power dissipation.

Colocated sensing: Each segment alignment actuator is instrumented with a colocated Kaman inductance position sensor. Each sensor has a 60 nanometer rms resolution below 5 Hz, and a measurement range of $\pm$ 1 mm.

Truss structure: The structure was designed and optimized to emulate a large telescope structure while being able to support the mirror segments in a 1-g environment. Its modal distribution contains several dense clusters and is fundamentally different from the well-spaced distribution of beamlike structures.

*See following page for an actual photograph of the ASCIE Test Bed.

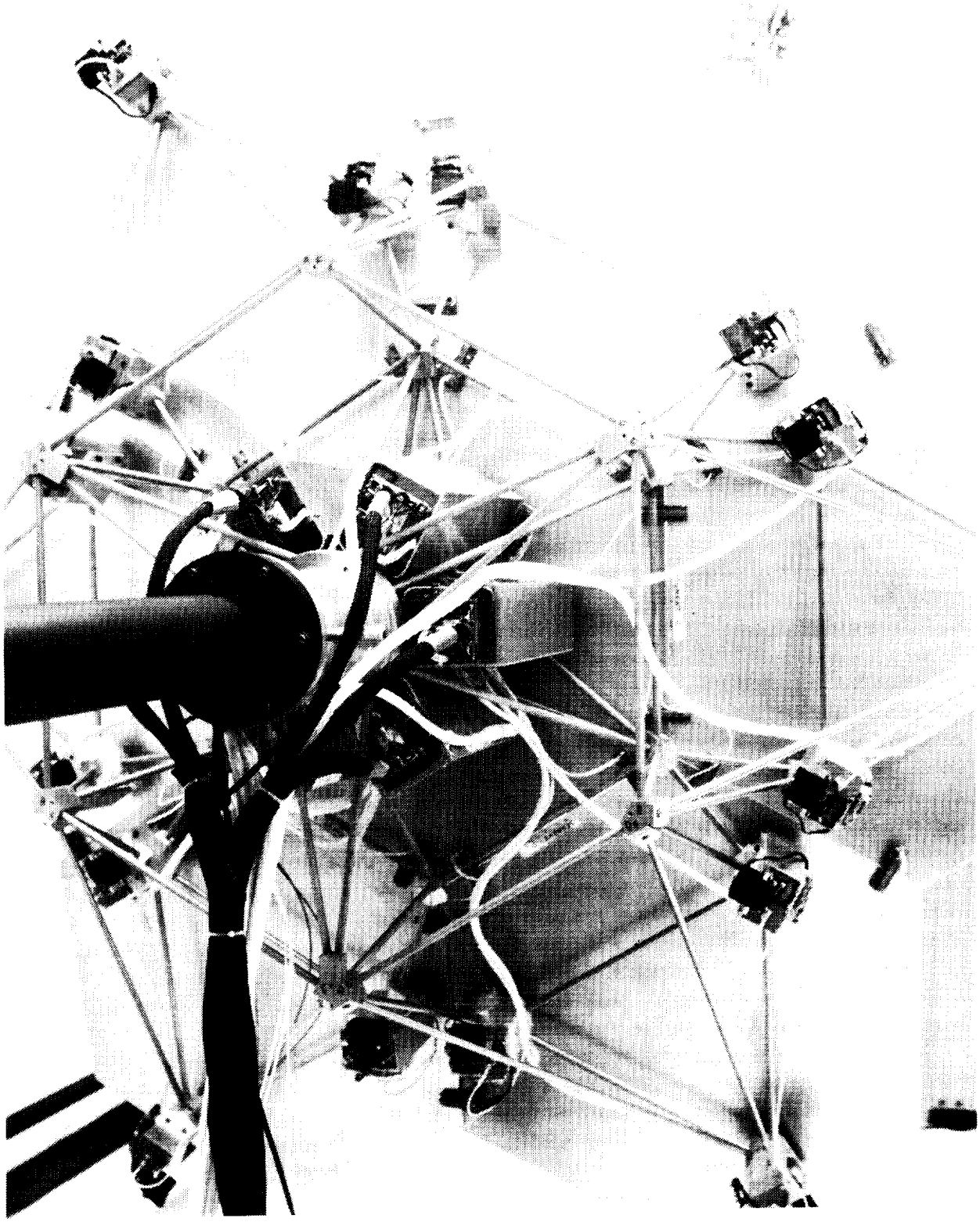

ASCIE Test Bed

Real-time processing and data acquisiton: The ASCIE computer and graphic set up includes an Array Processor, a mini computer, two PCs, and an input/output unit. The Array Processor is an AP-120B, a 12 MFlops machine with 64K of internal memory from Floating Point Systems, fully programmable from the Harris-800 mini computer. The Array Processor is the main computational unit and it is responsible for real-time control processing, signal generation, and real-time Direct Memory Access data transfers to a 256 Kbytes internal memory block residing on the Harris-800 mini computer. The Harris-800 and the PCs are used to monitor the ASCIE experiments via graphical displays of the Kaman sensor readings, the actuator commands, and the mirror segment piston and tilt misalignments. The input/output unit is composed of 32 16-bit analog to digital and 18 16-bit digital to analog converters.

3 CHOICE OF AN EXCITATION TECHNIQUE

System identification can be divided in two phases: a data acquisition phase and an analysis phase. The acquisition phase is particularly important because the quality of the test data determines the quality of the identified model. Good data acquisition requires exciting all of the dynamics of the test article and maintaining good signal to noise ratio via an appropriate choice of the excitation signals. Commonly used excitation signals include impulses, random, and sinusoidal signals. Few impulses or wide-band random excitations are needed to characterize the dynamics of a test article because the response of a system to such excitations is rich in dynamic information. In contrast, many sinusoidal excitations are needed to completely characterize a test article because sinusoidal test signals yield dynamic information at the test frequency only.

Impulse and random excitations allow fast testing, but in practice good signal to noise ratios can be difficult or impossible to achieve with them. Good signal to noise ratio in system identification means that the system response to the excitation is much larger than the system response to the natural disturbances in the whole test frequency range and in all the output dimensions. To ensure good signal to noise ratio, the magnitude of impulse excitations needed to test a complex structure like ASCIE would be destructive. Random excitations offer some more flexibility because filters can be used to concentrate or reduce the energy of the excitation in any desired frequency range. However the magnitude of the response of a multiple-input multiple-output lightly damped system can be quite different depending on the output dimension considered. Consequently if one attempts to maintain good signal to noise ratio in all output dimensions using shaped random signals in some frequency range containing resonant frequencies one may end up resonating the system excessively. Of course, filters could be found to properly shape the excitation in all the input dimensions. This could only be achieved through an iterative testing procedure, because the design of the filters then requires the a priori knowledge of the model of the test article to be found which is impractical.

In contrast, using sinusoidal excitations, it takes much more time to test a system, but it is relatively easy to maintain a given signal to noise ratio and yet ensure non-destructive testing because sinusoidal signals act at a single frequency and in a single input dimension at a time. For this work, we therefore opted for sinusoidal excitations. The complete data acquisition procedure followed for ASCIE is detailed in the data acquisition section, 6.3. The remaining of this section explains how we implemented sinusoidal testing at a given frequency and for a given input direction:

- Two digital sine waves of the same frequency and 90 degrees out of phase are generated by

the Array Processor (AP) and used to construct 18 digital sine waves of the same frequency and different amplitudes and phases.

$$u(n) = uc * cos(2 * \pi * n * of/sf) + us * sin(2 * \pi * n * of/sf)$$

n is the normalized time, $u(n)$ is a vector of size 18, u is the vector sequence of the 18 digital sine waves, π is the number pi = 3.14159..., of is the test frequency, sf is the sampling frequency, uc and us are two constant vectors of size 18 used to vary the amplitudes and phases of the 18 sine waves.

- The 18 digital sine waves are converted into 18 analog signals using 18 digital to analog converters (a2ds). The resulting 18 analog signals are used to command simultaneously the 18 ASCIE segment alignment actuators.

- The 24 analog edge sensor measurements (or the 18 colocated sensor measurements) are converted into 24 (resp. 18) digital signals using 24 (resp. 18) analog to digital converters (d2as) and recorded in real time. The digital signals are then analyzed to extract the coherent (in phase) and the quadrature (out of phase) responses of the ASCIE system to the sinusoidal excitation u. During the analysis, the biases and the harmonic components of the vector response are also extracted.

$$y(n) = yc * cos(2 * \pi * n * of/sf) + ys * sin(2 * \pi * n * of/sf)$$

n is the normalized time, $y(n)$ is a vector of size 24 (resp. 18), y is the vector sequence of the 24 (resp. 18) fundamental digital sine wave responses, yc is the constant vector of size 24 (resp. 18) of the coherent responses, ys is the constant vector of size 24 (resp. 18) of the quadrature responses, of is the oscillator frequency of the sine excitation, sf is the sampling frequency.

4 CHOICE OF AN OPTIMIZATION CRITERION

System identification from measured frequency responses involves fitting the parameterized transfer function matrix of a theoretical linear time invariant system to a measured transfer function matrix at selected frequencies. A criterion is needed to quantify the error between the theoretical and the measured responses at the test frequencies. Most criteria quantify either the average or the peak of the absolute or relative error. To guide our choice, we first discuss the nature of the errors to be expected when dealing with a system like ASCIE.

4.1 Nature of the errors to be expected

We shall classify the identification errors in two categories: stochastic errors, and systematic errors.

Stochastic errors reflect our inability to access the true behavior of the system being tested. Sensor noise, seismic disturbances, laboratory air turbulence, laboratory temperature changes, and measurement unrepeatability for example contribute to these errors in the ASCIE experiments. Long term variations also contribute in the ASCIE experiment since the testing lasted several weeks. The magnitude of these errors can be reduced to a negligible part of the response by careful

experimentation (e.g. vibration isolation, temperature controlled chambers, thermally stabilized electronics) and by careful data acquisition (e.g. averaging to improve repeatability, filtering to reduce the effect of sensor noise and stochastic disturbances).

Systematic errors reflect our inability to capture the true behavior of the system being tested using "reasonable size" linear systems. System nonlinearities are the main source of these errors. As we shall discuss below, the choice of a criterion in the ASCIE experiment is driven by the systematic errors which can be large and highly structured.

To test the ASCIE linearity, the non colocated frequency response of the ASCIE primary mirror and support structure between 15 and 18 Hz was measured for two different amplitudes of the test signals. In the first measurement, the overall amplitude of the segment alignment force excitation was set to give a constant 50 μm root mean squares measured edge sensor response throughout the frequency sweep. In the second measurement, the overall amplitude of the force excitation was set to give a constant 100 μm root mean squares response. The amplitude of the excitation was therefore approximately twice that of the first measurement. Figure (1) and Figure (2) show the principal gains of the two measured transfer function matrices versus frequency.

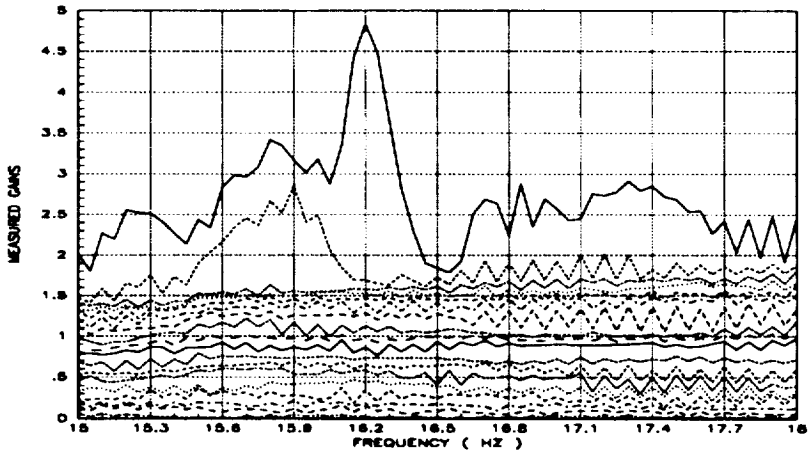

Figure 1: Measured non colocated frequency response of ASCIE for low amplitude test signals

Table (1) contains the dynamic parameters of the two 4-mode-models (Figure (3), and (4)) fitted to the measured frequency responses. It shows about 1% variation in the modal frequencies and up to 50% variation in the modal dampings between the two measurements. The ASCIE response therefore depends highly on the amplitude of the test signals which is typical of nonlinearities. No matter how good the measurements are, the fit errors will remain large because of these nonlinearities.

To illustrate, now a posteriori, the kind of fit error to be expected in the ASCIE identification experiment, we have taken the 50 mode colocated ASCIE identified model (Figure (9)), and perturbed randomly its modal frequencies by 1% or less, and its modal dampings by 10% or less. We then plotted the gains of the absolute error (Figure (5)) and of the relative error (Figure (6)) thus generated. The errors are relatively large. They are representative of what can be expected by fitting a linear model to the measured response of a system which exhibits significant nonlinearities.

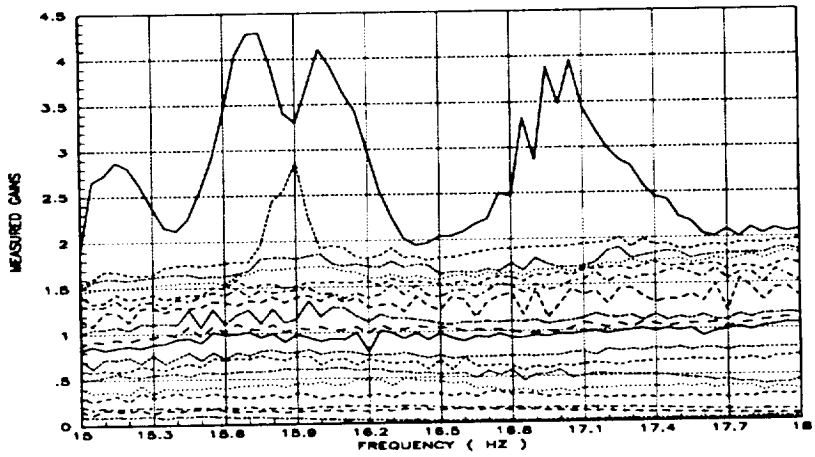

Figure 2: Measured non colocated frequency response of ASCIE for high amplitude test signals

	LOW AMPLITUDE TEST SIGNAL		HIGH AMPLITUDE TEST SIGNAL	
MODE NUMBER	DAMPING %	FREQUENCY (HZ)	DAMPING (increase %) %	FREQUENCY (increase %) (HZ)
1	2.26	15.16	1.91 (-16 %)	15.03 (-0.9 %)
2	1.71	15.81	0.94 (-45 %)	15.73 (-0.5 %)
3	0.78	16.20	1.01 (+29 %)	16.04 (-0.9 %)
4	3.51	17.38	1.65 (-53 %)	17.09 (-1.6 %)

Table 1: Measured modal parameters for two different amplitude test signals

For instance, Figure (5) should be compared to Figure (21) which shows the actual absolute error between the calculated and the measured ASCIE colocated frequency response.

The above observations have far reaching consequences. Most shift invariant identification techniques are based on the premise that the underlying system to be identified is linear. All the errors according to these techniques are treated as measurement errors. This premise is false in the ASCIE experiment and we would like to emphasize further the fundamental differences between measurement and systematic errors. Experimentally, it is possible to quantify how good the measurements are. For instance, bounds and variances of the measurement errors can be estimated, and used a priori in an identification algorithm. Deviations from linearity in contrast cannot be treated as measurement errors because they cannot be quantified a priori without being very conservative. For instance, according to Figure (5) an overall bound on the identification error would be 4 (the peak response of the system is about 8). Non conservative error bounds in this case are highly structured. Constructing such bounds would require the a priori knowledge of the

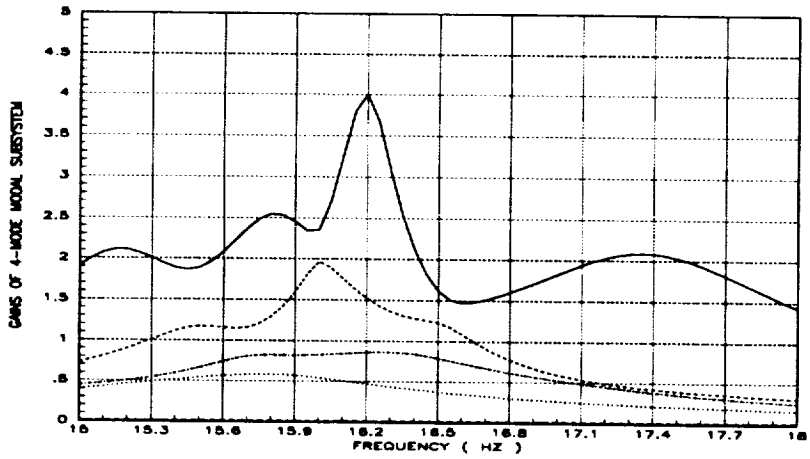

Figure 3: Calculated non colocated modal frequency response of ASCIE for low amplitude segment alignment input forces

model to be found which of course is impractical.

4.2 Relative versus absolute error

Criteria based on the relative error require that the number of measured responses be equal to the number of input forces. When this is not the case, the measurements or the input forces must be constrained, or generalized inverses must be used. For instance, for ASCIE in its non colocated configuration, a geometric transformation could be used to map the 24 edge sensor measurements into 6 piston, 6 petal, and 6 twist motions of the outer mirror segments thus making the number of outputs and the number of inputs equal. However, because the folding motion of the outer mirror segments produces small relative displacements of the mirror segments at the sensor locations, the non colocated ASCIE system is ill-conditioned (the condition number of the static transformation is about 40). Relative error criteria would not appropriately quantify the fit errors in this case because relatively small measurement errors could make the measured frequency response singular and produce large relative errors. In general, relative error criteria are inappropriate for identification of ill-conditioned systems from noisy data. Even when the system is not statically ill-conditioned, ill-conditioning may still appear near the zeros of the system leading again to the problems mentioned above. We shall therefore only consider criteria based on the absolute error for this work.

4.3 Average versus peak errors

The ASCIE segmented optics and support structure exhibit significant nonlinearities. As discussed above, non conservative bounds on the identification errors cannot be developed a priori in this case, so H_∞ peak-error-based identification techniques cannot be used. Figure (5) and Figure (6) show that this is the case whether absolute or relative errors are considered.

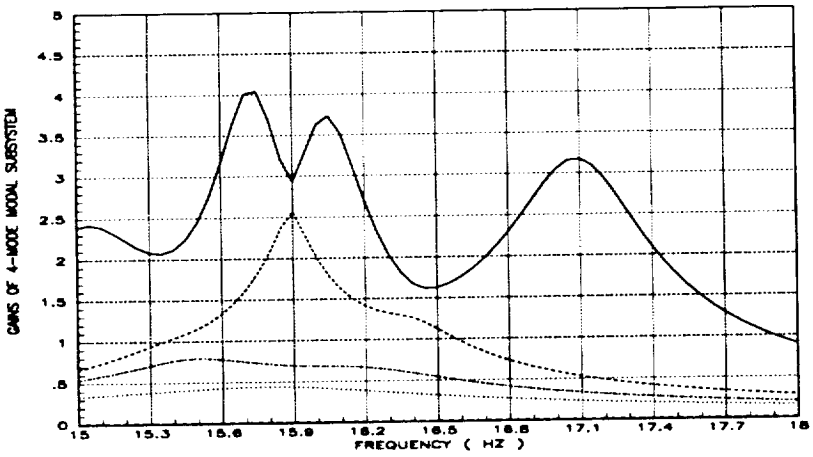

Figure 4: Calculated non colocated modal frequency response of ASCIE for high amplitude segment alignment input forces

Average-based identification techniques such as least-squares, in contrast, do not require any a priori error information: they correlate the measured data at the test frequencies to minimize an average of the modeling errors. As opposed to H_∞ methods, they do not guarantee any bound on the identification error; however, such a bound can always be found a posteriori. For the reasons exposed above, but also because its cost function is easy to compute, and relatively easy to optimize which is critical when dealing with large complex systems like ASCIE, least-squares identification will be used in this work.

Let $H(s)$ be the parameterized transfer function matrix of a theoretical system (s is the usual Laplace variable), let $H_1, \ldots, H_n$ be the ASCIE measured frequency responses at the test frequencies $j\omega_1, \ldots, j\omega_n$, respectively, the least-squares criterion J_0 is:

$$J_0(H) = \sum_{i=1}^{n} Trace\left[(H_i - H(j\omega_i))^*(H_i - H(j\omega_i))\right] \tag{1}$$

4.4 Overview of optimization strategy

The optimization of J_0 over the set of linear transfer function matrices is a difficult nonlinear optimization problem. About 50 modes are needed to model the dynamics of the ASCIE segmented optics and support structure up to 50 Hz. For the colocated identification problem, J_0 therefore depends on approximately 1900 modal parameters. Brute force optimization methods would require an excessive amount of computer time and would most certainly fail to converge if they were not started near a minimum. The proposed optimization strategy is a classical two step initialization-optimization. However, because of the complexity of the present identification problem, a lot of effort is put into the initialization procedure.

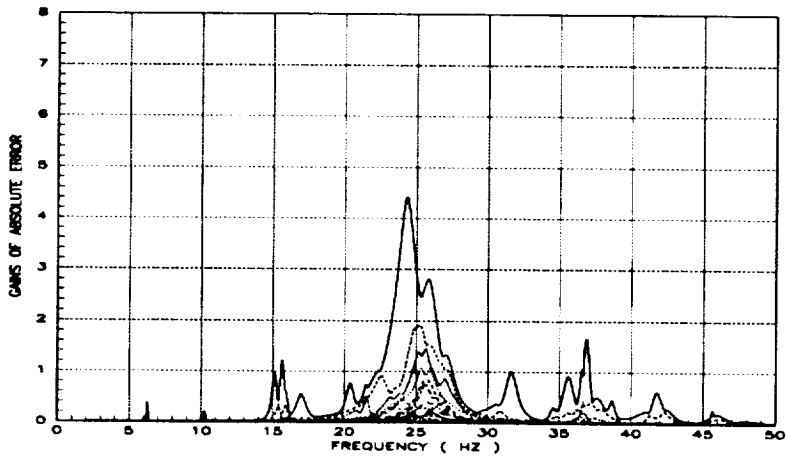

Figure 5: Absolute error generated by perturbing the modal parameters of the 50 mode colocated ASCIE identified model

4.4.1 Initialization procedure

The initialization attempts to find good estimates of the system modal characteristics, if possible, close to the global minimum of J_0. New algorithms are developed to this effect. Some of these algorithms give lower bounds on J_0 that can be used to test the proximity of the global minimum (the lower bounds are tight in the sense that if, for some theoretical model, the theoretical and the measured responses are identical, then the lower bound is achieved).

4.4.2 Optimization procedure

The optimization attempts, starting from the modal parameters estimated in the first step, to reach a minimum. An explicit 2nd order parameter subset optimization method is applied to this effect instead of standard global optimization methods which are computationally too intensive.

5 MODAL DESCRIPTION OF STRUCTURAL SYSTEMS AND MODAL TESTING

The small motions of a structure are best described by a set of partial differential equations. However because it is difficult to derive such a set of equations from physical principles, and because such a set of equations is difficult to use anyway, the dynamics of a structure are often described by a set of equations that describes the motion of the structure at a finite number of selected points called nodes. Such a set of equations is given by:

$$M\,\ddot{z} + L\,\dot{z} + K\,z = f \tag{2}$$

where M is the mass matrix, K is the stiffness matrix, L is the damping matrix, z is the vector of the displacements at the selected nodes, and f is the vector of the forces applied at the selected

C-4

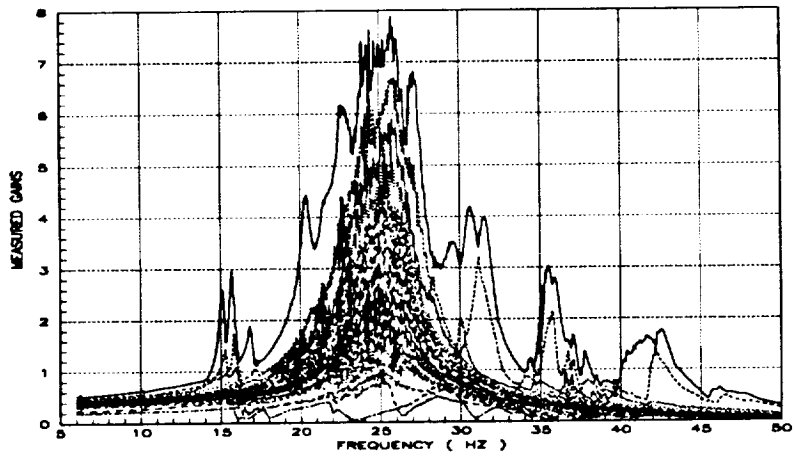

Figure 6: Relative error generated by perturbing the modal parameters of the 50 mode colocated ASCIE identified model

nodes. M and K are positive definite matrices. They can be constructed, using Finite Element Analysis, from the geometric and material properties of all the structural elements that make the system. In contrast, for most structures, analytical methods alone fail to construct the matrix L. L need not be symmetric. Very often, L is assumed to be relatively small, and in most Finite Element Analyses it is set to 0. The force vector f is typically composed of known (or control) forces u, and unknown environmental disturbance forces d. Control forces apply to only some of the nodes, so that the force vector can be rewritten:

$$f = E\,u + d \tag{3}$$

E is the control distribution matrix.

The displacements, the velocities, or the accelerations at some selected nodes may be measured. When only the displacements at some of the nodes are measured, the measurement equation is:

$$y = S\,z + e \tag{4}$$

S is the sensor distribution matrix. e is the measurement error vector.

5.1 Modal description and modal testing of structures with proportional damping

Under the proportional damping assumption, L is a linear combination of M and K. This assumption is often made for convenience, not on physical ground. The dynamic equations of the structure (2) can then equivalently be described by a set of dynamically uncoupled 2nd order ordinary scalar differential equations. Each of these equations describes what is called a natural structural mode. Such a set of equations is obtained using the modal transformation:

$$z = \Phi q \tag{5}$$

such that

$$\Phi^T M \Phi = I \tag{6}$$

$$\Phi^T K \Phi = \Omega^2 \tag{7}$$

where I is the identity matrix, and where Ω is the diagonal matrix of the modal frequencies. The columns of Φ are the mode shapes, and q is the vector of the modal coordinates. Under the proportional damping assumption, the matrices M, L, and K can be simultaneously diagonalized, so that we can also write:

$$\Phi^T L \Phi = 2 \xi \Omega \tag{8}$$

where ξ is the diagonal matrix of the modal dampings (or damping ratios).

The dynamic equations of the structure can then be rewritten:

$$\begin{cases} \ddot{q} + 2 \xi \Omega \dot{q} + \Omega^2 q = B_2 u + \Phi^T d \\ y = C_1 q + e \end{cases} \tag{9}$$

where we have defined $B_2 = \Phi^T E$ and $C_1 = S \Phi$. According to these definitions, the rows of B_2 are the mode shapes at the actuator locations, and the columns of C_1 are the mode shapes at the sensor locations.

5.1.1 Spectral description of structures with proportional damping

According to (9), the transfer function matrix from actuator commands to sensor measurements is:

$$H(s) = C_1(s^2 I + 2 \xi \Omega s + \Omega^2)^{-1} B_2 \tag{10}$$

5.1.2 Modal testing of structures with proportional damping

When the proportional damping assumption is satisfied, if one had an actuator at each of the structural nodes ($E = I$), one could excite each structural mode separately. For instance, to excite only the first mode, one would set $u = M \Phi_1 u_1$ where Φ_1 is the first column of the modal matrix Φ. When actuators are available at only some nodes, the best that can be done to excite a mode is to maximize the projection of the actuator force vector on the corresponding mode shape at the actuator location. Similarly, when the proportional damping assumption is satisfied, if one had a position sensor at each of the nodes (S=I), one could observe selectively each structural mode of the system. For instance, to observe only the first mode, one would form the linear combination of the measurements $q = \Phi_1^T M y$ where again Φ_1 is the first column of Φ. In general, this is not possible if sensors are available at only some nodes on the structure. In actual hardware however one would really need infinitely many actuators to excite a pure mode, and infinitely many sensors to observe a pure modal response, because the columns of the modal matrix Φ only interpolate the physical mode shapes of the real system at the nodes.

Modal testing involves using the actuators simultaneously to excite the structure and the sensors simultaneously to measure the structural response to isolate each mode of the structure and measure its characteristics. In practice, it is difficult to carry out because of the limited number of actuators

and sensors, and because the proportional damping assumption may be violated. Structural test engineers circumvent the first limitation by using many shakers and many accelerometers. This procedure is invasive because the extra hardware modifies the mass and inertia properties of the article being tested. The second limitation is not critical for very lightly damped structures.

Assuming that the mode shapes at the sensor and at the actuator locations are orthogonal, then testing pure modal response in actual hardware is easy because if a pure mode is being excited at a resonant frequency, the various displacements at the sensor locations are all in phase with respect to each other, and in quadrature with respect to the excitation. These properties form the theoretical basis for many current modal testing methods.

5.2 Modal description and modal testing of structures with nonproportional damping

When the proportional damping assumption is violated, it is still possible to find a set of dynamically uncoupled 2nd order ordinary scalar differential equations to describe the system. The non proportional damping allows a transfer of energy between modes. Consequently, a combination of force and rate control is needed to excite a pure mode, and similarly a combination of position and rate measurements is needed to observe a pure mode. From these physical considerations alone, the modal equations of a linear system with non proportional damping, assuming that such equations exist at all, must therefore have the following form:

$$\begin{cases} \ddot{q} + 2\,\xi\,\Omega\,\dot{q} + \Omega^2 q = B_1\dot{u} + B_2 u + B_{d1}\dot{d} + B_{d2} d \\ y = C_1 q + C_2 \dot{q} + D\,u + D_d d + e \end{cases} \tag{11}$$

where q is the vector of the modal coordinates, Ω is the diagonal matrix of the modal frequencies, and ξ is the diagonal matrix of the damping ratios. The distribution matrices involved in the above set of equations are not all independent. For instance, if these equations model a system with force command and position measurements then the following constraints must hold:

$$\begin{cases} D = -C_2 B_1 \\ D_d = -C_2 B_{d1} \\ C_1 B_1 + C_2(B_2 - 2\xi\Omega B_1) = 0 \\ C_1 B_{d1} + C_2(B_{d2} - 2\xi\Omega B_{d1}) = 0 \end{cases} \tag{12}$$

It is shown in Appendix C that the dynamic equations of a system with nonproportional damping, force commands, and position measurements can indeed equivalently be rewritten in the modal form postulated above.

5.2.1 Spectral description of structures with non proportional damping

According to (11),(12), the transfer function matrix of a structural system with non proportional damping, force commands, and position measurements is:

$$H(s) = (C_1 + s\,C_2)(s^2 I + 2\,\xi\Omega\,s + \Omega^2)^{-1}(s\,B_1 + B_2) - C_2 B_1 \tag{13}$$

where $C_1 B_1 + C_2(B_2 - 2\xi\Omega B_1) = 0$.

5.2.2 Modal testing of structures with non proportional damping

For a structure with non proportional damping, a combination of force and rate command is needed to excite a pure mode, and a combination of position and rate measurements is needed to observe a pure modal response. For a structure with non proportional damping, when a pure mode is being excited at a resonant frequency, the various displacements at the sensor locations are not in phase with respect to each other, and not in quadrature with respect to the excitation. It is therefore difficult to experimentally isolate the modes of a structure with non proportional damping to measure their modal characteristics. Standard vector force excitation, and standard tests for modal response purity fail in this case.

5.3 Reduced order modal description of structural systems

Infinitely many modes are needed to exactly describe the dynamic of a flexible structure. Only the lowest frequency modes however are needed in practice. One convenient way to model the effect of the "high" frequency modes at low frequencies is to assume that their response is quasi-steady, which is equivalent to recover static fidelity. For instance, consider the modal expansion of the transfer function matrix of a system with proportional damping:

$$H_\infty(s) = \sum_{i=1}^{\infty} \frac{c_i b_i}{s^2 + 2\xi_i\omega_i s + \omega_i^2} \tag{14}$$

Keeping the first n modes and assuming that the response of the other modes is quasi-steady, an approximation of H_∞ at low frequencies (say below ω_n) is:

$$H(s) = \sum_{i=1}^{n} \frac{c_i b_i}{s^2 + 2\xi_i\omega_i s + \omega_i^2} + \sum_{i=n+1}^{\infty} \frac{c_i b_i}{\omega_i^2} \tag{15}$$

or in matrix form with the obvious definitions:

$$H(s) = C(s^2 I + 2\,\xi\Omega\, s + \Omega^2)^{-1} B + D \tag{16}$$

5.4 Spectral descriptions used in this work

Two spectral descriptions will be used in the ASCIE identification. Both of them can account for non proportional damping.

The first description is closest to the physical system:

$$H(s) = C(M\, s^2 + L\, s + K)^{-1} B + D \tag{17}$$

C is then the sensor distribution matrix, B is the control distribution matrix, and D accounts for the contribution of the unmodeled modes at low frequencies. M, L, and K can be viewed as the mass, damping, and stiffness of the system respectively seen at the actuator and at the sensor locations.

The second description is a modal description:

$$H(s) = (C_1 + s\, C_2)(s^2 I + 2\,\xi\Omega\, s + \Omega^2)^{-1}(s\, B_1 + B_2) + D \tag{18}$$

with the physical constraint $C_1 B_1 + C_2(B_2 - 2\xi\Omega B_1) = 0$. This last description will be used for parameter optimization. No attempt however will be made to enforce the physical constraint which arises because only force commands and position measurements are used in the ASCIE experiment. This is not a serious shortcoming because any good model approximation to the physical system will tend to satisfy this constraint.

6 NEW ON-LINE MODAL TUNING, DATA ACQUISITION, AND EXPERIMENTAL RESULTS

On-line modal testing is useful for limited modal surveys. It was first proposed by Lewis and Wrisley [14]. Current on-line modal testing techniques were established in the late 70's early 80's [7]. The excitation technique closest to the one used in this work is called modal dwell. It requires tuning the polarities and the relative amplitudes at one frequency of several shakers located at discrete points on the structure to produce a pure modal response. Several methods, such the "amplitude-weighted sum of quadrature peaks" and the Asher [8] or Ibanez [15] determinant techniques, were developed to detect the presence of a mode and determine the force distribution to produce tuned modal responses. They assume that the response and the excitation, at a resonant frequency, are in quadrature. Delays, ill-conditioning of the type encountered with ASCIE in its non-colocated configuration, high modal density that alters the purity of the modal responses, all make these methods unreliable for testing complex systems.

Classical modal testing of large systems is costly. It requires a lot of instrumentation, cabling, and expensive data acquisition systems. Even though tuning techniques have been automated [16], they can still require a prohibitive testing time. This time is typically larger than the time required to measure the full frequency dependent system admittance matrix. The time to test complex flexible structures is therefore better spent measuring admittance matrices which have "all" the information about the system response. This relieves one from the requirement of exact tuning. Modal parameters are then obtained off-line by processing the measured spectral data, not experimentally. In testing ASCIE, the control hardware was used. No special purpose instrumentation was added, a situation similar to on-orbit testing of a spacecraft.

6.1 New on-line modal tuning technique

In view of the above limitations, new tuning techniques must be developed for modal tuning to become useful in practice. The approximate modal tuning objective used for ASCIE was to maximize the root mean squares displacement for a given root mean squares force excitation. This objective is the generalization of the single-input single-output force-displacement gain concept to the case of multiple excitation forces and multiple measured responses. At each frequency, to maximize this force-displacement gain, the relative magnitudes and the relative phases of the various sinusoidal forces applied to the test article must be adjusted. When the maximum is achieved, the corresponding normalized (unit) complex force vector is called a *major principal force vector*, the corresponding normalized (unit) complex displacement vector is called a *major principal displacement vector* at the test frequency.

Classical modal tuning (or modal dwell) techniques can be difficult to implement. Experimental factors such as number of excitations, number of responses, measurements non colocated with the

excitations, delays, non-proportional damping, lack of orthogonality of the mode shapes in high modal density regions, and ill-conditioning affect it or make it fail. In contrast, it is always very easy to tune the force vector to the maximum displacement/force gain at a given frequency. One way to do that is to measure the complex admittance matrix of the system at this frequency and compute its singular value decomposition [17]. The physical and the analytical data are then related as follows: the maximum singular value of the admittance matrix is the maximum displacement/force gain of the system; the corresponding right (input) singular vector of the admittance matrix is a major principal force vector; the corresponding left (output) singular vector of the admittance matrix is a major principal displacement vector.

For lightly damped structures, gain tuning and modal dwell are very closely related. Consider for example the modal expansion of the transfer function matrix of a lightly damped structure with proportional damping:

$$H(s) = \sum_{i=1}^{n} g_i \frac{c_i b_i}{s^2 + 2\xi_i \omega_i s + \omega_i^2} \tag{19}$$

where the c_i's and the b_i's are the normalized mode shapes at the sensor and the actuator locations, respectively, and the g_i's are scalars. At the resonant frequency ω_i, the response of the system will usually be dominated by the modal response of mode i:

$$H(j\omega_i) \sim g_i \frac{c_i b_i}{2\xi_i \omega_i^2} \tag{20}$$

which shows that the maximum gain of the system at the frequency ω_i is nearly $\sigma_i = \frac{g_i}{2\xi_i \omega_i^2}$, that a major principal force vector is nearly b_i that is the mode shape at the actuator locations, and that a major principal displacement vector is nearly c_i that is the mode shape at the sensor locations. The singular value decomposition of $H(j\omega_i)$ in this case is also approximately:

$$H(j\omega_i) \sim \sigma_i c_i b_i \tag{21}$$

Gain and modal tuning are therefore nearly equivalent. The former however has the significant advantage of being easy to achieve experimentally.

Based on these ideas, it is easy to devise experiments to measure the modal parameters of some mode. First perform a frequency sweep to measure the force-displacement system admittance matrix in some frequency range around the resonant frequency of the target mode. Then find analytically the maximum gain of the system in this frequency range by singular value analysis of the measured frequency response. The frequency where the maximum gain reaches its peak is the resonant frequency ω_i of the target mode, the right singular vector b_i^T of the admittance matrix at the frequency ω_i is the mode shape at the actuator locations, and the left singular vector c_i of the admittance matrix at the resonant frequency ω_i is the mode shape at the sensor locations. If the singular vectors c_i and b_i are not real, then they can be replaced by real vectors whose product best approximates $c_i b_i$. Once the mode shapes b_i^T and c_i are available, a new frequency sweep can be performed where the polarities and the relative magnitudes of the various forces are adjusted according to b_i^T and where a linear combination of all the responses is formed according to c_i. This sweep is analogous to a single-force-excitation single-response-measurement sweep and all the standard experimental techniques to test modal purity, and measure the resonant frequency and the modal damping of the target mode apply. For instance, phase displays can be used to test

modal purity and find the resonant frequency, and free decay from a forced response can be used to measure the modal damping.

6.2 Experimental demonstration of new on-line modal tuning technique

To illustrate the effectiveness of the experimental procedure described in the previous section, the non-colocated admittance matrix of the ASCIE segmented optics and support structure was measured between 22 and 33 Hz (Figure 7).

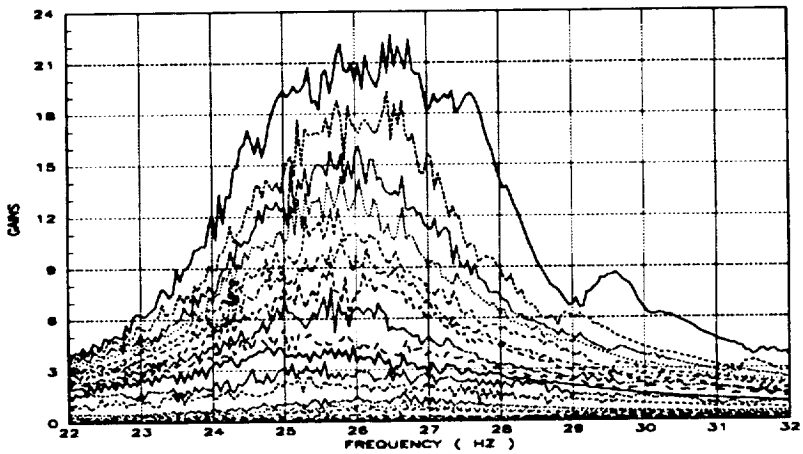

Figure 7: ASCIE non colocated frequency response in high modal density region

The singular value decomposition of the admittance matrix at 27 Hz was then computed to determine the mode shapes at the actuator and sensor locations of the dominant mode around this frequency (note that the resonant frequency does not need to be known exactly). A single-input single-output sweep using this mode shape information as described in the previous section was then performed.

(Figure 8) shows the measured modal response. The phase plot shows that the phase drops by 180 degrees as the sweep goes through the resonant frequency as it should for a pure mode response. The modal frequency and the damping ratio, obtained by curve fitting the modal response, are 26.9 Hz and 3.3% respectively.

Unlike current modal dwell techniques, gain tuning does not use any phase information. It is purely based on the dominance of the modal response of the target mode near the resonant frequency. Variations on the gain tuning technique which incorporate phase information are possible but will not be explored here.

Of course, gain tuning will fail to isolate a target mode if its response does not dominate the overall system response near its resonant frequency. This is the case in high modal density regions if the modes have resonant frequencies close to one another, if mode shape orthogonality is only approximately satisfied, and if the target mode has relatively low response. This is not however a limitation specific to gain tuning; current modal dwell techniques would also fail in this case. The fact is that it is in general impossible to experimentally isolate all the modes of a structure to

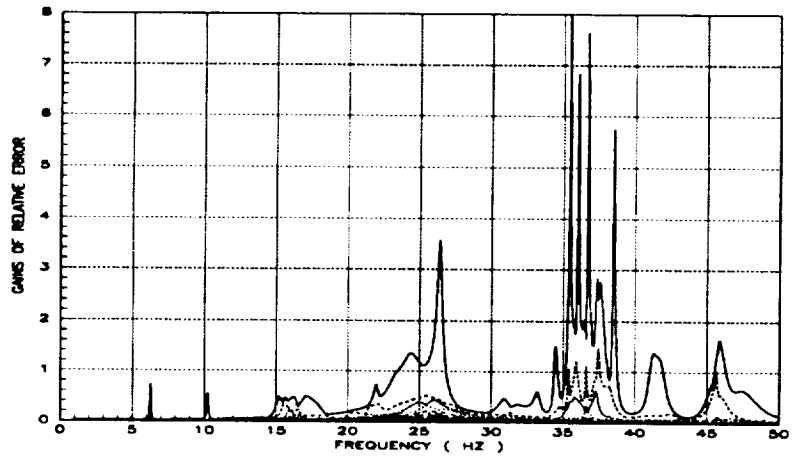

Figure 8: Frequency response of dominant mode around 27 Hz extracted by on-line modal tuning

measure their modal characteristics. Analytical techniques that can determine the modal properties of a structure without having to differentiate the modes must be used.

6.3 New data acquisition technique

In the previous section, we have introduced the concepts of principal gains, principal force vectors, and principal displacement vectors, and illustrated their importance in on-line modal tuning, an area the modal test engineers know well. The same concepts play a central part in the data acquisition procedure described next.

Recognizing the difficulty of getting accurate estimates of all the modal parameters of such a complex system like ASCIE using on-line modal tuning alone, the data acquisition process was focused on acquiring good data that could subsequently be analyzed off-line.

The data acquisition process is a linear, multiple-force-excitation, sinusoidal sweep between 1 and 50 Hz. The sweep dwells every 0.05 Hz. At each frequency, the data acquisition proceeds as follows:

(1)
- A set of 18 estimated orthonormal complex principal force vectors and estimated principal gains are defined. These gains give an estimate of the root mean squares response to a unit force excitation vector whose components are distributed according to the corresponding principal force vectors. The principal force vectors and the principal gains are set arbitrarily at the first test frequency. Subsequently they are updated from one test frequency to the next following a procedure described later.
- Two 90 degree out of phase digital reference sine waves at the test frequency are generated by the AP-120B Array Processor. These sine waves are modulated to produce 18 sinusoidal signals to drive the segment alignment actuators. The relative phases and amplitudes of these 18 sinusoidal signals are set according to the major principal force vector to produce maximum displacement per unit force, and the overall magnitude of

the excitation is set to give a 100 μm root mean squares displacement response. The excitation is then applied.

- The Harris-800 host computer waits for a specified length of time to allow the ASCIE structure to reach a steady state response, and then requests the response data. The reading of the 18 colocated Kaman position sensors (or the 24 non colocated Kaman position edge sensors) are then digitized and recorded in real-time together with the 18 discrete actuator commands in a 256 Kbyte buffer. Once the buffer is filled, the time response data are transferred into the local host computer memory and analyzed. The bias, the fundamental component at the excitation frequency, and a specified number of harmonics are extracted from the recorded signal time-histories. For each signal, a parameter indicative of the quality of the data, the Total Wave Distorsion, is computed. If a signal s is decomposed as:

$$s(t) = b + f(t) + h(t) + n(t) \tag{22}$$

where the scalar b is the bias, the function f is the fundamental component, the function h is the sum of a specified number of harmonics, and the function n is the noise, the Total Wave Distorsion TWD of the signal is defined as:

$$TWD = \frac{\|f\|}{\sqrt{\|h\|^2 + \|n\|^2}} \tag{23}$$

- The spectral data and the Total Wave Distorsion vector are stored in separate arrays.
- The excitation and measurement procedure just described in correspondence with the major principal force vector is repeated for the next principal force vector and so on until all the 18 orthonormal principal force vectors are considered.

(2)
- The transfer function matrix of the system is constructed from the measured spectral data, and its singular value decomposition is computed. The right singular vectors, and the singular values of this decomposition are the principal force vectors, and the principal gains respectively of the system at the test frequency.
- The test frequency, the spectral data, the 18 principal gains, and the matrix of all 18 Total Wave Distorsion vectors are stored on a disk file.

(3) The frequency is incremented and (1) and (2) are repeated. The principal force vectors and the principal gains computed at the last test frequency become the estimated principal force vectors and principal gains at the new test frequency.

The iteration lasts until the whole frequency range between 1 and 50 Hz is covered.

The whole measurement procedure has several important features worth emphasizing:

- For small frequency sweep increments, the principal force vectors will change only slightly from one test frequency to the next. Gain tuning is therefore approximately realized as the data acquisition progresses. According to the previous sections, this in turn means that modal dwell to the dominant modes of the system is also approximately realized as the data

acquisition progresses. The frequency sweep increment could be decreased to achieve modal frequency dwell when sharp increases in the maximum gain of the system are encountered which indicates that the sweep is approaching a resonant frequency, but we did not include this feature in our data acquisition procedure.

- The overall amplitude of the excitation is always set, to the extent possible, to give a prescribed overall displacement response. We have observed, by examining the values taken by the Total Wave Distorsion parameter that the quality of the data acquired this way is better than the quality of the data acquired by driving one actuator at a time. When the number of measured responses equals the number of excitations, the above excitation method could in fact be refined to produce nearly the same amplitude response at all the sensor stations. This uniform excitation method would give very good quality data but we did not implement it.

- The overall amplitude of the excitation is always set, to the extent possible, to give a prescribed overall displacement response. The overall amplitude of the excitation therefore decreases when passing through a resonant frequency. Modal test engineers have observed that this excitation technique reduces the effects of the nonlinearities. We think that this observation must be taken with caution. It is true that this excitation procedure can be used to ensure that the response will not exceed the working range of the instruments at any sensor station, and to ensure that the structure will not be damaged by being resonated excessively. This procedure is in a sense necessary for safe testing and yet maintaining good quality data. A nonlinear structure, however, exhibits different response depending on the amplitude of the excitation; varying the amplitude of the excitation continuously through the sweep might therefore not be the best strategy.

7 OFF-LINE MODAL CHARACTERIZATION, NEW ALGORITHMS AND APPLICATION TO ASCIE

This section describes new analytical techniques to extract the modal characteristics of a test article for its measured frequency response. These techniques are very closely related to the on-line gain-tuning-based-modal-dwell technique developed in the previous section, because they also extract modes on the basis of the dominance of their response in some frequency range around their resonant frequencies. Analytical modal separation is however easier to perform and more powerful than experimental modal dwell: the frequency response of the system is available for analysis over a whole frequency range and not just at the single test frequency; several modes can be extracted simultaneously, when the resonant frequencies are close to one another and the mode shapes are not orthogonal to each other; finally non dominant modes can be extracted from the residual frequency response after the contribution of the dominant modes to the system response has been removed. Like on-line modal dwell, the modal characteristics determined by analytical modal separation are not optimal because their value is based on the response of the system in some frequency range around the resonant frequencies and not on the system overall frequency response. They are nevertheless very useful to start global optimization procedures. The following section details the new algorithms and illustrates their application to the modal identification of

the colocated frequency response of the ASCIE segmented optics and support structure (Figure 9).

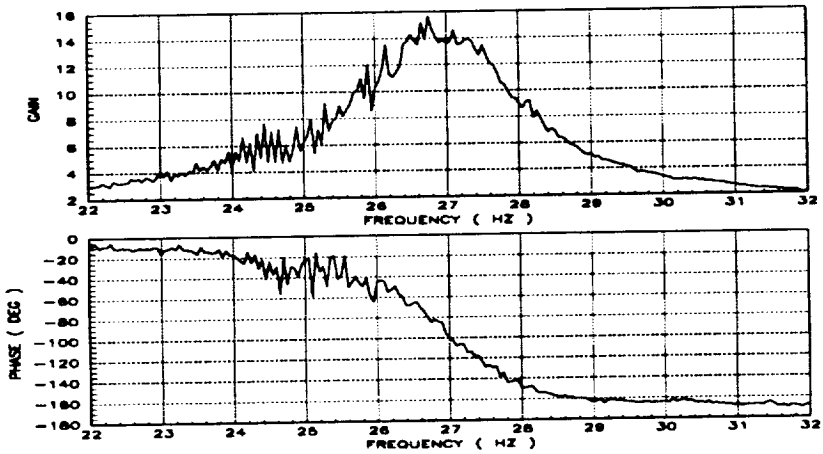

Figure 9: Measured colocated frequency response of ASCIE

7.1 Algorithms for extracting the combined response of several dominant natural modes in a given frequency range

Consider the colocated frequency response of the ASCIE segmented optics and support structure between 13 and 18 Hz (Figure (10)). We want to extract the modal response of the 4 dominant natural modes of ASCIE in this frequency range.

Extracting a single mode response involves determining the proper distribution of excitation forces and the proper linear combination of the measured responses (that is the mode shapes at the actuator and the sensor locations respectively) as in on-line modal dwell. Similarly, extracting a multiple mode response involves determining several distributions of excitation forces and several linear combinations of the measured responses. The distributions of excitation forces in this later case could be the mode shapes at the actuator locations, but they need not be. Independent linear combinations of the mode shapes are also perfectly appropriate. This fact is captured in the mathematical concept of range, that is the space spanned by multiple vectors. Accordingly, we shall call *modal spaces* the spaces spanned by the mode shapes of multiple modes at the actuator or the sensor locations. Thus modal spaces can equivalently be described by any maximum set of independent linear combinations of the mode shapes.

Let the theoretical frequency response of the ASCIE modal subsystem between 13 and 18 Hz be:

$$H(s) = C\,(M\,s^2 + L\,s + K)^{-1}B + D \tag{24}$$

where:

- the columns of C are independent linear combinations of the mode shapes at the sensor locations.

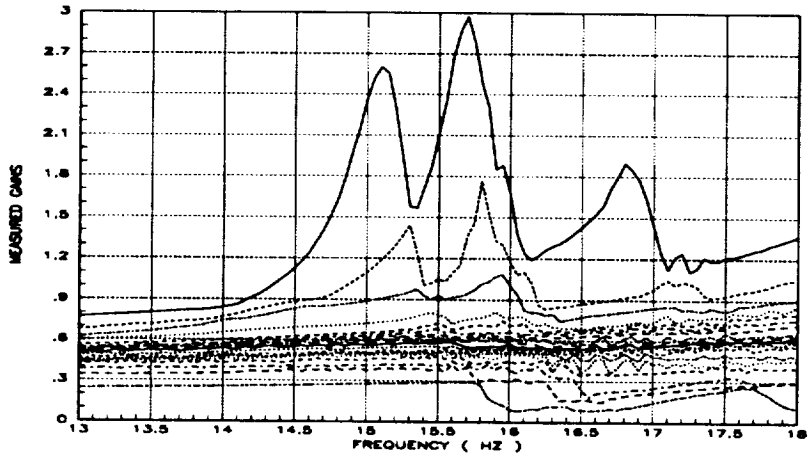

Figure 10: Measured ASCIE colocated frequency response between 13 and 18 Hz

- the rows of B are independent linear combinations of the mode shapes at the actuator locations.
- D accounts for the effects of the modes outside of the frequency range being analyzed.
- M, L, and K can be viewed as mass, damping, and stiffness matrices, respectively.

Without loss of generality, we shall assume that B and C are orthogonal matrices, that is $C^T C = I$ and $B\,B^T = I$.

Let $H_1, \ldots, H_n$ be the ASCIE measured frequency responses, and let $\Delta_1, \ldots, \Delta_n$ be the differences between the measured and the theoretical responses at the frequencies $j\omega_1, \ldots, j\omega_n$ respectively. The least-squares curve fitting problem would be to find the real matrices C, B, D, M, L, and K such that:

$$J(C, B, D, M, L, K) = \sum_{i=1}^{n} Trace(\Delta_i^* \Delta_i) \tag{25}$$

is minimized.

Instead of solving this problem exactly, which at present nobody knows how to do, we propose solving this problem approximately in three steps. In the first step, we estimate the modal space at the sensor locations by solving exactly a relaxed optimization problem. In the second step, dual of the first step, we estimate the modal space at the actuator locations. In the third step, we determine the modal dynamics.

7.1.1 Estimating the modal spaces at the sensor locations

Let $X_1, \ldots, X_n$ be the state of the theoretical system at the frequencies $j\omega_1, \ldots, j\omega_n$, then:

$$[H_1, \ldots, H_n] = C\,[X_1, \ldots, X_n] + D\,[I, \ldots, I] + [\Delta_1, \ldots, \Delta_n] \tag{26}$$

If $[X_1, \ldots, X_n]$ is allowed to be a general complex matrix X, then the minimization with respect to C, X, and D of

$$\tilde{J}(C, D, X) = \sum_{i=1}^{n} Trace(\Delta_i^* \Delta_i) \tag{27}$$

is equivalent to finding the best biased approximation to the matrix $[Re[H_1, \ldots, H_n], Im[H_1, \ldots, H_n]]$ by a matrix of lower rank. This problem is solved exactly in Appendices A and B and its solution defines uniquely the range of C, that is the estimated modal space at the sensor locations. Of course, since C is based on the dominant part of the frequency response in the frequency range being analyzed, C will be a close approximation to the true modal space of the target modal subsystem at the sensor locations only if the modal frequency response of this subsystem dominates the overall system frequency response.

The optimization problems with criteria J and $\tilde{J}$ are very closely related. If $\tilde{J}^*$ and J^* are the optimal values of J and $\tilde{J}$, respectively, then

$$\tilde{J}^* \leq J^* \tag{28}$$

$\tilde{J}$ is a lower bound for J. Thus if, in the course of minimizing J, values of J close to $\tilde{J}^*$ are obtained, we can be confident that a global minimum of J is being achieved. Furthermore, if, for some theoretical model, the theoretical and the measured frequency responses are identical, then the value of C obtained by minimizing $\tilde{J}$ corresponds to a global minimum of J. Direct optimization of J, in general, would not find a global minimum because J may have multiple minima.

7.1.2 Estimating the modal space at the actuator locations

The modal space at the actuator locations is determined in the dual manner.

7.1.3 Application: non parametric modal frequency response of ASCIE 4-mode-model between 13 and 18 Hz

The algorithm described above were applied to find the modal spaces at the sensor and at the actuator locations of a 4-mode model of ASCIE from the measured ASCIE frequency response between 13 and 18 Hz. Using these modal spaces, the "measured" frequency response of the modal subsystem can now be extracted from the measured overall system frequency response. This is done by considering only force distributions that belong to the modal space at the actuator locations, and only linear combinations of the measured responses that belong to the modal space at the sensor locations.

Analytically, if $H_{m1}, \ldots, H_{mn}$ denotes the estimated modal response at the frequencies $j\omega_1, \ldots, j\omega_n$, then:

$$H_{mi} = C^T (H_i - D)\, B^T \qquad i = 1 : n \tag{29}$$

The estimated non parametric frequency response of the 4-mode-subsystem between 13 and 18 Hz is shown in Figure (11). The frequency response of the residual system left after the modal subsystem is removed from the overall system frequency response is shown in Figure (12). This frequency response clearly illustrates that the modal response is well extracted.

To complete the modal identification, we now have to extract the dynamics of the 4-mode-subsystem with 4 inputs, 4 outputs, and with frequency response H_m, a problem much easier to solve than the original one with 18 inputs and 18 outputs.

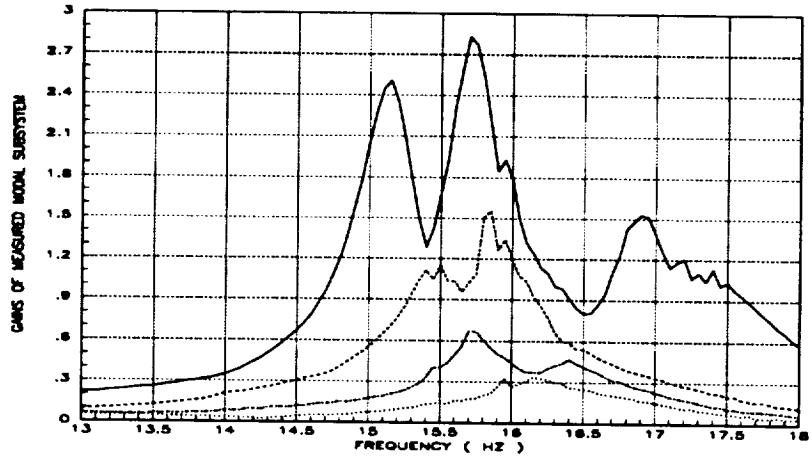

Figure 11: Non parametric frequency response of ASCIE 4-mode-model between 13 and 18 Hz

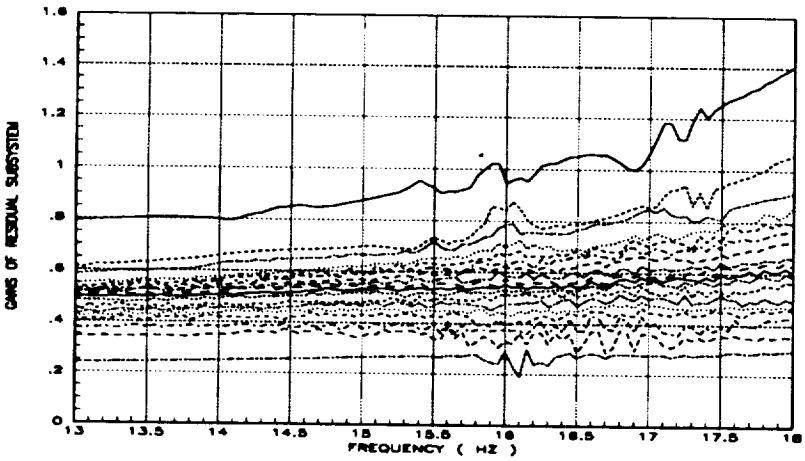

Figure 12: Residual ASCIE frequency response between 13 and 18 Hz after the estimated modal response is removed

7.1.4 Estimating the modal dynamics

Let the theoretical dynamic response of the modal subsystem be:

$$\bar{H}(s) = (M\ s^2 + L\ s + K)^{-1} \tag{30}$$

Let $\Delta_1, \ldots, \Delta_n$ be the difference between the theoretical and the measured modal responses at the frequencies $j\omega_1, \ldots, j\omega_n$ respectively. The least-squares curve fitting problem is to find the real matrices M, L, and K such that:

$$J(M, L, K) = \sum_{i=1}^{n} Trace(\Delta_i^* \Delta_i) \tag{31}$$

is minimized.

As a first step, we propose solving exactly a related linear least-squares problem. We have:

$$\begin{cases} H_{m1} = (M\ (j\omega_1)^2 + L\ (j\omega_1) + K)^{-1} + \Delta_1 \\ \ldots\ldots\ldots\ldots\ldots\ldots\ldots\ldots\ldots\ldots\ldots\ldots\ldots\ldots\ldots\ldots \\ H_{mn} = (M\ (j\omega_n)^2 + L\ (j\omega_n) + K)^{-1} + \Delta_n \end{cases} \tag{32}$$

What is often done [1], is to rewrite this set of equations as:

$$\begin{cases} H_{m1}(M\ (j\omega_1)^2 + L\ (j\omega_1) + K) = I + \Delta_1(M\ (j\omega_1)^2 + L\ (j\omega_1) + K) \\ \ldots\ldots\ldots\ldots\ldots\ldots\ldots\ldots\ldots\ldots\ldots\ldots\ldots\ldots\ldots\ldots\ldots\ldots\ldots\ldots\ldots\ldots \\ H_{mn}(M\ (j\omega_n)^2 + L\ (j\omega_n) + K) = I + \Delta_n(M\ (j\omega_n)^2 + L\ (j\omega_n) + K) \end{cases} \tag{33}$$

which is now a linear set of equations in M, L, and K, and solve the linear least-squares problem with criterion

$$\bar{J}(M, L, K) = \sum_{i=1}^{n} Trace(\bar{\Delta}_i^* \bar{\Delta}_i) \tag{34}$$

where $\bar{\Delta}_i = \Delta_i(M\ j\omega_i{}^2 + L\ j\omega_i + K)$, which is a frequency weighted version of the original least-squares problem. It is our experience that the estimates of M, L, and K obtained that way are usually very poor and cannot be used to start the optimization of the original least-squares problem with criterion J. What we propose instead, is to restore appropriate frequency weighting by rewriting the above set of equations as:

$$\begin{cases} H_{m1}(M\ (j\omega_1)^2 + L\ (j\omega_1) + K)H_{m1} = H_{m1} + \Delta_1(M\ (j\omega_1)^2 + L\ (j\omega_1) + K)H_{m1} \\ \ldots\ldots\ldots\ldots\ldots\ldots\ldots\ldots\ldots\ldots\ldots\ldots\ldots\ldots\ldots\ldots\ldots\ldots\ldots\ldots\ldots\ldots \\ H_{mn}(M\ (j\omega_n)^2 + L\ (j\omega_n) + K)H_{mn} = H_{mn} + \Delta_n(M\ (j\omega_n)^2 + L\ (j\omega_n) + K)H_{mn} \end{cases} \tag{35}$$

and to solve the new linear least-squares problem with criterion

$$\tilde{J}(M, L, K) = \sum_{i=1}^{n} Trace(\tilde{\Delta}_i^* \tilde{\Delta}_i) \tag{36}$$

where $\tilde{\Delta}_i = \Delta_i(M\ (j\omega_i)^2 + L\ (j\omega_i) + K)H_{mi}$. If M, L, and K can be found such that $\Delta_1, \ldots, \Delta_n$ are small, then $(M\ (j\omega_i)^2 + L\ (j\omega_i) + K)H_{mi} \sim I$ for $i = 1 : n$, so that the new optimization problem is nearly equivalent to the original one. It is however much easier to solve because it is linear.

The optimization of $\tilde{J}$ gives estimates for the dynamic parameters M, L, and K which can be used to start the optimization of J.

7.1.5 Application: Calculated modal frequency response of ASCIE 4-mode-model between 13 and 18 Hz

The above dynamic estimation procedure was applied to the ASCIE 4-mode-subsystem frequency response between 13 and 18 Hz to determine M, L, and K. The corresponding theoretical frequency response is shown in Figure (13) and the fit error is shown in Figure (14).

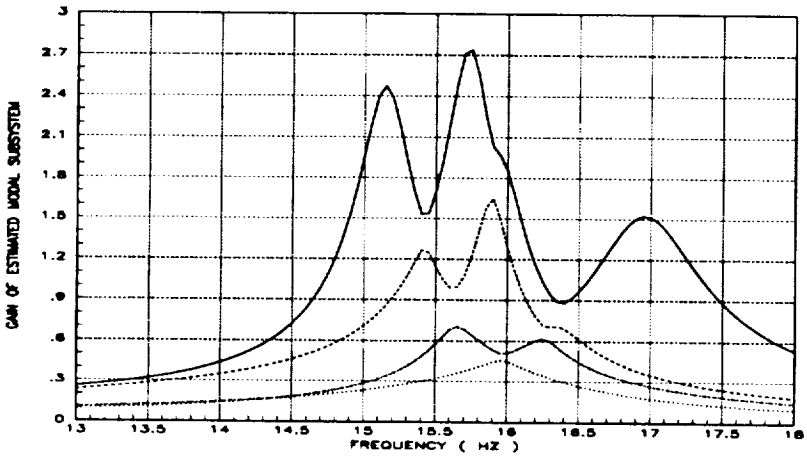

Figure 13: Calculated ASCIE initial 4-mode-model frequency response between 13 and 18 Hz

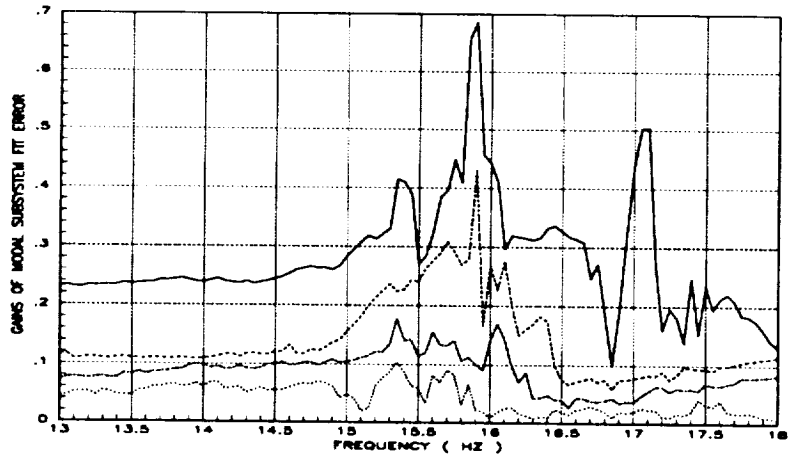

Figure 14: ASCIE initial modal response fit error between 13 and 18 Hz

J was then optimized using an explicit 2nd order Newton-Raphson iterative algorithm and using the above values of M, L, and K as starting parameters. The frequency response of the theoretical modal subsystem and of the corresponding residual subsystem is shown in Figure (15) and Figure (16), respectively.

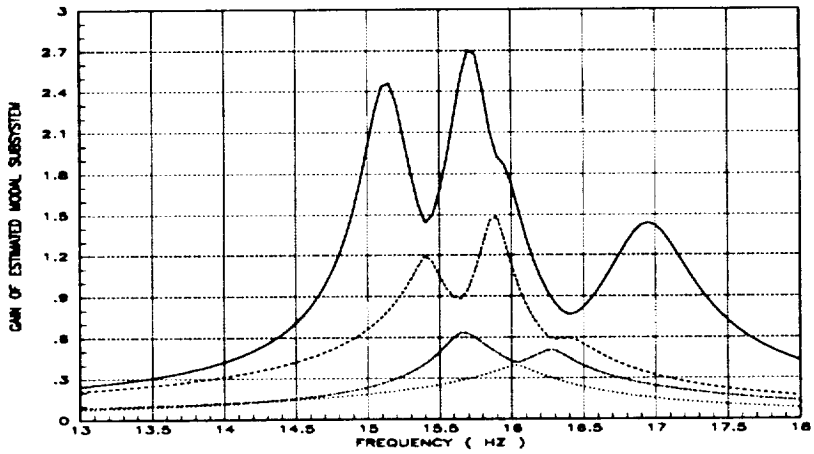

Figure 15: Calculated ASCIE optimal 4-mode-model frequency response between 13 and 18 Hz

7.1.6 Practical comments

This section describes and illustrates the application of new algorithms to extract the modal characteristics of a system from its measured frequency response. In the above example, 4 dominant modes were simultaneously extracted from the colocated frequency response of ASCIE between 13 and 18 Hz. By focusing the analysis on smaller frequency ranges, the same algorithms can be used to extract one mode at a time. At present, the extraction procedure is interactive: the user decides in what frequency range he wants to focus the analysis, and how many modes he wants to extract simultaneously.

We have found it useful to extract a single mode at a time, particularly in high modal density regions. In doing so we gained the assurance that a mode was indeed extracted each time. When to terminate the iterative extraction procedure is a matter of judgement. We always did so when, in any part of the spectrum, the phase of the dominant non parametric modal frequency response varied widely. For instance, Figure (17) shows the residual response of ASCIE between 20 and 29 Hz after 27 modes are extracted. Figure (18) shows the non parametric modal frequency response of the dominant part of the residual frequency response between 25.25 and 25.70 Hz (extracting this non parametric response is always the first step in extracting a mode in our procedure). Although the gain plot seems to indicate the presence of a mode around 25.5 Hz, the phase varies widely. The non parametric frequency response is therefore not the response of a pure mode.

As a last comment, the contribution of the modes already extracted, outside of the frequency range being analyzed, can be removed from the frequency response before starting the analysis. This usually improves the quality of the modal data.

7.2 Modal characterization of ASCIE between 1 and 50 Hz

This section explains how the modal characteristics of the ASCIE segmented optics and support structure between 1 and 50 Hz were obtained from its measured colocated frequency response (Figure (9)).

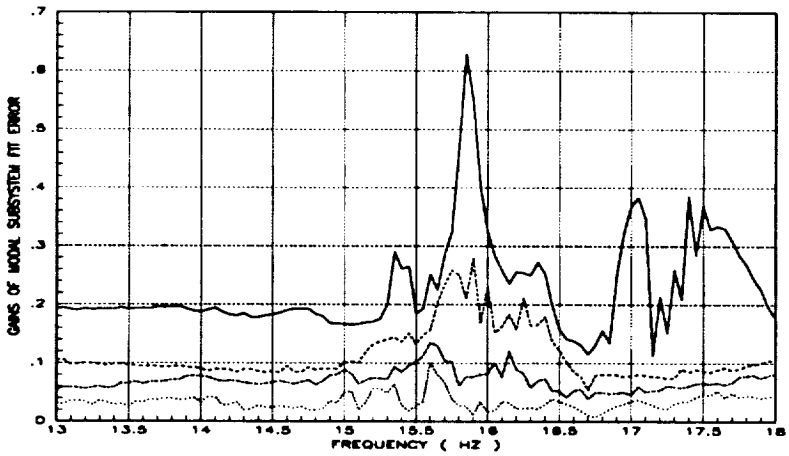

Figure 16: ASCIE optimal modal response fit error between 13 and 18 Hz

The main idea consists in isolating the modes according to their resonant frequencies and according to their mode shapes (spatial separation) to break the global characterization problem into simpler ones. Frequency separation is easy to perform by visual inspection of the system frequency response: the dominant modes with similar frequencies are grouped together. For instance, the ASCIE colocated frequency response was partitioned over 6 frequency ranges: 1 Hz to 13 Hz, 13 Hz to 18 Hz, 20 Hz to 29 Hz, 28 Hz to 33 Hz, 33 Hz to 39 Hz, and 39 Hz to 50 Hz. On each frequency range, when frequency alone failed to isolate modes, spectral and spatial separation was used concurrently: the analytical modal separation algorithms described and illustrated in section 7.1 were used to iteratively extract the modes from the measured frequency response one mode at a time.

8 OFF-LINE DYNAMIC CHARACTERIZATION, ALGORITHMS AND APPLICATION TO ASCIE

In the previous section, simple yet effective algorithms were developed to compute "good" estimates of the modal characteristics of ASCIE from its frequency response. Frequency separation, spatial separation, and modal dominance were used to extract natural modes one at a time. In general, however, it is not possible to exactly differentiate modes. Some of the deficiencies of analytical modal separation are:

- In the process of extracting the natural modes of ASCIE in the high modal density region, we noticed that some modes have close resonant frequencies and similar mode shapes at the actuator or the sensor locations. The algorithms do not guarantee that accurate modal characteristics are determined in this situation.

- If the extraction process of the previous section is iterated too many times in an attempt to extract modes with relatively low modal response, one may end up extracting more modes

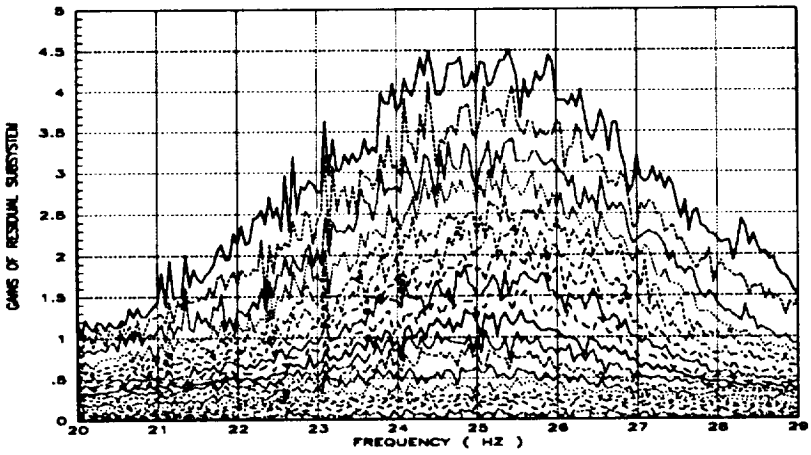

Figure 17: Residual frequency response between 20 and 29 Hz after complete modal extraction

than actually exist in the frequency range being analyzed. For instance, assume that some error is made in calculating the mode shape at the actuator location of a dominant mode whose response is

$$P(s) = g\frac{c\,b}{s^2 + 2\xi\omega s + \omega^2} \tag{37}$$

Let b, $\hat{b}$, and $\Delta b = b - \hat{b}$ be the actual value, the calculated value, and the error associated with the mode shape at the actuator location. Then assuming that all the other modal parameters have been estimated exactly, the residual frequency response once the estimated modal response has been removed will contain a term of the form $\Delta P(s) = g\frac{c\,\Delta b}{s^2+2\xi\omega s+\omega^2}$ which looks like the frequency response of a pure mode with low modal response.

- Analytical modal separation is based on modal dominance, frequency separation, and spatial separation. Consequently, the accuracy of the modal parameters determined applying this method degrades as the contribution of the modes outside of the frequency range being analyzed and of the modes not yet extracted within the frequency range being analyzed, increases.

Because of the above deficiencies, it is possible to improve on the values of the modal parameters of ASCIE determined in the previous section by performing a global analysis of the complete frequency response. In the next sections, we address the problem of extracting the linear dynamics of a system from its measured frequency response by least-squares curve fitting.

8.1 Limitations of current curve fitting techniques

Many algorithms were developed for Single-Input Single-Output (SISO) complex curve fitting problems, and particular attention was paid to eliminating numerical ill-conditioning using various parameterizations [18–20]. Most of them solve the original nonlinear least-squares problem by iteratively solving a frequency reweighted linear least-squares problem. The initialization is similar

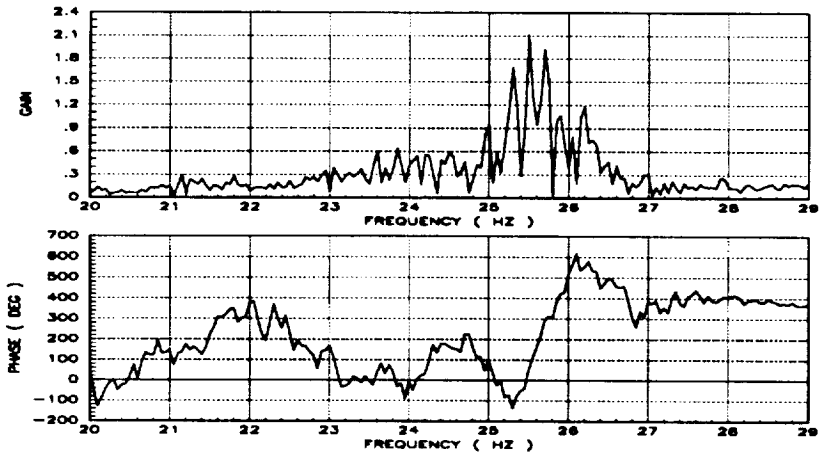

Figure 18: Non parametric frequency response of ASCIE 1-mode-model estimated from the residual frequency response of ASCIE between 25.25 and 25.70 Hz

to the initialization procedure used to estimate the dynamics of a modal system in section 7.1.4. However, because of the particular problem being solved, it was then very easy to restore proper frequency weighting. This is not the case in general SISO problems and this issue may be more important than numerical ill-conditioning. Some of the SISO techniques have been generalized to Single-Input Multiple-Output (SIMO) problems[21], but not to the Multiple-Input Multiple-Output (MIMO) curve fitting problems. At present, MIMO problems are reduced to a series of SIMO problems.

Analytical modal identification techniques and modal test engineers face the same problems. Experimentally, modal testing fails when it becomes impossible to isolate modes on the basis of their frequency separation, spatial separation, and modal dominance. Similarly, the curve fitting problem becomes numerically ill-conditioned under the same conditions. This problem is exacerbated in SISO problems because spatial separation is lost in this case. Although analytical techniques can numerically deal successfully with much more complex systems than the test engineer can experimentally, they cannot deal with the complexity of the ASCIE response in the high modal density regions. To illustrate this point, the frequency response of ASCIE from a single segment alignment actuator to a single edge sensor was plotted in Figure (19). The amplitude response is extremely complex and SISO curve fitting techniques would not be able to differentiate true modes from "noise modes" in this case. The phase plot shows similar complexity. This differentiation problem would still arise, although to a lesser extent, if SIMO responses and SIMO curve fitting techniques were considered.

Even assuming that the 18 SIMO ASCIE identification problems in the high modal density region between 20 and 29 Hz could be solved, one would still be faced with the problem of putting together 18 dynamic models, each of order approximately 40. Eliminating the redundant modes using balanced model order reduction [22] would then require solving Lyapunov equations of order approximately 700 !

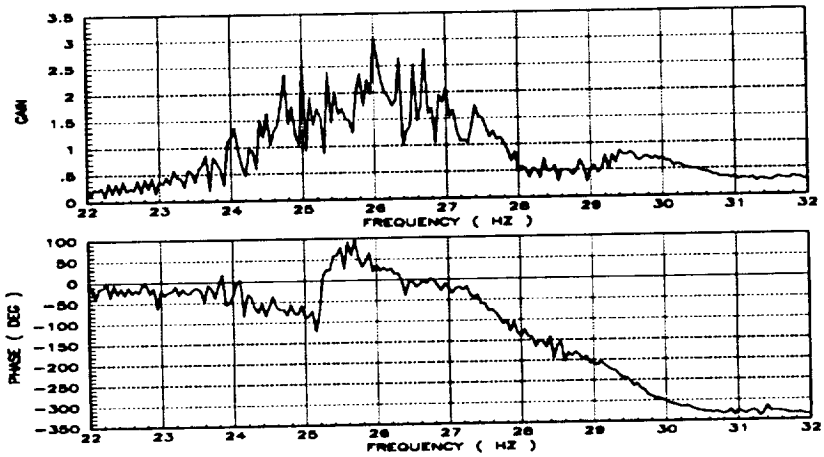

Figure 19: Modal differentiation failure when using classical frequency sweep

8.2 Multiple-Input Multiple-Output curve fitting for ASCIE

In section 7, new algorithms were developed and applied to find what the number of modes and what the modal characteristics of ASCIE are on 6 different frequency ranges. 6 modal subsystems were thus identified. These models can now be used to initialize a global optimization procedure. The objective of this section is to combine these 6 modal subsystems and to correct for the deficiencies of analytical modal separation techniques. This is done in two steps. In the first step, further analysis is performed on each frequency range to reduce the difference between the measured and the theoretical modal responses and if possible reduce the order of the corresponding modal subsystem. In the second step, the various models are combined and a global optimization of the least-squares cost function is attempted. In the following section, we describe the optimization strategy used first to optimize the 6 modal subsystems on their respective frequency range, and next to optimize the combined subsystems.

8.2.1 Subset parameter optimization

Let the theoretical transfer function matrix of a general damped oscillatory system be:

$$H(s) = (C_1 + s\,C_2)\,(s^2 I + 2\xi\Omega s + \Omega^2)^{-1}(s\,B_1 + B_2) + D \tag{38}$$

Let $H_1, \ldots, H_n$ be the measured frequency responses, and let $\Delta_1, \ldots, \Delta_n$ be the differences between the measured and the theoretical responses at the frequencies $j\omega_1, \ldots, j\omega_n$ respectively. The least-squares identification problem is to find the real matrices $C = [C_1, C_2]$, $B = [B_1, B_2]$, D, and the diagonal matrices $\xi > 0$ and $\Omega > 0$ such that:

$$J(C, B, D, \xi, \Omega) = \sum_{i=1}^{n} Trace(\Delta_i^* \Delta_i) \tag{39}$$

is minimized.

The global minimization of J for large systems is impractical. The length of the parameter vector constructed from the coefficients of B, C, D, ξ, and Ω that would have to be optimized to fit a linear model to the frequency response of ASCIE between 20 and 29 Hz would be over 1800. Brute force explicit 2nd order optimization algorithms would therefore take an excessive amount of computer time to run, and would require more work space than is currently available with most computers.

As an alternative, we propose to successively and iteratively optimize C, B, D, and $[\xi\Omega, \Omega^2]$. The same method was proposed in [23] to solve the model reduction problem which is similar to the present least-squares identification. This method, called parameter subset optimization, operates like the QR algorithm when it is used to find the minimum of a positive definite quadratic form (the QR algorithm finds the optimum by solving a finite number of line searches). Although parameter subset optimization does not enjoy the nice properties of the QR algorithm, we have always found it very efficient in practice.

The choice of the parameter subsets C, B, D, and $[\xi\Omega, \Omega^2]$ takes advantage of the structure of the least-squares identification problem. Since the cost function J is quadratic and convex in C, B, and D respectively, the corresponding optimization problems can be solved explicitly. The most difficult part is to optimize J with respect to $[\xi\Omega, \Omega^2]$. Fortunately, this problem involves relatively few parameters so that an explicit 2nd order Newton-Raphson algorithm can be used.

8.2.2 ASCIE modal subsystem optimization

6 ASCIE modal subsystems were extracted from the measured ASCIE frequency response over 6 different frequency ranges using analytical modal separation. As a first step to improve the accuracy of the modal parameters of each modal subsystem, an attempt is made to get values for the modal parameters free from the influence of the modes that do not belong to the subsystem. Thus, for each of the 6 frequency ranges defined above, the measured ASCIE frequency response was corrected by eliminating the estimated contribution of the modes outside of this frequency range, and the corresponding modal subsystem was optimized to match the residual modal frequency response (assume true modal response) thus calculated. Parameter subset optimization was applied to carry out the optimization.

As a second step, each modal subsystem was screened for possible modal redundancy and reoptimized. Balanced model order reduction was used to eliminate the redundant modes. The model order reduction was stopped when the elimination of any mode would have increased the value of the least-squares cost function by at least 1% . The number of modes of the modal subsystem between 20 and 29 Hz was thus reduced from 27 to 21. The number of modes of the modal subsystem between 33 and 39 Hz was reduced from 13 to 11. The orders of the 4 other subsystems were not reduced. With current SIMO least-squares curve fitting techniques, we would have had to reduce the number of modes of the modal subsystem between 20 and 29 Hz from approximately 18x21=378 to 21, and the number of modes of the modal subsystem between 33 and 39 Hz from approximately 18x13=234 to 11. Our method is more effective because it leads to a much lower modal redundancy.

8.2.3 Combining the modal subsystems

The ASCIE modal subsystems were combined and the resulting model was optimized to match the complete measured ASCIE frequency response using parameter subset optimization. This last step yielded less than a 1% decrease in the least-squares cost function. As for ASCIE, this step may well be unnecessary in many applications.

The frequency response of the identified model after optimization is given in Figure (20), and the corresponding residual response in Figure (21). A list of the identified dynamic parameters is given in Table (2). The first three modes are stand modes.

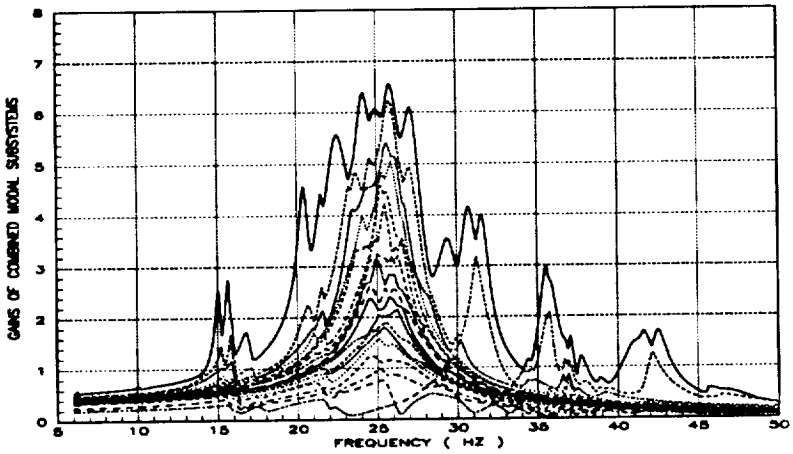

Figure 20: Calculated colocated frequency response of ASCIE

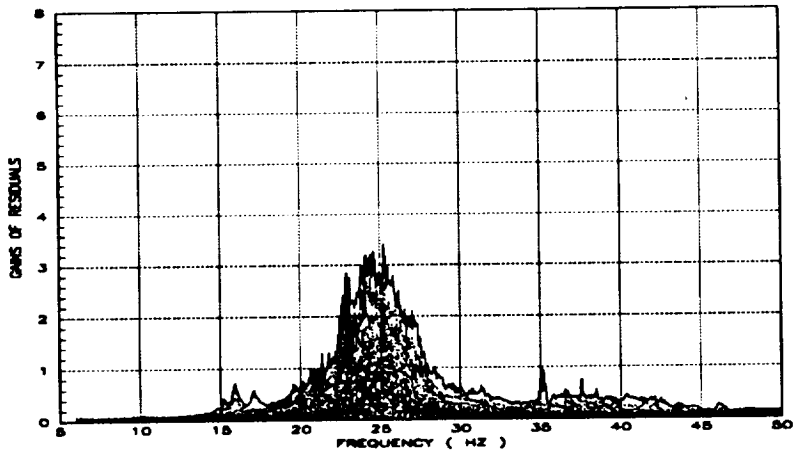

Figure 21: Residual ASCIE colocated frequency response after the optimized modal response is removed

MODE NUMBER	DAMPING %	FREQUENCY (HZ)	MODE NUMBER	DAMPING %	FREQUENCY (HZ)
1	0.90	4.9172	26	2.65	27.0039
2	0.31	6.2855	27	2.30	27.1858
3	0.72	10.1845	28	3.63	27.2201
4	1.28	15.0804	29	2.49	29.5919
5	1.17	15.6929	30	2.03	30.6646
6	1.01	15.9060	31	1.54	31.5755
7	2.30	16.8985	32	0.73	34.5256
8	1.79	20.4568	33	1.20	35.5957
9	1.05	21.5582	34	0.43	35.6220
10	4.21	22.4873	35	1.01	35.7824
11	3.94	23.7036	36	2.07	36.5263
12	4.90	24.0046	37	0.27	36.6676
13	3.31	24.2425	38	0.70	36.7465
14	5.27	24.3552	39	0.48	37.0040
15	2.75	24.3952	40	2.52	37.2631
16	3.80	24.9325	41	0.60	37.5024
17	2.93	24.9918	42	1.06	37.8245
18	7.33	25.2170	43	0.62	38.7592
19	3.18	25.4578	44	2.16	41.1248
20	4.06	25.7026	45	0.83	41.5539
21	2.64	25.8462	46	1.26	42.4540
22	3.42	25.9054	47	0.16	45.6241
23	2.97	25.9286	48	1.13	45.7434
24	3.89	26.1478	49	1.58	46.3683
25	2.78	26.3024	50	2.75	47.6578

Table 2: Modal frequencies and damping ratios of ASCIE 50 mode model

9 CONCLUSION

This paper reports on advances in four areas of system identification of complex flexible structures from frequency responses:

- data acquisition: a method that maintains, to the extent possible, a specified signal to noise ratio is developed to measure frequency responses using sinusoidal test signals.
- on-line modal tuning: an experimental procedure is developed to isolate modes to measure their characteristics on the basis of their spectral separation, spatial separation, and the dominance of their response.
- off-line analytical modal separation: new algorithms are developed to determine the modal characteristics of a system from its measured frequency response on the basis of spectral separation, spatial separation, and modal response dominance.

- curve fitting: a parameter subset optimization method is proposed that takes advantage of the structure of the non linear least-squares identification problem and reduces it to successively and iteratively solving two linear least-squares optimization problems and one non linear least-squares problem of relatively small size. The method can deal with much more complex systems than standard optimization techniques.

The new methods are applied to the modal characterization of the ASCIE segmented optics test-bed. They coped successfully with the problem of estimating over 2000 modal parameters, and resolving modal clusters with a modal density of 5 modes/Hz.

The new methods are combined into a constructive system identification procedure that breaks the global modeling problem into smaller ones easier to solve. As a result, they can be used to model systems even more complex than ASCIE which is critical for future applications. They also are suitable for on-orbit modal testing of spacecrafts because they do not require any special purpose instrumentation.

Aknowledgement: The authors would like to thank Ernie Perez, Paul Reshatoff, and Don Zacharie for their outstanding technical support.

A Approximation of a matrix by one of lower rank

Given a matrix H of rank n, the problem is to find a matrix $\hat{H}$ of rank $nr < n$ such that the Euclidian norm of the error $H - \hat{H}$ is minimized. The following theorem holds:

Theorem A.1 *Let $\sum_{i=1}^{n} \sigma_i u_i v_i^T$ be a singular value decomposition of H where $\sigma_1 \geq \sigma_2 \geq \ldots \geq \sigma_n > 0$, then of all the matrices of rank nr, $\hat{H} = \sum_{i=1}^{nr} \sigma_i u_i v_i^T$ is a best approximation of H in the Euclidian norm sense.*

In matrix form, denoting $C = [u_1, \ldots, u_{nr}]$ and $X^T = [\sigma_1 v_1, \ldots, \sigma_{nr} v_{nr}]$, then $\hat{H} = C\ X$ is a best approximation of H of rank nr in the Euclidian norm sense.

B Biased approximation of a matrix by one of lower rank

Given a matrix H of rank n and a full row rank matrix U, the problem is to find a matrix $\hat{H}$ of rank $nr < n$ and a matrix D such that the Euclidian norm of the error $H - (\hat{H} + D\ U)$ is minimized. The following theorem holds:

Theorem B.1 *Let $U^{\perp}$ be an orthogonal complement of U ($U^{\perp} U^{\perp T} = I$ and $U\ U^{\perp T} = 0$). Let $\sum_{i=1}^{n} \sigma_i u_i v_i^T$ be a singular value decomposition of $H\ U^{\perp T}$ where $\sigma_1 \geq \sigma_2 \geq \ldots \geq \sigma_n \geq 0$, then, of all the matrices of rank nr, $\hat{H} = (\sum_{i=1}^{nr} \sigma_i u_i v_i^T) U^{\perp}$ is a best biased approximation of H in the Euclidian norm sense. The bias matrix coefficient D is then $D = H\ U^T (U\ U^T)^{-1}$.*

Proof: Any matrix $\hat{H}$ of rank nr can be written as the product of two full rank matrices C and X of rank nr:

$$\hat{H} = C\ X \tag{40}$$

The problem is to find C, X, and D to minimize:

$$J = Trace\left[(H - (C\,X + D\,U))^T(H - (C\,X + D\,U))\right] \tag{41}$$

The optimization problem is convex in C, X, and D respectively, but not with respect to C and X simultaneously.

Since

$$\begin{aligned} X &= X\,(I - U^T(U\,U^T)^{-1}U) + X\,U^T(U\,U^T)^{-1}U \\ &= X\,U^{\perp T}U^{\perp} + X\,U^T(U\,U^T)^{-1}U \end{aligned}$$

we have:

$$C\,X + D\,U = C\,X\,U^{\perp T}U^{\perp} + (D + X\,U^T(U\,U^T)^{-1})\,U \tag{42}$$

We can therefore assume without loss of generality that $X\,U^T = 0 \quad \Leftrightarrow \quad X = X_1 U^{\perp}$ for some X_1. The first order condition of optimality with respect to D then gives:

$$D = H\,U^T(U\,U^T)^{-1} \tag{43}$$

which is independent of both C and X !

The cost function J then becomes:

$$J = Trace\left[(H\,U^{\perp T} - C\,X_1)^T(H\,U^{\perp T} - C\,X_1)\right] \tag{44}$$

The problem is now to approximate $H\,U^{\perp T}$ by a matrix of rank nr. Its solution is a simple application of the theorem of Appendix A.

□

Remark B.1 *It can be shown that, generically, C is unique up to an invertible right transformation.*

C Relationship between the modal and the physical dynamic equations of an oscillatory system

In this section, we show that the dynamic equations of a system with nonproportional damping, force commands, and position measurements can indeed equivalently be rewritten in the modal form postulated in section 5.2.

Rewrite the dynamic equations of the system (2) in first order form:

$$\begin{bmatrix} \dot{z} \\ \ddot{z} \end{bmatrix} = \begin{bmatrix} 0 & I \\ -M^{-1}K & -M^{-1}L \end{bmatrix} \begin{bmatrix} z \\ \dot{z} \end{bmatrix} + \begin{bmatrix} 0 \\ M^{-1}E \end{bmatrix} u + \begin{bmatrix} 0 \\ M^{-1} \end{bmatrix} d \tag{45}$$

and define the state space transformation $V = \begin{bmatrix} V_1 & V_{12} \\ V_{21} & V_2 \end{bmatrix}$:

$$\begin{bmatrix} z \\ \dot{z} \end{bmatrix} = \begin{bmatrix} V_1 & V_{12} \\ V_{21} & V_2 \end{bmatrix} \begin{bmatrix} x_1 \\ x_2 \end{bmatrix} \tag{46}$$

such that:

$$\begin{bmatrix} 0 & I \\ -M^{-1}K & -M^{-1}L \end{bmatrix} \begin{bmatrix} V_1 & V_{12} \\ V_{21} & V_2 \end{bmatrix} = \begin{bmatrix} V_1 & V_{12} \\ V_{21} & V_2 \end{bmatrix} \begin{bmatrix} 0 & I \\ -\Omega^2 & -2\,\xi\,\Omega \end{bmatrix} \tag{47}$$

The dynamic equations of the system can then equivalently be rewritten:

$$\begin{cases} \begin{bmatrix} \dot{x_1} \\ \dot{x_2} \end{bmatrix} = \begin{bmatrix} 0 & I \\ -\Omega^2 & -2\,\xi\,\Omega \end{bmatrix} \begin{bmatrix} x_1 \\ x_2 \end{bmatrix} + \begin{bmatrix} \bar{B}_1 \\ \bar{B}_2 \end{bmatrix} u + \begin{bmatrix} \bar{B}_{d1} \\ \bar{B}_{d2} \end{bmatrix} d \\ y = \begin{bmatrix} \bar{C}_1 & \bar{C}_2 \end{bmatrix} \begin{bmatrix} x_1 \\ x_2 \end{bmatrix} + e \end{cases} \tag{48}$$

where we have defined:

$$\begin{cases} \left[\begin{array}{c|c} \bar{B}_1 & \bar{B}_{d1} \\ \bar{B}_2 & \bar{B}_{d2} \end{array}\right] = \begin{bmatrix} V_1 & V_{12} \\ V_{21} & V_2 \end{bmatrix}^{-1} \left[\begin{array}{c|c} 0 & 0 \\ -M^{-1}E & -M^{-1} \end{array}\right] \\ \begin{bmatrix} \bar{C}_1 & \bar{C}_2 \end{bmatrix} = \begin{bmatrix} S & 0 \end{bmatrix} \begin{bmatrix} V_1 & V_{12} \\ V_{21} & V_2 \end{bmatrix} \end{cases} \tag{49}$$

From the last set of differential equations, we find:

$$\begin{cases} \ddot{x}_1 + 2\,\xi\,\Omega\,\dot{x}_1 + \Omega^2 x_1 = \bar{B}_1\dot{u} + (\bar{B}_2 + 2\,\xi\Omega\bar{B}_1)u + \bar{B}_{d1}\dot{d} + (\bar{B}_{d2} + 2\,\xi\Omega\bar{B}_{d1})d \\ y = \bar{C}_1 x_1 + \bar{C}_2\dot{x}_1 - \bar{C}_2\bar{B}_1 u - \bar{C}_2\bar{B}_{d1}d + e \end{cases} \tag{50}$$

That is a set of equations identical to the postulated modal equations (11) if we define:

$$\begin{cases} q = x_1 \\ \left[\begin{array}{c|c} B_1 & B_{d1} \\ B_2 & B_{d2} \end{array}\right] = \left[\begin{array}{c|c} \bar{B}_1 & \bar{B}_{d1} \\ \bar{B}_2 + 2\,\xi\Omega\bar{B}_1 & \bar{B}_{d2} + 2\,\xi\Omega\bar{B}_{d1} \end{array}\right] \\ \begin{bmatrix} C_1 & C_2 & D & D_d \end{bmatrix} = \begin{bmatrix} \bar{C}_1 & \bar{C}_2 & -\bar{C}_2\bar{B}_1 & -\bar{C}_2\bar{B}_{d1} \end{bmatrix} \end{cases} \tag{51}$$

Furthermore these equations yield the constraints (12) as follows:

$$\begin{cases} D = -C_2 B_1 \\ D_d = -C_2 B_{d1} \\ C_1 B_1 + C_2(B_2 - 2\xi\Omega B_1) = \bar{C}_1\bar{B}_1 + \bar{C}_2\bar{B}_2 = \begin{bmatrix} S & 0 \end{bmatrix} V\, V^{-1} \begin{bmatrix} 0 \\ M^{-1}E \end{bmatrix} = 0 \\ C_1 B_{d1} + C_2(B_{d2} - 2\xi\Omega B_{d1}) = \bar{C}_1\bar{B}_{d1} + \bar{C}_2\bar{B}_{d2} = \begin{bmatrix} S & 0 \end{bmatrix} V\, V^{-1} \begin{bmatrix} 0 \\ M^{-1} \end{bmatrix} = 0 \end{cases} \tag{52}$$

Unicity The dynamic of a system with non proportional damping can equivalently be described by many different sets of modal equations. One convenient way to parameterize all the possible sets of modal equations that describe a given system is to introduce three complex matrices

$$\begin{cases} B = B_r + j\,B_i \\ B_d = B_{dr} + j\,B_{di} \\ C = C_r + j\,C_i \end{cases} \tag{53}$$

and to rewrite the modal equations as follows:

$$\begin{cases} \ddot{q} + 2\,\xi\,\Omega\,\dot{q} + \Omega^2 q = B_i\dot{u} + (\xi\Omega B_i + \sqrt{I-\xi^2}\Omega B_r)u + B_{di}\dot{d} + (\xi\Omega B_{di} + \sqrt{I-\xi^2}\Omega B_{dr})d \\ y = (C_r\sqrt{I-\xi^2}\Omega + C_i\xi\Omega)q + C_i\dot{q} - C_iB_iu - C_iB_{di}d + e \end{cases} \tag{54}$$

For a system with force commands and position measurements the constraints then become:

$$\begin{cases} C_rB_i + C_iB_r = 0 \\ C_rB_{di} + C_iB_{dr} = 0 \end{cases} \tag{55}$$

The rows of B are then the complex mode shapes at the actuator locations, the rows of B_d the complex mode shapes at the node locations, and the columns of C the complex mode shapes at the sensor locations.

It can be shown that any two sets of modal equations with complex mode shapes (B, B_d, C), and ($\bar{B}$, $\bar{B}_d$, $\bar{C}$) respectively describe the same physical system if and only if there exists a complex diagonal and non singular matrix α such that:

$$\begin{cases} B = \alpha\,\bar{B} \\ B_d = \alpha\,\bar{B}_d \\ C = \bar{C}\,\alpha^{-1} \end{cases} \tag{56}$$

Complex mode shapes are thus defined up to a complex scalar multiplication. This limits significantly their usefulness in practice.

References

[1] Lorell K., Aubrun J-N., Zacharie D., Perez E., 'Development of a Precision, Wide-Dynamic-Range Actuator For Use In Active Optical Systems', Proc. 23rd Aerospace Mechanisms Symposium, pp. 139–156, 1989.

[2] Stroud R., Bonner C., Chambers G., 'Modal Testing Options for Spacecraft Developments', Society of Automotive Engineers Transactions, 1978.

[3] Moonen M., VanDerValle J., 'QSVD Approach to On and Off-Line State Space Identification', International Journal of Control, Vol. 51, no. 5, 1990.

[4] Juang J., Pappa R., 'An Eigenvalue Realization Algorithm for Modal Parameter Identification and Model Reduction', Journal of Guidance, Control and Dynamics, Vol. 8, pp. 620–627, Sept.-Oct. 1985.

[5] Allemang R., Shelley S., Brown D., Zhang Q., 'Practical Experience with Identification of Large Flexible Structures', Proceedings of the American Control Conference, 1991.

[6] Bayard D., Hadaegh F., Yan Y., Scheid R., Mettler E., Milman M., 'Frequency Domain Identification Experiment on a Large Flexible Structure', Proceedings of the American Control Conference, 1990.

[7] Stroud R., Smith S., Hamma G., 'MODALAB - A New System of Structure Dynamic Testing', The Shock and Vibration Bulletin, No. 46, pp. 153–175, August 1976.

[8] Asher G., 'A Method of Normal Mode Excitation Utilizing Admittance Measurements', Proceedings of the National Specialists' Meeting on Dynamics and Aeroelasticity, pp. 69–76, Forth Worth, Texas, November 1958.

[9] Smith S., Woods A., 'A Multiple Driver Admittance Technique for Vibration Testing of Complex Structures', The Shock and Vibration Bulletin, No. 42, Part 3, January 1972.

[10] Balas G., Doyle J., 'Identification for Robust Control of Flexible Structures', Proceedings of the American Control Conference, 1990.

[11] Anderson B.D.O., Antoulas A., 'Rational Interpolation and State-Space Realizations', Proceedings of the 29th Conference on Decision and Control, Hawaii, December 1990.

[12] Gu G., Khargonekar P., 'Linear and Nonlinear Algorithms for Identification in H_∞ with Error Bounds', Proceedings of the American Conference, June 1991.

[13] Gu G., Misra P., 'Identification of Linear Time-Invariant Systems', Proceedings of the American Control Conference, June 1991.

[14] Lewis R., Wrisley D., 'A system for excitation of pure natural modes of complex structures', Journal of Aerospace Sciences, Vol. 17, No. 11, pp. 705–722, November 1950.

[15] Ibanez P., 'Force Appropriation by Extended Asher's Method', presented at the SAE Aerospace Engineering and Manufacturing Meeting, San Diego, CA, December 1976.

[16] Ryan R. et al., 'Dynamic Testing for Large Systems', NASA TM-78307, Sept. 1980.

[17] Golub G., Van Loan C., *Matrix computations*, 1983, Hopkins.

[18] Levy E., 'Complex Curve Fitting', IRE Transactions on Automatic Control, Vol. AC-4, May 1959, pp. 37–44.

[19] Spanos J., Mingori D., 'A Newton Algorithm for Complex Curve Fitting', Proceedings of the American Control Conference, Boston, MA, June 1991.

[20] Adcock J., 'Curve fitter for pole-zero analysis', Hewlett-Packard Journal, January 1987.

[21] Dailey R., Lukich M., 'MIMO transfer function curve fitting using Chebyschev polynomials', SIAM 35th Anniversary Meeting, Denver, Colorado, 1987.

[22] Moore B., 'Principal Component Analysis in Linear Systems: Controllability, Observability, and Model Reduction', IEEE Transactions on Automatic Control, AC 26, No. 1, Feb. 1981.

[23] Carrier A., 'Modeling and Shape Control of a Segmented-Mirror-Telescope', Stanford University PhD Thesis, Department of Aeronautics and Astronautics, March 1990.

ACTIVE SUSPENSION DESIGN FOR A LARGE SPACE STRUCTURE GROUND TEST FACILITY

Thomas Lange, Clemens Schlegel
German Aerospace Research Establishment
8031 Wessling, Germany

INTRODUCTION

The expected future high performance requirements for Large Space Structures (LSS) enforce technology innovations such as active vibration damping techniques e.g. by means of structure integrated sensors and actuators. The implementation of new technologies like that requires an interactive and integrated structural and control design with an increased effort in hardware validation by ground testing.

During the technology development phase generic system tests will be most important covering verification and validation aspects up to the preparation and definition of relevant space experiments. For many applications using advanced designs it is deemed necessary to improve existing testing technology by further reducing disturbances and gravity coupling effects while maintaining high performance reliability. A key issue in this context is the improvement of suspension techniques.

The ideal ground test facility satisfying these requirements completely will never be found. The highest degree of reliability will always be obtained by passive suspension methods taking into account severe performance limitations such as non-zero rigid body modes, restriction of degrees of freedom of motion and frequency response limitations. Passive compensation mechanisms, e.g. zero-spring-rate mechanisms, either require large moving masses or they are limited with respect to low-frequency performance by friction, stiction or other non-linear effects.

With active suspensions these limitations can be removed to a large extent thereby increasing the range of applications. Despite an additional complexity which is associated with a potential risk in reliability their development is considered promising due to the amazing improvement of real-time control technology which is still continuing.

THE ACTIVE SUSPENSION TEST SETUP

The basic idea of an active suspension device is the combination of a bias spring designed to support the weight load at the hinge, augmented by an actuator which in a defined range compensates for the spring stiffness via positive displacement feedback (Figure 1). The artificial negative stiffness adds up with the passive one to an overall stiffness close to zero,

without the penalty of excessive weight or undesired additional eigendynamics. The potential advantages in performance are as follows:

- the overall stiffness is easily adjustable by choosing an appropriate gain factor,
- the relative error of the resulting differential dynamic forces can be kept small by using appropriate precision control hardware and software,
- an increased dynamic range becomes feasible owing to the reduced overall moving suspension mass.

As a reference test item a beam shaped truss structure has been selected which can be regarded as a typical substructure for LSS or at least as a basic element of potential space experiments. The principal test setup, as depicted in Figure 2, comprises three functional levels which logically are strictly separated:

- the active suspension mechanism with local control of associated suspension rods,
- the active vibration control which "sees" an ideal truss beam under approximately zero-g conditions,
- reference sensors and stimulation actuators for test evaluation.

In contrast to passive methods the active suspension permits optimal decoupling of bending from torsional degrees of freedom and the full compensation of pendulous rigid body modes. As shown in Figure 3 this becomes possible by equidistant clustered suspension units with the horizontal ones exhibiting negative overall stiffness to counteract gravity induced pendulous forces. Using kinematic decoupling algorithms, this technique can also be applied for non-symmetrical cross-sections. A practical advantage is the shortness of the suspension cable which is limited primarily by mechanical design tolerances, e.g. with respect to the radial load of the linear guidance bearing.

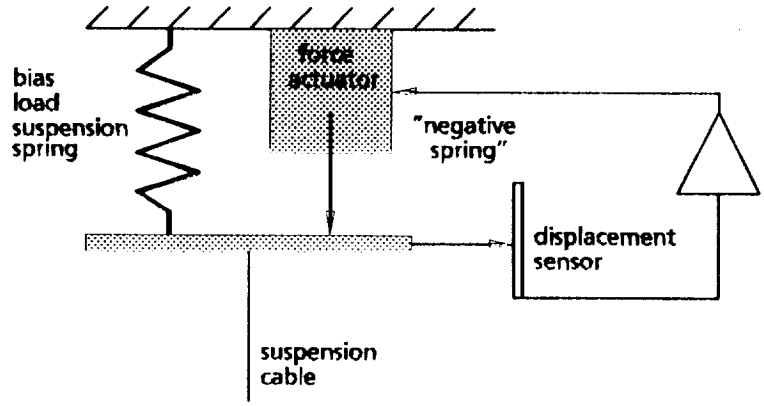

Figure 1. Active suspension principle.

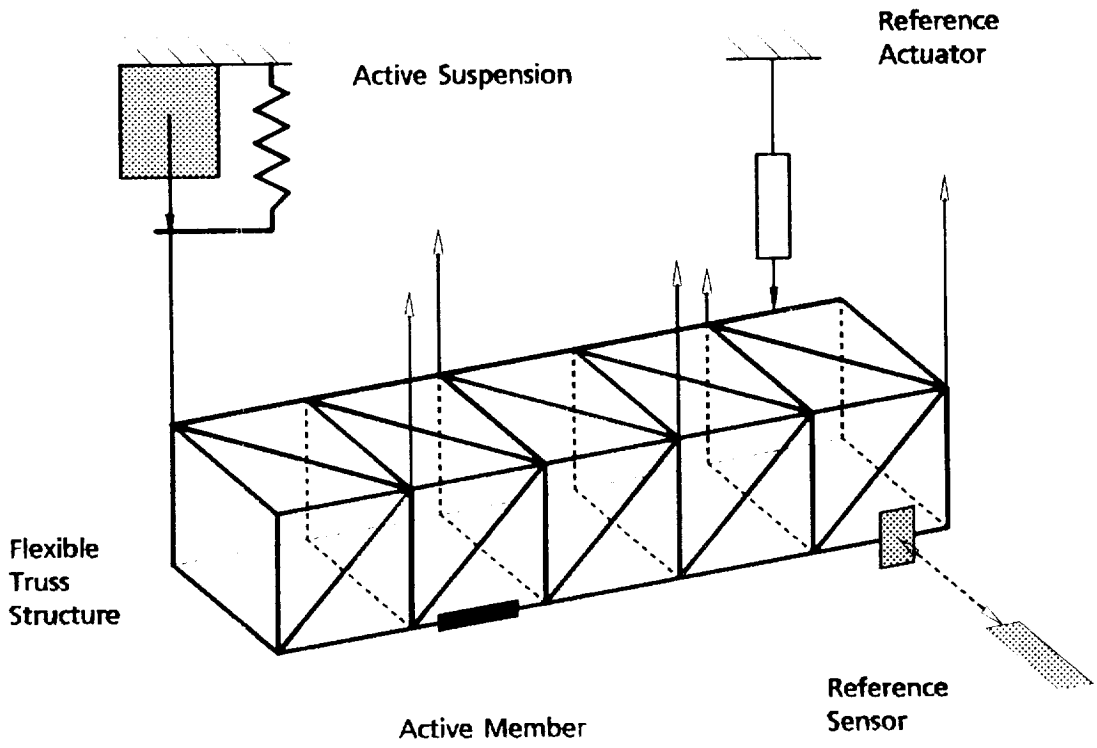

Figure 2. Principle configuration of test setup.

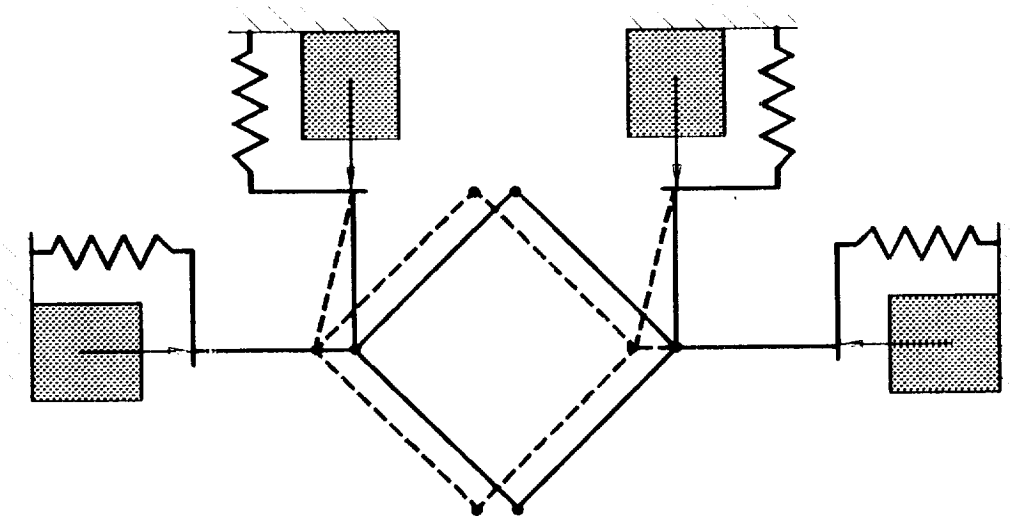

Figure 3. Optimal decoupling from gravity forces by an active suspension.

With such a compensated test setup new applications become feasible, since the suspension rods no longer have to be attached to long distance fixtures usually mounted at the lab ceiling. With a moving base it will be possible to investigate structure dynamics and control under large angle motions, e.g. slewing maneuvers. Although full gravity compensation by this suspension technique is approximative, depending on the number of hinge points, this new testing approach will help to enhance the design validation relevance for many applications.

DESIGN REQUIREMENTS FOR AN ACTIVE SUSPENSION UNIT

There are three basic functions which the suspension unit has to support with a defined accuracy:

- the passive weight compensation being free from hysteresis and acting with limited relative stiffness about equilibrium,
- the static compensation of the spring characteristic with low residual stiffness and noise,
- the dynamic compensation of moving mass inertial forces depending on the required operational bandwidth.

The interaction of forces and the compensation loops are shown in the functional diagram of Figure 4. The active functions have different associated frequency bands. While static compensation requires low-pass filtering to prevent measurement noise from deteri-

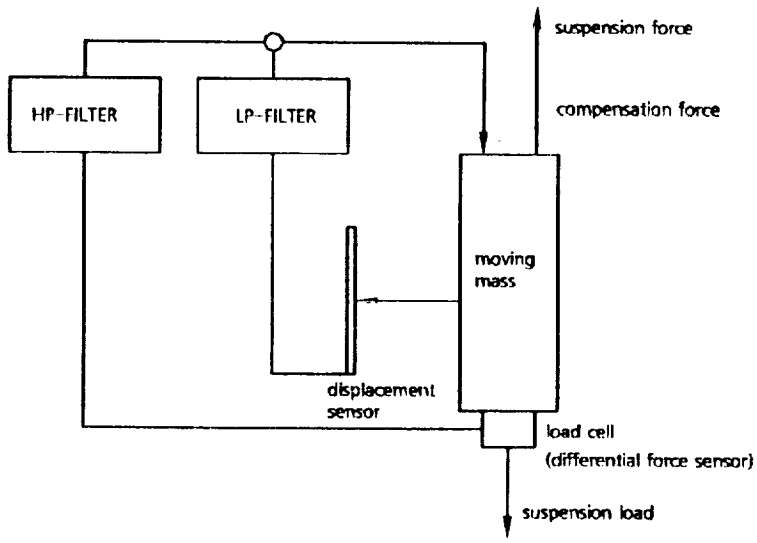

Figure 4. Active suspension force compensation loop

orating performance, the dynamic compensation is operating via high-pass filter to exclude the bias weight load measurement from feedback.

The system requirements to be satisfied by the basic functions are defined as to comprise a large number of applications which are likely to come in the foreseeable future. A large class of generic LSS control validation models including unscaled but moderately sized space experiments [1] are assumed to be covered by the following requirements:

Table 1. Requirements for an Active Suspension Unit

bandwidth	<30 Hz	(structural damping assumed with no additional active vibration damping required for higher frequencies)
load per hinge	100 N	(may be higher on expense of bandwidth)
max. displacement	±3 cm	(including open-loop tests)

The size of the suspension unit is largely defined by the required weight load and displacement range. This affects the passive spring device and the related force interaction with the actuator. But respective specifications depend on the selected design approach and hence not directly on the test item itself.

The dynamic environment however has a direct impact on the design. Respective actuator reaction force compensation requirements depend largely on the test operation mode:

- Closed-loop tests:

  Amplitudes are small with active vibration damping and hence not considered critical with respect to the dynamic feedback of inertial suspension forces.

- Open-loop tests:

  Depending on the stimulation mode, i.e. on the distribution of input energy over the structural modes large vibration amplitudes may occur. Therefore this operation mode is regarded most critical.

The worst case is obtained with all participating modes oscillating in-phase, e.g. immediately after an impulsive stimulation. More relevant for open-loop damping measurements however are sinusoidal and pass-band noise tests which permit extended measurement duration. These tests exhibit less overshoot and hence require less maximum dynamic compensation forces.

Assuming that the modal frequency distribution of a truss beam will be not too much different from that of an Euler-Bernoulli beam the assessment of the required dynamic compensation forces can be done analytically. The worst case in terms of response amplitude

is obtained for the suspension unit at the tip end of the beam with collocated stimulation. At this location then all mode shapes add up with a non-zero contribution as indicated in Figure 5.

The dynamic compensation force is derived from the required stimulation amplitude permitting a reasonably accurate evaluation of the structural motion. For wide-band excitation the unequal energy distribution with respect to the structural modes requires the full utilization of the admitted displacement range in order to include the low vibration frequencies. For single frequency excitation on the other hand the required peak acceleration or displacement depends on the evaluation instruments used. In both cases, the structural damping is not relevant since the stimulation input will always have to be adapted to the required measurement output.

The undefined input stimulation quantity is eliminated from the beam model equations by utilizing the expected output value as outlined above. The analysis for the three types of stimulation, which is omitted here, yields to the following results for the respective specific compensation forces:

- impulsive: $\ddot{y}_{max} < 45 \frac{m}{s^2} \approx 4.6g \quad (t = \Delta t)$
- white noise: $\ddot{y}_{max} < 1g \quad (3\sigma)$
- sinusoidal: $\ddot{y}_{max} < 1g$

These requirements are not very challenging for common actuators and motors available today. The low-noise performance however requires a more or less non-conventional design at the expense of available output power. This becomes evident from the detailed design analysis.

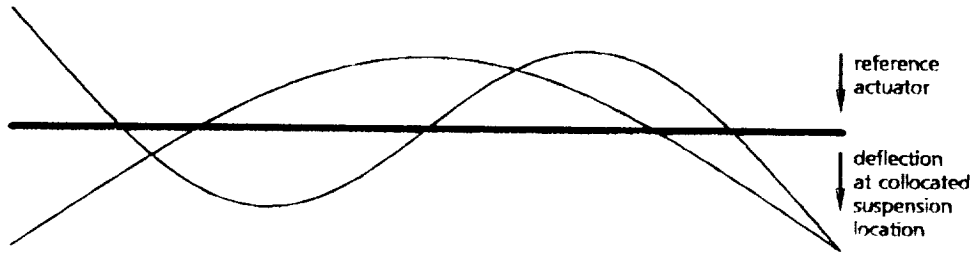

Figure 5. Beam model for dynamic analysis.

DESIGN CONCEPT

The minimization of disturbance and noise associated with the active suspension design requires precision technology. On the other hand high precision hardware may be extremely expensive, which then becomes a practical realization problem, particularly if many of these suspension units are required for an LSS control test setup. With the increasing capability of modern real-time control processors, however, which are available at even decreasing cost, this problem can be solved. A non-linear characteristic, e.g., can more easily be calibrated by respective functions in the processor than by complex mechanical adjustment procedures.

The design is determined by the method used for weight support and by the interaction with the compensation actuator. The basic solution for the passive weight support is a torsional spring. It is superior to a coil spring in terms of preloading capability and less sensitive with respect to the dynamic interference with the suspension forces. A design problem is however the force diversion, as the variation of the effective lever arm with the angle of rotation has an influence on the resulting suspension force vector.

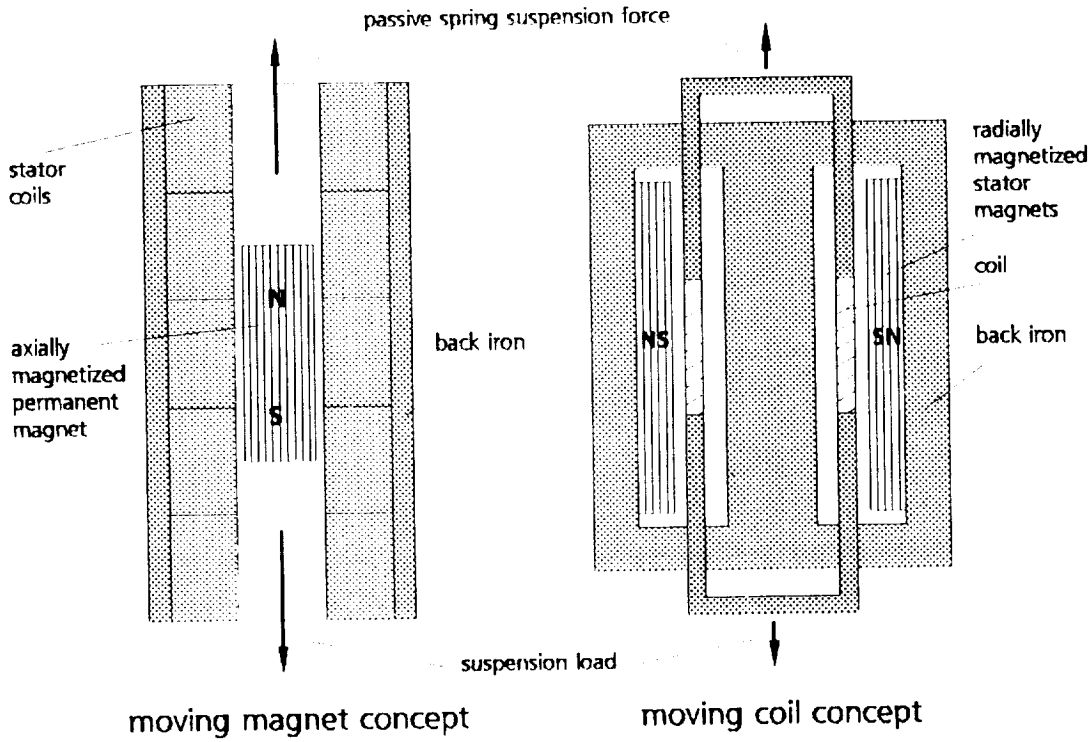

Figure 6. Electrodynamic actuator design options.

To minimize both friction effects and overall moving mass a linear motor design has been selected delivering the compensation forces. The optimal design in terms of noise and repeatability is the electrodynamic actuator which in contrast to ordinary DC-motors is characterized by

- absence of hysteresis effects which is a prerequisite to achieve high linearity performance,
- virtually noise free performance since commutation or cogging effects are excluded,
- direct force control without using high-authority control loops.

In principle two types of electrodynamic actuators are possible as illustrated in Figure 6:

1. A permanent magnet is moving in the center of controlled stator coils.

   Mechanically, this design is simple since the moving part is a concentrated mass in the center, collocated to the external load force vector. With control applied to the stator, there are no electrical leads to the moving part. Moreover, a modular adaptation to an arbitrary working range is easily possible by adding further stator coils. However, there is a long distance to the magnetic return path which decreases the force to input power efficiency.

2. An actuator coil is moving in the air gap of a radial magnetic field which is completely guided in an iron feedback.

   This design is mechanically more complex since the air gap enclosing the moving actuator coil must be narrow to minimize the magnetic stray field. The efficiency however is by principle exceeding that of the moving magnet concept.

Problems which are common to either approach are design limitations due to the non-linearity of the magnetic field characteristic. Moreover, to avoid stick-slip effects, the moving part has to be integrated into special linear contactless bearings. Hence a special development is necessary, taking into account the specific drawback features in a trade-off analysis.

Moving Magnet Actuator Concept

Due to the wide air gap associated with this approach, output force is largely dependent on displacement. As shown by the typical characteristic in Figure 7, force rapidly decreases with increasing displacement from a maximum. That is defined by the tip end of the permanent magnet being located approximately in the center of the excited coil. With increasing ratio of coil length vs. displacement the decay becomes smoother, but at the expense of a reduced effectiveness of force vs. electrical input power.

The solution to this problem is already indicated by Figure 6, where the moving magnet option is illustrated by an assembly of axially stacked coils which are simultaneously controlled depending on the relative magnet position. The efficiency of this device is dependent both on the geometrical dimensions of magnet and coil and on the control method.

Force controlled motion over a long distance may be very useful also for other applications such as handling objects under zero-g conditions. Potential benefits are in addition to the inherent modularity the accuracy and reproducibility of the exerted force.

Optimal Electromechanical Design

The optimal design of a moving magnet actuator is not straightforward due to the complex electromagnetical field distribution over a large air gap. Hence the axial force, which according to Ampère's law results from the cross-product of local field vector and the current through the stator coil windings, requires the solution of a volume integral of the form

$$F_z = G_\varphi \int_V B_r dV \tag{4.1}$$

with

G_φ = current density with respect to the coil cross-section

B_r = radial component of the emerging magnetic flux density

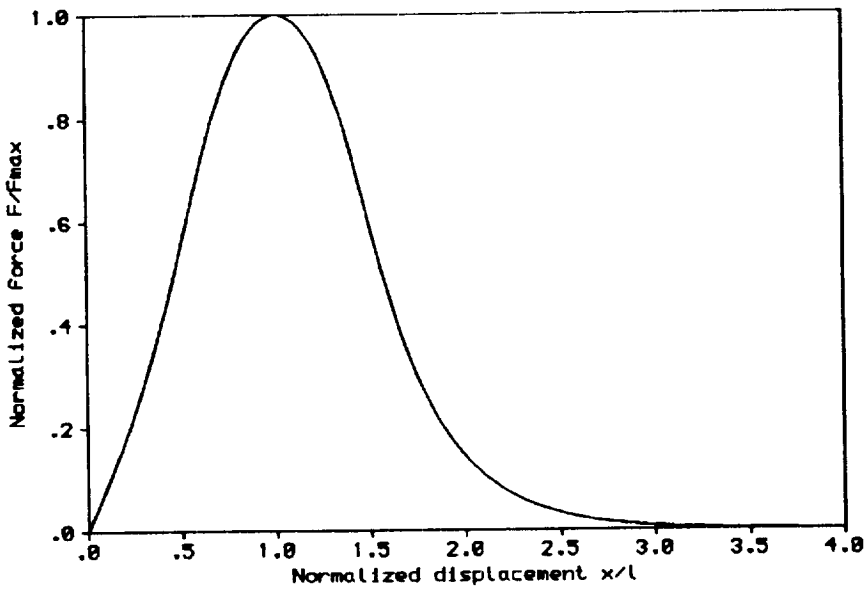

Figure 7. Coil/magnet force vs. displacement characteristic.

V = volume enclosed by the coil winding

To obtain a more general solution specific design parameters shall be eliminated from evaluation of Eq. (4.1). Assuming rare earth magnets, a remanent flux density of 1.2 T can be expected which is about the maximum to be achieved for modern NdFeB-magnets. Specific coil wiring data are replaced by more general parameters yielding an expression for the current density which is only dependent on coil geometrical dimensions and input power:

$$G_\varphi = \frac{1}{2}\sqrt{\frac{\sigma}{\rho}\,\frac{P}{(r_o^2 - r_i^2)l}} \tag{4.2}$$

with

$\sigma = \sigma_d d^2$ = normalized wiring constant

σ_d = Ampère turns per unit cross sectional area for wire diameter, d

ρ = specific ohmic wire resistance

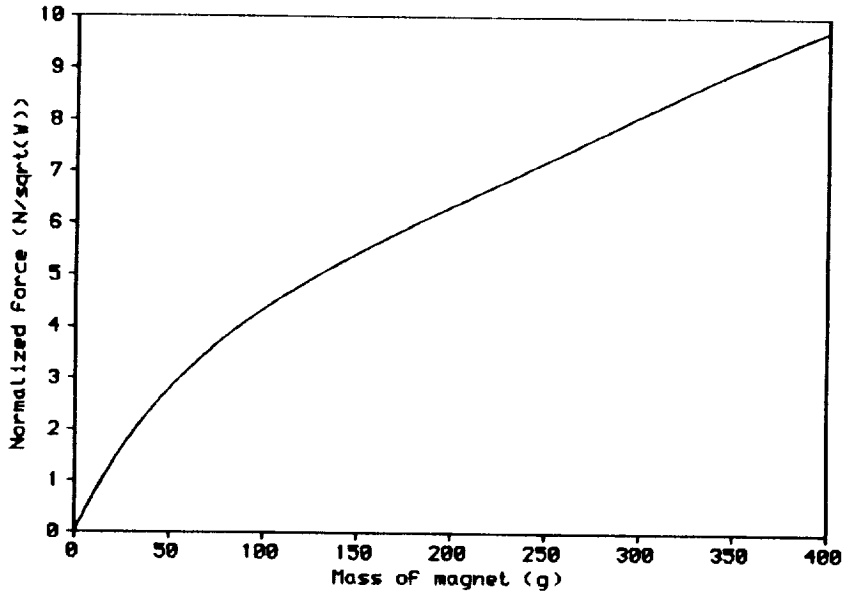

Figure 8. Optimal design diagram.

r_o , r_i = outer, inner coil radius

l = coil length

P = ohmic power loss

Then, after dividing the output force by the square root of input power, a function is obtained where only the geometrical coil/magnet parameters remain to be optimized. The result, which is computed by iteratively solving the magnetic field equations and the force integral, is shown in Figure 8. The force calculation is based upon the reference position and the ratio of magnet to coil length of two by one as shown in Figure 6, with the two coils at the tip ends of the magnet being simultaneously excited.

The required compensation force, f, depends on the dynamic force to moving mass ratio, q_m, and on the spring restraint force, F_c, yielding:

$$f(m) = F_c + q_m (m + M) \tag{4.4}$$

with M denoting the moving mass without the actuator magnet mass, m; i.e. the equivalent spring mass, attachments, rods etc.

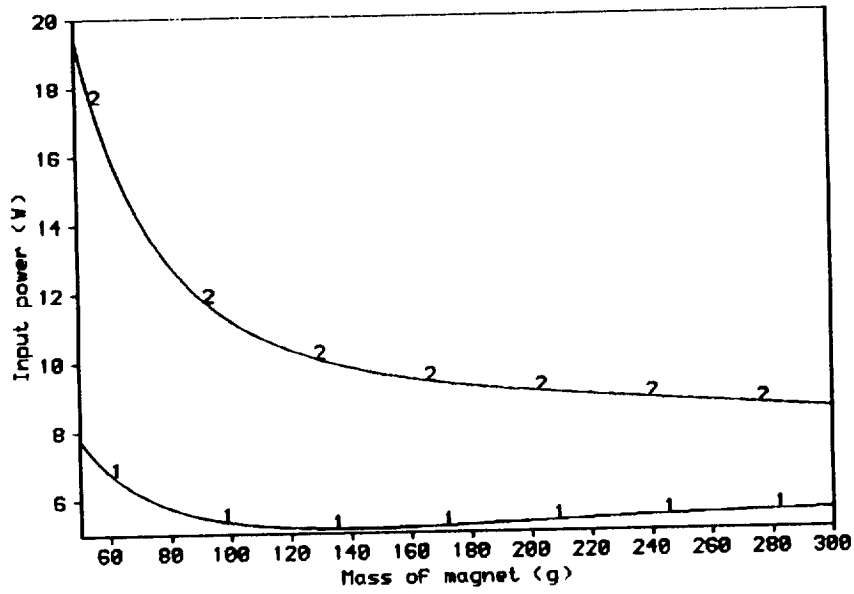

Figure 9. Input power vs. moving mass performance (graph 1: M = 100g, graph 2: M = 200g).

The most decisive design data to evaluate trade-off solutions are input power and magnet mass. A respective function is obtained by elimination of force using Eq. (4.4). The result is shown in Figure 9 for two different masses, M, and with a maximum spring restraint force F_c of 1 N.

Inspection of these performance diagrams shows at least with respect to the electromechanical voice coil design, that solutions with moderate technical effort in terms of input power and size of the moving magnet can be found to be realized with reasonable costs.

Optimal Gain Control

The actuator force is generated by simultaneously controlling all coils by dedicated wide-band current amplifiers.Their input signals are computed from the force command signal via individual displacement dependent gain factors.

The gain control law is applied to an arbitrary number of coils. A set of four coils, migrating with the magnet position, is actually involved, being controlled by a non-zero gain factor. In the reference position, as shown in Figure 10, coils No. (i + 1) and (i + 3), having maximum force efficiency, are controlled with maximum gain, while all other coils are idle.

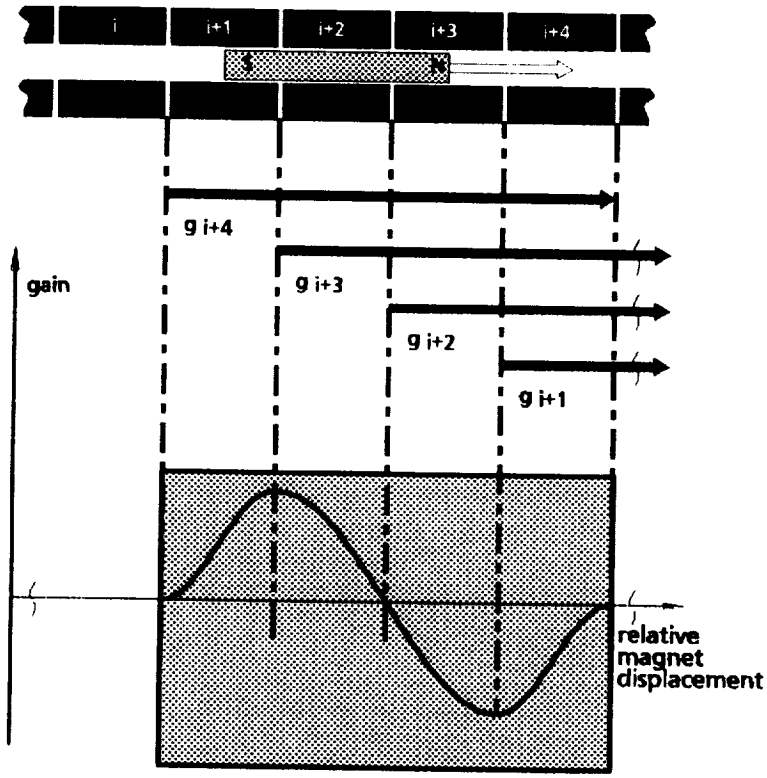

Figure 10. Gain control concept.

Starting out from this initial condition with the magnet moving to the right, the adjacent coils No. (i + 2) and No. (i + 4) are increasingly included into the magnetic driving field generation, while the rating of No. (i + 1) and (i + 3) is decreasing. This follows from the individual gain functions, $g_{i,k}$, which are sections of the overall gain function, shifted by the relative magnet position. After one coil length displacement, control continues periodically with the new set of coils controlled with maximum gain. The continuous change of gain factors is illustrated by corresponding arrows above the gain function graph.

The primary goal of gain control is an output force which is strictly proportional to the input command and independent from magnet displacement, x. This requires the four partial gain functions to satisfy for all locations, x

$$\sum_{j=i+1}^{i+4} g_j(x)\, F_j(x) = F_o = \text{const.} \tag{4.5}$$

with F_j representing the respective partial force characteristic.

In addition to this basic functional requirement a smooth variation of gain with displacement is desirable to avoid any AC transients from entering control. This applies in particular for the end of the gain function when a coil is dismissed from control. At this location therefore a zero derivative is provided to achieve a "soft commutation" performance.

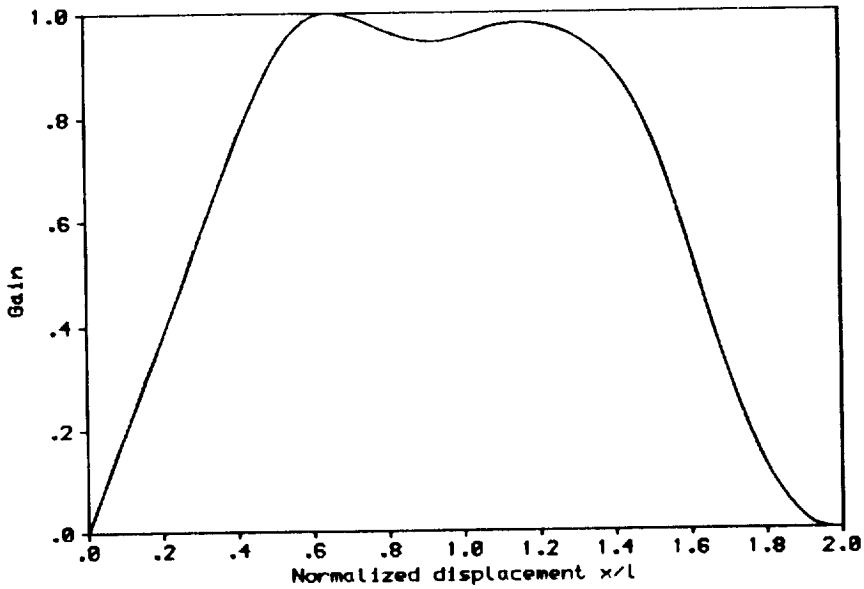

Figure 11. Typical gain characteristic.

All of these conditions are set as constraints for a quadratic optimization. The minimization function has the form

$$J = \int_{-2l}^{2l} [k_1 g(x)^2 + k_2 g''(x)^2] dx \tag{4.6}$$

with the second derivative of the gain function being included to minimize the average curvature. The weight factors k_1 and k_2 have to be selected by a trade-off to achieve acceptable smoothness on account of the average input power. A typical result is shown in Figure 11. For this design, maxima are found outside the reference position at x/l = 1. Accordingly, the average increase of input power as compared to that required for the reference position, is about 20 percent.

Moving Coil Actuator Concept

For most standard applications this concept would be preferred due to the higher efficiency as mentioned above. However, to enable a wide frequency band application, the coil AC resistance has to be low enough to avoid excessive input control voltages. This can only be realized by coil sectors opposed to multipole magnets with the individual coils not enclosing the center back iron [2].

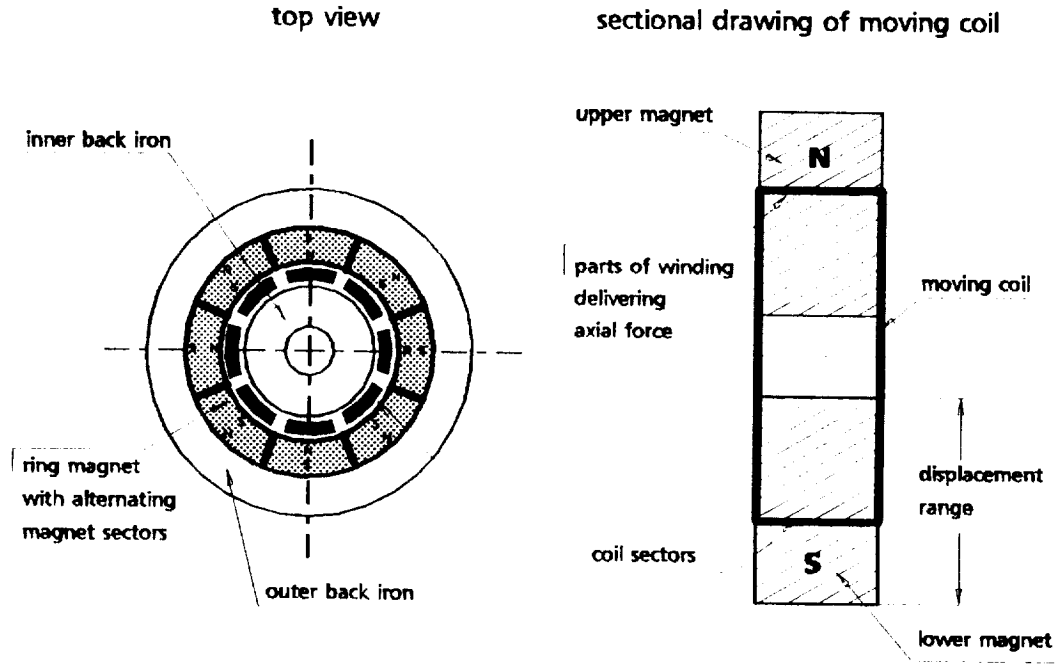

Figure 12. Multipole moving coil actuator.

A design problem arises with the desired range of displacement. As shown schematically in Figure 12, there is only a relatively short part of the winding delivering an axial force component. Moreover, two multipole stator magnet arrangements each extended over the full displacement range plus coil width must be provided ending up in a rather lengthy and complex mechanical design.

For DC applications a less complex design can be utilized employing one set of radial magnets and a simple cylindrical moving coil as shown in Figure 13. Feasibility studies have shown that this approach can be successfully used for the bias load suspension replacing the supporting spring and thereby removing spring restraint forces and mechanical interface design problems. For the specific design envisaged the radial magnets are replaced by a set of stacked rectangular magnets for cost reasons. They are attached to the circumference of the back iron. The moving part has ribs attached to a center shaft which is supported by an air bearing. By linking all external forces to the center shaft bending torques can be minimized.

As a result of electrodynamic model investigations a total moving mass of about 400 g and a required input power of 26 W is necessary to balance a 100 N external load. The main design problem here is the back iron flux saturation. Despite local saturation effects due to the non-uniform flux distribution, a satisfactory design is obtained with a moving coil diameter of about 14 cm and an air gap and magnet depth both measuring 1 cm.

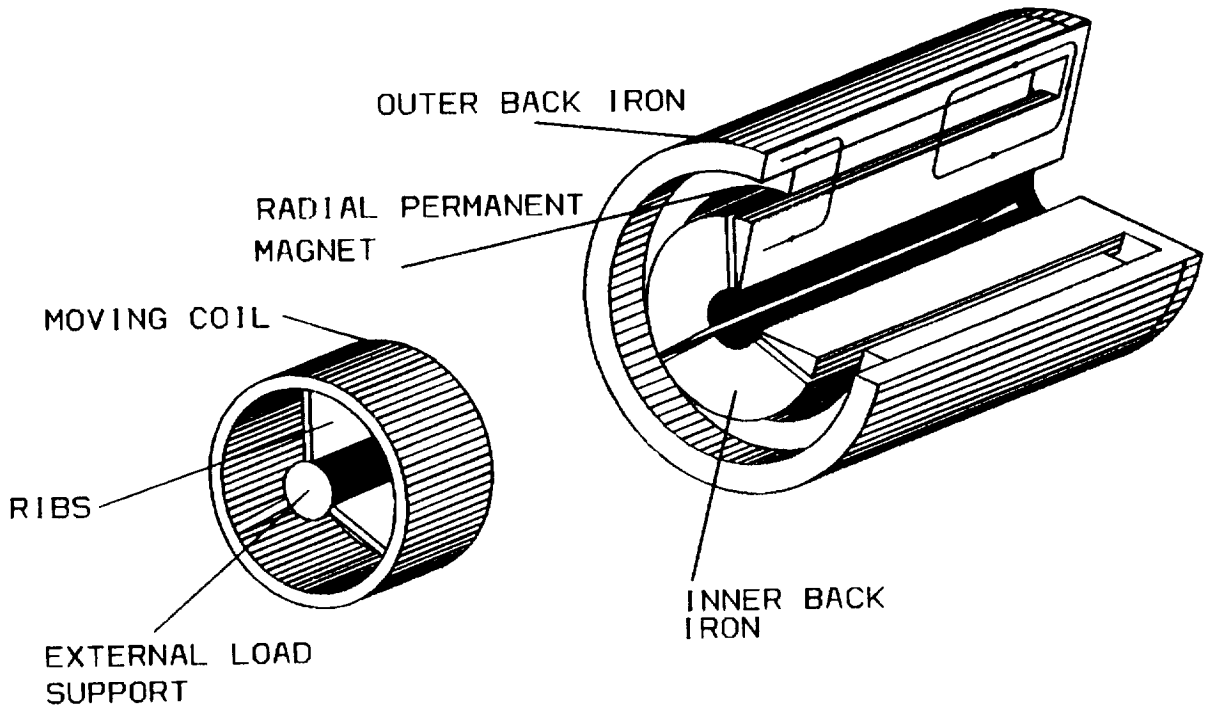

Figure 13. Moving coil actuator with unipolar stator magnet.

The obvious advantage of this approach is the virtual absence of displacement dependent forces with a computed error of a few tenths of a percent. This is achieved at the expense of a large moving mass. Extrapolating the results obtained so far it should be possible to achieve also larger forces. The additional weight penalty in terms of required actuator moving mass is estimated not to exceed about five percent of the supported load. The design limit, which is far beyond the design parameters under consideration here, is given by the increasing DC power with the associated heat transfer problem and by a potential demagnetization of the stator magnets.

DESIGN OF A LABORATORY MODEL

The development of the active suspension test facility is done stepwise starting out with prototype functional laboratory models. The first model which has been realized is a low-cost

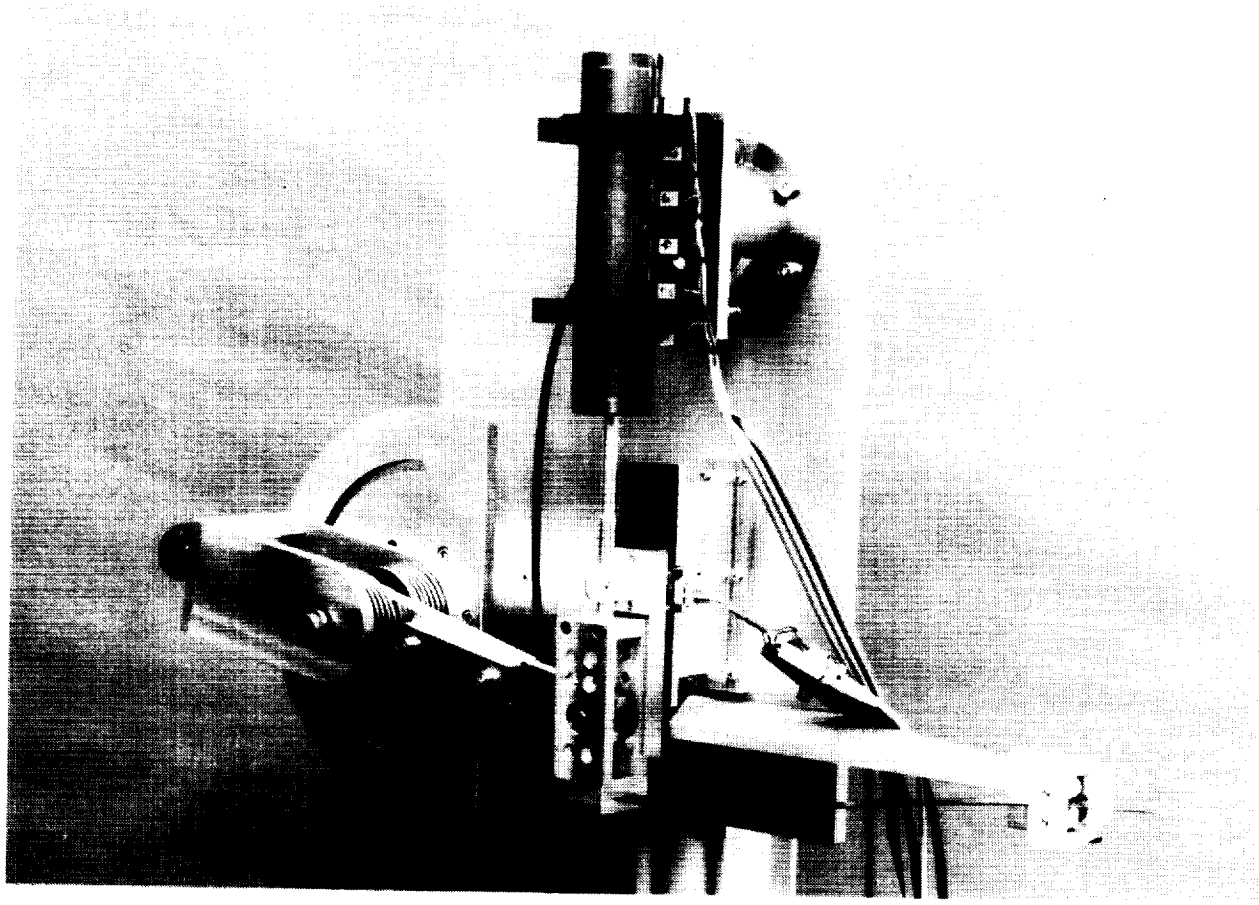

Figure 14. First functional test setup.

test stand composed of very basic mechanical elements to verify the moving magnet design concept.

Mechanical Test Setup

The functional test setup employs a 6 coil actuator, a torsional spring with a preload to be set manually by a lever and a linear ball bearing sled to guide the moving permanent magnet. The load attached to the sled is an adjustable spring-mass system. As shown in Figure 14, a fairly large force diversion lever arm is provided which is equipped with a ball bearing length compensation mechanism.

The displacement sensor is a simple off-the shelf optical incremental device. With the coil housing mounted to a piezoelectric force transducer, the force exerted on the coil can be measured while the bearing friction forces remain excluded.

Control Processor and Electrical Interface

The control hardware is based upon a high-speed digital signal processor (DSP) with associated fast I/O interface hardware. For system development it is used with a PC/AT host. In the final version it can be operated stand-alone under control of an on-chip EPROM. The main features of a typical control board currently being used is as follows:

- 16 bit fixed point DSP, 160 ns cycle time, 4 k words of memory,
- 6 pulse-width modulated outputs, high resolution & accuracy,
- two 16 bit incremental sensor I/F's with noise filters,
- various high speed ADC's and DAC's,
- 16 bit selectable I/O ports.

Special current control amplifiers have been provided to be controlled by the pulse-width modulators via an analog switch interface. Direct digital current switching has been avoided in favor of a continuous high-impedance control to suppress damping currents from the moving magnet induction voltages.

The control S/W design is supported by a development system permitting direct input of the matrices associated with the standard linear dynamic equations usually being applied for control design. Moreover, the implementation of non-linear functions is supported, realized by table look-up. In addition, on-line tracing of dynamic variables is possible. By this means, S/W development costs can be reduced to a large extent.

Test Results

The first problem to be solved has been the implementation of the gain characteristic. To this end, the force vs. displacement characteristic of each single coil has been determined.

Although no special manufacturing or wiring technique has been used the measurements showed satisfying agreement with the electromagnetic model calculations. The results were obtained by evaluation of the AC force on the stator housing due to a sinusoidal coil stimulation.

After implementation of the gain characteristic the compensated system was stimulated by a constant current input command while the moving magnet was freely oscillating with the spring-mass eigenfrequency. Although the compensation seemed to work properly, no final results are available yet since the current amplifiers started drifting. An appropriate electronics re-design is necessary to remove this malfunction.

The next step before determination of the frequency response characteristic will be the implementation of an air bearing in conjunction with the moving-coil bias load compensation. With the dynamic feedback included this will be the final functional test to validate or modify the concept if necessary before entering the first series production.

CONCLUSIONS

Active suspension tests are valuable for CSI design and validation problems, particularly if optimal dynamic zero-g simulation on ground is required. The technology becomes practically feasible with the advent of modern signal processors which are able to realize complex control tasks in real-time within the frequency range of controlled structures.

Test equipment design problems can be effectively reduced by this technology which decreases also the overall system cost. However, high accuracy results can only be achieved by a precision actuator for dynamic force compensation. The testing requirement of large structural deflection amplitudes for open-loop reference tests leads to the development of a special electrodynamic force actuator. A feasible solution in terms of reasonable mechanical effort is the moving magnet actuator although it is not very effective with respect to the required input power. A linear gain control method, including soft commutation, has been developed and successfully tested using an experimental suspension test setup. A potential spin-off application is the utilization of the force transducer as a manipulator for handling objects under zero-g conditions.

The moving coil actuator in a special configuration has been selected as a candidate to replace the bias weight suspension spring. Feasibility studies have shown that this is possible under the given operational conditions with a moving mass weight corresponding to about 5 percent of the suspended load. Considering the almost zero stiffness force and a further reduction of mechanical calibration effort, this approach has been selected as a promising alternative.

During the subsequent development steps the suspension unit will be optimized on a subsystem level before starting with the initial series production of a few suspension clusters for system level verification.

Due to the approximative gravity compensation in a wide frequency range with the active suspension approach, LSS control verification and system level validation should become

increasingly relevant. However, by no means well approved standard test methods will be ruled out, since the achievement of an optimum result will always require a well determined combination of complementary tests.

REFERENCES

[1] DLR/DORNIER, *Investigation of the Attitude and Orbit Control System Modelling for Flexible Space Platforms;* ESTEC Contract No. 6839/86/NL/MAC(SC).

[2] Fenn, R.C., et al., SatCon Technology Corporation, *An Active Magnetic Suspension for Space-Based Microgravity Vibration Isolation,* Active Noise and Vibration Control, 1990, NCA-Vol.8.

Modeling, System Identification, and Control of ASTREX

N. S. Abhyankar, J. Ramakrishnan, K.W. Byun

Dynacs Engineering Company
34650 U. S. 19N, Suite 301
Palm Harbor, FL 34684

A. Das, Lt. D. F. Cossey, J. Berg

OLAC PL/STS
Edwards AFB, CA 93523-5000

ABSTRACT

The modeling, system identification and controller design aspects of the ASTREX precision space structure are presented in this work. Modeling of ASTREX is performed using NASTRAN, TREETOPS and I-DEAS. The models generated range from simple linear time-invariant models to nonlinear models used for large angle simulations. Identification in both the time and frequency domains are presented. The experimental set up and the results from the identification experiments are included. Finally, controller design for ASTREX is presented. Simulation results using this optimal controller demonstrate the controller performance. Finally the future directions and plans for the facility are addressed.

1 Introduction:

The modeling, system identification and control of the Advanced Space Structures Technology Research Experiments (ASTREX) are the focus of this paper. ASTREX is an evolving test bed situated at the Phillips Laboratory, Edwards AFB, CA. The unique features of the experimental facility include the three-axis large angle slewing maneuver capability and the active tripod members with embedded piezoelectric sensors and actuators. The slewing and vibration control will be achieved with a set of Reaction Control System (RCS) thrusters, a reaction wheel, active members, control moment gyros (CMGs), and linear precision actuators (LPACT). A dedicated control and data acquisition computer is used to command and control this operation. The structure will be fully operational in the near future for implementing the control strategies to maneuver it to achieve retargeting and vibration suppression.

The paper is organized in the three major sections, namely modeling, identification and control. A general description of the testbed is given in the following section.

Description:

The ASTREX structure consists of two major parts; a vertical pedestal (1) 5 meters high supporting the test article (2) through an airbearing system (ABS). The test article is balanced in the floating configuration over the airbearing system by a 180 psi compressed airflow. The central part of the test article, called the hub, is directly connected to the hemispherical ball of ABS. The truss surrounding the hub is constructed by a set of 3" outer diameter graphite epoxy tubes with end fittings and the specially designed 'star nodes'. This primary structure

is connected to the front piece, called secondary, via a tripod made up of composite tubes and consisting of embedded sensors and actuators. The triangular secondary structure supports the reaction wheel and the simulated secondary mirror. A tertiary structure situated behind the primary balances the secondary and houses electronics/ power supply for the data acquisition and control. In addition, a couple of cylindrical masses placed on the sides simulate the trackers. Six sets of triangular plates attached on the front face of the test article simulate a primary mirror. The test article is shown in Figure 1. From its neutral floating configuration, it can undergo ± 20deg roll (local), ± 20deg pitch, and 'unlimited' (± 180deg revolutions) rotation about the vertical axis, limited only by the length of cables and air hoses from the ground.

The RCS thrusters are mounted on the corners of the hexagonal primary structure. Two 8 lb thrusters are placed on the top and bottom nodes for roll control. A set of four 200 lb and 8 lb RCS thrusters are placed near the remaining four corners. Their plate mounts are connected to the primary via truss members. These four thruster units can be rotated on the plate mounts to direct the thrust line by ± 30 deg with respect to the line joining centers of primary and secondary (test article z axis). With the secondary facing 30 deg down, its designed attitude, the thruster line can range between 0 to 60 deg down with respect to the ground. The 500 psi air supply to thrusters is provided by two 30 gallon tanks encased in the hub. The tanks are joined to the thrusters by a set of hoses, ball valves and air filters.

The structure is instrumented with several linear accelerometers which are connected to a set of Butterworth filters. The filtered signals can be acquired remotely by a CDAC unit with a VAX 3100 as a front end computer. It is equipped with Matrixx/ autocode/ real-time-monitor/ system build features to command actuator signals and acquire data from sensors as well as actuators. The computer requires discretized (as against continuous) forms of the control law algorithm for implementation. The CDAC is a parallel processor based system having 32 input and 32 output channel connections for transfer of analog data.

At present, the electronics for the active struts are being installed. Several angular rate sensors will be placed at different locations for line-of-sight error measurements. A set of CMGs and LPACTs will also be positioned on the test article to add slewing and vibration control power to the existing actuators.

2 Modeling:

Over time, the ASTREX structure has grown to be a complicated structure with hundreds of individual parts and bolted joints. An attempt is made to document the distances, dimensions and masses of each component to result in a finite element model (FEM) formatted as a NASTRAN data deck. The input file is grouped into the following components for ease of modification and understanding.

- Pedestal (Figure 2)
- Hub
- Hub-pedestal interface mount
- Primary truss with mirrors and trackers

- Secondary structure
- Tertiary structure and connections
- Tripod (a new component FEM is being developed.)
- Tripod to primary connection/feet plates, etc.
- Thruster mounts and thrusters
- Instruments (mainly concentrated masses)

The complete ASTREX structure is shown in Figure 3. All the above parts are discretized into elements of the types bars, triangular plates, quadrilateral plates, rigid connections and concentrated masses. The grids and their locations are defined in two cartesian coordinate systems: one for the pedestal (x vertically upward, y to the right and z horizontal) and another for the test article (x locally upward, y to the right and z facing secondary). This arrangement leads to a simplified configuration since the test article is allowed to pivot at the top node of the pedestal. The pivot point grid 139 on the primary (primary axes 0.,0.,0.127m) is coincidental with the pedestal origin at grid 501. The pedestal grids are numbered 501 to 599, and the corresponding elements are numbered 401-450 (CBAR) 801-856 (CQUADA4). These numbers have been fixed and it helps in isolating the pedestal model from the test article model for center of gravity/mass balancing checks and implementation on the multibody dynamics software such as TREETOPS. In all there are 537 grids and over 1000 elements including concentrated masses. Masses of individual components are matched with those in the model. All the grids and elements are arranged such as to resemble the structure physically. The inertia properties of the test article are as follows:

Mass = 5091.9 kg,

Center of gravity node: Grid 139

The inertia matrix in x, y, and z local coordinates relative to C.G. location in kg m^2 is

22239.30226 14.63632488 211.0207350
14.63632488 15680.06974 8.164874955
211.0207350 8.164874955 22270.35766

The NASTRAN input file is set up to perform either normal modes analysis (solution 3) or static analysis (solution 1). During the normal modes analysis, the original structural dynamical system is converted into normalized modal formulation: the dynamical equation $M\ddot{\mathrm{x}}+C\dot{\mathrm{x}}+K\mathrm{x}=F$ with M the mass matrix, C the viscous damping matrix, K the stiffness matrix, x the physical degrees of freedom, and F the force vector, becomes $\ddot{\eta}+2\zeta\omega\dot{\eta}+\omega^2\eta = \Phi^T F$ for mass normalization such that $\Phi^T M\Phi$ is an identity matrix. In this equation, η is the modal amplitude vector, ω the diagonal matrix of structural frequencies, Φ the eigenvector matrix, ζ the diagonal matrix of viscous damping factors, and an overdot signifies time differentiation.

The output for solution 3 can be obtained in three formats. The standard output includes eigenvalues, mode shapes, modal element stresses, and restraint forces induced by user supplied or automatically generated point constraints. A constraint check is performed by observing the values of rotational degrees of freedom in eigenvector matrices, providing restraints wherever large values occur and then confirming that the reaction forces produced by these restraints are negligibly small. The standard output is processed by an off-line computer program which uses the eigenvectors, eigenvalues, actuator-sensor information, damping, etc. to generate the control system matrices as a linear time invariant system. In

addition, specifically for ASTREX, the output matrix C for line of sight (LOS) is formulated by combining the optical sensitivity data (provided by Boeing) with various displacements at selected node locations on the primary, secondary and tertiary mirrors. This procedure is used to estimate the mirror motion for each of these three mirrors. The procedure of constructing the output matrix C has been detailed in [1]. The resulting state space model is:

$$\begin{aligned} \dot{x} &= Ax + Bu + Dw \\ y &= Cx \\ z &= Mx + Hu \end{aligned}$$

where A, B, D, C, M, and H are constant matrices and vectors x, u, y, z, and w symbolize states, input, output, measurements, and noise, respectively.

The second output form (output2 module) is generated using the ALTER sequence in NASTRAN for loading into the I-DEAS, Integrated Design and Analysis Software. In the I-DEAS' graphics environment, the model can be viewed and analyzed. This is achieved by selecting appropriate modules and steps in the I-DEAS' menu interactively. The pre-processing analysis and post-processing can all be performed using I-DEAS. For analysis purposes, only the finite element geometry is needed. For viewing the mode shapes in the deformed geometry form or in animation, the mode shapes from NASTRAN output2 are essential. The solution can as well be constructed entirely in the I-DEAS - FEM - Model Solution mode. (For system identification or test correlation, the I-DEAS - TEST module is utilized). In the FE module, the component weights can be evaluated by grouping several different components and evaluating their masses (element-solid properties) according to the assigned groups. As an output, strain energy distribution can also be obtained in the model solution.

The third form of the output (output5 module) is generated using the ALTER sequence for TREETOPS operations. Considering the test article and the pedestal as two individual bodies, separate flex files are generated. In TREETOPS, the problem is set-up as two flexible bodies with two hinges. These id's are the NASTRAN internal id's equivalent to the grid numbers defined by the user. The software allows one to select a different number of modes for bodies by specifying modes retained in the analysis. Upon execution, both the TREEFLX and TREETOPS synthesize multi-bodies as a single structure with pre-assigned degrees of freedom on hinge connections. The single structure with various kinds of sensors, actuators, functions generators, and controllers can be analyzed dynamically for the controlled response, especially during the large angle slew maneuver. (Both linearized and nonlinear formulations are implemented in TREETOPS). An LOS sensor subroutine as well as a controller represented in terms of dynamical matrices can be augmented externally. Other relevant features of TREETOPS include generation of eigenvalues of the combined structure (EIGEN), frequency response function plots, modal cost analysis, and time history of excitations and controlled responses. ASTREX models are generated using the above software.

Modeling is very crucial in quantifying the physical structure. Physical resemblance of the model to the actual structure is just the first step (pretest) in the modeling procedures. Acquiring data during the modal testing and identifying modal parameters of the structure formsthe next step. Validation and tuning the structural parameters for model matching are extremely important. With the modeling aspects complete, the system identification of ASTREX is now presented.

3 System Identification:

Model identification in the time domain seeks to solve the inverse problem of deriving a mathematical model that matches, in some sense, the output of a physical system. Identification experiments allow the precise characterization of the physical structure. Some of the parameters obtained from the identification procedures include modal parameters such as frequency, damping ratios and time-domain models such as state space characterizations. For the time domain identification, the q Markov covariance equivalent realization (q COVER) is used which is briefly presented here for the sake of completeness.

3.1 q - COVER Theory:

The objective of the q-Markov COVER identification is to develop state space matrices of a discrete dynamic system given by

$$\hat{x}(k+1) = \hat{A}\hat{x}(k) + \hat{B}u(k), \hat{x}(0) = \hat{x}_0 \quad (1)$$

$$\hat{y}(k) = \hat{C}\hat{x}(k) + \hat{D}u(k) \text{ for } k \geq 0 \quad (2)$$

with input u, output $\hat{y}$, the states $\hat{x}$ and the time sequence parameter k; the state covariance matrix

$$\hat{X} = \lim_{k\to\infty} E\hat{x}(k)\hat{x}^*(k) = \hat{A}\hat{X}\hat{A} + \hat{B}\hat{B}^* \quad (3)$$

is assumed to be positive definite. The infinite pulse response sequence H_i (also called Markov parameters) and corresponding autocorrelation sequence R_i (also called covariance parameters) with i $\rightarrow \infty$ relate to the output data as follows:

$$y(k) = H_0u(k) + H_1u(k-1) + H_2u(k-2) + ... = \sum_{i=0}^{\infty} H_iu(k-i)$$

and

$$R_i = \lim_{k\to\infty} Ey(k+i)y^*(k)$$

The system in eq. 1, along with the positive definite assumption on the state covariance, is said to be a q-Markov COVER of the system generating the above infinite data sequences, if the first q and q–1 terms of $\{H_i\}_0^\infty$ and $\{R_i\}_0^\infty$ are equal to those of the finite data sequences $\{\hat{H}_i\}_0^q$ and $\{\hat{R}_i\}_0^{q-1}$. Both sequences $\hat{H}_i$ and $\hat{R}_i$ can be expressed in terms of matrices $(\hat{A}, \hat{B}, \hat{C}, \hat{D})$. The quadruple $(\hat{A}, \hat{B}, \hat{C}, \hat{D})$ is extracted in an inverse manner from the experimental data obtained by exciting the structure by a finite series of pulses. The realization problem, finding all minimal stable q-Markov COVERs given $\{\hat{H}_i\}_0^q$ and $\{\hat{R}_i\}_0^{q-1}$, is based on the factorization and projection of two data matrices $\mathbf{D_q}$ and $\bar{\mathbf{D}}_\mathbf{q}$(functions of a finite number of Markov and Autocorrelation parameters) obtained from the pulse response data:

$$\mathbf{D}_q \triangleq \mathbf{R}_q - \mathbf{H}_q\mathbf{H}_q^*$$

$$\bar{\mathbf{D}}_q \triangleq \mathbf{R}_q - \bar{\mathbf{H}}_q\bar{\mathbf{H}}_q^* \quad (4)$$

The interested reader is directed to references [2,3] for more details and proofs. The data acquisition procedure in the ASTREX lab for conducting the identification experiments is now presented.

3.2 Data acquisition:

The data required for the system identification has been obtained from accelerometers and selected RCS thrusters (8-lb) through a control and data acquisition computer. A block diagram, given in Figure 4, describes the acquisition process. The locations for accelerometers are carefully selected based on expectations of capturing all the relevant structural modes. These accelerometers and thruster pin-outs are connected to a coaxial junction box situated on the tertiary structure. Signals from the accelerometers, powered by a constant current amplifier, are filtered and amplified prior to acquisition with the help of a set of 8^{th} order Butterworth filters having a 200 Hz bandwidth and the capability to amplify signals 34 times maximum. The data acquisition is monitored through a parallel processor CDAC having a VAX3100 as the front end computer. CDAC is also linked to the ABS computer to transfer information from gimbals, LVDTs, and encoders connected to ABS. The sampled data is saved in the ASCII format specifically to transport to other software such as MATRIXX, I-DEAS TEST, etc. to perform system identification. The identification of a large structure such as ASTREX is best performed using the techniques suitable for multi-input multi-output systems. The application of the q-Markov COVariance Equivalent Realization (COVER) algorithm to ASTREX is now presented.

3.3 Identification of ASTREX:

Markov and autocorrelation parameters of the system to be identified are determined from the experimental data. There are two approaches to this problem:

(i) Excite the system by a pulse input to obtain the Markov parameters and by a white noise input to obtain the autocorrelation factors.

(ii) Obtain both the Markov and autocorrelation parameters from the pulse response.

The second approach is used in this work since one experiment yields both the Markov and autocorrelation data.

Identification experiments were conducted on the ASTREX test article in August 1991. The compressed air thruster developed by Boeing was used in the experiments. The details of the identification experiment and the results are described as follows.

The actuators used in system identification were the 8 lb bidirectional thrusters. The thrusters are designed to operate using compressed air at 500 psi. At the time of testing, however, a 150 psi compressor was used to provide the compressed air (a new 500 psi compressor is now fully operational). Additionally, there was a pressure drop to 70 psi across the air filters. Based on this pressure and the thruster operation mode (blow down) a thrust of about 3 lbs was achieved. The input voltage versus thrust command of the actuator was linear. The tank pressure changed from 150 psi to a 100 psi during this test. The identification tests were conducted using 4 millisecond pulses with a 2 second data sampling time per experiment.

3.4 Identification at 250 Hz:

Four actuators and thirty-one sensors were used in the identification experiment. The actuators were located on the primary truss. The sensor locations and their identification numbers are shown in Table 1. Piezoelectric accelerometers with limits ± 5 g were used as sensors in this experiment. Channel 1 of the CDAC was used to record the input voltage from the thrusters, while channels 2-32 were used to record the accelerometer outputs. Since the pulse was of a low magnitude and short duration (4 ms), the gain on the Butterworth filters was set to 34. This resulted in a significantly better signal-to-noise ratio ($\simeq 8$). The noise in the outputs were essentially downstream of the Butterworth filter. The q-Markov covariance equivalent realization technique with pulse inputs was used in the identification work. The pulse input is applied one-at-a-time at each actuator location. For consistency in measurement, each experiment was repeated 10 times. At the first actuator location, the pulse was applied 10 times, at 2 second intervals. This was repeated at the other three locations and the raw data files were obtained.

The data collection and processing procedure is shown in Figure 5. For the first identification run, the data from experiment one was averaged and detrended. Then the q-COVER algorithm was applied to the six outputs given in Table 2 for 50^{th} order Markov COVER. The applied pulse amplitudes to thrusters are: [0.9122, 0.9246, 0.8903, 0.908]. The intensities are the square of these amplitudes. From the singular value plot of the matrix $\mathbf{D}_q$, a 50^{th} order state space realization is derived. Figures 6 and 7 show the correlation between the time responses of the identified data from channels 2 and 5 versus the lab time history data. The FFT for these output channels is shown in Figure 8 (Solid line represents LAB data dashed line represents IDM response). The eigenvalues in the 10-30 Hz range for the identified model are given in Table 3. A frequency response function was also generated between 0-50 Hz using a tripod accelerometer and the first actuator. The results from the time domain identification are close to the frequency domain results.

3.5 Frequency Response Function:

It is well known that a system's transfer function corresponding to any input/output pair can be represented graphically in the Laplace plane by plotting the system's complex poles and zeros. The poles of a second order viscously damped system are intimately related to the modal natural frequencies and modal damping ratios. Therefore the knowledge of a system's poles is sufficient for the identification of the modal parameters. In order to determine all the poles of interest, one has to investigate multiple sets of input/output pairs. The frequency response function (FRF) is the ratio of the output to the input of a system with respect to the frequency of excitation.

A single-input single-output (SISO) transfer function measurement between two locations on ASTREX was performed using the HP3562A dual channel analyzer. The structure was excited by a shaker at the left-top node on the shaker in the horizontal direction (z global). A force transducer situated between the shaker and the structure provides the analog input source level. A collocated accelerometer record was used to obtain a frequency response function (FRF) shown in Figure 9. This is the latest FRF of the structure after the new TRW active struts were installed. The frequencies 10.25 and 10.625 are classified to be bending in the yz and xz planes, respectively. Large numbers of such FRFs will be needed to identify the frequencies, mode shapes, and damping accurately. This FRF of the present ASTREX configuration provides one with a modal survey of the test article.

4 Control:

Control design procedure and results with related methods are presented in this section. The procedure shown in Figure 10 can be represented by the following steps: frequency weighting on LOS outputs, model reduction using Modal Cost Analysis(MCA), and reduced-order controller design using Output Variance Control (OVC). Now the OVC and MCA methods are discussed. Their applications can be found in [5,6].

4.1 OVC Theory:

The objective of the OVC problem is to design a controller that minimizes input energy subject to inequality constraints on the output variances. From the application standpoint, only the discrete form of the OVC theory is presented here.

Consider the following time-invariant, stabilizable and detectable continuous system state space model:

$$\begin{aligned} \dot{x}_p &= A_p x_p + B_p u + D_p w_p \\ y &= C_p x_p \\ z &= M_p x_p + v_p \end{aligned} \tag{5}$$

where $x_p \in R^{n_x}$, $y \in R^{n_y}$, $z \in R^{n_z}$, and $u \in R^{n_u}$ are the state, output, measurement and control vectors, respectively. The disturbance vector $w \in R^{n_w}$ is a zero mean white noise process with intensity $E\left\{w_p(t)w_p^*(\tau)\right\} = W_p\delta(t-\tau)$ while the measurement noise v_p has an intensity $V_p\delta(t-\tau)$. The objective is to design an full order controller

$$\begin{aligned} u &= Gx_c \\ \dot{x}_c &= A_c x_c + Fz \end{aligned} \tag{6}$$

which minimizes the control energy

$$J = E_\infty(u^T R u) = tr\, RGX_cG^T\,, \tag{7}$$

where $X_c = E_\infty x_c x_c^T$ is the controller variance, subject to equations 5 and 6 and satisfies the output variance inequality constraints

$$E_\infty\, y_i^2(t) \le \sigma_i^2 \quad i = 1, 2, \ldots, n_y \tag{8}$$

Defining a new state vector x as $x = \left[(x_p - x_c)^T \quad x_c^T\right]^T$, equations 5 and 6 can be written as

$$\dot{x} = Ax + Dw \tag{9}$$

$$y = Cx \tag{10}$$

where

$$A = \begin{bmatrix} A_p - FM_p & A_p - FM_p + B_pG - A_c \\ FM_p & A_c + FM_p \end{bmatrix}$$

$$D = \begin{bmatrix} D_p & -F \\ O & F \end{bmatrix}, \quad C = [C_p\ C_p], \quad u = [0\ \ G]\,x, \quad w = \begin{bmatrix} w_p \\ v_p \end{bmatrix} \tag{11}$$

The state covariance matrix of the system (9) becomes

$$X \triangleq E_\infty(xx^*) = \begin{bmatrix} P & X_{12} \\ X_{12}^T & X_c \end{bmatrix} \tag{12}$$

and the state covariance of the plant (5) becomes $X_p = P + X_c$, where P is the error covariance matrix and

$$W = \begin{bmatrix} W_p & 0 \\ 0 & V_p \end{bmatrix} \tag{13}$$

The OVC problem is expressed as an equivalent nonlinear programming problem in which an augmented objective function is minimized. The inequality variance constraint in the necessary conditions is handled via Kuhn-Tucker conditions. The solution of the necessary conditions results in the following algorithm for a discrete system.

4.2 OVC Algorithm for the Discrete System:

Given data $\{A_p, B_p, C_p, D_p, M_p, W_p, V_p, Q_o, R, \sigma_i, \epsilon_i, n\}$

where $Q_o > 0$ is a diagonal matrix

Step 1: Compute the Filter gains F through Riccati solution P by satisfying

$$\begin{aligned} 0 &= A_pPA_p^T - P - A_pPM_p^T(V_p + M_pPM_p^T)^{-1}M_pPA_p^T + D_pW_pD_p^T \\ F &= A_pPM_p^T(V_p + M_pPM_p^T)^{-1} \end{aligned} \tag{14}$$

Step 2: Compute the maximal accuracy solution

$$y_i^2 \text{ (Max. Accuracy)} = \left[C_pPC_p^T\right]_{ii} \tag{15}$$

Computation is terminated if $\sigma_i^2 < [C_pPC_p^T]_{ii}$ for any i.

Step 3: Compute the controller gain matrix G through Riccati solution $\tilde{K}$

$$\begin{aligned} 0 &= A_p^T\tilde{K}A_p - \tilde{K} - A_p^T\tilde{K}B_p(R + B_p^TKB_p)^{-1}B_p^T\tilde{K}A_p + Q_k \\ G &= -(R + B_p^TKB_p)^{-1}B_p^T\tilde{K}A_p \end{aligned} \tag{16}$$

Solve the controller covariance equation

$$0 = (A + BG)X_c(A + BG)^T - X_c + F(V + M_pPM_p^T)F^T \tag{17}$$

Compute the output variance

$$(y_{i_{RMS}})^2 = [C_p(P + X_c)C_p^T]_{ii} = [C_pX_pC_p^T]_{ii} \tag{18}$$

Step 4: Verify the convergence condition

$$[y^2_{i_{RMS}} - \sigma_i^2]Q_{ii} \leq \epsilon_i \text{ for all } i \text{ STOP}$$

OR update Q_k as $Q_{k+1} = [\ \frac{y^2_{i_{RMS}}}{\sigma_i^2}\ ]^n Q_k$ and return to step 3.

The necessary condition for the OVC problem is the same as that of the LQ class of problems with some diagonal output weighting matrix that is iteratively updated. From the above equation, it turns out that if $E_\infty y_\alpha^2(t) < \sigma_\alpha^2$, then the corresponding weighting q_α approaches 0. Physically this means that this particular output $y_\alpha(t)$ is not critical to the design and the constraint $T_\alpha \leq \sigma_\alpha^2$ is not necessary. It is, of course, not known *a priori* which constraints will be binding, and so all constraints must be stated in the problem. More details on the OVC method can be found in reference [9]. While there is no convergence proof for the algorithm, experience shows that the algorithm will converge if the tuning parameter n is sufficiently small.

4.3 Modal Cost Analysis (MCA):

The evaluation model is reduced to Riccati solvable dimensions by the MCA method. The reduced order model is called the design model. The controller is designed based on this model. The contribution of the mode i to the scalar cost function is called "modal cost." Modes are truncated such that the design model retains a percentage of the cost of the evaluation model.

Consider the system in modal coordinates

$$\begin{aligned} \dot{\eta}_i &= \lambda_i \eta_i + b_i^* u \qquad i = 1, \ldots, n_x \\ y &= \sum_{i=1}^{n_x} C_i \eta_i \qquad \eta_i(0) = 0 \end{aligned}$$

with the scalar cost function

$$V = \sum_{\alpha}^{n_u} \int_o^\infty y^{\alpha^*}(t) Q y^\alpha(t) dt$$

where $y^\alpha(t)$ is the response to $u_\alpha(t) = \mu_\alpha \delta(t)$. For the modal coordinate η_i, the modal cost is given by

$$V_{\eta_i} = [X_m\ C_m^*\ Q\ C_m]$$

where

$$\begin{aligned} 0 &= X_m A_m^* + A_m X_m + B_m \mathcal{U} B_m^* \\ \mathcal{U} &= diag \begin{bmatrix} \mu_1^2 & & \\ & \ddots & \\ & & \mu_{nu}^2 \end{bmatrix} \end{aligned}$$

and $A_m = diag\,[\ldots \lambda_i \ldots]$ with B_m and C_m being corresponding modal input/output coefficient matrices. From the computational viewpoint, closed form solutions of the Lyapunov

equation in modal coordinates are used. Furthermore, some of the calculations are carried out in the real Jordan form coordinates yielding the appropriate design model.

The controller design iterations use the integrated MCA-OVC formulation. The design model determined by the MCA approach depends on the output weighting matrix Q, which reflects the importance of each output. The OVC approach iteratively determines the Q matrix that yields a controller satisfying output inequality constraints. Thus the model reduction procedure is influenced by the designed controller. The integrated procedure is implemented as follows. Based on an initial weighting matrix, Q_o, the MCA approach is used to design a reduced-order model which is followed by the OVC loop. The OVC loop yields a new Q matrix. This matrix Q is now used in the MCA procedure to design a new reduced order model. Controller design is repeated until the reduced-order model ceases to change.

4.4 Design Results:

An 82^{nd}-order finite element model, with a 4 msec sample period, is used as the ASTREX model. Eight accelerometers and ten RCS jets are mounted on the test article; four 200-lb jets are primarily used for slews, four 8-lb jets are used for vibration control, and two 8-lb jets coupled to each other control roll motion. The RCS jets are assumed to have first-order lags with their corner frequencies at 30 Hz, while the accelerometers are assumed to have high bandwidth. Thus the order of the composite system (also the evaluation model) consisting of ASTREX, actuator, and sensor dynamics is 91.

For vibration suppression study, only the six 8-lb jet locations are used as control input channels, while all the jet locations are considered as disturbance input channels. The noise intensity matrices W and V for actuator and sensor noises are defined as

$$W = \text{diag } [2.02,\ 2.02,\ 2.02,\ 2.02,\ 2.02,\ 1260,\ 1260,\ 1260,\ 1260]\ N^2$$
$$V = \text{diag } [1.0,\ 1.0,\ 1.0,\ 1.0,\ 1.0,\ 1.0,\ 1.0,\ 1.0] \times 10^{-6}\ g^2$$

where g is the gravity acceleration constant. The output y to be controlled consists of the x and y components of the LOS outputs in the primary ($losP$), secondary $x_(losS)$, tertiary ($losT$) mirrors, and the average of the three (los):

$$y^T = [x_{losP},\ x_{losS},\ x_{losT},\ x_{los},\ y_{losP},\ y_{losS},\ y_{losT},\ y_{los}]$$

The reduced-order controller is sought in discrete time domain for ease of implementation on the CDAC. A 24^{th} order controller is designed based on the MCA-OVC algorithm such that the LOS output and control variances are minimized. As shown in Figure 10, the LOS outputs are weighted using a frequency-dependent function accounting for the actuator dynamics and also the control bandwidth. Also, unfavorable frequency components, such as the pedestal vibration modes, are directly augmented in the controlled output matrix along with the LOS outputs. Then the iterative use of the MCA and OVC algorithms tune the performance of the closed-loop system.

The controller is evaluated on the 91^{st}-order evaluation model. The open-loop variances of the composite system are given by

$$[9.0,\ 16.6,\ 0.013,\ 16.9,\ 3.6,\ 9.9,\ 0.010,\ 11.8]\ \text{arcsec}^2$$

The LOS output variances realized by the controller are

$$[6.7,\ 9.1,\ 0.010,\ 10.3,\ 2.5,\ 5.9,\ 0.010,\ 7.2]\ \text{arcsec}^2$$

The control variances are also listed as follows:

$$[10.7,\ 20.2,\ 15.4,\ 13.4,\ 26.0]\ \text{N}^2$$

Figure 11 shows the time response plot of typical outputs. The secondary mirror LOS outputs achieve moderate reductions in the output variances with low control input variances. The frequency components at 3 to 5 Hz, appearing in the primary mirror LOS outputs, are due to pedestal structure vibration, and require larger control effort for suppression. The controller designed for vibration suppression can now be implemented on ASTREX. Although implementation is beyond the scope of this paper, the procedure is presented nevertheless for the sake of completeness.

4.5 Implementation:

The CDAC has the software MATRIX$_X$, Autocode, and System_build which generate signals for actuators, and acquire data. The operation is performed by building block diagrams to process data in either continuous or discrete system form. For implementation, however, only the discretized control gain matrix form can be used, and thus the controller should be designed in a discretized version. The control 'superblock' basically relates sensor inputs to the actuator inputs, and depends on the method of controller design. For ASTREX, the encoder data converted in terms of quaternions or Euler angles, mainly for slewing, together with measurements of LOS error/accelerometers for vibration suppression can form the sensor data. At present, the control signals are of thrusters (14 total) and for reaction wheel (1). Monitoring of the control process is done in the interactive animation software. It is also to be noted that, due to their interactive nature, both the slewing and vibration must be controlled simultaneously. In other words, for ASTREX, both motions cannot be isolated from one another.

5 Plan:

The following items are currently in the planning stage.

- Component FEM for the tripod active struts.
- Evaluation of dynamic characteristics of thrusters (14) and reaction wheel.
- Acquisition, installation, and testing of LOS sensors.
- A detailed modal survey.
- Model updates based on the experimental data.
- Closed-loop vibration and slewing control.

6 Concluding Remarks

The modeling, identification and controller simulation aspects of the ASTREX testbed are presented in this paper. A precision space structure such as ASTREX provides the structural dynamics and control community with a testbed in which to test and implement emerging technologies. With the establishment of the baseline identification procedures, future updates to ASTREX can be easily handled. A comprehensive look at the modeling, identification and some controller synthesis approaches to ASTREX have been presented. With the structural/hardware development complete, future directions include large closed loop slewing experiments on ASTREX.

7 References

1. *Updated ASTREX State Space Model*, Dynacs Eng. Co., Oct. 90.

2. A.M. King, U.B. Desai and R.E. Skelton, *A Generalized Approach to q-Markov Covariance Equivalent Realizations for Discrete Systems,* 1987 American Control Conference, Minneapolis, MN.

3. U.B. Desai and R.E. Skelton, *Partially Nested q-Markov Covariance Equivalent Realizations,* CTAT, Vol. 3, No. 4, pp. 323-342, December 1987.

4. C. Hsieh, R.E. Skelton and F.M. Damra, *Minimum Energy Controllers with Inequality Constraints on Output Variance*, Opt. Control Appl. & Methods, vol. 10, pp. 347-366, 1989.

5. J. Ramakrishnan, K.W. Byun, R. Skelton, and Lt. D.F. Cossey, *ASTREX Controller Design: OVC and OCC Approach*, NASA-DOD Conference, Orlando, FL, pp. 202-213, Nov. 1990.

6. A. Hu, R.E. Skelton, G.A. Norris and D.F. Cossey, *Selection of Sensors and Actuators with Applications to the ASTREX Facility*, Proceedings of the 4th NASA/DoD CSI Conference, Orlando, FL, Nov. 1990.

Table 1: ASTREX Sensor Locations

CDAC Channel	ASTREX Node #	Sensor Connector #	x	y	z	Comments
1	Thruster				√	
2	197	56		√		Tripod Upper
3	218	43	√			Secondary Backface
4	195	60		√		Tripod Left
5	206	58		√		Tripod Upper
6	196	64		√		Tripod Right
7	204	61	√			Tripod Left
8	196	63	√			Tripod Right
9	197	55	√			Tripod Upper
10	205	65	√			Tripod Right
11	195	59	√			Tripod Left
12	218	44		√		Secondary
13	204	62		√		Tripod Left
14	204	70			√	Tripod Left
15	247	21			√	Primary
16	197	67			√	Tripod Upper
17	196	71			√	Tripod Right
18	206	68			√	Tripod Upper
19	205	72			√	Tripod Right
20	15	51	√			Tertiary
21	223	45		√		Secondary
22	250	26	√			Primary
23	195	69			√	Tripod Left
24	205	66		√		Tripod Right
25	233	33			√	Primary
26	244	4		√		Primary
27	238	16		√		Primary
28	245	22		√		Primary
29	241	11			√	Primary
30	26	54			√	Tertiary
31	1	52		√		Tertiary
32	206	57	√			Tripod Upper

Table 2: Identification Input Channels

Output #	Channel #	Location
1	2	Tripod
2	5	Tripod
3	7	Tripod
4	10	Tripod
5	11	Tripod
6	12	Secondary Plane

Table 3: ID Model Eigenvalues

$\underline{\omega}$(Hz)	ζ
10.2	0.8578
13.662	0.0226
14.3	0.1072
18.713	0.0243
19.24	0.0253
23.13	0.0334
27.22	0.0066
28.72	0.0104

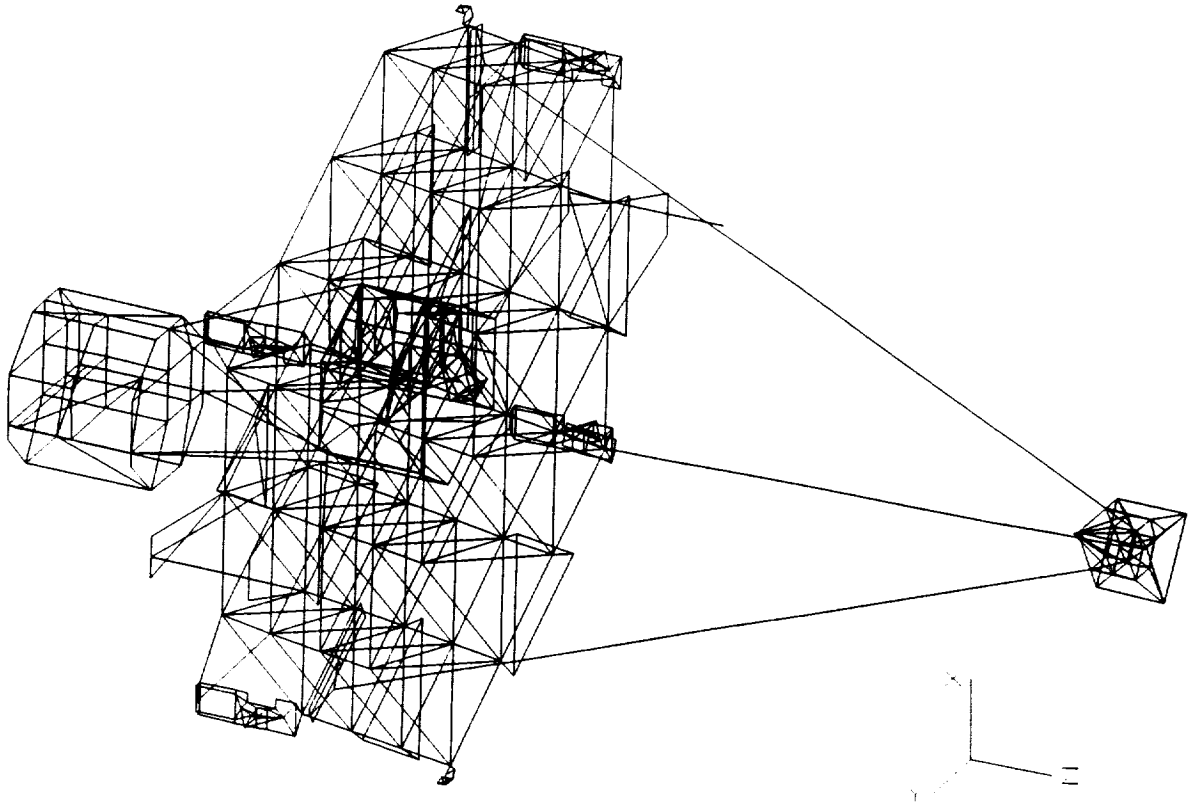

Figure 1: Test article substructure.

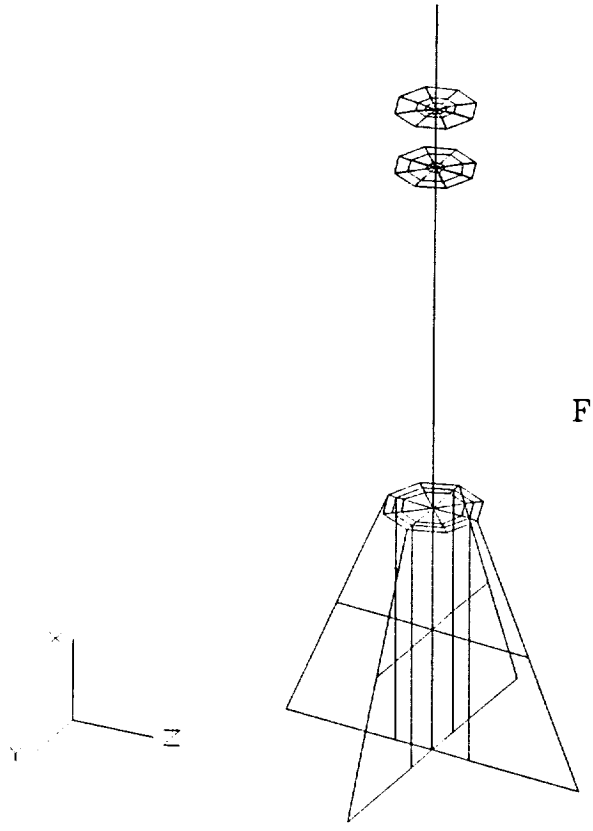

Figure 2: Pedestal substructure.

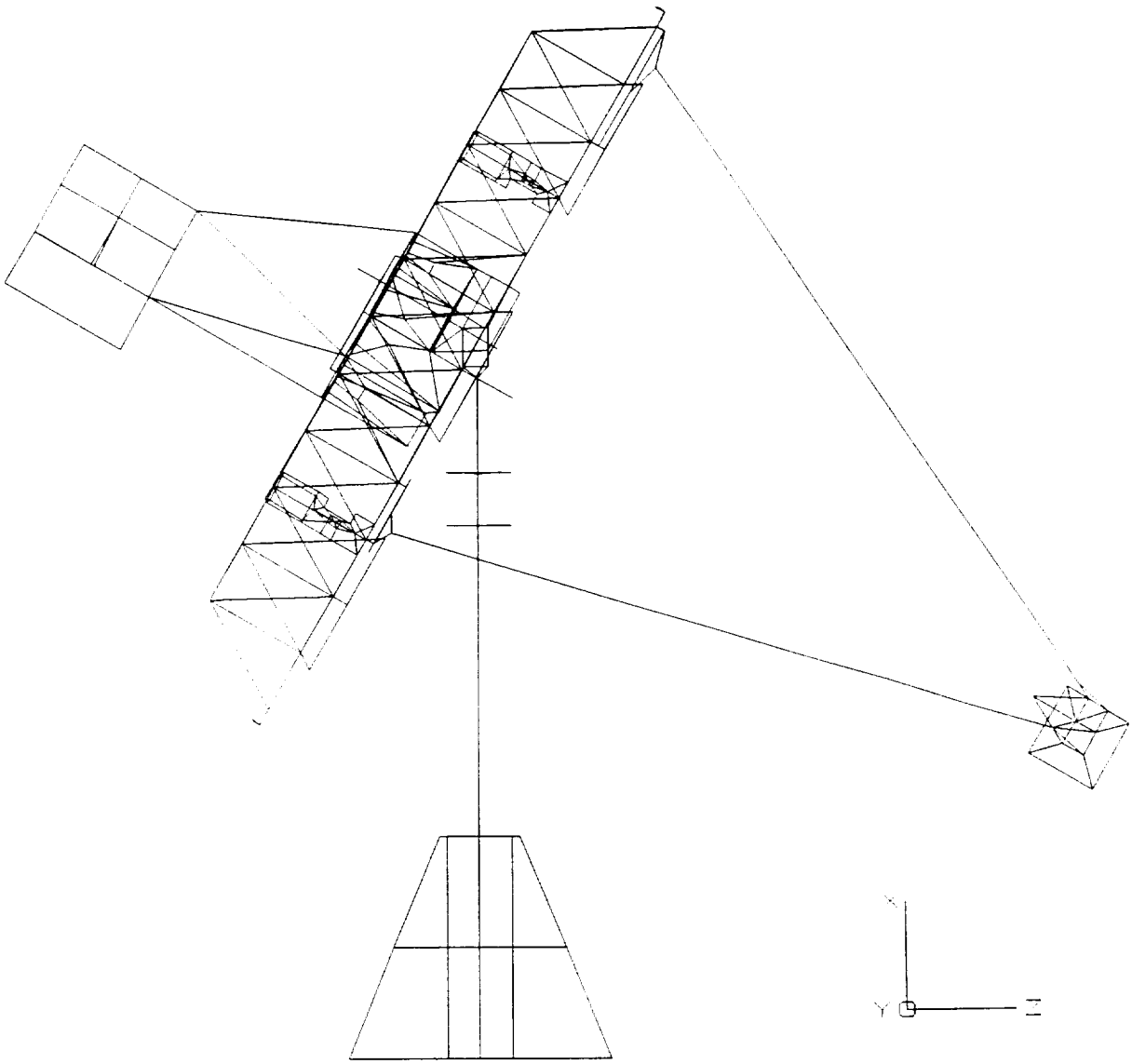

Figure 3: Complete ASTREX structure.

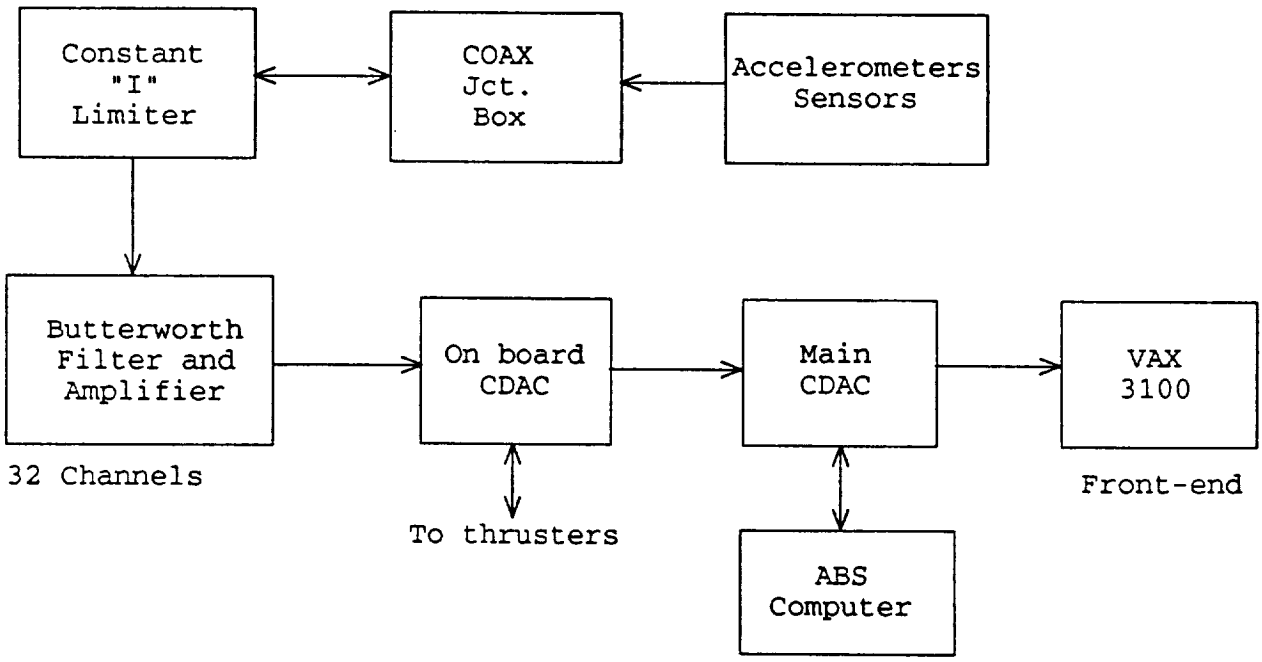

Figure 4: Data acquisition process.

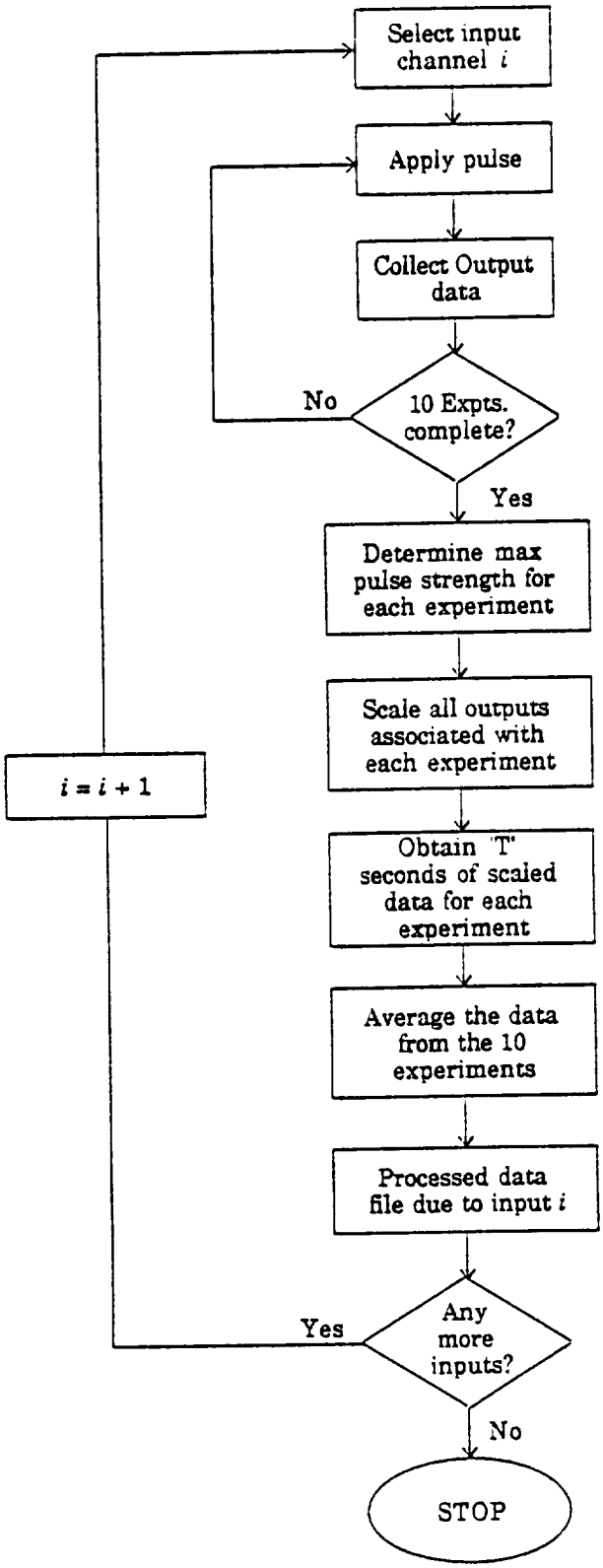

Figure 5: Data collection and processing procedure.

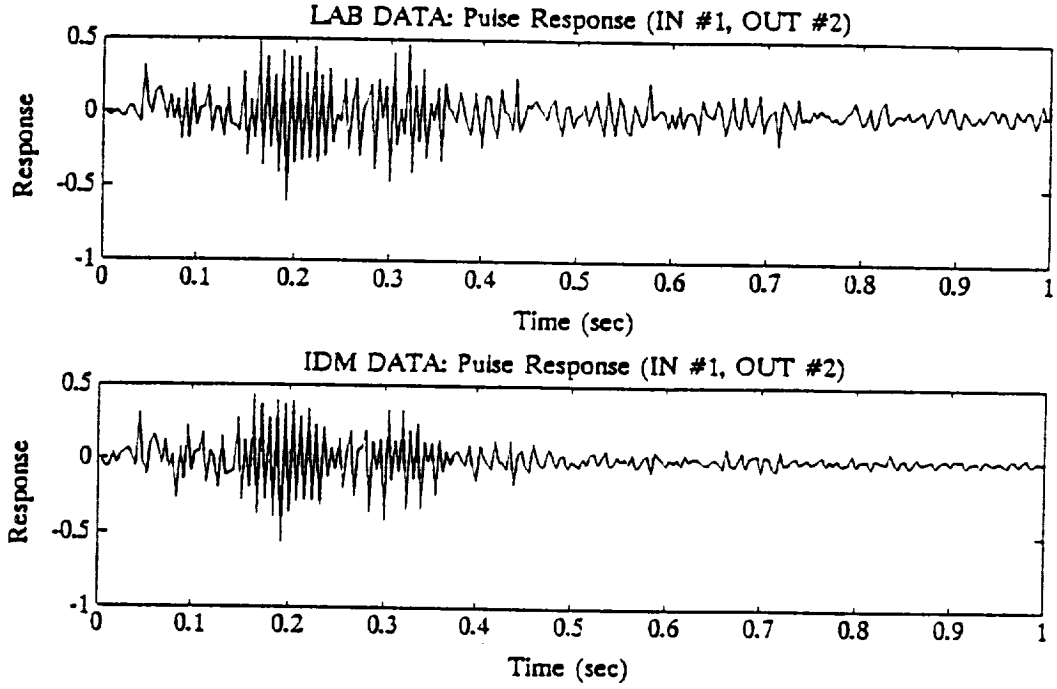

Figure 6: Pulse response: lab data vs. IDM (Identified) data, channel 2.

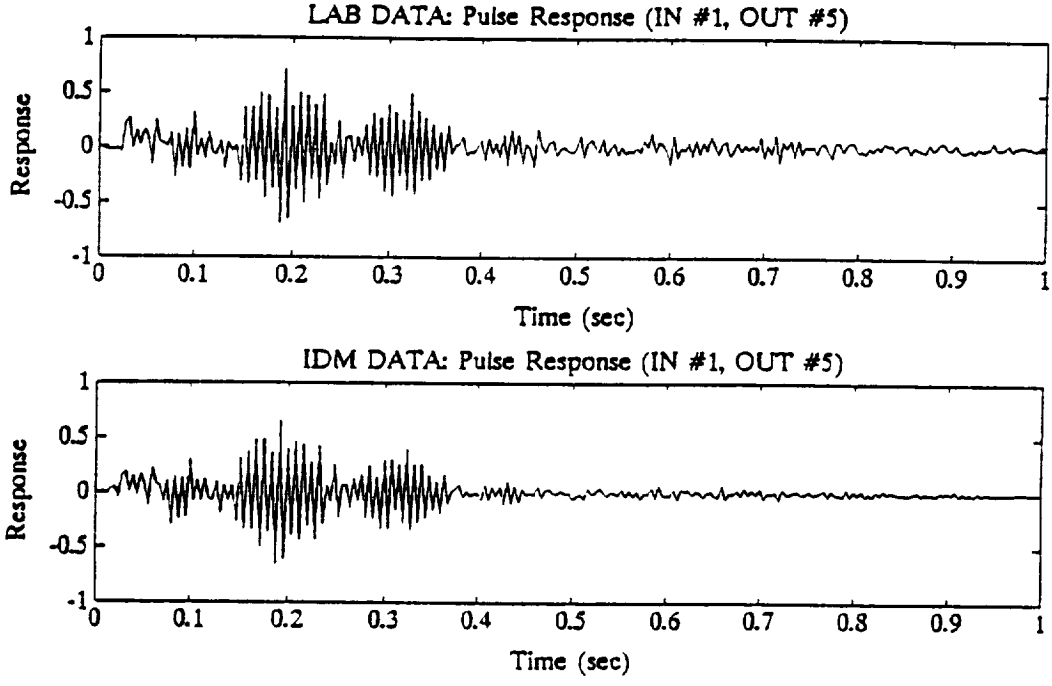

Figure 7: Pulse response: lab data vs. IDM (Identified) data, channel 5.

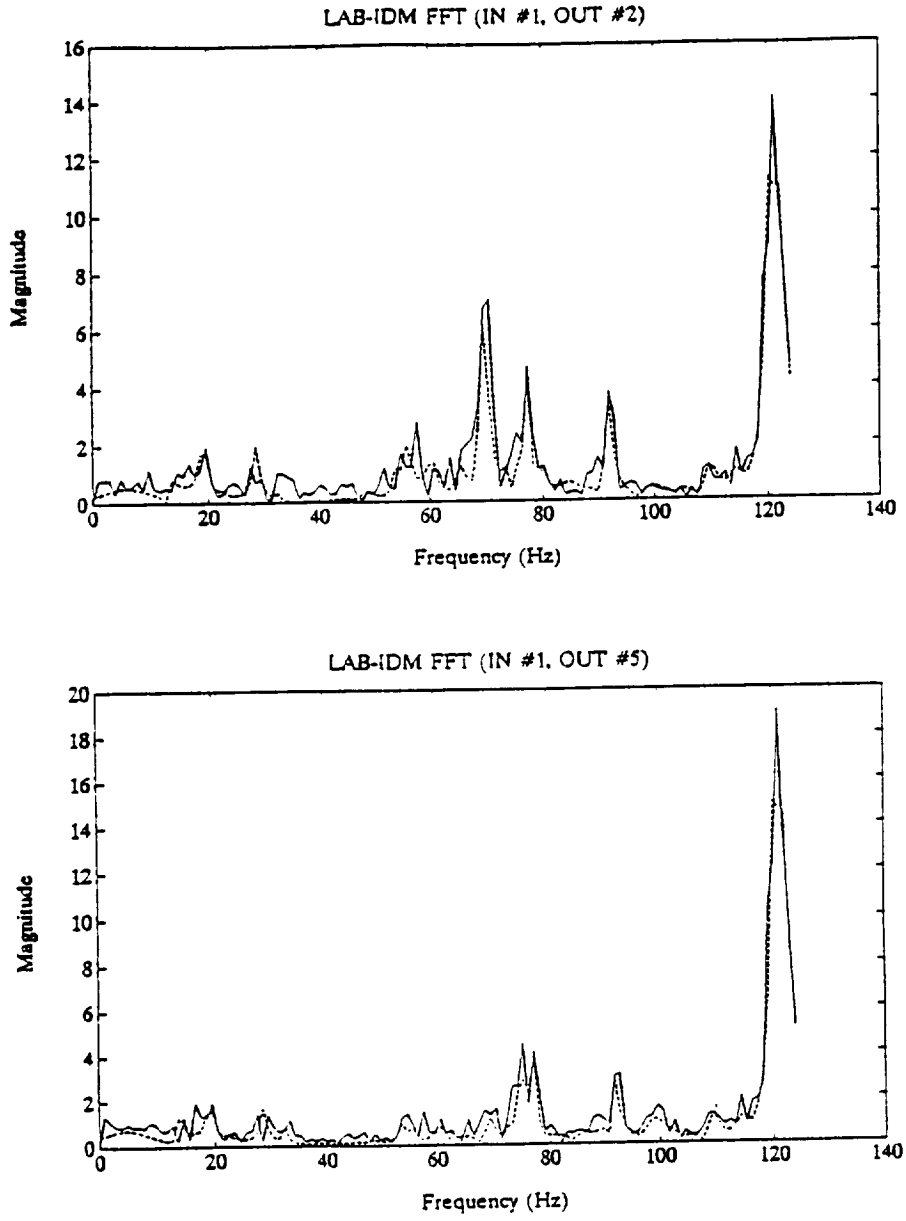

Figure 8: Frequency response: lab data vs. IDM (Identified) data, channels 2 and 5.

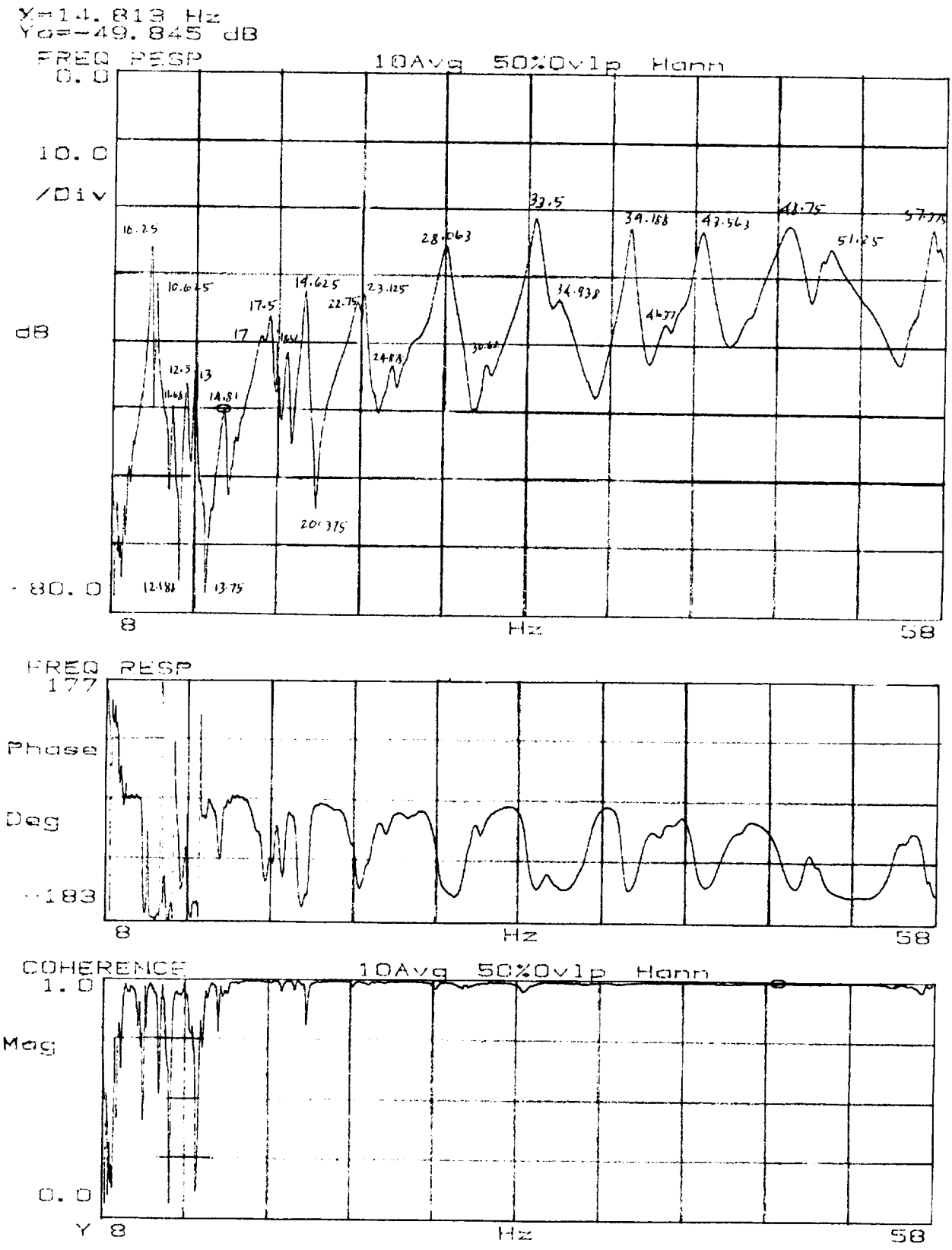

Figure 9: FRF (Bode plot) from the HP3562A analyzer.

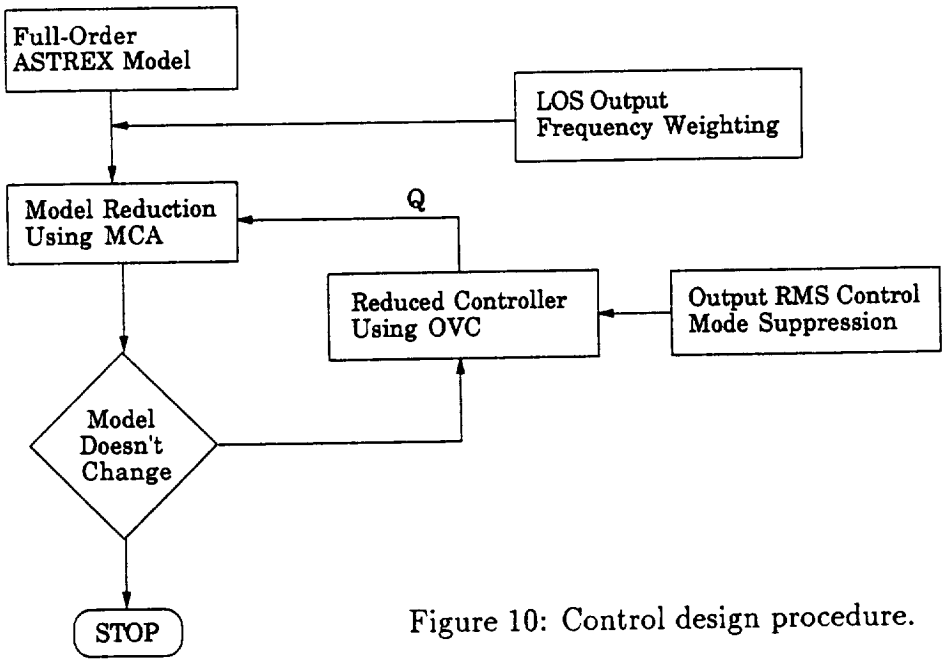

Figure 10: Control design procedure.

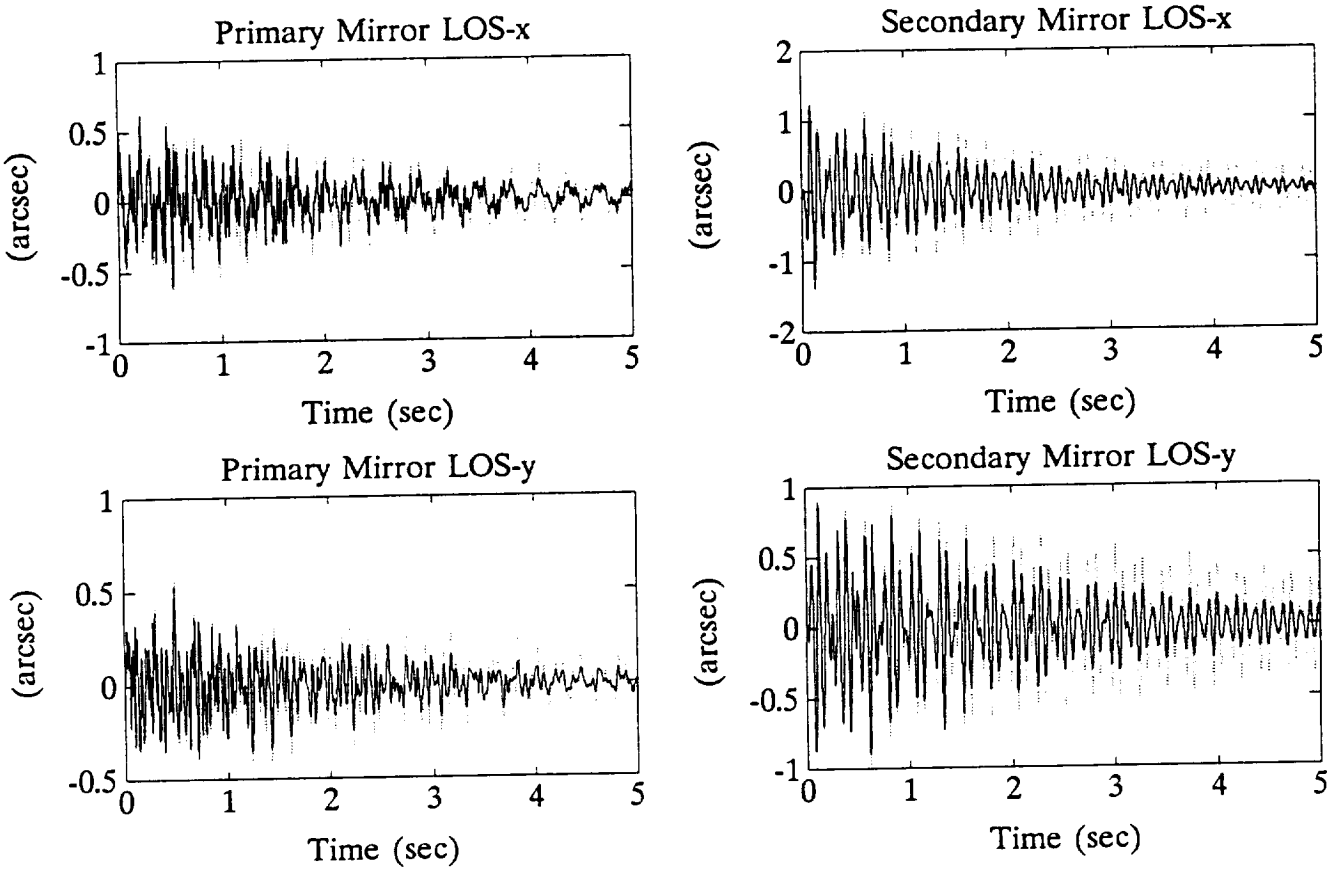

Figure 11: Pulse response to disturbance channel 6.

ANALYSIS, DESIGN, AND TESTING OF A LOW COST, DIRECT FORCE COMMAND LINEAR PROOF MASS ACTUATOR FOR STRUCTURAL CONTROL

G.L. Slater
Professor
Department of Aerospace Engineering
and Engineering Mechanics

Stuart Shelley
Research Assistant Professor
Department of Mechanical, Industrial, and Nuclear
Engineering

University of Cincinnati

Mark Jacobson
Undergraduate student
Department of Mechanical Engineering
The Ohio State University

Abstract

In this paper, the design, analysis, and test of a low cost, linear proof mass actuator for vibration control is presented. The actuator is based on a linear induction coil from a large computer disk drive. Such disk drives are readily available and provide the linear actuator, current feedback amplifier, and power supply for a highly effective, yet inexpensive, experimental laboratory actuator. The device is implemented as a force command input system, and the performance is virtually the same as other, more sophisticated, linear proof mass systems.

Introduction

Vibration suppression for large flexible structures in space requires some means of transferring the mechanical vibration energy into heat. A popularly proposed solution to implement this in realizable hardware is the linear proof mass actuator (or "Linear Momentum Exchange Device"). (see Refs. 1-3) The linear actuator achieves control by accelerating a mass along a linear track. The force driver is a linear motor, which applies a force to the moving mass, and hence by Newton's Laws, an equal and opposite force applied to the structure on which the actuator is mounted. If an ideal "velocity sensor" is used to apply the driving signal to a "perfect" force actuator, we have the classical force-velocity collocated control scheme, which is guaranteed to be energy dissipative, and results in a stable, damped structure.

The use of linear proof-mass actuators for control has long been recognized as a useful technique for implementing this type of control scheme. In addition to action as a control actuator, an alternate application of this device is as a force producer, where it acts essentially as a mechanical shaker. As a shaker, this device is capable of exciting the structure through a force input at the physical location of the mounting between the actuator and the structure.

The construction of linear proof mass actuators is conceptually quite simple, yet in practice, tends to be difficult to implement. They are heavy, the desired friction free linear track motion is difficult to maintain due to the precision alignment required for the linear motion, stiction in the bearings, and magnetization of the bearings and other materials. For laboratory experimentation, the construction of such actuators may be an expensive, time consuming task. The purpose of this paper is to report on an easy, low-cost implementation of a proof mass actuator which may be suitable for laboratory studies.

Proof Mass Actuator Description

The key element being proposed here to construct a proof mass actuator is to utilize the head actuation mechanism from a hard disk drive. For this application it is relatively easy to find obsolete disk drives, which are fairly large, heavy, and very reliable. The mechanism in these older drives is a sophisticated implementation of a common voice coil moving in a magnetic field. The primary advantages of these actuators are: (1) They are fairly large, hence they are easy to work with in a laboratory environment, (2) the mechanisms are very precise and reliable. The suspension system and track of the actuator are very smooth with low friction, and (3) the primary electronic component in the actuators is a high precision constant current DC amplifier. The constant current feature eliminates the back emf effect seen in a constant voltage drive system, hence there is almost no interaction of the actuator dynamics with the structure on which it is mounted.

The proof mass actuators constructed in our laboratory were constructed from old Hewlett Packard HP7925D disk drives. These are relatively old (circa 1980), fairly large drives which are obsolete for use as data storage devices. Nevertheless, the electronics and actuation are still perfectly good, and the head positioning subsystem of the disk drive makes an excellent proof mass actuator. This consists of a linear actuator, with approximately a four inch stroke, plus the power supply and regulator. For laboratory work this actuator produces several advantages. First it is reasonably inexpensive! Surplus drives of this type are commonly available for several hundred dollars. It is likely that most organizations have drives of this or other similar types, sitting around as unused, surplus equipment. Secondly, the linear actuator is fairly large, making it relatively easy to work on and modify. (Of course, it is also large and heavy making it less than desirable for a realistic space actuator. For our

purposes, however, this is not viewed as a major problem.)

The mass moves within a coil of approximately three inches in diameter. Current passing through the coil produces a magnetic field, which produces a force on the mass moving within the coil. The standard mass of the actuator moving within the coil is quite small, especially in comparison to the fixed mass of the actuator. Because there is ample room on the actuator, additional mass was added to make the device more efficient in producing force without being track limited. The primary limitation on the amount of mass that can be added is the bearing which guides the actuator on its track. For our design we rather arbitrarily used a nominal 2.2 kg additional mass on the actuator to reduce the stroke required especially at low frequencies.

The current driving the coil comes from a current amplifier which produces a current proportional to the input voltage. The specifications for the power supply and amplifier can be found in the manufacturer's documentation but should be measured in situ to get the correct value for your individual system. For the HP drives used the manual specifies the amplifier gain as 1.2 amp/v. Laboratory measurements obtained a value closer to 1 amp/v, with some slight variations within the group of amplifiers tested. The actuator itself was tested by constraining the actuator mass and using a load cell to measure the force produced by the coil. For the system tested the nominal value of this gain was found to be between 1-2 lb/amp. This value can vary widely between systems and is very sensitive to the track alignment in the system. The nominal force constant in the system is close to the upper figure. Disassembly of, or damage to, the permanent magnet during construction can reduce the magnetic flux and reduce the force constant toward the lower value. Nevertheless it is easy to see from this value that the actuator can be very effective in producing a force on the attaching structure.

Conversion to a Force Actuator

The only physical changes required to the actuator are the addition of a proof mass to the coil to decrease the stroke required to produce a given force, and the addition of an LVDT to give feedback for the position of the moving mass. The physical layout of the actuator is shown on Figure 1. For testing purposes, an accelerometer was mounted on the proof mass, to give a direct force readout. This accelerometer could also be used for feedback signals if required, but in the current implementation the acceleration feedback was not required. The LVDT used was a TransTek Model No. 244. The LVDT response is linear over about a two inch range. The LVDT requires an external power supply and has internal electronics that produce a significant phase lag in the measurement. Phase lag was measured to be 52 degrees at 100 Hz and varied approximately linearly with frequency. The linear velocity transducer (LVT) had no significant dynamics and was found to have a gain of 0.05 v/(in/sec). Using these parameters the system block

diagram was modeled as shown in Figure 2. The overall transfer function (neglecting the dynamics of the LVDT) are a second order system

$$\frac{F}{V} = \frac{K_a K_f s^2}{s^2 + K_a K_f K_V s + K_a K_f K_D}$$

where $K_{(.)}$ indicates an appropriate gain with
- a - Amplifier
- f- Force/current constant
- V- LVT transducer gain
- D- LVDT gain

A simple operational amplifier circuit was added to sum the LVT and LVDT signals, and to allow relative scaling of the signals to the amplifier. The general schematic of this circuit is shown in Figure 3. For our purposes the gains were set to give a low frequency cutoff of about three Hertz. Initial tests showed a lot of high frequency noise corrupting these feedback signals and causing very poor performance. Shielding all the leads from the sensors to the op-amps, and adding a number of small capacitors to the circuitry as shown on the figure, ultimately eliminated this problem and made the system respond very nicely.

Test results

Tests of the actuator show that this device performs very well as a force command proof mass actuator over a large frequency range. Figures 4 a,b show the measured transfer function from voltage input to force output (as measured by an accelerometer) for the actuator mounted in a bench test. The input used here is a one volt random input. The force output level is approximately 1.6 lb/v. As seen, the force output is extremely flat from about 2 Hz to over 200 Hz. The phase plot (not shown here) is generally quite flat but does exhibit noticeable phase shift at frequencies below about 5 Hz. In initial tests, the proof mass was not exactly centered on the axis of the moving coil. This produced noticed ripples in the response curves starting at about 50 Hz due to exciting structural dynamics of the actuator frame. Centering the mass produces the smooth response shown in the figure. Linearity of the device was tested by applying a sinusoidal voltage and plotting the voltage -force relationship. These results are shown in Figure 5. If perfectly linear, the curve should be a straight line. As seen in the figure there is slight non-linearity, and a small amount of hysteresis, but overall we judge the response to be extremely good.

Several of these actuators have been constructed and mounted on a five meter test structure in the Structural Dynamics Research Laboratory at the University of Cincinnati. The truss structure is shown in Figure 6. The bench tests previously described were

repeated on the test structure to verify that the proof mass actuator continued to operate as expected when subjected to the dynamics of the truss frame. The truss is mounted vertically and suspended from the ceiling to simulate a free-free horizontal suspension. A number of large aluminum plates are used as attachment points for the actuators described here. The large masses on the truss produce a set of dynamics with significant modes at low frequency. A typical frequency response of acceleration response to force input at one of the actuator mounting points is shown in Figure 7. Numerous modes exist on the truss throughout the frequency range tested. The bench test shown in Figure 4 was repeated with the actuator mounted on the structure. These results are shown in Figure 8. There is very little difference between the two sets of curves, indicating that the actuator dynamics have negligible interaction with the truss dynamics.

Conclusions

The intent of this paper is to present the details of the construction of a low cost proof mass actuator, suitable for research into the dynamics and control of large flexible structures. The actuators were constructed from surplus disk drive actuators for a relatively modest cost. Neglecting the cost of the drive (which we in fact obtained at no cost) the total expenditure for equipment was less than about three hundred dollars. (Normally the surplus disk drive itself may cost a comparable amount if purchased). The analysis and test results show how this relatively simple concept can be used as a highly effective linear proof mass actuator suitable for control purposes, or as a mechanical shaker. We have constructed over five of these systems and their performance is fairly reliable and repeatable. Current studies are under way to use these actuators in on-line identification schemes for structures and for vibration suppression control experiments.

References

1. J.Sulla,J-N Juang, L. Horta, "Analysis and Application of a Velocity Command Motor as a Reaction Mass Actuator", AIAA Dynamics Specialist Conf., Long Beach, CA, 1990.

2. J. Sharkey, H. Waites, G. Doane, "Distributed Control using Linear Momemtum Control Devices", NASA TM-100308, October, 1987.

3. D. C. Zimmerman, D. J. Inman, "On the Nature of the Interaction Between Structures and Proof-Mass Actuators, J. of Guidance, Control, and Dynamics, Vol. 13, Jan-Feb, 1990.

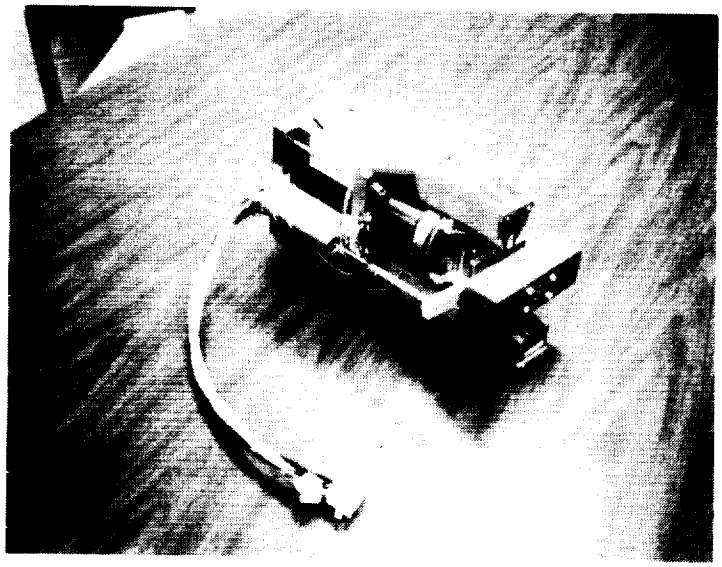

Figure 1 Proof Mass Actuator

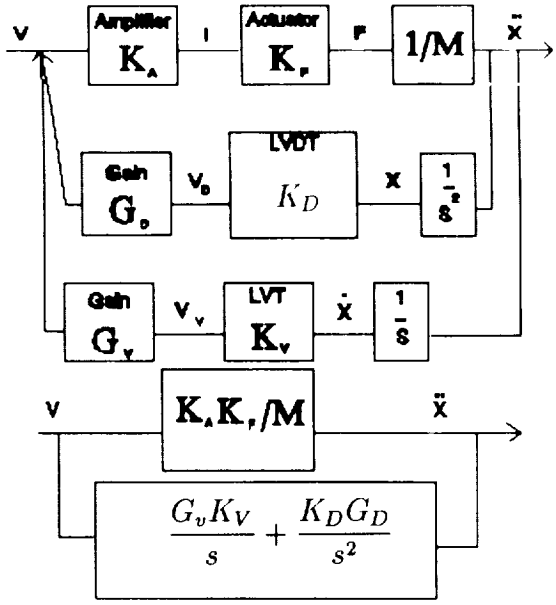

Figure 2 Block diagram of actuator feedback loop

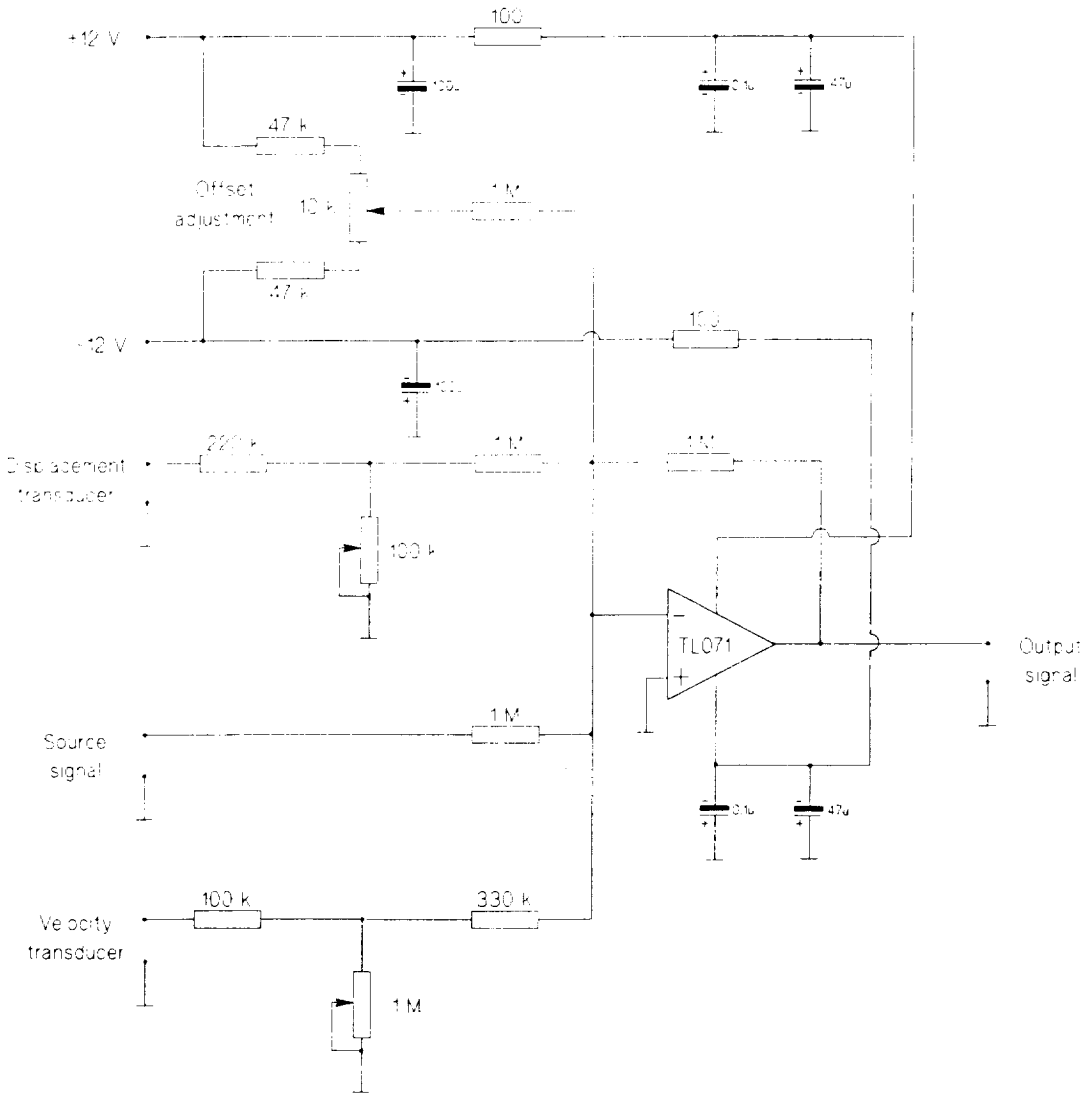

Figure 3 Op-amp circuit for conditioning of sensor signals to input amplifier

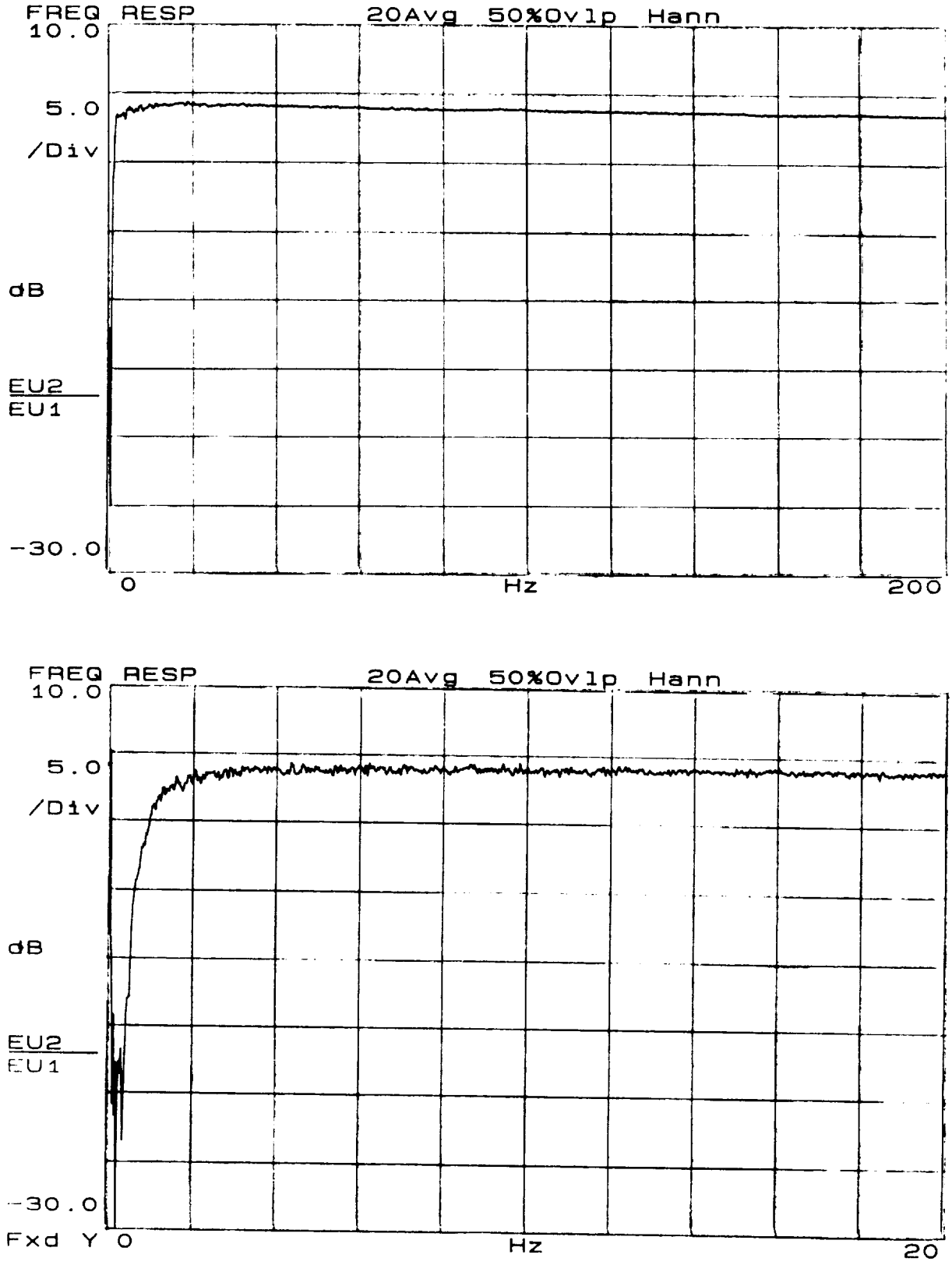

Figure 4 Transfer function magnitude for force output to voltage command (Bench Test). (a) 0-200 Hz (b) 0-20 Hz.

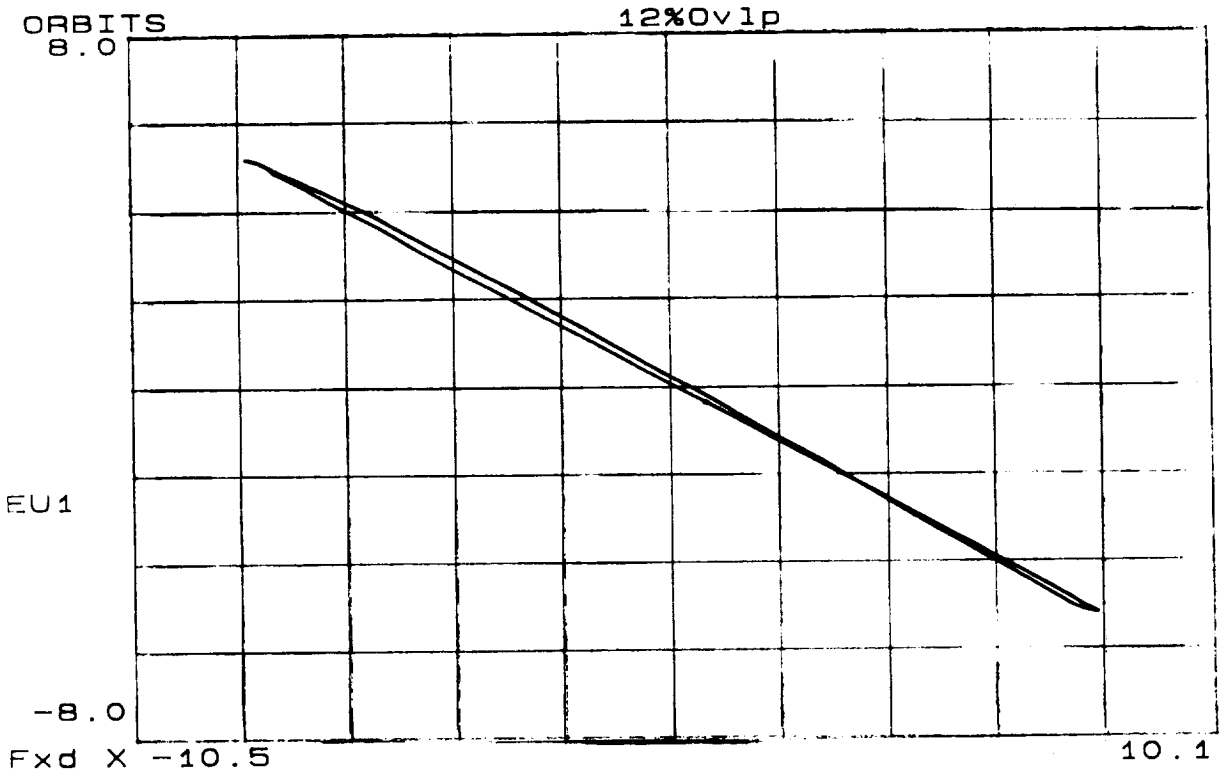

Figure 5 Force-voltage curve showing linearity of the actuator. (Reference signal is 5 v at 20 Hz.)

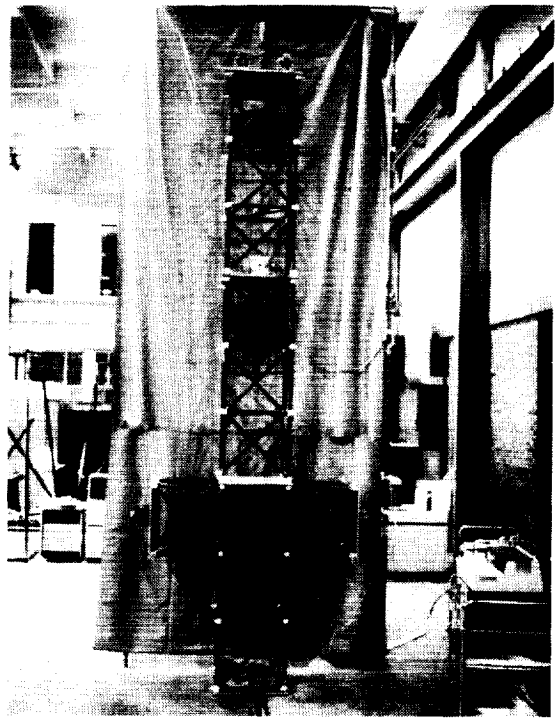

Figure 6 Laboratory truss structure used in test

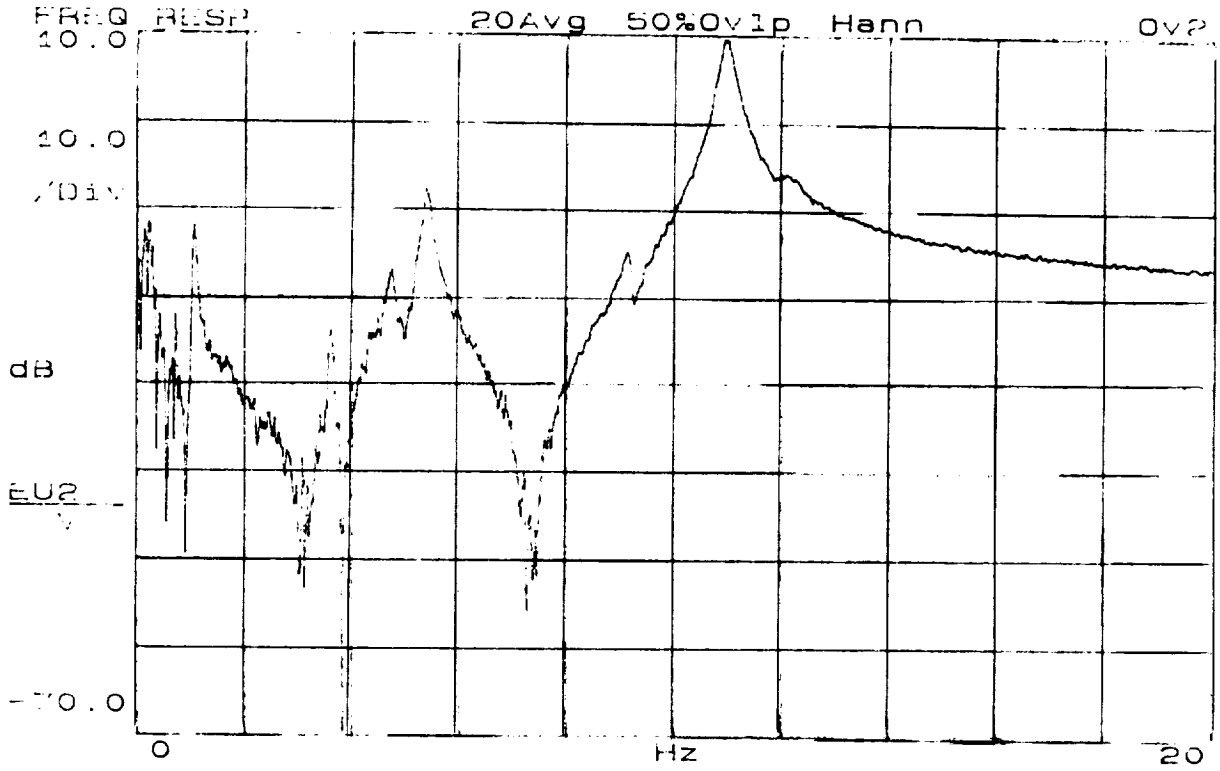

Figure 7 Frequency response of the truss structure (Acceleration/force)

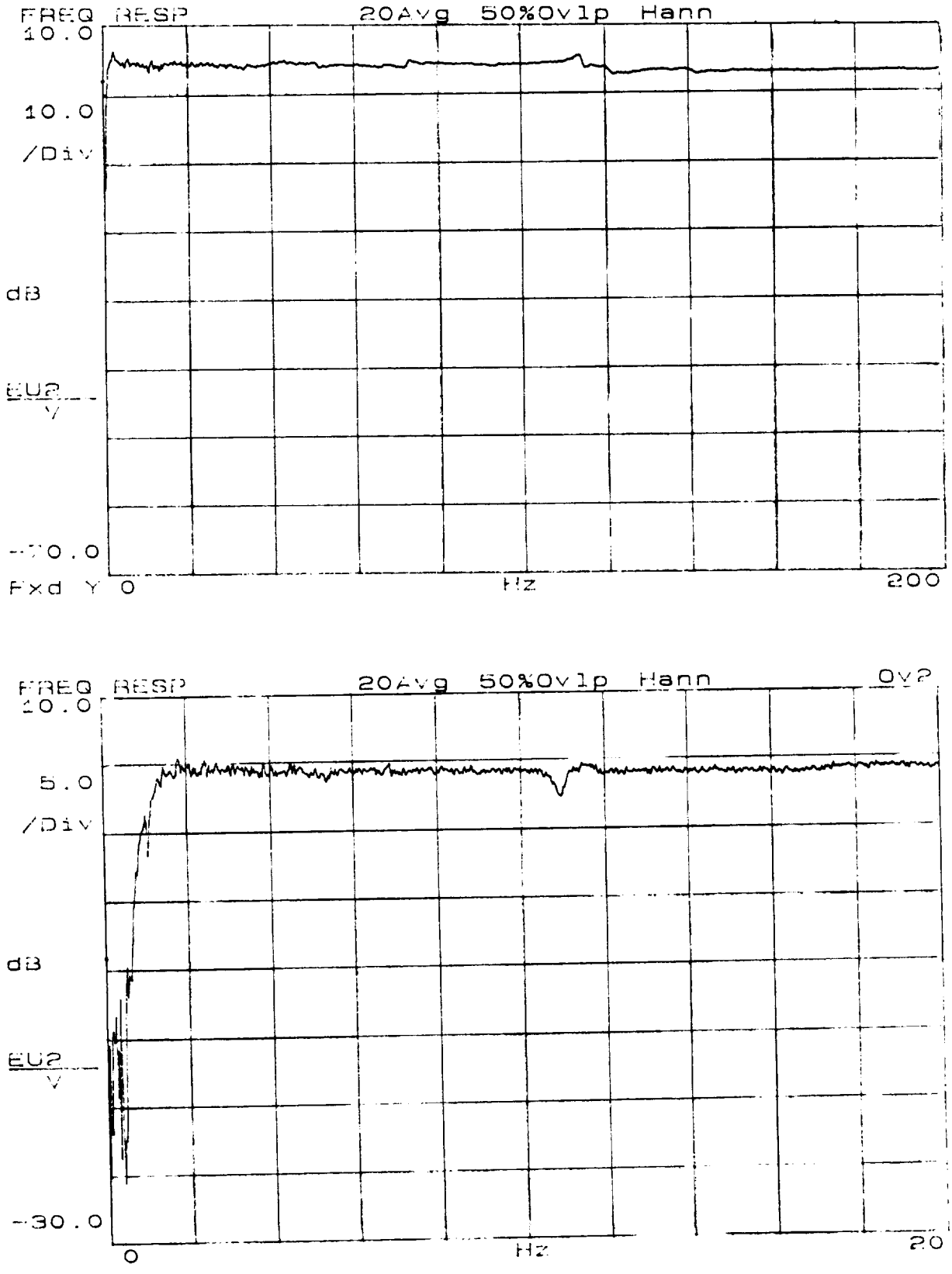

Figure 8 Transfer function magnitude for force output to voltage command (On structure). (a) 0-200 Hz (b) 0-20 Hz.

CSI FLIGHT EXPERIMENT PROJECTS OF THE NAVAL RESEARCH LABORATORY

Shalom Fisher
Naval Research Laboratory
Washington, D. C.

ABSTRACT

The Naval Research Laboratory (NRL) is involved in an active program of CSI flight experiments. The first CSI flight experiment of the Naval Research Laboratory, the Low Power Atmospheric Compensation Experiment (LACE) dynamics experiment, has successfully measured vibrations of an orbiting satellite with a ground-based laser radar. The observations, made on January 7, 8 and 10, 1991, represent the first ever measurements of this type. In the tests, a narrowband heterodyne CO_2 laser radar, operating at a wavelength of 10.6 microns, detected vibration induced differential-Doppler signatures of the LACE satellite. Power spectral densities of forced oscillations and modal frequencies and damping rates of free-damped vibrations were obtained and compared with finite element structural models of the LACE system. Another manifested flight experiment is the Advanced Controls Technology Experiment (ACTEX) designed to demonstrate active and passive damping with piezo-electric (PZT) sensors and actuators. This experiment was developed under the management of the Air Force Phillips Laboratory with integration of the experiment at NRL. It is to ride as a secondary, or "piggyback," experiment on a future Navy satellite.

LACE SATELLITE: DESIGN AND FLIGHT HARDWARE OF DYNAMICS EXPERIMENT

The first of the CSI flight experiments of the Naval Research Laboratory (NRL) is the Low Power Atmospheric Compensation Experiment (LACE) dynamics experiment. The experiment was a low-cost "piggyback" opportunity, secondary to the primary LACE mission. Its design was initiated at meetings held at NRL in May and June of 1988. Costs were kept low, and rapid integration of the experiment into the satellite design was made possible because the LACE satellite was built and launched by NRL, i.e., design and integration of the experiment took place at the same facility. The LACE satellite was launched on February 14, 1990 into a 540 km altitude circular orbit of 43^0 inclination. The structural configuration of the LACE spacecraft is illustrated in Figure 1. Three deployable/retractable booms of maximum length 45.72 m (150 ft) are mounted on a rectangular parallelepiped bus of mass 1,200 kg. The zenith directed gravity gradient boom has a magnetic damper at its tip; the forward or retro-boom is deployed along the velocity vector; the balance boom is mounted and deployed counter to the velocity. The tip end of the retro-boom carries a reflector plate on which an array of glass corner cubes is mounted. The glass corner cubes are intended to reflect visible light for the primary LACE mission. Attitude stabilization to within about 1^0 libration amplitude is accomplished by the gravity gradient torques and by a constant speed momentum wheel. Constant rate boom deployment/retraction maneuvers are remotely controlled through a ground based telemetry link.

The dynamics experiment flight hardware consists of three germanium corner reflectors, as shown in Figure 1. One of the reflectors is included in the array of corner cubes mounted on the end of the retro-reflector boom; one is on the bottom of the bus, and the third one is on the end of the balance boom. The germanium has an index of refraction of 4.0 for light of wavelengths between 1.8 microns and 15 microns. With this very high index of refraction, light striking the reflector surface at angles of 20^0 or greater will be reflected. Therefore, a ground-based light source will see a return signal even for the satellite at a low elevation angle.

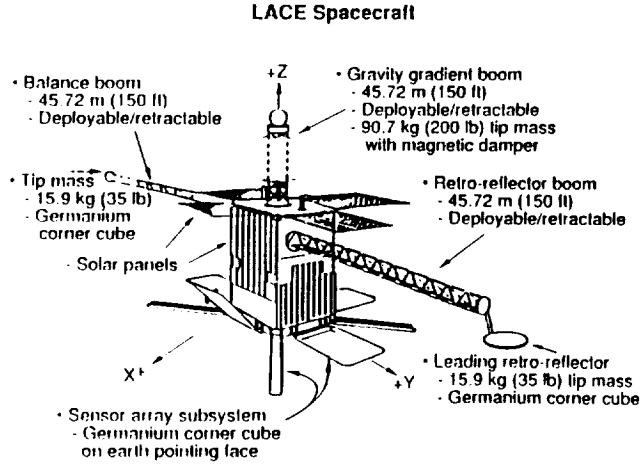

FIGURE 1: Design of the LACE satellite showing placement of germanium corner reflectors.

The laser illuminations are made with the MIT Lincoln Laboratory's Firepond laser radar located in Westford, MA as shown in Figure 2. The Firepond radar used for the illuminations is a narrowband, CO_2 laser radar operating at 10.6 microns. The aperture of the laser telescope is 1.2192 m (48 in), giving a nominal diffraction limited footprint of about 5 m at a range of 550 km (minimum target range). A 0.6096 m (24 in) telescope, boresighted with the CO_2 telescope, can track in visible light either passively by reflected sunlight or actively with a 25 watt, 514.5 nm Argon-ion laser. Acquisition and tracking are assisted by the Millstone L-band radar located nearby. The Millstone radar also supplies target frequency information for range-rate (Doppler) acquisition. Observations are made with the sun 10^0 to 30^0 below the horizon, either before sunrise or after sunset. In this "terminator mode," the site is in darkness but the satellite is still in sunlight. The CO_2 illuminations are limited by NORAD to windows unique to each pass, and by a safety requirement that the elevation angle must be 30^0 or more.

With the Firepond apparatus, vibration measurements were made on January 7, 8 and 10, 1991 (denoted hereafter in this report as days 91007, 91008 and 91010). The targeting of LACE was accomplished with active tracking by means of the Argon-ion laser targeted on the retroreflector array of glass corner cubes at the tip of the lead boom.

Before and during the targeting, vibrations of the LACE satellite structure were excited by retraction of the lead boom from 24.38 m (80 ft) to 4.572 m (15 ft). The reflector on the lead boom tip and the reflector on the bus were simultaneously illuminated, after the boom length decreased to 9.144 m (30 ft), to provide differential Doppler measurements of the relative motion between the end of the boom and the spacecraft body. Simultaneous observations could only be made for a boom length of 9.144 m (30 ft) or less because of the narrow width of the laser beam. The relative motion includes boom vibration as well as the rigid-body satellite motion and the boom retraction motion.

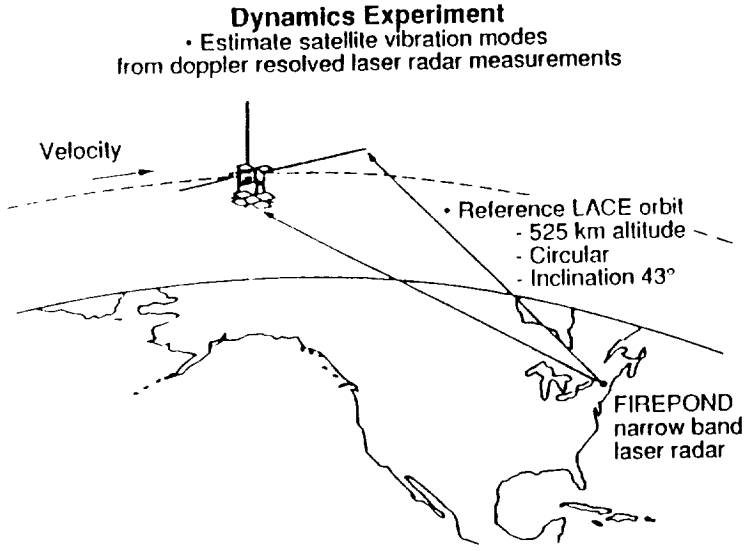

FIGURE 2: On-orbit targeting of LACE with the Firepond narrowband laser radar.

OBJECTIVES OF THE DYNAMICS EXPERIMENT

With the dynamics experiment, the primary design goal was to perform on-orbit system identification, i.e. to measure modal frequencies and damping ratios of the satellite structure as stated in Figure 3. The large size of the LACE structure precluded ground tests of the dynamics of the deployed structure or tests of boom deployment dynamics prior to launch. The damping ratios, measured by the experiment, provide a useful assessment of the amount of vibration damping intrinsic to the type of deployable/retractable truss structures used in LACE. Such structures are used in a number of space applications, i.e., the Voyager magnetometer booms and in the Galileo spacecraft. The on-orbit system identification provides a mechanism to validate finite element structural models of the satellite system; to refine and improve them, and to measure the level of vibration induced by boom deployments/retractions.

- Unique opportunity to measure effects of disturbances on spacecraft flexure; give boom vibration knowledge during LACE spacecraft operations.
- Goal is to perform on-orbit system identification: vibration frequencies, damping and amplitude ratios.
- Assess flexible structural modelling accuracies:

  deployment/retraction vibrations
  finite element models (FEM): NASTRAN
  dynamics simulation models: DISCOS, treetops
  deployment dynamics: DART

- Facilitate control of jitter and rapid slews in future spacecraft.

FIGURE 3.

KEY POINTS OF THE DYNAMICS EXPERIMENT

Figure 4 states the significant events of the dynamics experiment. The LACE satellite was launched on February 14, 1990. As previously mentioned, observations of vibrations of the LACE satellite were made on January 7, 8 and 10, 1991 (denoted in this report as days 91007, 91008 and 91010). In the observations, the Firepond narrowband laser radar telescope, boresighted with the visible light radar, observed differential Doppler reflections from the germanium corner reflectors on the lead boom and body of the spacecraft after the boom length reached 9.144 m (30 ft) or less. The laser Doppler measurement window of day 91007 observed about 38 seconds of forced dynamics motion of the lead boom while the boom was being retracted. The window of day 91008 contained about 68 seconds of retraction data and 25 seconds of free-decay data after retraction was stopped. Day 91010 data contained about 45 seconds of useful free-decay data after retraction was stopped.

- LACE spacecraft launched February 14, 1990
  altitude at launch 540 km, circular, 43° inclination
- LACE satellite built and launched by Naval Research Lab.
- Dynamics experiment is a low-cost "piggyback" experiment.
- Germanium corner cubes (3) serve as targets for Firepond laser radar of MIT Lincoln Laboratory, Westford, Mass.
- Corner cubes installed on LACE on December 22, 1989.
- Laser Doppler data collected on January 7, 8 and 10, 1991.
- Observed forced vibration and free-damped oscillations.

FIGURE 4:

COMPENSATION FOR RIGID BODY MOTION AND BOOM RETRACTION

In addition to the vibrational motion, the Doppler data includes the rigid body motion of the spacecraft as well as the boom retraction speed of about .076 m/sec (.25 ft/sec). Since the spacecraft is gravity-gradient stabilized it rotates once per orbit in inertia space at a uniform rate. However, from the ground, its aspect angle changes at a variable rate with time; the rate appears to be a maximum when the spacecraft is at its maximum elevation angle, as illustrated in Figure 5. These aspect angle changes and aspect angle rate changes have several effects on the observed Doppler shifted laser return:

1. The rigid body motion and boom retraction speed will bias the vibration motion. It will be shown that the boom retraction speed is several times larger than the vibration speed.

2. The frequency separation between the apparent rigid body motion and the lowest vibrational mode of 0.019 Hz is small. Therefore the observability of this mode is affected.

3. The observed damping factors of the detected modes will be biased by an amount that depends upon the position of the satellite in the sky. The calculated damping factors will be smaller for observations with the satellite ascending to its maximum elevation angle, than for observations with the satellite descending.

The effects of this apparent motion are treated by calculating the apparent rigid body motion during the observation period using the spacecraft orbital rate, range, the boom lengths and boom retraction rate. The bias produced by the rigid body motion is subtracted from the observed motion. The change in observed damping with aspect angle is corrected by dividing the damping factor by the cosine of the angle between the LOS vector and the pitch plane.

Figure 5 appears on the following page.

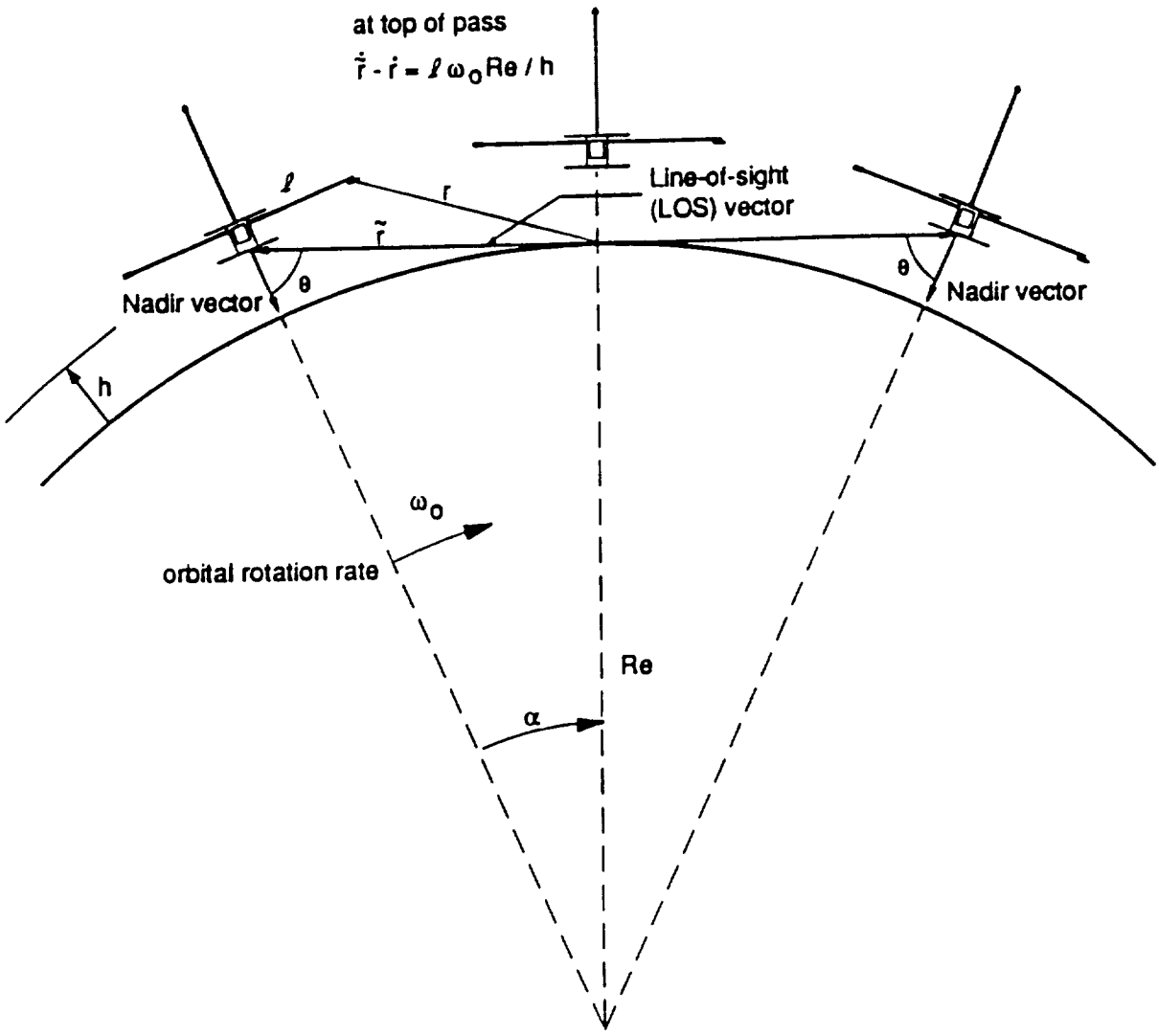

FIGURE 5: Rotation of LACE as observed from a ground site.

OBSERVED STRUCTURAL VIBRATIONS

Figure 6 shows observed data from day 91008. The figure shows forced vibration data to about 67 seconds, followed by about 28 seconds of free-decay vibration data, on which is superimposed a simulation of the rigid-body motion and boom retraction rate. The simulation comes fairly close to the median of the observed vibration data: orbital uncertainties and uncertainties in the boom retraction rate could account for the slight discrepancy between the real and computed central body motion. It can be seen that the amplitude of the forced vibration is about 20 mm/sec. The boom retraction rate is about 75 mm/sec. Figure 7 shows a power spectral density plot obtained by Hamming weighting the data of the entire temporal window and computing the power spectrum. The nominal resolution of the resultant spectrum is 0.01 Hz. The result indicates the presence of multiple vibration frequencies. Values of observed vibration frequencies are listed as follows: 0.12 Hz, 0.28 Hz, 0.51 Hz, 1.03 Hz, 1.25 Hz, 1.29 Hz, 1.31 Hz, 1.41 Hz, 1.45 Hz, 1.55 Hz, and 2.46 Hz. The accuracy of these measurements has not been determined due to the limited number of observations.

The time-frequency analysis of the forced oscillation data from day 91008 is presented in Figure 8. Represented in this way, the data clearly indicate that modes in the 0.28 Hz regime and in the higher 1.25 Hz - 2.46 Hz regime increase in frequency as the boom retracts. The figure also indicates the relative stability of the 1.03 Hz frequency, a frequency close to the driving frequency of the boom deployment mechanism.

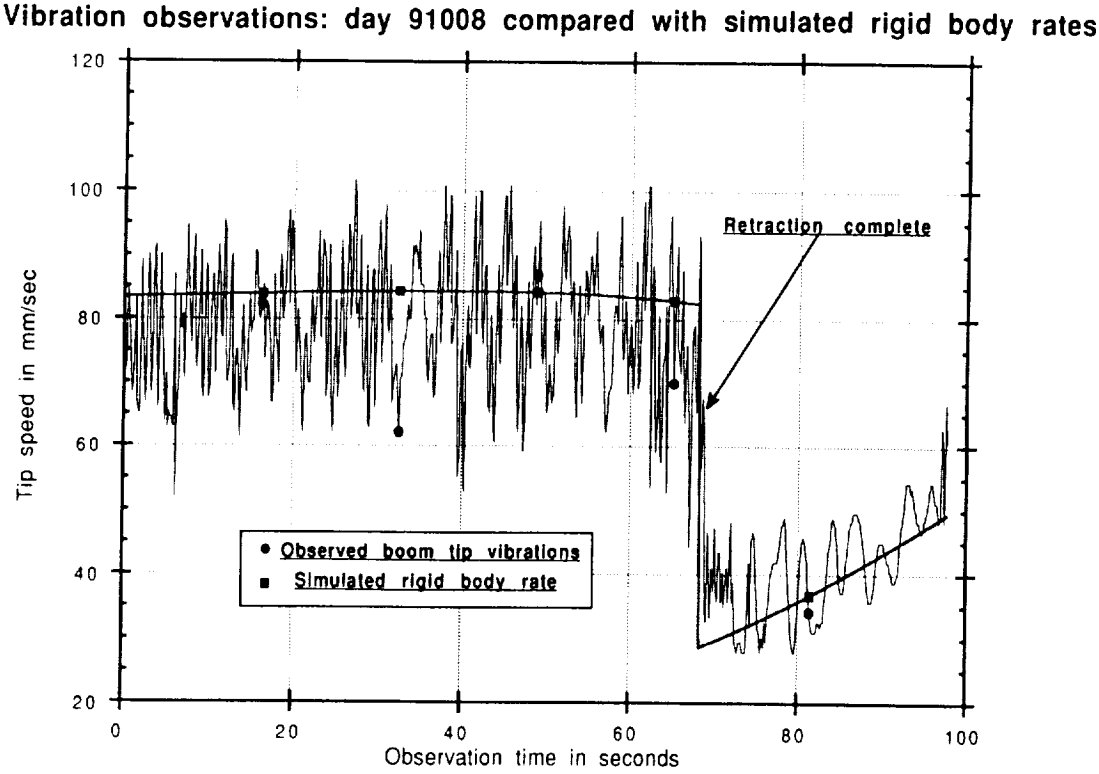

FIGURE 6: Observed vibration of LACE on day 91008.

Figures 7 and 8 appear on the following pages.

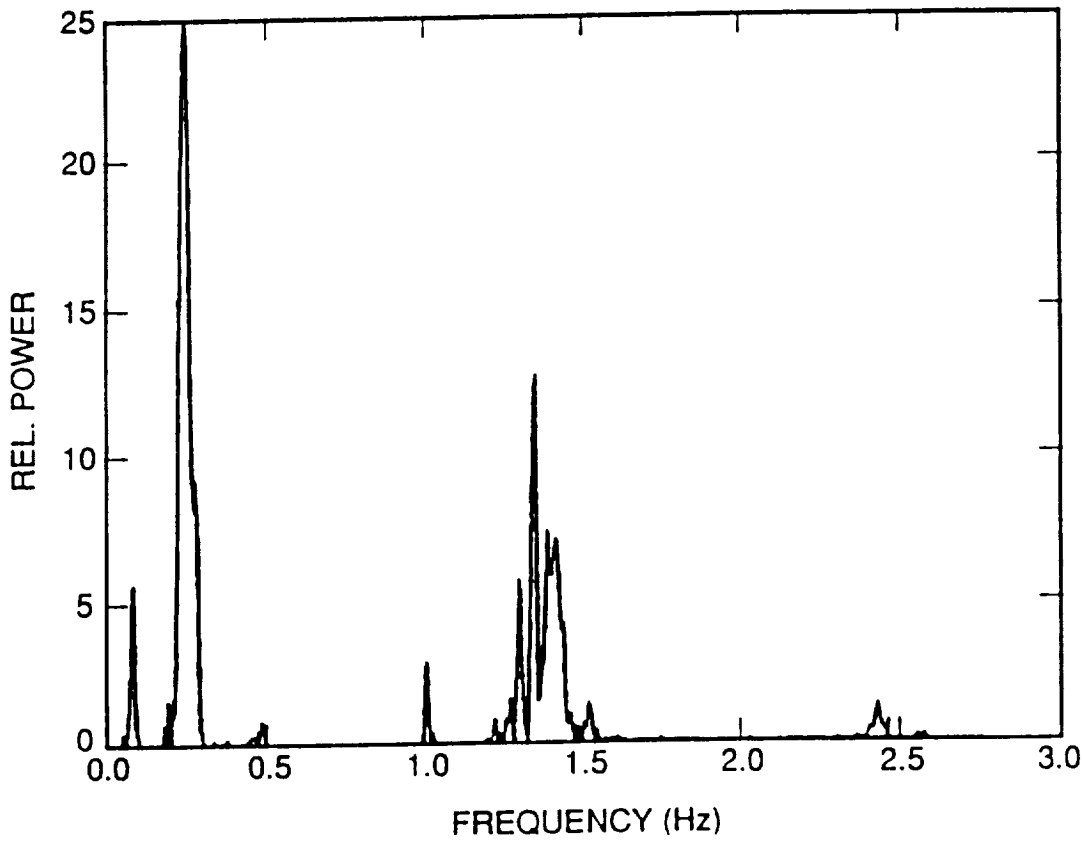

FIGURE 7: Power spectral density plot of vibrations observed during boom retraction.

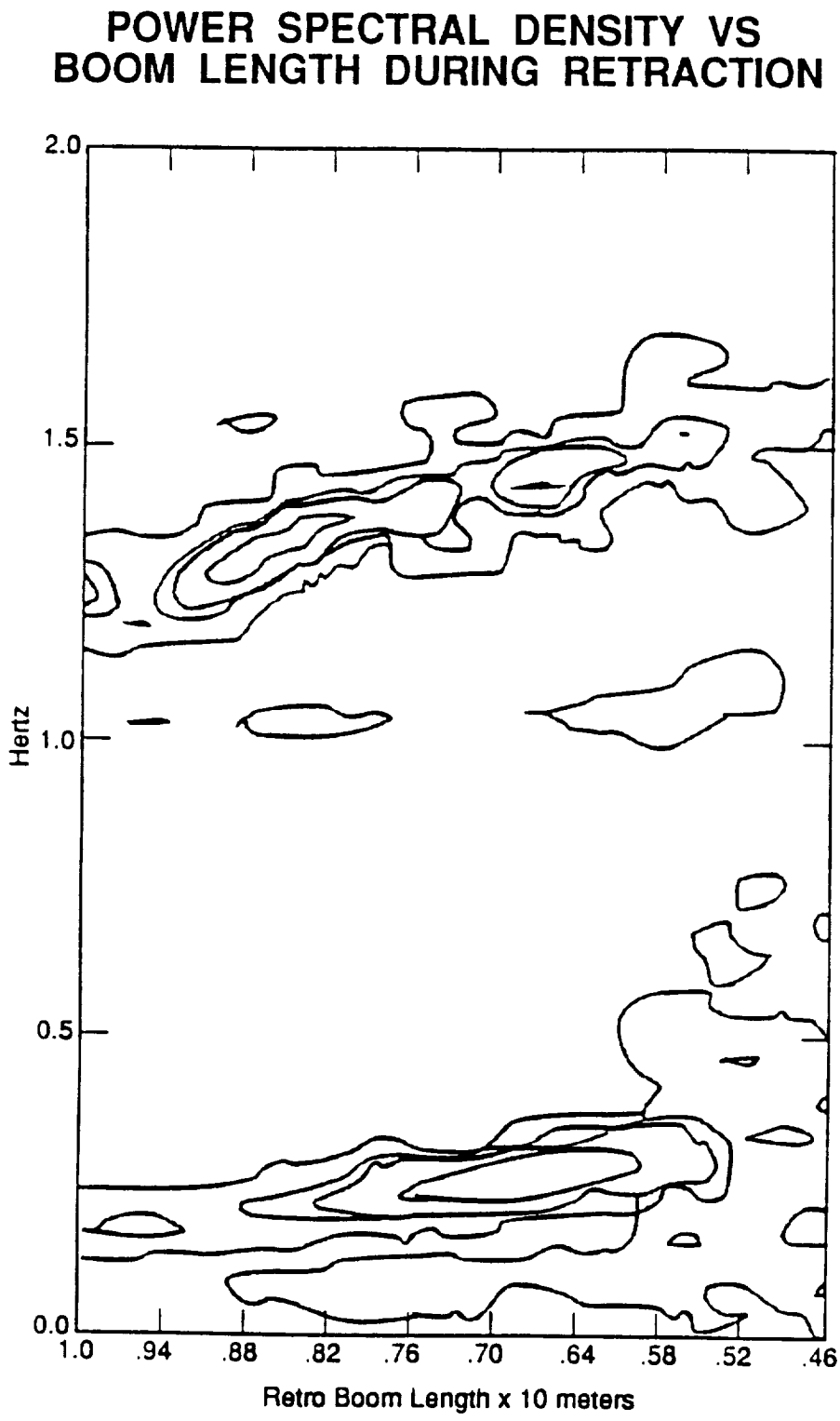

FIGURE 8: Forced oscillation frequencies versus boom length during retraction.

COMPARISON BETWEEN FEM MODES AND OBSERVED MODES

The eigensystem realization algorithm[1] (ERA) was used to calculate values of the observed modal frequencies and damping factors. Table 1 shows a comparison between the ERA derived modes (order = 8) and modes computed with a finite element (FEM) structural model. The finite element model used was a "stick" model in which the booms were modelled as simple beams rather than as trusses. Table 1 also shows the boom tip modal displacements obtained from the FEM model. The displacements are normalized so that the maximum displacment is 1.0. The observable modes are those with substantial modal displacement, Δz, perpendicular to the boom axis and coplanar with the line-of-sight vector and a vector along the boom axis. The lowest ERA derived mode of .019 Hz does agree quite well with the lowest FEM calculated mode. However, the day 91010 observation period was about 45 seconds, i.e., it was close to the 53 second period of that mode. Therefore, the agreement in frequency between the observed and calculated mode may be coincidental. The other observed modal frequencies of 0.124 Hz, 0.335 Hz and 0.547 Hz agree within 10% of the modal frequencies for the more highly observable modes. Another interesting feature of the comparison is the presence of the FEM mode at 0.646 Hz, which should have been observed, but was not. The close spacing between the FEM mode of 0.577 Hz and the mode at 0.646 Hz might have produced a nonlinear modal coupling that resulted in a combination mode at a frequency different from either, at 0.547 Hz. A more detailed modelling scheme with the booms modelled as full trusses might produce a closer agreement with the observations.

TABLE 1: Comparison of ERA-identified modal frequences with FEM modes.

Comparison of observed with modes computed from FE modelling (stick model)			
EI = 1.55 * 10^4 N - m^2		GJ = 5.74 * 10^2 N - m^2	
Obs freq	**FEM freq**	**tip modal displacements**	
		Δz	**Δx**
*0.019 Hz	0.019 Hz	.010	--
	0.110 Hz	.001	.05
	0.112 Hz	.002	.09
•0.124 Hz	0.125 Hz	.09	.004
	0.258 Hz	.009	--
	0.297 Hz	--	.08
•0.335 Hz	0.316 Hz	.10	.006
	0.320 Hz	.02	.02
•0.547 Hz	0.577 Hz	.14	.124
	0.646 Hz	.127	.135
	0.819 Hz	.004	--

•Denotes modes observed.* Not positively identified

OBSERVED MODAL DAMPING

An important result of the dynamics experiment is a measurement of the modal damping of the LACE satellite as shown in Table 2. The damping shown in Table 2 was also obtained with the ERA algorithm. The damping of the .547 Hz mode seems quite high and is an indication that the mode may have anomalous characteristics, i.e. it may be a combination of modes and not a simple mode. However, the computed damping of the other modes at 0.019 Hz, 0.124 Hz and 0.335 Hz is comparable to the values of 1.4% to 2.7% measured for the Voyager magnetometer boom by the Marshall Space Flight Center, Huntsville, Ala.[2] and values of 1.2% to 3.5% measured at the Canadian Communications Research Centre, Ottawa, Canada[3] for an astromast of design similar to the LACE booms.

A flight experiment that can be compared with the LACE dynamics experiment is the Solar Array Flight Experiment [4]. In that experiment a boom similar to the LACE booms was deployed with a solar blanket and attached tension wires for an 18 hour period on board the space shuttle. The vibration damping of modes out of the plane of the solar blanket can be compared with our results. These out-of-plane modes had damping factors of 3% to 6% depending on day/night. This damping was higher than ours, possibly because of the tension wires[5].

TABLE 2: ERA-identified damping of the observed modes.

System vibrations: ERA compared to FEM model		
frequency	% damping	FEM simulation
0.019 Hz	1.8	1st mode: 0.019 Hz
0.124 Hz	2.3	4th mode: 0.125 Hz
0.335 Hz	2.1	7th mode: 0.316 Hz
0.547 Hz	10.4	9th mode: 0.577 Hz

CONCLUSIONS FROM LACE DYNAMICS EXPERIMENT

The dynamics experiment performed on the low power atmospheric compensation experiment satellite has established the feasibility of ground-based laser measurements of vibrations, slews and deployments in orbiting satellites. The technique can be applied to health monitoring of large structures such as the space station. The experiment has demonstrated that velocity resolutions of 1.8 mm/sec are attainable with the current narrowband Firepond apparatus of the MIT Lincoln Laboratory.

ADVANCED CONTROLS TECHNOLOGY EXPERIMENT (ACTEX)

The ACTEX experiment, illustrated in Figure 9, is a secondary payload, manifested to fly on a future Navy spacecraft. The experiment is being built at the present time and will be exposed to space on the outside of the flight deck. Of course the electronics, comprised of a computer and solid state data recorder, are below deck for shielding and thermal control. The experiment includes three graphite-epoxy struts with embedded piezo-electric (PZT) sensors and actuators. Two of the struts are wrapped with mylar thermal insulation blankets, while the other strut is painted. One of the stuts has an extra set of PZT actuators to excite vibrations of the system.Thermistors are placed on the struts for temperature measurements. Both the top plate and mounting bracket contain three-axis accelerometers, with a heater on the top plate. The tripod is about 0.6 m (24 in) in length and weighs about 8.2 kg (18 lbs).

The experiment is intended to demonstrate that the technology of embedded PZT's is mature enough to be used on space based payloads. It is also intended to demonstrate the application of PZT's for passive and active vibration control in a large space structure. Different control algorithms, based on changing gains, filter cutoffs or sensor averages, can be telemetered to the experiment computer. The dynamic change mechanism (DCM) is attached to one of the struts. It contains a nitinol wire with attached electrodes. Passing a current through the wire pulls the strut snugly against the top plate, thereby increasing the strut stiffness. The purpose is to test the capability of modifying the control laws to damp out vibrations in the presence of on-orbit structural changes. An additional goal of the experiment is to evaluate the effect of radiation, thermal cycling and atomic oxygen erosion on the experiment performance over a three year lifetime.

Figure 9 appears on the following page.

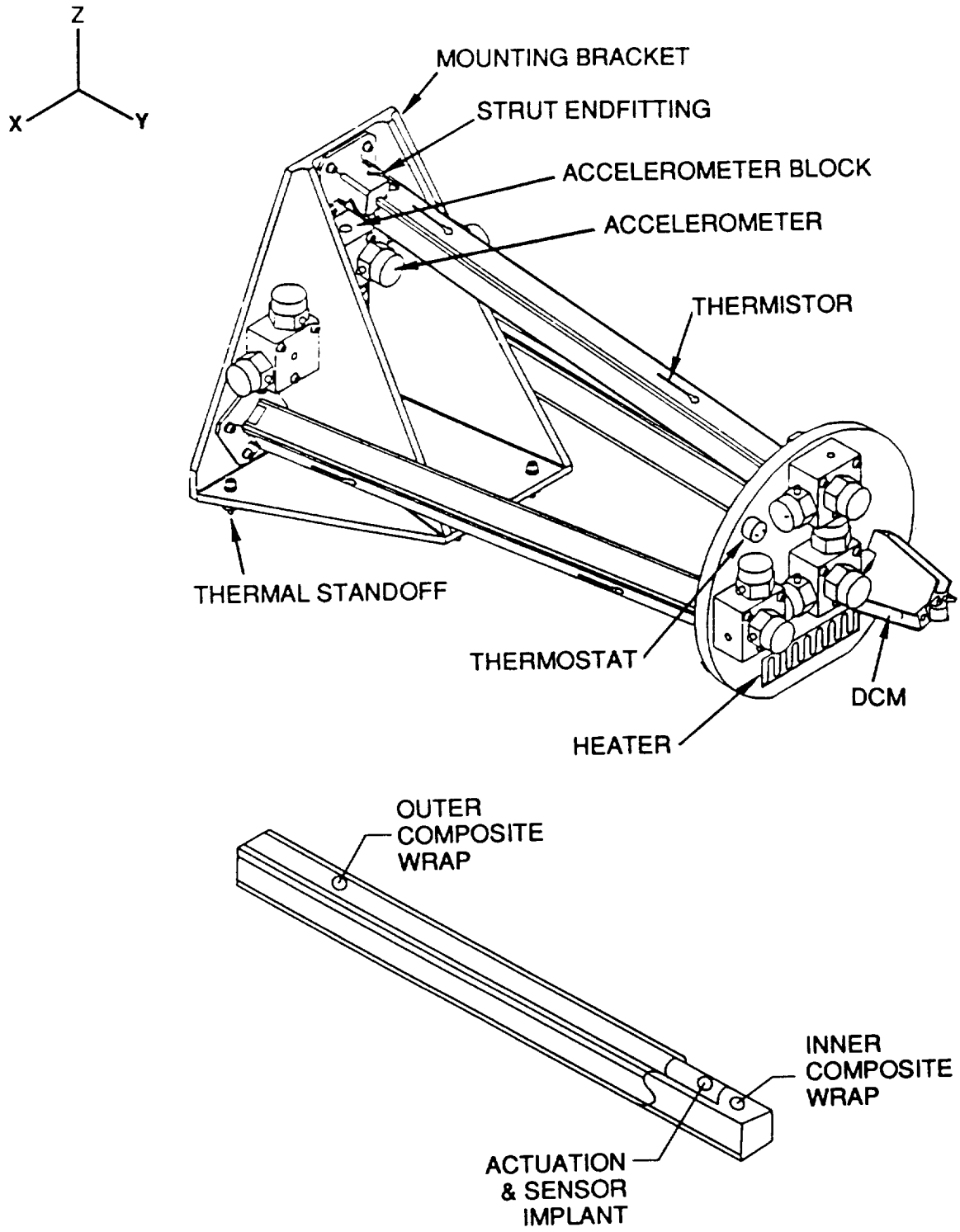

FIGURE 9: Design of the ACTEX experiment.

REFERENCES

1. Juang, J.N. and Pappa, R.S.,"An Eigensystem Realization Algorithm (ERA) for Modal Parameter Identification and Model Reduction," *Journal of Guidance, Control and Dynamics*, Vol 8, No. 5, 1985, pp. 620-627.

2. Johnson, G. D., "Modal Tests of the Voyager Magnetometer Boom," Marshall Space Flight Center, Huntsville, Ala., Reference Letter ET 53 (83-98), 2H Waites, Oct. 24, 1983.

3. Soucym Y, and Vigneron, F. "Modelling and Identification of the Structural Properties of an Astromast," Communications Research Center, CRC Report No. 1374, Ottawa, Can., November, 1983.

4. Lockheed Missiles and Space Co.,"Solar Array Flight Experiment Final Report," Marshall Space Flight Center, Huntsville, Ala., Contract NASA-31352, Report No. LMSC-F087173, April 1986.

5. Young, L.E. and Pack, H.C. Jr. "Solar Array Flight Experiment/Dynamic Augmentation Experiment," NASA Technical Paper 2690, Marshall Space Flight Center, Huntsville, Ala., 1987.

REPORT DOCUMENTATION PAGE

Form Approved
OMB No. 0704-0188

1. AGENCY USE ONLY *(Leave blank)*	2. REPORT DATE	3. REPORT TYPE AND DATES COVERED
	February 1993	Conference Publication

4. TITLE AND SUBTITLE
Fifth NASA/DoD Controls-Structures Interaction Technology Conference

5. FUNDING NUMBERS
590-14-41-01

6. AUTHOR(S)
Jerry R. Newsom, Compiler

7. PERFORMING ORGANIZATION NAME(S) AND ADDRESS(ES)
NASA Langley Research Center
Hampton, VA 23681-0001

8. PERFORMING ORGANIZATION REPORT NUMBER
L-17174

9. SPONSORING/MONITORING AGENCY NAME(S) AND ADDRESS(ES)
National Aeronautics and Space Administration
Washington, DC 20546-0001
Department of Defense
Washington, DC 20301

10. SPONSORING/MONITORING AGENCY REPORT NUMBER
NASA CP-3177, Part 2

11. SUPPLEMENTARY NOTES

12a. DISTRIBUTION/AVAILABILITY STATEMENT
Unclassified-Unlimited

Subject Category 18

12b. DISTRIBUTION CODE

13. ABSTRACT *(Maximum 200 words)*

This publication is a compilation of the papers presented at the Fifth NASA/DoD Controls-Structures Interaction (CSI) Technology Conference held in Lake Tahoe, Nevada, March 3–5, 1992. The conference, which was jointly sponsored by the NASA Office of Aeronautics and Space Technology and the Department of Defense, was organized by the NASA Langley Research Center. The purpose of this conference was to report to industry, academia, and government agencies on the current status of controls-structures interaction technology. The agenda covered ground testing, integrated design, analysis, flight experiments and concepts.

14. SUBJECT TERMS
Controls-structures interaction; Large space systems; Flexible structures

15. NUMBER OF PAGES
365

16. PRICE CODE
A16

17. SECURITY CLASSIFICATION OF REPORT	18. SECURITY CLASSIFICATION OF THIS PAGE	19. SECURITY CLASSIFICATION OF ABSTRACT	20. LIMITATION OF ABSTRACT
Unclassified	Unclassified		

NSN 7540-01-280-5500

Standard Form 298(Rev. 2-89)
Prescribed by ANSI Std. Z39-18
298 102

NASA-Langley, 1993

National Aeronautics and
Space Administration
Code JTT
Washington, D.C.
20546-0001

Official Business

Penalty for Private Use, $300

SPECIAL FOURTH-CLASS RATE
POSTAGE & FEES PAID
NASA
PERMIT No. G27

NASA

POSTMASTER: If Undeliverable (Section 158 Postal Manual) Do Not Return